

AJNR

AMERICAN JOURNAL OF NEURORADIOLOGY

JANUARY 2014
VOLUME 35
NUMBER 1
WWW.AJNR.ORG

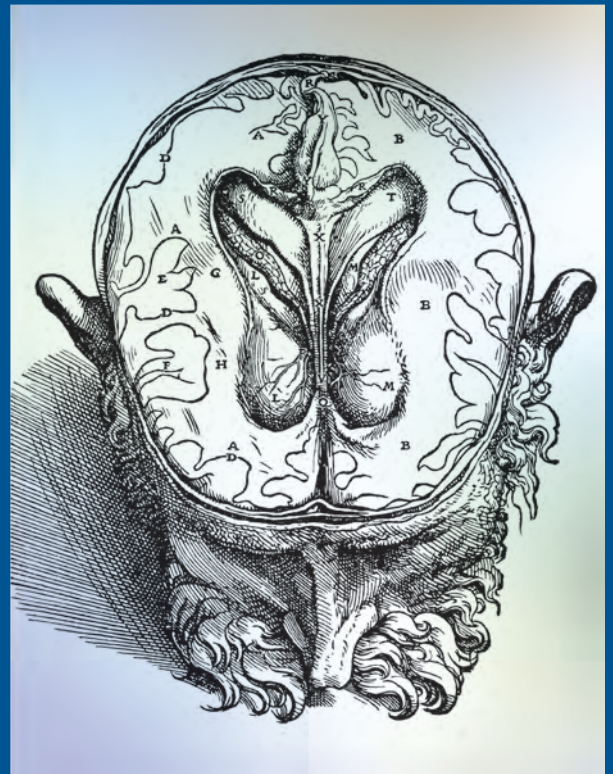
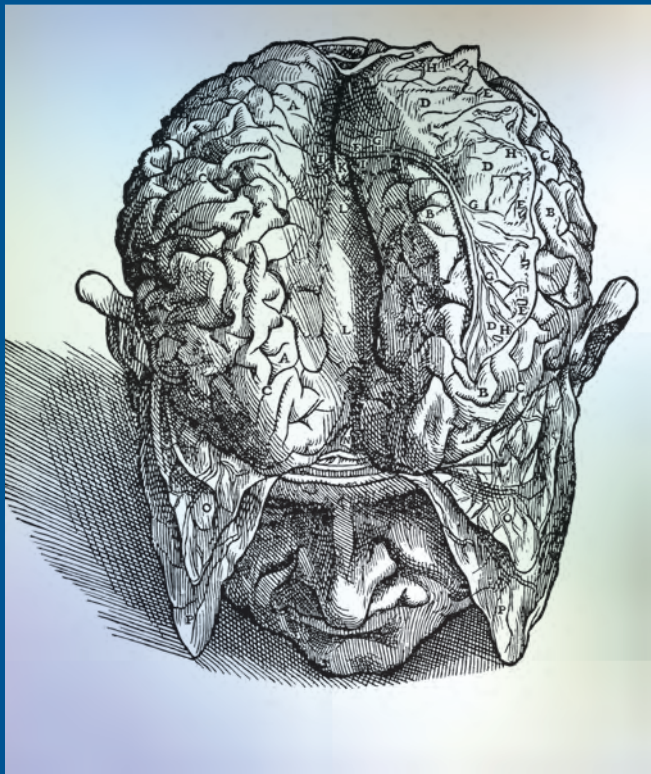
THE JOURNAL OF DIAGNOSTIC AND
INTERVENTIONAL NEURORADIOLOGY

Aneurysm screening in polycystic kidney
disease

Long-term white matter changes after severe
traumatic brain injury

Brain structural changes in patients with
drug-naïve schizophrenia

Official Journal ASNR • ASFNR • ASHNR • ASPNR • ASSR





MicroVention®
TERUMO

Dedicated to the development

The MicroVention family of neuroendovascular products:

HYDROGEL COIL PRODUCTS

HydroFrame®
HydroCoil® Embolic System

HydroSoft®
HydroCoil® Embolic System

HydroFill®
HydroCoil® Embolic System

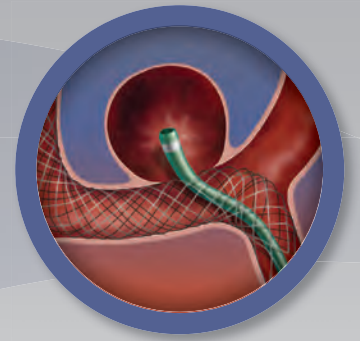


INTRALUMINAL PRODUCTS*

FRED™
Flow Re-Direction Endoluminal Device

LVIS™
Intraluminal Support Device

LVIS™ Jr.
Intraluminal Support Device



***CAUTION:**

The FRED™ system is an investigational device limited by U.S. law to investigational use.

The LVIS™/LVIS™ Jr. device is an investigational device limited by U.S. law to investigational use.

microvention.com

MICROVENTION, Headway, Headway Duo, Chaperon, Traxcess, HydroFrame, HydroFill, HydroSoft, VFC, HydroCoil, MicroPlex, Cosmos, HyperSoft, Compass, Scepter C, Scepter XC, V-Trak and V-Grip are registered trademarks of MicroVention, Inc. FRED, LVIS and LVIS Jr. are trademarks of MicroVention, Inc. Scientific and clinical data related to this document are on file at MicroVention, Inc. Refer to Instructions for Use for additional information. © 2013 MicroVention, Inc. 12/13



of innovative endovascular technologies



ACCESS PRODUCTS

Traxcess.

Guidewire

Chaperon.

Guiding Catheter

Headway.

Microcatheter

**Headway
Duo!**

microcatheter

Scepter

Occlusion Balloon
Catheter



PLATINUM COIL PRODUCTS

MICROPLEX.

coil system

COSMOS.

complex coil

COMPASS.

complex coil

VFC.

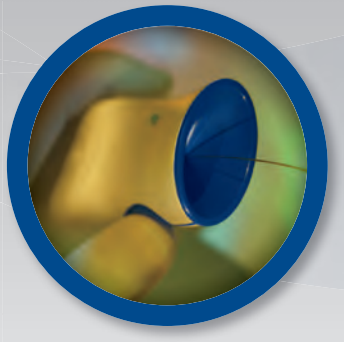
Versatile Range Fill Coil

HYPERSOFT.

finishing coil

HyperSoft 3D

complex coil



DELIVERY SYSTEM

V-Trak

**V-Trak
Soft**

V-Grip

MicroVention, Inc.

Worldwide Headquarters

1311 Valencia Avenue

Tustin, CA 92780 USA

MicroVention UK Limited

MicroVention Europe, S.A.R.L.

MicroVention Deutschland GmbH

PH +1.714.247.8000

PH +44 (0) 191 258 6777

PH +33 (1) 39 21 77 46

PH +49 211 210 798-0

ASNR 52ND ANNUAL MEETING & THE FOUNDATION OF THE ASNR SYMPOSIUM 2014

MAY 17-22 | Montreal ■ Palais des congrés de Montreal

ASNR 2014 PROGRAM CHAIR/PRESIDENT-ELECT - Gordon K. Sze, MD, FACR

THE FOUNDATION OF THE ASNR



The Foundation of the ASNR Symposium 2014: Inflammatory and Infectious Diseases of the CNS

SYMPOSIUM 2014:

- The Role of Inflammation and Infections in Stroke, Seizures, White Matter Diseases, etc.
- Advanced Imaging Techniques in the Evaluation of Inflammatory CNS Diseases
- Infectious Agents for Human Good: Oncolytic Viruses, Viral Vector Gene Therapy and Advanced Imaging

ADDITIONAL NEW EDUCATIONAL COURSE PROGRAM IN 2014 (concurrent program with the Symposium 2014): Inflammatory and Infectious Diseases

EDUCATIONAL COURSE 2014: with world class speakers including

- Anne G. Osborn, MD, Thomas P. Naidich, MD, Donald Resnick, MD, James G. Smirniotopoulos, MD, Jeffrey S. Ross, MD, Kelly K. Koeller, MD, FACR, David M. Yousem, MD, MBA, Laurie A. Loevner, MD, Peter M. Som, MD, Patricia A. Hudgins, MD, Robert D. Zimmerman MD, FACR, Hugh D. Curtin, MD, M. Judith Donovan Post, MD, FACR, and More...

ANNUAL MEETING:

- One-day **MINI SYMPOSIUM on STROKE** - Organized by Pina C. Sanelli, MD, MPH and Max Wintermark, MD
- One-day **MINI SYMPOSIUM on TUMORS** - Organized by Girish M. Fatterpekar, MD, MBBS, DNB, Whitney B. Pope, MD, PhD and Gordon K. Sze, MD, FACR
- Nobel Prize Laureate, Stanley Prusiner, MD, Keynote Speaker, on Prions and Alzheimer's Disease, Parkinson's Disease, and Other Neurodegenerative Disorders
- More "Hands-On" Experience Applicable to Your Practices
- Young Professionals Programming
- Expanded Self-Assessment Module (SAM) Session Programming Throughout the Week

PROGRAMMING DEVELOPED IN COOPERATION WITH THE...

- American Society of Functional Neuroradiology (ASFNR) David J. Mikulis, MD
- American Society of Head and Neck Radiology (ASHNR) Yoshimi Anzai, MD, MPH
- American Society of Pediatric Neuroradiology (ASPNR) Richard L. Robertson, MD
- American Society of Spine Radiology (ASSR) Meng Law, MD, MBBS, FRACR
- Society of NeuroInterventional Surgery (SNIS) Peter A. Rasmussen, MD



ASFNR ASHNR ASPNR ASSR SNIS

TO REQUEST PROGRAMMING AND REGISTRATION MATERIALS FOR THE ASNR 52ND ANNUAL MEETING, CONTACT:

ASNR 52ND ANNUAL MEETING

c/o American Society of Neuroradiology
800 Enterprise Drive, Suite 205
Oak Brook, Illinois 60523-4216

Phone: 630-574-0220
Fax: 630-574-0661
Email: meetings@asnr.org
Website: www.asnr.org/2014



Scan Now
to visit our website

AJNR

AMERICAN JOURNAL OF NEURORADIOLOGY

JANUARY 2014
VOLUME 35
NUMBER 1
WWW.AJNR.ORG

Publication Preview at www.ajnr.org features articles released in advance of print. Visit www.ajnrblog.org to comment on AJNR content and chat with colleagues and AJNR's News Digest at <http://ajnrdigest.org> to read the stories behind the latest research in neuroimaging.

EDITORIAL

PERSPECTIVES

- 1 **From Hard Drives to Flash Drives to DNA Drives** *M. Castillo*

REVIEW ARTICLES

- 3 **Should Patients with Autosomal Dominant Polycystic Kidney Disease Be Screened for Cerebral Aneurysms?** *M.N. Rozenfeld, S.A. Ansari, A. Shaibani, E.J. Russell, P. Mohan, and M.C. Hurley*
- 10 **Illustrated Review of the Embryology and Development of the Facial Region, Part 2: Late Development of the Fetal Face and Changes in the Face from the Newborn to Adulthood** *P.M. Som and T.P. Naidich*

HISTORICAL PERSPECTIVES

- 19 **Andreas Vesalius and Thomas Willis: Their Anatomic Brain Illustrations and Illustrators** *J.H. Scatliff and S. Johnston*

BRAIN

- 23 **Long-Term White Matter Changes after Severe Traumatic Brain Injury: A 5-Year Prospective Cohort** *J. Dinkel, A. Drier, O. Khalilzadeh, V. Perlberg, V. Czernecki, R. Gupta, F. Gomas, P. Sanchez, D. Dormont, D. Galanaud, R.D. Stevens, and L. Puybasset for NICER (Neuro Imaging for Coma Emergence and Recovery) Consortium*
- 30 **Patterns of Brain Structural Changes in First-Contact, Antipsychotic Drug-Naïve Patients with Schizophrenia** *M. Filippi, E. Canu, R. Gasparotti, F. Agosta, P. Valsecchi, G. Lodoli, A. Galluzzo, G. Comi, and E. Sacchetti*
- 38 **Comparison of Multiecho Postprocessing Schemes for SWI with Use of Linear and Nonlinear Mask Functions** *M.P. Quinn, J.S. Gati, L.M. Klassen, A.W. Lin, J.R. Bird, S.E. Leung, and R.S. Menon*
- 45 **Intracranial Imaging of Uncommon Diseases Is More Frequently Reported in Clinical Publications Than in Radiology Publications** *V.T. Lehman, D.A. Doolittle, C.H. Hunt, L.J. Eckel, D.F. Black, K.M. Schwartz, and F.E. Diehn*
- 49 **Does the Location of the Arterial Input Function Affect Quantitative CTP in Patients with Vasospasm?** *B.J. Shin, N. Anumula, S. Hurtado-Rúa, P. Masi, R. Campbell, R. Spandorfer, A. Ferrone, T. Caruso, J. Haseltine, C. Robinson, A. Gupta, and P.C. Sanelli*
- 55 **Morphologic, Distributional, Volumetric, and Intensity Characterization of Periventricular Hyperintensities** *M.C. Valdés Hernández, R.J. Piper, M.E. Bastin, N.A. Royle, S. Muñoz Maniega, B.S. Aribisala, C. Murray, I.J. Deary, and J.M. Wardlaw*
- 63 **Incidental Periventricular White Matter Hyperintensities Revisited: What Detailed Morphologic Image Analyses Can Tell Us** *F. Fazekas*

★ Indicates Editor's Choices selection

🔑 Indicates Fellows' Journal Club selection

🔑 Indicates open access to non-subscribers at www.ajnr.org

☰ Indicates article with supplemental on-line table

📷 Indicates article with supplemental on-line photo

📺 Indicates article with supplemental on-line video

EBM 1 Indicates Evidence-Based Medicine Level 1

EBM 2 Indicates Evidence-Based Medicine Level 2



Andreas Vesalius' original illustrations of the brain surface and transverse section.

-  **65 Accuracy of Vessel-Encoded Pseudocontinuous Arterial Spin-Labeling in Identification of Feeding Arteries in Patients with Intracranial Arteriovenous Malformations** *S.L. Yu, R. Wang, R. Wang, S. Wang, Y.Q. Yao, D. Zhang, Y.L. Zhao, Z.T. Zuo, R. Xue, DJJ. Wang, and J.Z. Zhao*
-  **72 Decreased T1 Contrast between Gray Matter and Normal-Appearing White Matter in CADASIL** *F. De Guio, S. Reyes, M. Duering, L. Pirpamer, H. Chabriat, and E. Jouvent*
-  **77 3T MRI Quantification of Hippocampal Volume and Signal in Mesial Temporal Lobe Epilepsy Improves Detection of Hippocampal Sclerosis** *A.C. Coan, B. Kubota, F.P.G. Bergo, B.M. Campos, and F. Cendes*
-  **84 MRI Findings in Autoimmune Voltage-Gated Potassium Channel Complex Encephalitis with Seizures: One Potential Etiology for Mesial Temporal Sclerosis** *A.L. Kotsenas, R.E. Watson, S.J. Pittock, J.W. Britton, S.L. Hoyer, A.M.L. Quek, C. Shin, and C.J. Klein*
-   **90 Intracranial Arteries in Individuals with the Elastin Gene Hemideletion of Williams Syndrome** *D.P. Wint, J.A. Butman, J.C. Masdeu, A. Meyer-Lindenberg, C.B. Mervis, D. Sarpal, C.A. Morris, and K.F. Berman*
-  **95 Evaluation of Diffusivity in the Anterior Lobe of the Pituitary Gland: 3D Turbo Field Echo with Diffusion-Sensitized Driven-Equilibrium Preparation** *A. Hiwatashi, T. Yoshiura, O. Togao, K. Yamashita, K. Kikuchi, K. Kobayashi, M. Ohga, S. Sonoda, H. Honda, and M. Obara*
- COMMENTARY
- 99 Diffusion-Weighted Imaging of the Pituitary Gland** *M.E. Mullins*
-  **100 Brain MR Findings in Patients with Systemic Lupus Erythematosus with and without Antiphospholipid Antibody Syndrome** *Y. Kaichi, S. Kakeda, J. Moriya, N. Ohnari, K. Saito, Y. Tanaka, F. Tatsugami, S. Date, K. Awai, and Y. Korogi*
-   **106 Prevalence of Radiologically Isolated Syndrome and White Matter Signal Abnormalities in Healthy Relatives of Patients with Multiple Sclerosis** *T. Gabelic, D.P. Ramasamy, B. Weinstock-Guttman, J. Hagemeyer, C. Kennedy, R. Melia, D. Hojnacki, M. Ramanathan, and R. Zivadinov*
-  **113 Right Insular Atrophy in Neurocardiogenic Syncope: A Volumetric MRI Study** *J.B. Kim, S.-i. Suh, W.-K. Seo, S.-B. Koh, and J.H. Kim*
-  **119 Cerebral Abnormalities in Adults with Ataxia-Telangiectasia** *D.D.M. Lin, P.B. Barker, H.M. Lederman, and T.O. Crawford*
- INTERVENTIONAL** *Published in collaboration with Interventional Neuroradiology*
- 124 Differences in the Angiographic Evaluation of Coiled Cerebral Aneurysms between a Core Laboratory Reader and Operators: Results of the Cerecyte Coil Trial** *I. Rezek, R.K. Lingineni, M. Sneade, A.J. Molyneux, A.J. Fox, and D.F. Kallmes*
-   **128 Last-Recorded P2Y12 Reaction Units Value Is Strongly Associated with Thromboembolic and Hemorrhagic Complications Occurring Up to 6 Months after Treatment in Patients with Cerebral Aneurysms Treated with the Pipeline Embolization Device** *J.E. Delgado Almandoz, B.M. Crandall, J.M. Scholz, J.L. Fease, R.E. Anderson, Y. Kadkhodayan, and D.E. Tubman*
-   **136 Computational Hemodynamics Analysis of Intracranial Aneurysms Treated with Flow Diverters: Correlation with Clinical Outcomes** *W. Chong, Y. Zhang, Y. Qian, L. Lai, G. Parker, and K. Mitchell*
-    **143 Cerebral Aneurysms Treated with Flow-Diverting Stents: Computational Models with Intravascular Blood Flow Measurements** *M.R. Levitt, P.M. McGah, A. Aliseda, P.D. Mourad, J.D. Nerva, S.S. Vaidya, R.P. Morton, B.V. Ghodke, and L.J. Kim*

- 149 **Potential for the Use of the Solitaire Stent for Recanalization of Middle Cerebral Artery Occlusion without a Susceptibility Vessel Sign** *Y.J. Bae, C. Jung, J.H. Kim, B.S. Choi, E. Kim, M.-K. Han, H.-J. Bae, and M.H. Han*
-   156 **Quantification of Internal Carotid Artery Flow with Digital Subtraction Angiography: Validation of an Optical Flow Approach with Doppler Ultrasound** *V. Mendes Pereira, R. Ouared, O. Brina, O. Bonnefous, J. Satwiaski, H. Aerts, D. Ruijters, F. van Nijnatten, F. Perren, P. Bijlenga, K. Schaller, and K.-O. Lovblad*
-  164 **Comparative Effectiveness of Ruptured Cerebral Aneurysm Therapies: Propensity Score Analysis of Clipping versus Coiling** *J.S. McDonald, R.J. McDonald, J. Fan, D.F. Kallmes, G. Lanzino, and H.J. Cloft*

HEAD & NECK

-  170 **Diffusion-Weighted Imaging of Orbital Masses: Multi-Institutional Data Support a 2-ADC Threshold Model to Categorize Lesions as Benign, Malignant, or Indeterminate** *A.R. Sepahdari, L.S. Politi, V.K. Aakalu, H.J. Kim, and A.A.K. Abdel Razek*
- 176 **4D-CT for Preoperative Localization of Abnormal Parathyroid Glands in Patients with Hyperparathyroidism: Accuracy and Ability to Stratify Patients by Unilateral versus Bilateral Disease in Surgery-Naïve and Re-Exploration Patients** *H.R. Kelly, L.M. Hamberg, and G.J. Hunter*
- 182 **Imaging Findings in Auto-Atticotomy** *M. Manasawala, M.E. Cunnane, H.D. Curtin, and G. Moonis*
- 186 **Tympanic Plate Fractures in Temporal Bone Trauma: Prevalence and Associated Injuries** *C.P. Wood, C.H. Hunt, D.C. Bergen, M.L. Carlson, F.E. Diehn, K.M. Schwartz, G.A. McKenzie, R.F. Morreale, and J.I. Lane*

SPINE

-  191 **Optimal Contrast Concentration for CT-Guided Epidural Steroid Injections** *P.G. Kranz, M. Abbott, D. Abbott, and J.K. Hoang*
-  196 **Intramedullary Spinal Cord Metastases: Visibility on PET and Correlation with MRI Features** *P.M. Mostardi, F.E. Diehn, J.B. Rykken, L.J. Eckel, K.M. Schwartz, T.J. Kaufmann, C.P. Wood, J.T. Wald, and C.H. Hunt*
-  202 **Analysis of Related Factors on the Deformity Correction of Balloon Kyphoplasty** *C. Xu, H.-X. Liu, and H.-Z. Xu*
-  207 **Vertebral Augmentation in Patients with Multiple Myeloma: A Pooled Analysis of Published Case Series** *O.A. Khan, W. Brinjikji, and D.F. Kallmes*

ONLINE FEATURES (www.ajnr.org)

LETTERS

- E1 **Est Modus in Rebus** *G. Guglielmi and F. Viñuela*
- E2 **Reply** *H.J. Cloft*

BOOK REVIEWS *R.M. Quencer, Section Editor*

Please visit www.ajnrblog.org to read and comment on Book Reviews.

Official Journal:

American Society of Neuroradiology
American Society of Functional Neuroradiology
American Society of Head and Neck Radiology
American Society of Pediatric Neuroradiology
American Society of Spine Radiology

EDITOR-IN-CHIEF

Mauricio Castillo, MD

Professor of Radiology and Chief, Division of Neuroradiology, University of North Carolina, School of Medicine, Chapel Hill, North Carolina

SENIOR EDITORS

Harry J. Cloft, MD, PhD

Professor of Radiology and Neurosurgery, Department of Radiology, Mayo Clinic College of Medicine, Rochester, Minnesota

Nancy J. Fischbein, MD

Professor of Radiology, Otolaryngology-Head and Neck Surgery, Neurology, and Neurosurgery and Chief, Head and Neck Radiology, Department of Radiology, Stanford University Medical Center, Stanford, California

Lucien M. Levy, MD, PhD

Professor of Radiology, Chief and Program Director of Neuroradiology, George Washington University Medical Center, Washington, DC

Jeffrey S. Ross, MD

Staff Neuroradiologist, Barrow Neurological Institute, St. Joseph's Hospital, Phoenix, Arizona

Pamela W. Schaefer, MD

Clinical Director of MRI and Associate Director of Neuroradiology, Massachusetts General Hospital, Boston, Massachusetts, and Associate Professor, Radiology, Harvard Medical School, Cambridge, Massachusetts

Charles M. Strother, MD

Professor of Radiology, Emeritus, University of Wisconsin, Madison, Wisconsin

EDITORIAL BOARD

Ashley H. Aiken, *Atlanta, Georgia*
A. James Barkovich, *San Francisco, California*
Walter S. Bartynski, *Charleston, South Carolina*
Barton F. Branstetter IV, *Pittsburgh, Pennsylvania*
Jonathan L. Brisman, *Lake Success, New York*
Julie Bykowski, *San Diego, California*
Donald W. Chakeres, *Columbus, Ohio*
Alessandro Cianfoni, *Lugano, Switzerland*
Colin Derdeyn, *St. Louis, Missouri*
Rahul S. Desikan, *San Diego, California*
Richard du Mesnil de Rochemont, *Frankfurt, Germany*
Clifford J. Eskey, *Hanover, New Hampshire*
Massimo Filippi, *Milan, Italy*
David Fiorella, *Cleveland, Ohio*
Allan J. Fox, *Toronto, Ontario, Canada*
Christine M. Glastonbury, *San Francisco, California*

John L. Go, *Los Angeles, California*
Wan-Yuo Guo, *Taipei, Taiwan*
Rakesh K. Gupta, *Lucknow, India*
Lotfi Hacein-Bey, *Sacramento, California*
David B. Hackney, *Boston, Massachusetts*
Christopher P. Hess, *San Francisco, California*
Andrei Holodny, *New York, New York*
Benjamin Huang, *Chapel Hill, North Carolina*
Thierry A.G.M. Huisman, *Baltimore, Maryland*
George J. Hunter, *Boston, Massachusetts*
Mahesh V. Jayaraman, *Providence, Rhode Island*
Valerie Jewells, *Chapel Hill, North Carolina*
Timothy J. Kaufmann, *Rochester, Minnesota*
Kenneth F. Layton, *Dallas, Texas*
Ting-Yim Lee, *London, Ontario, Canada*
Michael M. Lell, *Erlangen, Germany*
Michael Lev, *Boston, Massachusetts*
Karl-Olof Lovblad, *Geneva, Switzerland*
Lisa H. Lowe, *Kansas City, Missouri*
Franklin A. Marden, *Chicago, Illinois*
M. Gisele Matheus, *Charleston, South Carolina*
Joseph C. McGowan, *Merion Station, Pennsylvania*
Kevin R. Moore, *Salt Lake City, Utah*
Christopher J. Moran, *St. Louis, Missouri*
Takahisa Mori, *Kamakura City, Japan*

Suresh Mukherji, *Ann Arbor, Michigan*
Amanda Murphy, *Toronto, Ontario, Canada*
Alexander J. Nemeth, *Chicago, Illinois*
Laurent Pierot, *Reims, France*
Jay J. Pillai, *Baltimore, Maryland*
Whitney B. Pope, *Los Angeles, California*
M. Judith Donovan Post, *Miami, Florida*
Tina Young Poussaint, *Boston, Massachusetts*
Joana Ramalho, *Lisbon, Portugal*
Otto Rapalino, *Boston, Massachusetts*
Álex Rovira-Cañellas, *Barcelona, Spain*
Paul M. Ruggieri, *Cleveland, Ohio*
Zoran Rumboldt, *Charleston, South Carolina*
Amit M. Saindane, *Atlanta, Georgia*
Erin Simon Schwartz, *Philadelphia, Pennsylvania*
Aseem Sharma, *St. Louis, Missouri*
J. Keith Smith, *Chapel Hill, North Carolina*
Maria Vittoria Spampinato, *Charleston, South Carolina*
Gordon K. Sze, *New Haven, Connecticut*
Krishnamoorthy Thamburaj, *Hershey, Pennsylvania*
Kent R. Thielen, *Rochester, Minnesota*
Cheng Hong Toh, *Taipei, Taiwan*
Thomas A. Tomsick, *Cincinnati, Ohio*
Aquila S. Turk, *Charleston, South Carolina*
Willem Jan van Rooij, *Tilburg, Netherlands*
Arastoo Vossough, *Philadelphia, Pennsylvania*
Elysa Widjaja, *Toronto, Ontario, Canada*
Max Wintermark, *Charlottesville, Virginia*
Ronald L. Wolf, *Philadelphia, Pennsylvania*
Kei Yamada, *Kyoto, Japan*

EDITORIAL FELLOW

Falgun H. Chokshi, *Atlanta, Georgia*

YOUNG PROFESSIONALS ADVISORY COMMITTEE

Asim K. Bag, *Birmingham, Alabama*
Anna E. Nidecker, *Sacramento, California*
Peter Yi Shen, *Sacramento, California*

HEALTH CARE AND SOCIOECONOMICS EDITOR

Pina C. Sanelli, *New York, New York*

Founding Editor

Juan M. Taveras

Editors Emeriti

Robert I. Grossman, Michael S. Huckman,
Robert M. Quencer

Special Consultants to the Editor

Sandy Cheng-Yu Chen, Girish Fatterpekar,
Ryan Fitzgerald, Yvonne Lui,
Louise M. Henderson, Greg Zaharchuk

INR Liaisons

Timo Krings, Karel terBrugge

Managing Editor

Karen Halm

Electronic Publications Manager

Jason Gantenberg

Editorial Assistant

Mary Harder

Executive Director, ASNR

James B. Gantenberg

Director of Communications, ASNR

Angelo Artemakis

AJNR (Am J Neuroradiol ISSN 0195-6108) is a journal published monthly, owned and published by the American Society of Neuroradiology (ASNR), 800 Enterprise Drive, Suite 205, Oak Brook, IL 60523. Annual dues for the ASNR include \$170.00 for journal subscription. The journal is printed by Cadmus Journal Services, 5457 Twin Knolls Road, Suite 200, Columbia, MD 21045; Periodicals postage paid at Oak Brook, IL and additional mailing offices. Printed in the U.S.A. POSTMASTER: Please send address changes to American Journal of Neuroradiology, P.O. Box 3000, Denville, NJ 07834, U.S.A. Subscription rates: nonmember \$370 (\$440 foreign) print and online, \$300 online only; institutions \$430 (\$495 foreign) print and basic online, \$850 (\$915 foreign) print and extended online, \$355 online only (basic), extended online \$770; single copies are \$35 each (\$40 foreign). Indexed by PubMed/Medline, BIOSIS Previews, Current Contents (Clinical Medicine and Life Sciences), EMBASE, Google Scholar, HighWire Press, Q-Sensei, RefSeek, Science Citation Index, and SCI Expanded. Copyright © American Society of Neuroradiology.



From Hard Drives to Flash Drives to DNA Drives

M. Castillo, *Editor-in-Chief*

The word is now a virus.

William S. Burroughs, *The Ticket that Exploded*

Recently there has been another round of controversial news regarding genetically modified organisms (GMO). Perhaps the best known debate on these centers on corn. A recent French study showed severe kidney and liver abnormalities in rats that were fed this corn for up to 2 years.¹ Immediately afterward, Russia banned the use of this seed and the corn it produces. Because other studies have not confirmed this finding, the American media immediately released news stories stating that the French study was flawed and unscientific and that it represented just another round of propaganda by individuals who oppose GMO and the companies that produce the seeds (which are mostly American).² Salmon, with growth hormones that have been altered so that they not only grow faster but never stop growing, has also been in the news. Salmon is the third most-eaten seafood in the United States according to the National Fisheries Institute, and most of it is flown in from Chile, so growing enough of it here to feed Americans may actually be a good thing for the environment, even if its genes have been modified.³ All of these situations involve inserting or altering a specific gene in plant or animal deoxyribonucleic acid (DNA); thus, the genetic material in those organisms still serves its original purpose. However, what happens if we take our DNA, reconfigure it, and use it for something completely different from that for which it is intended? Cutting-edge genetic engineers are now synthesizing DNA so that it contains information much like a computer hard drive or solid memory chips. The capacity of DNA as a storage medium is staggering: All of the information contained on the entire Internet would fit into a device smaller than 1 cubic inch!

As our need for high-capacity information storage continues to increase, several researchers have begun to explore the possibility of using DNA for this purpose.⁴ The very fabric of life uses a binary code, but instead of the 1s and 0s computers use, the code in our DNA is composed of 4 letters: A, G, C, and T (adenine, guanine, cytosine, and thymine), which are paired into 2 nucleotide bases: A-T and G-C (hence a form of binary code). By changing the order of these 2 base nucleotide pairs, one can encode all different types of information in the same way a computer does by changing the order of 1s and 0s. Each nucleotide may encode 2 bits of information, and 1 g of single-stranded DNA can store 455 exabytes. One exabyte is equal to 1000 petabytes; 1 petabyte is equal to 1 quadrillion bytes, and so on. What this means is that in 1 g of single-stranded DNA, one can potentially store the equivalent

to 250 million DVDs! Computer chips are “planar” storage devices (obvious from their shape). One way to improve the capacity of a computer chip is to put several layers of circuits in it (making it 2D), but because DNA is 3D, it offers much more space. Memory cards are said to be reliable for up to 5 years after their initial use, but DNA-encoded information remains stable and readable for millennia.⁵ For purposes of timeless storage, DNA may be dried and then protected from water and oxygen, which gives it a nearly infinite stability.

DNA information storage is not new. It has been around since 1988, and one of the first successful projects came from the J. Craig Venter Institute, a nonprofit genomics research organization with facilities in 3 different US states. These investigators were able to encode 7920 bits into DNA.⁶ (Pridefully, in a synthetic cell, they encoded their names, 3 literary citations, and the address of an Internet site [Table].) Newer DNA-synthesizing techniques can alter the way base nucleotide pairs are formed, making it easier to encode information and thereafter read it. As mentioned previously, traditionally base pairs are A-T and G-C (remember that nucleotides are measured in pairs because DNA is usually double-stranded). Thus, the number of base pairs is equal to the number of nucleotides in 1 DNA strand. The problem with using the natural sequence of nucleotide base pairs for information encoding is that the G-C pair can be difficult to subsequently read. Therefore, new techniques use novel base pairs: A-C and G-T, which are easy to manufacture and thereafter interpret. With these 2 new base pairs, one also has a binary code: A-C for 0 and G-T for 1. At present, assembling long stable strands of DNA is difficult, so information needs to be parceled in smaller data blocks of DNA called “oligonucleotides” (by comparison, the human genome contains about 3 billion base pairs, so it is a very long strand and the amount of information that it contains is astonishing).

In a recent experiment, Church et al⁷ took one of their own books (nearly 54,000-words-long, including 11 images) and used a computer to convert it into a bit stream (they initially thought about encoding *Moby Dick*). They encoded all of the bits of the book into 159 oligonucleotides, each also containing information as to its general position within the text. The encoded DNA was then amplified by polymerase chain reaction* (PCR), and in this way, its base pairs could be assessed, read, and interpreted (similar techniques were used to map the human genome). During the entire process of writing, amplifying, and reading 5.27 megabits of information, only 10 bit errors occurred, a testament to how incredibly exact this technology is. Church et al were able to store in DNA 600 times more information than was previously possible. As amazing as this seems, one must add to it the fact that this technique used only in vitro procedures, avoiding the controversies of cloning and live genetic manipulations, and it was 100,000 times cheaper than other previous versions.

Synthetic DNA is exempt from the National Institutes of Health usage guidelines and is available to all with the means to

<http://dx.doi.org/10.3174/ajnr.A3482>

Works previously stored in DNA^a

Year of Experiment	Usage Description	Specific Contents
1988	Art	Microvenus image ^b
1998	Text	Text from the Bible, Genesis
2001	Text	Parts from a book by Dickens
2003	Text	Parts from "It's a Small World," the main song of a musical boat ride from Walt Disney ^c
2005	Text	"Tomten" a poem by Viktor Rydberg ^d
2010	Watermark	Watermark of a synthetic genome ^e

^a Adapted from Church et al.⁴

^b Image of the external female genitalia representing female Earth.

^c Encrypted into *Deinococcus Radiodurans*, a bacterium extremely resistant to inhospitable environments. Information resistant to the effects of a nuclear holocaust could be saved in similar cells.

^d A true example of "living poetry." For other similar projects, I suggest that you Google "Project Xenotext."

^e Watermarking a cell designed to contain information may help us keep track of it.

manufacture it. The cost of DNA synthesis drops 12-fold per year compared with that of newer electronic media (1.6-fold per year); thus, it is becoming widely available. For example, synthesizing a strand of DNA containing 100 million base pairs cost US \$10,000 in 2001 but only 10 cents today. Synthesizing and reading DNA for information-storage purposes will require 6–8 orders-of-magnitude improvement. Although this amount of improvement is significant, it will soon become a reality as handheld DNA sequencers become widely available and inexpensive. As the need to store untold amounts of information becomes more pressing, newer DNA-related technologies will be discovered and become less expensive.

In the supporting data from their article, Church et al⁷ also bring up some safety and ethical concerns with regard to their experiment. They state that the DNA fragments they used to encode their book are "unlikely" to replicate themselves or encode anything else that could be biologically active. They do not discard the possibility that if this DNA were left out in the wild, it could get incorporated into a living organism. This last observation seems unlikely because cells tend to expel DNA that is not theirs. However, what would happen if an organism incorporates this foreign DNA has not even been a matter of speculation. Could a cell produce proteins hitherto unknown? Will that cell die? It certainly will not help us improve our individual knowledge because our bodies lack mechanisms with which to read this DNA and move its information to our brains. Ninety-eight percent of our DNA is now considered to be "genetic junk" (that is, DNA with no apparent function), so perhaps the day will come when we can use this space to encode into each human cell our history and accumulated knowledge.

All of our knowledge placed into highly resistant and self-replicating cells sent out to space in miniships may be the best way to explore the possibility of other civilizations existing far away from ours. Security and defense agencies have also considered DNA storage as a means of encryption. This technique was inspired by the World War II microdot technique of Germany, in which an entire page of information was photographed and reduced to the size of the dot at end of this sentence. DNA microdots can be hidden in general genetic material with their locations known only to those who know the primers marking the beginning and end of their specific DNA segments, which can then be resolved and read with PCR.⁸ Therefore, information could cross

borders in cells and not be subject to Internet counterespionage, and if the person carrying the information is detained, the site harboring the information would be impossible to detect.

Some say that all science fiction eventually becomes reality, and certainly DNA information storage must have sounded like science fiction just a few years ago. In Frank Herbert's novel *Dune* (Clinton Book Company, 1965), spaceships are able to navigate only because their control systems know at all times the positions of all celestial bodies. This tremendous amount of information is not saved in a computer but rather in mutated humans (the Guild Navigators), each controlling a spaceship. The Navigators can do this because their DNA contains all of the information needed for space travel. If a human being has more than 10 trillion cells, it does not seem far-fetched that his or her DNA could contain all of the information in the universe.

Update

Since I wrote this Perspectives, investigators at the European Bioinformatics Institute have found a new and different way to encode information into DNA. Dr. King's "I Have a Dream" speech, a photo, a PDF of Watson and Crick's seminal article, and all of Shakespeare's sonnets were encoded using it. The new method allows for multiple copies of this special DNA to be accurately manufactured. The authors expect their product to last over 10,000 years if kept dry, cold, and dark. Because storing information in DNA is easier than reading it, they suggest that DNA may be the ideal method for keeping information that does not need to be frequently accessed and thus ideal for libraries and government records. Please see the article in *Nature* by Goldman et al.⁹

*In this situation, PCR is easy to use because the makeup of the DNA strand that needs to be amplified is known. Primers that start the reaction can be easily chosen, and specific zones may be amplified and then read.

REFERENCES

1. Séralini GE, Clair E, Mesnage R, et al. **Long term toxicity of Roundup herbicide and a Roundup-tolerant genetically modified maize.** *Food Chem Toxicol* 2012;50:4221–31
2. Zhu Y, He X, Luo Y, et al. **A 90-day feeding study of glyphosate-tolerant maize with the G2-aroA gene in Sprague-Dawley rats.** *Food Chem Toxicol* 2012;51:280–87
3. **No Drop at the Top of NFI's Top 10 Most Popular List.** <http://www.aboutseafood.com/press/press-releases/no-drop-top-nfi-s-top-10-most-popular-list>. Accessed December 7, 2012
4. Church GM, Gao Y, Kosuri S. **Next-generation digital information storage in DNA.** *Science* 2012;337:1628
5. Bonnet J, Colotte M, Coudy D, et al. **Chain and conformation stability of solid-state DNA: implications of room temperature storage.** *Nucleic Acids Res* 2010;38:531–46
6. Gibson DG, Glass JI, Lartigue C, et al. **Creation of bacterial cell controlled by a chemically synthesized genome.** *Science* 2010;329:52–56
7. Church GM, Gao Y, Kosuri S. **Next-generation digital information storage in DNA** (supplementary material). <http://www.sciencemag.org/content/suppl/2012/08/15/science.1226355.DC1/Church.SM.pdf>. Accessed December 7, 2012
8. Clelland CT, Risca V, Bancroft C. **Hidden messages in DNA microdots.** *Nature* 1999;399:533–34
9. Goldman N, Bertone P, Chen S, et al. **Towards practical, high-capacity, low-maintenance information storage in synthesized DNA.** <http://www.nature.com/nature/journal/vaop/ncurrent/full/nature11875.html>. Accessed February 5, 2012

Should Patients with Autosomal Dominant Polycystic Kidney Disease Be Screened for Cerebral Aneurysms?

M.N. Rozenfeld, S.A. Ansari, A. Shaibani, E.J. Russell, P. Mohan, and M.C. Hurley



ABSTRACT

SUMMARY: Autosomal dominant polycystic kidney disease is a genetic disorder affecting 1 in 1000 people worldwide and is associated with an increased risk of intracranial aneurysms. It remains unclear whether there is sufficient net benefit to screening this patient population for IA, considering recent developments in imaging and treatment and our evolving understanding of the natural history of unruptured aneurysms. There is currently no standardized screening protocol for IA in patients with ADPKD. Our review of the literature focused on the above issues and presents our appraisal of the estimated value of screening for IA in the setting of ADPKD.

ABBREVIATIONS: ADPKD = autosomal dominant polycystic kidney disease; GFR = glomerular filtration rate; IA = intracranial aneurysm; QALY = quality-adjusted life years; TOF = time-of-flight

Autosomal dominant polycystic kidney disease is a genetic disorder affecting 1 in 1000 people worldwide and is associated with an increased risk of intracranial aneurysms.¹ The average life expectancy of a patient with ADPKD ranges from 53 to 70 years, depending on the subtype.² It remains unclear whether there is sufficient net benefit in screening this patient population for IA, considering recent developments in imaging and treatment and evolving understanding of the natural history of unruptured aneurysms. There is currently no standardized screening protocol for IA in patients with ADPKD.

The criteria supporting an ideal screening program can be organized by the following: 1) disease: sufficient prevalence and morbidity in the target population; 2) diagnosis: technique efficacy and safety; and 3) therapy: treatment efficacy, safety, cost-effectiveness, and improved outcome with early treatment.^{3,4}

The following review of the literature focuses on these criteria and presents our appraisal of the estimated value of screening for IA in the setting of ADPKD.

DISEASE

Screening effectiveness is dependent on the natural history of the disease (Fig 1). Specific to IA, the preclinical phase between aneu-

rysm formation and symptom development/rupture can be variable and the clinical phase between symptom development and SAH/death can be short or nonexistent. The lead time (the time between aneurysm formation and the development of signs/symptoms) determines screening frequency and feasibility.

Prevalence

ADPKD has been associated with a widely variable reported prevalence of IA: 4%,^{5,6} 5%,⁷ 10%,⁸ 11.7%,⁹ 14%,¹⁰ 22.5%,⁵ and 41.2%.¹¹ Of the 18%–22% of patients with ADPKD who also have a family history of IA, reported prevalence rates are more tightly grouped (ie, 22%,⁷ 25.8%,⁹ and 27.3%^{5,10,12}). In comparison, the general population carries an estimated prevalence of 0.4%–6%, depending on the study.⁸ Most retrospective autopsy series and reviews put the general population prevalence between 2% and 3%.^{13–16}

In 1 large meta-analysis, ADPKD was found to be the single greatest risk factor for IA development—greater than atherosclerosis and family history of IA.⁸ In fact, 10% of patients with undiagnosed ADPKD will have IA rupture as their presenting symptom,¹³ and 6% of all patients with ADPKD will die due to subarachnoid hemorrhage.¹⁷ IA rupture is considered the most severe complication of ADPKD.¹⁸

The largest prospective screening study to date was recently published by Xu et al,¹⁹ with a sample size of 355 patients with ADPKD screened by 3T time-of-flight MRA. Of these, 12.4% were found to have an IA, with the percentage increasing to 21.6% in patients with a family history of IA or hemorrhagic stroke versus 11% prevalence in those without these risk factors. The prevalence was found to be as high as 23.3% in the 60- to 69-year-old

From the Department of Radiology (M.N.R., P.M.), St. Francis Hospital, Evanston, Illinois; and Department of Radiology (S.A.A., A.S., E.J.R., M.C.H.), Northwestern University Feinberg School of Medicine, Chicago, Illinois.

Please address correspondence to Michael N. Rozenfeld, MD, Department of Radiology, St. Francis Hospital, 355 Ridge Ave, Evanston, IL 60202; e-mail: mikerozenfeld@gmail.com

Indicates open access to non-subscribers at www.ajnr.org

<http://dx.doi.org/10.3174/ajnr.A3437>

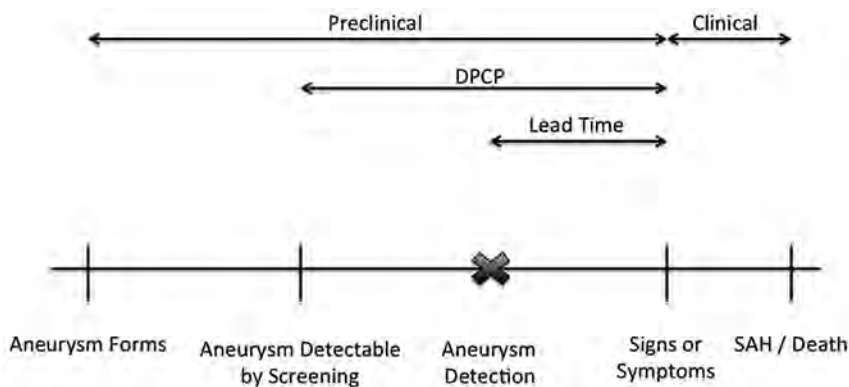


FIG 1. Specific to IA, the preclinical phase between formation and symptom development/rupture can be quite variable, and the clinical phase between symptom development and SAH/death can be quite short or nonexistent. Lead time is dependent on screening frequency. DPCP indicates detectable preclinical phase. Adapted from Morrison⁶⁵ by permission of Oxford University Press, USA.

Table 1: Aneurysm characteristics in patients with ADPCKD versus the general population

Characteristics	General Population	ADPCKD
Male/female distribution	71%–76% female	46%–58% female
Aneurysm location	80%–90% anterior circulation	90%–100% anterior circulation
Multiple aneurysms	35%	18%–31%

Table 2: Five-year cumulative rupture rates from the ISUIA trial for patients without a history of SAH

Artery	<7 mm	7–12 mm	13–24 mm	≥25 mm
Cavernous carotid	0%	0%	3%	6.4%
ACA/MCA/ICA	0%	2.6%	14.5%	40%
PCA, PcomA, vertebrobasilar	2.5%	14.5%	18.4%	50%

Note:—PCA indicates posterior cerebral artery; PcomA, posterior communicating artery; ACA, anterior cerebral artery.

group. All aneurysms, except for 1 giant aneurysm (25 mm), were <10 mm, though 11% were >7 mm (ie, of the original group, 1.36% had an aneurysm of >7 mm). All aneurysms were located in the anterior circulation (49% in the ICA, 26% in the MCA, 25% in the anterior communicating artery, and 2% in the anterior cerebral artery). Multiple aneurysms were found in 18.2% of patients. No correlation was found with hypertension, renal function, liver cysts, or duration of disease.

Data from the International Study of Unruptured Intracranial Aneurysms (ISUIA),²⁰ Stehbens,¹⁶ and Fox¹⁵ used to represent the general population data can be compared with those in larger series studies on patients with ADPCKD by Xu et al ($n = 355$),¹⁹ Schievink et al ($n = 41$),⁵ and Chauveau et al ($n = 71$) (Table 1).¹²

Morbidity

Intracranial aneurysms can cause local mass effect and thromboembolism; however, the most feared event is aneurysm rupture causing catastrophic SAH. Currently, the best prospective data regarding rupture risk come from the ISUIA trial.²⁰ These data support a 5-year cumulative rupture rate of 0%–50%, depending on the location and size of the aneurysm (Table 2), with anterior circulation aneurysms of <7 mm having extremely low rates of

rupture. Following the release of these data, the neurosurgical community exposed several weaknesses of the ISUIA study design. Specifically, ISUIA conducted a prospective but nonrandomized recruitment, predisposing it to selection bias in which small aneurysms deemed to be higher risk could have been excluded and prophylactically treated at the discretion of neurosurgeons on the basis of morphology or other risk factors (hypertension, smoking, alcohol abuse, family history). Patients with unruptured aneurysms were invited for inclusion, and their SAH-free survival was backdated to the time of their aneurysm diagnosis, whereas patients experiencing an SAH may not have been able to respond. Most

controversial was the discrepancy of the ISUIA findings based on the fact that a large proportion of ruptured IAs present with sizes <7 mm. One published 10-year series revealed a mean ruptured aneurysm diameter of only 7.5 mm.²¹ Finally, the subanalyses and post hoc grouping of the aneurysm sizes and locations rather than prospective validation of an a priori hypothesis were criticized.

Several explanations have attempted to reconcile the apparent size discrepancy for IA risk stratification. Wiebers et al²² suggested that aneurysms initially develop during a short time (hours to weeks), enlarging to a diameter that is constrained by the elasticity limits of the artery. If the aneurysm does not exceed the elasticity limit and remains unruptured, it undergoes compensatory stabilization via collagen formation. Once stabilized, however, larger aneurysms are at greater risk for further growth and rupture due to increased wall stress, according to the law of Laplace (exponentially increased wall stress with larger diameters). Matsubara et al²³ supported this theory; in their 17-month study, aneurysm growth/bleb formation directly correlated with aneurysm size because only 2.4% (<5 mm) and 9.1% (5–9 mm) of smaller aneurysms progressed versus 50% (10–20 mm) of larger aneurysms. Further analysis revealed that the percentage of aneurysms exhibiting growth increased with time: 1-, 2-, and 3-year cumulative rupture risks were 2.5%, 8%, and 17.6%. Burns et al²⁴ conducted a similar study with a longer follow-up of 47 months. The risk of aneurysm enlargement again correlated with aneurysm size: 6.9% (<8 mm), 25% (8–12 mm), and 83% (>13 mm).

Gibbs et al²⁵ evaluated 21 patients with ADPCKD with documented asymptomatic IA detected on screening examinations. All aneurysms were small (<6.5 mm). On follow-up, 1 aneurysm grew (by 1 mm), and 1 patient developed a new MCA aneurysm (2 mm) during the screening period (mean, 81 months). The authors recommended screening only patients with ADPCKD and a family history of aneurysm rupture or SAH. Because nearly 10% of the patients in this small study exhibited aneurysm growth or new aneurysm development, the reasoning behind the authors' conclusions is unclear. Their analysis was further complicated by nonsurgical interventions, including aggressive antihypertensive

therapy, lipid control, and tobacco cessation, which could potentially lower the risk of aneurysm growth and rupture.

A larger study by Schrier et al²⁶ evaluated the efficacy of re-screening 76 patients with ADPCKD 10 years after an initial screening examination with negative findings by using CTA, MRA, or DSA (depending on patient-specific factors). They found that 2 patients developed aneurysms in the interval period, though 1 may have previously existed on retrospective analysis. During 10 years, 1 patient developed a 10-mm vertebral artery aneurysm, a 10-mm extracranial ICA aneurysm, and a 4-mm MCA aneurysm requiring surgical clipping.

Following IA rupture, the patient faces a mortality risk ranging from 10% to 67%, depending on the study, with another 10%–38% becoming permanently dependent and disabled.^{12,27} Patients with ADPCKD with IA rupture have a mortality rate similar to that of the general population (46%),¹³ though they present with SAH earlier in life, with a mean age of 35–45 years, with 64% of aneurysms rupturing before the patient reaches 50 years of age.^{5,13,28,29} In a single study, 10% of aneurysms in patients with ADPCKD ruptured before the patients reached 21 years of age,¹³ significantly earlier than the rate of the general population (mean age, 50–54 years).^{27,30}

DIAGNOSIS

Imaging Modalities

Nonimaging-based screening/risk-stratification methods have been evaluated with little success. Markers such as renal function do not correlate with the risk of having an IA; up to 50% of patients with ADPCKD with IAs have completely normal renal function.³¹ No correlation has been found with liver cysts or mitral valve abnormalities, and 29% of these patients were normotensive.¹³ A correlation has been found with the duration of hypertension, but not with hypertension itself or duration since the diagnosis of ADPCKD.²¹

Evidence is emerging that the associated vascular defects in ADPCKD may be due to mutations in the *PKD1* and *PKD2* genes (located on the short arm of chromosome 16).^{32,33} Abnormalities of these genes in mouse models correspond with increased rates of arterial dissection, arterial rupture, and intracranial vascular abnormalities.³⁴ There is some evidence that the location of the genetic mutation may help prognosticate risk for IA in patients with ADPCKD (mutations in the 5' region of *PKD1* pose a higher risk than those at the 3' end), though further investigation would be needed before this information could be used in a clinical setting.³⁵

Traditionally, the criterion standard for IA evaluation has been conventional angiography or DSA, which yields a high spatial resolution of 0.1-mm² pixels, optimum contrast due to direct intra-arterial bolus delivery with background subtraction, and high temporal resolution (2–6 frames/s) that can depict flow patterns within an aneurysm. Modern flat-panel 3D DSA acquisitions can generate an isotropic volume dataset of 0.2 mm³, which can be visualized as a reconstructed 3D model or 2D multiplanar sections. The quality of DSA is operator-dependent, varying with the degree of vessel superselection, injection rates and volumes, and number of projections, including any supplementary 3D DSA with postprocessed reconstructions. Regions of compet-

itive flow such as at the vertebral-basilar junction and anterior communicating artery may be difficult to opacify due to a lack of contrast in the blood pool. Differences in geographic distortion and 2D planar imaging views can make subtle changes in aneurysm size difficult to assess on serial studies, unless 3D imaging is performed.

Recent advances in CT and MR imaging technology have made these modalities increasingly attractive options for IA screening. Multidetector CTA and 3T time-of-flight MRA can generate spatial resolutions of about 0.5-mm² per pixel, whereas previous generation scanners provided a resolution of 1 mm² per pixel. CTA relies on attenuation differences between iodinated contrast and surrounding tissues that can be suboptimal at the skull base in the presence of heavy mural calcification or metallic hardware. In fact, embolization coils and microsurgical clips used to treat IAs will cause metallic streak and beam-hardening artifacts on CTA, often yielding nondiagnostic scans. Furthermore, venous contamination seen with inadequately bolus-timed CTA can also limit assessment of the intracranial circulation.

Time-of-flight MRA relies predominantly on flow-related signal and, combined with suppression techniques, gives excellent contrast resolution with negligible interfering venous signal. Decreased temporal resolution with MRA predisposes it to motion artifacts, resulting in acquisition times that may require >5 minutes. In addition, turbulent flow can result in rapid dephasing and intraluminal signal loss, though these issues are less problematic on 3T MR imaging platforms. Contrast-enhanced TOF MRA is marred by venous signal, and the limited time window for dynamic contrast-enhanced arterial phase MRA results in relatively decreased spatial resolution. MR imaging–based techniques are sensitive to metallic susceptibility artifacts from either dental hardware or implanted devices and, at times, degrade images to nondiagnostic quality, as encountered with microsurgical aneurysm clips. Intraluminal stents are difficult to assess with noninvasive methods due to their intraluminal placement and cause moderate susceptibility artifacts on MRA. Although they may be better assessed with a postgadolinium protocol, confirmation with CTA or invasive DSA may be required for definitive diagnosis. Conversely, endovascular coils cause minimal MR imaging artifacts when ultrashort TEs are used with TOF MRA, permitting the assessment of residual filling in coiled aneurysms as an excellent screening technique for aneurysm recurrence.

Efficacy and Safety

Several studies have compared MRA and CTA with DSA with respect to diagnostic accuracy for IAs. According to a recent study, 3T TOF MRA demonstrated a screening sensitivity of 67% for aneurysms of <3 mm, 79% for those of 3–5 mm, and 95% for those of >5 mm.³⁶ Because many patients have multiple aneurysms (~30%),³⁷ a per-patient screening sensitivity is a more accurate metric for assessing the effectiveness of a technique. In this study, the per-patient screening sensitivity and specificity were 96% and 92%, respectively. Multidetector CTA had a slightly lower per-patient screening sensitivity of 95% and a slightly higher screening specificity of 96%. Another recent study focused on CTA revealed a similar screening sensitivity of 95% for aneurysms of >7 mm.³⁸ One study focused on small aneurysms

(<5 mm) and found CTA sensitivity to be higher than that of DSA with equivalent specificity.³⁹

Due to the relatively invasive nature of DSA and the small but definite risk of stroke as well as the cost, dedicated staff and time commitment, and patient discomfort involved in the procedure, DSA has become less attractive as a screening technique for IA. One study estimates the complication risk at 1.3%, with a 0.5% risk of permanent neurologic complications.⁴⁰

Noncontrast TOF MRA has become the primary noninvasive screening technique, with the advantage of avoiding the use of potentially nephrotoxic or allergenic contrast media and avoiding the placement of an IV line. Adding a gadolinium-enhanced MRA to the protocol may add the risk of the rare but serious nephrogenic systemic sclerosis. Nephrogenic systemic sclerosis is noted to occur in 1%–7% of patients with a GFR <30 mL/min due to the use of certain gadolinium-based compounds, though it is exceedingly rare in patients with normal GFR.⁴¹ General MR imaging contraindications include pacemakers, other implanted hardware, and occasionally claustrophobia. All intracranial clips will cause prominent susceptibility artifacts, and some older clips are MR imaging incompatible due to the risk of clip movement. All endovascular coils, stents, and liquid embolic materials are MR imaging compatible.

Because 50% of patients with ADPKD with aneurysms have normal renal function and many others have only slightly altered creatinine clearance, CTA using iodinated contrast media remains a viable option for many potential screening subjects. Risks of CTA include allergic reactions (0.18%–0.6%),⁴¹ contrast-induced nephrotoxicity or acute tubular necrosis, radiation, and intravenous extravasations. Contrast nephropathy is dependent on numerous factors including acute renal failure, dehydration, and elevated serum creatinine concentration or reduced GFR (<60 mL/min), though a serum creatinine level of <2 mg/dL is considered to be a sufficiently low risk for most patients with chronic renal failure.⁴¹ The radiation dose following a CTA of the head ranges from 1.6–1.9 mSv,⁴² which is roughly equivalent to the dose of an x-ray of the spine, 16 chest x-rays, or 7 months of background radiation.⁴³ Comparatively, the radiation dose for a noncontrast head CT is 1.7–2.7 mSv.⁴²

Cost

The cost of diagnostic imaging procedures varies among institutions. The 2012 Medicare technical reimbursement rate and the 2010 National 50th Percentile charge provide reliable figures for comparison (KnowledgeSource version 4.9.1; MedAssets, Alpharetta, Georgia). For CTA, the figures for Medicare and the National 50th Percentile are \$740 and \$2000 respectively. For MRA without contrast, the figures are \$718 and \$2050, whereas adding gadolinium to the study increases the reimbursement by \$300. Thus, there is no significant difference in the up-front cost of CTA versus MRA. In our experience, a small number of patients will require a CTA to clarify a finding on an initial MRA, whereas the opposite almost never occurs. With more widespread use of 3T MRA, this should become less common. Less measurable cost worth considering is incurred by the use of sedation with postprocedure observation, which would be more common with MRA due to the longer procedure time, and issues with claustro-

phobia. CTA carries the risk of contrast reaction or soft-tissue extravasation, which could require a period of observation or admission in the rare severe cases.

THERAPY

Following diagnostic screening and discovery of an IA, treatment versus conservative management must be contemplated. If treatment is deemed prudent, further study of the patient and aneurysm anatomy is required to determine whether microsurgical clipping or endovascular coil embolization is the preferred treatment. A multidisciplinary team experienced in both endovascular and microsurgical techniques along with neuro-critical care expertise, usually at a tertiary care center, is the ideal environment. Treatment decisions will depend on aneurysm size, location, anatomy/morphology (narrow/wide neck, saccular versus fusiform, incorporation of parent or branching vessels), patient age, comorbidities, and institutional/individual surgeon outcomes.

Efficacy and Safety

Microsurgical clipping and endovascular coil embolization have their inherent advantages and disadvantages, and a full comparison is beyond the scope of this review. While microsurgical clipping was previously the standard of care, coil embolization has matured rapidly in recent years and is a more frequent treatment alternative with technological advancements and the advent of adjunctive balloon and stent-assisted techniques.⁴⁴ Numerous studies have shown a lower periprocedural morbidity and mortality associated with endovascular treatment and lower rates of discharge to long-term care facilities.^{44,45} Some authors have suggested that >90% of aneurysms can now be effectively treated by using endovascular techniques.⁴⁶ However, the durability of coil embolization remains frequently debated due to the increased risk of residual aneurysm components or neck remnants, interval rupture or rebleeding (<1%), and the additional risk of retreatment. Despite these concerns, the largest and most recent retrospective analysis, by using the National Inpatient Sample data base, noted in-hospital mortality of 1.2% for clipping and 0.6% for coiling of unruptured aneurysms. In this study, the combined morbidity and mortality from coiling decreased from 6.2% to 4.3% versus clipping, which decreased from 16.9% to 13.2% during 2001–2008.⁴⁴ These outcomes are per procedure, and the risk per patient would increase in cases of retreatment, the latter being negligible after clipping.

Renowden et al⁴⁷ reported that 6% of 1631 patients required retreatment after coiling of 1834 mostly ruptured aneurysms. They found a lower morbidity in retreatment coiling procedures compared with the initial procedure: 3 cases of thromboembolism from 99 recoiling procedures. Overall, combined morbidity and mortality decreased from 14.8% to 7.6%. The important point is that due to modern techniques and increasing use of endovascular methods, treatment morbidity and mortality have significantly improved in comparison with the older risk-benefit analyses.

Nonsurgical interventions are a reasonable alternative to consider in treatment planning. Long-term hypertension has been correlated with an increased risk of IA rupture.⁴⁸ Patients on anticoagulants have a doubled mortality rate after IA rupture.⁴⁹

Other modifiable factors such as smoking, heavy alcohol consumption, oral contraceptive pills, atherosclerosis, ischemic heart disease in women, and hyperlipidemia have all been associated with an increased risk of aneurysmal SAH in the general population.⁵⁰ These risk factors have not, however, been specifically evaluated in the ADPCKD population. While there is no direct evidence that modification of these risk factors would then decrease the risk of rupture, it would seem judicious to address these factors with all patients after the diagnosis of an IA in the hopes of mitigating their risk.

Risk-Benefit Analysis

Multiple authors have addressed the risks and benefits of screening for IAs and their treatment. Crawley et al⁵¹ performed a risk-benefit analysis in 1999 focused on screening patients without polycystic kidney disease with a strong family history of IA and concluded that screening causes net harm. This was the only major analysis with a negative result; explanations include relying on pre-ISUIA data, relatively low MRA sensitivity/specificity (90%), relatively high treatment morbidity and mortality rates (8%), a relatively low incidence (9.8%), and a relatively low 0.8% annual risk of rupture.

One of the most complex risk-benefit analyses to date was performed by Takao and Nojo.⁵² Data were obtained from the prospective arm of the ISUIA and from large meta-analyses. Fifty years of age was chosen for their model because it approximated the mean age in the ISUIA trial. The choice of a 50-year-old cohort in this study was significant because as discussed earlier, 64% of patients with ADPCKD present with IA rupture before this age. Endovascular treatment was found to be effective from a risk-benefit standpoint in anterior circulation aneurysms of >7 mm, cavernous carotid aneurysms of >13 mm, and posterior circulation aneurysms <24 mm. Surgical repair was effective in anterior circulation aneurysms of >13 mm and in posterior circulation aneurysms of 7–12 mm.

Butler et al⁵³ conducted another comprehensive risk-benefit screening analysis. They determined that a single initial screening MRA in all 20-year-old patients with ADPCKD would increase the mean life expectancy without neurologic disability by 1 year. Hence, a 35-year-old patient would expect a mean 0.5-year increase in life expectancy; but declines in screening value were noted with increasing age. Of screened patients, those who have an aneurysm discovered and then treated will have an additional 10.8 years of life (on average) without neurologic deficit. Mitchell et al⁵⁴ reported similar findings in their risk-benefit analysis. Patients with a >20-year life expectancy were found to benefit from treatment for all posterior circulation aneurysms and all anterior circulation aneurysms of >7 mm.

Studies specifically evaluating the treatment of IAs in patients with ADPCKD are limited. As described earlier, these patients may have an increased risk of spontaneous dissection due to arterial wall abnormalities secondary to defects in the *PKD1* and *PKD2* genes. One study by Chapman et al⁶ showed a higher risk of transient complications after angiography in patients with ADPCKD (25%) versus controls (10%), though the complication rates of both groups appeared markedly elevated. Two of 32 patients with ADPCKD experienced transient carotid artery vaso-

spasm, and 1 had asymptomatic vertebral artery dissection without neurologic sequelae.

Cost-Effectiveness

While average initial hospital costs for endovascular coil embolization and surgical clipping are greater than Medicare reimbursement rates,⁵⁵ this alone does not address the overall cost of a screening program. Multiple authors have performed elaborate cost-effectiveness analyses regarding aneurysm screening and treatment in this population.

Takao and Nojo⁵² defined cost-effectiveness as a cost <\$100,000 per QALY, a commonly used value in the United States,⁵⁶ and found both endovascular treatment and surgical clipping to be valuable from a cost perspective in the treatment of IAs of >7 mm. The costs per QALY ranged from as low as \$600 for surgical clipping in anterior circulation aneurysms of >25 mm to \$482,500 for surgical clipping of posterior circulation aneurysms of <7 mm. If one used prospective data from Xu et al,¹⁹ 11% of the aneurysms discovered on initial screening in their study could be cost-effectively treated by using the analysis of Takao and Nojo. If one used retrospective data from Schievink et al,⁵ 35%–78% of the aneurysms in patients with ADPCKD could be treated cost-effectively on the basis of this analysis.

Butler et al⁵³ also addressed cost-effectiveness in their previously described study. As long as the aneurysm prevalence was above 1.1%, a general screening program in 20-year-old patients with ADPCKD was shown to be cost saving. Numerous studies have shown the general aneurysm prevalence in patients with ADPCKD to be at least 4%, and Xu et al¹⁹ demonstrated the prevalence in patients younger than 29 years of age to be 2.4%. No aneurysm size criteria were used in this study, and all aneurysms were hypothetically repaired surgically. Johnston et al⁵⁷ determined via their cost-utility analysis that any intracranial aneurysm that is symptomatic or >10 mm or any patient with a prior history of SAH could be cost-effectively treated with a net gain in QALY.

While most aneurysms of <7 mm have a low risk of rupture and may not require treatment, their early detection would result in a more concentrated follow-up, which may detect aneurysm growth indicative of an unstable lesion; the additional cost of such an approach would have to be factored in.

A very recent and detailed analysis by Bor et al⁵⁸ evaluated and compared numerous screening models. The study was specifically focused on patients (without ADPCKD) with a family history of 2 first-degree relatives with SAH and used an annual IA incidence of 0.3%–0.7% and an annual rupture risk of 1%–2%. While screening was cost-effective regardless of the model chosen, the largest health benefit was obtained by screening every other year from 20–80 years of age at a cost of \$20,000/QALY, well within the acceptable range in the United States. Their recommended model was screening every 7 years from 20–80 years of age at a cost of \$10,749/QALY, within the acceptable range in the United Kingdom and the Netherlands. The costs shown above compare favorably with those in other accepted screening programs and interventions such as digital mammography, colonoscopies, dialysis, and seatbelt use.^{59,60}

RECOMMENDATIONS

Currently, no official standardized societal recommendations exist for IA screening in patients with ADPKD, but various recommendations can be found in the literature. They include (only) screening patients with both ADPKD and a family history of IA or SAH, a prior aneurysm rupture, high-risk occupations, undergoing major elective surgery, or having a “warning headache” or severe anxiety regarding the issue.^{13,61–63} Weibers et al²² provided recommendations for following unruptured IAs in any high-risk population (including ADPKD): annual MRA/CTA for 2–5 years, then every 2–5 years thereafter if the aneurysms are stable. Butler et al⁵³ suggested screening every 2–3 years in patients with ADPKD with a family history of IA and every 5–20 years in those without. Torres et al⁶⁴ advised rescreening every 5–10 years in patients with initial negative screening examination findings. In patients with ADPKD with known aneurysms considered suitable for surveillance, they suggested biannual or annual imaging to confirm stability and then transitioning to less frequent intervals. Xu et al¹⁹ strongly recommended screening patients with ADPKD with a family history of IA or SAH, though they did not provide detailed guidelines or specifically comment on patients without this history.

If one incorporates the most recent data regarding the incidence, screening, treatment risk, and cost-benefit analyses, screening patients with ADPKD via CTA or MRA will improve life expectancy in a cost-effective and, at times, cost-saving manner. We recommend screening all patients with ADPKD by non-contrast 3T TOF MRA at the time of initial diagnosis with follow-up scans at intervals of, at most, 10 years and as short as 2 years, depending on patient-specific risk factors, including the following: family history of IA or SAH, prior SAH, neurologic symptoms, hypertension, smoking, alcohol abuse, high-risk professions (such as pilots), or those undergoing major elective surgery. We would consider coil embolization of most posterior circulation aneurysms and anterior circulation aneurysms of >7 mm, though treatment of smaller IAs may be contemplated on the basis of additional patient and aneurysm risk factors (including irregular morphology). Patients with aneurysms unsuitable for coil embolization with adjunctive balloon or stent-assisted techniques may be offered surgical clipping on multidisciplinary consensus. Newly diagnosed IAs would undergo biannual TOF MRA imaging for the first 2 years and every 2–5 years thereafter if stable. Appropriate medical management to reduce modifiable risk factors for aneurysm growth/rupture (smoking/alcohol cessation, antihypertensive therapy, and, when possible, avoidance of blood thinners) is also recommended.

REFERENCES

1. Dalgaard OZ. **Bilateral polycystic disease of the kidneys: a follow-up of 284 patients and their families.** *Acta Med Scan Suppl* 1957;328:1–255
2. Wilson P. **Polycystic kidney disease.** *N Engl J Med* 2004;350:151–64
3. Obuchowski NA, Graham RJ, Baker ME, et al. **Ten criteria for effective screening: their application to multislice CT screening for pulmonary and colorectal cancers.** *AJR Am J Roentgenol* 2001;176:1357–62
4. Black WC, Welch HG. **Screening for disease.** *AJR Am J Roentgenol* 1997;168:3–11
5. Schievink WI, Torres VE, Piepgras DG, et al. **Saccular intracranial aneurysms in autosomal dominant polycystic kidney disease.** *J Am Soc Nephrol* 1992;3:88–95
6. Chapman AB, Rubinstein D, Hughes R, et al. **Intracranial aneurysms in autosomal dominant polycystic kidney disease.** *N Engl J Med* 1992;327:916–20
7. Huston J 3rd, Torres VE, Sullivan PP, et al. **Value of magnetic resonance angiography for the detection of intracranial aneurysms in autosomal dominant polycystic kidney disease.** *J Am Soc Nephrol* 1993;3:1871–77
8. Rinkel GJ, Djibuti M, Algra A, et al. **Prevalence and risk of rupture of intracranial aneurysms: a systematic review.** *Stroke* 1998;29:251–56
9. Ruggieri PM, Poulos N, Masaryk TJ, et al. **Occult intracranial aneurysms in polycystic kidney disease: Screening with MR angiography.** *Radiology* 1994;191:33–39
10. Graf S, Schischma A, Eberhardt KE, et al. **Intracranial aneurysms and dolichoectasia in autosomal dominant polycystic kidney disease.** *Nephrol Dial Transplant* 2002;17:819–23
11. Wakabayashi T, Fujita S, Ohbora Y, et al. **Polycystic kidney disease and intracranial aneurysms.** *J Neurosurg* 1983;58:488–91
12. Chauveau D, Pirson Y, Verellen-Dumoulin C, et al. **Intracranial aneurysms in autosomal dominant polycystic kidney disease.** *Kidney Int* 1994;45:1140–46
13. de la Monte SM, Moore GW, Monk MA, et al. **Risk factors for the development and rupture of intracranial berry aneurysms.** *Am J Med* 1985;78:957–64
14. Inagawa T, Hirano A. **Autopsy study of unruptured incidental intracranial aneurysms.** *Surg Neurol* 1990;34:361–65
15. Fox JL, ed. *Intracranial Aneurysms.* New York: Springer-Verlag; 1983: 15–18
16. Stehbens WE. *Pathology of the Cerebral Blood Vessels.* St. Louis: Mosby; 1972:351–470
17. Fick GM, Johnson AM, Hammond WS, et al. **Causes of death in autosomal dominant polycystic kidney disease.** *J Am Soc Nephrol* 1995;5:2048–56
18. Fick GM, Gabow PA. **Hereditary and acquired cystic disease of the kidney.** *Kidney Int* 1994;46:951
19. Xu HW, Yu SQ, Mei CL, et al. **Screening for intracranial aneurysm in 355 patients with autosomal-dominant polycystic kidney disease.** *Stroke* 2011;42:204–06
20. Wiebers DO, Wisnant JP, Juston J 3rd, et al. **International Study of Unruptured Intracranial Aneurysms investigators: unruptured intracranial aneurysms—natural history, clinical outcome, and risks of surgical and endovascular treatment.** *Lancet* 2003;362:103–10
21. Wiebers DO, Whisnant JP, Sundt TM, et al. **The significance of unruptured intracranial saccular aneurysms.** *J Neurosurg* 1987;66:23–29
22. Wiebers DO, Piepgras DG, Meyer FB, et al. **Pathogenesis, natural history, and treatment of unruptured intracranial aneurysms.** *Mayo Clin Proc* 2004;79:1572–83
23. Matsubara S, Hadeishi H, Suzuki A, et al. **Incidence and risk factors for the growth of unruptured cerebral aneurysms: observation using serial computerized tomography angiography.** *J Neurosurg* 2004;101:908–14
24. Burns JD, Huston J 3rd, Layton KF, et al. **Intracranial aneurysm enlargement on serial magnetic resonance angiography: frequency and risk factors.** *Stroke* 2009;40:406–11
25. Gibbs G, Huston J, Qian Q, et al. **Follow-up of intracranial aneurysms in autosomal-dominant polycystic kidney disease.** *Kidney International* 2004;65:1621–27
26. Schrier R, Belz M, Johnson A, et al. **Repeat imaging for intracranial aneurysms in patients with autosomal dominant polycystic kidney disease with initially negative studies: a prospective ten-year follow-up.** *J Am Soc Nephrol* 2004;15:1023–28
27. Hop JW, Rinkel GJ, Algra A, et al. **Case-fatality rates and functional outcome after subarachnoid hemorrhage: a systematic review.** *Stroke* 1997;28:660–64
28. Lozano AM, Leblanc R. **Cerebral aneurysms and polycystic kidney disease: a critical review.** *Can J Neurol Sci* 1992;19:222–27

29. Chapman AB, Johnson AM, Gabow PA. **Intracranial aneurysms in patients with autosomal dominant polycystic kidney disease: how to diagnose and who to screen.** *Am J Kidney Dis* 1993;22:526–31
30. **Epidemiology of aneurysmal subarachnoid hemorrhage in Australia and New Zealand: incidence and case fatality from the Australasian Cooperative Research on Subarachnoid Hemorrhage Study (ACROSS).** *Stroke* 2000;31:1843–50
31. Chauveau D, Pirson Y, Verellen-Dumoulin C, et al. **Intracranial aneurysms in autosomal dominant polycystic kidney disease.** *Kidney Int* 1994;45:1140
32. Bichet D, Peters D, Patel AJ, et al. **Cardiovascular polycystins: insights from autosomal dominant polycystic kidney disease and transgenic animal models.** *Trends Cardiovasc Med* 2006;16:292–98
33. Kip SN, Hunter LW, Ren Q, et al. **[Ca²⁺]_i reduction increases cellular proliferation and apoptosis in vascular smooth muscle cells: relevance to the ADPKD phenotype.** *Circ Res* 2005;96:873–80
34. Hassane S, Claij N, Lantinga-van Leeuwen IS, et al. **Pathogenic sequence for dissecting aneurysm formation in a hypomorphic polycystic kidney disease 1 mouse model.** *Arterioscler Thromb Vasc Biol* 2007;27:2177–83
35. Rossetti S, Chauveau D, Kubly V, et al. **Association of mutation position in polycystic kidney disease 1 (PKD1) gene and development of a vascular phenotype.** *Lancet* 2003;361:2196
36. Hiratsuka Y, Miki H, Kiriyama I, et al. **Diagnosis of unruptured intracranial aneurysms: 3T MR angiography vs. 64-channel multidetector row CT angiography.** *Magn Reson Med Sci* 2008;7:169–78
37. Chauveau D, Pirson Y, Verellen-Dumoulin C, et al. **Intracranial aneurysms in autosomal dominant polycystic kidney disease.** *Kidney Int* 1994;45:1140
38. van Gelder JM. **Computed tomographic angiography for detecting cerebral aneurysms: implications of aneurysm size distribution for the sensitivity, specificity, and likelihood ratios.** *Neurosurgery* 2003;53:597–605, discussion 605–06
39. Villablanca J, Jahan R, Hooshi P, et al. **Detection and characterization of very small cerebral aneurysms by using 2D and 3D helical CT angiography.** *AJNR Am J Neuroradiol* 2002;23:1187–98
40. Willinsky RA, Taylor SM, TerBrugge K, et al. **Neurologic complications of cerebral angiography: prospective analysis of 2,899 procedures and review of the literature.** *Radiology* 2003;227:522–28
41. ACR Committee on Drugs and Contrast Media. *ACR Manual on Contrast Media, Version 8.* Reston, Virginia: American College of Radiology; 2012
42. Mnyusiwalla A, Aviv R, Symons S. **Radiation dose from multidetector row CT imaging for acute stroke.** *Neuroradiology* 2009;51:635–40
43. RadiologyInfo.org. Radiological Society of North America. What are x-rays and what do they do? 2012. http://www.radiologyinfo.org/en/pdf/sfty_xray.pdf. Accessed September 1, 2012
44. Brinjikji W, Rabinstein A, Nasr D, et al. **Better outcomes with treatment by coiling relative to clipping of unruptured intracranial aneurysms in the United States, 2001–2008.** *AJNR Am J Neuroradiol* 2011;32:1071–75
45. Alshekhlee A, Mehta S, Edgell RC, et al. **Hospital mortality and complications of electively clipped or coiled unruptured intracranial aneurysm.** *Stroke* 2010;41:1471–76
46. Pierot L, Spelle L, Vitry F. **Immediate clinical outcome of patients harboring unruptured intracranial aneurysms treated by endovascular approach: results of the ATENA study.** *Stroke* 2008;39:2497–504
47. Renowden SA, Koumellis P, Benes V, et al. **Retreatment of previously embolized cerebral aneurysms: the risk of further coil embolization does not negate the advantage of the initial embolization.** *AJNR Am J Neuroradiol* 2008;29:1401–04
48. Juvela S. **Prehemorrhage risk factors for fatal intracranial aneurysm rupture.** *Stroke* 2003;34:1852–57
49. Rinkel G, Prins N, Algra A. **Outcome of aneurysmal subarachnoid hemorrhage in patients on anticoagulant treatment.** *Stroke* 1997;28:6–9
50. Wardlaw J, White P. **The detection and management of unruptured intracranial aneurysms.** *Brain* 2000;123:205–21
51. Crawley F, Clifton A, Brown M. **Should we screen for familial intracranial aneurysm?** *Stroke* 1999;30:312–16
52. Takao H, Nojo T. **Treatment of unruptured intracranial aneurysms: decision and cost effectiveness analysis.** *Radiology* 2007;244:755–66
53. Butler W, Barker F, Crowell R. **Patients with polycystic kidney disease would benefit from routine magnetic resonance angiographic screening for intracerebral aneurysms: a decision analysis.** *Neurosurgery* 1996;38:506–15, discussion 515–16
54. Mitchell P, Gholkar A, Vindlacheruvu R, et al. **Unruptured intracranial aneurysms: benign curiosity or ticking bomb?** *Lancet Neurol* 2004;3:85–92
55. Brinjikji W, Kallmes D, Lanzino G, et al. **Hospitalization costs for endovascular and surgical treatment of ruptured aneurysms in the United States are substantially higher than Medicare payments.** *AJNR Am J Neuroradiol* 2012;33:1037–40
56. Laupacis A, Feeny D, Detsky A, et al. **How attractive does a new technology have to be to warrant adoption and utilization? Tentative guidelines for using clinical and economic evaluations.** *CMAJ* 1992;146:473–81
57. Johnston SC, Gress DR, Kahn JG. **Which unruptured cerebral aneurysms should be treated? A cost-utility analysis.** *Neurology* 1999;52:1806–15
58. Bor S, Koffjberg H, Wermer M, et al. **Optimal screening strategy for familial intracranial aneurysms: a cost-effectiveness analysis.** *Neurology* 2010;74:1671–79
59. Tosteson A, Stout N, Fryback D, et al. **Cost-effectiveness of digital mammography screening.** *Ann Intern Med* 2008;148:1–10
60. Tengs TO, Adams ME, Pliskin JS, et al. **Five-hundred life-saving interventions and their cost-effectiveness.** *Risk Anal* 1995;15:369–90
61. Pirson Y. **Extrarenal manifestations of autosomal dominant polycystic kidney disease.** *Adv Chronic Kidney Dis* 2010;17:173–80
62. Pirson Y, Chauveau D, Torres V. **Management of cerebral aneurysms in autosomal dominant polycystic kidney disease.** *J Am Soc Nephrol* 2002;13:269–76
63. Wakai S. **Polycystic kidneys and aneurysms.** *J Neurosurg* 1999;90:985–86
64. Torres V, Harris P, Pirson Y. **Autosomal dominant polycystic kidney disease.** *Lancet* 2007;369:1287–301
65. Morrison AS. **The natural history of disease in relation to measures of disease frequency.** In: Morrison AS. *Screening in Chronic Disease.* 2nd ed. New York: Oxford University Press; 1992:57

Illustrated Review of the Embryology and Development of the Facial Region, Part 2: Late Development of the Fetal Face and Changes in the Face from the Newborn to Adulthood

P.M. Som and T.P. Naidich



ABSTRACT

SUMMARY: The later embryogenesis of the fetal face and the alteration in the facial structure from birth to adulthood have been reviewed. Part 3 of the review will address the molecular mechanisms that are responsible for the changes described in parts 1 and 2.

Part 1 of this 3-part review primarily dealt with the early embryologic development of the face and nasal cavity. Part 2 will discuss the later embryonic and fetal development of the face, and changes in facial appearance from neonate to adulthood will be reviewed.

Formation of the Palate

Between the sixth and 12th weeks, the palate is formed from 3 primordia: a midline median palatine process and paired lateral palatine processes (Fig 1). In the beginning of the sixth week, merging of the paired medial nasal processes forms the intermaxillary process. From this, a wedge-shaped primary anterior mesenchymal mass extends posteriorly, between the internal surfaces of the developing maxillae, to form the primary palate (Fig 1B). The primary palate then gives rise to the premaxilla, the anterior median portion of the maxilla that encloses the 4 upper incisors. The secondary palate is the primordium of the remaining hard and the soft palates. Later in the sixth week, paired lateral palatine processes arise as medial mesenchymal projections from each maxillary process (Figs 1 and 2). Initially these grow inferiorly, between the developing tongue and the developing alveolus (see the sections on the mandible and teeth) (Fig 2A). However, as the maxilla and mandible elongate, the tongue is pulled downward away from the lateral palatal processes. During the seventh and eighth weeks (Fig 2B), the palatal shelves elevate into a horizontal position above the tongue (Fig 2C, -D). This change in orientation is facilitated by the release of hyaluronic acid by the mesenchyme of each palatal process. When the palatal shelves

first make contact, each is completely covered by a homogeneous epithelium. A special epithelium arises at the edge of each palatal shelf, facilitating the eventual fusion of these shelves. The epithelium on the nasal cavity surface of the palate will differentiate into columnar ciliated epithelium. The epithelium on the oral cavity side of the palate will differentiate into stratified squamous epithelium.

The 2 palatal shelves also fuse with the triangular primary palate anteromedially to form a y-shaped fusion line. The point of fusion of the secondary palatal shelves with the primary palate is marked in the adult by the incisive foramen. The fusion of the 2 palatal shelves also results in a lengthening of the nasal cavity and carries the posterior choana back toward the pharynx. Ossification gradually occurs in the primary palate and then extends into the palatal processes to form the hard palate. The posterior portions of the palatal processes do not ossify. Rather they extend posteriorly to the nasal septum and fuse to form the soft palate ad midline uvula.^{1,2}

Nasal Septum

The nasal septum develops downward and posteriorly from the internally merged medial nasal processes and the frontonasal process. Fusion between the nasal septum and the palatal processes starts anteriorly during the ninth week and is completed by the 12th week (Fig 2).^{1,2}

Mandible

During the fourth-to-fifth weeks, the mandibular processes gradually enlarge and merge in the midline. Between the fifth and eighth weeks, neural crest cells of the first pharyngeal arch give rise to left and right cartilaginous rods called the Meckel cartilages. These form the cores around which the membranous bone of the lower jaw develops. The mandibular processes form the lower lip, the lower jaw, and the lower cheek regions. The mentum marks the site where the 2 mandibular

From the Department of Radiology, Mount Sinai School of Medicine, New York University, New York, New York.

Please address correspondence to Peter M. Som, MD, Department of Radiology, The Mount Sinai Hospital, One Gustave Levy Place, New York, NY 10029; e-mail: Peter.Som@MSSM.edu

Indicates open access to non-subscribers at www.ajnr.org

<http://dx.doi.org/10.3174/ajnr.A3414>

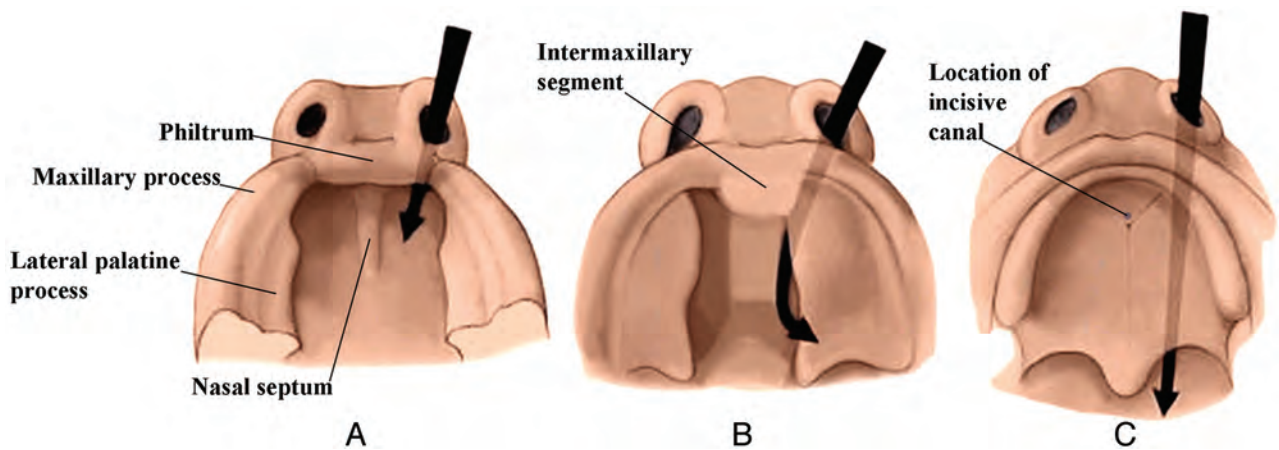


FIG 1. Drawings from below show the development of the palate from 6 to 7 weeks (A), 7 to 8 weeks (B), and 8 to 10 weeks (C). The lateral palatine processes grow medially and eventually merge in the midline and with the intermaxillary segment (primitive palate). The incisive canal marks the junction of the primitive and secondary palates. (Modified with permission from Levine HL, Clemente MP, eds. Chapter 1, Surgical Anatomy of the Paranasal Sinus. China: 2005. Sinus Surgery Endoscopic and Microscopic Approaches. Figures 1–3. Thieme Medical Publishers Inc., Georg Thieme Verlag Stuttgart).

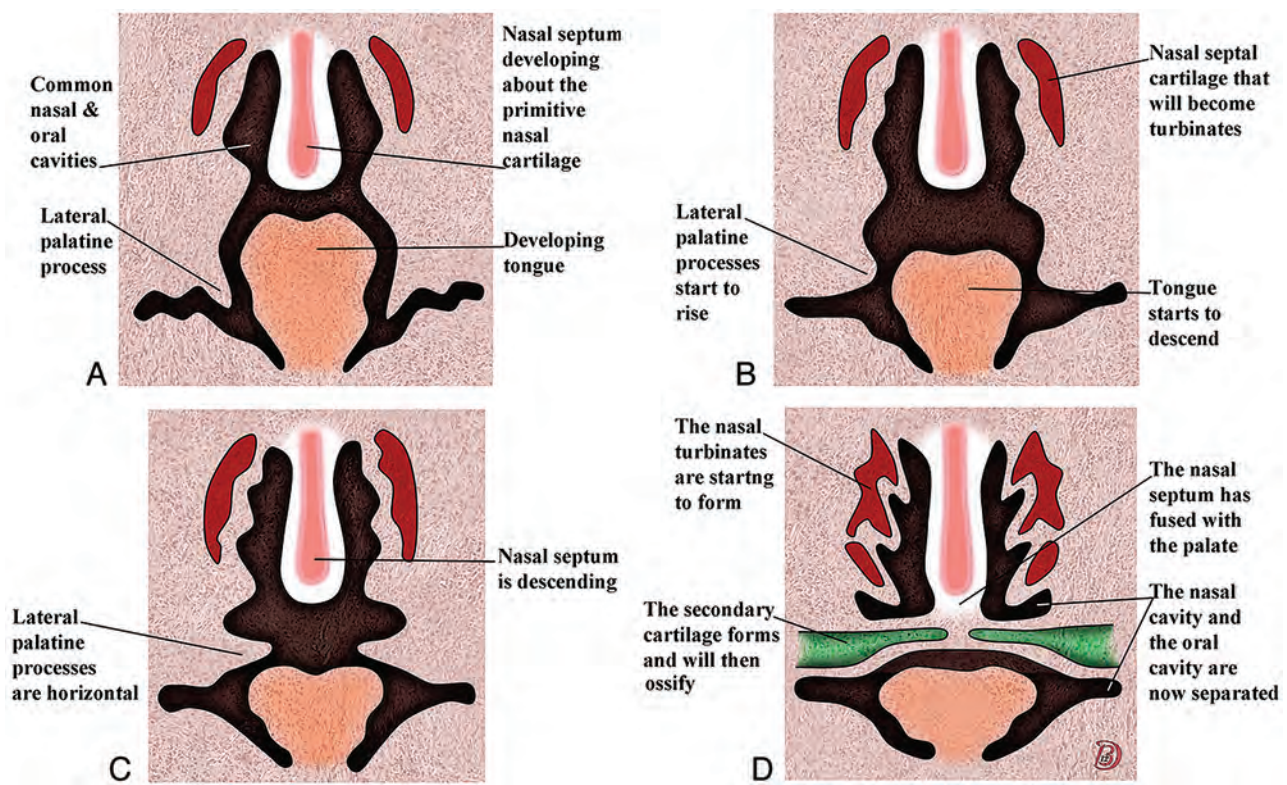


FIG 2. Serial frontal diagrams (A–D) from approximately 6–10 fetal weeks shown just posterior to the intermaxillary segment illustrate the progressive development of the secondary palate and its fusion with the nasal septum.

processes merge in the midline. A partial or incomplete merger of these mandibular processes forms the common midline chin dimple or cleft.

Gingiva, Lips, and Teeth

Until the end of the sixth week, the primordial jaws comprise only masses of mesenchymal tissue with no differentiation of the lips and gingivae. At the end of the sixth week, a curvilinear thickening of ectoderm, the labiogingival lamina, grows into the underlying mesenchyme. Most of this lamina degenerates, creating a labiogingival groove or sulcus between the lips and

gingivae (Fig 3A). A small midline remnant of the labiogingival lamina persists as the frenulum of the upper lip (Fig 3B).

Shortly after in the sixth week, a second lamina, the dental lamina, arises in the more buccal margin of the developing gingiva of both jaws. The dental lamina eventually will give rise to 10 spherical tooth buds that penetrate the mesenchyme of both jaws. The tooth buds first appear in the anterior mandible followed by the anterior maxilla. Budding then continues progressively posteriorly to form 10 deciduous teeth each in the maxilla and mandible. From about the 10th fetal month, deep

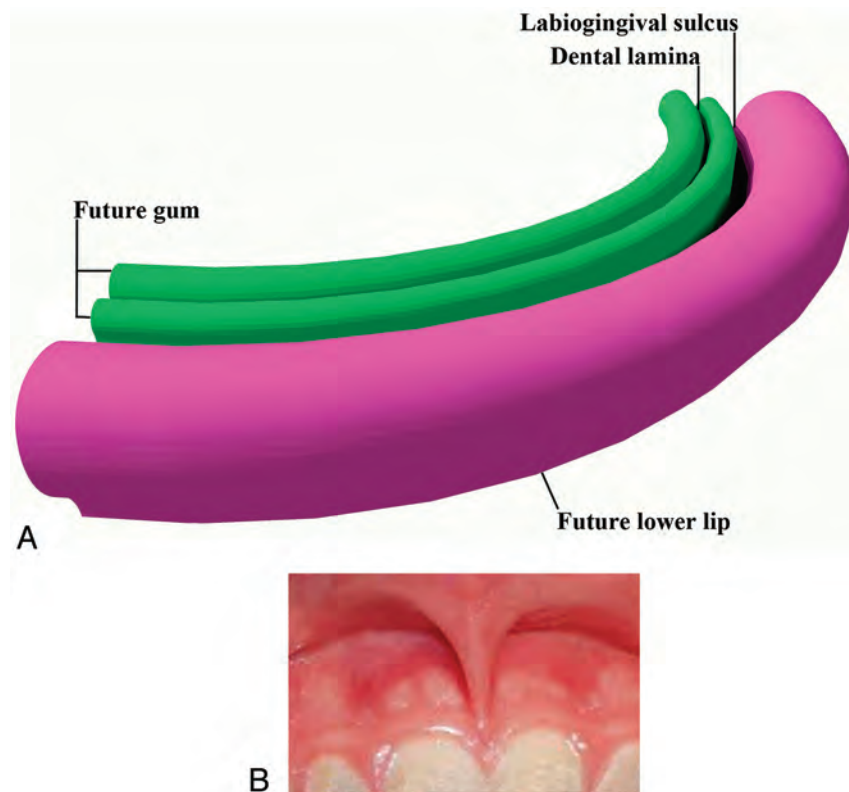


FIG 3. Drawing from above and in front (A) of the developing lips and gums. The labiogingival lamina develops in the common mesenchymal tissue of this region. When it dissolves, the labiogingival sulcus that remains separates the lips and gums. The dental lamina develops just behind this region and will give rise to the dental buds, which will form the deciduous and permanent teeth. B, Frontal photograph shows the frenulum of the upper lip, the only remaining vestige of the labiogingival lamina.

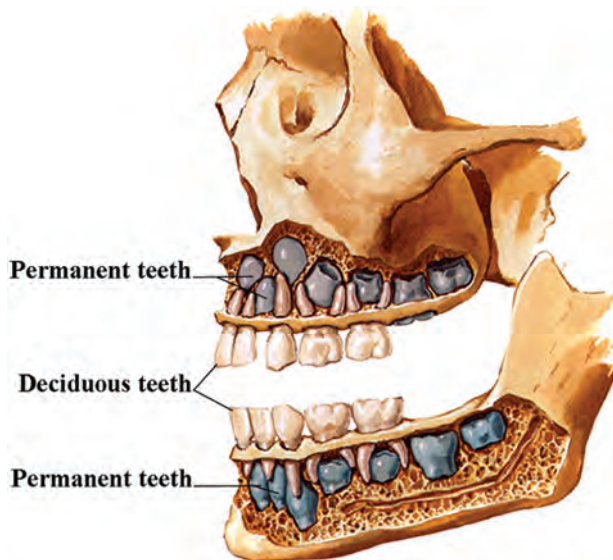


FIG 4. Lateral drawing of the developing teeth. Note that the permanent teeth (blue) develop medial to the deciduous teeth. (Modified with permission from Frank H. Netter, Atlas of Human Anatomy, 5th Edition, Saunders Elsevier, Philadelphia, 2011, Figure 56. Netter Illustrations from www.netterimages.com, ©Elsevier Inc, All rights reserved).

components of the dental lamina create the buds for the permanent teeth along the lingual aspects of the deciduous teeth (Fig 4). The permanent molar teeth have no deciduous precu-

sors and arise directly from posterior extensions of the dental laminae.

By the 10th week, a mesenchymal condensation called the “dental papilla” invaginates into each tooth bud, resulting in the formation of a cup-shaped enamel organ (Fig 5A). The enamel organ has an inner epithelium, an outer epithelium, and a middle enamel reticulum (enamel pulp) (Fig 5B, -E). The dental papilla contains attenuated collections of stellate cells, which eventually give rise to most of the tooth proper, including the pulp cavity, the dentin, and the vasculature of the tooth. The enamel organ and dental papilla are surrounded by a mesenchymal concentration called the “dental sac.” This sac will develop into the fibrous connective tissue (periodontal ligament) that attaches the roots of the teeth to the alveolar bone (Fig 5C). The inner enamel epithelium later differentiates into the ameloblasts that produce the tooth enamel. By the third month, the mesenchymal cells in the dental papilla adjacent to the inner enamel epithelium differentiate into odontoblasts. These produce predentin and deposit the predentin adjacent to the inner enamel epithelium (Fig 5C). In the sixth month, the predentin calcifies to become the dentin of the tooth.

The crown of the tooth refers to that part of the tooth covered by enamel and projecting above the gum line. The formation of the tooth root begins when the inner and outer enamel layers penetrate into the mesenchyme to form the epithelial root sheath (Hertwig epithelial root sheath) (Fig 5D). Root formation takes place after the crown formation has been completed. The root

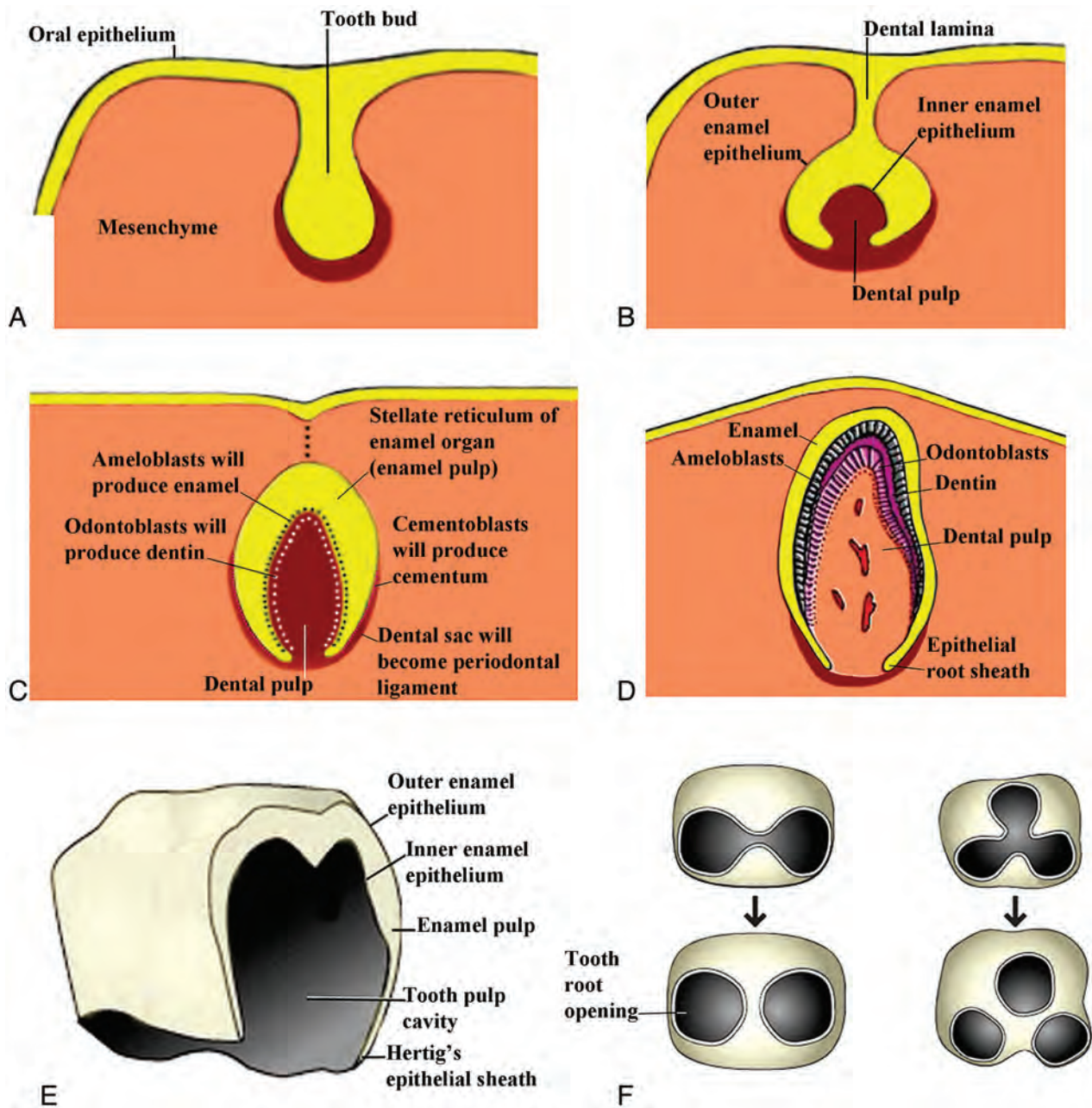


FIG 5. Drawings of the progressive development of the teeth from the tooth bud stage that comes from the dental lamina to the adult tooth. (Modified from <http://embryology.ch/anglais/sdigestive/gesicht05.htm> and www.embryo.chronolab.com/teeth.html).

canals arise through extension and later fusion of the enveloping root sheath (Fig 5F). The inner cells of the dental sac differentiate into cementoblasts, which will produce the cementum of the tooth. Increasing amounts of dentin reduce the pulp cavity to the narrow root canal through which the vessel and nerves pass. The deciduous teeth erupt through the gingiva from 6–24 months after birth.³

Facial Muscles

The facial muscles start to develop between the third and eighth weeks when the mesoderm of the second branchial arch starts to thicken just caudal to the first branchial groove. Between the sixth

and eighth weeks, sheet-like collections of premyoblasts and early myoblasts extend from this attenuated mesenchyme to form 5 laminae on each side of the face, which extend into the superficial portions of the future temporal, occipital, cervical, and mandibular regions. On each side of the face, the infraorbital lamina and the occipital platysma are the first laminae to appear (Fig. 6). Each infraorbital lamina forms the zygomaticus major, the zygomaticus minor, the levator labii superioris, the levator labii superioris alaeque nasi, the superior part of orbicularis oris, the compressor naris, the dilator naris, the depressor septi, the orbicularis oculi, the frontal belly of occipitofrontalis, the corrugator supercillii, and the procerus muscles. Each occipital lamina forms the occipital

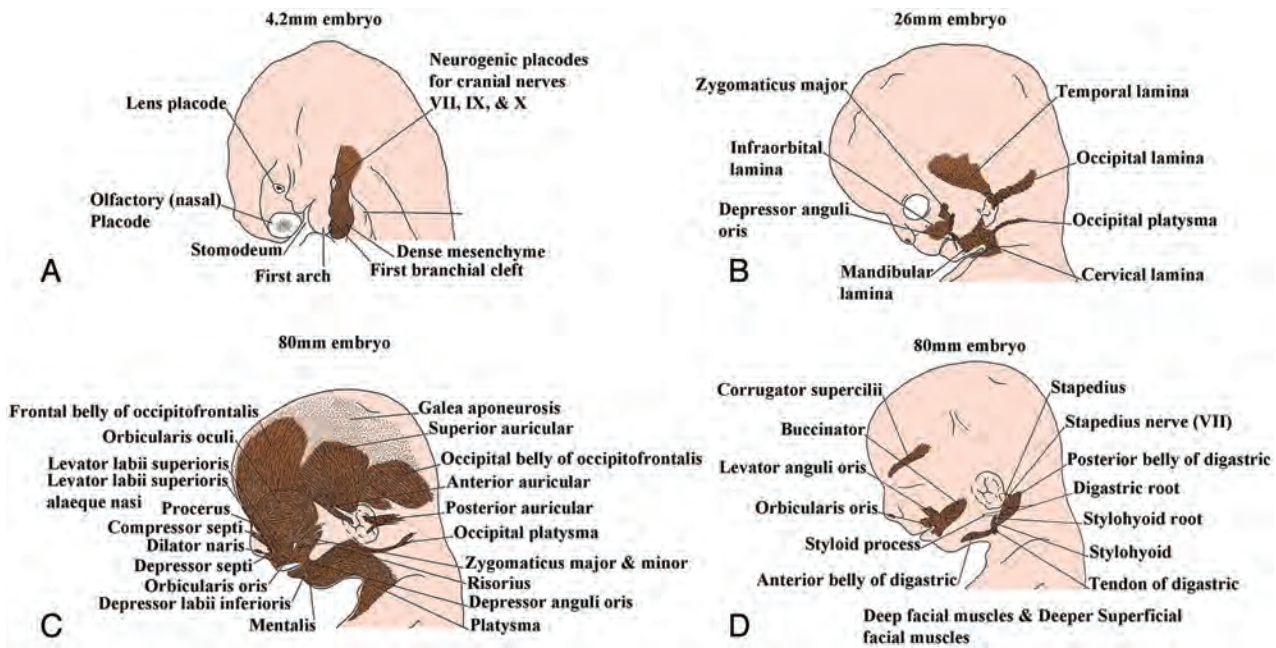


FIG 6. Sagittal drawings of the progressive development of the facial muscles from the dense mesenchyme that arises near the first branchial cleft. (Modified with permission from Gasser R. The Development of the Facial Muscles in Man. *Am J Anat* 1967;120:357–376).

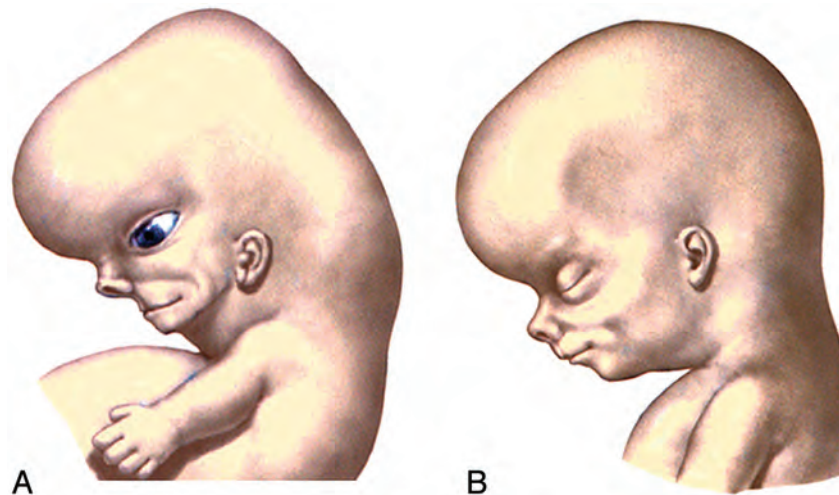


FIG 7. Lateral drawings of a 7- to 8-week embryo (A) and an 8- to 10-week fetus (B) show that the opening of the external auditory canal remains stationary but appears to rise because the progressive elongation of the jaw creates this impression. (Modified with permission from Netter's Atlas of Human Embryology. Edited by Cochard, L.R., PhD. 2002. Icon Learning Systems, Teterboro, New Jersey, Figure 9.27. Netter Illustrations from www.netterimages.com, ©Elsevier Inc, All rights reserved).

belly of the occipitofrontalis muscle. Each temporal lamina develops into the superior auricular muscles. Each mandibular lamina forms the mandibular part of platysma, the depressor labii inferioris, the mentalis, the risorius, the depressor anguli oris, the buccinator, and the levator anguli oris muscles. Mesenchymal cells adjacent to the first branchial cleft form the anterior auricular muscle on each side of the face. The deep muscles form separately for the mesoderm, and these muscles comprise the posterior belly of digastric, the digastric tendon, the stapedius, and the stylohyoid muscle on each side of the face.⁴

Remodeling of the Face

During the early fetal period, the nose is flat, the mandible appears small, and the orbits face laterally. These structures will grow into their adult configurations as facial development is completed. As the brain enlarges, the cranial vault expands to each side causing the orbits to face forward. The ostia of the external auditory canals remain stationary but appear to rise because the jaw elongates and grows downward (Fig 7). Early on, the stomodeum extends across nearly the full width of the embryonic face. By the seventh-to-eighth weeks, differential growth of the facial elements brings the eyes and lateral portions of the maxilla and mandible to a more



FIG 8. Drawing in an anterior oblique view of the late fetal face showing the contributions of the various facial processes. Green indicates the frontonasal process; yellow, the lateral nasal processes; purple, the medial nasal processes; orange, the maxillary processes; and blue, the mandibular processes.

frontal location. Although the expansion of the cranial vault does make the mouth appear smaller, it is the formation of the cheeks by progressive fusion of the maxillary with the mandibular processes at the lateral angles of the mouth that most reduces the size of the mouth. The coronal plane along which the oropharyngeal

membrane originally attached eventually corresponds to the plane of the Waldeyer ring. The progressive depth of this ring in the postnatal period is due to the dominant differential growth of the ventral face.

Summary of Contributions

The frontonasal process forms the forehead, the bridge, and dorsum of the nose and the nasal bones. The medial nasal processes form the columella of the nose, the philtrum, the perpendicular plate of the ethmoid bone and the vomer, the cribriform plates, and the primary palate. The lateral nasal processes form the sides and alae of the nose. The maxillary processes form the upper cheek regions and most of the upper lip, the maxilla, zygoma, and secondary palate. The mandibular processes form the chin, lower lip, lower cheek regions, and the mandible (Fig 8).

Pinna of the Ear

At the beginning of the sixth week, 6 auricular mesenchymal hillocks appear, 3 on either side of the first branchial cleft or groove. During the seventh week, the pinna of the ear will have taken its adult shape (Fig 9).

Eyelids

In the sixth week, the eyelids start to form from neural crest mesenchyme and from 2 cutaneous folds of ectoderm that grow over the cornea. The eyelids grow rapidly until they meet and fuse to each other in the 10th week. At this time, a persistent epithelial lamina arises between the eyelids. Between the 26th and 28th weeks before the eyelids reopen, eye lashes and small meibomian glands begin to differentiate from the common epithelial lining.

Later Facial Growth

At birth, the skull has a sagittal suture system that divides the cranium and face into left and right halves. Anteriorly, this system

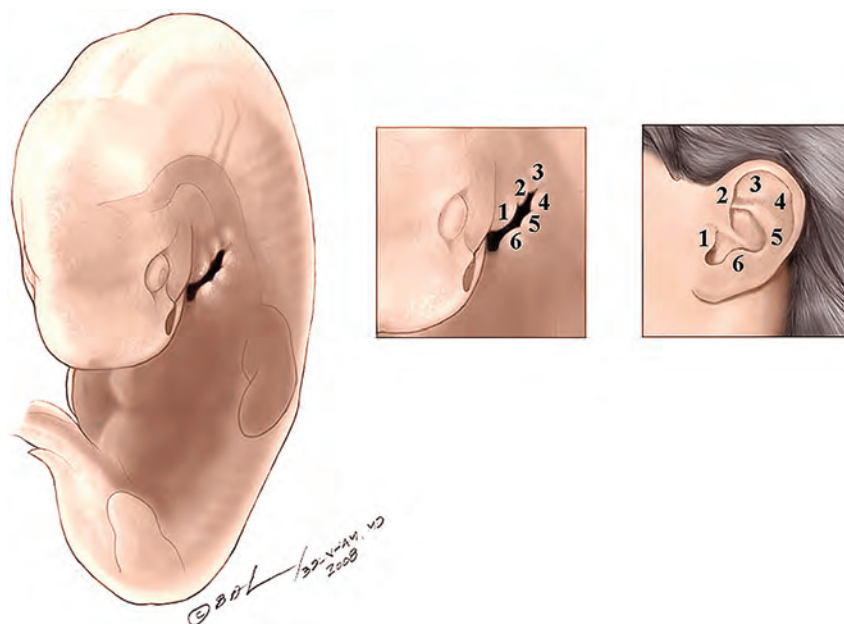


FIG 9. Lateral oblique drawings of the 6 hillocks that develop about the first branchial cleft and how they eventually form the pinna of the ear.

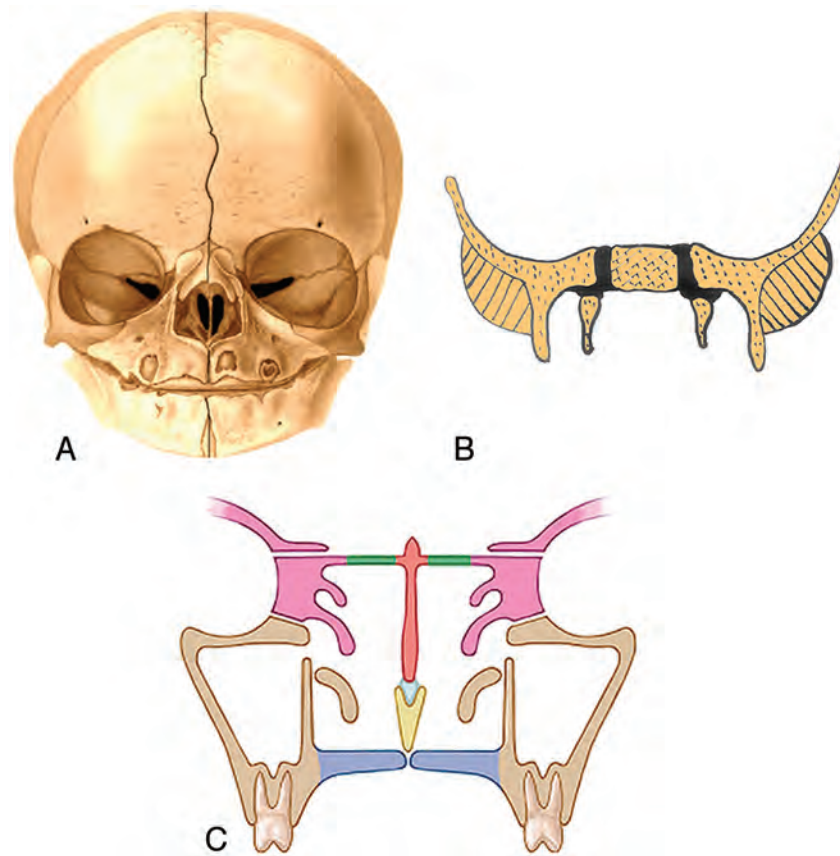


FIG 10. Frontal drawing of a neonate skull (A) shows the sagittal suture system that divides the cranium and face into 2 halves. This system is made up of the metopic suture, the internasal suture, the intermaxillary suture, and the mandibular symphysis (outlined with a black line). (Modified with permission from Sobotta: Atlas der Anatomie des Menschen. ©Elsevier GmbH, Urban & Fischer Verlag Munchen. Volume 1, Edited by Putz, R. and Pabst, R. Lippincott Williams and Wilkins, Philadelphia 2001, Figure 82). B, Frontal drawing of the body of the sphenoid bone, the greater sphenoid wings, and the cartilage between them (black). The sagittal suture system divides to run on either side of the body of the sphenoid bone because it is separated from the greater sphenoid wings by cartilage. C, Frontal drawing of the midfacial structures at approximately 3 years of age. The union of the ethmoid bodies (pink) with the perpendicular plate (orange) as a result of ossification of the cribriform plates (green) makes the ethmoid bone a single bone and stabilizes the interocular and upper nasal regions. The maxilla is beige; vomer, yellow; septal cartilage, light blue.

is made up of the metopic suture, the internasal suture, the intermaxillary suture, and the mandibular symphysis (Fig 10A). Posteriorly, the sagittal suture system splits around the body of the sphenoid bone, along the cartilage between the body of the sphenoid and the greater wings of the sphenoid (Fig 10B). The sagittal system does not bisect the entire skull however because other midline structures extend from the foramen magnum to the nasion. These structures comprise the basioccipit, basisphenoid, lesser wings of the sphenoid, the perpendicular plate of the ethmoid, and the interorbital portion of the frontal bone.⁵

By 8–9 weeks, the initial skeleton of the face is cartilaginous and composed of the nasal capsule in the upper face and Meckel cartilage in the lower face. The chondrocranium forms the skull base. By 12 weeks, most of the ossification centers have appeared in the membranous bones, and the enchondral ethmoid bone has started to ossify. Ossification then proceeds within these bones. During the late fetal period and until the first postnatal year, growth in the width of the craniofacial skeleton occurs at the midsagittal suture system. The main mechanism of this growth

is the progressive enlargement of the brain and growth of the cartilage between the body and greater wings of the sphenoid bone.

In the first year of life, the metopic suture unites, and soon after, the mandibular symphysis unites. Then the greater sphenoid wings unite with the sphenoid body. These changes close the midline sagittal suture system, and it ceases to be a growth site.⁵

At approximately 3 years, ossification of the cribriform plates unites the ethmoid bodies with the perpendicular plate, creating a single ethmoid bone and stabilizing the interocular and upper nasal regions (Fig 10C). It has been suggested that the progressive growth of the nasal septal cartilage “pushes” the midface forward and thus contributes to the facial antero-posterior growth.^{5,6}

After the third year, separation of the maxillary bones is still possible, as is separation of the zygomatic bone from the maxilla. However, with completion of the growth of the orbits between the seventh and 10th years, further outward movement of the maxilla and zygoma ceases at these sutures. Further growth of the upper facial skeleton takes place by surface bone deposition in association with internal bone resorption.⁵

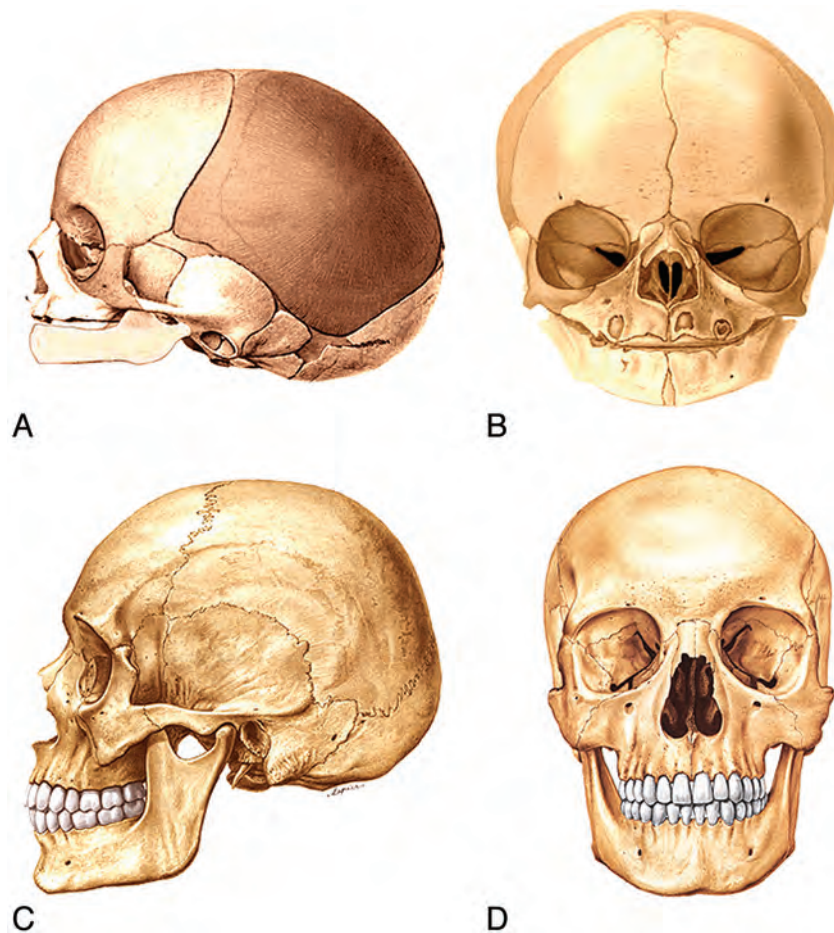


FIG 11. Lateral (A) and frontal (B) drawings of neonate facial bones and skull and adult facial bones and skull in the lateral (C) and frontal (D) views. In general, the facial structures grow proportionally more and for a longer time the further they are from the neurocranium. Thus, growth of the mandible begins later and continues longer than midfacial and orbital development. The forehead grows in an anterior and slightly upward direction. The forward and upward growth of the forehead contributes to elevation and widening of the nasal bridge. (Modified with permission from Sobotta: Atlas der Anatomie des Menschen. ©Elsevier GmbH, Urban & Fischer Verlag Munchen. Volume 1, Edited by Putz, R. and Pabst, R. Lippincott Williams and Wilkins, Philadelphia 2001, Figures 66, 68, 82 and 83).

Childhood to Adulthood Facial Remodeling

As one ages from childhood to adulthood, there is a constant growth and remodeling of the facial bones, which results in changes in the facial morphology. Overall, there is forward and downward growth of the face with progressing age. As a generality, the farther structures lie from the neurocranium, the longer they grow and the more they increase in size. Thus, growth of the mandible begins later and continues longer than does the growth of the midface and orbits.

During the first decade of life, the forehead grows in an anterior and slightly upward direction. This contributes to the elevation and widening of the nasal bridge (Fig 11B, -D).

The zygomatic/maxillary region grows progressively posteriorly as the dental arch becomes elongated by addition of new bone on the posterior margin of the maxilla. That part of the maxilla anterior to the zygomatic arch regresses while the posterior portion increases in size.^{6,7}

The backward movement of the malar region and the forward growth of the supraorbital region serve to draw out the anteroposterior dimensions of the face. The inferior orbital rim and the superior orbital rim are in the same coronal plane in the young

face, but in the older face, the supraorbital region protrudes forward of the cheek (Fig 12).

In the transverse plane, the maxillary bones and the ethmoid bodies grow apart from one another so that the interocular distance increases with age (Fig 12C). The movement of the nasal area combined with the malar movement results in an increase in the vertical size and the width of the upper part of each nasal cavity (Fig 12D). The mandibular ramus becomes progressively deeper in its anteroposterior dimension. The ramus also increases in vertical dimension, accommodating the marked downward growth of the nasomaxillary complex and the eruption of the teeth (Fig 12 A, -C).

The young face appears somewhat brachycephalic because it is relatively wide and vertically short. The dentition has not yet become fully established, and the jaws have not yet grown to their full vertical extent. The young face also appears small compared with the cranium when the craniofacial sizes are compared with an adult skull (Fig 11). Thus, compared with an adult face, the young face appears “cute,” with wide-set large eyes, a small jaw, a small “pug” nose, prominent cheeks, a high flat forehead

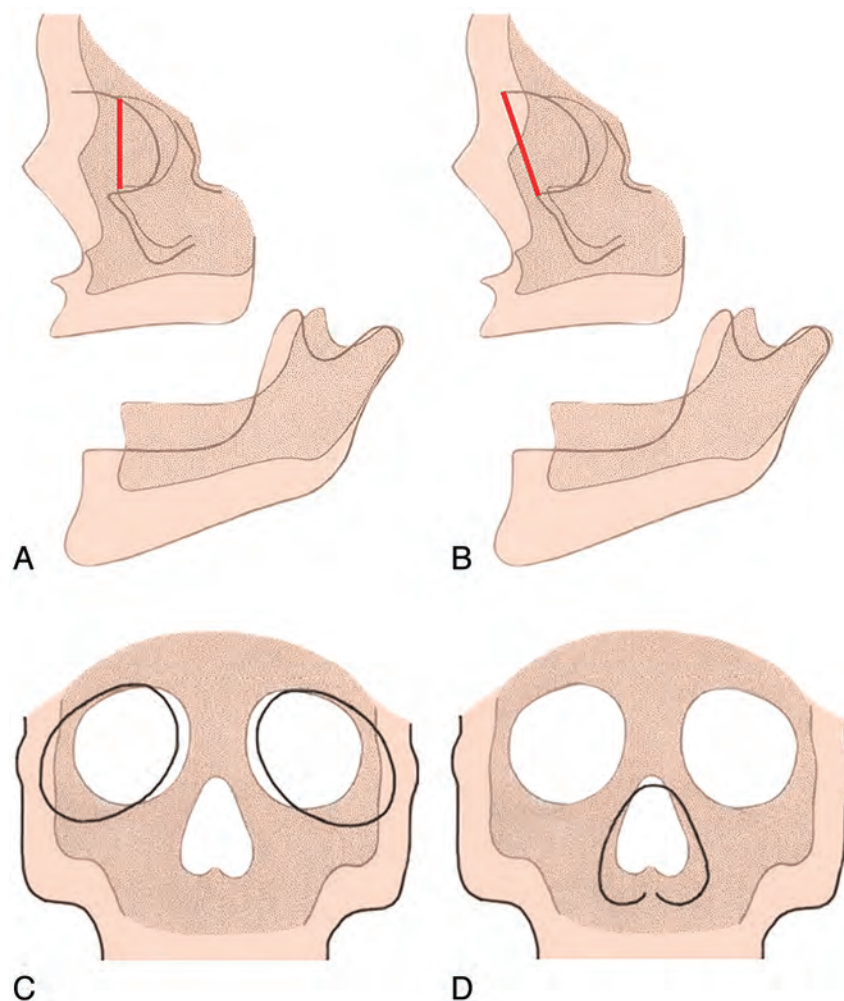


FIG 12. Lateral diagram of the fetal skull (A) (darker areas) and the adult skull (B) (lighter areas) shows that the inferior orbital rim and the superior orbital rim are in the same plane in the young face (dark line in A), but in the older face, the supraorbital region protrudes forward of the cheek (dark line in B). Frontal diagrams (C and D) show that as the maxillary bones and the ethmoid bodies separate from one another, this movement increases the lateral growth of the interocular distance. As a result, the orbits enlarge and shift laterally (C). The movement of the nasal area combined with the malar movement results in an increase in the vertical size and the width of the upper part of each nasal cavity (D). (Modified with permission from Enlow D. A Morphogenetic Analysis of Facial Growth. *Am J Orthodontics* 1966;52:283–299. Figures 1 and 4)

without full eyebrows ridges, a low nasal bridge, and a small mouth.

REFERENCES

1. Kim CH, Park HW, Kim K, et al. **Early development of the nose in human embryos: a stereomicroscopic and histologic analysis.** *Laryngoscope* 2004;114:1791–800
2. Warbrick JG. **The early development of the nasal cavity and upper lip in the human embryo.** *J Anat* 1960;94:351–62
3. Abrahams JJ, Poon CS, Hayt MW. **Embryology and anatomy of the jaw and dentition.** In: Som PM, Curtin HD, eds. *Head and Neck Imaging*. Philadelphia: Elsevier; 2011:1425–41
4. Gasser R. **The development of the facial muscles in man.** *Am J Anat* 1967;120:357–76
5. Scott JH. **The growth in width of the facial skeleton.** *Am J Orthod* 1957;43:366–71
6. Scott JH. **The growth of the cranio-facial skeleton.** *Ir J Med Sci* 1962;37:276–86
7. Enlow D. **A Morphogenetic analysis of facial growth.** *Am J Orthod* 1966;52:283–99
8. Levine HL, Clemente MP. **Surgical anatomy of the paranasal sinus.** In: Levine HL, Clemente MP, eds. *Sinus Surgery: Endoscopic and Microscopic Approaches*. New York: Thieme; 2005
9. Cochard LR, ed. *Netter's Atlas of Human Embryology*. Teterboro, New Jersey; Icon Learning Systems; 2002
10. Netter FL, Craig J, Machado C. netterimages.com. Netter Illustrations. Elsevier. www.netterimages.com. Accessed 2011
11. Human Embryology Organogenesis. 19.1. Face and upper foregut. <http://embryology.ch/anglais/sdigestive/gesicht05.html>. Accessed 2011
12. www.embryo.chronolab.com/teeth.html. Accessed 2011
13. Pultz HvR, Pabst R, eds. *Sobotta: Atlas der Anatomie des Menschen*. Philadelphia: Lippincott Williams and Wilkins; 2001

Andreas Vesalius and Thomas Willis: Their Anatomic Brain Illustrations and Illustrators

J.H. Scatliff and S. Johnston

ABSTRACT

SUMMARY: The brain illustrations of Vesalius and Willis were the first in anatomic history with pictorial accuracy. Their illustrations, illustrators, and methods are discussed. Woodcut blocks were used for the prints of figures in the Vesalian anatomy. Figures of the brain appear to be done after external fixation in the work of Willis.

With MR images of the brain now so clear, it is interesting to remember how the first true brain illustrations were done. Although the 3D reality of organ systems began with Da Vinci, it was Vesalius in Padua in the 1500s and his illustrations that led the way with brain drawings approaching those of the present. A hundred years after Vesalius, Thomas Willis and Christopher Wren in Oxford took the accurate depiction of the brain and its vessels further.

There are 25 woodcut figures of brains, reflected dura, skulls, and vessels in Andreas Vesalius' landmark anatomic text *The Fabric of the Human Body* (Latin: *De Humani Corporis Fabrica*) Book VII (Figs 1A, -B).¹ The identity of the artist who did the illustrations is uncertain. It may have been Von Calcar, a Fleming as was Vesalius.² It is known that Von Calcar was a pupil of Titian who lived and worked in Venice. With Vesalius in need of anatomic illustration 25 miles away in Padua, it is not hard to believe that Vesalius asked Titian to recommend an artist or artists.

Vesalius was known to conduct public dissections with as many as 500 observers, including officials of Padua or Bologna and faculty and students of their medical schools. The well-known title page il-

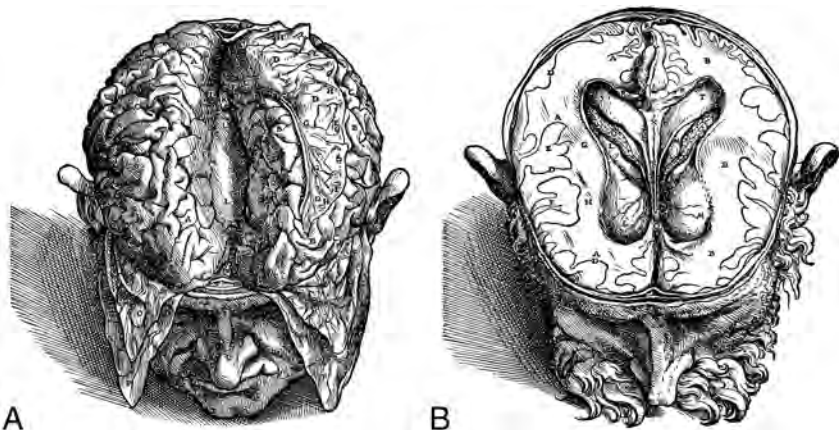


FIG 1. A, *De Humani Corporis Fabrica*, Book VII, Plate 3 L, Corpus Callosum; D, Falx Separated and Laid on Left Brain. B, Plate 4 E Gyri, GH White Matter O, Choroid Plexus. Modified courtesy of D. Garrison, Department of Classics, Northwestern University.

lustration of the *Fabrica* shows Vesalius (Fig 2) and a young man possibly sketching what Vesalius was dissecting. The man, however, may only be comparing Galenic anatomic observations with the findings of Vesalius. An older figure may be a symbolic rendition of Galen realizing that some of his anatomic observations 1400 years before were wrong. It is doubtful that an artist working with Vesalius was able to come close enough to the cadaver to accurately illustrate it in the sometimes carnival-like settings. From a medical student's description,³ Vesalius dissected rapidly and lectured while he dissected.

Later in a secluded area of the school in Padua, Vesalius may have shown the artist what he wanted drawn and labeled. There is no mention of body or organ preservation techniques at the time. Amputated heads were known to decompose more slowly, allowing the artist greater time to work. Possibly the artist had a photographic memory, allowing him to create drawings later, or from

From the Department of Radiology (J.H.S.), School of Medicine, University of North Carolina, Chapel Hill, North Carolina; and Department of Art History (S.J.), George Washington University, Washington, DC.

Please address correspondence to James Scatliff, MD, Department of Radiology, School of Medicine, CB7510, University of North Carolina, Chapel Hill, NC 27599-7510; e-mail: jiscatliff@med.unc.edu

<http://dx.doi.org/10.3174/ajnr.A3766>



FIG 2. Title page of *Fabrica*. The lower circle (right) may denote a figure representing Galen. The lower circle left is the anatomist Vesalius. The encircled figure above could be an artist drawing the dissection. Reprinted with permission from Saunders and O'Malley.²

sketches made as Vesalius dissected. The multiple figures in the frontispiece of the *Fabrica*, including one of Vesalius, were most probably completed in a studio rather than live. The nude figure clinging to the pillar on the left is most likely a topographic reminder of the anatomy in it.⁴

The artist, out of necessity, must have drawn rapidly, not only to avoid working with unpleasant odors but also in response to the urgency from Vesalius to complete his work. The time it took the artist to make individual drawings is not known. If Netter,⁵ 500 years later, can be used as a guide, multiple initial drawings are needed to portray the body in certain positions or in motion. For the final illustration of a stellate ganglion block, which Netter did for a CIBA Symposium article,⁵ as many as 8 preliminary sketches were used to show the position of the body, the stellate ganglion, and the needle direction for it. To produce the *Fabrica* with some dispatch, Vesalius may have encouraged the artist to maintain connections with dealers of art supplies and with skilled woodblock cutters in Venice. To prepare the *Fabrica* and the shorter *Epitome* drawings by Andreas Vesalius for printing, woodblock engravings were used. Some artists of the 16th century, including Albrecht Durer, cut illustrations directly into the woodblocks. The figures for Vesalius' work however were done by tracing the artist's drawing on the blocks.³

Although Venice was a major center for international book



FIG 3. Title page of *Cerebri Anatome* (2nd ed, 1664).⁸ Illustration shows Willis on the right of the cadaver. The figure in the left foreground may be Christopher Wren. Courtesy of Cushing/Whitney Medical Library, Yale University.

publication at the time, Vesalius decided to have both the *Fabrica* and the *Epitome* printed in Basel. What is amazing, 200 of the blocks survived until World War II, when they were destroyed in the Allied bombing of Munich. They had been discovered in the 1930s in an attic storage area of the University of Munich by Wiegand, who described them in the *Three Vesalian Essays*.³ The completed woodcut blocks were most likely shipped from Venice to Milan and then over the Alps to Basel in August 1542. The mode of transport of the blocks, the largest being approximately 10 × 17 inches (25.4 × 43.18 cm) is not known.

Basel, in Reformation Europe, with its political diversity and location on the other side of Alps, was farther from Rome and the possible prohibitions of the Church. It had also begun to rival Venice in the superiority of its printing. The Basel publisher of the *Fabrica* and *Epitome*, the philologist Johannes Oporinus,² directed a respected firm, known for the quality of its work. Oporinus was, in addition to being a publisher, a scholar of both Latin and Greek. Vesalius may have thought that with the philologist's help, his Latin text could be printed accurately. The marginal notes in Greek in the *Fabrica* may have been written by Oporinus. In addition, the distribution network in 1544 for the sale of his books was probably greater in Germany. It is interesting that Ve-

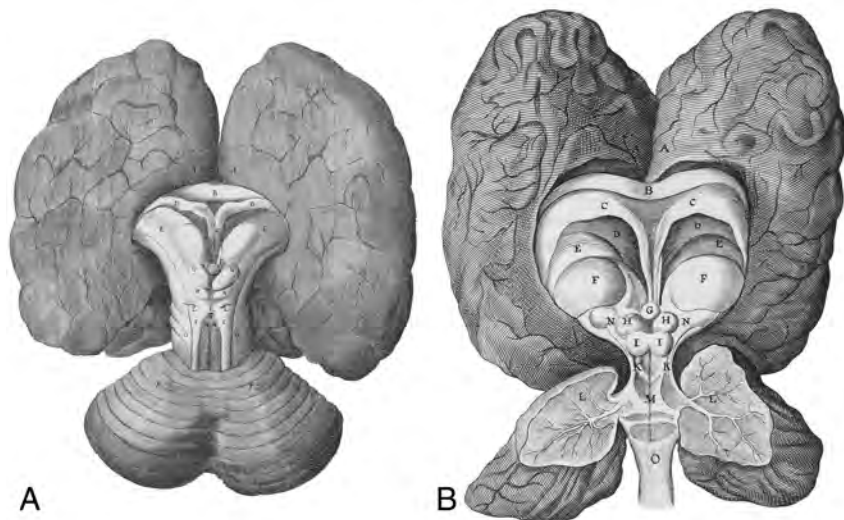


FIG 4. *Cerebri Anatome*, pages 43 and 51 (2nd ed, 1664).⁸ A, Base of the brain. B, Open brain. The darker color of the cerebral hemispheres and cerebellum is probably due to external fixation in wine and vinegar with the brain resting on its base in a receptacle. Courtesy of Rubenstein Rare Book and Manuscript Library, Duke University.



FIG 5. Surface (A) and interior (B) of a rabbit brain after 6 days showing the central area of brain not reached by fixative.

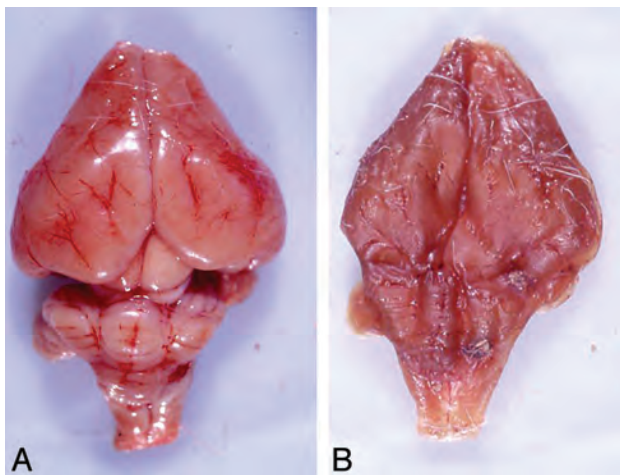


FIG 6. A, Rabbit brain without fixation 2 hours after removal from cranium. B, Loss of anatomic features of brain after 6 days without fixation.

salius, at the age of 28, left the University of Padua shortly after the publication of *Fabrica* and *Epitome* to become the personal physician to Emperor Charles V.

The anatomic information described in *Fabrica* and *Epitome* spread rapidly throughout Europe. It increased with a second printing of these books by the same firm in the 1550s by using the original woodblocks. The metal etching technique first used for armorial design replaced the woodblock technique beginning in the middle 1500s. The English engraver and publisher, Thomas Geminus, transferred drawings made for the *Fabrica* woodcuts to copper plates in 1545.⁶ By the middle of the 17th century, copper etching was used for the illustration of the anatomic observations of Thomas Willis and the Oxford school.

The first recording of Willis' brain dissection and observations came in his work, the *Cerebri Anatome*.⁷ It is known from a letter that Richard Lower, one of Willis' students, wrote to Robert Boyle that Willis began his human brain dissections in the fall of 1660.⁸ The dissections were conducted in the rooms of Christ Church, Willis' Oxford school, and in Willis' home and laboratory in Beam Hall, on Merten Street in Oxford. Willis gave Lower, who was 10 years younger, credit in his preface in the *Cerebri Anatome* for being a "skillful anatomist whose knife and wit I willingly acknowledge."⁷ It may be that Lower and Willis, along with Willis' Oxford associates, Thomas Millington and Edmund King, were principally involved in not only procuring bodies but also in the removal and fixation of brains for study, description, and illustration. This group made it possible for Willis to take time from his busy Oxford clinical practice to make the observations and preparation for the *Cerebri Anatome*. Christopher Wren was asked to do the illustrations.

Wren, a graduate of Oxford's Wadham College, was known not only for his intelligence and inventive mind but as an excellent mathematician, model builder, and draftsman.⁹ Willis stated in the preface of the *Cerebri Anatome* that "Wren delineates with his most skillful hand many of the figures of the brain and skull whereby work might be more exact."⁷ The frontispiece of the second edition of the *Cerebri Anatome* (Fig 3) quite possibly depicts Willis examining, with colleagues, a cadaver brain that has been exposed. In the fashionable dress of the time, the opposing figure may be Wren, the ascendant architect of the restoration of Charles II.

In all probability, Wren did not draw the brain before fixation; the dark cerebral hemispheres suggest fixation performed with the cerebral hemispheres up and covered with fixative. The brain could then be sketched later, anatomically intact, by Wren. The use of "spirits of wine" for organ preservation⁸ was described by Robert Boyle in the mid-1600s. Most likely the wine used was port, due to its higher alcohol content, mixed with vinegar. William Petty, an early Oxford colleague of Willis, purportedly kept a

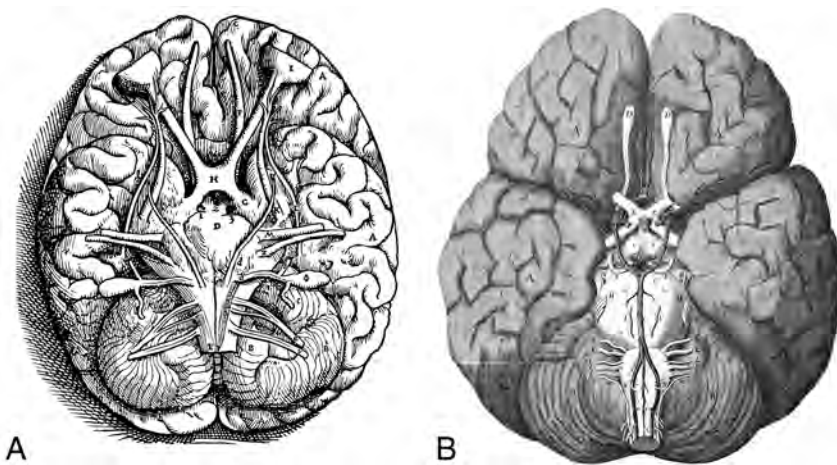


FIG 7. A, *Fabrica*, Book VII, Plate 24. The brain stem and nerves are inaccurately drawn due either to lack of fixation or unsatisfactory removal from the cranium. B, *Cerebri Anatome*, page 25. The brain stem with nerves and vessels, including the circle of Willis, is shown by Wren almost as in an architectural drawing. *Fabrica* courtesy of D. Garrison, Department of Classics, Northwestern University. *Cerebri Anatome* courtesy of Rubenstein Rare Book and Manuscript Library, Duke University.

corpse “soused and pickled.”⁸ With the brain resting on the bottom of the container, the fixative was unable to reach its interior; the Wren figures (Fig 4) from the *Cerebri Anatome* seem to bear this out. This observation is replicated with rabbit brains, as shown in Fig 5.

To study brain circulation, Willis, Lower, and Wren infused various liquids in the internal carotid arteries before fixation. Lower wrote to Boyle that all parts of the brain “were imbued with the same color after the carotids were injected.”⁸ There was no indication from Lower, however, that fixation of the brain was performed by carotid artery injection. The fact that the Wren drawing showed the brain stem in white is a further point in favor of external fixation of the brain without the brain stem being reached by the fixative. An alternative consideration is that Wren decided to contrast the cerebrum in a darker color than the brain stem, though differences in fixation seem more likely. The desiccation of the unfixed rabbit brain at 6 days (Fig 6) emphasizes the difference in the unfixed Vesalian brain drawn 100 years previously. Blood vessels and cranial nerves are not shown, and the brain stem is not well-defined. On the other hand, the Wren illustrations, though showing considerable detail, have an almost architectural appearance. A brain drawn for Vesalius is contrasted with that of Wren in Fig 7.

The preparation for printing, the printing, and the sale of the first and second editions of *Cerebri Anatome* are of interest. It would appear that a skilled German-Dutch engraver living in the Oxford area etched Wren’s drawings onto copper plates, along with Willis Latin text, for printing in the shop of James (Fletcher) Flesher.⁷ The site of Flesher’s printery is unknown but was probably close to St. Paul’s Cathedral, London. The title page of the Quarto Edition cites Flesher as the printer and Roycroft as the printer of the smaller Octavo Edition in 1664. The title page also indicates that the financing was by James Martyn and James Allestry and that the books were sold by them in their shop at The Sign of the Bell, adjacent to the churchyard of St. Paul’s, in 1664.⁷ Martyn and Allestry were booksellers for the Royal Society,

which may have prompted Willis and Wren, Society members, to use their services. The Great Fire of London of 1666 destroyed both the printing houses and the booksellers’ shops around St. Paul’s. Fortunately, the first 2 editions of the *Cerebri Anatome* were printed and sold before the fire. In all probability, the fire caused the next editions to be published in Amsterdam. The same copper plates used in London were used in the 1668 Amsterdam editions. Further publication of the *Cerebri Anatome* in Latin occurred in Lyon, Geneva, Amsterdam, and Venice between 1676 and 1681.

Although interest in illustrations of human anatomy including the brain went forward in the 18th century, publication with the impact of the *Fabrica* and *Cerebri Anatome* was not equaled until the 19th century.

The next major anatomic text of this time was *Gray’s Anatomy*, published in the mid-19th century. Two physicians working together, Henry Gray and Henry Carter, Gray’s illustrator, brought superb anatomic and functional information forward. Carter’s illustrations still appear in the current 40th edition of the book,¹⁰ along with the helpful color diagrams, radiographs, and images, as well as tissue and cellular anatomy revealed so clearly with scanning electron micrographs.

The 20th century anatomists and their illustrators, Pernkopf, Sobotta, Hollingshead, and Netter, to name but a few, have advanced the knowledge of the human brain and body immensely, beginning with the seminal works of Vesalius, Willis, and their illustrators.

Acknowledgments

The authors thank Jeremy Boomhower for his help in preparing the manuscript and Dwight Bellinger, DVM, for the preparation of the animal brains.

REFERENCES

1. Singer C. *Vesalius on the Human Brain*. London: Oxford University Press; 1952
2. Saunders JB, O’Malley CD. *The Illustrations from the Works of Andreas Vesalius of Brussels, 1514–1564*. Berkeley: University of California Press; 1950
3. Weigland W. *Three Vesalian Essays*. New York: Macmillan; 1952
4. Lind LR. *The Epitome of Andreas Vesalius*. New York; 1946
5. Netter FJ. *A Medical Illustration at Work*. *CIBA Symp* 1949;10:1087–92
6. Furdell EL. *Publishing and Medicine in Early Modern England*. Rochester, New York: University of Rochester Press; 2002
7. Willis T. *Cerebri Anatome*. 2nd ed. London, UK; Flesher J, 1664
8. Hughes JT. *Thomas Willis: 1621–1675: His Life and Work (Eponymists in Medicine Series)*. Dorchester, UK: Dorset Press; 1991
9. Jardine L. *On a Grand Scale: The Outstanding Career of Sir Christopher Wren*. London: HarperCollins; 2002
10. Standring S. *Gray’s Anatomy*. 40th ed. London, UK: Churchill Livingstone Elsevier; 2008

Long-Term White Matter Changes after Severe Traumatic Brain Injury: A 5-Year Prospective Cohort

J. Dinkel, A. Drier, O. Khalilzadeh, V. Perlberg, V. Czernecki, R. Gupta, F. Gomas, P. Sanchez, D. Dormont, D. Galanaud, R.D. Stevens, and L. Puybasset for NICER (Neuro Imaging for Coma Emergence and Recovery) Consortium



ABSTRACT

BACKGROUND AND PURPOSE: Extensive white matter damage has been documented in patients with severe traumatic brain injury, yet how this damage evolves in the long term is not well understood. We used DTI to study white matter changes at 5 years after traumatic brain injury.

MATERIALS AND METHODS: There were 8 healthy control participants and 13 patients with severe traumatic brain injury who were enrolled in a prospective observational study, which included clinical assessment and brain MR imaging in the acute setting (< 6 weeks) and 2 years and 5 years after injury. Only subjects with mild to moderate disability or no disability at 1 year were included in this analysis. DTI parameters were measured in 20 different brain regions and were normalized to values obtained in an age-matched control group.

RESULTS: In the acute setting, fractional anisotropy was significantly lower in the genu and body of the corpus callosum and in the bilateral corona radiata in patients compared with control participants, whereas radial diffusivity was significantly ($P < .05$) higher in these tracts. At 2 years, fractional anisotropy in these tracts had further decreased and radial diffusivity had increased. No significant changes were detected between 2 and 5 years after injury. The baseline radial diffusivity and fractional anisotropy values in the anterior aspect of the brain stem, genu and body of the corpus callosum, and the right and left corona radiata were significantly ($P < .05$) associated with neurocognitive sequelae (including amnesia, aphasia, and dyspraxia) at year 5.

CONCLUSIONS: DTI changes in major white matter tracts persist up to 5 years after severe traumatic brain injury and are most pronounced in the corpus callosum and corona radiata. Limited structural change is noted in the interval between 2 and 5 years.

ABBREVIATIONS: FA = fractional anisotropy; LI = axial diffusivity; Lt = radial diffusivity; MD = mean diffusivity; TBI = traumatic brain injury

Traumatic brain injury (TBI) represents a significant public health burden around the globe and is an important cause of death and lifelong disability.¹ Severe TBI accounts for only 10% of

these injuries, but it involves an extended stay in intensive care units and may cause subsequent long-term functional disability that needs long-term inpatient and outpatient rehabilitation.²

Beside focal lesions, moderate and severe TBI is associated with diffuse axonal injuries that manifest with little or no apparent damage in conventional neuroimaging but can be seen post-mortem on microscopy studies.³ Diffuse axonal injury can lead to a disconnection of critical cortical and subcortical pathways and might represent a neural basis for the cognitive dysfunction seen in the long term after TBI.³ Because conventional diagnostic imaging fails to appreciate the burden of microstructural white matter damage that occurs in TBI, it has limited ability to predict long-term outcome in a broad range of cognitive behavioral and functional impairments. DTI is an MR imaging technique that measures the properties of water diffusion.^{4,5} The degree of diffusion is characterized by 3 eigenvectors representing the diffusion in each orthogonal direction. Diffusion in white matter is particularly limited and anisotropic because of physical obstacles to water diffusion imposed by the myelin and axon membranes.^{6,7} The diffusion properties are believed to reflect

Received January 4, 2013; accepted after revision March 20.

From the Department of Radiology (J.D., O.K., R.G.), Massachusetts General Hospital, Harvard Medical School, Boston, Massachusetts; Department of Radiology (J.D.), University Hospital Heidelberg, Heidelberg, Germany; Departments of Neuroradiology (A.D., D.D., D.G.), Neurology (V.C.), and Anesthesiology and Intensive Care (P.S., L.P.), Pitié Salpêtrière Hospital, Assistance Publique-Hôpitaux de Paris, France; INSERM, UMR5 678 (V.P.) and INSERM, CRICM UMR 5975 (V.C.), Université Pierre et Marie Curie-Paris 6, Paris, France; Department of Anesthesiology and Intensive Care (F.G.), Louis Mourier Hospital, Colombes, France; and Division of Neuroscience Critical Care (R.D.S.), Department of Anesthesiology Critical Care Medicine, Johns Hopkins University School of Medicine, Baltimore, Maryland.

This study was funded by a grant from the French Ministry of Health (Projet Hospitalier de Recherche Clinique registration #P051061 [2005]) and from departmental funds from the Assistance Publique-Hôpitaux de Paris.

Please address correspondence to Pr. Louis Puybasset, Neuro-réanimation Chirurgicale Babinski, Département d'Anesthésie-Réanimation, Groupe Hospitalier Pitié-Salpêtrière, Université Pierre et Marie Curie, Paris 6, 47-83, Bd de l'hôpital; 75013 Paris, France; e-mail: louis.puybasset@psl.aphp.fr; louis.puybasset@me.com

Indicates open access to non-subscribers at www.ajnr.org

Evidence-Based Medicine Level 2.

<http://dx.doi.org/10.3174/ajnr.A3616>

many factors, including myelination and axonal attenuation and integrity.^{6,7}

DTI has shown promising results for depiction of neuropathologic changes in TBI, in which the microarchitecture of white matter may be altered. Although previous studies have shown the association of changes in DTI parameters of the white matter with different types of TBI (mild, moderate, or severe; in acute or chronic phase) and its outcome,⁶⁻¹⁵ limited evidence is available on the pattern of long-term changes in patients with chronic severe TBI. Studies have suggested evidence of active brain remodeling and neuroplasticity¹⁶ after TBI in children.¹⁷ However, the long-term white matter modifications in adults with TBI need to be further characterized. Knowledge of the time course and extent of these changes might yield better approaches for therapy and rehabilitation.¹⁸ Here, we undertook a prospective longitudinal study to determine the nature of white matter changes in a subset of patients with severe TBI who had moderate or no gross disability 1 year after injury by using DTI imaging. We hypothesized that microstructural cerebral alterations identified within the first weeks after the severe TBI would persist 2 and 5 years after injury.

MATERIALS AND METHODS

The institutional review board of Pitié Salpêtrière Hospital approved this study protocol. Informed consent was obtained from all study participants (legally authorized representative of the patients during the acute stage, patients themselves after recovery of consciousness, and healthy volunteers who served as control participants).

Patients

Patients with severe TBI (Glasgow Coma Scale, 3–8; posttraumatic amnesia > 7 days; and loss of consciousness > 24 hours¹) who were admitted to the intensive care unit were enrolled in this prospective study between March 2005 and March 2008. Inclusion criteria were 1) adult patients (≥ 18 years) and 2) moderate or no disability at 1 year (Glasgow Outcome Scale at 4 or 5). Exclusion criteria were 1) moribund patients (expected survival < 24 hours); 2) physiologic instability (eg, from hemodynamic instability, increased intracranial pressure, and/or rapidly deteriorating respiratory function) that would preclude MR imaging; 3) contraindication to the MR imaging; 4) penetrating head injury; and 5) a central nervous system condition such as stroke, brain tumor, or a neurodegenerative disease preceding TBI.

Control Participants

Eight age- and sex-matched healthy volunteers ($n = 8$; mean age, 32 ± 8 years; age range, 22–49 years; men) were enrolled in this study. They did not have a history of TBI or neurologic disease.

Clinical Data Collection

We collected data by using standardized case report forms including demographics, Glasgow Coma Scale, and cranial CT scan results. Head CT scans were performed within 48 hours after admission to the intensive care unit. A central study monitoring was performed to ensure data accuracy. The Glasgow Outcome Scale was assessed for all patients at 1 year post TBI. Baseline MR imaging was acquired as soon as clinically feasible (within 6 weeks after TBI). The MR imaging scans were repeated at 2 and 5 years after the TBI.

At 5 years, patients underwent a comprehensive neuropsychological evaluation. The level of disability on the basis of the Glasgow Outcome Scale, the disability rating scale, the extended Glasgow Outcome Score, and the modified Rankin Scale were assessed, the results of which will be reported separately. For the purposes of this study, patients were classified according to whether they had moderate cognitive sequelae (including amnesia, aphasia, and dyspraxia).

MR Imaging

Control participants underwent MR imaging by use of the same acquisition protocol as in the patients and underwent subsequent imaging after 2 years. MR imaging was performed on a 1.5T system (Signa; GE Healthcare, Milwaukee, Wisconsin) with the participants under sedation and mechanical ventilation for the first MR imaging and without any sedation for the follow-up MR imaging scans. The acquisition protocol included morphologic sequences (FLAIR, T2*-weighted gradient-echo, T2-weighted turbo spin-echo, T1-weighted 3D inversion recovery fast-spoiled gradient recalled), MR spectroscopy, and DTI. Only DTI results are presented in this study. DTI was performed by use of the following parameters: axial plane; 1 volume at b-value, 0 s/mm²; 24 directions; diffusion b-value, 700 s/mm²; section thickness, 5 mm; no gap; 20 sections; field of view, 32 × 32 cm; matrix size, 128 × 128; and 2 averages. The inferior section of the DTI acquisition was positioned at the junction between the pons and the medulla oblongata. Additional details on the DTI acquisition protocol are available in our prior study.¹⁹

MR Imaging Analysis

DTI images were preprocessed by use of FSL software (<http://www.fmrib.ox.ac.uk/fsl>).²⁰ The local diffusion parameters, namely, fractional anisotropy (FA), mean diffusivity (MD), axial diffusivity (L1), and radial diffusivity (Lt), were calculated²¹ for the entire brain in each patient and control participant. To make diffusion measures comparable between patients and participants, the FA, MD, L1, and Lt maps were registered on a 1 × 1 × 1 mm³ standard space image (Montreal Neurological Institute 152 space) by use of the tract-based spatial statistics procedure.²² Correction for distortions from eddy currents was performed by use of the $b=0$ images. The whole brain, including the pathologic regions, was registered by use of an automated nonrigid technique, and individual FA, MD, L1, and Lt values were projected on an alignment-invariant template for the brain. This procedure maps all available information to a common brain template and avoids misalignment among participants. A total of 20 ROIs for DTI analysis were selected, based on the ICBM-DTI-81 white matter atlas.²³ This atlas consists of 48 white matter tracts. Because some of these ROIs are very small and are subject to partial volume effects, we merged the initial 48 white matter tracts into 20 larger regions as published previously^{19,24} (in posterior fossa: 1- middle cerebellar peduncle; 2- anterior brain stem; 3- posterior brain stem; 4- right cerebral peduncle; 5- left cerebral peduncle; in deep brain: 6- genu of the corpus callosum; 7- body of the corpus callosum; 8- splenium of the corpus callosum; 9- right side anterior arm of the internal capsule; 10- left side anterior arm of the internal capsule; 11- right side posterior arm of the internal cap-

sule; 12- left side posterior arm of the internal capsule; in superficial brain regions: 13- right stratum sagittale; 14- left stratum sagittale; 15- right superior longitudinal fasciculus; 16- left superior longitudinal fasciculus; 17- right external capsule; 18- left external capsule; 19- right corona radiata; 20- left corona radiata). The regional DTI parameter extraction consisted of 3 steps: a nonlinear registration of the FA map to a template (provided by FSL), a projection of FA onto the FA template skeleton representing the centers of all tracts (also provided by FSL), and averaging of FA measures within the 20 ROIs restricted to the skeleton. The ROIs are placed automatically after nonrigid registration on a defined position on the common brain template. Furthermore, the registered maps were visually verified and were compared with the template. In total, the average values of FA, MD, L1, and Lt in these 20 ROIs resulted in 80 DTI biomarkers for each participant.

During the 5 years needed for the study, our MR scanner underwent 2 software updates. The sequence parameters were kept identical except for the TE, which had to be slightly modified (initial TE, 81 ms; then 85.9 ms; and finally 84.3 ms). To account for TE-related variability in raw DTI values and to make our results comparable with future studies, we normalized the raw DTI parameter values for each participant. For this purpose, every time our scanner undergoes a software, material, or sequence update, we scan several healthy participants for DTI metric normalization. We have constituted a very large dataset of reference values for our scanner that we use routinely for normalization in our clinical workflow and in previous studies.^{19,24} For this study, the raw FA, MD, L1, and Lt values in each of the 20 preselected ROIs of both patients and control participants were divided by the mean values of the corresponding reference group. Further details of MR image processing and normalization are provided in a previous publication.¹⁹

Statistical Analysis

We performed the statistical analysis by using SPSS software (version 16.0; IBM, Armonk, New York). The required sample size to detect a significant association at $\alpha = 0.05$ and with a power of 80% was estimated to be 15. Continuous variables are expressed as mean \pm standard deviation. Variables had normal distribution (according to the Kolmogorov-Smirnov test); therefore, parametric tests were used. One-way repeated-measures ANOVA was used to compare different DTI values between baseline and the follow-up steps, in patients with severe TBI. *P* values were corrected for multiple testing²⁵ (Bonferroni method), and only the corrected *P* values are presented in the study. One-way ANOVA (with Bonferroni post hoc) was used to compare baseline DTI values between healthy control participants and patients with TBI with and without neurocognitive sequelae. An independent sample *t* test was used to compare changes (year 2 vs baseline) in DTI values between patients and control participants. The level of significance was set at *P* < .05.

RESULTS

A total of 15 patients met the inclusion criteria during the study period. Two patients were dropped because of unwillingness to undergo the follow-up scans. There was no death or loss to follow-up in the remaining patients. The analysis was done in the 13

Patient characteristics

		Range
Age (y)	32.4 (9.0)	(18–49)
Men/women, <i>n</i>	13/0	—
GCS at admission, <i>n</i> (SD)	6 (4)	(3–8)
ICU stay duration (d)	47.5 (23.1)	(10–97)
Assisted ventilation duration (d)	33.1 (16.9)	(9–72)
Type of accident, <i>n</i> (%)		
MVA	10 (77)	—
Assault, fall, other	3 (23)	—
Hematoma, <i>n</i> (%) ^a		
Epidural	3 (23)	—
Subdural	1 (8)	—
Subarachnoid hemorrhage	8 (61)	—
Midline shift	3 (23)	—
Compressed third ventricle	4 (31)	—
Contusion, <i>n</i> (%) ^b	10 (77)	—
Neurosurgical intervention, <i>n</i> (%)	2 (15)	—
Neurologic sequelae, <i>n</i> (%)		
Amnesia	2 (15)	—
Aphasia	1 (8)	—
Dyspraxia	2 (15)	—

Note:—Variables are presented as mean (standard deviation) or number (percentage).

GCS indicates Glasgow Coma Scale; ICU, intensive care unit; SD, standard deviation; MVA, motor-vehicle collision.

^a Hematoma was defined as an area spontaneously hyperdense on the first CT scan.

^b Contusion was defined as a focal area appearing hypodense or of mixed density on the CT scan.

patients with severe TBI (Table 1) and in 8 control participants. There was no significant difference in age between patients and healthy control participants (patients: mean age, 32 \pm 9 years; age range, 18–49 years; control participants: mean age, 32 \pm 8 years; age range, 22–49 years). Initial (baseline) scan was obtained at a mean of 22 \pm 12 days (range, 12–58 days) after injury. Repeated scans were performed at a mean of 2.0 years (range, 1.8–2.1 years) and 5.0 years (range, 4.7–5.4 years) after TBI. The mean rescan time for healthy control participants was 2.0 \pm 0.08 years. The automatic segmentation software accurately recognized the 20 ROIs in all patients, even in the presence of intracranial pathologic features. A typical set of FLAIR and FA images of a patient is shown in Fig 1.

For healthy control participants, there was no difference in white matter measurable by DTI between baseline and year 2. In patients with severe TBI at baseline, FA values were significantly lower at the genu and body of the corpus callosum and the bilateral corona radiata compared with control participants (Fig 2), whereas Lt was significantly higher in the same regions. Repeated-measures ANOVA in patients with TBI (comparing baseline vs year 2 and year 5) revealed significant changes in FA and Lt (*P* < .05) in the anterior aspect of the brain stem, genu and body of the corpus callosum, and bilateral corona radiata (Fig 2). In a post hoc analysis, results were significant for baseline vs year 2; however, no significant difference was observed between year 2 and year 5.

Regarding L1 and MD, no significant difference was observed between patients and control participants at baseline. Repeated-measures ANOVA indicated that L1 did not significantly change during the 5-year observation period, whereas MD increased significantly in the genu and body of the corpus callosum and the bilateral corona radiata from baseline to 2 years (post hoc analysis

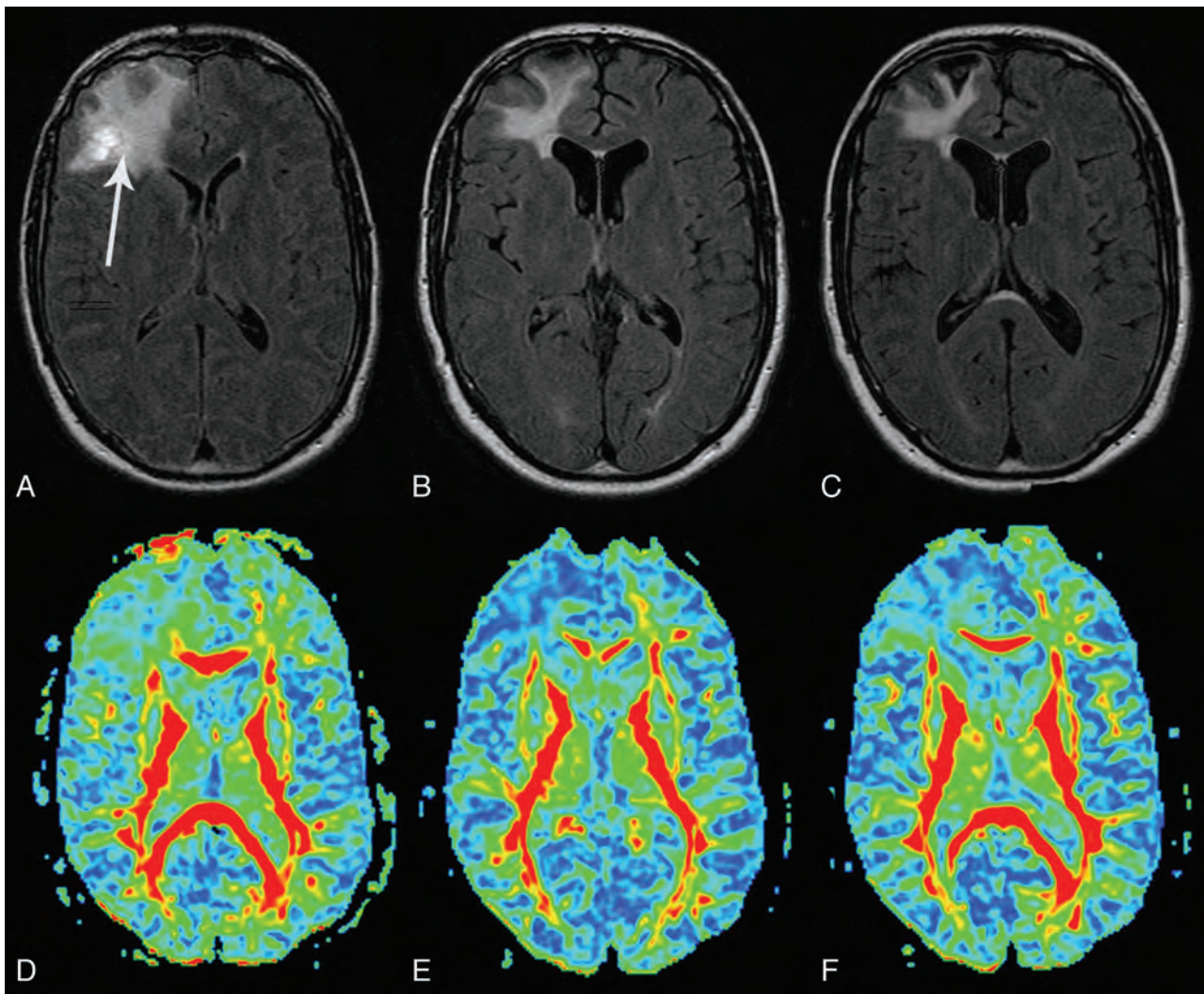


FIG 1. MR images of a patient with severe TBI at baseline (A and D), year 2 (B and E), and year 5 (C and F). On the conventional FLAIR images (A–C), the hyperintensity of the right frontal lobe (*arrow*) decreases with time with some minimal atrophic changes. The corresponding FA maps (D–F) are presented. In the acute setting, the normalized FA was slightly reduced in the genu (0.80) and body (0.92) of the corpus callosum and in the bilateral corona radiata (right: 0.96; left: 0.98) compared with control participants (normalized value = 1). At 2 years, most of the normalized FA values in these tracts had further decreased: genu (0.81) and body (0.79) of corpus callosum; corona radiata (right: 0.89; left: 0.96). At 5 years, the values slightly increased: genu (0.82) and body (0.85) of corpus callosum; corona radiata (right: 0.92; left: 0.97).

was significant for baseline vs year 2 but was not significant for year 2 vs year 5).

As presented in Fig 3, there were significant changes (year 2 vs baseline) in normalized FA (Fig 3A) and Lt (Fig 3B) at the anterior aspect of the brain stem, genu and body of the corpus callosum, and the right and left corona radiata in patients with TBI vs healthy control participants. At 5 years, neurocognitive sequelae were present in 5 patients (amnesia [$n=2$], aphasia [$n=1$], and dyspraxia [$n=2$]).

The baseline Lt and FA values at the anterior aspect of the brain stem, genu and body of the corpus callosum, and right and left corona radiata were significantly associated ($P < .05$) with these neurocognitive sequelae at year 5 (including amnesia, aphasia, and dyspraxia) (Fig 4).

DISCUSSION

In this study, we found that FA in the genu and body of the corpus callosum and in the bilateral corona radiata were significantly

lower in patients with severe TBI compared with control participants; these measures decreased significantly for the first 2 years after trauma and remained stable thereafter. The Lt in these same structures increased in the first 2 years and then remained stable.

These results indicate widespread white matter damage occurring in the setting of severe TBI and persisting with time, a finding that has been previously reported.^{14,26} The changes observed in FA were driven by alterations in radial (and not axial) diffusivity, suggesting that the underlying white matter alterations could be related to changes in myelin rather than axonal injury.^{6,27} The absence of changes for more than 2 years after TBI indicates that the most dynamic structural changes, and the window for therapeutic and rehabilitative intervention, may be limited beyond that time point.²⁸

A pattern suggestive of myelin damage in white matter rather than axonal injury has been identified by other groups.^{8,14,26,29} Ewing-Cobbs et al⁸ evaluated 41 children at a

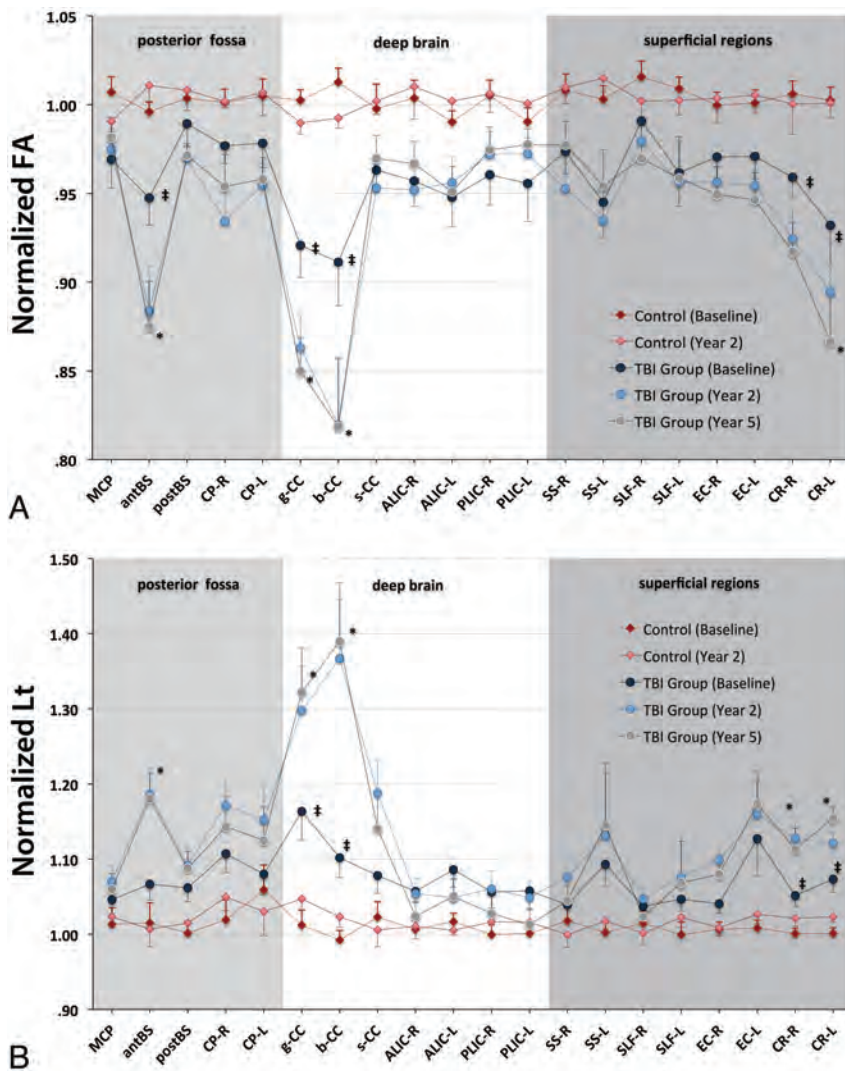


FIG 2. Normalized FA (A), and Lt (B) values of patients and control participants at baseline and follow-up steps. The x-axis represents the ROIs (in posterior fossa: 1- MCP: middle cerebellar peduncle; 2- antBS: anterior brain stem; 3- postBS: posterior brain stem; 4- CP-R: right cerebral peduncle; 5- CP-L: left cerebral peduncle; in deep brain: 6- g-CC: genu of the corpus callosum; 7- b-CC: body of the corpus callosum; 8-second-CC: splenium of the corpus callosum; 9- ALIC-R: right side anterior arm of the internal capsule; 10- ALIC-L: left side anterior arm of the internal capsule; 11- PLIC-R: right side posterior arm of the internal capsule; 12- PLIC-L: left side posterior arm of the internal capsule; in superficial brain regions: 13- SS-R: right stratum sagittale; 14- SS-L: left stratum sagittale; 15- SLF-R: right superior longitudinal fasciculus; 16- SLF-L: left superior longitudinal fasciculus; 17- EC-R: right external capsule; 18- EC-L: left external capsule; 19- CR-R: right corona radiata; 20- CR-L: left corona radiata). There were no significant differences in DTI parameters between baseline and year 2 in the control group and between year 2 and year 5 in the TBI group. †: $P < .05$; for comparison of baseline values between control participants and patients (corrected P). *: $P < .05$; for repeated-measures ANOVA in the patient group between baseline and follow-up steps. Data are presented as mean and standard error of mean (handles). The connection lines are for clarity.

mean of 39 months after severe TBI, demonstrating (compared with a control group) significantly reduced corpus callosum FA and increased Lt, whereas L1 remained unchanged. This pattern was also seen in a recent study by Farbota et al²⁹ on 12 patients with severe TBI. In a prospective cohort, Newcombe et al¹⁴ studied 68 patients who underwent MR imaging at a median of 11.8 months (range, 6.6 months to 3.7 years) after injury, finding significant decrements in FA in multiple structures including the corpus callosum, changes which were

associated with increases in Lt and with clinical outcomes. Sidaros et al²⁶ studied patients with severe TBI at 2 and 12 months after injury, demonstrating reductions in corpus callosum FA and increases in Lt. At 1 year, FA remained decreased and Lt increased particularly in patients with unfavorable outcome. Other authors have had slightly different results: In a study of 37 patients who underwent MR imaging with DTI at a mean of 8.9 years after TBI, Kraus et al⁶ found reduced FA in conjunction with increases in both Lt and L1 compared with matched control participants.

Our results also show that baseline FA and Lt measures of DTI (at the genu and body of the corpus callosum, anterior aspect of the brain stem, and right and left corona radiata) are associated with long-term cognitive sequelae in patients with severe TBI. Predicting neurobehavioral outcome in TBI is challenging because patients with similar clinical and radiologic characteristics in the acute phase of TBI may have markedly different outcomes ranging from death to complete recovery.^{2,13} In a prospective study, decreased regional FA in 4 major white matter tracts at 8 weeks was predictive of unfavorable outcome at 12 months.²⁶ Available evidence indicates that damage to critical areas such as the corpus callosum or brain stem correlate most highly with poor post-TBI prognosis.^{26,28,30} In a large multicenter study, we recently generated and validated a stringent prognostic model by integrating a composite DTI score of white matter tracts with available clinical and CT-scan variables. Furthermore, DTI metric analysis has not only the potential to be applied clinically in an individual patient for prognosis assessment but also may be used in follow-up to monitor the response to therapeutic and rehabilitation measures.

Some limitations should be considered on interpretation of our results. TBI is biologically and clinically heterogeneous and may have a range of radiologic features.² First, the results of this study could not be extrapolated to mild or moderate TBI, in which different temporal changes might occur. In addition, the heterogeneous spatial distribution of DTI and its various pathologic sequelae were a real challenge for ROI-based statistical analysis. In our study, the nonhomogeneous pattern of white matter injury was obvious in superficial brain regions, and

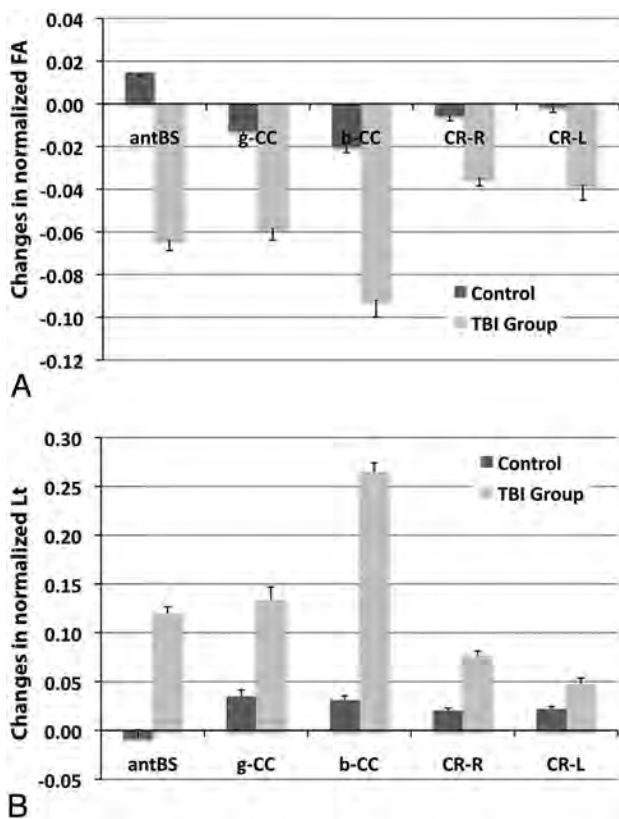


FIG 3. The changes (year 2 vs baseline) in normalized FA (A) and Lt (B) in the presented ROIs were significantly higher in the patients vs healthy control participants. $P < .05$ for comparison between patients and control participants in all of the presented ROIs.

the high variability of DTI metrics observed in these regions was probably the result of the heterogeneous nature of the pathologic findings in TBI.

Furthermore, because we did not perform imaging between baseline and 2 years on these patients, we could not precisely identify at which time point the white matter stops evolving. Given the small patient sample and the heterogeneity of the conventional MR imaging findings, we did not analyze the conventional morphologic sequences. We reported the results of the DTI metrics only.

In an ideal setting, brain tissue diffusion measurements should be independent of the MR imaging scanner and image acquisition parameters. However, a recent study has indicated variations in apparent diffusion coefficients and FA values when images are acquired on different scanners or when different acquisition protocols are used.¹⁹ Therefore, we implemented a normalization step, which makes our estimates of DTI parameters comparable with results found in other groups despite slightly different MR imaging parameters. We believe that this approach helps to overcome data heterogeneity in quantitative DTI studies and can be an important step in clinical application of quantitative DTI measures. This study was designed and conducted based on a predetermined sample size of 15 patients to have a power = 80% and $\alpha = 0.05$. Although we enrolled 15 patients in this study, 2 were dropped because of unwillingness to undergo the follow-up scan at 5 years. Therefore, larger long-term cohorts are needed to pro-

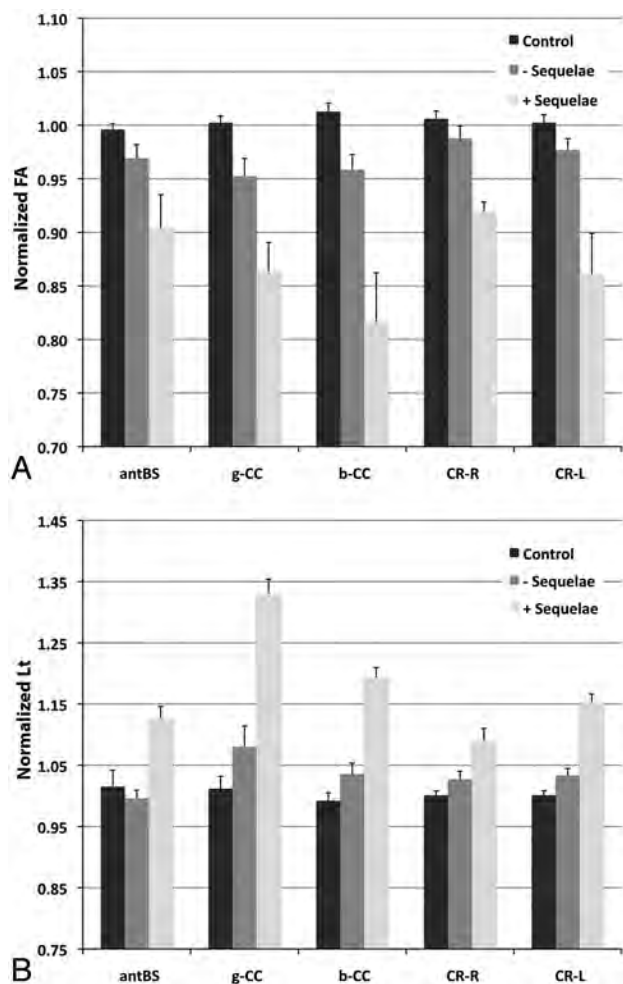


FIG 4. The normalized FA (A) and Lt (B) values at baseline were significantly different in patients with cognitive sequelae at year 5 (including amnesia, aphasia, and dyspraxia) vs healthy control participants. $P < .05$ for ANOVA among the groups and for comparison between healthy control participants and patients with sequelae in all of the presented ROIs.

vide a more comprehensive assessment and more thorough subgroup analysis.

CONCLUSIONS

This study demonstrates significant and durable changes in the corpus callosum and in the corona radiata in a cohort of patients with TBI who were observed during a 5-year period. These alterations evolved significantly between the initial assessment and up to 2 years from the injury, beyond which few additional changes were seen. These data suggest that therapeutic and rehabilitative measures after severe TBI may be monitored by DTI during an initial time window, beyond which the microarchitecture of the white matter measured by TBI stop evolving.

Disclosures: Vincent Perlberg—RELATED: Grant: Program "Investissements d'avenir" ANR-10-IAIHU-06; UNRELATED: Patents (planned, pending or issued): Patent Number FR 2975806 (A1).* Didier Dormont—RELATED: Grant: French Ministry of Health.* Comments: PHRC national (French Ministry of Health), Projet Hospitalier de Recherche Clinique #P051061. Damien Galanaud—RELATED: French Ministry of Health.* Comments: Projet Hospitalier de Recherche Clinique #P051061; UNRELATED: Consultancy: Olea Medical; Payment for Development of Educational Presentations: Sanofi Aventis; Travel/Accommodations/Meeting Expenses Unrelated to Activities

Listed: Olea Medical. Louis Puybasset—RELATED: Grant: DRC,* APHP,* Comments: Funding by the French government, PHRC 2005 paid for the software used in the study; UNRELATED: Patents (planned, pending or issued): Patent published (no fees or money), Comments: <http://patentscope.wipo.int/search/en/detail.jsf?docId=WO2012160316&recNum=1&maxRec=&office=&prevFilter=&sortOption=&queryString=&tab=PCT+Biblio>. *Money paid to institution.

REFERENCES

1. Saatman KE, Duhaime AC, Bullock R, et al. **Classification of traumatic brain injury for targeted therapies.** *J Neurotrauma* 2008;25:719–38
2. Narayan RK, Michel ME, Ansell B, et al. **Clinical trials in head injury.** *J Neurotrauma* 2002;19:503–57
3. Smith DH, Meaney DF, Shull WH. **Diffuse axonal injury in head trauma.** *J Head Trauma Rehabil* 2003;18:307–16
4. Wada T, Asano Y, Shinoda J. **Decreased fractional anisotropy evaluated using tract-based spatial statistics and correlated with cognitive dysfunction in patients with mild traumatic brain injury in the chronic stage.** *AJNR Am J Neuroradiol* 2012;33:2117–22
5. Basser PJ, Mattiello J, LeBihan D. **MR diffusion tensor spectroscopy and imaging.** *Biophys J* 1994;66:259–67
6. Kraus MF, Susmaras T, Caughlin BP, et al. **White matter integrity and cognition in chronic traumatic brain injury: a diffusion tensor imaging study.** *Brain* 2007;130:2508–19
7. Kumar R, Husain M, Gupta RK, et al. **Serial changes in the white matter diffusion tensor imaging metrics in moderate traumatic brain injury and correlation with neuro-cognitive function.** *J Neurotrauma* 2009;26:481–95
8. Ewing-Cobbs L, Prasad MR, Swank P, et al. **Arrested development and disrupted callosal microstructure following pediatric traumatic brain injury: relation to neurobehavioral outcomes.** *Neuroimage* 2008;42:1305–15
9. Akpinar E, Koroglu M, Ptak T. **Diffusion tensor MR imaging in pediatric head trauma.** *J Comput Assist Tomogr* 2007;31:657–61
10. Wilde EA, Chu Z, Bigler ED, et al. **Diffusion tensor imaging in the corpus callosum in children after moderate to severe traumatic brain injury.** *J Neurotrauma* 2006;23:1412–26
11. Wilde EA, McCauley SR, Hunter JV, et al. **Diffusion tensor imaging of acute mild traumatic brain injury in adolescents.** *Neurology* 2008;70:948–55
12. Lipton ML, Kim N, Park YK, et al. **Robust detection of traumatic axonal injury in individual mild traumatic brain injury patients: intersubject variation, change over time and bidirectional changes in anisotropy.** *Brain Imaging Behav* 2012;6:329–42
13. Betz J, Zhuo J, Roy A, et al. **Prognostic value of diffusion tensor imaging parameters in severe traumatic brain injury.** *J Neurotrauma* 2012;29:1292–305
14. Newcombe V, Chatfield D, Outtrim J, et al. **Mapping traumatic axonal injury using diffusion tensor imaging: correlations with functional outcome.** *PLoS One* 2011;6:e19214
15. Yuan W, Holland SK, Schmithorst VJ, et al. **Diffusion tensor MR imaging reveals persistent white matter alteration after traumatic brain injury experienced during early childhood.** *AJNR Am J Neuroradiol* 2007;28:1919–25
16. Levin HS. **Neuroplasticity following non-penetrating traumatic brain injury.** *Brain Inj* 2003;17:665–74
17. Wu TC, Wilde EA, Bigler ED, et al. **Longitudinal changes in the corpus callosum following pediatric traumatic brain injury.** *Dev Neurosci* 2010;32:361–73
18. Young JA, Tolentino M. **Neuroplasticity and its applications for rehabilitation.** *Am J Ther* 2011;18:70–80
19. Galanaud D, Perlberg V, Gupta R, et al. **Assessment of white matter injury and outcome in severe brain trauma: a prospective multi-center cohort.** *Anesthesiology* 2012;117:1300–10
20. Smith SM, Jenkinson M, Woolrich MW, et al. **Advances in functional and structural MR image analysis and implementation as FSL.** *Neuroimage* 2004;23 Suppl 1:S208–19
21. Pierpaoli C, Basser PJ. **Toward a quantitative assessment of diffusion anisotropy.** *Magn Reson Med* 1996;36:893–906
22. Smith SM, Jenkinson M, Johansen-Berg H, et al. **Tract-based spatial statistics: voxelwise analysis of multi-subject diffusion data.** *Neuroimage* 2006;31:1487–505
23. Mori S, Wakana S, Nagae-Poetscher L, et al. *MRI Atlas of Human White Matter.* Amsterdam: Elsevier; 2005
24. Luyt CE, Galanaud D, Perlberg V, et al. **Diffusion tensor imaging to predict long-term outcome after cardiac arrest: a bicentric pilot study.** *Anesthesiology* 2012;117:1311–21
25. Benjamini Y, Hochberg Y. **Controlling the false discovery rate: a practical and powerful approach to multiple testing.** *J Royal Stat Soc Ser B* 1995;57:289–300
26. Sidaros A, Engberg AW, Sidaros K, et al. **Diffusion tensor imaging during recovery from severe traumatic brain injury and relation to clinical outcome: a longitudinal study.** *Brain* 2008;131:559–72
27. Mac Donald CL, Dikranian K, Bayly P, et al. **Diffusion tensor imaging reliably detects experimental traumatic axonal injury and indicates approximate time of injury.** *J Neurosci* 2007;27:11869–76
28. Huisman TA, Schwamm LH, Schaefer PW, et al. **Diffusion tensor imaging as potential biomarker of white matter injury in diffuse axonal injury.** *AJNR Am J Neuroradiol* 2004;25:370–76
29. Farbota KD, Bendlin BB, Alexander AL, et al. **Longitudinal diffusion tensor imaging and neuropsychological correlates in traumatic brain injury patients.** *Front Hum Neurosci* 2012;6:160
30. Parvizi J, Damasio AR. **Neuroanatomical correlates of brainstem coma.** *Brain* 2003;126:1524–36

Patterns of Brain Structural Changes in First-Contact, Antipsychotic Drug-Naïve Patients with Schizophrenia

M. Filippi, E. Canu, R. Gasparotti, F. Agosta, P. Valsecchi, G. Lodoli, A. Galluzzo, G. Comi, and E. Sacchetti



ABSTRACT

BACKGROUND AND PURPOSE: Previous studies have suggested that structural changes do occur in the brain of patients with schizophrenia compared with healthy control participants. However, findings from such studies are inconclusive, probably because of the different methodologic approaches, the clinical heterogeneity of patient samples, and also the fact that patients enrolled were treated with antipsychotic drugs. The aim of this study was to investigate brain GM volumes and intrinsic structural WM changes in first-contact, antipsychotic drug-naïve patients with schizophrenia.

MATERIALS AND METHODS: A total of 43 first-contact, drug-naïve, patients with schizophrenia and 17 age-matched control participants were studied. All participants underwent T1-weighted MR imaging and DTI scans. Voxel-based morphometry and tract-based spatial statistics were used to compare GM volumes and WM DTI metrics between groups. MR imaging measures were correlated with the duration of the untreated psychosis and the clinical positive and negative symptoms.

RESULTS: Compared with control participants, patients with schizophrenia showed smaller volumes of the temporal, parietal, and occipital GM, and a pattern of decreased mean diffusivity and increased fractional anisotropy in the brain stem and cerebellum bilaterally, interhemispheric and cortico-cortical connections bilaterally, and right anterior and posterior limb of the internal capsule. In patients, decreased mean diffusivity and increased fractional anisotropy in several brain regions were related to a longer duration of the untreated psychosis and the severity of positive symptoms.

CONCLUSIONS: First-contact, drug-naïve, patients with schizophrenia present with volumetric and DTI changes, which correlated with their clinical features. This study increases our knowledge on the neural networks involved in the pathophysiologic mechanisms of schizophrenia.

ABBREVIATIONS: DARTEL = Diffeomorphic Anatomical Registration through Exponentiated Lie Algebra; DUP = duration of the untreated psychosis; FA = fractional anisotropy; MD = mean diffusivity; PANSS = Positive and Negative Syndrome Scales; MNI = Montreal Neurological Institute; TBSS = tract-based spatial statistics

In recent years, interest in the physiopathologic mechanisms of schizophrenia has increased dramatically. As normal brain functions are served by networks of cortical and subcortical areas,

disturbed communication (“dysconnectivity”) within and between brain regions may be the core pathologic feature of schizophrenia.¹ In this context, the contribution of neuroimaging techniques has proved to be relevant. Structural MR imaging studies have shown that reductions of GM volume occur in the brain of patients with schizophrenia compared with healthy control participants, though increased GM volumes of some subcortical regions have also been reported.² DTI studies of schizophrenic patients have disclosed an abnormal organization and integrity of several WM tracts of the brain. However, results are conflicting regarding which tracts are affected, with some DTI studies showing a marked involvement of the anterior pattern of brain WM regions in patients with schizophrenia, and others describing a posterior pattern of WM changes or even no difference compared with control participants.³

The inconclusive findings of previous studies are probably the result of the clinical heterogeneity of the samples and/or the dif-

Received November 16, 2012; accepted after revision February 4, 2013.

From the Neuroimaging Research Unit (M.F., E.C., F.A.) Institute of Experimental Neurology, Division of Neuroscience, and Department of Neurology (M.F., G.C.) San Raffaele Scientific Institute, Vita-Salute San Raffaele University, Milan, Italy; Department of Diagnostic Imaging (R.G., G.L.), Neuroradiology Unit, Brescia University School of Medicine, Spedali Civili, Brescia, Italy; Department of Mental Health (P.V., A.G., E.S.), Spedali Civili, Brescia, Italy; University Psychiatric Unit (P.V., E.S.), Brescia University School of Medicine, Brescia, Italy; Centre on Behavioural and Neurodegenerative Disorders (E.S.), Brescia University and EULO, Brescia, Italy.

Please address correspondence to Prof. Massimo Filippi, Neuroimaging Research Unit, Institute of Experimental Neurology, Division of Neuroscience, San Raffaele Scientific Institute, Vita-Salute San Raffaele University, Via Olgettina, 60, 20132 Milan, Italy; e-mail: m.filippi@hsr.it



Indicates article with an on-line appendix



Indicates article with supplemental on-line figure

<http://dx.doi.org/10.3174/ajnr.A3583>

Table 1: Sociodemographic and clinical features of patients and control participants

	Patients	Control Participants	P ^a
No.	43	17	
Age (range)	29.3 ± 7.4 (17–44)	30.7 ± 8.6 (19–50)	.687
Women (%)	19 (44%)	11 (65%)	.252
Education (y)	11.0 ± 3.4 (1–18)	15.2 ± 3.2 (9–19)	<.001
DUP (months)	7.9 ± 9.7 (1–40)	–	–
PANSS total score	100.8 ± 14.7 (64–125)	–	–
PANSS positive score	28.2 ± 6.4 (15–49)	–	–
PANSS negative score	23.0 ± 5.6 (12–34)	–	–
PANSS composite score	5.2 ± 7.4 (–8–21)	–	–

^a Mann-Whitney and Fisher exact test. Composite score (PANSS positive – PANSS negative score).

ferent MR imaging approaches used. In addition, most previous studies have enrolled medicated patients, and the effects of antipsychotic drugs and treatment duration on MR imaging findings were not taken into account. It is clear that studies based on untreated patients enrolled at an early stage of the disease represent the easiest and most rewarding strategy to overcome such an issue. To date, however, only a few studies^{4–9} have adopted this strategy showing WM changes compared with healthy participants in a variable pattern of brain regions including the splenium of the corpus callosum,^{4,6} superior longitudinal fasciculus,^{7,8} anterior⁹ and posterior⁴ limbs of the internal capsule, and fronto-occipital fasciculus.⁴ The relevance of DTI abnormalities in the early phase of schizophrenia is further supported by the positive association between positive symptoms and fractional anisotropy (FA) values of the superior and inferior longitudinal fasciculi and inferior fronto-occipital fasciculus in never-medicated patients with schizophrenia.^{5,10} In addition, most studies^{4–8} have investigated FA only, and none of them have assessed GM volumes in the same sample.

The aim of this study was to investigate whether volumetric and DTI changes, in FA, mean diffusivity (MD), and axial and radial diffusivity, are present in a relatively large sample of first-in-lifetime psychiatric contact, antipsychotic drug-naïve patients with a diagnosis of schizophrenia, compared with control participants, and to explore whether brain structural changes in these patients are associated with the duration of the untreated psychosis (DUP) and the severity of clinical positive and negative symptoms. We hypothesized that antipsychotic drug-naïve patients with schizophrenia show WM changes in cortical and subcortical connection systems, in both increased and decreased diffusion, and that such WM changes reflect the DUP and the severity of clinical symptoms. We also postulated that patients with schizophrenia in the early stage of the disease have GM volume loss in regions related to visual and episodic memory recall processing (ie, the occipital, temporal, and parietal lobes).

MATERIALS AND METHODS

Participants

Patients were recruited consecutively at the Department of Psychiatry, University School of Medicine, Brescia, Italy. Control participants were selected among the personnel of the Spedali Civili of Brescia and students of the University Brescia.

To be eligible, patients and control participants had to meet the following criteria: age between 18 and 50 years; antipsychotic drug-naïve and lack of exposure to other classes of psychopharmacologic agents for more than 2 consecutive weeks preceding

the enrollment; no family ties with other enrolled participants; a negative history of seizures and head trauma with loss of consciousness; no concomitant major medical conditions; Mini-Mental State Examination¹¹ score > 24; an IQ score on the Wechsler Adult Intelligence Scale-Revised¹² > 75; and no other causes of focal or diffuse brain damage, including lacunae, and extensive cerebrovascular disorders at routine MR imaging.

Furthermore, patients were included if they had a current *Diagnostic and Statistical Manual of Mental Disorders, (DSM-IV)*, diagnosis of schizophrenia¹³; no lifetime comorbidities with *DSM-IV*, Axis I disorders; a first-in-lifetime psychiatric contact; a level of understanding judged sufficient to give informed consent; and willingness to undergo an MR imaging examination before starting an antipsychotic drug. The diagnosis of schizophrenia and the exclusion of Axis I comorbidities were based on a detailed clinical interview complemented by a revision of all medical records.

For control participants, the group-specific inclusion/exclusion criteria were no lifetime evidence of any *DSM-IV*, Axis I disorder; a negative family history for psychosis and mood disorders in first-degree relatives; and willingness to perform an MR imaging examination.

A total of 43 patients with schizophrenia and 17 control participants were enrolled (Table 1). After complete description of the study to the participants, written informed consent was obtained. Participants also received an explicit guarantee of anonymity.¹⁴

Clinical Assessment

Participants were evaluated by a team of qualified and experienced psychiatrists, blinded to MR imaging data. Direct information from the patients, together with systematic interviews of at least 1 family member, was collected to date the age of onset of schizophrenia, operationally identified as when the first psychotic symptom with deterioration of function emerged. The interval elapsing between the first symptom and the first psychiatric contact defined the DUP.¹⁵ The Positive and Negative Syndrome Scales (PANSS)¹⁶ were administered to the patients.

MR Imaging Study

Within 2 weeks from the first clinical visit, brain MR imaging scans were obtained by use of 1.5T scanner. A detailed description of the MR imaging study is provided in the On-line Appendix. Tract-based spatial statistics (TBSS) was used to perform the multisubject DTI analysis. Voxel-based morphometry was run to assess GM volumes, by use of Statistical Parametric Mapping 8 (Wellcome Department of Imaging Neuroscience, London, UK).

Statistical Analysis

Demographic and clinical variables were compared between groups by use of the Fisher exact test, the Mann-Whitney *U* test, or the Kruskal-Wallis test as appropriate ($P < .05$; SPSS 13.0; IBM, Armonk, New York).

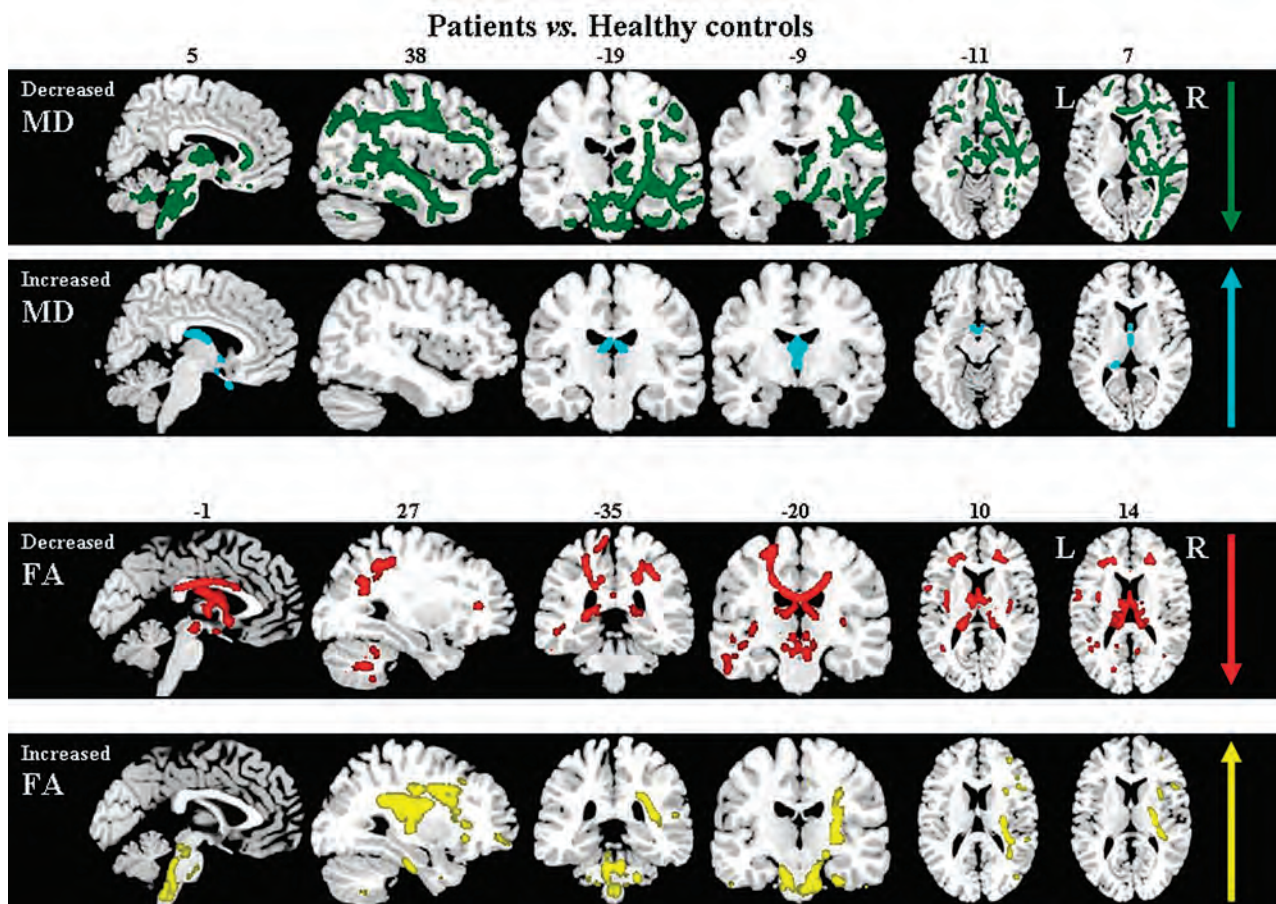


FIG 1. TBSS results in patients compared with healthy control participants. Voxelwise group differences are shown in cyan (*increased MD*), green (*decreased MD*), red (*decreased FA*), and yellow (*increased FA*). Results are overlaid on the sagittal, coronal, and axial sections of the Montreal Neurological Institute standard brain in neurologic convention (*right is right*) and are displayed at permutation-based $P < .05$, uncorrected.

DTI voxelwise statistics were performed by use of a permutation-based inference tool for nonparametric statistical thresholding.¹⁷ MD, FA, axial, and radial diffusivity values within the skeleton were tested between groups by use of a permutation-based 2-sample t test adjusted for age.¹⁷ Statistical maps were thresholded at $P < .05$ uncorrected for multiple comparisons.

Analyses of covariance were performed to assess GM volume differences between groups, with adjustment for age and total intracranial volume. Results were tested at $P < .001$ uncorrected, within at least 50 contiguous voxels. Furthermore, maps of the average percentage GM tissue loss in patients vs control participants were computed on the basis of the ratio, at each GM point, between the mean GM attenuation value at that point in the patient group and the corresponding mean GM attenuation value of the control group. The mean percentage GM tissue loss of clusters showing a significant between-group difference was also measured.

In patients, the associations of DUP and PANSS scores with DTI variables and GM volumes were tested by regression models in the FMRIB Software Library (<http://www.fmrib.ox.ac.uk/fsl>) and Statistical Parametric Mapping 8, respectively. Results were assessed at $P < .05$ for WM and $P < .001$ within 50 voxels for GM, uncorrected. The mean FA and MD values of the skeletonized voxels showing a significant correlation with clinical features were

calculated. Then, mean FA and MD values were correlated with DUP and PANSS by use of the Pearson coefficient adjusted for the participant age ($P < .05$; SPSS).

RESULTS

Demographic and Clinical Features

Compared with control participants, patients had similar age and sex but differed in length of education (Table 1).

WM Damage: TBSS

Patients compared with control participants showed an increased MD in the fornix and thalamic radiations bilaterally, and right olfactory bulb (Fig 1). In patients vs control participants, decreased MD was found in the posterior cerebellar lobe bilaterally, cerebral peduncles, pons and medulla oblongata, middle and inferior cerebellar peduncles, genu of the corpus callosum, middle cingulum, uncinate and parahippocampal tracts bilaterally, and right anterior and posterior limbs of the internal capsule, right thalamic radiations, right inferior fronto-occipital fasciculus, and right superior and inferior longitudinal fasciculi (Fig 1). Compared with control participants, patients had a decreased FA in the cerebral peduncles, thalamic radiations, fornix, corona radiata (with a left-side predominance), corpus callosum, superior longitudinal fasciculus (with a left-side predominance) bilaterally,

Table 2: Smaller GM volumes in patients vs control participants

Cluster Size (no. of Voxels)	Brain Region	Stereotaxic Coordinates (mm)			T Value	Percentage of Tissue Loss
		x	y	z		
322	Right fusiform gyrus	37	-54	-7	5.01	14
220	Left middle temporal lobe	-47	-54	19	4.08	14
53	Left middle temporal lobe	-60	-8	-13	3.65	8
52	Left postcentral gyrus	-37	-40	49	4.35	11
82	Right postcentral gyrus	37	-33	54	4.25	12
379	Left precuneus	-11	-46	42	4.07	12
51	Right middle cingulate	13	-54	33	3.66	9
85	Left superior occipital gyrus	-18	-97	8	3.77	17
154	Left cerebellum	-15	-42	-62	3.75	12
120	Left cerebellum	-34	-61	-32	3.59	6

Note:—No regions of increased GM volume were found in patients vs control participants.

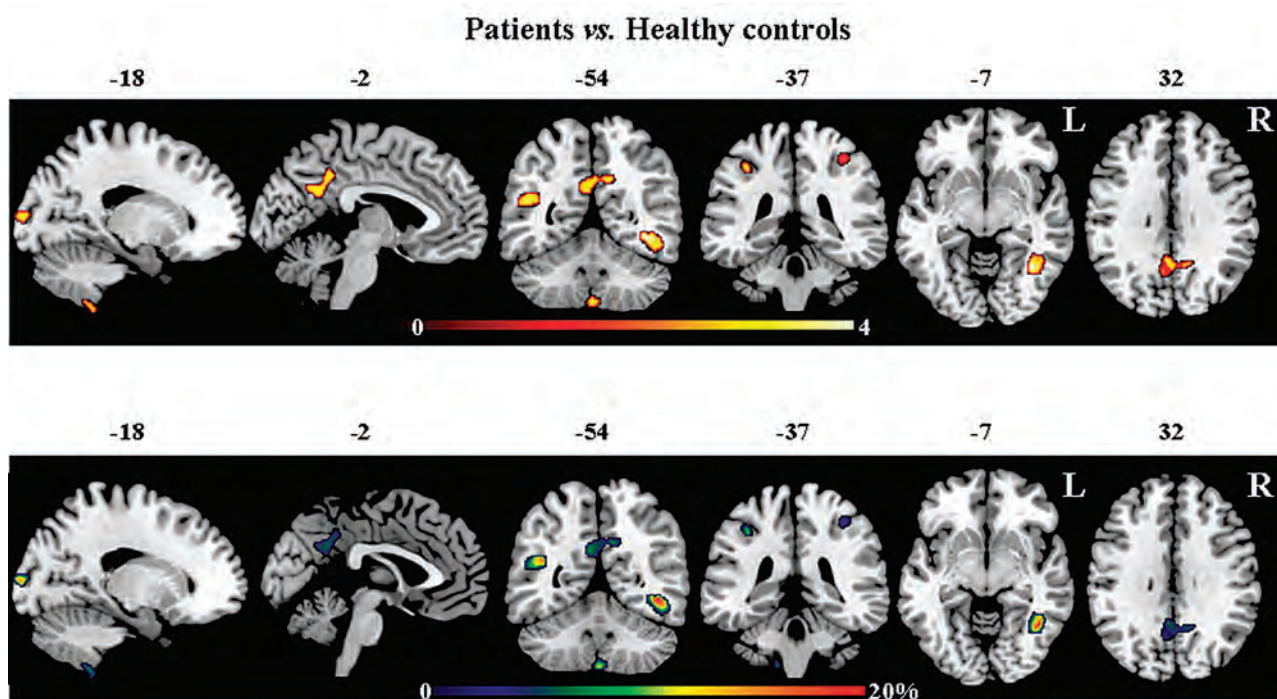


FIG 2. Voxel-based morphometry results showing smaller GM volumes in patients compared with healthy control participants. Results are overlaid on the sagittal, coronal, and axial sections of the MNI standard brain in neurologic convention (*right is right*) and are displayed at $P < .001$, uncorrected within at least 50 contiguous voxels. Color bars denote T values (*on the top*) and percentages of GM reduction (*at the bottom*). No region of increased GM volume was found in patients compared with control participants.

right superior cerebellar peduncle and posterior cerebellar lobe, and left olfactory bulb, left posterior parahippocampal tract, and left inferior fronto-occipital fasciculus (Fig 1). Compared with control participants, patients also had regions of increased FA in the cerebral peduncles, pons and medulla oblongata, middle and superior cerebellar peduncles bilaterally, and right posterior limb of the internal capsule, right external capsule, right frontoparietal part of the superior longitudinal fasciculus, and right parahippocampal tract (Fig 1).

Axial and radial diffusivity patterns resembled those of MD and FA in all contrasts. In all comparisons, patterns of decreased axial diffusivity mirrored those of reduced MD, while patterns of increased axial diffusivity reflected those of increased MD and decreased FA (On-line Figure). Patterns of decreased radial diffusivity reflected those of increased FA, whereas increased radial diffusivity reflected those of increased MD (On-line Figure).

GM Volumes: Voxel-Based Morphometry

Compared with control participants, patients showed smaller GM volumes of the bilateral postcentral gyrus; right fusiform gyrus and middle cingulate cortex; and left middle temporal and superior occipital gyrus, precuneus, and cerebellum (Table 2, Fig 2). In these regions, patients with schizophrenia had up to 20% GM loss relative to healthy control participants. No regions of increased GM volumes were found in patients compared with control participants.

Relationship between Clinical Features and GM and WM Damage

DUP. In patients, a negative relationship was found between DUP and MD values of the cerebral peduncles, pons and medulla oblongata, middle cingulum, parahippocampal tracts and inferior longitudinal fasciculi bilaterally, and right posterior limb of

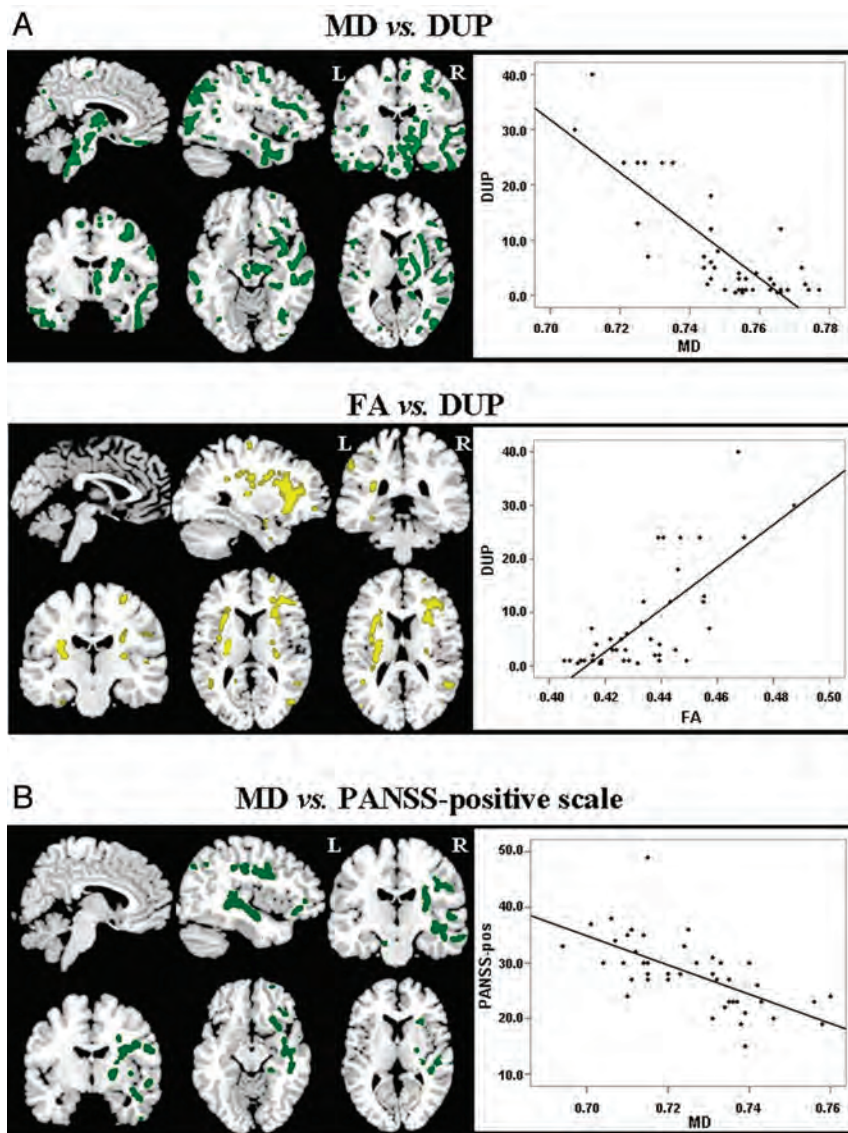


FIG 3. A, Relationships of the DUP with MD (green, negative correlation) and FA (yellow, positive correlation). B, Relationships between the PANSS-positive scores and MD (negative correlation). Results are overlaid on the sagittal, coronal, and axial sections of the MNI standard brain in neurologic convention (right is right) and are displayed at permutation-based $P < .05$, uncorrected.

the internal capsule, right thalamic radiations, right inferior fronto-occipital, and right uncinate fasciculi (Fig 3A). In patients, a positive relationship was found between DUP and FA values of the posterior limb of the internal capsule, superior longitudinal (with a left-side predominance) and inferior fronto-occipital fasciculi bilaterally, and the right uncinate fasciculi (Fig 3A). Pearson correlation coefficients were -0.81 for MD values and 0.82 for FA values ($P < .001$).

PANSS Scores. In patients with schizophrenia, MD values of the right middle and inferior cerebellar peduncles, uncinate and parahippocampal tracts, inferior longitudinal fasciculus, posterior limb of the internal capsule, inferior fronto-occipital and superior longitudinal fasciculi, and the left posterior cerebellar lobe were inversely related with the PANSS positive score (Fig 3B). The Pearson correlation coefficient was -0.69 ($P < .001$).

DISCUSSION

To our knowledge, this study is the first to investigate both microstructural WM and volumetric GM changes in a large group of first-contact, antipsychotic drug-naïve patients with schizophrenia. We observed that the brain of patients with schizophrenia is characterized by the coexistence of WM microstructural changes and reduced GM volumes in several brain regions since the clinical onset of the disorder. The inclusion of patients at the first psychotic event further highlights the precocity of the observed brain changes. Compared with control participants, patients with schizophrenia showed WM changes, in both higher and lower diffusion, of the following networks: the limbic system, the interhemispheric connections, the cortico-cortical systems, the motor system, and the cerebello-thalamo-cortical circuit. Patients with schizophrenia also had reduced GM volume mainly of the posterior brain regions. MR imaging changes observed in our patients may be the structural correlates of the “hypococonnectivity” and “hyperconnectivity” between brain regions that have been proposed to characterize cortical and subcortical connections in schizophrenia.¹⁸ The potential role of structural brain “disconnectivity”¹⁸ in determination of the clinical picture of schizophrenia is further suggested by the correlation analysis. Indeed, in patients with schizophrenia, we observed a positive correlation between DUP and FA, and a negative relationship of DUP and positive symptoms with MD values of the motor and the cortico-cortical systems, suggesting the dysfunctional nature of

the structural “hyperconnectivity” of these systems in untreated patients.

WM Findings

Compared with control participants, patients with schizophrenia showed decreased FA and increased MD in several regions corresponding to those observed in other studies that investigated never-medicated schizophrenic patients between 18 and 45 years old.⁴⁻⁸ Previous authors have found lower FA values in the fornix,⁷ thalamic radiations,⁸ corpus callosum,^{4,6,8} superior longitudinal^{7,8} and inferior fronto-occipital fasciculi,^{4,8} and the cortico-spinal tracts⁸ relative to healthy subjects. Our findings are also in agreement with previous studies in medicated schizophrenic patients showing decreased FA values in the corpus callosum, thalamic radiations, and superior longitudinal fasciculus (for a com-

prehensive review of WM findings in schizophrenia, please see Kyriakopoulos and Frangou et al¹⁹ and Peters et al¹). Postmortem studies have identified WM alterations in schizophrenia, which include microstructural abnormalities of the myelin and oligodendrocytes that may represent the pathologic substrate of the observed MD increases and FA decreases in the MR imaging results of our study and in previous MR imaging reports.²⁰

Different from other studies of first-episode antipsychotic drug-naïve patients with schizophrenia,⁴⁻⁹ we observed that patients also showed regions of increased FA and decreased MD values, likely reflecting structural “hyperconnectivity,”¹⁸ mainly in the brain stem, cerebellum, and in the interhemispheric and cortico-cortical WM connections. Some studies of patients with schizophrenia have found a similar pattern of DTI changes.^{21,22} It is interesting to note that a recent study detected both increased and decreased FA in untreated patients with schizophrenia in the corticopontine-cerebellar circuit,²¹ with the most inferior sections of the corticopontine tracts and the middle cerebellar peduncles showing higher FA values in patients compared with control participants (ie, exactly the same pattern that we observed in our present study; see the sagittal sections of FA:×-1 and MD:×5, Fig 1). Another DTI study of 12 first-episode patients with schizophrenia found an increased intervoxel coherence, which corresponds to high FA, in the thalamic radiations.²³ The pathophysiologic correlates of decreased MD and increased FA in patients with schizophrenia can be diverse. First, an increased WM fiber attenuation in patients with schizophrenia vs healthy participants is observed, as shown by postmortem studies investigating the WM architecture of patients with schizophrenia.²⁴ Second, there is decreased integrity of the corticopontine inhibitory GABAergic projections that may result in an increased axonal remyelination downstream,²¹ which, in turn, may cause a paradoxical decrease of MD and increase of FA as observed in our study. Third, an alternative, but not mutually exclusive, explanation may be related to the dopamine hypothesis of schizophrenia,²⁵ according to which a hyperdopaminergic status could lead to “overdemanding” neuronal activity able to initiate an increase of useless WM connections and, clinically, induce aberrant assignments of motivational salience to objects, people, and actions.

In patients with schizophrenia, we observed that the DUP correlated negatively with MD values and positively with FA values. In addition, we also found a negative correlation between MD of some cerebellar and cerebral regions and the severity of the clinical positive manifestations. A relationship between increased FA values of the fronto-occipital and temporolimbic tracts and more severe positive symptoms has been previously observed in never-medicated patients with schizophrenia^{5,10} and in medicated patients with schizophrenia with a history of auditory hallucinations and other positive symptoms.²⁶⁻²⁸ Overall, these findings suggest that the observed pattern of structural WM changes in patients with schizophrenia is already present before treatment initiation and is associated with the occurrence of positive clinical manifestations.

It is worth noting that MD and FA changes may be secondary to modifications of diffusion either parallel (axial diffusivity) or perpendicular (radial diffusivity) to the principal direction of the tensor.²⁹ Analysis of directional diffusivities may provide addi-

tional information on the underlying mechanisms of WM integrity loss.²⁹ Myelin breakdown is likely to be associated with increased diffusivity perpendicular to the WM tract, whereas axonal damage has been suggested to reflect diffusivity changes parallel to the primary fiber orientation.^{30,31} However, although study of axial and radial diffusivity helps to interpret MD and FA changes, radiopathologic correlations on the basis of investigation of these metrics remain controversial.³²

GM Findings

Drug-naïve patients with schizophrenia had reduced volumes of the temporal, parietal, and occipital cortices and cerebellum. Only a few studies have investigated GM volumes in patients with schizophrenia at the first psychotic episode and who are antipsychotic-naïve, and have shown a pattern of GM volume loss³³ similar to the one we observed.

Reduced volume of the fusiform gyrus (14% of tissue loss) is in line with the results of a neuropathologic study of patients with schizophrenia showing an 18% reduction of neuron attenuation in layers III and V of this region.³⁴ The fusiform gyrus plays a relevant role in face-processing integrating perception, memory, and emotion.³⁵ Reduced GM volume of this region may, therefore, be linked to a failure in facial identification and emotion and, thus, may lead to typical impairment of the empathic social interaction known to occur in these patients.³⁵ Previous structural MR imaging studies in medicated patients with schizophrenia also showed smaller volumes of the posterior cerebellum.³⁶ Cerebellar damage has been shown to be associated with negative symptoms and mood and behavioral dysregulation.³⁷ Reduced volume of the precuneus was also found in patients with schizophrenia and was associated with delusions of control.³⁸ We also detected reduced volume of the superior occipital region, which subtends perceptual functions known to be frequently altered in schizophrenia. In addition, compared with control participants, patients with schizophrenia showed smaller volumes of the middle temporal lobe. This region has been found to be atrophic in a study investigating GM attenuation in high-risk patients in whom psychosis later developed.³⁹

Study Strengths and Limitations

Having avoided the potential effects played by the chronicity of the disorder on brain MR imaging results and those associated with concomitant treatment, we believe that the presence of multiple structural brain changes in our patients may be conceivably seen as an early phenotypic expression of the processes involved in the pathophysiologic mechanisms of schizophrenia. However, our study was cross-sectional and, therefore, did not allow us to disentangle the role of neurodevelopmental and neurodegenerative abnormalities, which may both result in the observed MR imaging changes. The patients in our study did not undergo comprehensive cognitive testing and were not educationally matched with healthy control participants. However, the inclusion of participants with a Mini-Mental State Examination score > 24 and IQ > 75 should have reduced the effect of intellectual functions and educational level on the MR imaging results. In addition, although the exclusion of patients with a lifetime history of Axis I disorders precludes a major effect of cannabis abuse on our find-

ings, a possible influence of a sporadic use of cannabis during adolescence cannot be excluded.¹ In patients with recent-onset schizophrenia, a study found that cannabis use before age 17 years was related with increased FA in several brain regions, including the uncinate fasciculus, internal capsule, and frontal WM, compared with patients without a history cannabis use and compared with control participants.⁴⁰ In another study, the authors found that compared with cannabis-naïve patients with schizophrenia, patients who used cannabis showed increased FA in the splenium of the corpus callosum.⁴¹ Evidence of an association between increased FA and cannabis use comes from studies of cannabis users without major psychiatric illnesses, showing increased FA^{42,43} and reduced MD⁴² of several WM regions in these participants. All of these findings are compatible with the ability of the cannabinoid receptor stimulation to increase the oligodendrocyte transcription factor Olig2 as well as the expression of myelin basic protein.⁴⁴

Some technical limitations of this study also need to be considered. The diffusion tensor model is currently the framework most commonly used to relate the diffusion signal to the direction of the fibers. However, this model has been shown to be inadequate in voxels containing multiple fiber orientations (eg, “crossing fibers”).⁴⁵ Because complex crossing fibers tend to have decreased FA and increased MD, this issue may have influenced our findings. Many approaches have recently been proposed to address this issue, based on high-angular resolution DWI data,⁴⁶ and would help to clarify the nature of WM changes in patients with schizophrenia. Head motion can influence MR imaging studies, in particular when dealing with patients with psychiatric disorders. For this reason, structural images (3D T1 and DTI) were carefully checked, and none showed gross head motion artifacts. Furthermore, the DTI preprocessing used in our study includes a movement correction step (see On-line Appendix for further details). Finally, as in previous studies of patients with schizophrenia⁴⁷ and in accordance with the exploratory nature of the study design, group differences did not survive multiple comparisons correction, suggesting that structural brain changes in schizophrenia are subtle or that some of the significances may have been overestimated. However, we tried to minimize false-positive findings by using a relatively conservative statistical threshold in the voxel-based morphometry analysis, and by estimating the standard error of the *t* statistics by using a permutation approach in the TBSS analysis. In TBSS, we permuted the data 5000 times to obtain large, and consequently relatively conservative, standard errors of the *t* statistics. Such an approach is usually considered robust enough to allow the use of a canonical statistical threshold of .05.⁴⁸

ACKNOWLEDGMENTS

The study was partly supported by the Health Authority of the Lombardia Region (Project 153; www.sanita.regione.lombardia.it).

Disclosures: Massimo Filippi—UNRELATED: Board Membership: Teva Pharmaceutical Industries, Genmab A/S; Consultancy: Bayer Schering Pharma, Biogen Idec, Genmab A/S, Merck Serono, Peppen Corporation, Teva Pharmaceutical Industries; Grants/Grants Pending: Bayer Schering Pharma,* Biogen Idec,* Genmab A/S,* Merck Serono,* Teva Pharmaceutical Industries,* Fondazione Italiana Sclerosi Multipla,* Italian Ministry of Health,* CurePSP*; Payment for Lectures (including service on speaker bureaus): Bayer Schering Pharma, Biogen-Idec, Genmab A/S, Merck Se-

rono, Teva Pharmaceutical Industries; Travel/Accommodations/Meeting Expenses Unrelated to Activities Listed: Bayer Schering Pharma, Biogen Idec, Genmab A/S, Merck Serono, Teva Pharmaceutical Industries. Federica Agosta—UNRELATED: Grants/Grants Pending: Italian Ministry of Health*; Payment for Lectures (including service on speaker bureaus): Bayer Schering Pharma, Biogen Idec, Sanofi Aventis, Serono Symposia International Foundation; Travel/Accommodations/Meeting Expenses Unrelated to Activities Listed: Teva Pharmaceutical Industries. Paolo Valsecchi—UNRELATED: Payment for Lectures (including service on speaker bureaus): Abbott, AstraZeneca, Boehringer-Ingelheim, Bristol-Myers Squibb, Eli Lilly, Innova Pharma, Janssen-Cilag, Lundbeck, Pfizer, Wyeth Lederie. Giancarlo Comi—UNRELATED: Consultancy and Payment for Lectures (including service on speaker bureaus): Novartis, Teva Pharmaceutical Industries, Sanofi-Aventis, Genzyme, Marck Serono, Bayer Schering, Biogen-Dompè, Actelion. Emilio Sacchetti—UNRELATED: Board Membership and Consultancy and Payment for Lectures (including service on speaker bureaus): Abbott, Angelini, AstraZeneca Pharmaceuticals, Boehringer-Ingelheim, Bristol-Myers Squibb, Danippon Sumitomo Pharma, Eli Lilly, GlaxoSmith-Kline, Innova Pharma, Italfarmaco, Janssen-Cilag, Lundbeck, Otsuka, Pfizer, Rottapharm, Sanofi-Aventis, Servier, Shire Pharmaceuticals, Stroder, Wyeth Lederie. *Money paid to institution.

REFERENCES

- Peters BD, Blaas J, de Haan L. Diffusion tensor imaging in the early phase of schizophrenia: what have we learned? *J Psychiatr Res* 2010;44:993–1004
- Levitt JJ, Bobrow L, Lucia D, et al. A selective review of volumetric and morphometric imaging in schizophrenia. *Curr Top Behav Neurosci* 2010;4:243–81
- Ellison-Wright I, Bullmore E. Meta-analysis of diffusion tensor imaging studies in schizophrenia. *Schizophr Res* 2009;108:3–10
- Cheung V, Cheung C, McAlonan GM, et al. A diffusion tensor imaging study of structural dysconnectivity in never-medicated, first-episode schizophrenia. *Psychol Med* 2008;38:877–85
- Cheung V, Chiu CP, Law CW, et al. Positive symptoms and white matter microstructure in never-medicated first episode schizophrenia. *Psychol Med* 2011;41:1709–19
- Gasparotti R, Valsecchi P, Carletti F, et al. Reduced fractional anisotropy of corpus callosum in first-contact, antipsychotic drug-naïve patients with schizophrenia. *Schizophr Res* 2009;108:41–48
- Guo W, Liu F, Liu Z, et al. Right lateralized white matter abnormalities in first-episode, drug-naïve paranoid schizophrenia. *Neurosci Lett* 2012;531:5–9
- Pérez-Iglesias R, Tordesillas-Gutiérrez D, Barker GJ, et al. White matter defects in first episode psychosis patients: a voxelwise analysis of diffusion tensor imaging. *Neuroimage* 2010;49:199–204
- Zou LQ, Xie JX, Yuan HS, et al. Diffusion tensor imaging study of the anterior limb of internal capsules in neuroleptic-naïve schizophrenia. *Acad Radiol* 2008;15:285–89
- Szeszko PR, Robinson DG, Ashtari M, et al. Clinical and neuropsychological correlates of white matter abnormalities in recent onset schizophrenia. *Neuropsychopharmacology* 2008;33:976–84
- Folstein MF, Folstein SE, McHugh PR. “Mini-mental state”. A practical method for grading the cognitive state of patients for the clinician. *J Psychiatr Res* 1975;12:189–98
- Wechsler D. *WAIS-R Manual. Wechsler Adult Intelligence Scale Revised*. New York: The Psychological Corporation; 1981
- Association AP. *Diagnostic and Statistical Manual of Mental Disorders (DSM-IV) 4th ed*. Washington, DC: American Psychiatric Association; 1994
- Sacchetti E, Bocchio-Chiavetto L, Valsecchi P, et al. —G308A tumor necrosis factor alpha functional polymorphism and schizophrenia risk: meta-analysis plus association study. *Brain Behav Immun* 2007;21:450–57
- Craig TJ, Bromet EJ, Fennig S, et al. Is there an association between duration of untreated psychosis and 24-month clinical outcome in a first-admission series? *Am J Psychiatry* 2000;157:60–66
- Kay SR, Fiszbein A, Opler LA. The positive and negative syndrome scale (PANSS) for schizophrenia. *Schizophr Bull* 1987;13:261–76
- Nichols TE, Holmes AP. Nonparametric permutation tests for functional neuroimaging: a primer with examples. *Hum Brain Mapp* 2002;15:1–25

18. Innocenti GM, Ansermet F, Parnas J. **Schizophrenia, neurodevelopment and corpus callosum.** *Mol Psychiatry* 2003;8:261–74
19. Kyriakopoulos M, Frangou S. **Recent diffusion tensor imaging findings in early stages of schizophrenia.** *Curr Opin Psychiatry* 2009;22:168–76
20. Uranova N, Orlovskaya D, Vikhreva O, et al. **Electron microscopy of oligodendroglia in severe mental illness.** *Brain Res Bull* 2001;55:597–610
21. Koch K, Wagner G, Dahnke R, et al. **Disrupted white matter integrity of corticopontine-cerebellar circuitry in schizophrenia.** *Eur Arch Psychiatry Clin Neurosci* 2010;260:419–26
22. Sun Z, Wang F, Cui L, et al. **Abnormal anterior cingulum in patients with schizophrenia: a diffusion tensor imaging study.** *Neuroreport* 2003;14:1833–36
23. Federspiel A, Begre S, Kiefer C, et al. **Alterations of white matter connectivity in first episode schizophrenia.** *Neurobiol Dis* 2006;22:702–09
24. Chance SA, Highley JR, Esiri MM, et al. **Fiber content of the fornix in schizophrenia: lack of evidence for a primary limbic encephalopathy.** *Am J Psychiatry* 1999;156:1720–24
25. Guillin O, Abi-Dargham A, Laruelle M. **Neurobiology of dopamine in schizophrenia.** *Int Rev Neurobiol* 2007;78:1–39
26. Hubl D, Koenig T, Strik W, et al. **Pathways that make voices: white matter changes in auditory hallucinations.** *Arch Gen Psychiatry* 2004;61:658–68
27. Shergill SS, Brammer MJ, Fukuda R, et al. **Engagement of brain areas implicated in processing inner speech in people with auditory hallucinations.** *Br J Psychiatry* 2003;182:525–31
28. Seok JH, Park HJ, Chun JW, et al. **White matter abnormalities associated with auditory hallucinations in schizophrenia: a combined study of voxel-based analyses of diffusion tensor imaging and structural magnetic resonance imaging.** *Psychiatry Res* 2007;156:93–104
29. Basser PJ, Mattiello J, LeBihan D. **MR diffusion tensor spectroscopy and imaging.** *Biophys J* 1994;66:259–67
30. Beaulieu C. **The basis of anisotropic water diffusion in the nervous system—a technical review.** *NMR Biomed* 2002;15:435–55
31. Song SK, Sun SW, Ramsbottom MJ, et al. **Dysmyelination revealed through MRI as increased radial (but unchanged axial) diffusion of water.** *Neuroimage* 2002;17:1429–36
32. Wheeler-Kingshott CA, Cercignani M. **About “axial” and “radial” diffusivities.** *Magn Reson Med* 2009;61:1255–60
33. Bora E, Fornito A, Radua J, et al. **Neuroanatomical abnormalities in schizophrenia: a multimodal voxelwise meta-analysis and meta-regression analysis.** *Schizophr Res* 2011;127:46–57
34. Di Rosa E, Crow TJ, Walker MA, et al. **Reduced neuron density, enlarged minicolumn spacing and altered ageing effects in fusiform cortex in schizophrenia.** *Psychiatry Res* 2009;166:102–15
35. Vuilleumier P, Armony JL, Driver J, et al. **Effects of attention and emotion on face processing in the human brain: an event-related fMRI study.** *Neuron* 2001;30:829–41
36. Thomann PA, Roebel M, Dos Santos V, et al. **Cerebellar substructures and neurological soft signs in first-episode schizophrenia.** *Psychiatry Res* 2009;173:83–87
37. Tavano A, Grasso R, Gagliardi C, et al. **Disorders of cognitive and affective development in cerebellar malformations.** *Brain* 2007;130:2646–60
38. Blakemore SJ, Wolpert DM, Frith CD. **Abnormalities in the awareness of action.** *Trends Cogn Sci* 2002;6:237–42
39. Pantelis C, Velakoulis D, McGorry PD, et al. **Neuroanatomical abnormalities before and after onset of psychosis: a cross-sectional and longitudinal MRI comparison.** *Lancet* 2003;361:281–88
40. Peters BD, de Haan L, Vlioger EJ, et al. **Recent-onset schizophrenia and adolescent cannabis use: MRI evidence for structural hyperconnectivity?** *Psychopharmacol Bull* 2009;42:75–88
41. Dekker N, Schmitz N, Peters BD, et al. **Cannabis use and callosal white matter structure and integrity in recent-onset schizophrenia.** *Psychiatry Res* 2010;181:51–56
42. Bava S, Frank LR, McQueeney T, et al. **Altered white matter microstructure in adolescent substance users.** *Psychiatry Res* 2009;173:228–37
43. De Bellis MD, Van Voorhees E, Hooper SR, et al. **Diffusion tensor measures of the corpus callosum in adolescents with adolescent onset alcohol use disorders.** *Alcohol Clin Exp Res* 2008;32:395–404
44. Arévalo-Martín A, García-Ovejero D, Rubio-Araiz A, et al. **Cannabinoids modulate Olig2 and polysialylated neural cell adhesion molecule expression in the subventricular zone of post-natal rats through cannabinoid receptor 1 and cannabinoid receptor 2.** *Eur J Neurosci* 2007;26:1548–59
45. Alexander DC, Barker GJ, Arridge SR. **Detection and modeling of non-Gaussian apparent diffusion coefficient profiles in human brain data.** *Magn Reson Med* 2002;48:331–40
46. Tournier JD, Yeh CH, Calamante F, et al. **Resolving crossing fibres using constrained spherical deconvolution: validation using diffusion-weighted imaging phantom data.** *Neuroimage* 2008;42:617–25
47. Miyata J, Sasamoto A, Koelkebeck K, et al. **Abnormal asymmetry of white matter integrity in schizophrenia revealed by voxelwise diffusion tensor imaging.** *Hum Brain Mapp* 2012;33:1741–49
48. Good PI. *Permutation, Parametric, and Bootstrap Tests of Hypotheses*, 3rd ed. New York: Springer; 2005

Comparison of Multiecho Postprocessing Schemes for SWI with Use of Linear and Nonlinear Mask Functions

M.P. Quinn, J.S. Gati, L.M. Klassen, A.W. Lin, J.R. Bird, S.E. Leung, and R.S. Menon



ABSTRACT

BACKGROUND AND PURPOSE: SWI is an MR technique conventionally implemented with single-echo gradient-echo data. The purpose of this study was to compare single-echo SWI processing and 2 multiecho SWI processing schemes: postaverage, where an SWI image is created for each echo and then averaged to create a single volume; and frequency-based, where a SWI image is generated from an average frequency image. Linear and nonlinear mask functions were investigated for all 3 processing schemes.

MATERIALS AND METHODS: Comprehensive optimizations were performed. Single and multigradient-echo data were acquired at 3T in 10 volunteers. Contrast-to-noise ratio was measured in various structures. Visibilities of the same structures were ranked in different SWI images by trained raters.

RESULTS: When image evaluation was based on measurements of contrast-to-noise ratio, the nonlinear mask and frequency-based scheme were superior. However, when image evaluation was based on ranks of qualitative visibility, the linear mask and postaverage scheme were superior. Although the nonlinear mask and frequency-based scheme allow increased contrast of paramagnetic perturbers such as the globus pallidus, periventricular veins, red nucleus, and subthalamic nucleus, they do not necessarily increase the information content of the image; rather, they result in a harsh contrast that is visually unpleasing to radiologists and wherein more subtle structure is relatively less apparent.

CONCLUSIONS: Linearly masked postaverage SWI is the recommended implementation of multiecho SWI for radiologic use; however, nonlinearly masked frequency-based SWI may have use in computer-based segmentation or registration.

ABBREVIATIONS: CNR = contrast-to-noise ratio; GP = globus pallidus; OR = optic radiations; RN = red nucleus; STN = subthalamic nucleus

SWI is an MR imaging technique that exploits the effect of variations in magnetic susceptibility on gradient-echo signal to produce enhanced image contrast. Most MR imaging studies reconstruct only the magnitude image; phase is generally discarded. However, the phase data contain potentially useful information about inclusions in the imaging volume that change the

local magnetic field. SWI processing allows this information to be incorporated into the magnitude image because the underlying structure may not necessarily be visible on magnitude alone.¹

SWI was originally used to produce high-resolution venograms.² SWI has found additional uses in clinical and research settings because of its sensitivity to other physiologically relevant magnetic field perturbers such as blood products,³ iron,⁴ and calcium.⁵ However, single-echo SWI is useful in the visualization, but not the quantification, of field perturbers. Modifications of SWI allow simultaneous quantification of the nature or amount of the perturber. For example, the effective transverse relaxation rate (R_2^*), which can be extracted from multiecho gradient-echo data via voxelwise curve fitting, is a metric that scales linearly with iron concentration in the brain.⁶

Brainovich et al⁷ described a postprocessing scheme for dual-echo gradient-echo data. In this scheme, average phase and average magnitude volumes were generated and subsequently used to produce a single SWI volume. Denk and Rauscher⁸ used a multi-echo acquisition with 5 echoes to produce 5 SWI volumes that

Received December 13, 2012; accepted after revision February 14, 2013.

From the Departments of Medical Biophysics (M.P.Q., R.S.M.) and Medical Imaging (A.W.L., J.R.B., S.E.L.), The University of Western Ontario, London, Ontario, Canada; and Robarts Research Institute (M.P.Q., J.S.G., L.M.K., R.S.M.), London, Ontario, Canada.

This work was supported in part by grants from the Canadian Institutes of Health Research (MOP-111085) and Canada Research Chairs Program (R.S.M.), and from the Vanier Canada Graduate Scholarships Program (M.P.Q.).

Paper previously presented at: Annual Meeting of International Society for Magnetic Resonance in Medicine, May 10, 2012; Melbourne, Australia.

Please address correspondence to Matthew P. Quinn, Centre for Functional and Metabolic Mapping, Robarts Research Institute, 100 Perth Dr, London, Ontario, Canada, N6A5K8; e-mail: mquinn@robarts.ca

 Indicates open access to non-subscribers at www.ajnr.org

 Indicates article with supplemental on-line figures

<http://dx.doi.org/10.3174/ajnr.A3584>

were subsequently averaged to produce a single average SWI volume. They reported improvements in contrast-to-noise ratio (CNR) of veins compared with conventional SWI. In addition, they described computation of R_2^* maps as a natural extension of the multiecho acquisition. In all cases, a conventional linear-phase mask function for SWI was used. The use of alternative mask functions theoretically results in an increased CNR of the cerebral veins,⁹ though this claim has not been rigorously tested in vivo.

There are 2 main goals of this work: first, a comparison of 3 SWI postprocessing schemes (single echo and 2 multiecho methods); and second, a comparison of the conventional (ie, linear) mask function with a novel nonlinear mask function. We identified the following objectives: 1) to describe and outline modifications to previously published multiecho SWI, as well as describe a nonlinear mask function; 2) to optimize the number of mask function multiplications for all combinations of postprocessing scheme and mask function; and 3) to compare all postprocessing schemes and mask functions in vivo by using both quantitative and radiologic assessments.¹⁰

MATERIALS AND METHODS

Processing was performed in Matlab (MathWorks, Natick, Massachusetts) and FSL (<http://www.fmrib.ox.ac.uk/fsl>). Statistical analyses were performed in SPSS (IBM, Armonk, New York).

SWI Postprocessing Schemes

Three postprocessing schemes were compared: 1 for single-echo SWI and 2 for multiecho SWI. First, single-echo SWI processing involves background phase removal by using the homodyne method,¹¹ generation of a phase mask, and multiplication of the m^{th} power of the mask by the magnitude image.¹²

Second, the multiecho SWI method of Denk and Rauscher⁸ was modified and herein is referred to as the postaverage method. Postaverage multiecho SWI involves single-echo SWI processing on data from each echo, and averaging of the resulting images. Denk and Rauscher⁸ prescribe this technique with a linearly (in TE) increasing homodyne filter width to remove background contributions to phase from each echo to account for the additional phase wrapping at longer TE. We used a constant (with TE) filter size, as a compromise between eliminating phase wraps in later echoes and preserving the relevant contrast between echoes in a consistent manner.

Third, a frequency-based method for multiecho SWI was used and is based on the method described initially by Brainovich et al.⁷ For the image volume reconstructed from each echo, the background phase was removed by use of the homodyne method. Successive phase images were then temporally unwrapped by using Matlab's 1D unwrap function on the TE-dependent voxel data. Each unwrapped phase image was then divided by its corresponding TE to produce a frequency image. A weighted average of frequency was calculated from these individual frequency images: weights were inversely proportional to the variance of the frequency: $(\text{magnitude})^2 / (\text{TE})^2$. A mask was computed from the average frequency image, and its m^{th} power was multiplied by the average magnitude image for that section. This method is similar to what has been described by Brainovich et al⁷ but, in addition,

involves the temporal unwrapping of phase, as well as masking the weighted average of frequency maps rather than the arithmetic mean of the phase images. Although the mean of the frequency maps is a physical and intuitive quantity, the mean of the phase images used by Brainovich et al⁷ is not logical from a physical or mathematic perspective.

For the homodyne filter, a 2D Hann window (1 period of a raised cosine) with dimensions equal to 30% (for multiecho) or 20% (for single-echo) of the respective matrix dimensions, rounded to the nearest integer, was used. This constant width filter, in conjunction with the temporal phase unwrapping that was used, resulted in the ability to remove all relevant phase wraps.

SWI Mask Functions

Two different mask functions were compared. First, the conventional linear mask function was used. In general form, the linear mask, L , is defined as follows:

$$E1) \quad L(x) = \begin{cases} 0 & \text{if } x < -X \\ \frac{1}{X}(x + X) & \text{if } -X \leq x \leq 0 \\ 1 & \text{if } x > 0. \end{cases}$$

For single-echo and postaverage, $X = -\pi$ rad is used, with x in radians. For frequency-based SWI where x is in units of Hertz, X is set to the equivalent value: $(-\pi \text{ rad})(1 \text{ cycle}/2\pi \text{ rad})(1/\text{TE}_{\text{average}}) = 18.2 \text{ Hz}$, where $\text{TE}_{\text{average}}$ is the average of the TEs used (described below).

Second, a nonlinear mask function was used. This Hann-derived mask, H , is defined as follows:

$$E2) \quad H(x) = \begin{cases} 0 & \text{if } x < -X \\ \frac{1}{2} \left[1 + \cos\left(\frac{\pi x}{X}\right) \right] & \text{if } -X \leq x \leq 0 \\ 1 & \text{if } x > 0. \end{cases}$$

The values X and x can be expressed in either units of phase or frequency. X was set to π (for single-echo and postaverage) or the equivalent value of 18.2 Hz (for frequency-based SWI). Compared with the linear filter, it was expected that this filter would result in reduced image noise and increased contrast for negative phase/frequency structures.

MR Imaging

All scanning was performed on a 3T MR imaging scanner (Tim Trio; Siemens, Erlangen, Germany) by use of a 32-channel head coil. For evaluation and comparison of different SWI postprocessing schemes, 10 healthy volunteers were scanned (7 women; age, 28 ± 7 years). We collected data by using a single-echo 3D gradient-echo (TE, 20 ms; TR, 30 ms; bandwidth, 80 Hz/pixel; acquisition time, 6:28; fully flow-compensated) and multiecho 3D gradient-echo sequences (TE₁, 10 ms; echo spacing, 7 ms; 6 echoes; TR, 52 ms; bandwidth, 160 Hz/pixel; acquisition time, 11:12; first echo fully flow-compensated). For both sequences, common parameters were matrix, $448 \times 336 \times 60$; field of view, $224 \times 178 \times 60 \text{ mm}^3$; flip angle, 12°; section oversampling, 12.5%. Both acquisitions were accelerated with generalized auto-calibrating partially parallel acquisition ($R = 2$, reference lines =

24). Phase data from each channel were combined on-line by use of vendor software. This study was approved by the institutional review board. Informed consent was obtained in writing from all participants.

Six SWI volumes were created per participant: 3 postprocessing schemes with 2 mask functions each. The single-echo magnitude volume was registered to the first echo magnitude of the multiecho volumes to allow careful comparison of the different methods on individual vessels or regions, even if motion were present between the different volumes. Single-echo SWI volumes were computed, following which the magnitude registration parameters were applied.

Numeric Optimization

A 2D numeric phantom was created to evaluate the CNR of a vein by use of different postprocessing schemes and mask functions. The purpose of this simulation was to optimize the number of mask multiplications, m , for different postprocessing schemes. The phantom consisted of a 512×512 array. All pixels were assigned values of the effective transverse relaxation time, T_2^* (32 ms), and equilibrium signal, S_0 (425), based on their measured values in WM in the in vivo multiecho data. One column was designated the vein compartment and was assigned a frequency that was varied for different trials. All other pixels were assigned a frequency of zero for all trials. This is similar to a previously described simulation to optimize the number of mask multiplications for conventional SWI.¹²

We simulated the data by creating magnitude and phase image pairs for different TEs. At a given TE, signal magnitude was calculated according to $S(TE) = S_0 \exp(-TE/T_2^*)$. Phase was calculated as (frequency) \times (TE). Each magnitude and phase pair was converted into real and imaginary images, to each of which normally distributed noise with a standard deviation of 18 was added to ensure comparable signal-to-noise in simulated data when compared with periventricular WM by use of our acquisition parameters. The noisy real and imaginary images were then converted back to magnitude and phase.

We simulated a multiecho dataset by creating magnitude/phase pairs for TEs of 10, 17, 24, 31, 38, and 45 ms. From the same simulated multiecho data, 1 multiecho SWI image was generated according to each of the 4 possible combinations of multiecho postprocessing scheme (postaverage and frequency-based) and mask function (linear and nonlinear).

We simulated single-echo data by creating 1 magnitude/phase pair at a TE of 20 ms. Noise was decreased by a factor of $2^{0.5}$ to simulate decreased noise accompanying the reduction in bandwidth from 160 Hz/pixel in the multiecho acquisition to 80 Hz/pixel in the single-echo acquisition. In addition, the WM S_0 was decreased by 16% to account for the reduction in the steady-state signal accompanying the decrease in TR. For the simulated single-echo data, a single SWI image was produced with each mask function.

Contrast was measured as the difference in mean signals between 2 ROIs in the SWI volumes: one placed in the vein compartment, and one in the WM compartment. The CNR was calculated as this contrast divided by the standard deviation of the

signal in the latter ROI, which is the standard definition of CNR used in SWI numeric optimization.¹²

Visual Optimization

Values of m were also optimized by 3 radiology residents, each with 29 months of experience, who rated SWI images from 4 volunteers. For each volunteer, image volumes included each of the 6 SWI combinations processed with a range of m values. Images processed with the linear mask function were processed with m 's from 0–11, incremented in steps of 1. Images processed with the nonconventional filter were processed with m 's from 0–55, incremented in steps of 5. This larger range and coarser increment of m values were found to yield a similar range of contrasts to the images processed with the conventional mask. Raters were shown 24 sets of 12 volumes. The raters were not blinded to the value of m , but each set was presented in a random order to ensure that experience from early sets did not influence the rating of later sets. Rating instructions were as follows: "For each set, identify the single value of m which is optimal. When considering optimal m , consider SWI quality from a radiologic standpoint. Please consider how structure contrast as well as image noise is affected by choice of m . Specifically, you should consider the visibility of veins (both small veins such as those at the lateral ventricles, and large veins) as well as other structures that may be targeted with SWI, such as: red nucleus, subthalamic nucleus, globus pallidus." Each rater performed rating independently. To evaluate interrater agreement, a 2-way mixed-average measures interclass correlation coefficient was calculated for the pooled ratings.

ROI Analyses

For in vivo data, ROI analyses were used to compare optimized SWI techniques. For each participant, ROIs were drawn in the right hemisphere of single-echo, linearly masked SWI volume and propagated into the other volumes. Signal-to-noise ratio was approximated in the frontal WM of all participants as the mean divided by standard deviation of the signal in the ROI. CNR was measured between various anatomic structures (globus pallidus [GP], optic radiations [OR], periventricular veins, subthalamic nucleus [STN], and red nucleus [RN]) and the adjacent WM as the difference between mean values of signal in 2 ROIs (one in the structure of interest, one in the adjacent WM) divided by the standard deviation of signal in the WM ROI.

Visual Comparison

The same 3 raters evaluated the optimized SWI images with respect to visibility of the different structures. For each of the 10 volunteers, the 6 different SWI volumes were assigned a random letter for blinding purposes. Raters were instructed to rank the volumes from best (rank 1) to worst (rank 6) for different structures. Specific instructions were "consider: the contrast of the structure with surrounding tissue, the ability to resolve its borders, and how image noise influences visibility." Visibility was ranked for the same structures in which CNR was measured. The qualitative impression of SNR in the frontal WM was also ranked. Images were rated for severity of artifacts at the sinuses from least severe (rank 1) to most severe (rank 6).

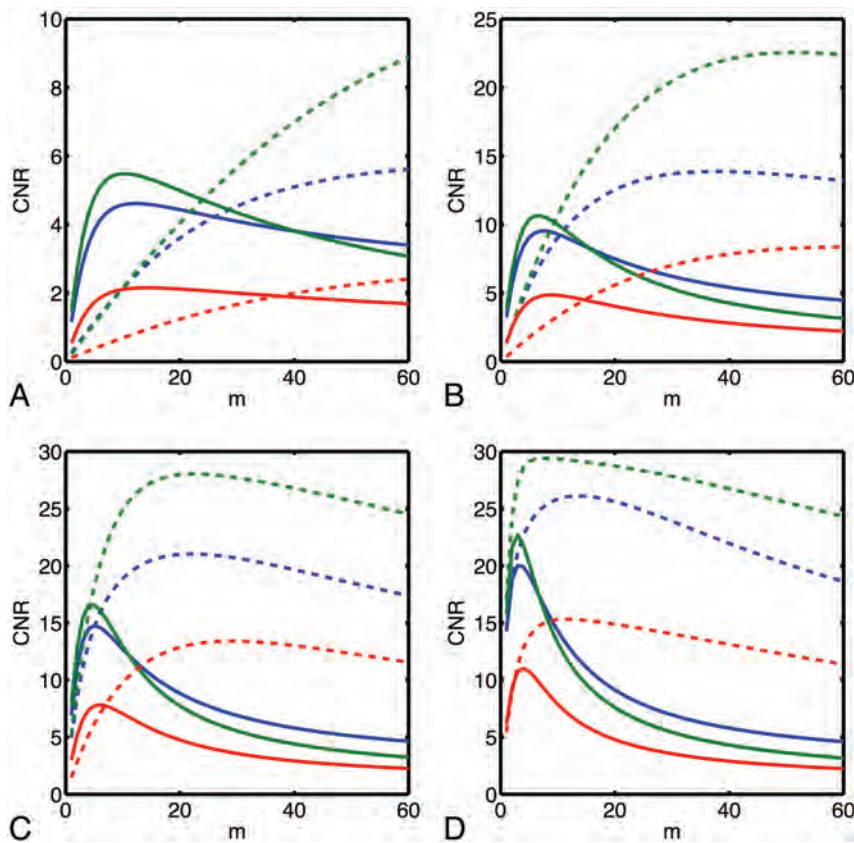


FIG 1. CNR vs number of mask multiplications (m) for different SWI postprocessing schemes (*red: single-echo, blue: postaverage, green: frequency-based*) and mask functions (*solid: linear, dashed: nonlinear*) as simulated for a vein of varying frequency in WM. Simulated frequencies were -1.0 Hz (A), -2.5 Hz (B), -5 Hz (C), and -10.0 Hz (D).

Optimization of m

	Simulation		Radiologist Rating
	Min. Optimal m^a	Max. Optimal m^b	Optimal m (Min ^c , Max ^d)
Single-echo			
Linear	4	17	6 (4,7)
Nonlinear	11	>60	35 (20,35)
Postaverage			
Linear	3	15	7 (5,10)
Nonlinear	14	>60	35 (25,45)
Frequency-based			
Linear	3	15	5 (2,7)
Nonlinear	8	>60	25 (20,40)

^{a,b} Minimal, maximal values, respectively, of m that yield maximal contrast-to-noise ratio for any frequency of vein simulated.

^{c,d} Minimal, maximal values, respectively, assigned by any of the 3 raters.

To evaluate interrater agreement, we calculated the interclass correlation coefficient on rankings of each structure analyzed. For each volunteer, for each combination of processing scheme and mask function, the 3 ranks assigned by the raters were averaged to create a mean rank. To separately test the significance of the 2 main effects (processing scheme and filter), for each level of each main effect, we added mean ranks across all levels of the other main effect. Nonparametric-related samples tests were then used to compare all levels of a given effect: the Friedman test for scheme and the Wilcoxon signed-rank test for filter. Where appropriate, the Wilcoxon test was used post hoc with Bonferroni correction.

RESULTS

Optimization of m

Plots of CNR as a function of m are presented (Fig 1) for several different choices of the frequency of the vein compartment of the numeric phantom. Optimal values of m depend strongly on the frequency of the vein; minimal and maximal values of optimal m over the range of frequencies investigated are presented in the accompanying Table. According to simulation, greater CNR is achievable with the nonlinear mask, though typically larger values of m are required. Simulation predicts that the frequency-based method allows the greatest CNR and that both multiecho methods are superior to single-echo SWI.

Optimization of m was also performed via visual rating of images. For measurement of the optimal value of m for a given processing combination, the median (across the 4 volunteers) of the median (across the 3 raters) is reported in the Table. In all cases, the optimal value as determined by the raters falls within the range of optimal values predicted by simulation. The interclass correlation coefficient was found to be 0.96, indicating excellent interrater agreement.

When implementing different SWI techniques herein, we use the values of m that are determined to be optimal by the raters.

In Vivo Data

Minimum intensity projections through 4 mm for a subset of a section at the level of the basal ganglia are shown in Fig 2 for all permutations of postprocessing scheme and mask function. An increase in SNR is apparent when single-echo images are compared with multiecho images. In general, the nonlinear mask function results in improved noise characteristics compared with the linear filter, and its use also dramatically enhances contrast in some regions (eg, for large veins [arrow in Fig 2F] and at the edges of the basal ganglia [arrowheads in Fig 2F]). Small veins that are not visible in single-echo SWI are readily detected in all implementations of multiecho SWI, such as at the horns of the ventricles (arrows in Fig 2B), though their appearance is smoother and more continuous when the linear filter and/or postaverage processing is used.

ROI Analyses

Normalized measurements of SNR and CNR are presented in On-line Fig 1. The nonlinear mask function results in a significantly larger SNR or CNR ($P < .05$ for GP, $P < .01$ for periventricular veins, STN; $P < .001$ for frontal WM, OR, or RN). The frequency-based scheme results in a significantly larger CNR or SNR than both postaverage and single-echo techniques, except

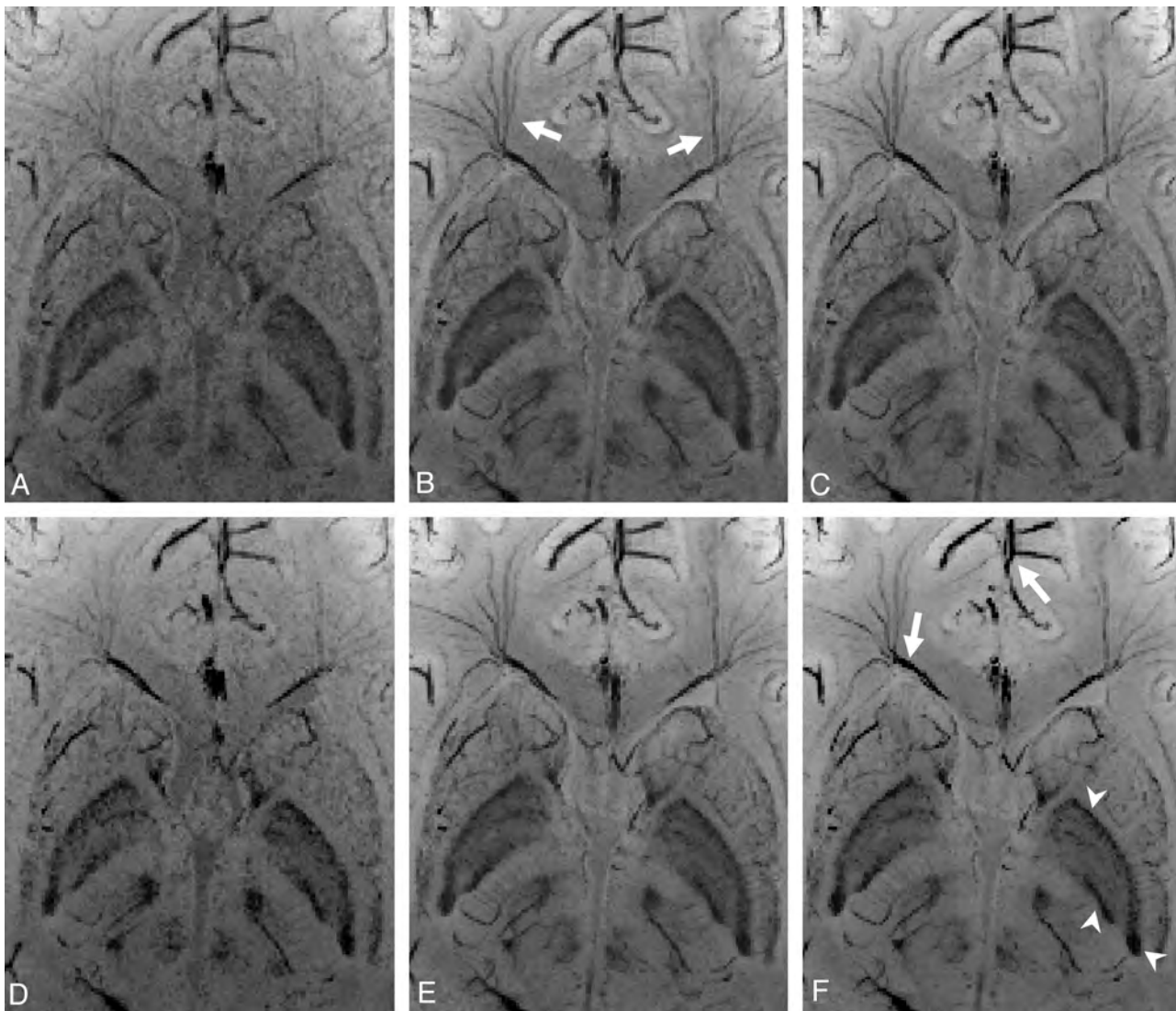


FIG 2. Minimum intensity projections through 4 mm at the basal ganglia for different SWI postprocessing schemes (*first column: single-echo, second column: postaverage, third column: frequency-based*) and mask functions (*first row: linear mask, second row: nonlinear mask*).

for GP, where no significant difference is detected between post-average and frequency-based processing, though both result in a significantly larger CNR than single-echo. Specific *P* values are presented for pair-wise comparisons of the processing scheme in On-line Fig 1.

Visual Comparison

Mean ranks are presented (On-line Fig 2) for qualitative impression of SNR of the frontal WM, and for visibility of various structures. For all paramagnetic perturbers (GP, STN, RN, and periventricular veins), the linear filter resulted in significantly ($P < .001$) greater visibility (equivalently, lower mean rank). The postaverage scheme resulted in significantly lower mean ranks than both frequency-based and single-echo schemes for these structures as well—except for the periventricular veins, where no significant differences were observed between postaverage and frequency-based processing. In contrast, for visibility of OR and SNR of the frontal WM, the nonlinear filter was ranked as significantly better ($P < .001$). For OR, the frequency-based scheme was significantly better than both single-echo and postaverage

schemes. Specific *P* values are presented for pair-wise comparisons of the processing scheme in On-line Fig 2. Mean ranks of artifact severity are presented (Fig 3). In general, the linear mask function results in less severe artifacts ($P < .001$); the postaverage scheme results in least severe artifacts. Interrater agreement, as assessed by the interclass correlation coefficient, was excellent (frontal WM, 0.88; GP, 0.93; OR, 0.85; periventricular veins, 0.82; STN, 0.91; RN, 0.93; artifacts, 0.96).

DISCUSSION

This study presents a comparison of 1) different SWI processing schemes; and 2) different mask functions, in SWI image quality as assessed by ROI analysis and visual rating.

SWI Optimization

Our choice of *m* for implementation in human data was based on optimized values as determined by radiologist raters. This is justified for several reasons: 1) in all cases, rater-optimized values fell within the range of optimal *m* predicted by simulation; 2) raters were instructed to consider the influence of *m* not only on the

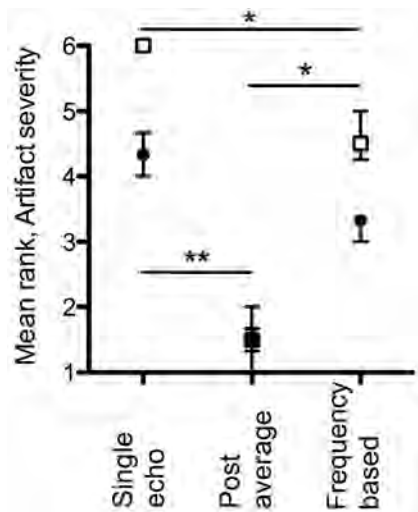


FIG 3. Mean rank of artifact severity at sinuses. Filled black circles: linear mask function; empty squares: nonlinear mask function. Points: median; bars: interquartile range ($n=10$). Illustrated are significant P values for pair-wise comparisons of postprocessing schemes (* $P < .05$, ** $P < .01$).

veins but also on other structures and noise; 3) there was excellent interrater agreement; and 4) radiologists are the end-users of SWI. Our optimal m value for linearly masked single-echo (ie, conventional) SWI was 6. In contrast, conventional SWI is virtually always implemented with $m=4$. This choice is influenced by a seminal SWI study¹² where CNR vs m was simulated for a comparable range of vein phases. As in our simulation, that study found that a lower m is required for maximal CNR for an increasingly large phase. Our raters found a slightly larger value of m to be most suitable. As our optimizations involved simulation and rating, they are more comprehensive than previous efforts. We have endeavored to choose values of m that are suitable for optimal visibility of a range of structures; however, if reoptimization is required for a specific application, it should be performed by trained raters.

In Vivo Data

For small veins, typical targets of SWI, ROI measurements in vivo agree with those predicted by simulation: optimal CNR can be achieved with the nonlinear mask implemented with a frequency-based processing scheme. This conclusion can be extended to a CNR of paramagnetic perturbers in general. However, according to visual assessment by trained raters, these same structures are most visible when SWI is performed with the linear mask and postaverage processing. This apparent contradiction highlights a discrepancy between CNR and the qualitative impression of visibility. Although the nonlinear filter and frequency-based scheme might independently result in more dramatic contrast (eg, at the edges of the GP in Fig 2), they do not necessarily increase the information content of the image compared with other implementations of multiecho SWI. Rather, their implementation can result in an image with harsher contrast wherein a more subtle structure is less apparent. Images appear “burnt out” when the contrast is too high, with scarce gradation in the grayscale, which was interpreted by raters as potential loss of information. It seems

that maximal contrast should not be the exclusive target when visibility is being optimized.

The nonlinear mask function and frequency-based processing demonstrated best performance with respect to the frontal WM and OR, a diamagnetic perturber, as judged by both quantitative measures in ROI analyses, and visual ranking. For both the frontal WM and OR, we do not expect the mean signal in an ROI to change after multiplication with the described mask functions, given their zero or positive frequency, respectively. Therefore, the improved performance of nonlinear mask function and frequency-based processing for the frontal WM and OR can be attributed to the reduced noise introduced into the image in these regions by these postprocessing strategies, given the absence of changes in mean signal or contrast.

One limitation of multiecho SWI is increased scan time. Fewer echoes or reduced coverage could be used to reduce scan time. As an alternative, if coverage were expanded to allow imaging of the entire supratentorial brain, scan time would be on the order of 20 minutes. In addition to SWI, it is possible to obtain many contrasts from this acquisition, including R_2^* maps, frequency maps, and quantitative susceptibility maps. Given the high-yield nature of this acquisition, the parameters recommended here are not unreasonable in a clinical setting.

Field Inhomogeneity Artifacts

Multiecho SWI processing, in particular postaverage, typically resulted in less severe field inhomogeneity artifacts compared with single-echo SWI. Denk and Rauscher⁸ showed that, by using a filter width that varies with TE, field inhomogeneity artifacts could be reduced further in postaverage processing while preserving contrast elsewhere in the image. To limit the matrix of comparisons in our present study, we elected not to investigate the effects of an adaptive filter, though we expect its use would result in further reduction of these artifacts.

Prospective Applications

Ultimately, our recommendation for SWI implementation depends on the desired application and allowed time. It is certainly clear that any implementation of multiecho SWI results in superior images to single-echo SWI.

For radiologic use, postaverage processing and the linear filter are favored. Given its favored performance for visualization of paramagnetic perturbers, this implementation of multiecho SWI seems especially well suited to the study of neurodegenerative diseases in which iron deposition is implicated. In addition, this technique might have a role in the study of traumatic brain injury, stroke, and other conditions where abnormalities in the vasculature or blood products are involved. One specific diagnostic application is assessing the presence of veins within WM lesions. At 7T, this has been demonstrated to be specific to multiple sclerosis¹³; however, current techniques at 3T lack the sensitivity to delineate such veins. Optimized multiecho SWI holds promise for reproducing these findings at clinical field strengths.

In our study, volunteers were free of pathologic conditions, and raters were thus only able to evaluate the visibility of normal structures. It is possible that the high-contrast, low-noise properties of either (or both) frequency-based processing and the nonlinear filter may facilitate more rapid detection of very

subtle pathologic conditions such as microbleeds. As an alternative, although frequency-based, nonlinearly filtered SWI may be undesirable for radiologic assessment, such an image may be optimal for automated tasks where high contrast and low noise would be favored, such as STN segmentation for electrode targeting, computer-based delineation of veins, or registration tasks.

CONCLUSIONS

Linearly masked postaverage SWI is the recommended implementation of multiecho SWI for radiologic use; however, nonlinearly masked frequency-based SWI may have use in computer-based segmentation or registration. A discrepancy between measures of CNR and subjective impressions of visibility was found, highlighting an important caution for SWI optimization.

Disclosures: Matthew Quinn—RELATED: Grant: CIHR operating grant.* Amy Lin—RELATED: Grant: CIHR operating grant.* Jeffery Bird—RELATED: Grant: CIHR operating grant.* Stephanie Leung—RELATED: Grant: CIHR.* Ravi Menon—RELATED: Grant: CIHR.* Comments: Operating grant that supported this research; UNRELATED: Grants/Grants Pending: Ontario Research Fund.* * Money paid to institution.

REFERENCES

- Haacke EM, Mittal S, Wu Z, et al. **Susceptibility-weighted imaging: technical aspects and clinical applications, part 1.** *AJNR Am J Neuroradiol* 2009;30:19–30
- Reichenbach JR, Venkatesan R, Schillinger DJ, et al. **Small vessels in the human brain: MR venography with deoxyhemoglobin as an intrinsic contrast agent.** *Radiology* 1997;204:272–77
- Sehgal V, Delproposito Z, Haddar D, et al. **Susceptibility-weighted imaging to visualize blood products and improve tumor contrast in the study of brain masses.** *J Magn Reson Imaging* 2006;24:41–51
- Haacke EM, Makki M, Ge Y, et al. **Characterizing iron deposition in multiple sclerosis lesions using susceptibility weighted imaging.** *J Magn Reson Imaging* 2009;29:537–44
- Wu Z, Mittal S, Kish K, et al. **Identification of calcification with MRI using susceptibility-weighted imaging: a case study.** *J Magn Reson Imaging* 2009;29:177–82
- Yao B, Li TQ, Gelderen P, et al. **Susceptibility contrast in high field MRI of human brain as a function of tissue iron content.** *Neuroimage* 2009;44:1259–66
- Brainovich V, Sabatini U, Hagberg GE. **Advantages of using multiple-echo image combination and asymmetric triangular phase masking in magnetic resonance venography at 3 T.** *Magn Reson Imaging* 2009;27:23–37
- Denk C, Rauscher A. **Susceptibility weighted imaging with multiple echoes.** *J Magn Reson Imaging* 2010;31:185–91
- Casciaro S, Bianco R, Franchini R, et al. **A new automatic phase mask filter for high-resolution brain venography at 3 T: theoretical background and experimental validation.** *Magn Reson Imaging* 2010;28:511–19
- Quinn MP, Klassen LM, Gati JS, et al. **Frequency-based multi-echo susceptibility weighted imaging.** In: Proceedings of the International Society for Magnetic Resonance in Medicine; May 5–11, 2012; Melbourne, Australia.
- Noll DC, Nishimura DG, Macovski A. **Homodyne detection in magnetic resonance imaging.** *IEEE Trans Med Imaging* 1991;10:154–63
- Haacke EM, Xu Y, Cheng YC, et al. **Susceptibility weighted imaging (SWI).** *Magn Reson Med* 2004;52:612–18
- Tallantyre EC, Dixon JE, Donaldson I, et al. **Ultra-high-field imaging distinguishes MS lesions from asymptomatic white matter lesions.** *Neurology* 2011;76:534–39

Intracranial Imaging of Uncommon Diseases Is More Frequently Reported in Clinical Publications Than in Radiology Publications

V.T. Lehman, D.A. Doolittle, C.H. Hunt, L.J. Eckel, D.F. Black, K.M. Schwartz, and F.E. Diehn



ABSTRACT

BACKGROUND AND PURPOSE: Descriptions of uncommon diseases with intracranial imaging abnormalities are often difficult to find in the radiology literature. We hypothesized that reported imaging findings of such conditions in the recent literature were more frequent in clinical compared with radiology journals.

MATERIALS AND METHODS: PubMed searches from December 1, 2007 to December 1, 2012 were performed for 5 uncommon CNS diseases with intracranial imaging manifestations: 1) Susac syndrome; 2) amyloid β -related angiitis; 3) Parry-Romberg syndrome/en coup de sabre; 4) transient lesion of the splenium of the corpus callosum; and 5) reversible cerebral vasoconstriction syndrome. Articles were classified as a case report, case series, or original research. Journals were categorized as radiology or clinical. The 1- and 5-year Impact Factors of the journals were recorded.

RESULTS: Two hundred two articles were identified for the 5 diseases, including 151 (74%) case reports, 26 case series (13%), and 25 original research articles (13%); 179 (89%) were published in nonradiology journals, compared with 23 (11%) in radiology journals. There was no significant difference between the mean 1- and 5-year Impact Factors of the radiology and clinical journals.

CONCLUSIONS: Recent reports of the selected uncommon diseases with intracranial manifestations are more frequent in clinical journals when compared with dedicated radiology publications. Most publications are case reports. Radiologists should review both radiology and clinical journals when reviewing imaging features of uncommon diseases affecting the brain. Lack of reporting on such disease in the radiology literature may have significant practice, educational, and research implications for the radiology community.

ABBREVIATIONS: ABRA = amyloid β -related angiitis; RCVS = reversible cerebral vasoconstriction syndrome

The frequency with which the radiology versus the clinical literature reports on the imaging findings and techniques of uncommon CNS diseases is not known. Although little has been published about the rates at which radiologists read specific medical journals, there is some evidence that radiologists tend to read radiology journals and that specialists tend to focus on clinical journals within their respective areas.¹⁻³ There is also evidence that journal articles are a preferred source of information for clinical decision-making by physicians.² It is important to characterize the avenues of knowledge dissemination, to direct radiologists and clinicians to the most likely primary resources that can help

optimize management of patients with an uncommon CNS disease.

In our day-to-day clinical practice, we have anecdotally found much of the relevant information on imaging findings about several uncommon CNS diseases in the clinical rather than the radiologic literature. However, this perception has not been confirmed with a systematic study of the medical literature. Additionally, the type of articles in which imaging of uncommon CNS disease is reported is not known but could be useful to investigate to increase understanding of the source of reported imaging findings. Many of the purported imaging features of uncommon CNS diseases may be found within case reports rather than within original research, in part because of low prevalence of disease and inherent difficulty with patient accrual. However, case reports have faced high rejection rates within the radiology literature, and some radiology journals no longer consider case reports for publication in recent years,⁴ even though a survey has indicated that many radiologists find case reports useful.⁵

Received March 5, 2013; accepted after revision April 5.

From the Department of Radiology, Mayo Clinic College of Graduate Medical Education, Rochester, Minnesota.

Please address correspondence to Vance T. Lehman, MD, Department of Radiology, 200 First St SW, Rochester, MN 55905; e-mail: lehman.vance@mayo.edu

 Indicates article with supplemental on-line appendix

 Evidence-Based Medicine Level 2.

<http://dx.doi.org/10.3174/ajnr.A3625>

To further investigate these unresolved questions, we selected 5 uncommon diseases with potentially important intracranial imaging manifestations. We hypothesized that reported imaging findings of such conditions in the recent literature were more frequent in clinical compared with radiology journals.

MATERIALS AND METHODS

CNS Conditions

Five uncommon conditions with important intracranial imaging manifestations were selected for review: Susac syndrome, transient lesion of the splenium of the corpus callosum, amyloid β -related angiitis (ABRA), Parry-Romberg syndrome/en coup de sabre, and reversible cerebral vasoconstriction syndrome (RCVS). Although the precise incidence of these conditions is not known with certainty, they were selected because 1) imaging plays an important role in diagnosis and/or management and 2) these are common enough that the authors have cumulatively seen cases of each in our subspecialized academic practice but evaluate each one infrequently. Multiple unrelated conditions were selected to evaluate for overall patterns in publication of topics relevant to neuroradiology rather than the publication pattern of a single condition. Because Parry-Romberg syndrome and en coup de sabre are now considered to be related along the same spectrum of morphea by many authorities in dermatology,⁶ they were considered together as Parry-Romberg syndrome/en coup de sabre.

PubMed Search

PubMed searches of the English literature from December 1, 2007 to December 1, 2012 were performed for the aforementioned conditions. We evaluated topics over a 5-year period to capture an adequate number of publications for analysis but limited our search to these recent years to ensure results are representative of current patterns of publication. All searches were performed between December 1, 2012 and December 10, 2012. The condition names and common synonyms were used as search terms to capture most of the relevant literature. The following search terms were used with an English language-only modifier: 1) Susac syndrome: "Susac syndrome OR Susac's syndrome," 2) transient lesion of the splenium of the corpus callosum: "(transient lesion OR reversible lesion) AND corpus callosum," 3) ABRA: "amyloid beta-related angiitis OR ABRA OR amyloid vasculitis," 4) Parry-Romberg syndrome/en coup de sabre: "Parry-Romberg syndrome OR en coup de sabre," and 5) RCVS: "reversible cerebral vasoconstriction syndrome OR RCVS OR Call-Fleming."

Inclusion Criteria

Included case reports or case series contained, at minimum, a description of the imaging findings as well as at least 1 figure demonstrating a radiologic image of the brain. A report of multiple cases with common diagnosis and pure description of findings was categorized as a case series. A publication with multiple cases that included a clearly defined systematic method of analysis of an imaging finding/technique or other pertinent aspect of the disease was designated original research. Included original research contained, at minimum, description of imaging findings of some included patients, though an actual figure of an example of an imaging finding was not required. Included intracranial imaging was cross-sectional (either CT or MR imaging), transcranial Doppler,

and/or angiographic (conventional DSA, MRA, or CTA). Original research articles that studied patients both with and without the target diagnosis, such as those with comparison of patients with ABRA and primary CNS vasculitis, were included. Imaging of the face without intracranial imaging, such as reports of extracranial head and neck findings in Parry-Romberg syndrome/en coup de sabre alone, was not sufficient for inclusion because the focus of this study was on intracranial findings.

Exclusion criteria were 1) wrong topic captured by search terms; 2) animal study; 3) review article, commentary, or editorial without concomitant incremental case report; 4) no images of the brain included for case reports or case series; 5) no description of imaging findings for an original research article; and 5) full-text not available when insufficient information for analysis was available in the abstract. The full text was analyzed whenever possible. For articles in which there was no abstract or insufficient information available within the abstract, an attempt was made to obtain the full text by our institutional librarians from the publisher or interlibrary loan. In these cases, if the librarians were unable to obtain the full text from the publisher without charge, the article could not be analyzed and was excluded.

Literature Search Analysis and Author Experience

The journal for each included article was recorded and categorized as radiology or clinical with consensus agreement among the authors. Radiology journals were those with a clear primary focus of reporting imaging findings/techniques. The authors reviewed all journals and arrived at consensus designation of each journal as in either the radiology or clinical category. A description of the type of imaging and imaging analysis in each original article was recorded. The articles within the most common radiology journal were examined to determine if they would fulfill current publication criteria (as of April 1, 2013). Additionally, although review, commentary, and editorial articles were not grouped with original reports and studies for the formal analysis, these could also serve as a source of information for radiologists and clinicians. Therefore, the journals of these publications were also categorized as radiology or clinical.

Six of the authors (V.T.L., D.F.B., C.H.H., F.E.D., K.M.S., L.J.E.) are board-certified radiologists with 1, 1, 2, 4, 5, and 7 years of postfellowship radiology experience, respectively. Four of the authors (C.H.H., F.E.D., K.M.S., L.J.E.) have obtained a Certificate of Added Qualification in neuroradiology. One author (D.A.D.) is a radiology resident. Two of the authors (D.F.B. and C.H.H.) also have board certification in clinical neurology, with 5 years of clinical neurology experience each.

The affiliation of each author of the included articles was noted. Articles were categorized as having either 1) at least 1 radiologist as an author or 2) no radiologist listed as an author. If a radiologist author was not identified but the affiliation of every author could not be confirmed, the article was excluded from the author analysis. If at least 1 radiologist as an author was identified, it was included regardless of the availability or type of other author affiliations.

The 2011 1-year and 5-year Impact Factors were recorded for each journal as a measure of frequency of journal citation. The Impact Factors were obtained from an on-line data base, *Journal Citation Reports*, which is published by Thomson Reuters.⁷ Journals that had no recorded Impact Factors were assigned Impact

Factor values of 0 for the purpose of data analysis. Mean Impact Factors of the radiology and clinical journals for each included article were compared with a paired *t* test. The mean Impact Factors were weighted to account for some journals having more than 1 article identified within this literature analysis; 95% CIs were calculated. *P* < .05 was considered statistically significant.

RESULTS

Literature Search

Four-hundred seventy-one publications were captured by the search terms. Two hundred sixty-nine were excluded from analysis for the following reasons: 1) wrong topic captured by search terms (*n* = 160, 59%); 2) animal study (*n* = 3, 1%); 3) review or commentary without incremental case report (*n* = 51, 19%); 4) no CNS images provided for a case report or series (*n* = 45, 17%); 5) full text unavailable when insufficient information was available in the abstract (*n* = 10, 4%); and 6) no imaging description for original research articles (*n* = 0, 0%).

Two hundred two publications (43% of 471) were identified within 12 radiology and 80 clinical journals. The most common radiology and clinical journals are listed in Table 1. The most common radiology journal was the *American Journal of Neuroradiology*, whereas the most common clinical journal was the *Journal of Neurologic Sciences*. Three of 5 (60%) of the articles in the *American Journal of Neuroradiology* were case reports or series with <5 patients and would no longer be considered for publication in this journal after July 1, 2011, whereas 2 (40%) were case series with >5 patients and would still be considered.⁸ A complete list of the journals identified and designation as radiology or clinical is catalogued in the On-line Appendix.

Table 2 details the categorization of publication of the clinical and radiology articles. The final study sample of 202 publications included 151 (74%) case reports, 26 case series (13%), and 25 original research articles (13%). Overall, 179 (89%) were published in non-radiology journals compared with 23 (11%) in radiology journals.

Table 1: The 3 most common radiology and clinical journals with the included diagnoses

Journal	No. of Articles
Radiology	
1) <i>AJNR Am J Neuroradiol</i>	5
2) <i>J Neuroimaging</i>	4
3) <i>Interv Neuroradiol</i>	3
Clinical	
1) <i>J Neurol Sci</i>	16
2) <i>Cephalgia</i>	13
3) <i>Neurol Sci</i>	9

Table 2: Frequency of identified publication in radiology and clinical journals

Journal Type	PRS	ABRA	TLCC	Susac	RCVS	Overall
Radiology						
Case reports	4	0	6	3	5	18
Case series	0	0	4	0	1	5
Original research	0	0	0	0	0	0
All publication categories	4	0	10	3	6	23
Clinical						
Case reports	17	8	35	21	52	133
Case series	3	1	7	2	8	21
Original research	1	4	1	4	15	25
All publication categories	21	13	43	27	75	179

Note:—PRS indicates Parry-Romberg syndrome; TLCC, transient lesion of the splenium of the corpus callosum.

Case reports were the most common form of publication for articles in both the radiology and the clinical literature, accounting for 18 of 23 (78%) and 133 of 179 (75%) of radiology and clinical articles, respectively. Additionally, 47 of 51 (92%) separate review, commentary, or editorial articles were within clinical journals.

A brief description of the identified original research articles is listed in the On-line Table. All 25 (100%) original research articles were in the clinical literature. Fifteen (60%) of the original research articles addressed RCVS, though each of the 5 diagnoses had at least 1 original research article. The role of imaging within these articles varied and included articles with a primary aim of characterizing imaging findings such as serial MRA examinations with RCVS⁹ or MR imaging findings of Susac syndrome at 7T,¹⁰ as well as articles primarily assessing an imaging technique or sequence, such as diffusion tensor imaging in Susac syndrome.¹¹

Author Affiliations

In 19 of 202 (9%) of articles, all in clinical journals, a radiologist author could not be confirmed and complete lists of author affiliations could not be found. Complete lists of author affiliations were available for 183 of 202 (91%) articles. Radiologists were authors in 98 of these 183 (54%) articles, including 22 of 23 (96%) articles in radiology journals and 76 of 160 (48%) articles in clinical journals.

Impact Factors

There was no significant difference between the mean 1- and 5-year Impact Factors (*P* values of .29 and .39, respectively) between radiology and clinical journals (Table 3). One-year Impact Factors did not exist for the journals of 1 of 23 (4%) articles in the radiology literature and for the journals of 21 of 179 (12%) articles in the clinical literature. Five-year Impact Factors did not exist for 2 of 23 (9%) articles in radiology journals and 31 of 179 (17%) articles in clinical journals.

DISCUSSION

In the present study, identified reports and original research of imaging features of each of the selected uncommon conditions with brain pathology were more frequent in the clinical compared with the radiology literature. Radiologists are under-represented as authors on such publications in the clinical literature. These findings have numerous implications for neuroradiology practice and patient care.

Description and analysis of imaging findings of CNS disease in the clinical literature is important for several reasons. Clinicians should know the utility of various neuroradiologic techniques to ensure the most appropriate test is requested for a given clinical scenario and should learn about new techniques as they become available. With many CNS pathologies, imaging findings can help

direct treatment, can be of prognostic significance, and can help to assess response to clinical treatment.

Clinicians aware of reports of imaging findings of neurologic disease in the clinical literature will probably expect consulted neuroradiologists to have knowledge of these imaging findings. If the primary targeted audience of the journals containing these reports is highly skewed toward physicians other than radiologists, it is possible that these imaging findings, or

Table 3: Mean Impact Factors of included radiology and clinical journals

Journal Type	1-Year Impact Factor		5-Year Impact Factor	
	Mean (95% CI)	P Value	Mean (95% CI)	P Value
Radiology	1.80 (1.25–2.36)	.29	1.87 (1.20–2.54)	.39
Clinical	2.84 (2.17–3.51)		2.66 (2.02–3.29)	

Note:—Journals with no listed impact factor were assigned values of “0” for the analysis in this table.

even the existence of the condition, will be under-recognized by radiologists. In fact, under-recognition of Susac syndrome by radiologists has been cited by Dr Susac.¹² Radiologists are potentially the first physicians to encounter findings suggestive of a rare CNS condition and have great potential to affect management. Specifically, radiologist under-recognition could initiate an incorrect, possibly invasive, diagnostic workup and delay both the correct diagnosis and the most appropriate therapy.

Although information of the reading habits of radiologists is scant, Andreisek et al³ previously suggested that physicians focus on literature published in journals targeted to their respective specialties.³ These authors compared 2 nearly identical, independently derived grading systems for spinal canal stenosis, one in the radiology literature and one in the orthopedic literature, as an example of duplicative and fragmented knowledge between the clinical and radiology literature. The findings of the present literature analysis indicate that it could be beneficial for radiologists to read, critique, and report imaging findings embedded in the non-radiology literature and to increase publication on these and similar CNS diseases within the radiology literature.

There are multiple potential explanations for the findings of this study. For example, clinical journals outnumber radiology journals. De-emphasis of case reports by radiology journals could also shift the balance of publication to clinical journals. Interestingly, most of included publications in the most common radiology journal in this study would not have been considered for publication in this journal after July 1, 2011, indicating some submissions since this date would presumably have been directed to other journals. Possibly in response to unmet demand for case report publication, several case report radiology journals have recently been introduced, but it is unclear if this will ultimately result in an increased number of radiology publications of uncommon CNS conditions. In addition, some publications containing imaging information potentially describe a new predisposing clinical condition, associated clinical symptoms or syndrome, treatment, affected demographic, or observed prognosis that might be most useful for a clinical audience. It is also possible that a single interested clinical specialist might see several patients with the same rare condition and publish his or her experience while the images of the individual patients are interpreted by several different radiologists. Additionally, lack of familiarity with conditions not reported in the radiologic literature may perpetuate a cycle wherein radiologists do not develop an interest in publishing on these uncommon conditions and remain unaware of new diagnostic issues. Other explanations include possible differences between neuroradiologists and neurologists in the degree of academic involvement, incentive to publish, and degree of subspecialization.

Although the Impact Factor ratings are not perfect measures of the value of an individual article or even a journal, the results of the current study indicate that the preponderance of articles on

the selected topics in the clinical versus radiology literature is not explained by a lower clinical journal Impact Factor.¹³ Radiologists were also authors in nearly half of articles within the clinical literature, indicating that lack of radiologist authorship should not account entirely for the proportional number of articles published within the clinical literature.

This literature analysis has several limitations. Only a limited number of conditions in a specified time period were evaluated, which could not capture all results from all potential search terms, search engines, neuroradiology diagnoses, or dates of publication. This study did not assess the actual rate of radiologist awareness of the imaging findings of the included conditions, references to the nonradiologic literature within radiology review articles, radiology textbooks, and/or radiology conferences. Rates of publication of imaging findings in nonradiology journals could differ with category or prevalence of a specific neuropathology and could differ across various subspecialty topics within radiology. A small number of articles were not included because of the lack of availability of all necessary information for data analysis. Finally, the Impact Factor analysis includes an assumption that articles in journals without listed Impact Factors can be represented.

CONCLUSIONS

This literature analysis demonstrates that uncommon conditions with potentially important CNS imaging findings are more often published in clinical rather than radiology journals, and radiologists are under-represented as authors on such publications. Radiologists should consider the use of broad literature searches and baseline journal reading to include clinical journals, as well as increasing the frequency of publication of imaging findings of uncommon conditions in the primary radiology literature.

REFERENCES

- Hunter TB, Marcus DS, Witzke DB. **Radiologists' perception of professional journals.** *Invest Radiol* 1993;28:706–09
- McKibbin KA, Haynes RB, McKinlay RJ, et al. **Which journals do primary care physicians and specialists access from an online service?** *J Med Libr Assoc* 2007;95:246–54
- Andreisek G, Hodler J, Steurer. **Uncertainties in the diagnosis of lumbar spinal stenosis.** *Radiology* 2011;261:681–84
- Ehara S, Takahashi K. **Reasons for rejection of manuscripts submitted to AJR by international authors.** *AJR* 2007;188:w113–16
- Skjennald A. **What do radiologists read and what do they want to read.** *Acta Radiol* 2006;47:757–58
- Tollefson MM, Witman PM. **En coup de sabre morphea and Parry-Romberg syndrome: a retrospective review of 54 patients.** *J Am Acad Dermatol* 2007;56:257–63
- Journal Citation Reports. <http://admin-apps.webofknowledge.com/JCR/JCR?PointOfEntry=Home&SID=2EI8nCC8ndBilc8dC4>. Thomson Reuters. 2013
- <http://www.ajnr.org/> Accessed April 1, 2013
- Yeh YC, Fuh JL, Chen SP, et al. **Clinical features, imaging findings, and outcomes of headaches associated with sexual activity.** *Cephalgia* 2010;30:1329–35
- Wuerfel J, Sinnaker T, Ringelstein EB, et al. **Lesion morphology at 7 Tesla MRI differentiates Susac syndrome from multiple sclerosis.** *Mult Scler* 2012;18:1592–99
- Kleffner I, Deppe M, Mohammadi S, et al. **Neuroimaging in Susac syndrome: focus on DTI.** *J Neurol Sci* 2010;299:92–96
- Susac JO. **Susac's syndrome.** *AJNR Am J Neuroradiol* 2004;25:351–52
- Seglen PO. **Why the impact factor of journals should not be used for evaluating research.** *BMJ* 1997;314:498–502

Does the Location of the Arterial Input Function Affect Quantitative CTP in Patients with Vasospasm?

B.J. Shin, N. Anumula, S. Hurtado-Rúa, P. Masi, R. Campbell, R. Spandorfer, A. Ferrone, T. Caruso, J. Haseltine, C. Robinson, A. Gupta, and P.C. Sanelli



ABSTRACT

BACKGROUND AND PURPOSE: In recent years, there has been increasing use of CTP imaging in patients with aneurysmal SAH to evaluate for vasospasm. Given the critical role of the arterial input function for generation of accurate CTP data, several studies have evaluated the effect of varying the arterial input function location in patients with acute stroke. Our aim was to determine the effect on quantitative CTP data when the arterial input function location is distal to significant vasospasm in patients with aneurysmal SAH.

MATERIALS AND METHODS: A retrospective study was conducted of patients with aneurysmal SAH admitted from 2005 to 2011. Inclusion criteria were the presence of at least 1 anterior cerebral artery or MCA vessel with a radiologically significant vasospasm and at least 1 of these vessels without vasospasm. We postprocessed each CTP dataset 4 separate times by using standardized methods, only varying the selection of the arterial input function location in the anterior cerebral artery and MCA vessels. For each of the 4 separately processed examinations for each patient, quantitative data for CBF, CBV, and MTT were calculated by region-of-interest sampling of the vascular territories. Statistical analysis was performed by using a linear mixed-effects model.

RESULTS: One hundred twelve uniquely processed CTP levels were analyzed in 28 patients (mean age, 52 years; 24 women and 4 men) recruited from January 2005 to December 2011. The average Hunt and Hess scale score was 2.89 ± 0.79 . The average time to CTP from initial presentation was 8.2 ± 5.1 days. For each vascular territory (right and left anterior cerebral artery, MCA, posterior cerebral artery), there were no significant differences in the quantitative CBF, CBV, and MTT generated by arterial input function locations distal to significant vasospasm compared with nonvasospasm vessels ($P > .05$).

CONCLUSIONS: Arterial input function placement distal to significant vasospasm does not affect the quantitative CTP data in the corresponding vascular territory or any other vascular territory in aneurysmal SAH.

ABBREVIATIONS: ACA = anterior cerebral artery; AIF = arterial input function; aSAH = aneurysmal subarachnoid hemorrhage; VSP = vasospasm

In recent years, there has been increasing use of CTP imaging in patients with aneurysmal subarachnoid hemorrhage (aSAH) to evaluate vasospasm (VSP). Several studies have reported CTP as a valuable tool for detecting perfusion deficits related to vasospasm,

described as focal areas of CBF reduction and/or MTT prolongation.¹⁻⁵ To obtain the CBF, MTT, and CBV maps, one performs postprocessing of the acquired dataset. Deconvolution-based postprocessing algorithms require selection of an arterial input function (AIF) to represent the actual injection rate of contrast as time-series data during its first pass in the artery. The mathematic algorithm “deconvolves” this arterial attenuation curve from the tissue attenuation curve to compute an impulse residue function. On the basis of the impulse residue function curve, CBF is calculated as the height of this curve, CBV is the area under the curve, and MTT is the area under the curve of the impulse residue function divided by its height.

Given the critical role of the AIF for generation of accurate CTP data, several studies have evaluated the effect of varying the AIF location in patients with acute stroke.⁶⁻⁸ These studies revealed no significant difference in the quantitative CTP data with AIF selection ipsilateral or contralateral to the side of MCA vessel

Received January 7, 2013; accepted after revision March 28.

From the Departments of Radiology (B.J.S., N.A., P.M., R.C., R.S., A.F., T.C., J.H., C.R., A.G., P.C.S.) and Public Health (S.H.-R., P.C.S.), Weill Cornell Medical College/New York–Presbyterian Hospital, New York, New York.

This work was supported by grant 5K23NS058387-04 from the National Institute of Neurological Disorders and Stroke (NINDS), a component of the National Institutes of Health (NIH). It was also funded by the Clinical and Translational Science Center (grant ULI-RR024996).

The contents of this publication are solely the responsibility of the authors and do not necessarily represent the official view of NINDS or NIH.

Please address correspondence to Pina C. Sanelli, MD, MPH, Department of Radiology, Weill Cornell Medical College–New York Presbyterian Hospital, 525 East 68th St, Box 141, New York, NY 10065; e-mail: pcs9001@med.cornell.edu

Indicates open access to non-subscribers at www.ajnr.org

<http://dx.doi.org/10.3174/ajnr.A3655>

occlusion in either the anterior cerebral artery (ACA) or MCA segments. However, AIF selection distal to an embolus revealed significant differences in the quantitative CTP data recommending avoidance of this location.⁹ It is unclear to what extent these findings are applicable to patients with aneurysmal subarachnoid hemorrhage because vasospasm results in narrowing rather than abrupt occlusion of the cerebral arteries. When significant vasospasm ($\geq 50\%$ narrowing) is present, perfusion deficits have been reported in the corresponding vascular territories,^{1,2} supporting the hypothesis that AIF selection distal to severe vasospasm could potentially affect quantitative CTP data. To date, there are no reports in the literature evaluating AIF placement in vasospasm. The purpose of this study was to determine the effect on quantitative CTP when the AIF location is distal to significant vasospasm in patients with aSAH.

MATERIALS AND METHODS

Study Design

A retrospective study of consecutive patients with aSAH enrolled in a prospective clinical trial was performed to compare quantitative CTP data when the AIF location is distal to significant vasospasm (AIF_{VSP}) versus without vasospasm (AIF_{non-VSP}). Patients were enrolled in an institutional review board–approved clinical trial at our institution from January 2005 to December 2011. aSAH was diagnosed by NCCT, CTA, DSA, and/or CSF analysis. The following inclusion criteria were applied in this study to compare quantitative CTP data when postprocessing occurred with AIF_{VSP} and AIF_{non-VSP} in each patient: 1) CTA performed at the same time as CTP to determine which vessels were in vasospasm at the time of CTP acquisition, 2) the presence of significant arterial narrowing related to vasospasm on CTA in at least 1 first-order segment of the ACA or MCA, and 3) the absence of significant vasospasm on CTA in at least 1 first-order segment of the ACA or MCA. The exclusion criteria were the following: 1) CTP with extreme patient motion or inadequate contrast bolus for which postprocessing could not be performed, and 2) CTP performed following treatment for vasospasm.

Retrospective chart review was performed to collect demographic data on the study population, including age, sex, Hunt and Hess scale grade, ruptured aneurysm location, and the day CTP was performed following aneurysm rupture.

CTA Scanning and Interpretation

CTA of the head was performed by using a standard scanning protocol at our institution with LightSpeed or Pro 16 scanners (GE Healthcare, Milwaukee, Wisconsin). The scanning parameters were 140 kV(peak) and 370 mA at 0.625-mm thickness. A total of 90 mL of nonionic iodinated contrast was administered intravenously at 4 mL/s by using a power injector. Standardized maximum intensity projection images were reconstructed in the coronal, sagittal, and axial planes.

CTA was used to determine the angiographic criteria for proximal vasospasm of the first-order cerebral vessels (A1 and M1 segments) on the basis of the arterial luminal narrowing compared with the normal parent vessel and baseline CTA performed on admission. On the basis of published data, significant vasospasm was defined as $\geq 50\%$ narrowing, because this threshold has been shown to be associated with CT perfusion deficits,^{1,2}

while no significant vasospasm was defined as $< 50\%$ narrowing. CTA examinations were interpreted by 2 observers, neuroradiologists who performed the clinical interpretation (with 7–27 years' experience) and another neuroradiologist (with 3 years' experience) blinded to all clinical and imaging information. Arterial caliber measurements were made by measuring the linear diameter of the lumen at the point of greatest narrowing, by using the imaging plane (axial source images or coronal or sagittal reformations) that demonstrated the most severe narrowing and then comparing this diameter with the native arterial luminal diameter on baseline imaging performed before the period of vasospasm. If no prior imaging was available, the normal-appearing vessel segment immediately proximal to the point of narrowing was used as a reference for normal vessel diameter. If this was also thought to be narrowed secondary to vasospasm, the contralateral vessel was used to approximate normal vessel caliber. If diffuse vasospasm was present and no prior imaging was available for comparison, research reader judgment based on previous clinical experience was used to assess the expected normal vessel caliber to grade vasospasm severity. For disagreements, a third neuroradiologist (with 11 years' experience) independently reviewed the examination in a blinded fashion.

CTP Scanning, Postprocessing, and Data Collection

CTP was performed during the typical time for vasospasm between days 6 and 10 following aneurysm rupture. There is a standard scanning protocol for CTP at our institution by using LightSpeed or Pro 16 scanners (GE Healthcare) with cine 4i scanning mode and 45-second acquisition at 1 rotation per second by using 80 kVp and 190 mA. A scanning volume of 2.0 cm was used, consisting of 4 sections at 5.0-mm thickness with its inferior extent selected at the level of the basal ganglia, above the orbits, to minimize radiation exposure to the lenses. Approximately 45 mL of nonionic iodinated contrast was administered intravenously at 5 mL/s by using a power injector with a 5-second delay.

We performed postprocessing of the acquired dataset into CBF, CBV, and MTT maps on an Advantage Workstation (GE Healthcare) by using CTP software, Version 3.0, using a deconvolution method. The postprocessing technique was standardized for all patients according to recommended guidelines,¹⁰ selecting the venous function as the superior sagittal sinus. While we maintained all postprocessing parameters constant, each CTP dataset was postprocessed 4 times by varying only the AIF location in the A2 segment of the right and left ACAs and M2 segment of the right and left MCAs (Fig 1). Placement of the AIF in the right- and left-sided A2 and M2 segments was performed by a neuroradiologist (with 11 years' experience) on the basis of the concurrent CTA.

Quantitative analysis was conducted by using a standardized method with contiguous region-of-interest placement, measuring 157 mm², sampling the cerebral cortex. Each CTP section in each functional map (CBF, MTT, and CBV) had up to 24 ROIs distributed in the following territories: approximately 6 ROIs in the ACA, 12 ROIs in the MCA, and 6 ROIs in the posterior cerebral artery. For accurate comparison of the quantitative CTP data derived from each of the 4 different AIF locations, a region-of-interest template was created for each patient to replicate the exact size and location of the region-of-interest sampling at each CTP level.

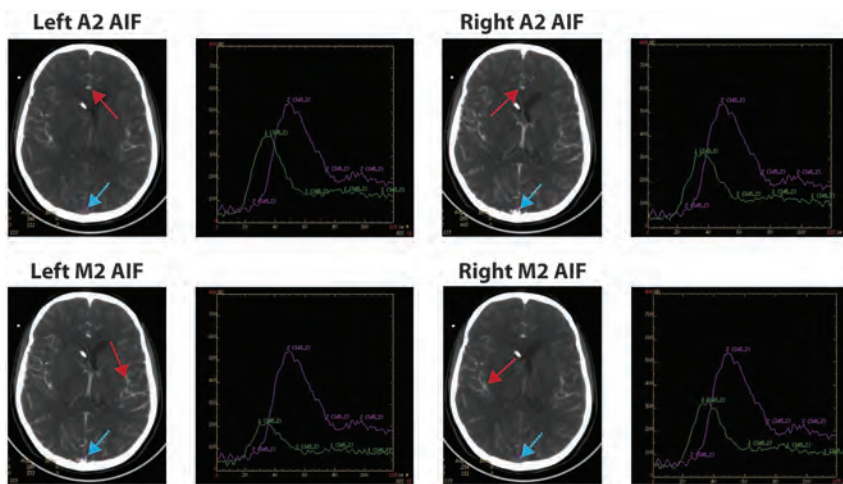


FIG 1. Examples of the standardized AIF locations selected according to the study protocol. The AIFs (red arrows) are placed in the right and left A2 and M2 segments of the ACA and MCA, respectively, within the same patient. The venous output function (blue arrows) is not varied and held constant within the same patient. The arterial attenuation curves (green) and venous attenuation curves (purple) generated by the respective arterial and venous functions are demonstrated to the right of each image. In this particular example, the AIF location in the left M2 segment is distal to vasospasm. Note, the reduced height of its arterial attenuation curve.

Table 1: Characteristics of the study population

Characteristic	Value
Age (mean) (yr)	52 ± 11
Sex: female	86% (24/28)
Hunt and Hess scale score (mean)	2.89 ± 0.79
Time to CTP (mean) (days) ^a	8.2 ± 5.1
Aneurysm site ^b	
Basilar	3.6% (1/28)
ICA	35.7% (10/28)
AcomA	14.3% (4/28)
ACA	3.6% (1/28)
MCA	32.1% (9/28)
PcomA	25% (7/28)
Multiple	25% (7/28)
First-order cerebral arteries ^c	
Significant vasospasm, AIF _{VSP} (≥50% narrowing)	56
No significant vasospasm, AIF _{non-VSP} (<50% narrowing)	54

Note:—AcomA indicates anterior communicating artery; PcomA, posterior communicating artery.

^a Time from initial diagnosis to CTP scanning.

^b Number of patients with an aneurysm at the specified site. Note that the total exceeds 100% because some patients had multiple aneurysms.

^c Two cerebral arteries could not be evaluated due to streak artifacts and motion.

Statistical Analysis

We performed a power analysis to determine the sample size needed for this study design, analyzing quantitative CTP data from 6 vascular territories (right- and left-sided ACA, MCA, and posterior cerebral artery) in each patient. Bonferroni adjustments were performed for multiple comparisons so that the significance level (α) remained at .05. An effect size for CBF of 5 mL/100 g/min was used, indicating that the study would be adequately powered to detect a mean CBF difference of 5 U (per vascular territory) between the AIF_{VSP} and AIF_{non-VSP} data. This more conservative approach by using a 5-U difference in CBF may not necessarily be clinically significant, but it is important in ensuring that the study design would detect small differences between AIF_{VSP} and AIF_{non-VSP} data. The remaining parameters in the power analysis

(mean, SD) were based on pilot data. The sample size calculation was performed by using PASS 2008, Version 8.0.13. All tests were performed as 2-tailed. A sample size of 112 CTP levels (28 patients) achieved 90% power with a significance level (α) of .05.

Quantitative analysis of the CTP parameters was performed by using a linear mixed-effects model. The response variable was CBF; the fixed effects in the model were vascular territory, AIF location, and AIF status (AIF_{VSP} and AIF_{non-VSP}). Subjects were included as random effects to account for multiple measures per subject. Differences in CBF values in the AIF_{VSP} and AIF_{non-VSP} data by vascular territory and AIF location were reported along with 95% confidence intervals. Overall, this model accounts for intersubject variability, variability in the number of vasospasm and nonvasospasm vessels among patients, variability in the number of measurements among patients,

and missing data. Most important, analysis for all 6 vascular territories can be performed by using this single fitted model. Similar models were fit for the CBV and MTT analysis. Statistical analysis was performed by a biostatistician and conducted by using R: A Language and Environment for Statistical Computing (<http://www.R-project.org>).

RESULTS

Study Population Characteristics

Twenty-eight consecutive patients with aSAH were included to achieve sufficient power for statistical analysis. The mean age was 52 ± 11 years. There were 86% (24/28) female and 14% (4/28) male patients. Table 1 demonstrates the characteristics of the study population.

One hundred twelve postprocessed CTP levels were derived from the 28 patients; each patient's acquired data were repeatedly postprocessed 4 times by varying only the AIF location (right- and left-sided A2 and M2 segments). Of the 112 A1 and M1 vessels assessed for this study, we required a third reader as a tie-breaker in 7.1% (8/112) of vessels. Analysis was performed at the level of the 6 vascular territories (right- and left-sided ACA, MCA, and posterior cerebral artery), resulting in 672 territories for each CBF, CBV, and MTT analysis.

Quantitative CTP Analysis by AIF Location

Figure 2A demonstrates the mean and 95% CI of the quantitative CTP for all vascular territories in both the AIF_{VSP} and AIF_{non-VSP} data according to each AIF location. There was no statistically significant difference in the quantitative CBF, CBV, and MTT for any of the AIF locations when they were distal to significant vasospasm.

Quantitative CTP Analysis by Vascular Territory

Figure 2B demonstrates the mean and 95% CI of the quantitative CTP for each vascular territory in both the AIF_{VSP} and AIF_{non-VSP} data. There was no statistically significant difference in the quan-

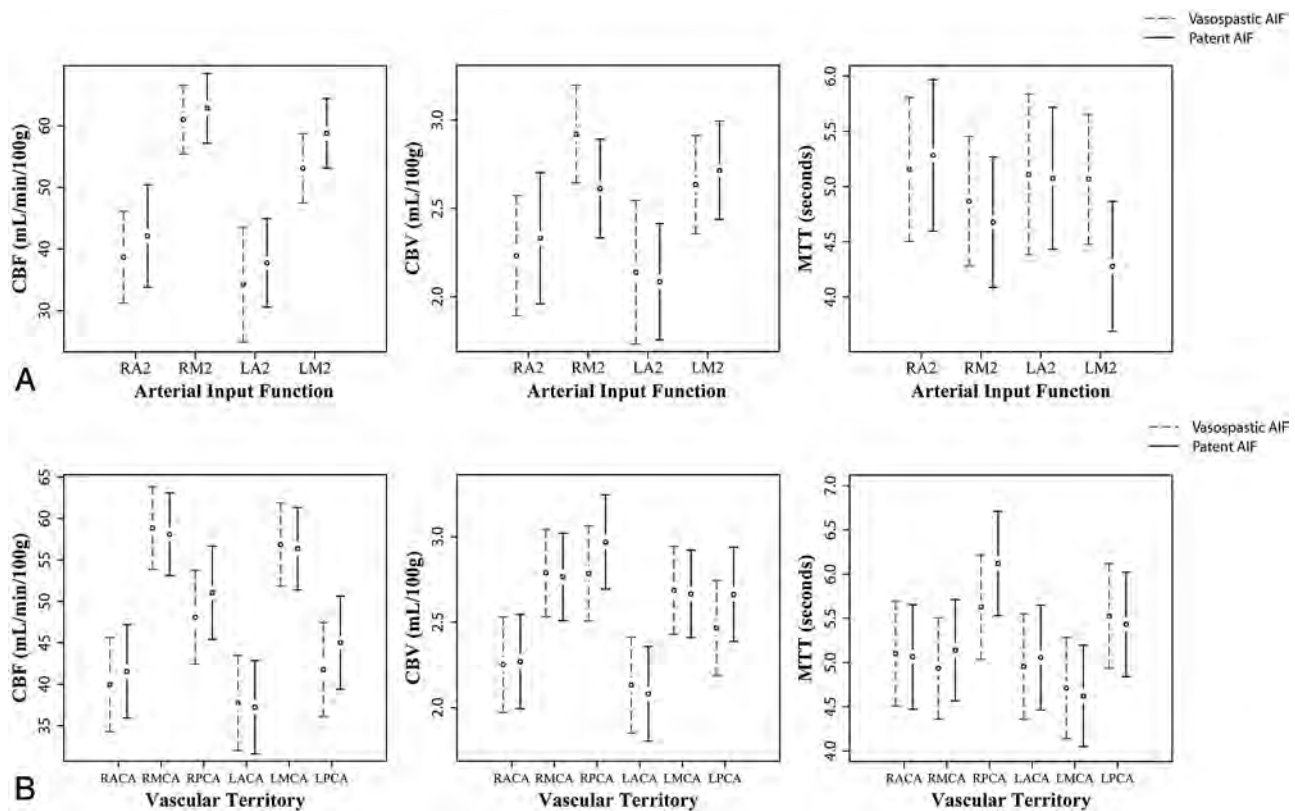


FIG 2. A, Model-adjusted mean and 95% CI bars are displayed for the quantitative CBF, CBV and MTT data for all the vascular territories according to the AIF location. The dashed line represents the quantitative data when AIFVSP was used for post-processing and the continuous line represents the quantitative data when AIFnon-VSP was used. B, Model-adjusted mean and 95% CI bars are displayed for the quantitative CBF, CBV and MTT data for each vascular territory when the AIF is located in a vessel with or without proximal vasospasm. The dashed line represents the quantitative data when AIFVSP was used for post-processing and the continuous line represents the quantitative data when AIFnon-VSP was used. ACA indicates anterior cerebral artery; and PCA, posterior cerebral artery.

Table 2: Model-adjusted mean and 95% CI for CBF, CBV, and MTT data classified by the vascular territory and AIF location in its supplying artery in both AIF_{VSP} and AIF_{non-VSP} data

Vascular Territory	Cerebral Blood Flow (mL/100 g/min)		Cerebral Blood Volume (mL/100 g)		Mean Transit Time (sec)	
	Mean	95% CI	Mean	95% CI	Mean	95% CI
R ACA						
RA2 AIF _{VSP}	38.68	31.23, 46.12	2.23	1.89–2.57	5.16	4.50–5.81
RA2 AIF _{non-VSP}	42.11	33.79–50.43	2.33	1.96–2.70	5.28	4.60–5.97
R MCA						
RM2 AIF _{VSP}	60.99	55.41–66.56	2.92	2.64–3.2	4.87	4.28–5.46
RM2 AIF _{non-VSP}	62.80	57.13–68.46	2.61	2.33–2.89	4.68	4.09–5.27
L ACA						
LA2 AIF _{VSP}	34.23	24.91–43.54	2.14	1.73–2.54	5.11	4.38–5.84
LA2 AIF _{non-VSP}	37.73	30.58–44.88	2.09	1.76–2.41	5.07	4.43–5.72
L MCA						
LM2 AIF _{VSP}	53.09	47.46–58.72	2.63	2.36–2.91	5.07	4.48–5.66
LM2 AIF _{non-VSP}	58.76	53.14–64.39	2.71	2.44–2.99	4.28	3.69–4.87

Note:—R indicates right; L, left.

tative CBF, CBV, and MTT for any vascular territory when the AIF location was distal to vasospasm.

Quantitative CTP Analysis by AIF Location and Its Corresponding Vascular Territory

An additional analysis was performed to evaluate quantitative CTP for the MCA and ACA territories when the AIF was located in its supplying artery in both the AIF_{VSP} and AIF_{non-VSP} data (Table 2). There was no statistically significant difference in the

quantitative CBF, CBV, and MTT for any vascular territory when the AIF location in its supplying artery was distal to vasospasm.

DISCUSSION

CTP has been increasingly used in patients with aSAH, given its reported high sensitivity and specificity to detect perfusion abnormalities thought to occur in vasospasm.^{1,3-5,10} Furthermore, several studies have reported quantitative threshold values for CBF and MTT to determine perfusion deficits for management and treatment of vasospasm.^{1,3,4,10} However, generation of

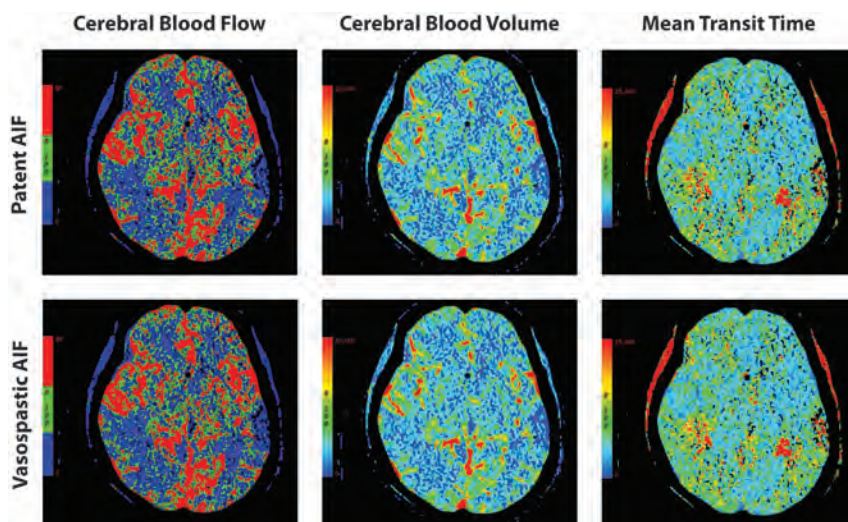


FIG 3. Functional maps of CBF, CBV, and MTT using an AIFVSP and AIFnon-VSP within the same patient. Top row represents the CTP maps for the AIF location in an A2 segment without vasospasm in the proximal ACA. Bottom row represents the CTP maps for the AIF location in an M2 segment distal to proximal vasospasm. There is no significant difference in the quantitative data between these 2 sets of CTP maps in this patient. In addition, the maps appear qualitatively similar with a small perfusion deficit in the left temporoparietal region.

accurate and reproducible quantitative CTP data relies on selecting an appropriate AIF. Standardization of AIF placement by using the A2 segment has been suggested in patients with acute stroke to improve its reproducibility.⁶ This approach is not feasible in patients with aSAH, given the diffuse and variable pattern of vasospasm.

A review of the literature reveals several studies demonstrating the robustness of various AIF locations in patients with acute stroke.^{6-9,11} These studies found that major variations in the AIF location, whether ipsilateral or contralateral to the affected territory, had no significant effect on the quantitative CTP data.^{6,8,9,11} Additionally, the ACA and even the superficial temporal artery may be used as appropriate AIF locations in patients with acute stroke, regardless of the cortical region affected; using these locations may assist in its standardization.^{6,8,9,11} Most important, placement of the AIF in a vessel distal to the embolus has been shown to affect the quantitative CTP data by overestimating MTT and underestimating CBF values due to the marked delay or lack of contrast distal to the clot.⁹ It is physiologically plausible that marked delay in contrast arrival distal to a vessel in significant vasospasm may also occur in patients with aSAH, affecting the quantitative CTP data, but to our knowledge, this has never been studied.

Significant vasospasm, defined as $\geq 50\%$ arterial narrowing, has been found to result in perfusion deficits,^{1,2} suggesting that this degree of arterial narrowing is hemodynamically significant and potentially could result in delay of contrast arrival in the distal vessel. On the basis of digital subtraction angiography, delay in contrast arrival was found in vessels distal to significant vasospasm,¹² with associated diminished height and prolongation of the arterial attenuation curve.¹³ Our study revealed no statistically significant difference in the quantitative CBF, CBV, or MTT data between AIF_{VSP} and AIF_{non-VSP} data (Fig 3) according to the AIF location and vascular territory. Furthermore, there was no quantitative difference in these CTP parameters in the ACA or MCA

vascular territories when the AIF location was in its supplying artery distal to significant vasospasm. Even though our software does not use delay-correction that would likely have demonstrated differences between AIF_{VSP} and AIF_{non-VSP} CTP data if present, these findings suggest that the deconvolution-based algorithm is robust to alterations in the arterial attenuation curve occurring in significant vasospasm. Similar findings in patients with acute stroke were reported for deconvolution-based algorithms, with delay-insensitive techniques producing less pronounced differences in quantitative CTP data when AIF placement distal to the embolus was used.⁹ Another possible explanation is that the delay in contrast arrival distal to vasospasm is not as severe as that distal to an occlusive embolus, thereby not significantly affecting CTP quantitation.

These results have several potential implications for patient care in centers using CTP in patients with aSAH. First, flexibility in selecting the AIF location in patients with vasospasm is valuable, given the challenges with streak artifacts from surgical clips or coils and motion degradation in this population. Second, it is not always known at the time of postprocessing the CTP whether a vessel is in vasospasm when selecting the AIF location. Our study suggests that the presence of significant vasospasm does not have to be determined from CTA before selecting an AIF location. Third, given that many postprocessing software programs have fully or semiautomated processing methods to rapidly generate CBF, CBV, and MTT data, our study supports the selection of variable AIF locations in the A2 or M2 segments by automated computer algorithms. Last, AIF placement is not a limiting factor in postprocessing CTP data in patients with diffuse vasospasm.

There are several limitations in our study to be considered. We were not able to assess collateral circulation and communicating arteries with great certainty because these vessels were below the diagnostic threshold of the concurrent CTA. Documentation of the collateral circulation would have been helpful to further explore possible explanations of why significant vasospasm does not affect the quantitative data, especially because vasospasm has been shown to delay blood flow and collateral circulation can potentially help maintain perfusion, as seen in acute stroke.¹⁴⁻¹⁶ However, the effect of collateral flow on perfusion has not been well-studied in vasospasm and remains uncertain. In addition, AIF location in the posterior circulation was not evaluated because many CTP examinations in this study captured limited areas of the posterior circulation. Finally, because no statistically significant difference was detected between AIF_{VSP} and AIF_{non-VSP} CTP data, the risk of our study being underpowered might be considered as a possible limitation. However, because we were statistically powered to detect differences that are even below the threshold of what many would not consider a clinically significant difference in CBF (5 U), this is unlikely to have affected the

significance or validity of our findings. Finally, although we chose a software package without delay-correction that would likely have demonstrated differences between AIF_{VSP} and $AIF_{non-VSP}$ CTP data if present, this work will require future validation across multiple software platforms, including those with algorithms involving delay-correction, to ensure generalizability across variable postprocessing techniques.

CONCLUSIONS

AIF placement distal to significant vasospasm does not significantly affect the quantitative CTP data in the corresponding vascular territory or any other vascular territory in patients with aSAH. Therefore, vasospasm status should not necessarily influence the selection of the AIF location in either the ACA or MCA segments. This information may be helpful in selecting an AIF location in patients with challenging aSAH with diffuse vasospasm and streak artifacts from aneurysm repair or motion.

Disclosures: Benjamin J. Shin—UNRELATED: Stock/Stock Options: I own stock in Amazon, Activision, Disney, Intel, and Verizon (all unrelated). Sandra Hurtado-Rúa—RELATED: Grant: National Center for Advancing Translational Sciences (NCATS) grant ULI-RR024996,* Comments: This project was supported in part by funds from the Clinical Translational Science Center (CTSC) and NCATS, grant ULI-RR024996. Ranita Campbell—RELATED: Other: Summer Internship Program, Comments: This project was supported in part by funds from the CTSC and NCATS, grant ULI-RR024996. Thomas Caruso—RELATED: Fees for Participation in Review Activities, Such as Data Monitoring Boards, Statistical Analysis, Endpoint Committees, and the Like: Weill Cornell Medical College, Comments: Weill Cornell Medical College paid me a salary that was in return for my input in collecting data for the research stage of the manuscript. Christopher Robinson—UNRELATED: Grants/Grants Pending: Medical Scientist Training Program grant.* Pina C. Sanelli—RELATED: Grant: NINDS NIH grant.* *Money paid to the institution.

REFERENCES

- Dankbaar JW, Rijdsdijk M, van der Schaaf IC, et al. Relationship between vasospasm, cerebral perfusion, and delayed cerebral ischemia after aneurysmal subarachnoid hemorrhage. *Neuroradiology* 2009;51:813–19
- Aralasmak A, Akyuz M, Ozkaynak C, et al. CT angiography and perfusion imaging in patients with subarachnoid hemorrhage: correlation of vasospasm to perfusion abnormality. *Neuroradiology* 2009;51:85–93
- Sanelli PC, Ugorec I, Johnson CE, et al. Using quantitative CT perfusion for evaluation of delayed cerebral ischemia following aneurysmal subarachnoid hemorrhage. *AJNR Am J Neuroradiol* 2011;32:2047–53
- Nabavi DG, LeBlanc LM, Baxter B, et al. Monitoring cerebral perfusion after subarachnoid hemorrhage using CT. *Neuroradiology* 2001;43:7–16
- Binaghi S, Colleoni ML, Maeder P, et al. CT angiography and perfusion CT in cerebral vasospasm after subarachnoid hemorrhage. *AJNR Am J Neuroradiol* 2007;28:750–58
- Wintermark M, Lau BC, Chien J, et al. The anterior cerebral artery is an appropriate arterial input function for perfusion-CT processing in patients with acute stroke. *Neuroradiology* 2008;50:227–36
- Bisdas S, Konstantinou GN, Gurung J, et al. Effect of the arterial input function on the measured perfusion values and infarct volumetric in acute cerebral ischemia evaluated by perfusion computed tomography. *Invest Radiol* 2007;42:147–56
- Sanelli PC, Lev MH, Eastwood JD, et al. The effect of varying user-selected input parameters on quantitative values in CT perfusion maps. *Acad Radiol* 2004;11:1085–92
- Ferreira RM, Lev MH, Goldmakher GV, et al. Arterial input function placement for accurate CT perfusion map construction in acute stroke. *AJR Am J Roentgenol* 2010;194:1330–36
- Wintermark M, Ko NU, Smith WS, et al. Vasospasm after subarachnoid hemorrhage: utility of perfusion CT and CT angiography on diagnosis and management. *AJNR Am J Neuroradiol* 2006;27:26–34
- Sheikh K, Schipper MJ, Hoeffner EG. Feasibility of superficial temporal artery as the input artery for cerebral perfusion CT. *AJR Am J Roentgenol* 2009;192:W321–29
- Ohkuma H, Manabe H, Tanaka M, et al. Impact of cerebral microcirculatory changes on cerebral blood flow during cerebral vasospasm after aneurysmal subarachnoid hemorrhage. *Stroke* 2000;31:1621–27
- Iwabuchi S, Yokouchi T, Hayashi M, et al. Intra-arterial administration of fasudil hydrochloride for vasospasm following subarachnoid hemorrhage: analysis of time-density curve with digital subtraction angiography. *Neurol Med Chir (Tokyo)* 2006;46:535–39, discussion 540
- Knutsson L, Larsson EM, Thilmann O, et al. Calculation of cerebral perfusion parameters using regional arterial input functions identified by factor analysis. *J Magn Reson Imaging* 2006;23:444–53
- Calamante F, Gadian DG, Connelly A. Delay and dispersion effects in dynamic susceptibility contrast MRI: simulations using singular value decomposition. *Magn Reson Med* 2000;44:466–73
- Endo S, Branson PJ, Alksne JF. Experimental model of symptomatic vasospasm in rabbits. *Stroke* 1988;19:1420–25

Morphologic, Distributional, Volumetric, and Intensity Characterization of Periventricular Hyperintensities

M.C. Valdés Hernández, R.J. Piper, M.E. Bastin, N.A. Royle, S. Muñoz Maniega, B.S. Aribisala, C. Murray, I.J. Deary, and J.M. Wardlaw



ABSTRACT

BACKGROUND AND PURPOSE: White matter hyperintensities are characteristic of old age and identifiable on FLAIR and T2-weighted MR imaging. They are typically separated into periventricular or deep categories. It is unclear whether the innermost segment of periventricular white matter hyperintensities is truly abnormal or is imaging artifacts.

MATERIALS AND METHODS: We used FLAIR MR imaging from 665 community-dwelling subjects 72–73 years of age without dementia. Periventricular white matter hyperintensities were visually allocated into 4 categories: 1) thin white line; 2) thick rim; 3) penetrating toward or confluent with deep white matter hyperintensities; and 4) diffuse ill-defined, labeled as “subtle extended periventricular white matter hyperintensities.” We measured the maximum intensity and width of the periventricular white matter hyperintensities, mapped all white matter hyperintensities in 3D, and investigated associations between each category and hypertension, stroke, diabetes, hypercholesterolemia, cardiovascular disease, and total white matter hyperintensity volume.

RESULTS: The intensity patterns and morphologic features were different for each periventricular white matter hyperintensity category. Both the widths ($r = 0.61, P < .001$) and intensities ($r = 0.51, P < .001$) correlated with total white matter hyperintensity volume and with each other ($r = 0.55, P < .001$) for all categories with the exception of subtle extended periventricular white matter hyperintensities, largely characterized by evidence of erratic, ill-defined, and fragmented pale white matter hyperintensities (width: $r = 0.02, P = .11$; intensity: $r = 0.02, P = .84$). The prevalence of hypertension, hypercholesterolemia, and neuroradiologic evidence of stroke increased from periventricular white matter hyperintensity categories 1 to 3. The mean periventricular white matter hyperintensity width was significantly larger in subjects with hypertension (mean difference = 0.5 mm, $P = .029$) or evidence of stroke (mean difference = 1 mm, $P < .001$). 3D mapping revealed that periventricular white matter hyperintensities were discontinuous with deep white matter hyperintensities in all categories, except only in particular regions in brains with category 3.

CONCLUSIONS: Periventricular white matter hyperintensity intensity levels, distribution, and association with risk factors and disease suggest that in old age, these are true tissue abnormalities and therefore should not be dismissed as artifacts. Dichotomizing periventricular and deep white matter hyperintensities by continuity from the ventricle edge toward the deep white matter is possible.

ABBREVIATIONS: DWMH = deep white matter hyperintensities; IQR = interquartile range; PVWMH = periventricular white matter hyperintensities; WMH = white matter hyperintensities

The presence of brain white matter hyperintensities is a common neuroradiologic finding in older individuals without disease¹ and in those with neurologic disease. They appear on CT

as areas of decreased attenuation. On MR imaging, they appear as areas of increased signal intensity in T2-weighted and FLAIR brain images and as hypointense areas in T1-weighted images. White matter hyperintensities (WMH) are typically separated into periven-

Received February 11, 2013; accepted after revision March 21.

From the Brain Research Imaging Centre (M.C.V.H., M.E.B., N.A.R., S.M.M., B.S.A., J.M.W.), College of Medicine and Veterinary Medicine (R.J.P.); Division of Health Sciences (Medical Physics) (M.E.B.); and Department of Psychology (C.M., I.J.D.), University of Edinburgh, Edinburgh, UK.

M.C. Valdés Hernández and R.J. Piper contributed equally to this work.

This work was funded by Age UK and the UK Medical Research Council as part of the project “Disconnected Mind: LBC1936” (<http://www.disconnectedmind.ed.ac.uk/>); the Centre for Cognitive Ageing and Cognitive Epidemiology (<http://www.ccace.ed.ac.uk/>) (G0700704/84698); and the Row Fogo Charitable Trust. Funding from the Biotechnology and Biological Sciences Research Council, the

Engineering and Physical Sciences Research Council, and the Economic and Social Research Council is gratefully acknowledged. Imaging was performed in the Brain Research Imaging Centre (<http://www.bric.ed.ac.uk/>), a Scottish Imaging Network, A Platform for Scientific Excellence Collaboration center.

Paper previously presented at: 36th European Society of Neuroradiology Annual Meeting, September 19–23, 2012; Edinburgh, Scotland.

Please address correspondence to María C. Valdés Hernández, MD, Brain Research Imaging Centre, Neuroimaging Sciences, University of Edinburgh, Western General Hospital, Crewe Rd, Edinburgh EH4 2XU, UK; e-mail: mvhernan@staffmail.ed.ac.uk

Indicates open access to non-subscribers at www.ajnr.org

<http://dx.doi.org/10.3174/ajnr.A3612>

tricular or deep categories.² Periventricular white matter hyperintensities (PVWMH) are regarded as hyperintensities adhering to a “continuity rule,” so that they are confluent with and extend away from the ventricular wall.^{2,3} Deep white matter hyperintensities (DWMH), conversely, are said to be separated from the PVWMH by at least 1 voxel⁴ and reside within the deep white matter.

It is not clear from previous investigations whether the innermost segment of PVWMH is indeed white matter pathology or is a mere manifestation of artifacts from CSF flow signal. PVWMH that exhibit a regular pattern and are narrower than 2 voxels have been considered true white matter abnormalities by some,^{2,3} whereas others classified them as artifacts.⁵ However, no evidence has been provided to support these conventions.

The criteria for separating WMH into PVWMH or DWMH have typically relied on rules of continuity of WMH from the lateral ventricles,^{6,7} but distance from the ventricular edges has also been proposed. For example, PVWMH have been reported to penetrate as much as 7 and 13 mm into the brain parenchyma,^{8,9} and any WMH found within 3 mm from the ventricular wall have been proposed to belong to a distinct subtype, “juxtaperiventricular.”⁶ Some studies^{2,10} render these classifications artificial. Others claim that they are arbitrary¹¹ and contrary to pathologic evidence of common vascular mechanisms, or they have suggested that PVWMH and DWMH volumes are highly correlated and have found that their spatial analysis failed to identify distinct subpopulations for PVWMH and DWMH.¹² Thus, a robust analysis of PVWMH morphology, distribution, and clinical correlates is required to determine a more appropriate classification of these hyperintense regions and their associations.

The purpose of this study was to characterize PVWMH more clearly by their spatial distribution, signal intensity, and relationship to risk factors. The analyses were designed to test 3 hypotheses concerning the definition and classification of PVWMH: 1) A hyperintense thin white line detected along the rim of the lateral ventricle is not a manifestation of a partial volume effect (artifacts) but is evidence of abnormal tissue; 2) PVWMH and DWMH dichotomization is possible and appropriate by a compound rule of continuity from the ventricular surface, unique distribution patterns, and morphologic characteristics; and 3) both PVWMH and DWMH are associated because they have similar distributional properties and common risk factors and therefore are potentially part of the same disease process.

MATERIALS AND METHODS

Subjects and Brain MR Imaging Acquisition

Brain axial FLAIR images and self-reported clinical data were obtained from 667 participants of the Lothian Birth Cohort 1936 (353 males and 314 females), a group of community-dwelling individuals without dementia, 72–73 years of age (mean, 72.7 ± 0.7 years) at the time of scanning and data collection. This cohort was recruited as part of the Disconnected Mind project (<http://www.disconnectedmind.ed.ac.uk>), an investigation of the aging brain and related cognitive changes.¹³ Formal written consent from all subjects and ethical approval were acquired.

MR imaging was conducted in the Brain Research Imaging Centre, University of Edinburgh (<http://www.bric.ed.ac.uk>). A Signa Horizon HDx 1.5T clinical scanner (GE Healthcare, Mil-

waukee, Wisconsin), equipped with a self-shielding gradient set and a manufacturer-supplied 8-channel phased-array head coil, was used to acquire FLAIR-weighted datasets (TR/TE/TI = 9002/147.38/2200 ms, 4-mm section thickness, matrix = 256 × 256, and 15.63-Hz bandwidth) among other sequences. Full details of the MR imaging protocol have been published previously.¹⁴

Categorization of PVWMH

We defined 4 categories to describe the morphologic and distributional properties of the PVWMH on the basis of visual rating scales^{2,15,16} and distinctions arising from clinical studies.^{2,16,17} These categories were the following (Fig 1): 1) a thin white line on the borders of the ventricles (corresponding to the commonly termed “pencil-thin” rims²); 2) a thick rim characterized by attenuated PVWMH with irregular boundaries; and 3) extended PVWMH characterized by either large caps at the horns of the ventricles or wide hyperintense areas that penetrate into the DWMH and can converge with DWMH. These 3 categories are in correspondence with Fazekas visual rating scale PVWMH categories 1, 2, and 3, respectively. An additional category (4) “subtle extended PVWMH” was considered for subjects with extensive evidence of “dirty” or ill-defined, subtle, pale PVWMH¹⁸ and noncontinuous and diffuse periventricular hyperintensities, with varying and erratic intensity patterns emerging from the lateral ventricle wall, as described previously.^{10,18,19} These were much less well-defined and much less intense than the very obvious white hyperintensities classed in 1–3 above. Each FLAIR image was visually assessed by 2 observers, blinded to each other’s results and to any other information (ie, clinical or obtained from image processing or other visual rating scales). Discrepant borderline cases were discussed until agreement was reached. A random subsample ($n = 70$) was assessed twice by both observers separately; the intraclass correlation coefficient was 0.98.

Quantitative Measurement of Intracranial and WMH Volumes

The intracranial volume (ie, contents within the inner skull table including brain tissue, CSF, veins, and dura), with an inferior limit on the axial section just superior to the tip of the odontoid peg at the foramen magnum, was extracted semiautomatically by using the T2*-weighted sequence, with the Object Extraction Tool in Analyze (AnalyzeDirect, Mayo Clinic, Rochester, Minnesota) followed by manually editing.

WMH were segmented semiautomatically on the quantized color image obtained after fusing coregistered FLAIR and T2*-weighted sequences, mapping them in green and red respectively, and applying minimum variance quantization. This technique is described in Valdés Hernández et al,²⁰ validated elsewhere,²¹ and implemented by MCMxxxVI_ALE (a tool freely available from (www.sourceforge.net/projects/bric1936)). Intracranial volume was used to correct WMH volumes for head size.

Intensity Analysis

The intensity of PVWMH was measured by using a tool Intensity Analyzer (freely downloadable from <http://www.sourceforge.net/projects/bric1936>). This tool allows a straight line to be plotted on an MR imaging section to generate a uniform readout of the normalized signal-intensity profile along the plotted line (y-axis) ver-

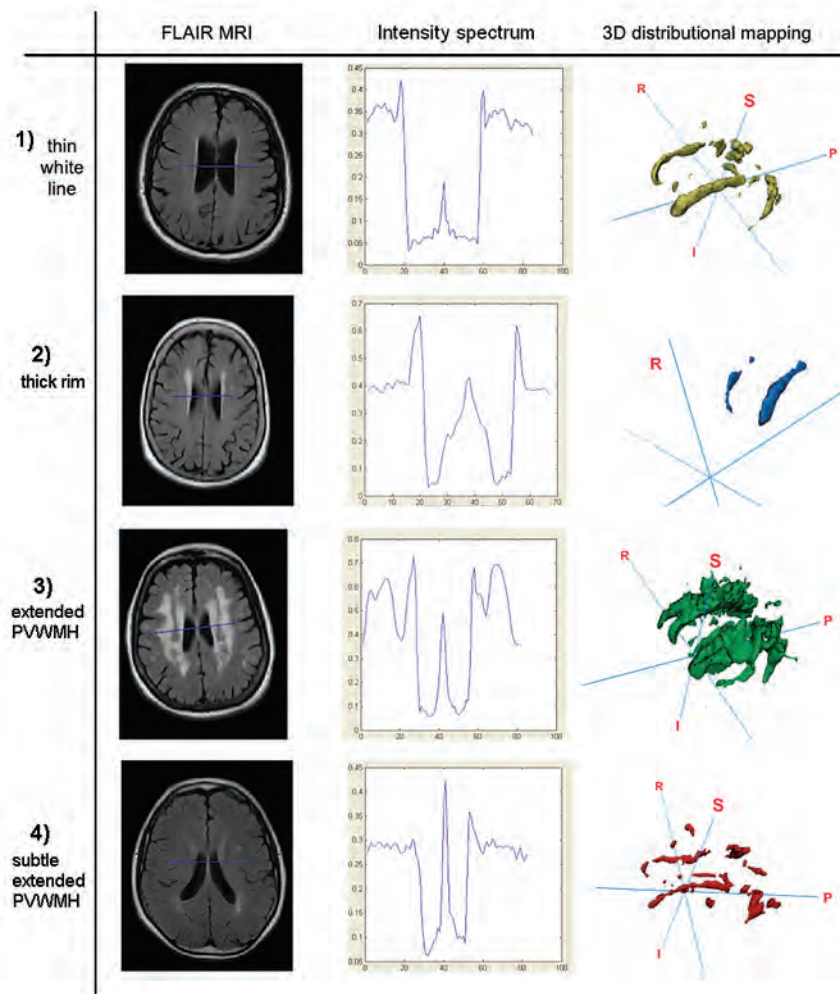


FIG 1. Representative images from each category. From top to bottom: 1) thin white line, 2) thick rim, 3) extended PVWMH, and 4) subtle extended PVWMH. From left to right: axial FLAIR MR imaging, readout from the novel Intensity Analyzer tool, and 3D distributional mapping of WMH. The Intensity Analyzer axes: x, width in millimeters; y, signal intensity (percentage peak from the adjacent lateral trough).

sus its normalized length (x-axis). From each scan, we chose a section toward the top of the lateral ventricles (just after the basal ganglia disappears) and drew a line perpendicular to the interventricular septum starting at the left hemispheric white-gray matter boundary and finishing at the corresponding right boundary, taking care that it crossed the area where the width of the PVWMH was closer to the mean width visually estimated (Fig 1). In all cases, we measured the width of the PVWMH (distance from the edge of the ventricles to the end of the first spike along the plotted line) and their peak intensity (expressed as the percentage increase with respect to the mean intensity of the adjacent lateral trough).

The aforementioned criterion for determining the intensity of the PVWMH was cross-checked as follows: We placed squared regions of interest (2×2 mm) at the central and innermost region of the hyperintensity rim on 4 consecutive sections by using Analyze 10.0 on a subsample of 10% of the subjects selected randomly from each PVWMH category and calculated the mean intensity of those regions. The mean intensity of the healthy white matter was calculated by placing a square (5×5 mm) region of

interest bilaterally in the frontal white matter (selected for the relative absence of WMH).²¹

3D Distributional Visualization of WMH

3D distributional visualization of WMH was conducted representing in 3D the binary masks of the WMH of the random subsample mentioned above by using the surface builder tool in Mango software (University of Texas Health Science Center, Houston, Texas; <http://ric.uthscsa.edu/mango>). This was to determine whether the spatial separation between PVWMH and DWMH is an artificial convention on the basis of 2D visualization.¹²

Statistical Analysis

In addition to the imaging measurements, we analyzed smoking status and clinical data: the presence or absence of hypertension, diabetes, hypercholesterolemia, and cardio- and cerebrovascular disease. Subjects were classified as having cerebrovascular disease if the subject either self-reported stroke or transient ischemic attack or had neuroradiologic evidence of previous stroke on MR imaging, determined as explained elsewhere.²⁰

The Kruskal-Wallis test with a post hoc Dunn test was used to identify significant differences between categories and groups of participants with/without the presence of risk factors, and the Spearman test was used to assess the correlations. For all statistical tests, we used GraphPad-Prism, Version 5.0 (GraphPad Software, San Diego, California). Statistical significance was set at $P < .05$ (2-tailed). Results are presented as median and interquartile range (IQR) (25%–75%) unless stated otherwise.

RESULTS

Characteristics of the Sample

In total, 327 (49.17%) subjects had hypertension, 67 (10.08%) had diabetes (type 1, $n = 7$ and type 2, $n = 60$), 278 (41.80%) had hypercholesterolemia, and 178 (26.77%) had a history of cardiovascular disease (Table). From the total number of subjects with cerebrovascular disease, 44 (6.62%) self-reported a history of stroke and 95 (14.33%) had neuroradiologic confirmation of a previous stroke. The median WMH volume was 7.7 mL (IQR = 13.6 mL).

Categorization of PVWMH

Only 2 subjects did not exhibit any evidence of PVWMH, leaving 665 (99.7%) subjects who were divided into 4 categories as follows: thin white line, 273 (41.05%); thick rim, 233 (35.04%); ex-

Characteristics of the sample

Category of PVWMH	No. of Subjects	Smokers		Hyper-tension		Diabetes		Hyper-cholesterolemia		History of Cardiovascular Disease		History of Cerebrovascular Disease	
		No.	%	No.	%	No.	%	No.	%	No.	%	No.	%
Thin white line	273	143	52.38	120	43.96	30	10.99	103	37.73	74	27.11	32	11.72
Thick rim	233	127	54.51	126	54.08	26	11.16	106	45.49	62	26.61	44	18.88
Extended PVWMH	90	47	52.22	50	55.56	6	6.67	48	53.33	24	26.67	30	33.33
Subtle extended PVWMH	69	35	52.24	31	46.27	5	7.46	21	31.34	18	26.87	9	13.43
Total	665	352	52.93	327	49.17	67	10.08	278	41.80	178	26.77	115	17.29

Note:—Cardiov. Indicates cardiovascular; Cerebrov., cerebrovascular.

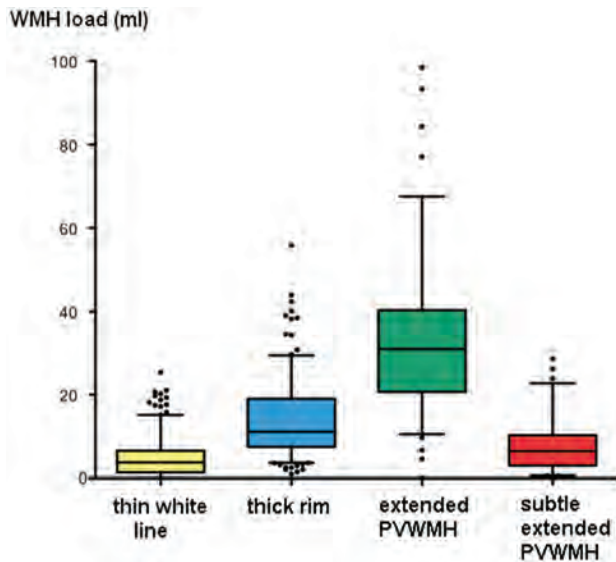


FIG 2. Box-and-whisker plot showing the distribution of PVWMH across the categories. Boxes indicate 25%–75% interquartile range; horizontal lines in boxes, median width; whiskers, 5%–95% range; dots, detected outliers that reside outside the whisker range. The distribution of total WMH volumes across these categories is widespread (maximum = 98.38 mL), but differences among all categories are statistically significant.

tended PVWMH, 90 (13.53%); and subtle extended PVWMH, 69 (10.08%) (Table). The distribution of total WMH volumes across these categories was widespread (from almost none to maximum = 98.38 mL), but statistically significant volumetric differences were found among all categories (thin white line median = 3.77 mL, IQR = 1.39–6.65 mL; thick rim = 11.13 mL, IQR = 7.47–19.03; extended PVWMH = 31.02 mL, IQR = 20.73–40.33; subtle extended PVWMH = 6.46 mL, IQR = 3.02–10.26) (Fig 2).

Intensity Analysis

The Intensity Analyzer tool identified signature intensity patterns and features for each morphologic category. Figure 1 shows a representative case of each category with the output from the Intensity Analyzer and the 3D visualization of the WMH. The PVWMH mean width and mean intensity amplitudes were directly and highly correlated with each other ($\rho = 0.55$, $P < .001$) for the whole sample.

Subjects with PVWMH categorized as thin white lines exhibited expected thin widths (3.2 mm, IQR = 2.63–3.78) and sharp intensity peaks (33.99% increase from the adjacent lateral trough, IQR = 23.46–44.74). Compared with the thin white line category, both width and intensity (mean increase with respect to the

adjacent lateral trough) were significantly greater in both the thick rim (5.29 mm, IQR = 4.69–6.14; 53.16%, IQR = 40.15–66.64) and extended PVWMH (6.17 mm, IQR = 5.14–7.56; 56.22%, IQR = 44.26–71.53) categories. Subtle extended PVWMH exhibited multiple small-intensity peaks proximal to the ventricles and ill-defined boundaries of the PVWMH (as expected). This category was found to have a median width of 3.86 mm (IQR = 2.70–5.00 mm) and a median intensity amplitude of 16.44% (IQR = 10.18–21.16), the latter being significantly lower than all other categories (Fig 3).

The difference between the sampled intensity of the healthy white matter, equivalent to the mean intensity measured from the adjacent lateral trough (as in “Materials and Methods”), and the PVWMH rim was significantly smaller in the thin white line category compared with the thick rim (mean difference = 54.82%) and extended PVWMH (mean difference = 68.31%) categories. This means a gradual increase in the intensity of the PVWMH from the ventricular wall toward the deep white matter, with an increase in the load of white matter changes.

Volumetric Analysis

Overall, the widths of PVWMH were found to be highly correlated ($P < .001$) with WMH volume, uncorrected ($\rho = 0.61$) and corrected by intracranial volume ($\rho = 0.62$). The WMH volume (corrected and uncorrected) was significantly correlated with the width of 3 PVWMH category groups separately without excluding outliers (ie, outside the 5%–95% range): thin white matter ($\rho = 0.32$, $P < .001$); thick rim ($\rho = 0.61$, $P < .001$); and extended PVWMH, ($\rho = 0.44$, $P < .001$), but not with the subtle extended PVWMH ($\rho = -0.20$, $P = .11$). Similarly, an overall significant correlation ($P < .001$) was found between mean intensity amplitude and WMH volume uncorrected ($\rho = 0.45$) and corrected by intracranial volume ($\rho = 0.42$) in all categories with the exception of the diffuse subtle extended PVWMH ($\rho = 0.02$, $P = .84$).

Distributional Analysis

Among 665 subjects, we found only 1 subject who exhibited a PVWMH width of >13 mm (14.71 mm). In the extended PVWMH category (mean PVWMH width = 6.52 ± 0.2 mm), 57/90 conformed to <7 mm, and 71/90 to <8 mm, leaving only 19/90 subjects within the sample for whom these distances may not be applicable.

The 3D representation of the WMH showed that subjects in the thin white line category had WMH that strictly adhered to the ventricle walls; however, regions of discrete DWMH were also present. In both the thin white line and thick rim categories, PVWMH were disconnected from hyperintensities in the deep

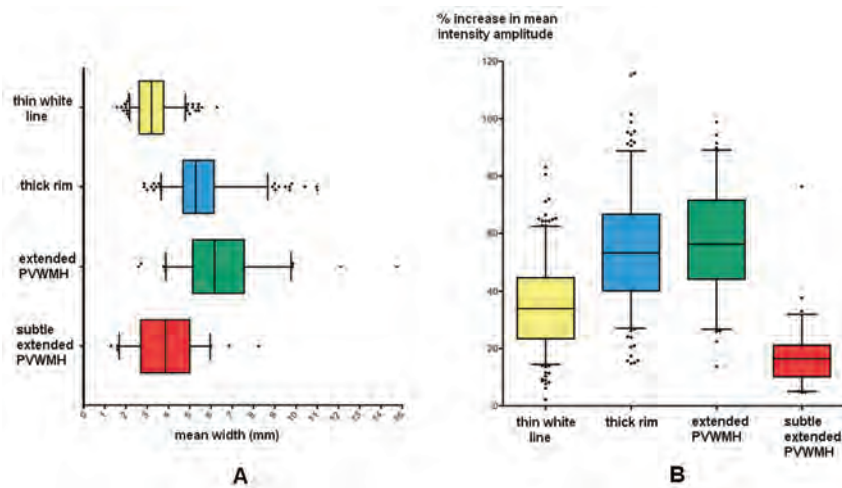


FIG 3. Box-and-whisker plots showing the distribution of PVWMH. Mean width (A) and mean intensity amplitude (percentage peak from adjacent lateral trough) (B) across the different categories. Boxes indicate 25%–75% interquartile range; horizontal lines in boxes, median width; whiskers, 5%–95% range; dots, detected outliers that reside outside the whisker range.

white matter and subcortical regions, albeit the visual impression of continuity can be observed in 2D MR imaging. In the extended PVWMH category, extensive confluence was found between periventricular white matter intensities and DWMH. In this category, regions of nonconfluence were typically found lateral to the midventricular PVWMH as “pockets” of healthy white matter between periventricular white matter intensities and DWMH regions. 3D representation of the WMH of those subjects with diffuse subtle extended PVWMH revealed highly erratic and fragmented distributions of both PVWMH and DWMH (Fig 1).

Relationship with Vascular Risk Factors

A stepwise increase was found in the percentage of subjects falling within each of the first 3 categories (thin white line, thick rim, extended PVWMH) and their histories of hypertension, hypercholesterolemia, and evidence of stroke (Fig 4A). PVWMH were significantly wider in subjects with hypertension ($P = .03$) and evidence of stroke ($P < .001$), regardless of the category (Fig 4B).

DISCUSSION

It has previously been suggested that PVWMH of <2 voxels wide are a manifestation of a partial volume effect⁵ or, alternatively, artifacts due to CSF pulsation.²² In this study, the PVWMH rim mean signal intensity in the thin white line that borders the ventricles was highly correlated and proportional with both total burden (volume) of WMH and the width of PVWMH (maximum of 3 mm for this category), as well as in the 2 categories for which such a result would be obvious: PVWMH penetrating into the deep white matter and large caps confluent with DWMH. An artifactual phase shift effect (produced by CSF pulsation) or truncation artifacts (common in areas where high and low signals are adjacent to each other) would not show these correlations. These findings suggest that these thin PVWMH are evidence of true white matter abnormalities. However, it does not mean that artifacts do not occur at the ventricle wall but, rather, that these artifacts cannot be identified by measurements of PVWMH width or signal intensity on FLAIR MR imaging.

On the basis of vascular neuroanatomy, it has been suggested that the boundary of PVWMH and DWMH may lie within a 3- to 13-mm watershed zone.^{8,23} For our sample, the mean width of the PVWMH in the extended PVWMH category agreed with more specific suggestions that PVWMH may be separately identified from DWMH by distance thresholds^{4,9} of <7 or <8 mm. For scans on the third category (extended PVWMH), 8 mm also seemed an adequate distance for considering the boundary between PVWMH and DWMH. Previous investigations have found that volumetric measures of the ventricles,²⁴ intracranial space, and brain tissue are highly variable between subjects. In this birth cohort, the use of WMH volume uncorrected or corrected either for brain tissue or intracranial volume has been demonstrated not to affect the analysis of

WMH load²⁰ as the results presented here corroborate.

Evidence of advanced leukoaraiosis on intensity analysis reveals a typical pattern (extended PVWMH) of a juxtaperiventricular signal-intensity peak followed by another DWMH peak. This pattern is also found on 3D distributional mapping, but only at the PVWMH rim do the surrounding caps of the frontal and occipital horns exhibit extensive confluence with DWMH. This commonly found trough of signal intensity at the PVWMH rim may mark the boundary of the periventricular white matter hyperintensities and DWMH distinction and may conform to a dichotomy on the basis of rules of continuity to the ventricle.^{6,7} This distinction, less informative than advanced distributional probabilistic atlases, has proved valid in clinical practice and research.

We found a positive and significant association between PVWMH width and hypertension, which is a small-vessel disease risk factor considered to be more highly associated with DWMH.^{2,5,25-27} However, an alternative interpretation of this finding is that higher widths are associated with higher total WMH volumes and thus are due to an indirect association, or that certain areas of PVWMH that penetrate into the deep WM should be considered DWMH. Evidence of subependymal defects, transudation of ventricular CSF, and impaired cerebral autoregulation in patients with hypertension who have severe PVWMH has been reported previously.²⁸ We also found that PVWMH were significantly wider in subjects with evidence of stroke, but not in smokers, and in subjects with a history of hypercholesterolemia, diabetes, or cardiovascular disease. The percentage of subjects with hypertension, hypercholesterolemia, and evidence of stroke increased with increasing total WMH volume in thin, thick rim, and extended PVWMH categories.

The extensive presence of diffuse subtle PVWMH, also commonly termed “dirty-appearing white matter,” has been rarely reported in the literature. Ge et al¹⁰ found that such regions, most often found in proximity to the ventricles, exhibit a signal greater than healthy white matter but lower than established WMH.

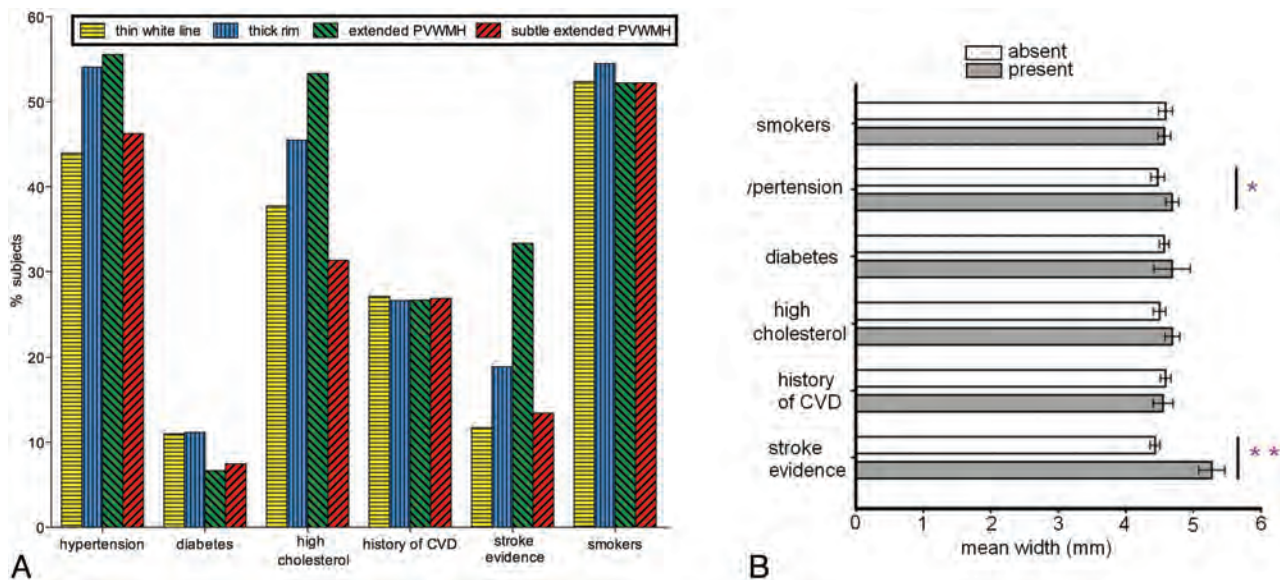


FIG 4. A, Percentage of subjects with vascular risk factors: hypertension, diabetes (type 1 and 2), hypercholesterolemia, smoking history, and history of cardio- and cerebrovascular disease. B, PVWMH mean width found in subjects with either the presence or absence of vascular risk factors. Mean width is significantly higher in those with hypertension (+4.81%, $P = .03$) and evidence of stroke (+18.97%, $P < .001$).

The current investigation confirms this finding in 67 subjects (10.08%), with mean intensity amplitudes for these WMH significantly lower than those in other WMH categories and higher than those in healthy white matter. The underlying pathologic processes were not explored in this study, but the fact that no correlations were found between the width or intensity of this type of PVWMH and WMH total volume or the vascular risk factors explored in this study supports the suggestion that diffuse subtle extended PVWMH are evidence of evolving, preactive WMH,²⁹ and/or secondary degenerative processes remote from established WMH,¹⁹ which can be confirmed on a follow-up scanning wave of these subjects. WMH segmentation and 3D distributional mapping confirm that these are ill-defined¹⁸ and fragmented regions.

The study strengths are that to our knowledge, this is the first study that jointly analyzes in detail the morphologic, distributional, volumetric, and intensity characteristics of PVWMH in an attempt to provide evidence about the nature (ie, real lesion or artifactual) of the periventricular thin hyperintense rim that commonly appears in brain FLAIR scans. A large sample size provided robust estimates of effect. Careful blinding of the analyses and a narrow age range to avoid confounding factors are also among the strengths of the study. Each conclusion resulted from a combination of multiple types of assessments, all conducted blinded to each other's results: visual (based on clinically proved visual rating scales and outcomes), computational, and clinical (vascular risk factors). The Intensity Analyzer tool presented is relatively fast, taking only <5 minutes to assess the width and intensity for a single subject (including the manual placing of the measuring line), and allows linear measurements, histogram, and voxel-based intensity analyses of tissues and anomalies on MR images. We used coregistered FLAIR and T2*-weighted images and multispectral data fusion to segment the WMH.²¹ Combinations of multiple sequences have proved to largely remove the artifactual confound.^{30,31}

The study also has limitations. Despite the fact that visual assessment and categorization of PVWMH in “borderline” cases were discussed and agreed on between the 2 observers, the distinction from 1 category to another was not clear in some cases. Also, because WMH segmentations and volumes were not divided into periventricular white matter hyperintensities and DWMH as previous investigators have done,^{7,12} the associations of WMH volume with other parameters are not sensitive to differences between periventricular white matter hyperintensities and DWMH. Another limitation is that the data used in our analysis merely indicated whether the vascular risk factor was present or absent, not allowing detailed analyses of these variables (such as blood pressure measurement) as performed by other investigators.^{25,26}

The analysis presented here used a semiquantitative PVWMH visual rating scale. Although the intra-/interobserver agreements on the categorization process were 0.99 and 0.97, respectively, a fully automatic quantitative WMH mapping^{9,24} will allow a more detailed study of the WMH distribution. This study used data obtained from community-dwelling individuals. The distribution patterns of PVWMH categories and widths might differ in disease cohorts.

Recommendations for Further Investigation

Few studies have reported or addressed the pathologic correlates of periventricular white matter hyperintensities and DWMH.³² Further investigation is needed to identify reliable indicators of artifacts on brain MR imaging. Using pathologic samples may also allow the comparison of PVWMH on MR imaging with pathologic evidence of white matter abnormalities and may resolve the problem of the extent of PVWMH caused by artifacts. Referral to or combination with other sequences such as T1-, T2-, and proton attenuation-weighted MR imaging; the use of sequence coregistration; and multiple-level assessment of morphometric features³³ may otherwise guide the distinctions explored here (ie,

between categories of PVWMH, PVWMH and DWMH, or thin white line and artifacts). Determining the significance of the fragmentation found in thin white line and diffuse PVWMH categories may also be achievable. These findings might indicate true white matter abnormalities and artifacts or might instead identify inaccuracies in segmentation (due to difficulties of definition from surrounding tissues¹⁹).

This study advocates considering the use of quantitative measures of intensity with other features like volume and distribution in the study of WMH. The methodology followed here, though not intended to make recommendations for the definitive ranges of PVWMH (collectively or in different categories), complements the qualitative assessment of WMH with quantitative measures of PVWMH width and intensity.

The 3D visualization techniques presented here and in other studies⁷ should be explored further in studies of WMH to clarify the spatial distribution of WMH, enabling stronger conclusions about defining subtypes, etiology, and progression. This study supports the contention that 3D analysis avoids some of the limitations of 2D axial analysis,¹² which allowed identifying otherwise undetected fragmented patterns of PVWMH.

CONCLUSIONS

PVWMH intensity levels, distribution, and association with risk factors and disease suggest that in old age, these are true tissue abnormalities and therefore should not be dismissed as artifacts. Dichotomizing periventricular white matter hyperintensities and DWMH by continuity from the ventricle edge toward the deep white matter is possible.

Disclosures: Maria del Carmen Valdés Hernández—RELATED: Grant: Age UK,* UK Medical Research Council.* Comments: The work was funded as part of the project Disconnected Mind: LBC 1936 (<http://www.disconnectedmind.ed.ac.uk/>). UNRELATED: Employment: Row Fogo Charitable Trust.* Susana Muñoz Maniega—RELATED: Grant: Age UK,* UK Medical Research Council.* Comments: The work was funded by Age UK and the UK Medical Research Council as part of the project Disconnected Mind: LBC 1936 (<http://www.disconnectedmind.ed.ac.uk/>). Benjamin S. Aribisala—RELATED: Grant: Age UK,* UK Medical Research Council.* Comments: The work was funded as part of the Disconnected Mind Project, UNRELATED: Employment: Medical Research Council.* Mark E. Bastin—RELATED: Grant: UK Medical Research Council.* Ian J. Deary—RELATED: Grant: Age UK,* Medical Research Council.* Comments: Funds for cohort recruitment and brain imaging. UNRELATED: Board Membership: Medical Research Council, Comments: small sum for attending Neurosciences and Mental Health Board. Joanna M. Wardlaw—RELATED: Grant: Row Fogo Trust.* Comments: academic grant to institution to support the work. *Money paid to the institution.

REFERENCES

- Wen W, Sachdev P. **The topography of white matter hyperintensities on brain MRI in healthy 60- to 64-year-old individuals.** *Neuroimage* 2004;22:144–54
- Fazekas F, Chawluk JB, Alavi A, et al. **MR signal abnormalities at 1.5 T in Alzheimer's dementia and normal aging.** *AJR Am J Roentgenol* 1987;149:351–56
- Krishnan KR, Boyko OB, McDonald WM, et al. **Magnetic-resonance morphometry: Image-analysis methodology development for affective disorder.** *Depression* 1993;1:159–71
- Brickman AM, Sneed JR, Provenzano FA, et al. **Quantitative approaches for assessment of white matter hyperintensities in elderly populations.** *Psychiatry Res* 2011;193:101–06
- Payne ME, Fetzer DL, MacFall JR, et al. **Development of a semi-automated method for quantification of MRI gray and white matter lesions in geriatric subjects.** *Psychiatry Res* 2002;115:63–77
- Kim KW, MacFall JR, Payne ME. **Classification of white matter lesions on magnetic resonance imaging in elderly persons.** *Biol Psychiatry* 2008;64:273–80
- Ramirez J, Gibson E, Quddus A, et al. **Lesion Explorer: a comprehensive segmentation and parcellation package to obtain regional volumetrics for subcortical hyperintensities and intracranial tissue.** *Neuroimage* 2011;54:963–73
- Sachdev P, Chen X, Wen W. **White matter hyperintensities in mid-adult life.** *Curr Opin Psychiatry* 2008;21:268–74
- van der Lijn F, Verhaaren BF, Ikram MA, et al. **Automated measurement of local white matter lesion volume.** *Neuroimage* 2012;59:3901–08
- Ge Y, Grossman RI, Babb JS, et al. **Dirty-appearing white matter in multiple sclerosis: volumetric MR imaging and magnetization transfer ratio histogram analysis.** *AJNR Am J Neuroradiol* 2003;24:1935–40
- Appelman AP, Vincken KL, van der Graaf Y, et al. **White matter lesions and lacunar infarcts are independently and differently associated with brain atrophy: the SMART-MR study.** *Cerebrovasc Dis* 2010;29:28–35
- DeCarli C, Fletcher E, Ramey V, et al. **Anatomical mapping of white matter hyperintensities (WMH): exploring the relationships between periventricular WMH, deep WMH, and total WMH burden.** *Stroke* 2005;36:50–55
- Deary IJ, Gow AJ, Taylor MD, et al. **The Lothian Birth Cohort 1936: a study to examine influences on cognitive ageing from age 11 to age 70 and beyond.** *BMC Geriatr* 2007;7:28
- Wardlaw JM, Bastin ME, Valdés Hernández MC, et al. **Brain aging, cognition in youth and old age and vascular disease in the Lothian Birth Cohort 1936: rationale, design and methodology of the imaging protocol.** *Int J Stroke* 2011;6:547–59
- van Straaten EC, Fazekas F, Rostrup E, et al. **Impact of white matter hyperintensities scoring method on correlations with clinical data: the LADIS study.** *Stroke* 2006;37:836–40
- Enzinger C, Fazekas F, Ropele S, et al. **Progression of cerebral white matter lesions: clinical and radiological considerations.** *J Neurol Sci* 2007;257:5–10
- Conijn MM, Kloppenborg RP, Algra A, et al. **Cerebral small vessel disease and risk of death, ischemic stroke, and cardiac complications in patients with atherosclerotic disease: the Second Manifestations of ARterial disease-Magnetic Resonance (SMART-MR) study.** *Stroke* 2011;42:3105–09
- Moore GR, Laule C, Mackay A, et al. **Dirty-appearing white matter in multiple sclerosis: preliminary observations of myelin phospholipid and axonal loss.** *J Neurol* 2008;255:1802–12, discussion 1812
- Filippi M, Rocca MA. **Dirty-appearing white matter: a disregarded entity in multiple sclerosis.** *AJNR Am J Neuroradiol* 2010;31:90–91
- Valdés Hernández MC, Morris Z, Dickie DA, et al. **Close correlation between quantitative and qualitative assessments of white matter lesions.** *Neuroepidemiology* 2013;40:13–22
- Hernández MC, Ferguson KJ, Chappell FM, et al. **New multispectral MRI data fusion technique for white matter lesion segmentation: method and comparison with thresholding in FLAIR images.** *Eur Radiol* 2010;20:1684–91
- Bakshi R, Caruthers SD, Janardhan V, et al. **Intraventricular CSF pulsation artifact on fast fluid-attenuated inversion-recovery MR images: analysis of 100 consecutive normal studies.** *AJNR Am J Neuroradiol* 2000;21:503–08
- Mayer PL, Kier EL. **The controversy of the periventricular white matter circulation: a review of the anatomic literature.** *AJNR Am J Neuroradiol* 1991;12:223–28
- Jongen C, van der Grond J, Anbeek P, et al. **Construction of periventricular white matter hyperintensity maps by spatial normalization of the lateral ventricles.** *Hum Brain Mapp* 2009;30:2056–62
- Murray AD, Staff RT, Shenkin SD, et al. **Brain white matter hyperintensities: relative importance of vascular risk factors in nondemented elderly people.** *Radiology* 2005;237:251–57
- Godin O, Tzourio C, Maillard P, et al. **Antihypertensive treatment**

- and change in blood pressure are associated with the progression of white matter lesion volumes: the Three-City (3C)-Dijon Magnetic Resonance Imaging Study. *Circulation* 2011;123:266–73
27. de Leeuw FE, de Groot JC, Oudkerk M, et al. Hypertension and cerebral white matter lesions in a prospective cohort study. *Brain* 2002;125:765–72
 28. Pantoni L, Garcia JH. Pathogenesis of leukoaraiosis: a review. *Stroke* 1997;28:652–59
 29. De Groot CJ, Bergers E, Kamphorst W, et al. Post-mortem MRI-guided sampling of multiple sclerosis brain lesions: increased yield of active demyelinating and (p) reactive lesions. *Brain* 2001; 124:1635–45
 30. Admiraal-Behloul F, van den Heuvel DM, Olofsen H, et al. Fully automatic segmentation of white matter hyperintensities in MR images of the elderly. *Neuroimage* 2005;28:607–17
 31. Klöppel S, Abdulkadir A, Hadjideometriou S, et al. A comparison of different automated methods for the detection of white matter lesions in MRI data. *Neuroimage* 2011;57:416–22
 32. McAleese KE, Firbank M, Hunter D, et al. Magnetic resonance imaging of fixed post mortem brains reliably reflects subcortical vascular pathology of frontal, parietal and occipital white matter. *Neuropathol Appl Neurobiol* 2013;39:485–97
 33. Scully M, Anderson B, Lane T, et al. An automated method for segmenting white matter lesions through multi-level morphometric feature classification with application to lupus. *Front Hum Neurosci* 2010;4:27

Incidental Periventricular White Matter Hyperintensities Revisited: What Detailed Morphologic Image Analyses Can Tell Us

Soon after the introduction of MR imaging, periventricular hyperintensities started to vex the scientific community.¹ While they may be a consequence of distinct disorders such as multiple sclerosis causing focal periventricular lesions or increased intraventricular pressure giving rise to extending hyperintense rims around the lateral ventricles, most periventricular white matter hyperintensities (PVWMH) constitute an unexpected or incidental finding similar to hyperintensities in the deep white matter (DWMH).² Thus, numerous studies have attempted to clarify the etiology and clinical consequences of these signal abnormalities and their association with one another. These investigations often led to quite contradictory results which is not fully surprising given the variability with which PVWMH and DWMH have been quantified up to combining signal abnormalities at both locations in 1 rating scale.^{3,4} Observed anatomic overlap and a close correlation of PVWMH and DWMH volumes also led to the suggestion that their separation was arbitrary and not warranted,⁵ despite evidence for histopathologic differences.^{6,7} Still others completely dismissed linear areas of PVWMH as artifacts,⁸ contributing to the uncertainty of how to deal with this frequently noted phenomenon.

After a period of stagnation, the work of Valdés Hernández et al, “Morphologic, Distributional, Volumetric, and Intensity Characterization of Periventricular Hyperintensities,”⁹ now promises to move the field forward again. Using MRI obtained from a large cohort of community-dwelling subjects without dementia, these investigators undertook accurately quantifying the maximum intensity and width of hyperintense signal changes observed with different categories of PVWMH, such as a thin white line, a thick rim, or penetrating toward or confluent with DWMH.¹⁰ In parallel, they also generated 3D reconstructions of all white matter hyperintensities (WMH). These showed that PVWMH were clearly discontinuous with DWMH in all categories, except for rare instances with PVWMH penetrating toward or confluent with DWMH. As would be expected, maximum signal intensity and width increased with the semiquantitative classification of PVWMH severity, and this change was accompanied by an increase in the prevalence of hypertension, hypercholesterolemia, and neuroradiologic evidence of stroke.

Neither these observations nor the close correlation of PVWMH widths and signal intensities with WMH volumes confirms or refutes speculations on a common pathomechanism for PVWMH and DWMH. Presented findings, however, clearly substantiate the prevailing morphologic separation of PVWMH and DWMH and indicate the availability of relatively simple and robust tools for their more refined assessment. This should open new avenues, especially for longitudinal evaluations. Furthermore, the fact that a close correlation between WMH volume and mean intensity and width of the signal was also seen for linear PVWMH strongly disputes a mainly artifactual genesis of such signal changes.

Valdés Hernández et al⁹ also call attention to another finding that should be followed up. In approximately 10% of investigated individuals, the authors observed “dirty” or ill-defined subtle, pale changes in the periventricular white matter, which they termed “subtle extended PVWMH.” This category of periventricular signal abnormality was characterized by ill-defined boundaries and multiple small intensity peaks, which were significantly lower than those observed in all other categories. Likewise there was also no association between mean intensity and width of the signal and WMH volume seen with this category of PVWMH. Thus far “dirty white matter” on proton-attenuation or T2-weighted (FLAIR) images has received attention primarily in MS, in which it appears to indicate subtle tissue damage either as a consequence of the inflammatory process or secondary to degeneration.¹¹ Ge et al¹² thought that such areas might indicate prelesional changes.

In this context, it is interesting that a more recent study investigating morphologic factors related to the subsequent growth of DWMH also described subtle FLAIR hyperintensities of the brain tissue as one of the indicators of subsequent lesion development and expansion.¹³ Notwithstanding the superior sensitivity and undoubted contribution of quantitative techniques like diffusion tensor and magnetization transfer imaging for assessing microstructural tissue changes, these observations indicate that even conventional images may contain valuable information regarding the identification of individuals with a high probability of showing progression of white matter changes. Attention to subtle tissue

changes on FLAIR may thus constitute another possibility for improving our insight into PVWMH development and help in selecting individuals for whom the institution of preventive therapeutic strategies might be most timely.¹⁴ Clearly this hypothesis will need to be validated by longitudinal studies.

REFERENCES

1. Zimmerman RD, Fleming CA, Lee BC, et al. **Periventricular hyperintensity as seen by magnetic resonance: prevalence and significance.** *AJR Am J Roentgenol* 1986;146:443–50
2. Brant-Zawadzki M, Fein G, Van Dyke C, et al. **MR imaging of the aging brain: patchy white-matter lesions and dementia.** *AJNR Am J Neuroradiol* 1985;6:675–82
3. Mäntylä R, Erkinjuntti T, Salonen O, et al. **Variable agreement between visual rating scales for white matter hyperintensities on MRI: comparison of 13 rating scales in a poststroke cohort.** *Stroke* 1997;28:1614–23
4. Kapeller P, Barber R, Vermeulen RJ, et al. **Visual rating of age-related white matter changes on magnetic resonance imaging: scale comparison, interrater agreement, and correlations with quantitative measurements.** *Stroke* 2003;34:441–45
5. DeCarli C, Fletcher E, Ramey V, et al. **Anatomical mapping of white matter hyperintensities (WMH): exploring the relationships between periventricular WMH, deep WMH, and total WMH burden.** *Stroke* 2005;36:50–55
6. Gouw AA, Seewann A, van der Flier WM, et al. **Heterogeneity of small vessel disease: a systematic review of MRI and histopathology correlations.** *J Neurol Neurosurg Psychiatry* 2011;82:126–35
7. Schmidt R, Schmidt H, Haybaeck J, et al. **Heterogeneity in age-related white matter changes.** *Acta Neuropathol* 2011;122:171–85
8. Payne ME, Fetzter DL, MacFall JR, et al. **Development of a semi-automated method for quantification of MRI gray and white matter lesions in geriatric subjects.** *Psychiatry Res* 2002;115:63–77
9. Valdés Hernández MD, Piper RJ, Bastin ME, et al. **Morphologic, distributional, volumetric, and intensity characterization of periventricular hyperintensities.** *AJNR Am J Neuroradiol* 2014;35:55–62
10. Fazekas F, Chawluk JB, Alavi A, et al. **MRI signal abnormalities at 1.5 T in Alzheimer's dementia and normal aging.** *AJR Am J Roentgenol* 1987;149:351–56
11. Filippi M, Rocca MA. **Dirty-appearing white matter: a disregarded entity in multiple sclerosis.** *AJNR Am J Neuroradiol* 2010;31:390–91
12. Ge Y, Grossman RI, Babb JS, et al. **Dirty-appearing white matter in multiple sclerosis: volumetric MR imaging and magnetization transfer ratio histogram analysis.** *AJNR Am J Neuroradiol* 2003;24:1935–40
13. de Groot M, Verhaaren BF, de Boer R, et al. **Changes in normal-appearing white matter precede development of white matter lesions.** *Stroke* 2013;44:1037–42
14. Schmidt R, Berghold A, Jokinen H, et al. **White matter lesion progression in LADIS: frequency, clinical effects, and sample size calculations.** *Stroke* 2012;43:2643–47

F. Fazekas

Department of Neurology
Medical University Graz
Graz, Austria

<http://dx.doi.org/10.3174/ajnr.A3714>

Accuracy of Vessel-Encoded Pseudocontinuous Arterial Spin-Labeling in Identification of Feeding Arteries in Patients with Intracranial Arteriovenous Malformations

S.L. Yu, R. Wang, R. Wang, S. Wang, Y.Q. Yao, D. Zhang, Y.L. Zhao, Z.T. Zuo, R. Xue, D.J.J. Wang, and J.Z. Zhao



ABSTRACT

BACKGROUND AND PURPOSE: Identifying feeding arteries of intracranial AVMs is very important for preoperative evaluation. DSA remains the reference standard for diagnosis but is invasive. Our aim was to evaluate the diagnostic accuracy of vessel-encoded pseudocontinuous arterial spin-labeling in identifying feeding arteries of intracranial AVMs by using DSA as the criterion standard.

MATERIALS AND METHODS: Eighteen patients with AVMs were examined with vessel-encoded pseudocontinuous arterial spin-labeling and DSA. Three postlabeling delays (postlabeling delay = 1, 1.3, and 1.6 seconds) were applied in 6 patients, and a single postlabeling delay (1 second) was applied in the remainder. Perfusion-weighted images were decoded into individual vascular territories with standard and relative tagging efficiencies, respectively. The supply fraction of each feeding artery to the AVM was calculated. The within-subject ANOVA was applied to compare supply fractions acquired across 3 postlabeling delays. Receiver operating characteristic analysis curves were calculated to evaluate the diagnostic accuracy of vessel-encoded pseudocontinuous arterial spin-labeling for identifying the feeding arteries of AVMs.

RESULTS: There were no significant differences in supply fractions of the 3 major arteries to AVMs acquired with 3 postlabeling delays ($P > .05$). For vessel-encoded pseudocontinuous arterial spin-labeling with standard labeling efficiencies, the area under the receiver operating characteristic analysis curve was 0.942. The optimal cutoff of the supply fraction for identifying feeding arteries was 15.17%, and the resulting sensitivity and specificity were 84.62% and 93.33%, respectively. For vessel-encoded pseudocontinuous arterial spin-labeling with relative labeling efficiencies, the area under the receiver operating characteristic analysis curve was 0.957. The optimal cutoff of the supply fraction was 11.73%, which yielded an 89.74% sensitivity and 93.33% specificity.

CONCLUSIONS: The contribution fraction of each feeding artery of the AVM can be reliably estimated by using vessel-encoded pseudocontinuous arterial spin-labeling. Vessel-encoded pseudocontinuous arterial spin-labeling with either standard or relative labeling efficiencies offers a high level of diagnostic accuracy compared with DSA for identifying feeding arteries.

ABBREVIATIONS: ASL = arterial spin-labeling; AUC = area under the ROC curve; LICA = left internal carotid artery; PLD = postlabeling delay; RICA = right internal carotid artery; ROC = receiver operating characteristic analysis; VA = vertebral artery; VE-PCASL = vessel-encoded pseudocontinuous arterial spin-labeling

Intracranial AVMs are congenital vascular abnormalities with ≥ 1 feeding artery and without a normal intervening capillary bed. The principal presentation of an AVM is parenchymal hem-

orrhage, which accounts for 2%–4% of overall hemorrhagic strokes¹ and confers significant morbidity and mortality. AVMs may increase in size and show vascular remodeling with time. The management of AVMs includes microsurgery, stereotactic radiosurgery, embolization, and multimodality treatments. Residual lesions may exist after microsurgery, though with a low incidence.^{2,3} Complete obliteration with stereotactic radiosurgery requires approximately 1–3 years to complete, and a cure is not always achieved.⁴ For a large AVM, partial embolization is performed to make it amenable to further surgery or radiosurgery.⁵ The identification of feeding arteries of an AVM and calculation of corresponding contribution

Received December 31, 2012; accepted after revision March 17, 2013.

From the Department of Neurosurgery (S.L.Y., Rong Wang, S.W., D.Z., Y.L.Z., J.Z.Z.), Beijing Tiantan Hospital, Capital Medical University, Beijing, China; State Key Laboratory of Brain and Cognitive Science (Rui Wang, Z.T.Z., R.X.), Beijing MRI Center for Brain Research, Institute of Biophysics, Chinese Academy of Sciences, Beijing, China; Department of Neurosurgery (Y.Q.Y.), Beijing Jishuitan Hospital, Peking University, Beijing, China; Department of Neurology (D.J.J.W.), University of California, Los Angeles, Los Angeles, California; and University of California, Los Angeles–Beijing Joint Center for Advanced Brain Imaging (R.X., Rui Wang, D.J.J.W.), Los Angeles, California and Beijing, China.

This work was supported by Natural Science Foundation of China of Tiantan Hospital (30830101), the National Institutes of Health (grants R01-MH080892, R01-NS081077 and R01-EB014922), the Ministry of Science and Technology of China (grant 2012CB825500), and the CAS Knowledge Innovation Project (grant KSCX2-YW-R-259).

Please address correspondence to Jizong Zhao, MD, Department of Neurosurgery, Beijing Tiantan Hospital, No. Six Tiantan Xili, Chongwen District, Beijing 100050, China; e-mail: zhaojz205@gmail.com

Indicates open access to non-subscribers at www.ajnr.org

<http://dx.doi.org/10.3174/ajnr.A3638>

fractions are helpful for standard microsurgical operations, in which the arterial feeders are generally occluded first, followed by excision of the nidus, and finally resection of the draining veins.⁶ Information about feeding arteries can also help in determining the sequence of arteries to be managed. A reliable, safe, and convenient imaging technology with the capability of identifying feeding arteries would be highly desirable for frequent examinations of AVMs.

DSA remains the criterion standard for the diagnosis and evaluation of intracranial AVMs. In our institution (Beijing Tiantan Hospital), it is usually performed just before the operation to identify feeding arteries and corresponding draining veins. As an invasive technique, DSA exposes both doctors and patients to the radiation of x-rays and carries potential risks related to contrast agents and the experience of the operators.⁷ Although these results are rare, DSA may cause vessel injury, stroke, and even death, which is most concerning.⁸ Various MRA techniques have been explored for the evaluation of AVMs, such as 4D time-resolved dynamic MRA with or without contrast enhancement.^{9,10} Arterial spin-labeling (ASL) offers a method for quantifying regional CBF by using magnetically labeled arterial blood water as an endogenous tracer.¹¹ While delayed arterial transit may cause underestimation of tissue perfusion in patients with stroke, the opposite effect—the rapid transit of labeled blood through arteriovenous shunts—can be exploited for direct visualization and, potentially, quantification of arteriovenous shunting.^{12,13} More recently, pseudocontinuous ASL has been introduced, which uses a train of discrete radio-frequency pulses to mimic flow-driven adiabatic inversion and combines the continuous superior signal-to-noise ratio of ASL and the higher tagging efficiency of pulsed ASL.¹⁴ Vessel-encoded pseudocontinuous arterial spin-labeling (VE-PCASL) is a time-efficient method for

mapping multiple vascular territories by using x and y gradients to encode arteries within the labeling plane.¹⁵ It has been applied in the evaluation of collateral circulation in ischemic cerebrovascular diseases in previous studies.^{16,17}

In this study, we applied VE-PCASL in patients with intracranial AVMs to identify feeding arteries of AVMs on the basis of the estimated supply fractions of the arteries. Due to the presence of noise in the supply fraction maps and potential contamination of ASL signals between vessels, a cutoff or threshold was applied on the estimated supply fraction to identify the “true” feeding arteries of AVMs. The accuracy of VE-PCASL for identifying feeding arteries at various cutoff values of the supply fraction was evaluated by using DSA as the criterion standard.

MATERIALS AND METHODS

Patients

This study was approved by the institutional review boards, and written informed consent was obtained from all participants. The inclusion criteria were patients diagnosed with intracranial AVMs and without other brain lesions who were scheduled for DSA examination at Beijing Tiantan Hospital. The general contraindications for MR imaging examination were applied as the exclusion criteria.

DSA Technique

DSA was performed according to a standard protocol during routine clinical examinations on a biplane angiography system (Advantx LCV+; GE Healthcare, Hertfordshire, UK). A 5F diagnostic catheter was navigated into the bilateral internal carotid, external carotid, and vertebral arteries (VAs) (6 vessels), respectively, via the right femoral artery to acquire standard anteroposterior and lateral projections, each by manual delivery of a 5- to 7-mL iodinated contrast agent injection per run (iodixanol, Visipaque; GE Healthcare, Co. Cork, Ireland).

MR Imaging

MR imaging was performed on a 3T Tim Trio system (Siemens, Erlangen, Germany) by using a body coil transmitter and a 12-channel head coil as a receiver. First, a sagittal localizer scan was performed for anatomic reference; then TOF MRA was performed to select the right and left ICAs and vertebral arteries, on the basis of which the tagging plane was determined (Fig 1). The labeling offset from the center of the imaging slab was 80 mm. In this axial tagging plane, the ICAs and vertebral arteries had an

approximately trapezoidal arrangement and the direction of flow was predominantly inferior-to-superior. The image sections were positioned parallel to the labeling plane. Postlabeling delay (PLD) was set at 3 time points (1, 1.3, and 1.6 seconds) in 6 patients and at a single time point of 1 second in the remaining 12 patients. Imaging parameters were as follows: TR/TE/flip angle = 3000 ms/10 ms/90° for PLD = 1 second (while TR = 3.3 seconds for PLD = 1.3 seconds and TR = 3.6 seconds for PLD = 1.6 seconds), FOV = 220 × 220 mm², 12 sections with a 6-mm thickness and 1.5-mm gap, matrix

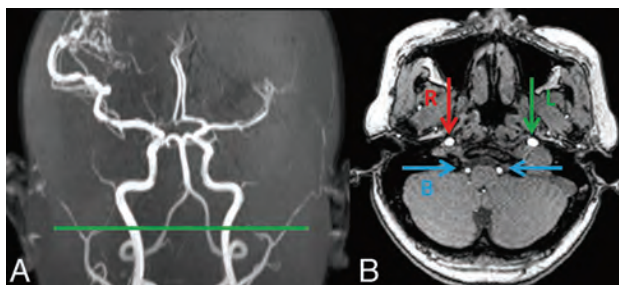


FIG 1. Labeling plane on the coronary (A) and transverse (B) MRA images. Arrows show RICA (R), LICA (L), and vertebral basilar arteries (B).

Table 1: Modified Hadamard encoding matrix based on estimated relative labeling efficiencies of the 18 patients with AVMs

A	-1.0000	-1.0000	-1.0000	1.0000
	1.0000	1.0000	1.0000	1.0000
	-0.9200 ± 0.083	0.1600 ± 0.186	0.7100 ± 0.340	1.0000
	0.9200 ± 0.083	-0.1600 ± 0.186	-0.7100 ± 0.340	1.0000
	0.9700 ± 0.105	-0.5300 ± 0.112	0.9700 ± 0.105	1.0000
	-0.9700 ± 0.105	0.5300 ± 0.112	-0.9700 ± 0.105	1.0000
A ⁺	-0.1087 ± 0.0312	0.1087 ± 0.0312	-0.3067 ± 0.0210	0.3067 ± 0.0210
	0.1125 ± 0.0387	-0.1125 ± 0.0387		
	-0.3233 ± 0.031	0.3233 ± 0.031	0.0000	-0.0000
	-0.3333 ± 0.0402	0.3333 ± 0.0402		
	-0.0680 ± 0.0446	0.0680 ± 0.0446	0.3067 ± 0.0210	-0.3067 ± 0.0210
	0.2209 ± 0.0528	-0.2209 ± 0.0528		
	0.1667	0.1667	0.1667	0.1667
	0.1667	0.1667		

Note:—Data are means.

size = 64×64 , 7/8 partial k -space, 120 measurements, and 2D EPI readout. We performed 6 cycles of VE-PCASL: global tag, control, tag of the left-versus-right ICA, tag of ICA versus the vertebralbasilar artery.¹⁵ The total scanning time was 6.2 minutes for 1 PLD and 20 minutes for 3 PLDs.

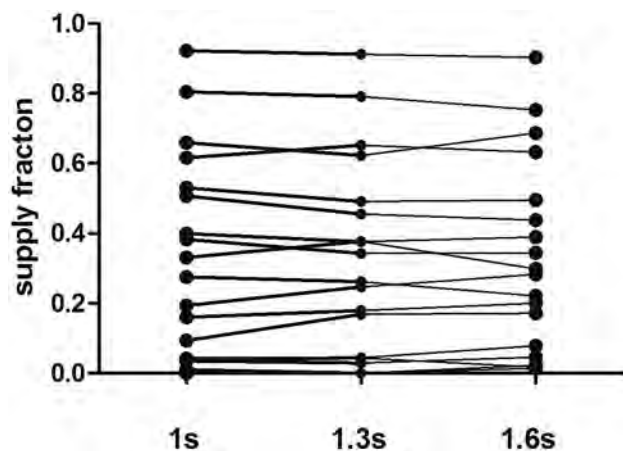


FIG 2. For the 6 patients (18 vessels) with 3 PLDs, there are no significant differences in the supply fractions with relative labeling efficiencies ($P > .05$).

Table 2: Demographic data on the studied population and characterization information of AVMs

Patient No.	Age (yr)	Sex	Spetzler-Martin Classification	Major Feeding Arteries Diagnosed by DSA		
				RICA	LICA	VA
1	23	M	S2EIV0	0	1	1
2	21	M	S2E0V1	1	1	1
3	34	M	S2E0V0	0	1	1
4	44	M	S2EIV1	1	1	1
5	27	F	S3EIV0	1	0	1
6	22	F	S3EIV1	1	1	1
7 ^a	40	M	S2E0V0	0	1	1
8 ^a	46	F	S2E0V0	1	1	1
9 ^a	31	F	S2EIV0	1	0	1
10 ^a	47	F	S2EIV0	1	0	1
11 ^a	13	M	S1E0V0	0	1	1
12 ^a	39	M	S2E0V0	1	0	0
13	27	F	S2EIV0	1	0	1
14	31	M	S3EIV0	1	1	1
15	25	M	S1EIV0	0	1	1
16	47	M	S2E0V0	1	0	1
17	39	F	S1EIV1	0	1	1
18	28	F	S1E0V0	0	1	0

Note:—S indicates the size of the cerebral AVM nidus (1, <3 cm; 2, 3–6 cm; 3, >6 cm); E, eloquence of adjacent brain (0, noneloquent; 1, eloquent); V, venous drainage pattern (0, superficial draining vein; 1, deep draining vein).

^a Patients who had 3 PLD time points. Zero and 1 indicate arteries that have or have not contributed to AVM lesions.

Table 3: Different cutoff values of the supply fraction of feeding arteries of the AVM and the resulting sensitivity and specificity with standard or relative labeling efficiencies respectively

Cutoff Value	Standard		Relative	
	Sensitivity	Specificity	Sensitivity	Specificity
0%	100%	0	100%	6.67%
5%	97.44%	40%	97.44%	66.67%
10%	92.31%	73.33%	89.74%	80%
15%	84.62%	93.33%	82.05%	93.33%
20%	76.92%	93.33%	79.49%	93.33%
25%	74.36%	93.33%	69.23%	93.33%

Data Processing

Raw EPI images were corrected for motion. Global perfusion-weighted images were obtained by subtraction of the globally tagged images from the control images. CBF was calculated according to previous studies.¹⁸ A standardized 12-voxel region of interest was placed in the contralateral basal ganglia on the signal-intensity difference (global perfusion) image to measure the mean value and SD. Basal ganglia signal (mean) + 8 SDs was set as the threshold to generate a mask for the AVM lesion on the global perfusion image.¹²

The 6 cycles of EPI images were averaged and decoded into individual vascular territories corresponding to the left ICA, right ICA, and VA, with standard and relative tagging efficiencies,¹⁵ respectively. The standard tagging efficiency matrix was adopted from previous studies.¹⁵ In addition, the relative tagging efficiency for each artery (assuming that the efficiency of nonselective labeling is 1) was measured directly from the experimental data by using the histogram method in each subject.¹⁹ The estimated relative tagging efficiencies were then used in the construction of the modified Hadamard encoding matrix (Table 1).

The AVM mask determined on global perfusion images was overlaid on individual perfusion maps of the 3 main feeding arteries. The contributions of the 3 main arteries to the AVM

lesion were quantified by calculating supply fractions.¹⁹ The supply fraction was defined as CBF values of all voxels within the AVM mask on individual CBF maps (CBF_{ind}) divided by the summation of CBF values of the 3 main arteries—that is, $CBF_{ind} / (CBF_{LICA} + CBF_{RICA} + CBF_{VA}) \times 100\%$.

Analysis

Two experienced neurosurgeons (both with >10 years' experience) who were blinded to the results of VE-PCASL reviewed DSAs in a random order to identify the major arteries that supplied the AVM lesions. In each patient, each of the 3 major arteries (a total of 54 arteries) was labeled zero or 1 as feeding arteries of the AVM. In cases of disagreement, a consensus was sought. Two experienced researchers reviewed the ASL perfusion-weighted images independently in a random order. Image quality was scored from 5 to 1, corresponding to excellent, good, fair, poor, or uninterpretable, respectively. The Cohen κ was obtained to evaluate interobserver agreement on image quality. The κ coefficient of agreement was graded as follows: 0–0.2 = poor to slight; 0.21–0.4 = fair; 0.41–0.6 = moderate; 0.61–0.8 = excellent; 0.81–0.99 = nearly perfect; 1.0 = perfect.²⁰

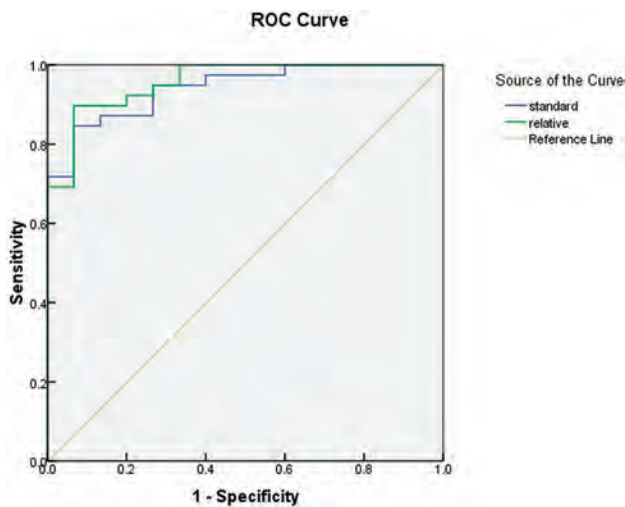


FIG 3. ROC curves of VE-PCASL with standard (blue line) and relative (green line) labeling efficiencies, respectively, for the identification of feeding arteries, and the AUC is larger for relative labeling efficiencies.

Receiver operating characteristic analysis (ROC) curves were generated from the supply fractions of the 3 major arteries obtained by VE-PCASL with PLD = 1 second, by using the Statistical Package for the Social Sciences, Version 16.0 (IBM, Armonk, New York). The area under the ROC curve (AUC) was calculated to compare the diagnostic accuracy of VE-PCASL with standard and relative labeling efficiencies, respectively. The cutoff of the supply fraction was determined as the value that achieved a targeted balance between sensitivity and specificity. In the present study, the value of the supply fraction associated with the maximal sum of sensitivity and specificity was chosen as the optimal cutoff.

Statistical analyses were performed by using within-subject ANOVA to compare supply fractions acquired with different PLDs. The data processing was performed with Matlab R2009a (MathWorks, Natick, Massachusetts).

RESULTS

Patients

Between December 2011 and November 2012, eighteen consecutive patients (8 women/10 men; mean age, 32.8 ± 10.8 years) with intracranial AVMs were recruited for this prospective study. All 18 patients demonstrated no other lesions in the brain, and 1

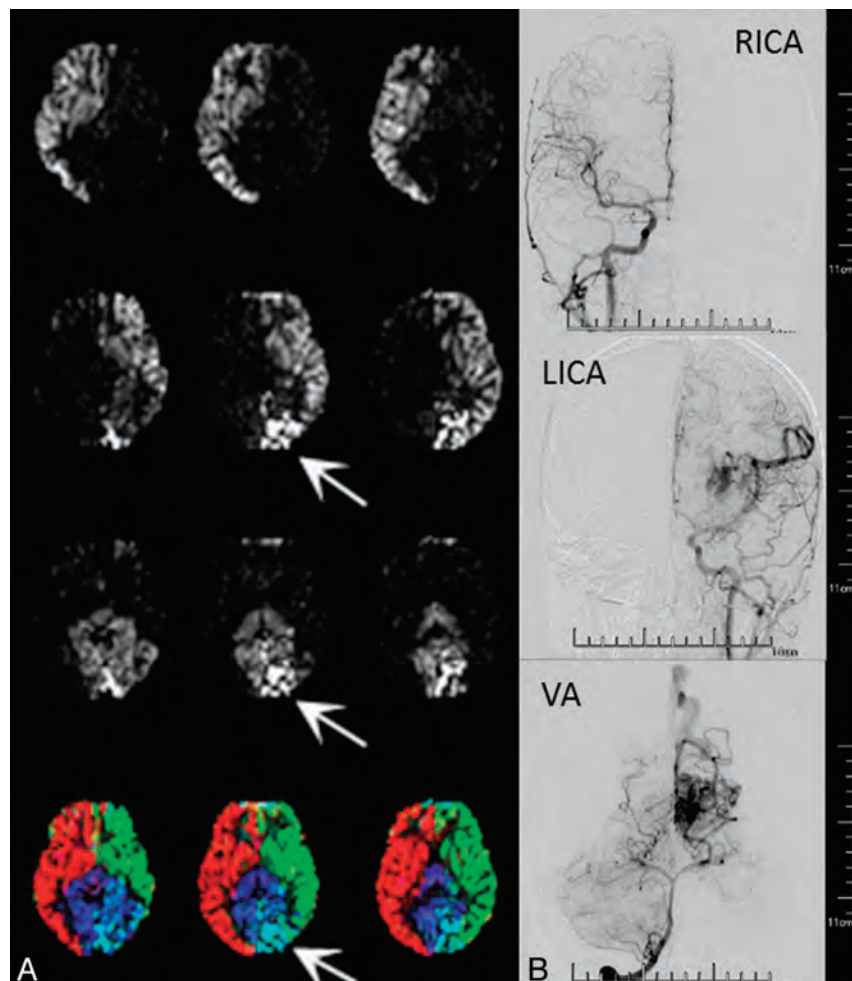


FIG 4. Patient 1, a 23-year-old man. He had headaches and blurred vision in both eyes for half a year. The supply fractions of the left ICA, VA, and right ICA were 52.59%, 46.75%, 0.66% and 49.27%, 50.71%, 0 with standard and relative labeling efficiencies, respectively, showing good agreement between the 2 methods. A, VE-PCASL with standard labeling efficiency (arrows show the AVM lesion). B, DSA shows that the AVM lesion is fed by the left ICA and VA.

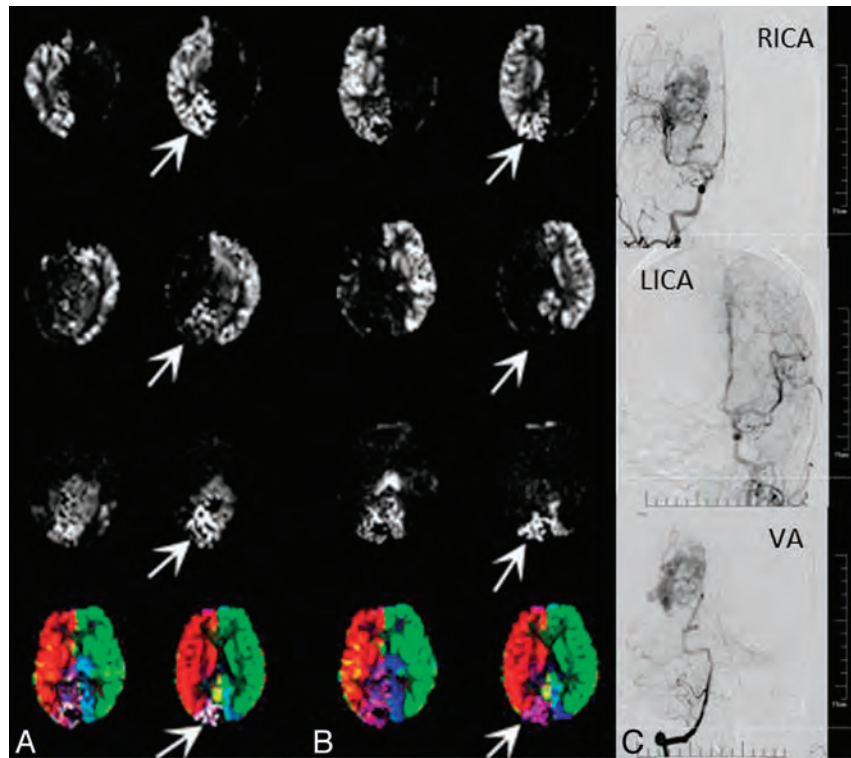


FIG 5. Patient 13, a 27-year-old woman. She had a sudden severe headache accompanying a visual field defect 2 months ago, which was confirmed as spontaneous intraventricular hemorrhage by CT. **A**, VE-PCASL with standard labeling efficiencies shows relatively poor separation of left-versus-right ICA perfusion territories, and there are abnormally high signals in the left ICA perfusion territory with the supply fraction of 14.31%, mismatching the results of DSA. **B**, VE-PCASL with relative labeling efficiencies shows an improved separation, and there are fewer abnormally high signals from the left ICA perfusion territory with the supply fraction of 1.14% (arrows show the AVM lesion). **C**, DSA shows that the AVM lesion is fed by the VA and right ICA.

patient had an interventional operation to partially embolize the AVM lesion. The demographic data of the studied population are listed in Table 2. The time interval between preoperative DSA and VE-PCASL was 2~40 days (mean = 11.7 ± 14.1 days).

Image Quality

The identification of feeding arteries of the AVM was consistent between the 2 neurosurgeons on the basis of DSA reports. VE-PCASL was performed successfully in all 18 patients in whom AVM lesions could be identified with obviously high CBF values. The average score of image quality of the ASL maps was 4.36 ± 0.72 . The κ coefficient was 0.723 between the 2 raters, which indicates excellent agreement.

Reliability of VE-PCASL

Supply fractions of individual feeding arteries to the AVM lesions were successfully obtained by using both standard and relative tagging efficiencies, respectively. For the 6 patients with 3 PLDs, there were no significant differences in the supply fractions obtained at 3 PLDs ($P > .05$, Fig 2).

Diagnostic Accuracy of VE-PCASL

The diagnostic accuracy of VE-PCASL assessed by ROC showed high sensitivity and specificity at various cutoff levels for both standard and relative labeling efficiencies (Table 3). Both methods yielded a high diagnostic accuracy with an $AUC > 0.9$ ($P < .01$) (Fig 3).

For VE-PCASL encoded with standard labeling efficiencies, the ROC curve showed that the cutoff of 15.17% supply fraction is optimal for identifying feeding arteries to the AVM. For that cutoff level (ie, supply fraction $\geq 15.17\%$), the sensitivity was 84.62% and the specificity was 93.33%, the positive predictive value was 97.06%, and the negative predictive value was 70%. The AUC was 0.942 ($P < .01$), indicating a high level of accuracy (Fig 4).

VE-PCASL with relative labeling efficiencies showed an improved ability to discriminate ASL signals from different arteries. This resulted in an improved sensitivity while maintaining the specificity with a decreased cutoff of supply fractions. The AUC for this method was 0.957, and the optimal cutoff of the supply fraction was 11.73%, which led to an 89.74% sensitivity, 93.33% specificity, 97.22% positive predictive value, and 77.78% negative predictive value. The AUC by using relative labeling efficiencies was greater than that of standard labeling efficiencies, though there were no significant differences between the AUCs of the 2 decoding methods (Fig 5).

However, VE-PCASL with relative labeling efficiencies was not perfect. Figure 6 shows an AVM located in the right occipital lobe that was fed by the VA and right ICA on DSA. VE-PCASL with standard labeling efficiencies showed abnormally high signals in the left ICA perfusion territory with a supply fraction of 27.53%, mismatching the results of DSA. VE-PCASL with relative labeling efficiencies reduced the supply fraction of the left ICA to

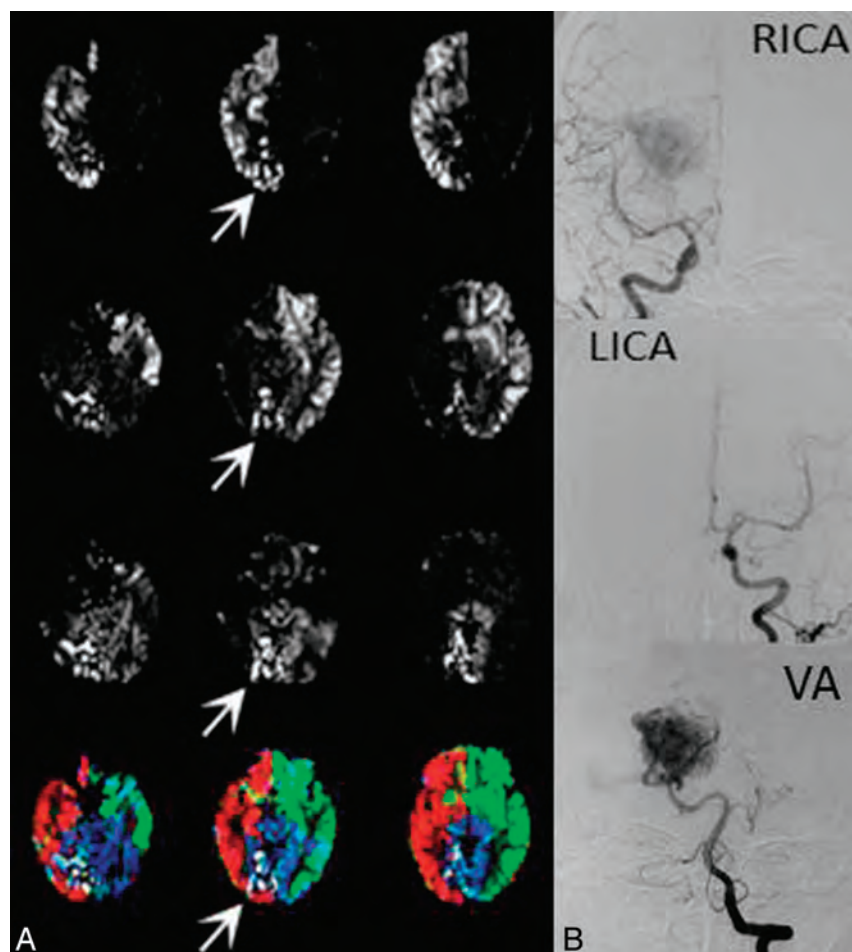


FIG 6. Patient 9, a 31-year-old woman. She had dizziness for approximately 2 years. VE-PCASL with standard labeling efficiencies showed abnormally high signals in the left ICA perfusion territory with the supply fraction of 27.53%, mismatching the results of DSA. A, VE-PCASL with relative labeling efficiencies shows reduced abnormal signals with the supply fraction of 25.67% but still fails to match the results of DSA (arrows show the AVM lesion). B, DSA shows that the AVM lesion is fed by the VA and right ICA.

25.67% but still failed to match the results of DSA. There were still hyperintensities in the left ICA perfusion territory.

DISCUSSION

VE-PCASL is a recently introduced time-efficient method for mapping multiple vascular territories. It can estimate the fraction of CBF supplied by each artery by using x-y gradients to encode the major arteries within the labeling plane. The imaging process is conceptually similar to that of conventional angiography without the use of x-rays or iodinated contrast agents. As a result, VE-PCASL has engendered increasing attention in the evaluation of cerebrovascular disorders such as steno-occlusive disease, aneurysms, and AVMs. However, 1 shortcoming of VE-PCASL is its sensitivity to magnetic field inhomogeneity effects at the labeling location, which affects tagging efficiencies of individual arteries.²¹ Furthermore, for AVMs, there is clearance of tagged blood by venous flow due to the lack of a normal capillary network, which would lead to inaccuracy in quantifying CBF. In the present study, we estimated the relative tagging efficiencies of 3 major arteries in each individual patient by using the histogram method. We also applied 3 different PLDs to check whether the supply fraction can be estimated reliably. The results were relatively stable across different PLDs; this finding indicates that VE-PCASL can provide a

reliable estimation of supply fractions of individual arteries despite several potential confounding factors such as relaxation and venous outflow of the labeled blood.

Optimal Hadamard encoding assumes that all inflowing blood is either fully inverted or fully relaxed for each tagging cycle, and there are equal numbers of tag and control conditions for each vessel.¹⁵ This assumption may not be realistic because of vessel geometry and variations in tagging efficiencies due to field inhomogeneity effects. As a result, the discrimination of arteries may not be perfectly achieved and there may be contamination of ASL signals from different arteries. This result may not be prominent in healthy populations but would be noteworthy in AVM lesions in which CBF is abnormally high. To circumvent this problem, Wong¹⁵ proposed a histogram-based method for estimating vessel-specific labeling efficiencies from VE-PCASL data, which were applied in the construction of the encoding matrices to improve the separation of supplying arteries within vascular territories.

Overall, VE-PCASL with both standard and relative labeling efficiencies showed a high level of accuracy in identifying feeding arteries (AUC = 0.942 and 0.957). In the present study, the optimal cutoff was chosen as a balance between sensitivity and specificity (maximal sum). Because no statistical significance was observed, it is too

soon to conclude that VE-PCASL with relative labeling efficiencies has better performance compared with that of standard labeling efficiencies. VE-PCASL with both standard and relative labeling efficiencies awaits further evaluation in larger scale clinical studies.

Various MR imaging techniques have been applied as noninvasive and radiation-free methods for the evaluation of intracranial AVMs. However, the subjective interpretation of feeding arteries may be viewer-dependent. VE-PCASL evaluates feeding arteries and AVM lesions differently than TOF-MRA or DSA. It does not display the vascular architecture directly but provides a quantitative estimate of supply fractions of individual arteries, which can be displayed in color scales. The fractional supply was calculated to evaluate the role of each feeding artery quantitatively rather than by qualitative approaches without standardization. In addition, it can help to determine dominant feeding arteries, the pattern of which would influence the chances for complete or subtotal obliteration of AVM lesions.²² The cutoff or threshold of the supply fraction should be determined according to the clinical purpose. For example, if the purpose was for preliminary screening of feeding arteries, the lower cutoff (higher sensitivity) should be applied, while a higher cutoff (higher specificity) should be chosen for precise identification of feeding arteries.

In addition to the advantages of a quantitative evaluation of supply fractions, VE-PCASL can display the spatial relationship between AVM lesions and functional or eloquent cortices, which would provide valuable information for neurosurgical operations. Furthermore, VE-PCASL can evaluate hypoperfused areas around the AVM to probe a potential “steal phenomenon” related to the AVM lesion.¹² Recently, VE-PCASL has also been expanded to encode branches of the circle of Willis, even without prior knowledge of vessel positions.²³

A limitation of our study is that the number of patients was relatively small; thus, the selection of the cutoff may serve as a reference rather than a criterion. Another limitation is that we did not label bilateral external carotid arteries with VE-PCASL, which may also contribute to the feeding of intracranial AVMs (1 AVM in this study was confirmed to be fed partially by ipsilateral external carotid artery on DSA). However the latter problem has recently been resolved technically¹⁷ and labeling bilateral external carotid arteries can be applied in assessments of AVM lesions in the future.

CONCLUSIONS

Quantitative supply fractions of feeding arteries to intracranial AVMs can be reliably estimated with VE-PCASL. VE-PCASL with either standard or relative labeling efficiencies demonstrated a high level of accuracy for identifying feeding arteries of AVMs. Even though VE-PCASL cannot replace DSA for clinical diagnosis currently, it can act as preoperative adjunct to estimate relative contributions of feeding arteries.

Disclosures: Rong Xue—RELATED: Grant: Ministry of Science and Technology of China.* Chinese Academy of Sciences Knowledge Innovation Project.* Danny JJ. Wang—RELATED: Grant: National Institutes of Health. *Money paid to the institution.

REFERENCES

- Hernesniemi JA, Dashti R, Juvela S, et al. **Natural history of brain arteriovenous malformations: a long-term follow-up study of risk of hemorrhage in 238 patients.** *Neurosurgery* 2008;63:823–29, discussion 829–31
- Pik JH, Morgan MK. **Microsurgery for small arteriovenous malformations of the brain: results in 110 consecutive patients.** *Neurosurgery* 2000;47:571–75, discussion 575–77
- Klimo P Jr, Rao G, Brockmeyer D. **Pediatric arteriovenous malformations: a 15-year experience with an emphasis on residual and recurrent lesions.** *Childs Nerv Syst* 2007;23:31–37
- van Beijnum J, van der Worp HB, Buis DR, et al. **Treatment of brain arteriovenous malformations: a systematic review and meta-analysis.** *JAMA* 2011;306:2011–19
- Spetzler RF, Martin NA, Carter LP, et al. **Surgical management of large AVM's by staged embolization and operative excision.** *J Neurosurg* 1987;67:17–28
- Yarsargil MG, Curcic M, Kis M, et al. *Microneurosurgery (IIIB)*. Stuttgart, Germany and New York: Thieme; 1988
- Willinsky RA, Taylor SM, TerBrugge K, et al. **Neurologic complications of cerebral angiography: prospective analysis of 2,899 procedures and review of the literature.** *Radiology* 2003;227:522–28
- Hankey GJ, Warlow CP, Sellar RJ. **Cerebral angiographic risk in mild cerebrovascular disease.** *Stroke* 1990;21:209–22
- Hadizadeh DR, von Falkenhausen M, Gieseke J, et al. **Cerebral arteriovenous malformation: Spetzler-Martin classification at subsecond-temporal-resolution four-dimensional MR angiography compared with that at DSA.** *Radiology* 2008;246:205–13
- Yu S, Yan L, Yao Y, et al. **Noncontrast dynamic MRA in intracranial arteriovenous malformation (AVM): comparison with time of flight (TOF) and digital subtraction angiography (DSA).** *Magn Reson Imaging* 2012;30:869–77
- Detre JA, Leigh JS, Williams DS, et al. **Perfusion imaging.** *Magn Reson Med* 1992;23:37–45
- Wolf RL, Wang J, Detre JA, et al. **Arteriovenous shunt visualization in arteriovenous malformations with arterial spin-labeling MR imaging.** *AJNR Am J Neuroradiol* 2008;29:681–87
- Pollock JM, Whitlow CT, Simonds J, et al. **Response of arteriovenous malformations to gamma knife therapy evaluated with pulsed arterial spin-labeling MRI perfusion.** *AJR Am J Roentgenol* 2011;196:15–22
- Wu WC, Fernandez-Seara M, Detre JA, et al. **A theoretical and experimental investigation of the tagging efficiency of pseudocontinuous arterial spin labeling.** *Magn Reson Med* 2007;58:1020–27
- Wong EC. **Vessel-encoded arterial spin-labeling using pseudocontinuous tagging.** *Magn Reson Med* 2007;58:1086–91
- Wu B, Wang X, Guo J, et al. **Collateral circulation imaging: MR perfusion territory arterial spin-labeling at 3T.** *AJNR Am J Neuroradiol* 2008;29:1855–60
- Dang Y, Wu B, Sun Y, et al. **Quantitative assessment of external carotid artery territory supply with modified vessel-encoded arterial spin-labeling.** *AJNR Am J Neuroradiol* 2012;33:1380–86
- Wang J, Alsop DC, Li L, et al. **Comparison of quantitative perfusion imaging using arterial spin labeling at 1.5 and 4.0 Tesla.** *Magn Reson Med* 2002;48:242–54
- Kansagra AP, Wong EC. **Quantitative assessment of mixed cerebral vascular territory supply with vessel encoded arterial spin labeling MRI.** *Stroke* 2008;39:2980–85
- Landis JR, Koch GG. **The measurement of observer agreement for categorical data.** *Biometrics* 1977;33:159–74
- Wong EC. **Quantifying CBF with pulsed ASL: technical and pulse sequence factors.** *J Magn Reson Imaging* 2005;22:727–31
- Cohadon F, Dolenc VV, Lobo Antunes J, et al. *Advances and Technical Standards in Neurosurgery*. (vol. 24). New York: Springer-Verlag; 1998
- Wong EC, Guo J. **Blind detection of vascular sources and territories using random vessel encoded arterial spin labeling.** *MAGMA* 2012;25:95–101

Decreased T1 Contrast between Gray Matter and Normal-Appearing White Matter in CADASIL

F. De Guio, S. Reyes, M. Duering, L. Pirpamer, H. Chabriat, and E. Jouvent



ABSTRACT

BACKGROUND AND PURPOSE: CADASIL is the most frequent hereditary small-vessel disease of the brain. The clinical impact of various MR imaging markers has been repeatedly studied in this disorder, but alterations of contrast between gray matter and normal-appearing white matter remain unknown. The aim of this study was to evaluate the contrast alterations between gray matter and normal-appearing white matter on T1-weighted images in patients with CADASIL compared with healthy subjects.

MATERIALS AND METHODS: Contrast between gray matter and normal-appearing white matter was assessed by using histogram analyses of 3D T1 high-resolution MR imaging in 23 patients with CADASIL at the initial stage of the disease (Mini-Mental State Examination score > 24 and modified Rankin scale score ≤ 1; mean age, 53.5 ± 11.1 years) and 30 age- and sex-matched controls.

RESULTS: T1 contrast between gray matter and normal-appearing white matter was significantly reduced in patients compared with age- and sex-matched controls (patients: 1.35 ± 0.08 versus controls: 1.43 ± 0.04, $P < 10^{-5}$). This reduction was mainly driven by a signal decrease in normal-appearing white matter. Contrast loss was strongly related to the volume of white matter hyperintensities.

CONCLUSIONS: Conventional 3D T1 imaging shows significant loss of contrast between gray matter and normal-appearing white matter in CADASIL. This probably reflects tissue changes in normal-appearing white matter outside signal abnormalities on T2 or FLAIR sequences. These contrast alterations should be taken into account for image interpretation and postprocessing.

ABBREVIATIONS: CADASIL = cerebral autosomal dominant arteriopathy with subcortical infarcts and leukoencephalopathy; NAWM = normal-appearing white matter; MMSE = Mini-Mental State Examination

Cerebral autosomal dominant arteriopathy with subcortical infarcts and leukoencephalopathy (CADASIL) is a hereditary small-vessel disease of the brain secondary to mutations of the *NOTCH3* gene.¹ Conventional MR imaging markers have been repeatedly investigated in this disorder.²⁻⁵ The impact of lacunar lesions detected on T1-weighted sequences seems more impor-

tant than that of white matter lesions observed on FLAIR sequences.⁶ Recently, various measures of brain and cortical atrophy were shown to be related to clinical worsening.^{7,8}

As reported in the context of Alzheimer disease,⁹ contrast between gray matter and normal-appearing white matter (NAWM) may be altered in CADASIL. This could have important implications for both image interpretation in the clinical setting and postprocessing in research studies. So far however, the alterations of MR imaging T1 contrast between GM and NAWM have not been evaluated in CADASIL. The aim of the present study was to assess potential contrast alterations between GM and NAWM on T1-weighted images in patients with CADASIL at the initial stage of the disease compared with age- and sex-matched individuals.

MATERIALS AND METHODS

Participants

Patients with CADASIL without dementia (Mini-Mental State Examination [MMSE] score > 24)¹⁰ and without significant disability (modified Rankin Scale score ≤ 1)⁶ were recruited from

Received January 15, 2013; accepted after revision April 4.

From University Paris Diderot (F.D.G., H.C., E.J.), Sorbonne Paris Cité, Paris, France; Department of Neurology (S.R., H.C., E.J.), Lariboisière Hospital, Paris, France; Institute for Stroke and Dementia Research (M.D.), Medical Centre, Klinikum der Universität München, Ludwig-Maximilians-University, Munich, Germany; and Division of Neurogeriatrics (L.P.), Department of Neurology, Medical University of Graz, Graz, Austria.

This work was supported by grants from the Fondation Planiol, the Fondation NRJ-Institut de France, and an FP6 ERANET NEURON (01 EW1207) and was helped by the French CADASIL Foundation.

Please address correspondence to Eric Jouvent, MD, Hôpital Lariboisière, 2 Rue Ambroise Paré, 75010 Paris, France; e-mail: eric.jouvent@lrb.aphp.fr

Indicates open access to non-subscribers at www.ajnr.org

<http://dx.doi.org/10.3174/ajnr.A3639>

Characteristics of patients with CADASIL and healthy controls

	Patients with CADASIL (n = 22)	Healthy Controls (n = 29)	P Value
Age (yr) (mean) (range)	53.5 ± 11.1, 32.1–74.5	53.8 ± 11.0, 30.1–71.4	.73
Male sex (No.) (%)	11/22 (50%)	15/29 (52%)	.88
Right-handed (No.) (%)	22/22 (100%)	28/29 (97%)	.99
Level of education (yr)	11.7 ± 3.9	13.6 ± 3.5	.08
MMSE (mean) (median) (range)	28.5, 29, 25–30	29.0, 29, 26–30	.26
Brain volume in mm ³ (mean)	1017202 ± 113233	1003640 ± 84340	.64 (.61) ^a
Normalized GM peak (mean)	0.30 ± 0.05	0.31 ± 0.05	.48 (.45) ^a
Normalized WM peak (mean)	0.59 ± 0.06	0.67 ± 0.09	.001 (.001) ^a
Contrast between GM and NAWM (mean)	1.35 ± 0.08	1.43 ± 0.04	.001 (<10 ⁻⁵) ^a
White matter lesion volume, (mean) (median) (range) in mm ³	97972.9, 76256.6, 7249.8–267095.1	NA	–
Lacunar lesion volume (mean) (median) (range) in mm ³ (n = 14/22, 64%) ^b	526.1, 290.1, 14.0–1974.7	NA	–
No. of microhemorrhages (mean) (median) (range) (n = 8/22, 36%) ^b	6.5, 2.5, 1–32	NA	–

Note:—NA indicates not applicable; –, no test performed.

^a P value adjusted for age and sex.

^b In patients with such lesions (number given in parentheses).

our French data base on a voluntary basis. Twenty-three patients were included. Thirty healthy controls from a local volunteer data base were age- and sex-matched. A local ethics committee validated the protocol.

Clinical Assessment

All participants underwent a comprehensive neuropsychological evaluation preceded by a clinical psychological interview. Global cognitive performances were assessed by using the MMSE.¹⁰ This widely used global cognitive battery scores from 0 to 30. As a general rule, patients with a score under 24 are considered to have dementia.¹¹ Disability was assessed by using the modified version of the Rankin Scale (from 0, no disability, to 5, major disability), in which scores ≤1 denote no disability.⁶ Other tests, including those of visual object or spatial perception and verbal or visual episodic memory and the evaluation of attention and executive processes, were performed but are not detailed here because they were not relevant to the present study.

MR Imaging Protocol

3D T1 images were acquired with a 3T Tim Trio MR imaging scanner (Siemens, Erlangen, Germany) equipped with a 12-channel head coil, by using a single standard MPRAGE sequence (in-plane resolution = 1 × 1 mm², section thickness = 1.1 mm, TR = 2300 ms, TE = 2.98 ms, TI = 900 ms, flip angle = 9°). Within 6 months, as part of another ongoing longitudinal study, patients also underwent an MR imaging protocol on a 1.5T Signa scanner (GE Healthcare, Milwaukee, Wisconsin) with 3D T1 fast-spoiled gradient echo (in-plane resolution = 1.02 × 1.02 mm², section thickness = 0.8 mm, TR = 9 ms, TE = 2 ms, flip angle = 20°), FLAIR (in-plane resolution = 1 × 1 mm², section thickness = 5.5 mm, TR = 8402 ms, TE = 161 ms, TI = 2002 ms), and T2* gradient echo (in-plane resolution = 1 × 1 mm², section thickness = 5.5 mm, TR = 500 ms, TE = 15 ms) sequences, from which lesion masks, volumes of lacunar lesions and of white matter hyperintensities, and the number of cerebral microhemorrhages were obtained as previously reported.^{6,7}

Image Processing

3D T1-weighted images were segmented to obtain brain masks for GM and WM by using the Morphologist pipeline of BrainVISA (<http://www.brainvisa.info>), which relies on a histogram analysis algorithm performed after a first step consisting of field inhomogeneity bias correction.¹²

Lacunar lesions were defined on T1-weighted images as hypointense lesions with a signal identical to that of CSF, a diameter of >3 mm, and a distinct shape from that of enlarged perivascular spaces.¹³ Microhemorrhages were defined as rounded foci of signal loss with a diameter inferior to 5 mm on gradient-echo sequences and distinct from vascular flow voids, leptomeningeal hemosiderosis, or nonhemorrhagic mineralization. Masks of white matter hyperintensities were obtained from FLAIR sequences by applying an adaptive threshold derived from the signal-intensity histogram and were manually corrected afterward only if necessary, as previously detailed.¹⁴ Registration matrices between FLAIR and 3D T1 sequences were calculated with the FLIRT rigid body registration algorithm (www.fmrib.ox.ac.uk/fsl) and then were applied on masks of white matter hyperintensities by using nearest neighbor interpolation to obtain binary masks of white matter lesions in the space of the 3D T1 sequence, as previously reported.⁷ In patients, histograms of bias-corrected 3D T1 images were computed within the brain mask and outside the lesion mask to study GM and NAWM. Histograms were computed on whole GM and WM in control subjects. To ensure that computing histograms in smaller and/or different volumes did not systematically bias our results, we checked analyses after random attribution of lesion masks of patients to MR imaging scans of control subjects. The contrast between GM and NAWM was defined as the ratio of the intensity level corresponding to the NAWM peak and the one corresponding to the GM peak. Image intensity was normalized between subjects according to their minimum values (representing at least 1000 voxels) and to the intensity level of the vitamin E capsule that was placed before MR imaging acquisition to indicate the right side of the subject.

Statistical Methods

R software (<http://www.R-project.org>) was used for statistical analyses. Group comparisons were made according to variable types and distributions. For numeric variables, we used *t* tests when variables were normally distributed, taking into account the equal or unequal variances of the 2 groups. When the assumption of normality was violated, the Wilcoxon rank sum tests were used. For categorical variables, χ^2 tests were used. Contrast differences between groups were adjusted for age and sex, which may influence tissue contrast,¹⁵ by using ANCOVA.

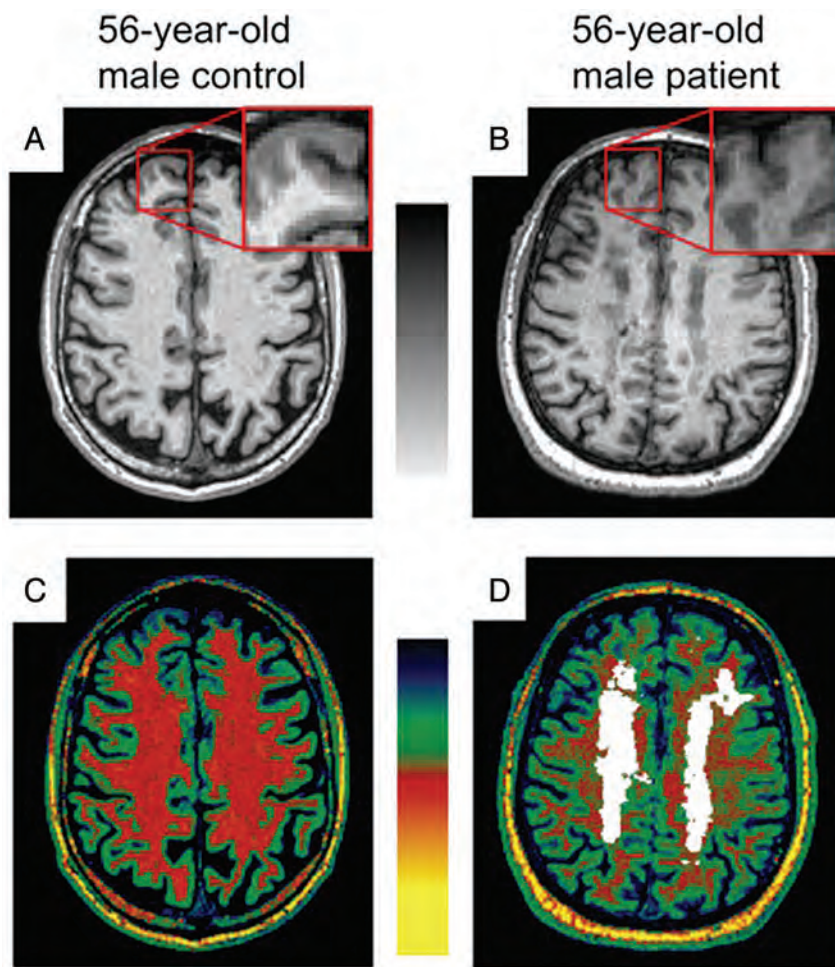


FIG 1. Reduction of T1 contrast between gray matter and normal-appearing white matter. Axial 3D T1 image after intensity normalization of a 56-year-old healthy male subject (A) and a 56-year-old male patient with CADASIL (B) with zoom boxes showing reduced contrast between gray matter and normal-appearing white matter in CADASIL because NAWM appears darker. Color-coded images are enhancing the global heterogeneity of NAWM outside the lesions determined on FLAIR (overlaid in white) in the patient with CADASIL (D) compared with the homogeneous white matter in the control subject (C). The signal of subcutaneous fat, similar for the 2 subjects, may serve as a reference for visual inspection.

RESULTS

One control subject did not undergo MR imaging, and histogram analysis failed for 1 patient with CADASIL due to a single peak detection, leaving 22 patients and 29 control subjects for analyses. Characteristics of the 2 groups are reported in the Table. Age, sex, level of education, MMSE score, and brain volumes did not significantly differ between patients and controls.

We observed a significant contrast reduction between GM and NAWM in patients compared with controls, which persisted after adjustment for age and sex as illustrated in Fig 1 (patients: 1.35 ± 0.08 versus controls: 1.43 ± 0.04 , $P < 10^{-5}$). These contrast alterations were mainly driven by modifications of NAWM because normalized values showed a decreased NAWM peak in patients (patients: 0.59 ± 0.06 versus controls: 0.67 ± 0.09 , $P = .001$) but no difference in GM peaks (Fig 2).

Applying white matter lesion masks of patients on scans of control subjects randomly did not alter the NAWM peak computation (unchanged in 14 subjects, mean variation of 0.2% in the other 8 subjects).

In patients, linear regression modeling showed that contrast between GM and NAWM was strongly related to the logarithm of white matter lesion volume after adjustment for age and sex (estimate: -0.09 ; SE: 0.01; $P < 10^{-4}$). The contrast was not related to the volume of lacunar lesions (estimate: -4.97 ; SE: 2.99; $P = .12$) or to the number of microhemorrhages (estimate: -0.002 ; SE: 0.003; $P = .38$).

In patients, we also observed a marginal linear relationship between MMSE scores and contrast between GM and NAWM after adjustment for age and sex (estimate: 9.6; SE: 4.4; P value = .04). No other association with other clinical outcomes was significant.

DISCUSSION

In the present study, we observed significant contrast alterations between NAWM and GM in patients with CADASIL compared with age- and sex-matched healthy subjects, long before the appearance of disability. Our results seemed mainly related to a global reduction of NAWM T1 signal in patients with CADASIL. These findings are in line with previous data obtained in CADASIL that showed alterations of the NAWM by using magnetization transfer¹⁶ or diffusion tensor imaging.¹⁷ In contrast to these sophisticated methods, our results were obtained on conventional T1-weighted images by using simple post-processing steps and were easily confirmed by visual inspection of patient scans compared with controls (Fig 1).

The decreased signal in NAWM observed in patients with CADASIL may be explained by diffuse white matter edema as recently reported.¹⁸ An increase in water content would induce longer T1 and thus reduce signal in T1-weighted images. Demyelination, neuronal degeneration, or regional iron concentration may also be involved in these signal changes.¹⁹

Contrast reduction was previously observed in normal aging²⁰ and was proposed as an alternative marker of tissue loss in Alzheimer disease.⁹ Here, the contrast reduction was strongly and independently related to the extent of WM lesions in patients. A correlation between average magnetization transfer imaging metrics of the NAWM and lesion volume was previously reported in CADASIL, which authors attributed to Wallerian degeneration secondary to axonal injury.¹⁶

Our results may have consequences for postprocessing of 3D T1 images in research studies. Indeed, high-resolution 3D T1 acquisitions are necessary so far to perform fine-tissue segmentation, voxel-based morphometry studies, and advanced image techniques such as cortical surface analysis⁷ or cortical

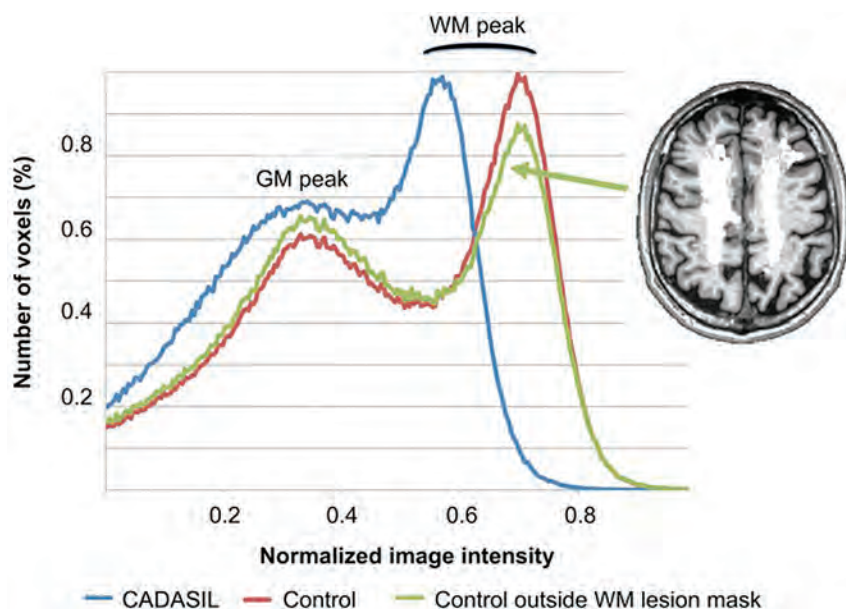


FIG 2. 3D T1 intensity histograms in a patient with CADASIL and a control subject. Normalized histograms computed within the brain and outside the white matter lesion masks for the 56-year-old patient with CADASIL and control subject of Fig 1. For the control subject, a histogram is redrawn after exclusion of voxels corresponding to the white matter lesion mask of the patient (overlaid in white). While the gray matter peak is roughly the same between subjects, the white matter peak is left-shifted in the patient with CADASIL, leading to a reduced contrast between GM and NAWM. Computation of the histogram for the control subject outside the lesion mask (randomly allocated from a patient with CADASIL) did not change WM peak and contrast values.

thickness estimation⁸ through dedicated software, and it has been demonstrated that contrast properties could influence cortical thickness measures.^{9,21} Contrast alterations may also serve as a visual clue to the diagnosis of CADASIL because they do not seem to be as severe in other types of small-vessel disease of the brain, but further studies will be necessary to evaluate this hypothesis.

We observed a significant relationship between MMSE scores and contrast changes in patients with CADASIL. However, this finding should be interpreted cautiously because MMSE scores lay within normal ranges and the *P* value was marginally significant (.04). Moreover, we did not observe any other association between cognitive tests and contrast changes in patients. Further studies with larger samples and patients with more severe disease will help to determine the clinical significance of T1 contrast changes.

Our study has some limitations. FLAIR sequences were not part of the 3T protocol because it was designed for a cortical morphology study. Control subjects had no lesion mask, and histograms were computed on the whole WM. However, we showed that applying WM lesion masks of patients on control scans randomly did not change the results. Besides, at least some part of WM lesions are hypointense on T1-weighted images. Therefore, lesions potentially included in the WM would have induced a decreased contrast in controls, which is the opposite of what we found (ie, an increased contrast in controls). FLAIR sequences for patients were obtained within 6 months by using 1.5T acquisitions and 5-mm-thick sequences. Hypointense lesions on T1 may thus appear outside lesion masks determined on FLAIR. However, the extension of white matter lesions in nondisabled patients

with CADASIL in such a short period is negligible, unlikely to alter our results.⁷ Moreover, manual corrections performed to include potential hypointense lesions on T1 secondary to this time interval or to other potential sources such as variation of field strength, differences in section thickness between FLAIR and 3D-T1, or registration imprecisions and not overlaid by lesion masks did not alter our results (data not shown).

Another limitation of our study was the global computation of the contrast between GM and NAWM, not allowing a regional quantification of contrast reduction. This global measure was thought to be more robust, given the large variability of WM lesion extent in patients with CADASIL, and highlighted a diffuse biologic mechanism occurring in whole NAWM. Finally, the signal normalization chosen to compare NAWM mean intensity across subjects was not perfect because the vitamin E capsule was not equally placed on subjects and therefore was dependent on gradient nonlinearity effects and field

heterogeneities. However, the large differences observed between the 2 groups in NAWM and not in GM could not be explained only by field heterogeneities.

Our study also has several strengths. There was a high homogeneity between groups in terms of age and sex, which was important, given the effect of age on contrast. Patients and controls were imaged with the same MR imaging scanner and protocol, with special care to reproduce acquisition conditions. The histogram-based technique to compute the tissue contrast is simple but was robust and adapted to patients with large WM lesions, leading to straightforward and original results.

CONCLUSIONS

Conventional 3D T1 imaging shows significant loss of contrast between GM and NAWM as soon as the early stages in CADASIL. These contrast alterations should be taken into account for both image interpretation and postprocessing. Whether these alterations can be used as a new biomarker in CADASIL or in other small-vessel diseases of the brain requires further investigation.

ACKNOWLEDGMENTS

The authors acknowledge Jocelyne Ruffié, Veronique Joly-Testaud, Laurence Laurier, and Chantal Ginisty for the recruitment process of patients and controls.

Disclosures: François De Guio—RELATED: Grant: ERA-NET-Funded Collaborative Network MESCOG.* Comments: The network is funded under the ERA-Net scheme in FP6 2007–2011 by the European Commission. Marco Duering—UNRELATED: Grants/Grants Pending: BMBF/DZNE, Travel/Accommodations/Meeting Expenses Unrelated to Activities Listed: United Leukodystrophy Foundation. Hugues Chabriat—UNRELATED: Board Membership: Lundbeck, Janssen, Comments: steer-

ing or safety committees. *Consultancy*: Lundbeck, Janssen, *Comments*: during the past 5 years. **Money paid to the institution*.

REFERENCES

1. Chabriat H, Joutel A, Dichgans M, et al. **CADASIL**. *Lancet Neurol* 2009;8:643–53
2. Yousry TA, Seelos K, Mayer M, et al. **Characteristic MR lesion pattern and correlation of T1 and T2 lesion volume with neurologic and neuropsychological findings in cerebral autosomal dominant arteriopathy with subcortical infarcts and leukoencephalopathy (CADASIL)**. *AJNR Am J Neuroradiol* 1999;20:91–100
3. Singhal S, Rich P, Markus HS. **The spatial distribution of MR imaging abnormalities in cerebral autosomal dominant arteriopathy with subcortical infarcts and leukoencephalopathy and their relationship to age and clinical features**. *AJNR Am J Neuroradiol* 2005;26:2481–87
4. van Den Boom R, Lesnik Oberstein SA, van Duinen SG, et al. **Subcortical lacunar lesions: an MR imaging finding in patients with cerebral autosomal dominant arteriopathy with subcortical infarcts and leukoencephalopathy**. *Radiology* 2002;224:791–96
5. Duering M, Zieren N, Herve D, et al. **Strategic role of frontal white matter tracts in vascular cognitive impairment: a voxel-based lesion-symptom mapping study in CADASIL**. *Brain* 2011;134:2366–75
6. Viswanathan A, Godin O, Jouvent E, et al. **Impact of MRI markers in subcortical vascular dementia: a multi-modal analysis in CADASIL**. *Neurobiol Aging* 2010;31:1629–36
7. Jouvent E, Mangin JF, Duchesnay E, et al. **Longitudinal changes of cortical morphology in CADASIL**. *Neurobiol Aging* 2012;33:1002.e29–36
8. Duering M, Righart R, Csanadi E, et al. **Incident subcortical infarcts induce focal thinning in connected cortical regions**. *Neurology* 2012;79:2025–28
9. Grydeland H, Westlye LT, Walhovd KB, et al. **Improved prediction of Alzheimer's disease with longitudinal white matter/gray matter contrast changes**. *Hum Brain Mapp* 2013;34:1775–85
10. Folstein MF, Folstein SE, McHugh PR. **"Mini-mental state": a practical method for grading the cognitive state of patients for the clinician**. *J Psychiatr Res* 1975;12:189–98
11. Jagust W, D'Esposito M. *Imaging the Aging Brain*. New York: Oxford University Press; 2009
12. Jouvent E, Viswanathan A, Mangin J-F, et al. **Brain atrophy is related to lacunar lesions and tissue microstructural changes in CADASIL**. *Stroke* 2007;38:1786–90
13. Zhu YC, Dufouil C, Mazoyer B, et al. **Frequency and location of dilated Virchow-Robin spaces in elderly people: a population-based 3D MR imaging study**. *AJNR Am J Neuroradiol* 2011;32:709–13
14. Viswanathan A, Guichard JP, Gschwendtner A, et al. **Blood pressure and haemoglobin A1c are associated with microhaemorrhage in CADASIL: a two-centre cohort study**. *Brain* 2006;129:2375–83
15. Cho S, Jones D, Reddick WE, et al. **Establishing norms for age-related changes in proton T1 of human brain tissue in vivo**. *Magn Reson Imaging* 1997;15:1133–43
16. Iannucci G, Dichgans M, Rovaris M, et al. **Correlations between clinical findings and magnetization transfer imaging metrics of tissue damage in individuals with cerebral autosomal dominant arteriopathy with subcortical infarcts and leukoencephalopathy**. *Stroke* 2001;32:643–48
17. Chabriat H, Pappata S, Poupon C, et al. **Clinical severity in CADASIL related to ultrastructural damage in white matter: in vivo study with diffusion tensor MRI**. *Stroke* 1999;30:2637–43
18. Yao M, Jouvent E, Duing M, et al. **Extensive white matter hyperintensities may increase brain volume in cerebral autosomal-dominant arteriopathy with subcortical infarcts and leukoencephalopathy**. *Stroke* 2012;43:3252–57
19. Kong L, Herold C, Stieltjes B, et al. **Reduced gray to white matter tissue intensity contrast in schizophrenia**. *PLoS One* 2012;7:e37016
20. Salat DH, Lee SY, van der Kouwe AJ, et al. **Age-associated alterations in cortical gray and white matter signal intensity and gray to white matter contrast**. *Neuroimage* 2009;48:21–28
21. Salat DH, Chen JJ, van der Kouwe AJ, et al. **Hippocampal degeneration is associated with temporal and limbic gray matter/white matter tissue contrast in Alzheimer's disease**. *Neuroimage* 2011;54:1795–802

Cerebral Aneurysms Treated with Flow-Diverting Stents: Computational Models with Intravascular Blood Flow Measurements

M.R. Levitt, P.M. McGah, A. Aliseda, P.D. Mourad, J.D. Nerva, S.S. Vaidya, R.P. Morton, B.V. Ghodke, and L.J. Kim



ABSTRACT

BACKGROUND AND PURPOSE: Computational fluid dynamics modeling is useful in the study of the hemodynamic environment of cerebral aneurysms, but patient-specific measurements of boundary conditions, such as blood flow velocity and pressure, have not been previously applied to the study of flow-diverting stents. We integrated patient-specific intravascular blood flow velocity and pressure measurements into computational models of aneurysms before and after treatment with flow-diverting stents to determine stent effects on aneurysm hemodynamics.

MATERIALS AND METHODS: Blood flow velocity and pressure were measured in peri-aneurysmal locations by use of an intravascular dual-sensor pressure and Doppler velocity guidewire before and after flow-diverting stent treatment of 4 unruptured cerebral aneurysms. These measurements defined inflow and outflow boundary conditions for computational models. Intra-aneurysmal flow rates, wall shear stress, and wall shear stress gradient were calculated.

RESULTS: Measurements of inflow velocity and outflow pressure were successful in all 4 patients. Computational models incorporating these measurements demonstrated significant reductions in intra-aneurysmal wall shear stress and wall shear stress gradient and a trend in reduced intra-aneurysmal blood flow.

CONCLUSIONS: Integration of intravascular dual-sensor guidewire measurements of blood flow velocity and blood pressure provided patient-specific computational models of cerebral aneurysms. Aneurysm treatment with flow-diverting stents reduces blood flow and hemodynamic shear stress in the aneurysm dome.

ABBREVIATIONS: CFD = computational fluid dynamics; WSS = wall shear stress; WSSG = wall shear stress gradient; TCD = transcranial Doppler ultrasonography; pcMRA = phase-contrast MRA

Flow-diverting stent technology¹ is thought to reduce blood flow (and hence hemodynamic stresses) inside cerebral aneurysms, promoting thrombosis and lowering rupture risk.² How-

ever, 15–35% of aneurysms treated with flow-diverting stents remain patent at midterm angiographic follow-up.^{3–6} Risk factors for persistent aneurysm patency include previous aneurysm treatment and female sex, though accurate predictors of treatment failure and delayed hemorrhagic complications have not been completely elucidated.^{7–9}

Computational fluid dynamics (CFD) modeling of aneurysms and the surrounding cerebral vasculature allows investigators to study important hemodynamic characteristics such as wall shear stress (WSS)^{10,11} and wall shear stress gradient (WSSG),¹² which have been implicated in aneurysm growth, rupture, and treatment failure.¹³ Recently, CFD analysis has been applied to the effects of flow-diverting stent treatment in an attempt to understand how flow diversion affects aneurysm hemodynamics for both treatment success¹⁴ and complication avoidance.^{15–17} However, these reports did not use patient-specific measurements of blood flow velocity and blood pressure when creating CFD models, which may have affected their results.^{18,19}

Received February 26, 2013; accepted after revision April 14.

From the Departments of Neurological Surgery (M.R.L., P.D.M., J.D.N., R.P.M., B.V.G., L.J.K.), Mechanical Engineering (P.M.M., A.A.), Applied Physics Laboratory (P.D.M.), Bioengineering (P.D.M.), and Radiology (P.D.M., S.S.V., B.V.G., L.J.K.), University of Washington, Seattle.

This work was supported by NINDS/NIH grant R03NS078539, and in part by US Army Medical Research and Materiel Command contract No. W81XWH-11-1-0109, an unrestricted grant from Volcano Corporation, San Diego, California, and the generous support of Mark Robison and family.

Paper previously presented as an abstract at: American Society of Mechanical Engineering 2013 Summer Bioengineering Conference, June 26–29, 2013, Sun River, Oregon.

Please address correspondence to Louis J. Kim, MD, Box 359924, Department of Neurological Surgery, Harborview Medical Center, 325 9th Ave, Seattle, WA 98104; e-mail: ljkiml@u.washington.edu

Indicates open access to non-subscribers at www.ajnr.org

Indicates article with supplemental on-line appendix.

Indicates article with supplemental on-line figure.

<http://dx.doi.org/10.3174/ajnr.A3624>

We incorporated patient-specific measurements of blood flow velocity and blood pressure in the peri-aneurysmal environment into the boundary conditions of CFD to determine the hemodynamic effects of flow-diverting stents on unruptured aneurysms.

MATERIALS AND METHODS

Population

Four patients with unruptured cerebral aneurysms were included in this institutional review board–approved prospective study, and informed consent was obtained. Patient, aneurysm, anatomic, and device characteristics are shown in On-line Table 1. All patients underwent endovascular flow-diverting stent placement by use of the Pipeline Embolization Device (Covidien/ev3, Irvine, California) under isoflurane inhalational anesthesia. The aneurysm in patient 1 was also partially coiled. Patient temperature, hematocrit, and end-tidal CO₂ were recorded. Three-dimensional rotational angiography was obtained before aneurysm treatment, and contrast-enhanced flat panel CT was obtained after treatment for stent visualization.²⁰

Patient-Specific Data Collection

Blood flow velocity and blood pressure were measured by use of the dual-sensor pressure and Doppler velocity guidewire (ComboWire, Volcano Corporation, Rancho Cordova, California) and workstation (ComboMap, Volcano). The tip of the 0.014-inch wire contains a piezoresistive pressure sensor and piezoelectrode Doppler device that emits a 45° sonography beam that measures velocity 5 mm beyond the tip. This wire has been used to measure patient-specific blood pressure and blood flow velocity in both coronary²¹ and cerebral vessels,^{22,23} with excellent anatomic specificity and correlation to measured blood flow.²⁴ In the current study, pressure and velocity were sampled every 5 ms, and peak systolic, diastolic, and average pressures and velocities were calculated automatically by the workstation on the basis of the cardiac cycle.

Before aneurysm treatment, the dual-sensor guidewire was placed in 2 predetermined peri-aneurysmal locations: 1) proximal petrous carotid artery, and 2) 5 mm distal to the aneurysm neck. The wire was oriented along the long axis of vessel flow to maximize the flow velocity signal, and radiographs of the location of the wire were obtained. Blood pressure and blood flow velocity were recorded for at least 10 cardiac cycles at each location before wire removal. After aneurysm treatment, the wire was reintroduced and the same measurements were taken again at all locations. Effort was made to reproduce the exact wire locations during pretreatment measurements as recorded in previous radiographs. Blood pressure and blood flow velocity measurements were exported to a workstation for CFD analysis.

Computational Modeling

Three-dimensional reconstructions of the vessels were created from the rotational angiographic images by use of the Vascular Modeling Toolkit (Bergamo, Italy; www.vmtk.org). Ophthalmic and posterior communicating arteries and other small side-branching vessels were eliminated from each model, except for the posterior communicating artery in patient 1 because they had a negligible effect on hemodynamic calculations (On-line Appendix). A “virtual stent” was placed into each reconstruction for

posttreatment simulations by inserting a saddle-shaped surface to the location of the stent boundary on the basis of its location in the posttreatment CT. The stent was modeled as a thin, porous surface with specified pressure-loss coefficients, taken from a previous study²⁵ that computed the pressure drops over low-porosity flow-diverting stents. Pressure drops were parameterized as 2 unique loss coefficients integrated into our CFD model (On-line Appendix). In patient 1 (in whom the aneurysm was partially coiled), a shear and shear gradient value of zero was assigned to the area of the aneurysm dome excluded after coiling, and the remaining volume was used for hemodynamic calculations. Tetrahedral meshes were generated for all simulations by use of the ANSYS Gambit package, release 2.4 (ANSYS, Canonsburg, Pennsylvania). The characteristic width of the computational mesh cells was 0.2 mm for all cases. Simulations were executed by use of ANSYS Fluent, release 12.1 (ANSYS), a finite-volume-based solver. The blood was assumed to be incompressible and Newtonian, with an attenuation of 1050 kg/m³ and viscosity of 3.5 cP.

At the proximal vessel, the time-dependent Womersley velocity profile was prescribed by use of velocity measurements from the dual-sensor guidewire at position 1 (petrous carotid artery). These measured velocities were matched to the centerline velocity of the Womersley flow and used as inflow conditions, incorporating the cross-sectional vessel area from the pretreatment and posttreatment 3D vessel reconstructions (Fig 1, On-line Appendix). At distal vessels, pressures were prescribed by use of measurements from the dual-sensor guidewire at position 2 (5 mm distal to the aneurysm neck) for use as outflow conditions. Velocity and pressure waveforms were phase-averaged over at least 10 cardiac cycles before CFD modeling. Flow rates were computed directly from the wire-derived Womersley velocity profile. Slight changes in heart rate, mean arterial pressure, and blood flow after treatment were incorporated into posttreatment CFD models. The CFD simulations were computed over 3 cardiac cycles, and the first 2 cycles were excluded from analysis to ensure that the simulation was independent of the initializing condition. Intra-aneurysmal blood flow, WSS, and WSSG were calculated over the entire aneurysm volume in each patient (On-line Appendix). Flow rates, WSS, and WSSG were determined both at the moment of peak systole and averaged over an entire cardiac cycle. Pressure drops were also simulated between the 2 wire locations (petrous carotid artery and 5 mm distal to the aneurysm neck), without patient-specific guidewire-derived pressure values. Statistical comparisons were made by use of the Student *t* test.

RESULTS

Patient-Specific Measurements

Proximal blood flow velocity and distal blood pressure measurements were successful in all 4 patients both before and after treatment. Blood flow velocity and flow rates at position 1 (petrous carotid, used for inflow velocity boundary conditions) are shown in Table 1. Flow rates are presented both as an average over the entire cardiac cycle and at the moment of peak systole. The differences between pretreatment and posttreatment velocity and blood flow (both average and peak systolic) at the petrous carotid artery were not significant ($P > .17$).

Table 1: Dual-sensor guidewire measurements of peak systolic blood flow velocity and flow rate used for inflow boundary conditions

n	Blood Flow Velocity, cm/s		Flow Rate, mL/min			
			Averaged Over Cardiac Cycle		At Peak Systole	
	Pre	Post	Pre	Post	Pre	Post
1	46.92	47.11	165.45	154.83	328.88	236.36
2	37.18	37.28	101.92	110.04	147.52	156.28
3	42.05	46.3	137.20	149.09	209.78	239.12
4	48.17	53.37	170.240	191.02	269.69	311.23
Average	43.58	46.02	143.70	151.25	238.97	235.75
Standard deviation	5.02	6.63	31.44	33.15	77.98	63.31
P		.17		.34		.92

Note:—Pre indicates pretreatment; post, posttreatment.

Complications

There were no intraprocedural or periprocedural complications associated with the use of the dual-sensor guidewire. No vascular injury, thromboembolic event, or new neurologic deficit was observed in any patient.

Computational Modeling

Modeling of WSS and WSSG is shown for each patient in Fig 1. Colorized maps of the top row of each panel demonstrate pretreatment conditions, the middle row shows posttreatment, and the bottom row shows the effect of treatment, as calculated by the difference between pretreatment and posttreatment. In patient 1, after flow diversion and partial coiling, both WSS and WSSG were reduced at the aneurysm neck and impact area of the wall opposite the inflow zone (Fig 1A). In patient 2, the sidewall aneurysm demonstrated similar findings of WSS and WSSG reduction in the neck and impact area, with corresponding increase in the downstream parent vessel (Fig 1B). Modeling of patient 3, with a more spherical aneurysm, showed reduction in WSS in nearly the entirety of the aneurysm dome and neck and a slight increase in WSSG in the neck midpoint (Fig 1C). WSS and WSSG were reduced in the small sidewall aneurysm of patient 4, with increases in these parameters in the surrounding parent vessel (Fig 1D).

The wire-based CFD calculations of the effects of flow-diverting stent treatment on intra-aneurysmal hemodynamics are shown in Table 2. Reduction of all parameters was observed in all patients, with significant decreases in WSS and peak-systolic WSSG and trends in reduced blood flow ($P = .07$) and cardiac cycle-averaged WSSG ($P = .06$). Simulated pressure drops across the entire CFD model are shown in On-line Table 2. The average and peak-systolic change in pressure drop after treatment were -0.09 ± 0.26 mm Hg and -0.85 ± 2.08 mm Hg, respectively. The differences were not significant ($P = .55$ and $.47$).

DISCUSSION

We have successfully incorporated patient-specific measurements of blood flow velocity and blood pressure into CFD modeling of unruptured cerebral aneurysms before and after treatment with flow-diverting stents. The method of applying patient-specific boundary conditions to CFD modeling and quantifying the effects of flow-diverting stents on aneurysmal hemodynamics has not been previously reported. This method may improve the ability of CFD to determine hemodynamic factors associated with treatment, including aneurysm occlusion, persistent patency, or delayed hemorrhagic complications.

The premise of aneurysmal flow diversion is the reduction of blood flow into the aneurysm dome, promoting intra-aneurysmal thrombosis and promoting endothelialization of the stent wall, which reconstructs the parent vessel excluding the aneurysm. Reduction of hemodynamic stress is thought to be crucial in achieving this goal, and the determination of such stress is a key application of CFD analysis.¹⁴ We observed a reduction of flow rate, WSS, and WSSG in the aneurysmal domes. Previous reports of CFD modeling for aneurysmal flow diversion have shown similar reductions in intra-aneurysmal velocity and WSS, though WSSG has not been consistently described.^{2,14,17} We also observed a (nonsignificant) increase in blood flow in the parent vessel after treatment, possibly the result of the exclusionary effect of flow diversion on aneurysmal blood capacitance.

Increased pressure within the aneurysm dome has been suggested as a possible mechanism for delayed aneurysm rupture after flow-diverting stent treatment. However, in the current study, blood pressure measurements in peri-aneurysmal locations did not change substantially after aneurysm treatment, nor did simulated pressure drops. This is in contrast to a previous CFD report of large pressure drops¹⁶ and increased mural tension¹⁷ after flow diversion but similar to previous CFD^{26,27} and in vivo²⁸ intra-aneurysmal pressure measurements that did not demonstrate changes after flow-diverting stent treatment. Although we did not measure pressure within the aneurysm lumen directly, it is unlikely that a substantial intraluminal increase occurred in the face of such small pressure drops, especially considering the lack of preaneurysmal stenosis in the aneurysms we studied.

Average peak inflow velocity in the petrous carotid artery pretreatment and posttreatment was 43.58 cm/s and 46.02 cm/s, respectively, with a mean flow rate of 143.70 mL/min. Studies of sonography²⁹ and phase-contrast MRA (pcMRA)³⁰ velocities of healthy volunteers showed average flow rates of 234 and 277 mL/min, respectively. The use of idealized assumptions of blood flow velocity and blood pressure (rather than patient-specific measurements) as boundary conditions would have significantly affected the results of our hemodynamic calculations.^{18,31,32} The origin of our lower flow rate values is unclear; however, healthy volunteers in studies of reference velocity were younger than our patients (average age, 28 ± 7 years). Age is inversely correlated to the measured flow rate in the cerebral vasculature in some studies³³ but not in others.³⁴ However, we are confident that our direct physiologic measurements with the use of the dual-sensor guidewire were accurate when measuring such parameters in vivo, as shown in animal studies comparing such measurements with direct measurements of blood flow.²⁴

Efforts to improve the accuracy of CFD for better applicability to an individual patient's treatment have led to the incorporation of patient-specific blood flow measurements derived from trans-

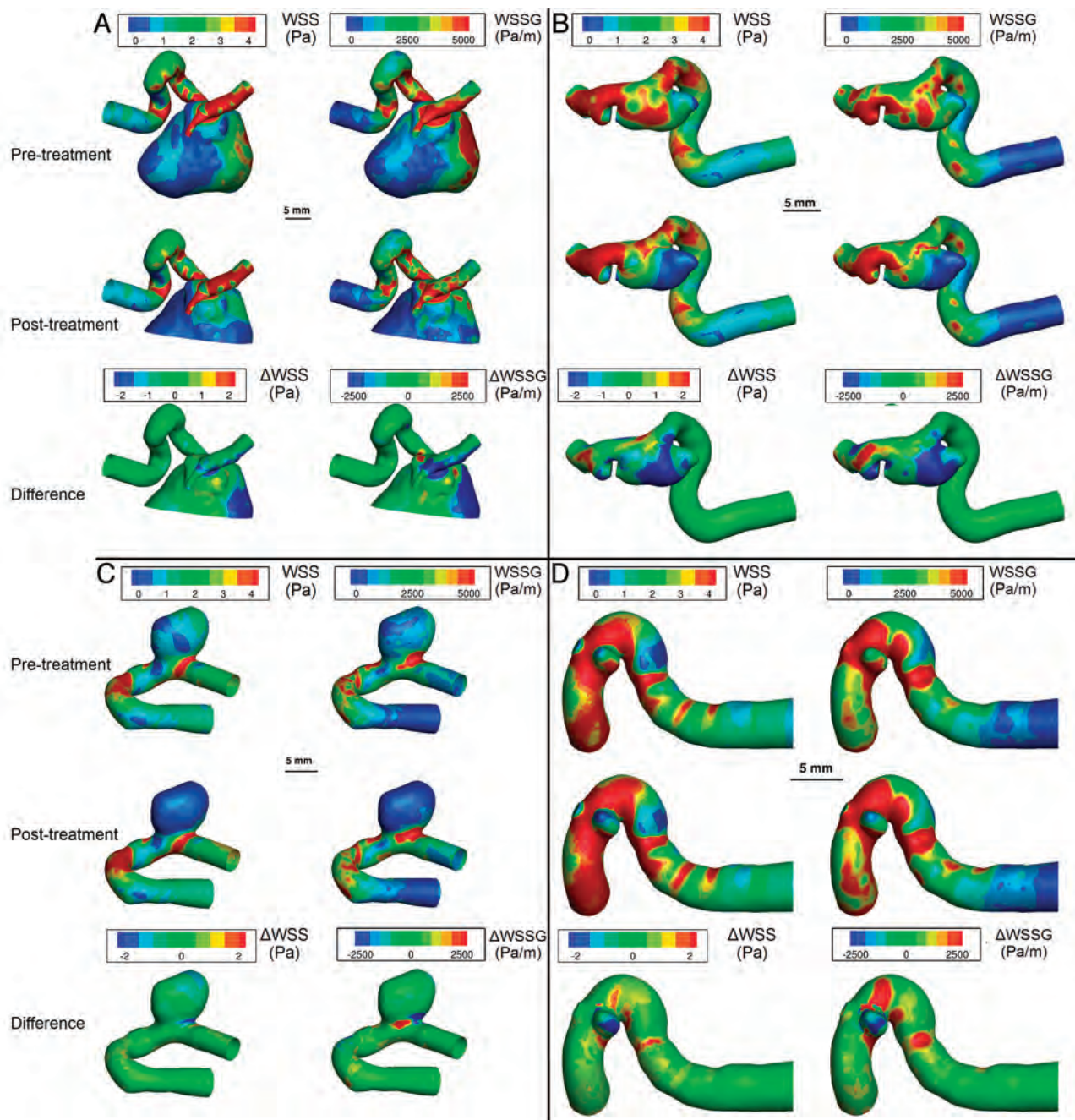


FIG 1. Computational models of 4 aneurysms (A–D) integrating patient-specific dual-sensor guidewire measurements of blood flow velocity and pressure. Wall shear stress and wall shear stress gradient are shown before and after treatment (top and middle rows, respectively). The difference (bottom row) represents the effect of treatment on WSS (Δ WSS) and WSSG (Δ WSSG).

Table 2: Computational model-based calculations of intra-aneurysmal hemodynamics before and after flow-diversion treatment with the use of patient-specific boundary conditions from the dual-sensor guidewire

Measure		Pretreatment	Posttreatment	% Change	P
Blood flow, mL/min	Time-averaged	81.36	51.38	−39.33%	.07
	Peak systolic	123.25	88.28	−28.84%	.07
WSS, Pa	Time-averaged	1.99	0.92	−56.77%	.03
	Peak systolic	3.92	2.20	−51.89%	.01
WSSG, Pa/m	Time-averaged	2807.95	1730.70	−43.38%	.06
	Peak systolic	6261.35	4236.05	−42.93%	.04

cranial Doppler ultrasonography (TCD)^{35,36} or pcMRA^{37–39} as input conditions. Acquiring flow rates by use of TCD is fast and noninvasive but may not be accurate in the vertebrobasilar sys-

tem⁴⁰ or in small-caliber vessels or in those near the skull base⁴¹ and cannot be obtained in up to 16% of patients lacking adequate temporal bone windows.⁴² When compared with TCD⁴³ and tra-

ditional CFD,⁴⁴ flow rates acquired with pcMRA have a lower temporal resolution and may underestimate peak velocity by up to 30%, especially in smaller-diameter vessels.⁴⁴ This degree of error may substantially influence WSS results.^{18,44} Additionally, pcMRA velocity data must be acquired outside of the angiographic workflow, are both time-consuming and expensive to acquire, and require transport that may be dangerous in critically ill patients.⁴⁵ These disadvantages reduce the utility of pcMRA- and TCD-derived flow velocities.

The dual-sensor guidewire has several advantages over the above techniques in acquiring patient-specific measurements. Unlike TCD, it can be used in a highly anatomically specific manner in any major blood vessel, including in the vertebrobasilar system, and does not require temporal bone windows. Advantages over pcMRA include the real-time integration of blood flow velocity measurements during angiography, without transport to and from MR imaging. In addition, a previous report of direct comparison between blood flow velocity measured by pcMRA and the dual-sensor guidewire showed that pcMRA underestimated peak systolic velocity, which could alter CFD-derived hemodynamic calculations.²³ Finally, neither TCD nor pcMRA acquire blood pressure measurements, whereas the dual-sensor nature of the guidewire allows additional integration of this physiologic parameter into CFD modeling. To our knowledge, the incorporation of pressure change data into boundary condition calculations for aneurysmal CFD modeling has not been previously reported. Application of this technique in follow-up studies may help to determine hemodynamic factors responsible for success or failure of flow-diverting stent treatment.

This study has several limitations. First, a small number of patients were studied with variable aneurysmal size and morphology, reducing the study's generalizability (though aneurysm location, vessel diameter, measured velocity, and waveform morphology were similar among all 4 studied patients). Second, although we attempted to recreate the exact location of the dual-sensor guidewire in pretreatment and posttreatment conditions, small variations in the location or angle of the wire may have influenced blood pressure and velocity measurements. Third, the position of the virtual stent in posttreatment CFD and the CFD-derived velocities may not precisely match their in vivo locations. These localization errors were minimized by use of multiple-projection radiographs and 3D volumes to plan virtual wire and stent placement. Fourth, changes in patient systemic hemodynamic status over the course of treatment may have influenced velocity and pressure measurements through the variance of systemic blood pressure, temperature, and end-tidal CO₂. Fifth, subtle changes in stent porosity caused by deformity in curved cerebral vessels was not incorporated into CFD simulations.¹⁵ Finally, though the wire was manipulated in an attempt to measure the most robust velocity signal, it is possible that the measured blood flow velocity was not perfectly aligned within the center of the vessel, resulting in slight underestimations or error in these measurements.⁴⁶

CONCLUSIONS

We have successfully incorporated dual-sensor guidewire measurements of blood pressure and blood flow velocity into patient-specific CFD analyses of unruptured cerebral aneurysms before

and after flow-diverting stent treatment. In accordance with the therapeutic intent of flow-diverting stents, significant intra-aneurysmal reductions in WSS and WSSG and a trend in reduced blood flow were observed after treatment.

ICMJE Disclosures: Michael Levitt—*RELATED: Grant:* 1) National Institutes of Health/National Institute of Neurological Disease and Stroke,* 2) Volcano Corporation.* *Comments:* 1) In the form of grant 1R03NS078539 (Co-investigator), 2) In the form of an unrestricted grant without influence on study design, data collection or interpretation, or manuscript editing (Co-investigator); *OTHER RELATIONSHIPS:* This study was supported by the manufacturer of the dual-sensor Doppler guidewire (Volcano Corporation) through a grant made to the Departments of Neurological Surgery and Radiology, University of Washington. The sponsor was shown the final manuscript but had no role in the study design, data collection, data analyses or interpretation. Patrick McGah—*RELATED: Grant:* NIH-NINDS.* *Comments:* R03 grant to support the research. Alberto Aliseda—*RELATED: Grant:* National Institutes of Health.* *Comments:* R03 from NINDS. Sandeep Vaidya—*RELATED: Grant:* Volcano.* Basavaraj Ghodke—*RELATED:* 1) NIH/NINDS.* 2) Volcano Corporation.* *Comments:* 1) Institutional grant 1R03NS078539 (co-investigator) and 2) Clinical study idea (co-principle investigator); *UNRELATED: Other:* Covidien/ev3, *Comments:* Proctor, under \$5000; *OTHER RELATIONSHIPS:* This study was supported by the manufacturer of the dual-sensor Doppler guidewire (Volcano Corporation) through a grant made to the departments of Neurological Surgery and Radiology, University of Washington. The sponsor was shown the final manuscript but had no role in the study design, data collection, data analyses or interpretation. Louis Kim—*RELATED: Grant:* NIH R03 grant,* Mark Robison private donation grant.* *Comments:* I am PI on this NIH grant that primarily funded the work in this report. I received a private sector donation from Mark Robison explicitly used for cerebrovascular research. These funds partly funded equipment costs for this study; *Other:* Volcano Inc research grant.* *Comments:* I am co-PI of this privately funded grant that contributed to equipment and personnel costs; *UNRELATED: Consultancy:* Aesculap, *Comments:* Consultant neurosurgeon for this medical device company; *Grants/Grants Pending:* Department of Defense grant on surgical robotics*; *Stock/Stock Options:* Spi Surgical, *Comments:* Early-stage surgical robotics company, co-founder and shareholder (*money paid to institution).

REFERENCES

1. Lylyk P, Miranda C, Ceratto R, et al. **Curative endovascular reconstruction of cerebral aneurysms with the Pipeline embolization device: the Buenos Aires experience.** *Neurosurgery* 2009;64:632–42
2. Zhang Y, Chong W, Qian Y. **Investigation of intracranial aneurysm hemodynamics following flow diverter stent treatment.** *Med Eng Phys* 2013;35:608–15
3. McAuliffe W, Wycoco V, Rice H, et al. **Immediate and midterm results following treatment of unruptured intracranial aneurysms with the Pipeline embolization device.** *AJNR Am J Neuroradiol* 2012;33:164–70
4. O'Kelly CJ, Spears J, Chow M, et al. **Canadian experience with the Pipeline embolization device for repair of unruptured intracranial aneurysms.** *AJNR Am J Neuroradiol* 2013;34:381–87
5. Piano M, Valvassori L, Quilici L, et al. **Midterm and long-term follow-up of cerebral aneurysms treated with flow diverter devices: a single-center experience.** *J Neurosurg* 2013;118:408–16
6. Yu SC, Kwok CK, Cheng PW, et al. **Intracranial aneurysms: midterm outcome of Pipeline embolization device: a prospective study in 143 patients with 178 aneurysms.** *Radiology* 2012;265:893–901
7. Hampton T, Walsh D, Tolia C, et al. **Mural destabilization after aneurysm treatment with a flow-diverting device: a report of two cases.** *J Neurointerv Surg* 2011;3:167–71
8. Velat GJ, Fargen KM, Lawson MF, et al. **Delayed intraparenchymal hemorrhage following Pipeline embolization device treatment for a giant recanalized ophthalmic aneurysm.** *J Neurointerv Surg* 2012; 4:e24
9. Kulcsar Z, Houdart E, Bonafe A, et al. **Intra-aneurysmal thrombosis as a possible cause of delayed aneurysm rupture after flow-diversion treatment.** *AJNR Am J Neuroradiol* 2011;32:20–25
10. Shojima M, Oshima M, Takagi K, et al. **Magnitude and role of wall shear stress on cerebral aneurysm: computational fluid dynamic study of 20 middle cerebral artery aneurysms.** *Stroke* 2004; 35:2500–05

11. Miura Y, Ishida F, Umeda Y, et al. **Low wall shear stress is independently associated with the rupture status of middle cerebral artery aneurysms.** *Stroke* 2013;44:519–21
12. Meng H, Wang Z, Hoi Y, et al. **Complex hemodynamics at the apex of an arterial bifurcation induces vascular remodeling resembling cerebral aneurysm initiation.** *Stroke* 2007;38:1924–31
13. Li C, Wang S, Chen J, et al. **Influence of hemodynamics on recanalization of totally occluded intracranial aneurysms: a patient-specific computational fluid dynamic simulation study.** *J Neurosurg* 2012;117:276–83
14. Kulcsar Z, Augsburger L, Reymond P, et al. **Flow diversion treatment: intra-aneurysmal blood flow velocity and WSS reduction are parameters to predict aneurysm thrombosis.** *Acta Neurochir (Wien)* 2012;154:1827–34
15. Mut F, Cebal JR. **Effects of flow-diverting device oversizing on hemodynamics alteration in cerebral aneurysms.** *AJNR Am J Neuroradiol* 2012;33:2010–16
16. Cebal JR, Mut F, Raschi M, et al. **Aneurysm rupture following treatment with flow-diverting stents: computational hemodynamics analysis of treatment.** *AJNR Am J Neuroradiol* 2011;32:27–33
17. Hassan T, Ahmed YM, Hassan AA. **The adverse effects of flow-diverter stent-like devices on the flow pattern of saccular intracranial aneurysm models: computational fluid dynamics study.** *Acta Neurochir (Wien)* 2011;153:1633–40
18. Venugopal P, Valentino D, Schmitt H, et al. **Sensitivity of patient-specific numerical simulation of cerebral aneurysm hemodynamics to inflow boundary conditions.** *J Neurosurg* 2007;106:1051–60
19. Marzo A, Singh P, Larrabide I, et al. **Computational hemodynamics in cerebral aneurysms: the effects of modeled versus measured boundary conditions.** *Ann Biomed Eng* 2011;39:884–96
20. Levitt MR, Cooke DL, Ghodke BV, et al. **“Stent view” flat-detector CT and stent-assisted treatment strategies for complex intracranial aneurysms.** *World Neurosurg* 2011;75:275–78
21. Bach RG, Kern MJ. **Practical coronary physiology: clinical application of the Doppler flow velocity guide wire.** *Cardiol Clin* 1997;15:77–99
22. Ferns SP, Schneiders JJ, Siebes M, et al. **Intracranial blood-flow velocity and pressure measurements using an intra-arterial dual-sensor guidewire.** *AJNR Am J Neuroradiol* 2010;31:324–26
23. Schneiders JJ, Ferns SP, van Ooij P, et al. **Comparison of phase-contrast MR imaging and endovascular sonography for intracranial blood flow velocity measurements.** *AJNR Am J Neuroradiol* 2012;33:1786–90
24. Chaloupka JC, Viñuela F, Kimme-Smith C, et al. **Use of a Doppler guide wire for intravascular blood flow measurements: a validation study for potential neurologic endovascular applications.** *AJNR Am J Neuroradiol* 1994;15:509–17
25. Augsburger L, Reymond P, Rufenacht DA, et al. **Intracranial stents being modeled as a porous medium: flow simulation in stented cerebral aneurysms.** *Ann Biomed Eng* 2011;39:850–63
26. Larrabide I, Aguilar ML, Morales HG, et al. **Intra-aneurysmal pressure and flow changes induced by flow diverters: relation to aneurysm size and shape.** *AJNR Am J Neuroradiol* 2013;34:816–22
27. Shobayashi Y, Tateshima S, Kakizaki R, et al. **Intra-aneurysmal hemodynamic alterations by a self-expandable intracranial stent and flow diversion stent: high intra-aneurysmal pressure remains regardless of flow velocity reduction.** *J Neurointerv Surg* 2013; 5 Suppl 3:iii38–42
28. Schneiders JJ, Vanbavel E, Majoie CB, et al. **A flow-diverting stent is not a pressure-diverting stent.** *AJNR Am J Neuroradiol* 2013;34:E1–4
29. Reymond P, Bohraus Y, Perren F, et al. **Validation of a patient-specific one-dimensional model of the systemic arterial tree.** *Am J Physiol Heart Circ Physiol* 2011;301:H1173–82
30. Ford MD, Alperin N, Lee SH, et al. **Characterization of volumetric flow rate waveforms in the normal internal carotid and vertebral arteries.** *Physiol Meas* 2005;26:477–88
31. Karmonik C, Yen C, Grossman RG, et al. **Intra-aneurysmal flow patterns and wall shear stresses calculated with computational flow dynamics in an anterior communicating artery aneurysm depend on knowledge of patient-specific inflow rates.** *Acta Neurochir (Wien)* 2009;151:479–85
32. Karmonik C, Yen C, Diaz O, et al. **Temporal variations of wall shear stress parameters in intracranial aneurysms—importance of patient-specific inflow waveforms for CFD calculations.** *Acta Neurochir (Wien)* 2010;152:1391–98
33. Melamed E, Lavy S, Bentin S, et al. **Reduction in regional cerebral blood flow during normal aging in man.** *Stroke* 1980;11:31–35
34. Hoi Y, Wasserman BA, Xie YJ, et al. **Characterization of volumetric flow rate waveforms at the carotid bifurcations of older adults.** *Physiol Meas* 2010;31:291–302
35. Hassan T, Ezura M, Timofeev EV, et al. **Computational simulation of therapeutic parent artery occlusion to treat giant vertebrobasilar aneurysm.** *AJNR Am J Neuroradiol* 2004;25:63–68
36. Sun Q, Groth A, Aach T. **Comprehensive validation of computational fluid dynamics simulations of in-vivo blood flow in patient-specific cerebral aneurysms.** *Med Phys* 2012;39:742–54
37. Jou LD, Quick CM, Young WL, et al. **Computational approach to quantifying hemodynamic forces in giant cerebral aneurysms.** *AJNR Am J Neuroradiol* 2003;24:1804–10
38. Bousset L, Rayz V, Martin A, et al. **Phase-contrast magnetic resonance imaging measurements in intracranial aneurysms in vivo of flow patterns, velocity fields, and wall shear stress: comparison with computational fluid dynamics.** *Magn Reson Med* 2009; 61:409–17
39. Rayz VL, Bousset L, Acevedo-Bolton G, et al. **Numerical simulations of flow in cerebral aneurysms: comparison of CFD results and in vivo MRI measurements.** *J Biomech Eng* 2008;130:051011
40. Sviri GE, Ghodke B, Britz GW, et al. **Transcranial Doppler grading criteria for basilar artery vasospasm.** *Neurosurgery* 2006;59:360–66
41. Turner CL, Higgins JN, Kirkpatrick PJ. **Assessment of transcranial color-coded duplex sonography for the surveillance of intracranial aneurysms treated with Guglielmi detachable coils.** *Neurosurgery* 2003;53:866–71
42. Ackerstaff RG, Suttorp MJ, van den Berg JC, et al. **Prediction of early cerebral outcome by transcranial Doppler monitoring in carotid bifurcation angioplasty and stenting.** *J Vasc Surg* 2005;41:618–24
43. Chang W, Landgraf B, Johnson KM, et al. **Velocity measurements in the middle cerebral arteries of healthy volunteers using 3D radial phase-contrast HYPRFlow: comparison with transcranial Doppler sonography and 2D phase-contrast MR imaging.** *AJNR Am J Neuroradiol* 2011;32:54–59
44. Cebal JR, Putman CM, Alley MT, et al. **Hemodynamics in normal cerebral arteries: qualitative comparison of 4D phase-contrast magnetic resonance and image-based computational fluid dynamics.** *J Eng Math* 2009;64:367–78
45. Waydhas C. **Intrahospital transport of critically ill patients.** *Crit Care* 1999;3:R83–89
46. Mynard JP, Wasserman BA, Steinman DA. **Errors in the estimation of wall shear stress by maximum Doppler velocity.** *Atherosclerosis* 2013;227:259–66

Potential for the Use of the Solitaire Stent for Recanalization of Middle Cerebral Artery Occlusion without a Susceptibility Vessel Sign

Y.J. Bae, C. Jung, J.H. Kim, B.S. Choi, E. Kim, M.-K. Han, H.-J. Bae, and M.H. Han

ABSTRACT

BACKGROUND AND PURPOSE: Absence of the MCA susceptibility vessel sign (negative MCA susceptibility vessel sign) on gradient recalled-echo MR imaging in acute stroke is commonly associated with in situ stenosis and thrombotic occlusion. We evaluated the effectiveness and safety of the Solitaire stent as the first-line device for the recanalization of MCA occlusion with a negative MCA susceptibility vessel sign.

MATERIALS AND METHODS: Thirty-eight consecutive patients presenting with acute ischemic stroke due to MCA occlusion were treated by using the Solitaire AB stent alone or combined with thrombolytic drugs. Among these patients, 11 (7 men and 4 women; median age, 70 years; range, 49–89 years) who underwent multimodal stroke MR imaging before the endovascular procedure and had no MCA susceptibility vessel sign on the initial gradient recalled-echo MR imaging were included in this study. The primary end point was the recanalization of the occluded artery evaluated by the arterial occlusive lesion score. Clinical outcome was assessed at discharge and 90 days, as was the degree of residual MCA stenosis or reocclusion.

RESULTS: Successful recanalization (arterial occlusive lesion score \geq II) without balloon angioplasty was obtained in 9 patients (81.8%). Six patients (54.5%) had an mRS score of \leq 2 at 90 days. After a median of 147 days, no patient showed reocclusion on follow-up imaging. There were no symptomatic intracerebral hemorrhages.

CONCLUSIONS: The Solitaire stent is a feasible tool as the first-line device for multimodal endovascular recanalization therapy in acute ischemic stroke with a negative MCA susceptibility vessel sign. It has a good rate of successful and complete recanalization and is a fast yet safe procedure.

ABBREVIATIONS: GRE = gradient recalled-echo; SVS = susceptibility vessel sign

The Solitaire stent (Covidien/ev3, Irvine, California) was initially developed as a device for assisting coil embolization of intracranial aneurysms.^{1–3} However, its ability to be completely and safely retrieved after full deployment allows it to be used as a device for mechanical thrombectomy in patients with acute thromboembolic stroke. Many reputable studies have shown that entrapping and extracting the thromboembolus by using the Solitaire stent is fast and effective in vascular recanalization, espe-

cially when treating large arterial occlusions, including MCA occlusion.^{4–8}

Thromboembolus in the MCA is known to create the MCA susceptibility vessel sign (SVS) on gradient recalled-echo (GRE) MR imaging.^{9,10} This sign results from a T2-shortening effect of intracellular deoxyhemoglobin in the acute stage of a red blood cell clot.⁹ Thus, the MCA SVS is more commonly seen in red blood cell–dominant and mixed clots and can reflect the clot composition.^{9,11,12} Cho et al¹² also showed that the SVS on GRE MR imaging was more commonly associated with cardioembolic stroke (77.5%) than other stroke subtypes (25.5%, $P < .001$). They suggested that the relatively greater thrombus burden in a cardioembolism may increase the conspicuity of SVS, so the SVS could be more frequently observed in cardioembolic stroke.

In contrast to the presence of the SVS, its absence is generally associated with a small amount of thrombus; fibrin-rich thrombus, a potential target for chemical thrombolysis; or an in situ steno-occlusive lesion, which could be an indication for angio-

Received November 7, 2012; accepted after revision February 1, 2013.

From the Departments of Radiology (Y.J.B., C.J., J.H.K., B.S.C., E.K.) and Neurology (M.-K.H., H.-J.B.), Seoul National University Bundang Hospital, Gyeonggi-do, Republic of Korea; and Department of Radiology and Institute of Radiation Medicine (M.H.H.), Seoul National University College of Medicine, Seoul, Korea.

Paper previously presented at: 68th Korean Congress of Radiology, October 18–20, 2012; Seoul, Republic of Korea.

Please address correspondence to Cheolkyu Jung, MD, Department of Radiology, Seoul National University Bundang Hospital, 300, Gumi-dong, Bundang-gu, Seongnam-si, Gyeonggi-do, 463-787, Republic of Korea; e-mail: cheolkyu.jung.ni@gmail.com

<http://dx.doi.org/10.3174/ajnr.A3562>

plasty.^{11,12} Consequently, we can assume that mechanical thrombectomy by using the Solitaire stent could be less effective in acute ischemic stroke with a negative MCA SVS, which could represent an in situ steno-occlusive lesion. To our knowledge, there has been no report demonstrating the effectiveness of the Solitaire stent in acute ischemic stroke with a negative MCA SVS. The purpose of our study was to evaluate the effectiveness and safety of mechanical thrombectomy by using the Solitaire stent in acute ischemic stroke with a negative MCA SVS.

MATERIALS AND METHODS

The institutional review board approved this retrospective study protocol and waived informed consent.

Patients

In our institution from September 2010 to March 2012, thirty-eight consecutive patients (21 men and 17 women; median age, 70 years; range, 49–89 years) presenting with acute ischemic stroke from an MCA occlusion were treated by using the Solitaire AB stent alone or combined with thrombolytic drugs. Among them, the patients who underwent multimodal MR imaging before the endovascular procedure and who had no MCA SVS on initial GRE MR imaging were included in our study.

The patients were divided into 3 different categories according to the interval change in their neurologic symptoms: “Fluctuating” symptoms indicated neurologic deficits that waxed and waned, “progressive” symptoms were defined as neurologic deficits that got worse as time passed, and “stable” symptoms referred to neurologic deficits that were maintained before the endovascular procedure.

Stroke MR Imaging Protocol and Analysis

MR imaging was performed by using a 1.5T or 3T unit (Gyrosan Intera; Philips, Best, the Netherlands) with a sensitivity encoding head coil. Patients underwent MR imaging by using the following routine stroke protocol in our institution before the endovascular procedure: DWI, TOF 3D angiography of the extracranial and intracranial arteries, GRE T2*-weighted imaging, MR perfusion, and gadolinium-enhanced T1- and T2-weighted FLAIR imaging. An average of 20 minutes was required for each routine stroke protocol MR imaging.

Acquisition parameters for GRE T2*-weighted images were set as follows: TR, 750–800 ms; TE, 10–15 msec; section thickness, 5 mm; intersection gap, 1 mm; FOV, 250 × 250 mm; flip angle, 20°.

All images were reviewed by 2 experienced neuroradiologists (B.S.C. and J.H.K.) who had 5 and 20 years of experience, respectively. If any discrepancy arose, the 2 readers analyzed images in consensus. First, the presence of the MCA SVS, defined as a hypointense signal change within the MCA with the diameter exceeding that of the contralateral vessel, was assessed on GRE MR imaging.⁹ The patients who had the MCA SVS were excluded from our study. Second, DWI-ASPECTS was estimated by the method of Barber et al.¹³

Procedural Techniques

All procedures were performed on a biplanar system (Integrus Allura 12/12; Philips) by a single neurointerventionalist. Initial

diagnostic cerebral angiography was performed via the transfemoral approach to identify the occluded MCA segment and to assess the collateral degree.

The proximal occluded segment of the MCA was defined on conventional angiography.^{14,15} The MCA trunk (M1) extends from the ICA bifurcation to the MCA trunk before secondary division. The MCA branches (M2) start from the secondary division. They course upward and over the insula and end at the top of the Sylvian fissure where they reach the apex of the circular sulcus. The MCA distal branches (M3 and M4) begin at the top of the circular sulcus and end at the surface of the lateral end of the Sylvian fissure.

A 6F balloon-guided catheter (Cello; Covidien/ev3 Neurovascular, Irvine, California; or Optimo; Tokai Medical Products, Aichi, Japan) was placed in the proximal cervical ICA. Then, a microcatheter (Prowler Select Plus; Codman Neurovascular, Miami Lakes, Florida; or Rebar 27; ev3) was advanced in the occluded vessel and navigated distal to the clot. Following this procedure, the Solitaire AB stent was advanced and deployed from a few millimeters distal to the clot. After immediate flow restoration was confirmed, the stent was kept deployed for approximately 3–10 minutes to ensure the entrapment of the clot. Afterward, the balloon guide was inflated and the microcatheter and stent were withdrawn gently, under the application of negative suction pressure, through the guiding catheter to prevent distal migration of the clot while retrieving the guide and microcatheter. When thrombectomy by using the Solitaire stent failed or partial recanalization was achieved, an intra-arterial thrombolytic agent (urokinase) was injected inside the clot. Intra-arterial and/or intravenous Aggrastat was infused during the procedure in selected patients who were without high risk of intracranial hemorrhage. The patients who had been under medication with anticoagulants or antithrombotics were not selected. Postprocedural cerebral angiography was performed to assess the recanalization status after the whole procedure.

Outcome Assessment

The degree of recanalization of the occluded MCA segment was evaluated with the arterial occlusive lesion score suggested by Khatri et al.¹⁶ Successful recanalization was defined as an arterial occlusive lesion score \geq II, and complete recanalization, as an arterial occlusive lesion score of III.

On admission, clinical outcomes were assessed by 2 experienced neurologists (M.K.-H. and H.-J.B.) and their faculty. The mRS score for evaluation of the functional independence level was also recorded at discharge and 90 days after the procedure. A good clinical outcome was defined as an mRS score \leq 2 at discharge or at 90 days. On the patient's follow-up TOF MRA or CTA, the degree of residual MCA stenosis was determined. The degree of residual stenosis was graded according to the stenosis diameter as follows: normal (0%), mild (<50%), moderate (50%–69%), severe (\geq 70%), and occlusion (no visualization of the MCA segment distal to the occlusion).¹⁷

Complications associated with the procedure were also assessed. The major adverse events were the following: 1) device-associated complications, including arterial dissection, vessel perforation, or distal embolization; 2) procedural reocclusion of the

Table 1: Patient characteristics and procedural outcome

Case	Sex	Age (yr)	Side	Occluded Artery	Tandem Stenosis	Other Extra- or Intracranial				Onset to Recan.			FU Artery Status		
						Atherosclerosis ^a	IV rt-PA	Add-On Methods	UK × 10 ³	Tirofiban	AOL Score	Puncture (hr)	Time (min)	First FU (period)	Last FU (period)
1	F	89	R	Branch	Yes	Yes	Yes	IAT	140	IA	II	3.6	103	Moderate (1 day)	Moderate (4 mo)
2	M	49	L	Branch	No	Yes	Yes	IAT	0	IA + IV	III	50	11	Severe (1 day)	Severe (12 mo)
3	F	85	L	Trunk	No	Yes	No	IAT	80	IA	III	17.5	38	Severe (1 day)	Severe (5 days)
4	M	59	L	Trunk	Yes	Yes	Yes	None	0	None	0	15.2	NA	Occlusion (6 days)	Moderate (5 mo)
5	M	53	R	Trunk	No	No	No	None	0	None	III	12	25	Mild (2 days)	Mild (3 mo)
6	F	73	R	Trunk	No	Yes	No	IAT	80	None	II	14	45	Moderate (1 day)	Severe (7 mo)
7	M	49	R	Trunk	No	No	No	IAT	80	None	I	6.2	NA	Occlusion (5 days)	NA
8	M	73	R	Trunk	No	Yes	No	None	0	None	III	9.1	27	NA	NA
9	M	56	R	Trunk	No	Yes	No	IAT, balloon	60	IV	III	14.8	87	Severe (1 day)	Mild (4 days)
10	F	76	L	Trunk	No	No	No	None	0	None	II	21.7	42	Severe (4 days)	NA
11	M	70	R	Trunk	No	Yes	No	None	0	None	III	11	31	Severe (4 days)	NA

Note:—R indicates right; L, left; IAT, intra-arterial chemical thrombolysis; balloon, balloon angioplasty; IA, intra-arterial; UK, urokinase; AOL, arterial occlusive lesion; Recan. Time, time from puncture to recanalization; NA, not applicable; FU, follow-up.

^aThe presence of multifocal atherosclerosis at extra- or intracranial arteries.

intracranial artery; 3) symptomatic intracranial hemorrhage; and 4) death. Symptomatic intracranial hemorrhage was any hemorrhage demonstrated on the follow-up imaging leading to an interval decrease in the NIHSS score ≥ 4 from baseline or the lowest NIHSS score between admission and 7 days or to death.^{18,19}

Statistical Analysis

Continuous variables were expressed as the median value and range. Categorical variables were expressed as frequency by using percentages.

RESULTS

Of 38 patients with MCA occlusion, 11 (28.9%) (7 men and 4 women; median age, 70 years; range, 49–89 years) were confirmed as having a negative MCA SVS. Among them, 5 (45.5%) showed the onset of fluctuating symptoms, 3 (27.3%) had progressive symptoms, and the remainder (27.3%) had stable symptoms. The median DWI-ASPECTS calculated on the basis of initial MR imaging was 8 (range, 5–9).

All 11 patients had complete occlusion of 1 MCA segment on initial angiography. Nine of 11 patients (81.8%) were confirmed to have an occlusion at the M1 segments. The remaining 2 patients (18.2%) had occluded M2 segments. Tandem stenosis was noted in 2 patients (18.2%): One patient had a left M1 occlusion with mild stenosis of the left proximal cervical ICA, and the other patient had a right M2 occlusion with mild stenosis of the right proximal cervical ICA.

Before the procedure, 2 of 11 patients (18.2%) underwent intravenous thrombolysis with rtPA. The median time from symptom onset to puncture was 14 hours (range, 3.6–50.0 hours). As an add-on method, intra-arterial thrombolysis with urokinase was performed in 6 patients (54.5%). One patient

(9.1%) underwent additional balloon angioplasty for the occluded segment. Systemic or intra-arterial infusion of tirofiban was used in 4 patients (36.4%) when the occluded artery was recanalized; 2 patients (18.2%) received intra-arterial tirofiban loading and 1 (9.1%) received intravenous loading. One patient (9.1%) underwent intra-arterial tirofiban loading followed by intravenous maintenance. The overall clinical and procedural characteristics of the patients are shown in Tables 1 and 2.

Procedural Outcome

Of 11 patients with negative MCA SVS, successful and complete recanalization was obtained in 9 (81.8%) and 6 patients (54.5%), respectively. Successful and complete recanalization without balloon angioplasty was achieved in 72.7% and 45.5%, respectively. After we excluded 2 patients with an arterial occlusive lesion score of 0 or I, the median time from puncture to recanalization was 38 minutes (range, 11–103 minutes).

Clinical Outcome

All patients were successfully followed for a median of 252 days (range, 113–547 days). Of 11 patients, 4 (36.4%) had an mRS ≤ 2 at discharge and 6 (54.5%) had an mRS ≤ 2 at 90 days.

Patient Follow-Up

The first follow-up CTA or MRA of patients with a negative MCA SVS was performed in 10 patients after a median of 1.5 days (range, 1–6 days) from arrival at the emergency department. The degree of residual MCA stenosis on the first follow-up imaging was mild in 1 patient (9.1%), moderate in 2 (18.2%), severe in 5 (45.5%), and occlusion in 2 (18.2%); all these features were pres-

Table 2: Patient clinical features and clinical outcomes

Case	Symptom Pattern	DWI ASPECTS			NIHSS		mRS	mRS at
		Baseline	HT	sHT	Baseline	Discharge	Discharge	90 Days
1	Fluctuating	8	No	No	20	10	4	4
2	Fluctuating	9	No	No	3	2	2	1
3	Fluctuating	7	No	No	17	4	4	3
4	Fluctuating	6	No	No	17	15	5	3
5	Progressive	5	Yes	No	6	1	1	1
6	Fluctuating	7	No	No	6	6	3	2
7	Progressive	8	No	No	7	8	4	3
8	Stable	6	No	No	15	7	4	4
9	Stable	8	No	No	15	2	1	1
10	Progressive	8	No	No	7	8	4	2
11	Stable	8	No	No	5	0	0	1

Note:—HT indicates hemorrhagic transformation; sHT, symptomatic hemorrhagic transformation.

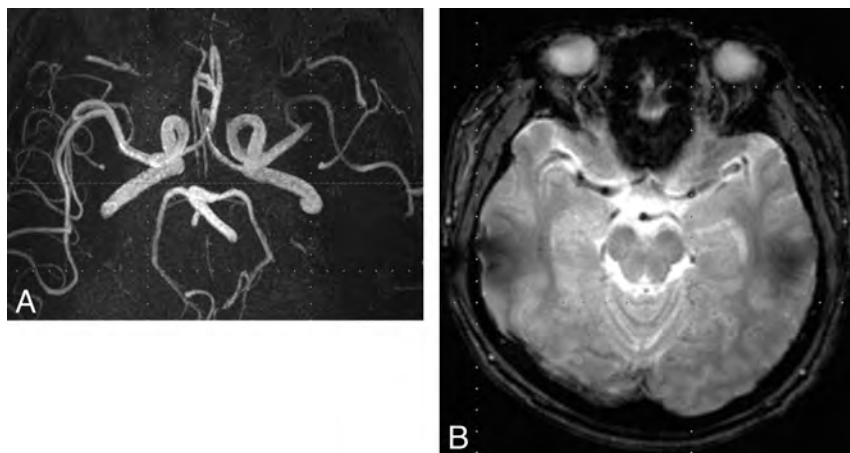


FIG 1. MR imaging in a 49-year-old man with acute ischemic stroke. A, MRA shows the occlusion of the superior division of the left MCA. B, On GRE MR imaging, the MCA SVS was absent.

on the initial baseline imaging. There was no case with reocclusion on the first follow-up imaging.

The second or last follow-up was after a median of 147 days (range, 25–367 days) in 7 of 11 patients (63.6%); 4 patients did not have available follow-up imaging after the initial one. On the final follow-up imaging, mild residual stenosis was shown in 2 patients (18.2%); moderate, in 2 patients (18.2%); and severe, in another 3 patients (27.3%). None of the cases showed reocclusion on the final follow-up imaging or symptom recurrence.

In 1 of 11 patients (9.1%) (case 5) with right M1 occlusion, focal hemorrhage in the head portion of the right caudate nucleus was observed on the 3-hour follow-up CT after recanalization. However, no symptomatic hemorrhage was detected after the procedure. Procedural reocclusion occurred in 2 cases. Other than this, no complication, such as arterial dissection, vascular perforation, or distal embolism, developed in any patient. There was no procedure-related or other-cause mortality.

Representative Case

Case 2. A 49-year-old man visited the emergency department of our institution with fluctuating motor aphasia and dysarthria. Symptom onset time was 2 days before the hospital visit, and his initial NIHSS score was 3. The patient underwent MR imaging with a stroke protocol, and an occlusion of the left M2 segment of the MCA with multiple small infarctions in the left

basal ganglia and subcortical white matter was confirmed (Fig 1A). The DWI-ASPECTS was 9. No initial MCA SVS was demonstrated (Fig 1B).

Because his symptoms worsened to an NIHSS score of 13 immediately after the MR imaging, intravenous rtPA infusion was initiated, and endovascular recanalization therapy for the left M2 occlusion was performed. The occlusion of the left M2 segment was also confirmed by conventional angiography (Fig 2A). Immediate flow restoration of the occluded segment was achieved by temporary Solitaire stent deployment in the occluded segment for 5 minutes (Fig 2B). After the Solitaire stent was removed, in situ moderate stenosis of the occluded segment was identified by postprocedural angiography (Fig 2C). Therefore, an additional intra-arterial loading of 500 mcg of tirofiban was performed manually, followed by intravenous maintenance. Mechanical recanalization alone took approximately 11 minutes, and the entire intra-arterial thrombolysis procedure took approximately 38 minutes.

DISCUSSION

To date, the Solitaire stent has been known to be effective for flow restoration

in acute ischemic stroke, especially for mechanical thrombectomy in an acute occlusion of the large intracranial artery.^{4-8,20,21} However, it is unknown whether the Solitaire stent could be used as a thrombectomy device and could be effective in recanalizing an in situ steno-occlusive lesion. In this study, we performed multimodal endovascular recanalization therapy by using the Solitaire stent as a first-line device for 38 MCA occlusions, and 11 MCA occlusions (28.9%) were verified as not showing the MCA SVS on GRE MR imaging. The rate of negative MCA SVS was in accordance with a previous report.⁹ Among these 11 MCA occlusions with negative MCA SVS, successful recanalization without balloon angioplasty was achieved in 72.7% of the patients, with a median recanalization time of 38 minutes (range, 11–103 minutes). Several case series describing thrombectomy by using the Solitaire stent have reported successful recanalization, with a success rate between 62% and 100%.^{4-8,20,21} However, the first multicenter, prospective, randomized trial for the Solitaire system (the Solitaire With the Intention For Thrombectomy [SWIFT] trial) showed that successful recanalization (Thrombolysis in Myocardial Infarction grade 2 or 3) without symptomatic intracranial hemorrhage was achieved in 61% of the Solitaire group.⁸ Thus, our results do not appear to be worse than those of the SWIFT trial. This finding suggests the possibility that Solitaire thrombectomy, with or without chemical thrombolysis, could result in successful, rapid, and safe arterial

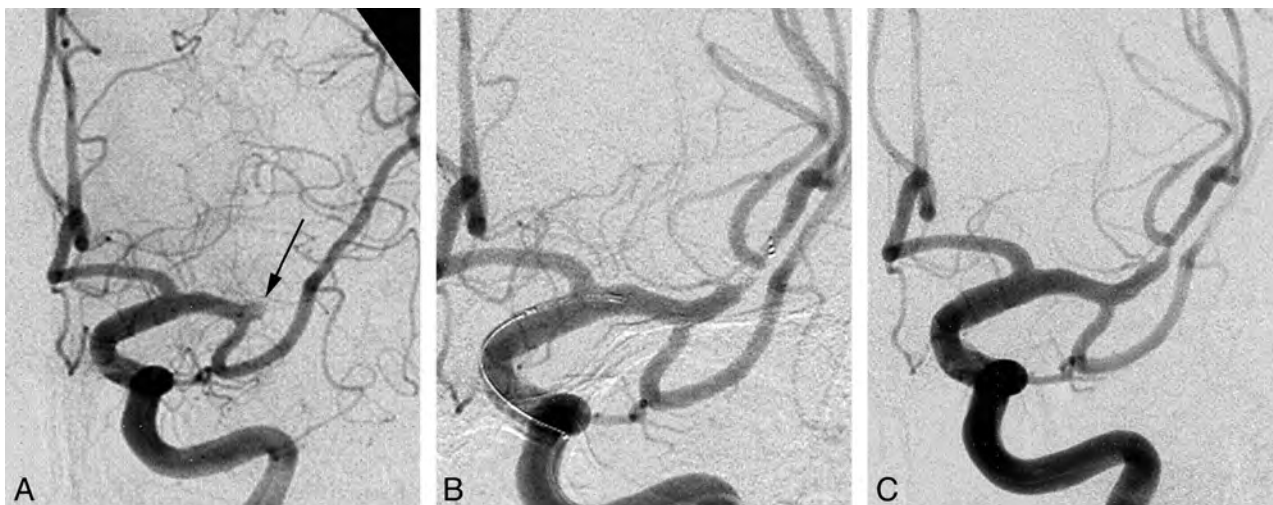


FIG 2. A, Initial conventional angiography shows complete occlusion of the left M2 segment of the MCA (arrow). B, Conventional angiography shows immediate blood flow restoration achieved by Solitaire stent deployment. C, After mechanical thrombectomy, moderate stenosis is noted at the occlusion site.

recanalization with balloon angioplasty or permanent stent placement, even in cases without the MCA SVS.

Some case series have shown that an in situ steno-occlusive lesion is related to incomplete vessel recanalization and may require additional balloon angioplasty or permanent stent placement.²² Balloon angioplasty with or without stent placement as a first-line method could have some disadvantage in the setting of hyperacute or acute ischemic stroke. First, the rate of adverse events could be higher without antithrombotic premedication, partly due to plaque vulnerability.²³⁻²⁵ Dorn et al²⁵ reported that the rate of adverse events was 87.5% for acute stroke with complete occlusion but 8.3% for a scheduled angioplasty procedure. Second, anatomic factors such as vessel tortuosity, occlusion length, or diameter of the proximal or distal portion of occlusion, as well as the neurointerventionalist's experience, could be critical for the technical success and procedural outcome of balloon angioplasty.²⁶ Finally, whether aggressive medical therapy or angioplasty with or without stent placement in combination with aggressive medical therapy is the better treatment method for symptomatic intracranial stenosis is still under debate.^{26,27} Consequently, we considered that balloon angioplasty with or without stent placement was the second option for acute ischemic stroke without the SVS.

The theoretic background for this interesting result could be found in studies of the relationship of atherosclerotic plaque and thrombus formation.^{28,29} Arterial atherosclerotic plaques can induce intraluminal thrombus formation at the site of maximal stenosis or just distal to it. This phenomenon, known as "atherothrombosis," is due to the advanced lipid core of the atherosclerotic plaque, which is rich in tissue factors that activate platelets and promote coagulation if released into the blood by either rupture or ulceration of the plaque.³⁰ Thus, vulnerable plaques with intra-arterial thrombus may act as the cause of acute ischemic stroke with in situ stenosis rather than hemodynamic instability.^{26,28} Because the MCA SVS reflects clot composition and burden, the atherothrombus may exist without demonstrating the MCA SVS on GRE MR imaging because of a different clot composition or a small amount of

clotting.^{11,12} Moreover, even in the vessel showing MCA SVS, a concurrent atherothrombus with in situ atherosclerotic stenosis may be present. Therefore, considering the possibility of an underlying atherothrombus in the stenotic artery, we can conclude that mechanical thrombectomy by using the Solitaire stent could be effective, even in acute ischemic stroke without the MCA SVS, by removing the thrombus within stenotic lesion.

Rapid arterial rethrombosis is associated with high-grade residual stenosis and usually occurs at the site of the initial occlusion, resulting in reocclusion of the recanalized artery.³¹ Because platelet activation is a key step in thromboembolism in the reocclusion of an in situ steno-occlusive lesion,³¹⁻³⁴ intravenous or intra-arterial glycoprotein IIb/IIIa inhibitors could be effective for preventing reocclusion.^{32,34} On the basis of the findings of the Abciximab in Emergency Treatment of Stroke Trial, which showed an increased rate of symptomatic or fatal intracranial hemorrhage,³⁵ we used intravenous or intra-arterial tirofiban in our study only when no contraindication existed.

Another interesting finding was that the percentage of patients who demonstrated fluctuating symptoms was relatively high in our study. Several reports have suggested that fluctuating symptoms might be a manifestation of intracranial vascular occlusion with marginal blood flow supplied by collateral circulation.³⁶ In particular, fluctuating symptoms may suggest existing but unstable and insufficient collateralization,³⁷ which means that intervention including thrombolytic therapy should be considered for patients with this pattern of symptoms. We thought that fluctuating symptoms could be one of the surrogate markers to predict in situ stenosis as the cause of the occlusion.

There are a few limitations to our study. First, this was a preliminary report including only a small number of patients. Second, for this retrospective study, we chose consecutive patients who underwent endovascular intervention with the Solitaire stent due to acute neurologic deficits caused by MCA occlusion. This choice led to an unavoidable selection bias. Third, the high section thickness of the GRE sequence (5 mm) could

give false-negative results regarding the MCA SVS. Third, the follow-up imaging technique and the interval between each follow-up was not consistent among the patients. The precise comparison of the degree of vessel stenosis is not possible. Therefore, a large randomized prospective study needs to be performed, and the effectiveness of the Solitaire stent should be proved with statistical analysis.

CONCLUSIONS

The Solitaire stent is a feasible tool as a first-line device for endovascular intervention in acute ischemic stroke without the MCA SVS. It not only provides a good rate of successful and complete recanalization but also enables rapid yet safe vascular recanalization without reported complications. The most likely theory for its function is that the removal of the atherothrombus by Solitaire thrombectomy results in arterial recanalization, but the exact pathologic mechanism is still unclear. To confirm this theory, further prospective studies with long-term follow-up should be conducted.

Disclosures: Hee-Joon Bae—UNRELATED: Board Membership: Bayer Korea, Boehringer Ingelheim Korea, Bristol-Myers Squibb Korea, MSD Korea, Novartis Korea, Consultancy: YuYu Pharmaceutical Co, Grants/Grants Pending: ESAI-Korea,* Sanofi-Aventis Korea,* Bayer-Korea,* Ostuka Korea,* Pfizer Inc,* Dae Woong Pharmaceutical Co,* Daichi Sankyo,* Yuhan Corporation,* Dong-A Pharmaceutical Co, Payment for Lectures (including service on Speakers Bureaus): Bayer Korea, AstraZeneca Korea, MSD Korea, Bristol-Myers Squibb Korea, Novartis Korea, Ostuka Korea, Pfizer Korea, Daichi Sankyo Korea, Handok Pharmaceuticals Co, Payment for Manuscript Preparation: Bayer Korea, Ostuka Korea, Moon Hee Han—UNRELATED: Consultancy: MicroVention.* *Money paid to the institution.

REFERENCES

- Henkes H, Flessler A, Brew S, et al. **A novel microcatheter-delivered, highly-flexible and fully-retrievable stent, specifically designed for intracranial use.** *Interv Neuroradiol* 2003;9:391–93
- Lubicz B, Collignon L, Raphaeli G, et al. **Solitaire stent for endovascular treatment of intracranial aneurysms: immediate and mid-term results in 15 patients with 17 aneurysms.** *J Neuroradiol* 2010;37:83–88
- Klisch J, Eger C, Sychra V, et al. **Stent-assisted coil embolization of posterior circulation aneurysms using Solitaire ab: preliminary experience.** *Neurosurgery* 2009;65:258
- Castaño C, Dorado L, Guerrero C, et al. **Mechanical thrombectomy with the Solitaire AB device in large artery occlusions of the anterior circulation: a pilot study.** *Stroke* 2010;41:1836–40
- Stampfl S, Hartmann M, Ringleb PA, et al. **Stent placement for flow restoration in acute ischemic stroke: a single-center experience with the Solitaire stent system.** *AJNR Am J Neuroradiol* 2011;32:1245–48
- Breckenfeld C, Schroth G, Mordasini P, et al. **Impact of retrievable stents on acute ischemic stroke treatment.** *AJNR Am J Neuroradiol* 2011;32:1269–73
- Nayak S, Ladurner G, Killer M. **Treatment of acute middle cerebral artery occlusion with a Solitaire AB stent: preliminary experience.** *Br J Radiol* 2010;83:1017–22
- Saver JL, Jahan R, Levy EI, et al, for the SWIFT Trialists. **Solitaire flow restoration device versus the Merci retriever in patients with acute ischaemic stroke (SWIFT): a randomised, parallel-group, non-inferiority trial.** *Lancet* 2012;380:1241–49
- Rovira A, Orellana P, Alvarez-Sabín J, et al. **Hyperacute ischemic stroke: middle cerebral artery susceptibility sign at echo-planar gradient-echo MR imaging.** *Radiology* 2004;232:466–73
- Flacke S, Urbach H, Keller E, et al. **Middle cerebral artery (MCA) susceptibility sign at susceptibility-based perfusion MR imaging:**

clinical importance and comparison with hyperdense MCA sign at CT. *Radiology* 2000;215:476–82

- Liebeskind DS, Sanossian N, Yong WH, et al. **CT and MRI early vessel signs reflect clot composition in acute stroke.** *Stroke* 2011;42:1237–43
- Cho KH, Kim JS, Kwon SU, et al. **Significance of susceptibility vessel sign on T2*-weighted gradient echo imaging for identification of stroke subtypes.** *Stroke* 2005;36:2379–83
- Barber PA, Hill MD, Eliaziw M, et al. **Imaging of the brain in acute ischaemic stroke: comparison of computed tomography and magnetic resonance diffusion-weighted imaging.** *J Neurol Neurosurg Psychiatry* 2005;76:1528–33
- Smith WS, Sung G, Starkman S, et al. **Safety and efficacy of mechanical embolectomy in acute ischemic stroke: results of the MERCI trial.** *Stroke* 2005;36:1432–38
- Fiehler J, Knudsen K, Thomalla G, et al. **Vascular occlusion sites determine differences in lesion growth from early apparent diffusion coefficient lesion to final infarct.** *AJNR Am J Neuroradiol* 2005;26:1056–61
- Khatri P, Neff J, Broderick JP, et al. **Revascularization end points in stroke interventional trials: recanalization versus reperfusion in IMS-I.** *Stroke* 2005;36:2400–03
- Wong K, Lam WWM, Liang E, et al. **Variability of magnetic resonance angiography and computed tomography angiography in grading middle cerebral artery stenosis.** *Stroke* 1996;27:1084–87
- Wahlgren N, Ahmed N, Davalos A, et al. **Thrombolysis with alteplase for acute ischaemic stroke in the Safe Implementation of Thrombolysis in Stroke-Monitoring Study (SITS-MOST): an observational study.** *Lancet* 2007;369:275–82
- Larrue V, von Kummer R, Müller A, et al. **Risk factors for severe hemorrhagic transformation in ischemic stroke patients treated with recombinant tissue plasminogen activator: a secondary analysis of the European-Australasian Acute Stroke Study (ECASS II).** *Stroke* 2001;32:438–41
- Miteff F, Faulder K, Goh A, et al. **Mechanical thrombectomy with a self-expanding retrievable intracranial stent (Solitaire AB): experience in 26 patients with acute cerebral artery occlusion.** *AJNR Am J Neuroradiol* 2011;32:1078–81
- Costalat V, Machi P, Lobotesis K, et al. **Rescue, combined, and stand-alone thrombectomy in the management of large vessel occlusion stroke using the Solitaire device: a prospective 50-patient single-center study.** *Stroke* 2011;42:1929–35
- Ueda T, Sakaki S, Nochide I, et al. **Angioplasty after intra-arterial thrombolysis for acute occlusion of intracranial arteries.** *Stroke* 1998;29:2568–74
- Suh DC, Kim JK, Choi JW, et al. **Intracranial stenting of severe symptomatic intracranial stenosis: results of 100 consecutive patients.** *AJNR Am J Neuroradiol* 2008;29:781–85
- Suh DC, Kim EH. **The therapeutic time window related to the presenting symptom pattern, that is, stable versus unstable patients, can affect the adverse event rate of intracranial stenting.** *Stroke* 2009;40:e588–89, author reply e590
- Dorn F, Prothmann S, Wunderlich S, et al. **Stent angioplasty of intracranial stenosis: single center experience of 54 cases.** *Clin Neuro-radiol* 2012;22:149–56
- Abou-Chebl A, Steinmetz H. **Critique of “Stenting versus aggressive medical therapy for intracranial arterial stenosis” by Chimowitz, et al in the New England Journal of Medicine.** *Stroke* 2012;43:616–20
- Chimowitz MI, Lynn MJ, Derdeyn CP, et al. **Stenting versus aggressive medical therapy for intracranial arterial stenosis.** *N Engl J Med* 2011;365:993–1003
- Ogata J, Masuda J, Yutani C, et al. **Mechanisms of cerebral artery thrombosis: a histopathological analysis on eight necropsy cases.** *J Neurol Neurosurg Psychiatry* 1994;57:17–21
- Komotar RJ, Mocco J, Wilson DA, et al. **The natural history of intracranial carotid artery atherosclerosis.** *Neurosurg Focus* 2005;18:e5

30. Rauch U, Osende JI, Fuster V, et al. **Thrombus formation on atherosclerotic plaques: pathogenesis and clinical consequences.** *Ann Intern Med* 2001;134:224
31. Heo JH, Lee KY, Kim SH, et al. **Immediate reocclusion following a successful thrombolysis in acute stroke: a pilot study.** *Neurology* 2003;60:1684–87
32. Mangiafico S, Cellierini M, Nencini P, et al. **Intravenous glycoprotein IIb/IIIa inhibitor (tirofiban) followed by intra-arterial urokinase and mechanical thrombolysis in stroke.** *AJNR Am J Neuroradiol* 2005;26:2595–601
33. Torgano G, Zecca B, Monzani V, et al. **Effect of intravenous tirofiban and aspirin in reducing short-term and long-term neurologic deficit in patients with ischemic stroke: a double-blind randomized trial.** *Cerebrovasc Dis* 2010;29:275–81
34. Kwon JH, Shin SH, Weon YC, et al. **Intra-arterial adjuvant tirofiban after unsuccessful intra-arterial thrombolysis of acute ischemic stroke: preliminary experience in 16 patients.** *Neuroradiology* 2011;53:779–85
35. Adams HP Jr, Effron MB, Torner J, et al. **Emergency administration of abciximab for treatment of patients with acute ischemic stroke: results of an international phase III trial: Abciximab in Emergency Treatment of Stroke Trial (AbESTT-II).** *Stroke* 2008;39:87–99
36. Johnston DC, Hill MD. **The patient with transient cerebral ischemia: a golden opportunity for stroke prevention.** *CMAJ* 2004;170:1134–37
37. Jakubowska MM, Michels P, Müller-Jensen A, et al. **Endovascular treatment in proximal and intracranial carotid occlusion 9 hours after symptom onset.** *Neuroradiology* 2008;50:599–604

Quantification of Internal Carotid Artery Flow with Digital Subtraction Angiography: Validation of an Optical Flow Approach with Doppler Ultrasound

V. Mendes Pereira, R. Ouared, O. Brina, O. Bonnefous, J. Satwinski, H. Aerts, D. Ruijters, F. van Nijnatten, F. Perren, P. Bijlenga, K. Schaller, and K.-O. Lovblad



ABSTRACT

BACKGROUND AND PURPOSE: Digital subtraction angiography is the reference standard technique to evaluate intracranial vascular anatomy and used on the endovascular treatment of vascular diseases. A dedicated optical flow-based algorithm was applied to DSA to measure arterial flow. The first quantification results of internal carotid artery flow validated with Doppler sonography are reported.

MATERIALS AND METHODS: We included 22 consecutive patients who underwent endovascular procedures. To assess the sensitivity of the algorithm to contrast agent–blood mixing dynamics, we acquired high-frame DSA series (60 images/s) with different injection rates: 1.5 mL/s ($n = 19$), 2.0 mL/s ($n = 18$), and 3.0 mL/s ($n = 13$). 3D rotational angiography was used to extract the centerline of the vessel and the arterial section necessary for volume flow calculation. Optical flow was used to measure flow velocities in straight parts of the ICAs; these data were further compared with Doppler sonography data. DSA mean flow rates were linearly regressed on Doppler sonography measurements, and regression slope coefficient bias from value 1 was analyzed within the 95% confidence interval.

RESULTS: DSA mean flow rates measured with the optical flow approach significantly matched Doppler sonography measurements (slope regression coefficient, $b = 0.83 \pm 0.19$, $P = .05$) for injection rate = 2.0 mL/s and circulating volumetric blood flow < 6 mL/s. For injection rate = 1.5 mL/s, volumetric blood flow < 3 mL/s correlated well with Doppler sonography ($b = 0.67 \pm 0.33$, $P = .05$). Injection rate = 3.0 mL/s failed to provide DSA–optical flow measurements correlating with Doppler sonography because of the lack of measurable pulsatility.

CONCLUSIONS: A new model-free optical flow technique was tested reliably on the ICA. DSA-based blood flow velocity measurements were essentially validated with Doppler sonography whenever the conditions of measurable pulsatility were achieved (injection rates = 1.5 and 2.0 mL/s).

ABBREVIATIONS: OF = optical flow; RMSE = relative root mean square errors; IR = injection rate; CA = contrast agent; USD = Doppler sonography; 3DRA = 3D rotational angiography

Even though digital subtraction angiography has traditionally been confined to standard anatomy assessment, quantification of blood flow based on DSA is becoming an important topic that could help neurointerventionists in making adequate periprocedural decisions. Some reports have described new techniques based on DSA that are able to assess flow or flow changes

during treatment of stented aneurysms.^{1,2} However, the development of clinically useful tools based on the integration of engineering, hemodynamic and physiologic knowledge still requires improved translation of biofluid mechanical information into clinical applications.³ X-ray video densitometry, based on the detection of the displacement of radiopaque contrast material through the vascular system, has been studied since the early 1960s and has been divided into 2 main classes: tracking and computational methods.⁴ Sarry et al⁵ estimated the flow by using an inverse advection model. Bogunović and Lončarić⁶ proposed the combination of DSA and 3D rotational angiography (3DRA), using an analysis of the time-attenuation curves. Rhode et al⁷ developed a model-based and weighted-optical field (OF) approach to improve already existing techniques and compared the results with simulation data, while Imbed et al^{8,9} developed a similar approach on the femoral artery and simulated angiographic data. Waechter et al¹⁰ developed a model-based approach to measure flow in the cerebral arteries.

Received October 8, 2012; accepted after revision March 28, 2013.

From the Interventional Neuroradiology Unit (V.M.P., R.O., O. Brina, K.-O.L.), Service of Neurosurgery (P.B., K.S.), and Service of Neurology (F.P.), University Hospital of Geneva, Geneva, Switzerland; and Medisys Research Laboratory (O. Bonnefous, J.S.) and Interventional X-Ray (H.A., D.R., F.v.N.), Philips Healthcare, Best, the Netherlands.

This work was supported by Swiss National Funds (SNF 32003B_141192 and SNF 320000_121565).

Please address correspondence to Vitor Mendes Pereira, MD, MSc, Interventional Neuroradiology, University Hospital of Geneva, Rue Gabrielle-Perret-Gentil, 4 Geneva, Switzerland 1211; e-mail: vitormpbr@hotmail.com

Indicates open access to non-subscribers at www.ajnr.org

Indicates article with supplemental on-line table

<http://dx.doi.org/10.3174/ajnr.A3662>

These approaches were all limited in case of fast flows, required longer straight-vessel segments, and were affected by low signal-to-noise ratios. A dedicated algorithmic scheme was developed to reduce instabilities due to temporal and spatial noise and to cope with fast flows, to address these issues.¹¹ Essentially, we used only the modulation by the cardiac cycle to extract flow-velocity values. The OF principle was then applied to the pulsating component of dye-concentration signal.¹¹ In this article, the first clinical results of the proposed algorithm applied to the ICA are reported. The clinical implementation and verification against Doppler ultrasound (USD) data in a consecutive cohort of patients are described, and the limits of the current technique are discussed.

MATERIALS AND METHODS

Clinical Data

The study protocol was approved by our institutional ethics committee (NEC 07–056). Between 2008 and 2009, all patients undergoing angiographic investigation or endovascular treatment for intracranial aneurysms in our department were considered for recruitment. Patients with intraventricular drainage, hydrocephalus, or hematoma were excluded because of a possible unstable intracranial pressure that could interfere with intracranial flow during the procedure and image acquisition. We included prospectively 22 consecutive patients with ruptured or unruptured intracranial aneurysms. All patients were evaluated under general anesthesia. A 5F 0.038-inch diagnostic catheter (Cook, Bloomington, Indiana) was placed selectively in the ICA (3 cm after the common carotid bifurcation) by using a femoral approach. The angiographic examinations were performed with a monoplane angiographic C-arm Allura FD20 system (Philips Healthcare, Best, the Netherlands). Every patient underwent 3DRA to acquire the 3D vascular anatomy with an injection rate (IR) = 3 mL/s during 6 seconds. An optimized projection, offering the best view of the vessel segment, was chosen for flow-rate measurement with the fewest overlapping vessels. High-speed DSA (60 frames/s with the 1024 × 1024 detector pixel matrix) was acquired in 10 seconds. The radiation exposure was equivalent to 2-frames-per-second sequences in terms of dose level. Two or 3 DSA acquisitions by using different contrast agent IRs were obtained for each patient. The contrast agent (CA) was iopamidol (Iopamiro 300; Bracco, Milan, Italy), and the injection duration was 3 seconds. CA was injected with an Imaxeon Avidia angiographic contrast injector (Medrad, Indianola, Pennsylvania). IRs were randomly selected before each acquisition among 3 protocols: 1.5 mL/s ($n = 19$), 2.0 mL/s ($n = 18$), and 3.0 mL/s ($n = 13$).

Optical Flow Principle

The OF-based algorithm used in this study to measure internal carotid flows was based on both 2D DSA and 3DRA image data.¹¹ The blood-contrast flow-velocity fields were measured from 2D DSA sequences. The injected contrast material was diluted in the blood stream while being transported through the vascular network. The pulsating contrast patterns generated by dye injection under the effect of the cardiac cycle were captured in DSA sequences. The main improvement provided by this approach consisted of extracting only the cardiac modulation from the signal, while discarding the low-frequency wash-in and washout compo-

nents. The OF approach is a mass-conserving technique, which was applied in an image-processing algorithm to extract velocity and flow curves. The second step consisted of projecting the DSA sequence on the arterial centerline extracted from the 3DRA data to generate the 2D “contrast wave map” or “flow map,” which defines the effective progression of the contrast wave along the arterial axis. Then, a 1D OF scheme was applied iteratively on the contrast wave map to extract the velocity profile. The iterative process was stopped when the quadratic error was no longer decreasing. The high-frame-rate acquisition was allowed to reduce constraints on the required arterial segment length and, therefore, to address more complex arterial geometries such as in cerebral vessels. For average velocities as high as 60 cm/s for instance, the required arterial segment length was approximately 20 mm to allow a proper warping, which was largely achieved at a frame rate of 60 Hz (2 times 10 mm). If $C(t, z)$ is the physiologically modulated contrast attenuation at instant time t , and z is the curvilinear axial position along the centerline, displacement velocity $V(t, z)$ satisfies the differential contrast wave equation:

$$1) \quad \frac{\partial C(t, z)}{\partial t} + \frac{\partial C(t, z)}{\partial z} V(t, z) = 0.$$

If $S(z)$ is the arterial cross-section at z , the volume flow curve is given by

$$2) \quad Q(t) = \frac{1}{L} \int_L S(z) V(t, z) dz,$$

where L is the curvilinear length of the arterial segment. $S(z)$ is measured from the segmented vasculature in the 3DRA dataset.

Figure 1 summarizes the whole velocity-extraction process,¹¹ starting from the DSA and 3DRA acquisitions (Fig 1A). The centerline of the artery was used to determine the curvilinear path represented by z . The contrast-level intensity along the curvilinear length z , namely the flow map or contrast wave map,^{10,12} is represented in Fig 1B. The velocity profile extracted from the flow map along with the volumetric flow is represented in Fig 1C.

To ensure good mixing between CA and blood, we selected the region of interest in the ICA at least 10 arterial diameters from the injection site.¹³ The region of measurement was reachable by sub-mandibular USD examination.

The presence of physiologic pulsatility in the contrast material motion pattern is effectively required for our OF algorithm¹¹ and was correlated with injection rate quotient (IQR) metric I_q ,

$$3) \quad I_q = \frac{Q_i}{Q_D},$$

where Q_i is the IR (milliliters per second) and Q_D is the time-average USD volume flow measure (milliliters per second). It has been shown, by comparing cardiac cycles measured from both electrocardiogram and time-intensity curves, that for $I_q \leq 1.2$, the physiologic pulsating character is conserved in a CA motion pattern.¹⁴

Doppler Measurement (USD)

The ICAs were examined by an experienced investigator with a 5- to 11-MHz color-coded duplex linear probe connected to an Aplio 770A scanner (Toshiba Medical Systems, Tokyo, Japan) by

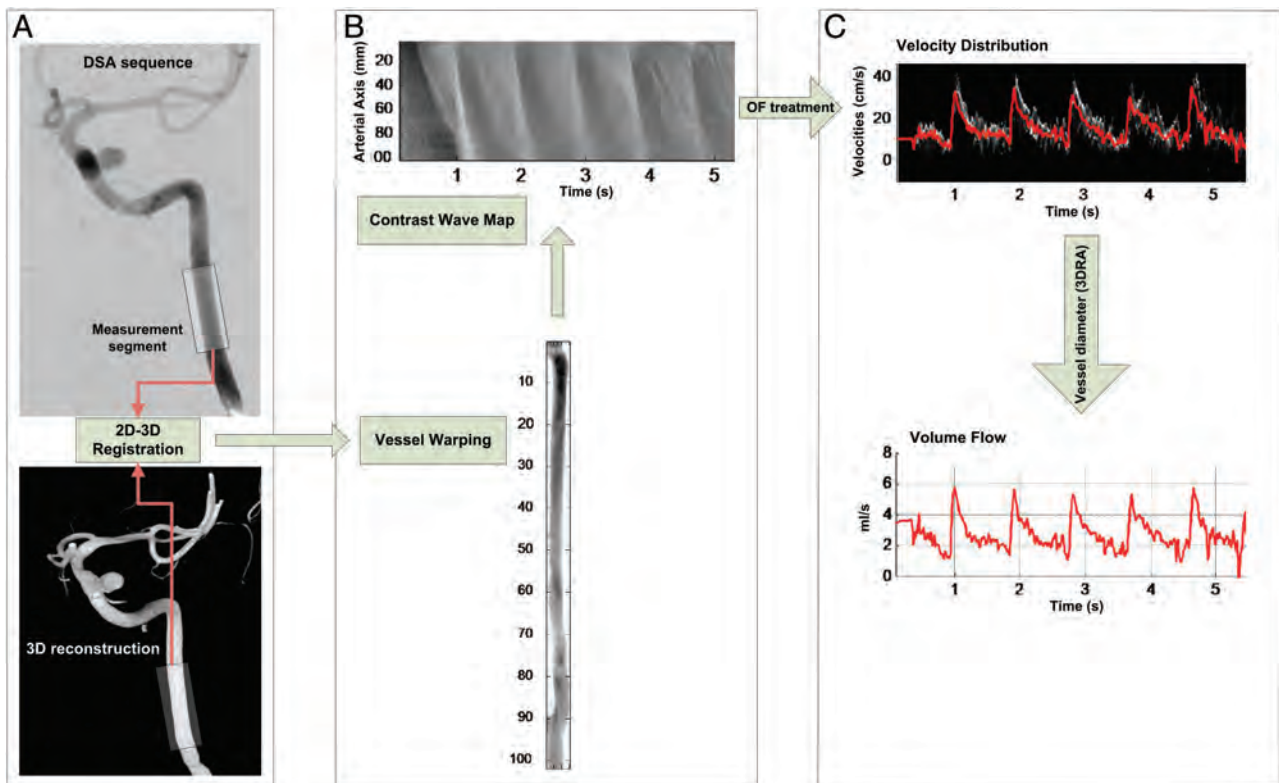


FIG 1. Flowchart illustrating the treatment of DSA images to calculate the blood flow of patient 3. First, the 2D images are superimposed on the 3DRA to scale the distances on the 2D images (A). Next, the contrast values are distributed over a straight model (B) to extract a flow map from the contrast sequence. Last, the flow map is analyzed by using the optical flow principle to estimate flow velocity curves (C). The volume flow rate curve is estimated by using the section of the artery measured from the 3DRA volume.

using a standard technique.¹⁵ The sample volume, adjusted to the size of the artery, was placed in the ICA with a submandibular approach, to obtain velocity waveforms. Its placement was adjusted around the site of measurements to acquire the higher color-coded signal. The angle-corrected mean velocity, peak systolic velocity, and end-diastolic velocity were determined by tracing the maximum frequency envelope of the waveform. The reference flow curves, based on Womersley solutions, were extracted with a Matlab (MathWorks, Natick, Massachusetts) program from images of velocity profiles acquired with USD. The vessel diameter needed to estimate the volumetric flow rate was measured on the 3D reconstruction. For cases in which several USD measures were acquired, repeatability was estimated.

Statistics and Regression Analysis

The validation process was performed by using linear regression fit between Q_D (Doppler) and Q_x (x-ray). Q_D was either a single USD time-average flow rate measure ($n = 6$) or an average of several measures ($n = 16$). Q_x was the time-average measure provided by the OF method. A robust fitting technique was used to reduce the impact of outliers by iteratively reweighting least squares with a bisquare weighting function ($r = 4.6$)^{16,17}

$$4) \quad Q_x = b \cdot Q_D.$$

The slope b and offset a were the regression coefficients of the robust fit model. The analysis was made for every injection rate group separately (1.5, 2.0, and 3.0 mL/s) and for several Q_D thresholds ($Q_D \leq 3.0, \leq 4.0, \leq 5.0, \leq 6.0, \leq 7.0$ mL/s) to test the

volume flow limits of the current OF technique prototype. Ideally, the 95% CI of the regression slope estimate should contain the value 1. The y -intercept a coefficient was proportional to the CA injected volume flow and was not taken into account in the validation process because of the lack of knowledge of this factor.¹⁸ Nonparametric Wilcoxon rank sum U tests and the Kruskal-Wallis H test were used to test statistics for the continuous data: b -slope regression coefficient, injection rate quotient, and Doppler measurement precision. If the H test was significant among 3 groups, the U test was performed to find out which of the differences were statistically significant. The significance level was fixed to $\alpha = .05$.

RESULTS

The On-line Table summarizes the measurements from USD and DSA. The average Doppler flow rate of the whole patient sample was 3.2 ± 0.3 mL/s ($n = 22$). Of the 22 patients, 16 had at least 2 Doppler measures in the submandibular On-line ICA segment: 11 with relative root mean square errors (RMSE) $< 10\%$ and the rest with RMSE between 10% and 25%. This precision did not depend on the circulating mean flow rate ($P = .13$).

Impact of Volume Flow on X-Ray Flow Measurement

Q_x volume flow quantification was regressed on the reference USD Q_D for each injection rate (1.5 mL/s, 2.0 mL/s, and 3.0 mL/s) and for each Q_D threshold subsample (≤ 3 mL/s, ≤ 4 mL/s, ≤ 5 mL/s, ≤ 6 mL/s, ≤ 7 mL/s). Figure 2 illustrates the results for both $Q_D \leq 4$ mL/s (left) and $Q_D \leq 7$ mL/s (right) subsamples. For $Q_i = 1.5$ mL/s (Fig 2A, -B), the regression slopes were $b = 0.49$ (95% CI,

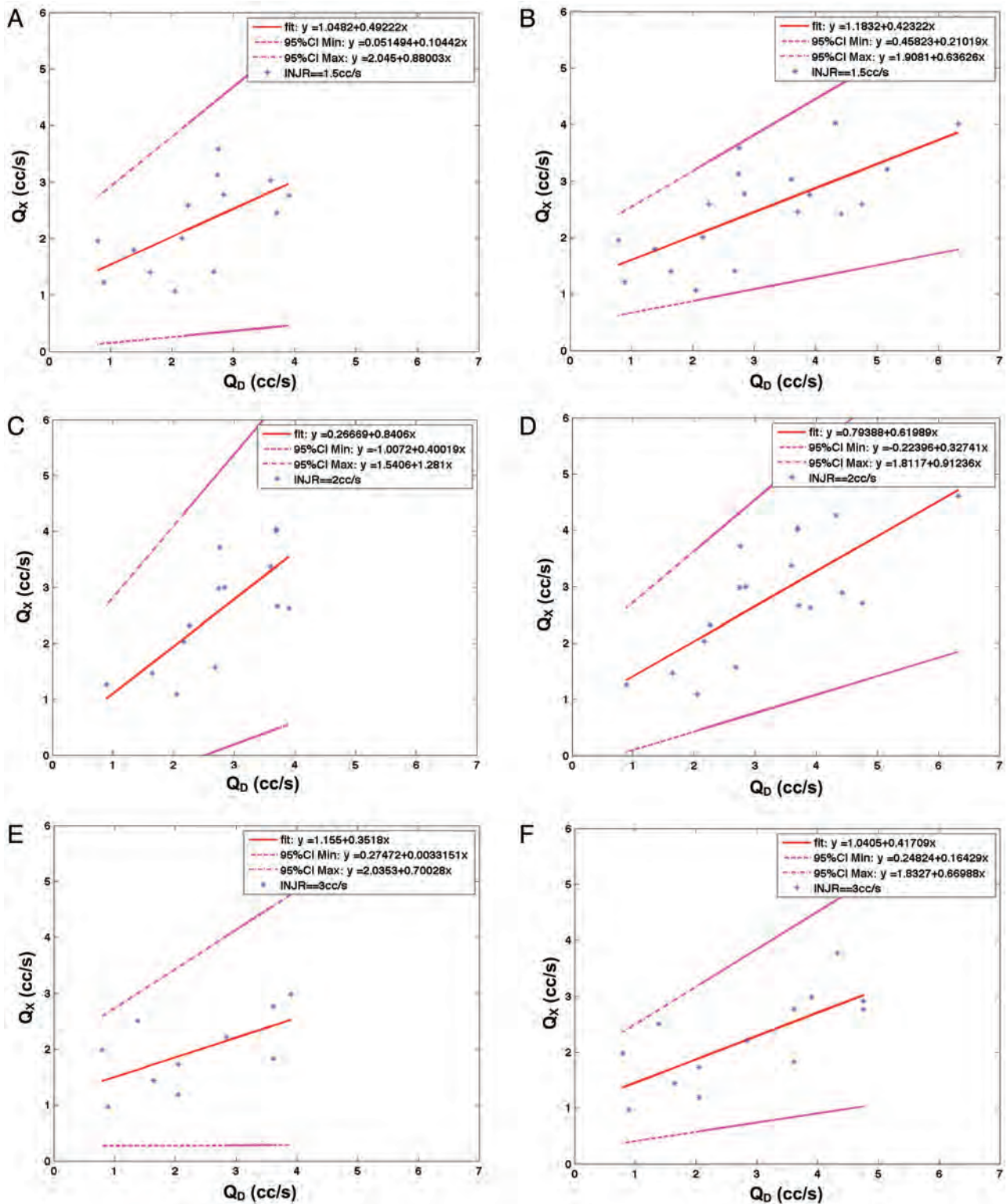


FIG 2. A and B, The regression fit at $Q_i = 1.5$ mL/s for $Q_D \leq 4$ mL/s (left) and $Q_D \leq 7$ mL/s (right). Q_x is represented on the y-axis, and Q_D , on the x-axis. The data (blue star points), fit (red line), and 95% CI limits (magenta) are all represented. C and D, The regression fit at $Q_i = 2.0$ mL/s for $Q_D \leq 3$ mL/s (left) and $Q_D \leq 7$ mL/s (right). Q_x is represented on the y-axis and Q_D on the x-axis. The data (blue star points), fit (red line), and 95% CI limits (magenta) are all represented. E and F, The regression fit at $Q_i = 3.0$ mL/s for $Q_D \leq 3$ mL/s (left) and $Q_D \leq 7$ mL/s (right). Q_x is represented on the y-axis, and Q_D , on the x-axis. The data (blue star points), fit (red line), and 95% CI limits (magenta) are all represented.

0.10–0.88; $R^2 = 0.72$) (Fig 2A) and $b = 0.42$ (95% CI, 0.21–0.63; $R^2 = 0.84$) (Fig 2B), respectively. For $Q_i = 2.0$ mL/s (Fig 2C, -D), the slopes were $b = 0.84$ (95% CI, 0.40–1.28; $R^2 = 0.76$) (Fig 2C)

and $b = 0.62$ (95% CI, 0.33–0.91; $R^2 = 0.81$) (Fig 2D), respectively. For $Q_i = 3.0$ mL/s (Fig 2E, -F), the slopes were $b = 0.35$ (95% CI, 0.03–0.67; $R^2 = 0.71$) (Fig 2E) and $b = 0.42$ (95% CI,

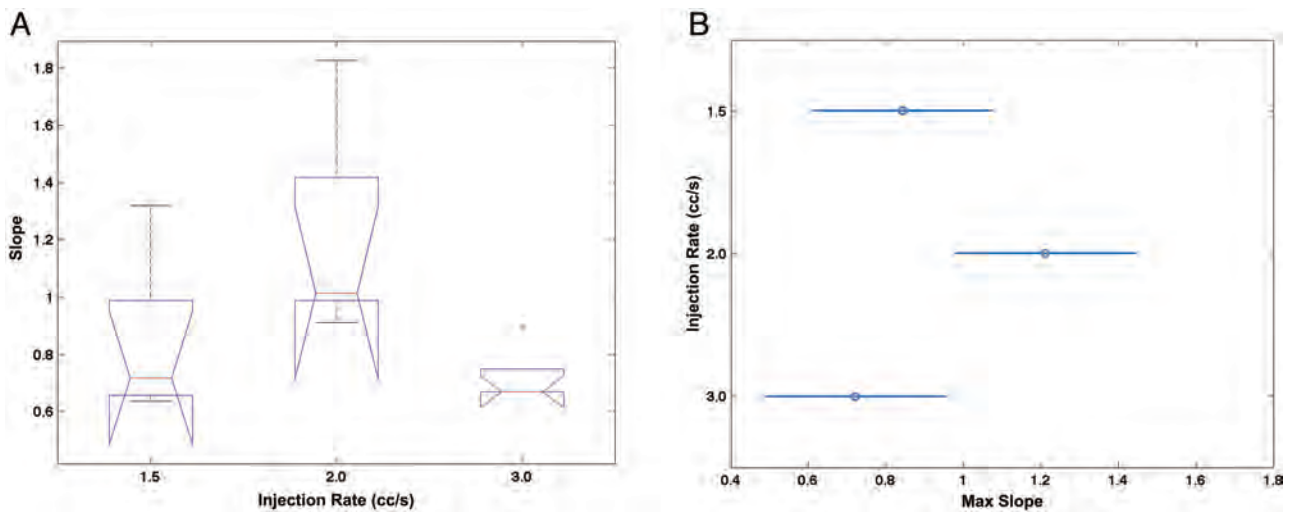


FIG 3. A, the boxplot for the fitted slope (y-axis) at 1.5, 2.0, and 3 mL/s (x-axis). Each boxplot represents the 5 slope values fitted for each Q_D subsample, with Q_D thresholds ≤ 3.0 , ≤ 4.0 , ≤ 5.0 , ≤ 6.0 , and ≤ 7.0 mL/s. B, results of the nonparametric ANOVA multiple comparison of the regression slope upper limit (x-axis) for each injection rate group (y-axis). These summarize the corresponding maximum slope values of 0.84, 1.21, and 0.72 with an SE of 0.12. The 95% CI error margins are also represented.

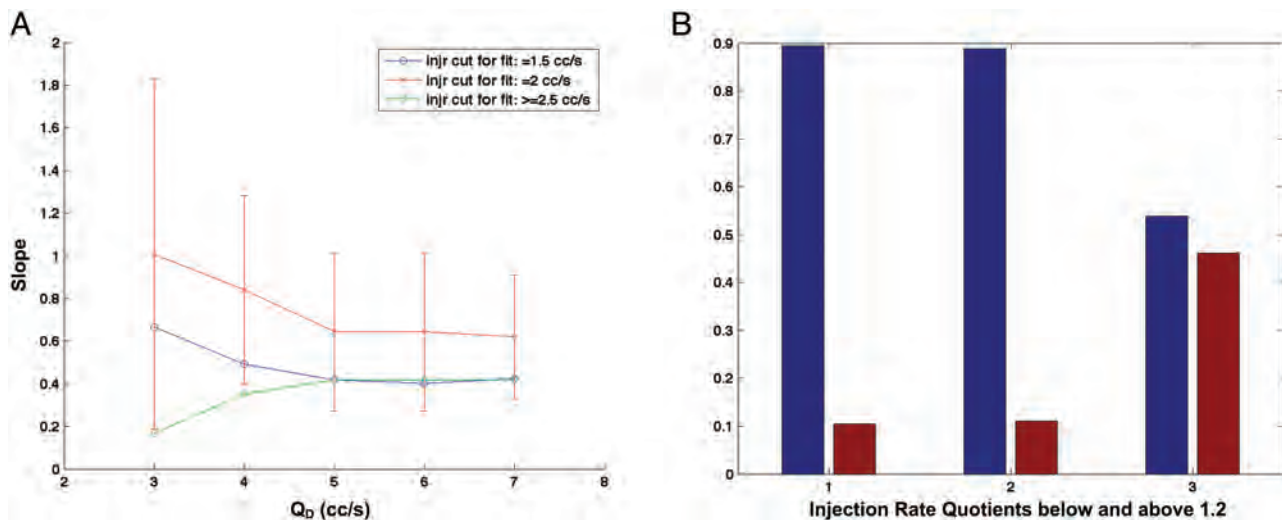


FIG 4. A, Slope versus Q_D for injection rates $Q_i = 1.5$ (blue), 2.0 (red), and 3.0 mL/s (green). The 95% CI limits have been superimposed to $Q_i = 2.0$ mL/s points. The graph shows that the slope bias calculated is not significantly different from 1 up to $Q_D = 6$ mL/s ($P > .05$). The $Q_i = 1.5$ mL/s group (blue points) follows the same evolution trend as $Q_i = 2.0$ mL/s, though with accentuated bias. A nonsignificant slope bias is likely for the Q_D range below 3 mL/s ($P = .06$). B, Injection rate quotients for $Q_i = 1.5$ mL/s (group 1), 2.0 (group 2), and 3.0 mL/s (group 3). The blue bars correspond to quotients < 1.2 , and the red bars, to quotients > 1.2 . The fact that the $Q_i = 1.5$ and 2.0 mL/s groups are reconstructed in similar ways with minimum slope bias, unlike the $Q_i = 3.0$ mL/s group, is partly due to differences in injection rate quotients ($P = .01$).

0.16–0.67; $R^2 = 0.80$) (Fig 2F), respectively. The slope bias from 1 significantly increased with the Q_D threshold for both $Q_i = 1.5$ and 2.0 mL/s groups. Unlike the 2 other IRs, the slope bias for $Q_i = 3.0$ mL/s followed a decreasing trend with increasing Q_D .

Sampling Effect on the Regression Slope Coefficient

The comparison of the regression slope coefficient among Q_i groups (Fig 3A) indicated that the only significant difference was between the $Q_i = 2.0$ mL/s and $Q_i = 3.0$ mL/s groups ($P = .0015$). The mean slopes, if sampling errors were ignored, were 0.48, 0.75, and 0.35 for $Q_i = 1.5$, 2.0, and 3.0 mL/s, respectively, with SE = 0.06. The corresponding slope upper values for the respective Q_i values were 0.84, 1.21, and 0.72, respectively, with a SE of 0.12 (Fig 3B). The $Q_i = 3.0$ mL/s group was significantly biased compared

with both $Q_i = 1.5$ mL/s and 2.0 mL/s ($P = .039$). For each CA injection rate Q_i , the sampling effect on slope driven by Q_D cutoffs at 3.0, 4.0, 5.0, 6.0, and 7.0 mL/s is plotted in Fig 4A. The error bars are superimposed for the group $Q_i = 2.0$ mL/s. For this group, the slope bias was not significant up to $Q_D = 6$ mL/s. Above $Q_D = 5$ mL/s, flow quantification was not sensitive to sampling. For $Q_i = 1.5$ mL/s, slope bias was significant ($P < .05$) for sampling cutoffs of > 3 mL/s; and for $Q_i = 3.0$ mL/s, the slope bias was effective for the whole sample ($P = .0004$).

Injection Rate Quotient

The ratio between the injection rate and the mean blood flow is illustrated in Fig 4B. The groups $Q_i = 1.5$ and 2.0 mL/s were not different ($P = .85$), while both of them were different from the

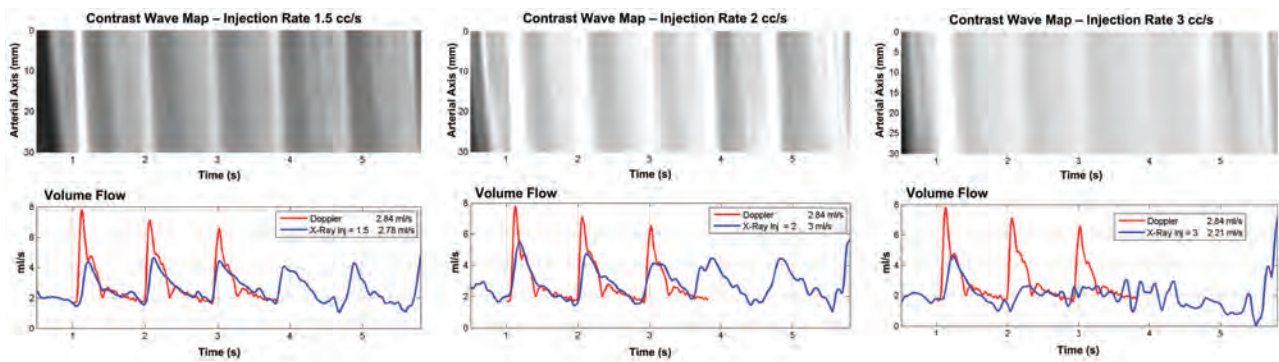


FIG 5. Comparison of contrast wave maps (top) and flow curves (bottom) for patient 13 for different IRs: IR = 1.5 mL/s (left), IR = 2.0 mL/s (middle), and IR = 3.0 mL/s (right). The red and blue curves in the bottom images correspond to USD and DSA measurements.

$Q_i = 3.0$ mL/s group ($P = .01$). In the first 2 groups, 90% of the data points had an injection rate quotient < 1.2 , implying that physiologic information and modulation were conserved in contrast-motion patterns.¹⁴ In the $Q_i = 3.0$ mL/s group, 45% of the points had an injection rate quotient > 1.2 . Therefore, the optical flow measures significantly matched the Doppler outcome for 2.0 mL/s injected cases when circulating blood flow ranged between 1 and 6 mL/s. With a 1.5 mL/s injection rate, flow measures matching was for circulating blood flow ranging from 1 to 3 mL/s. Figure 5 shows, for case 13, the contrast wave maps and flow curves corresponding to IR = 1.5, 2.0, and 3.0 mL/s. As one can notice, the contrast wave maps corresponding to IR = 1.5 and 2.0 mL/s show the best premises for velocity extraction (several pulses) compared with IR = 3.0 mL/s (1 detectable pulse).

DISCUSSION

Quantification of the Flow through DSA

The DSA-based approach represents a logical evolution of the criterion standard method for intracranial vascular anatomy assessment. Although DSA is an imaging technique used for endovascular treatments, the lack of tools for periprocedural quantitative flow measurements did not ease real-time therapeutic decision-making.^{1,2} The advantages for measuring blood velocity and flow changes during the procedure are numerous. For instance, one could evaluate the hemodynamic effect of an angioplasty in a stenotic segment for vasospasm or intracranial stenosis or the impact on the intra-aneurysmal hemodynamics of a flow-diverter stent to decide whether to place another one or coils.^{1,2} Other possible applications could be in acquiring patient-specific boundary conditions (flow curves) for computational flow dynamics. Different methods have been proposed to quantify both flow changes and characteristics from DSA sequences.^{3,7,10-12,19} However, most could not provide a reasonable level of confidence for clinical applications because of their inability to fully cope with both the complex advective and diffusive dispersion of the dye in blood stream and the complex pulsatile nature of the flow in the artery.³ Additionally, not all studies paid attention to CA injection protocols that might alter the physiologic modulation of CA motion waveform.^{13,20-22} This physiologic modulation is a key factor in dealing with the mixing problems related to CA transport in quantifying blood flow. The extraction of the modulated component with proper filtering is a necessary step that will condition the performance of such a functional algorithm. Con-

trary to the technique of Waechter et al,¹⁰ which also extracted the modulated component, our OF algorithm is model-free and can be applied to quantify flow in both the vessels and aneurysms.¹

In our study, we used 3 different IRs: 1.5, 2.0, and 3.0 mL/s. The Craya-Curtet number was 0.5–0.9 with a 5F catheter of 0.035-inch inner diameter, the tip of which was positioned at least a 10-artery diameter below the measurement zone.¹³ Measurable flow pulsatility was obtained for IR = 1.5 mL/s and 2 mL/s (injection rate quotient ≤ 1.2).^{13,14} Consequently, the OF technique performance was reasonably high, with slightly better results for 2 mL/s and for volume flows of < 6 mL/s. The performance with IR 1.5 mL/s was lower than expected because of the larger dilution of the dye with a deleterious effect on signal-to-noise ratio. The injection at 3 mL/s presented excessive reflux at the injection site, which altered the matching between dye and blood-flow dynamics in the region of interest.

General Trend of the OF Method

The general trend of our current OF algorithm was to measure flow with an underestimated slope bias that depends on the injection rate: 0.48, 0.75, and 0.35 for $Q_i = 1.5$ mL/s, 2.0 mL/s, and 3.0 mL/s, respectively, with RMSE = 0.06. Those values do not take into account sampling errors. The maximum slope value variations (95% CI) over the whole Q_D show that the slope bias for $Q_i = 1.5$ and 2.0 mL/s was not statistically significant (the maximum slope is, respectively, 0.84 and 1.21, with RMSE = 0.12, $P = .05$), unlike that for IR = 3.0 mL/s group. This general trend is consistent with the fact that the performance of the OF method depends first on the presence of the physiologic information on contrast wave maps and, consequently, on the injection rate quotient (≤ 1.2).

Thorough examinations of slope dependency with Q_D show that the slope bias for group IR = 2.0 mL/s was not statistically significant ($P > .05$) up to 6 mL/s, setting the limit on reliable velocity measurement to 60 ± 6 cm/s, taking into account the average inlet diameter of 4.8 mm and the relative RMSE = 0.12. For the IR = 1.5 mL/s group, the slope bias was small, within $Q_D \leq 3.0$ mL/s, and increased with Q_D . As Q_D increases, the corresponding CA signal-to-noise ratio is reduced, possibly because poor mixing occurs at the injection site due to high Craya-Curtet number.^{7,13} Consequently, intensity gradients in 2D images would have been overestimated in the denominator of the OF equation. More improvements to the OF technique are expected

in the near future to cope uniformly with different injection rates and flow rates.

Study Limitations

Doppler Measurements. The OF trend and limitations presented in the above section are discussed under the assumption that USD measures are infinitely accurate, which is, in fact, not correct. Biases due to geometric spectral broadening and to angulations between the beam direction and the vessel axis may lead to an overestimate of the USD velocity of approximately 30%.²³ The Doppler measurement repeatability inherent to the experienced investigator was reasonable (<23%). However, the mean-flow-rate repeatability of the measurements was <15% in 13 of 16 cases that had at least 2 USD measures, and for the other 3, it was ≤23%. The volumetric flow shapes were similar for repeated measures.

Acquisition Protocol. Sources of mismatch between OF and USD could have been due to the delay between the 2 acquisitions or to inaccurate estimates of the parent artery diameter from the 3D geometry. The diameter is influenced by the threshold selection and by the location of the measurement on the artery, which could deviate from the USD measurement zone. In this work, we focused on the most rectilinear part of the internal carotid artery to ensure the reliability of USD velocity measurements. In the submandibular part of ICA, the vessel narrowing is negligible within the OF measurement-segment length (2 cm). The range of flow rates in the ICA is quite exhaustive to validate the method. Nevertheless, it will be necessary to validate in other cerebral vessel locations where flow rates are smaller.

CONCLUSIONS

The DSA-based OF approach can be used to measure circulating flows in ICAs. The OF measure was validated with USD for flows up to 6 mL/s with CA injected at 2.0 mL/s and up to 3 mL/s with CA injected at 1.5 mL/s. The values obtained from the IR = 3.0 mL/s group were significantly biased because only partial dynamic information was propagated to the CA motion pattern. Improvements to the OF technique are expected in the near future to improve the accuracy and uniformity of velocity measurements over ranges of flow rates and injection rates. The capability of using this technique during the procedures and assessing fast flows in cerebral vessels would open new insights in intraoperative therapeutic decision-making.

APPENDIX

Statistical Analysis

The linear regression method we used applies generally to cases in which the independent variable (Q_D) is free from errors. In such situations, the robust fitting method consistently rejects the outliers and focuses on the bulk attenuation of data points. In our case, because 16 of 22 points were characterized by an estimated error on Q_D , errors-in-variables regression methods would have been used (eg, Deming regression) to avoid underestimating the regression coefficients. Some OF and Doppler measures were unique, and using Deming-like regression would have led to speculations on relative variances. Requiring that all data points have more than a single measure simultaneously in either OF or Dopp-

ler would have reduced the number of points by 50%. The robust regression fit is then a reasonable compromise to capture trends of the optical flow method.

The H test is generally performed among groups that are statistically independent. In our study, Q_D cutoff-based subsampling created the 3 IR (Q_i) groups. However, with such a low number of points (5) in each group, the lack of that statistical independence should not have dramatic consequences, given the level of precision and accuracy that we were dealing with.

USD

For several decades, the potential of Doppler instruments to measure volume flow rates at the same time as velocity waveforms has been discussed.²⁴ One article has reviewed all of the factors of inaccuracy and provided the orders of magnitude of the errors that were derived from the Doppler acquisition constraints and that were evaluated during validation tests.²³ Validation experimentation estimates the performance of the technique with in vivo and in vitro tests.²⁵ The authors found errors in the range of 5%–54% for in vivo experiments and errors <18% for in vitro flow-phantom experiments.

Disclosures: Vitor Mendes Pereira—RELATED: Grant: Swiss National Foundation.* Odile Bonnefous—UNRELATED: Employment: Philips Research Paris. Jean Stawiaski—UNRELATED: Employment: Philips Research. Fred van Nijnatten—UNRELATED: Employment: Philips Medical Systems Nederland BV (a Philips Healthcare Company). Hans Aerts—UNRELATED: Employment: Philips Healthcare. Daniel Ruijters—UNRELATED: Employment: Philips Healthcare.*Money paid to the institution.

REFERENCES

1. Pereira VM, Bonnefous O, Ouared R, et al. A DSA-based method using contrast-motion estimation for the assessment of the intra-aneurysmal flow changes induced by flow-diverter stents. *AJNR Am J Neuroradiol* 2013;34:808–15
2. Jou LD, Mawad ME. Analysis of intra-aneurysmal flow for cerebral aneurysms with cerebral angiography. *AJNR Am J Neuroradiol* 2012;33:1679–84
3. Lieber BB, Siebes M, Yamaguchi T. Correlation of hemodynamic events with clinical and pathological observations. *Ann Biomed Eng* 2005;33:1695–1703
4. Shpilfoygel SD, Close RA, Valentino DJ, et al. X-ray videodensitometric methods for blood flow and velocity measurement: a critical review of literature. *Med Phys* 2000;27:2008–23
5. Sarry L, Peng YJ, Boire JY. Blood flow velocity estimation from x-ray densitometric data: an efficient numerical scheme for the inverse advection problem. *Phys Med Biol* 2002;47:62
6. Bogunović H, Lončarić S. Blood flow and velocity estimation based on vessel transit time by combining 2D and 3D X-ray angiography. *Med Image Comput Comput Assist Interv* 2006;9(pt 2):117–24
7. Rhode KS, Lambrou T, Hawkes DJ, et al. Novel approaches to the measurement of arterial blood flow from dynamic digital x-ray images. *IEEE Trans Med Imaging* 2005;24:500–13
8. Imbed B, Meunier J, Mongrain R, et al. Optical flow assessment of parabolic velocity profile in cineangiography: a simulation study. In: *Proceedings of the 17th International Conference of the Engineering in Medicine and Biology Society*, Montreal, Canada, September 20–25, 1995
9. Imbed B, Meunier J, Mongrain R, et al. Blood flow assessment from optical flow in cineangiography. In: *Proceedings of the 17th International Conference of the Engineering in Medicine and Biology Society*, Montreal, Canada, September 20–25, 1995
10. Waechter I, Bredno J, Barratt DC, et al. Quantification of blood flow from rotational angiography. *Med Image Comput Comput Assist Interv* 2007;10(pt 1):634–41

11. Bonnefous O, Pereira VM, Ouared R, et al. **Quantification of arterial flow with digital subtracted angiography (DSA).** *Med Phys* 2012;39:6264–75
12. Waechter I, Bredno J, Hermans R, et al. **Model-based blood flow quantification from rotational angiography.** *Medical Image Anal* 2008;12:586–602
13. Lieber BB, Sadasivan C, Hao Q, et al. **The mixability of angiographic contrast with arterial blood.** *Med Phys* 2009;36:5064–78
14. Ouared R, Brina O, Bonnefous O, Groth A, Brunjs T, Babic D, Bijlenga P, Schaller K, Lovblad KO, Pereira VM. **Intracranial aneurysms: study of x-rays time-intensity-curves (TIC) pulsatility.** In: *Proceedings of 2nd International Conference on Mathematical and Computational Biomedical Engineering*, Washington DC. March 30-April 1, 2011
15. Forteza AM, Krejza J, Koch S, et al. **Ultrasound imaging of cerebrovascular disease.** In: Babikian VL, Wechsler L, Higashida RT [eds.]. **Imaging Cerebrovascular Disease.** Philadelphia: Butterworth-Heinemann; 2003, pp. 3–35.5
16. Holland PW, Welsch RE. **Robust regression using iteratively reweighted least-squares: theory and methods.** *Communications in Statistics: Theory and Methods* 1977;6:813–27
17. Street JO, Carroll RJ, Ruppert D. **A note on computing robust regression estimates via iteratively reweighted least squares.** *The American Statistician* 1988;42:152–54
18. Mulder G, Bogaerds AC, Rongen P, et al. **The influence of contrast agent injection on physiological flow in the circle of Willis.** *Med Eng Phys* 2011;33:195–203
19. Tenjin H, Asakura F, Nakahara Y, et al. **Evaluation of intra-aneurysmal blood velocity by time-density curve analysis and digital subtraction angiography.** *AJNR Am J Neuroradiol* 1998;19:1303–07
20. Sadasivan C, Cesar L, Seong J, et al. **An original flow diversion device for the treatment of intracranial aneurysms: evaluation in the rabbit elastase-induced model.** *Stroke* 2009;40:952–58
21. Sadasivan C, Cesar L, Seong J, et al. **Treatment of rabbit elastase-induced aneurysm models by flow diverters: development of quantifiable indexes of device performance using digital subtraction angiography.** *IEEE Trans Med Imaging* 2009;28:1117–25
22. Sadasivan C, Lieber BB, Cesar L, et al. **Angiographic assessment of the performance of flow diverters to treat cerebral aneurysms.** In: *Proceedings of the 28th Annual International Conference of the Engineering in Medicine and Biology Society*, New York, New York. August 31-September 3, 2006;3210–13
23. Hoskins PR. **Accuracy of maximum velocity estimates made using Doppler ultrasound systems.** *Br J Radiol* 1996;69:172–77
24. Burns PN. **Measuring volume flow with Doppler ultrasound: an old nut.** *Ultrasound Obstet Gynecol* 1992;2:238–41
25. Holland CK, Clancy MJ, Taylor KJ, et al. **Volumetric flow estimation in vivo and in vitro using pulsed-Doppler ultrasound.** *Ultrasound Med Biol* 1996;22:591–603

Comparative Effectiveness of Ruptured Cerebral Aneurysm Therapies: Propensity Score Analysis of Clipping versus Coiling

J.S. McDonald, R.J. McDonald, J. Fan, D.F. Kallmes, G. Lanzino, and H.J. Cloft



ABSTRACT

BACKGROUND AND PURPOSE: The relative merits of treating ruptured aneurysms with clipping versus coiling continue to be a topic of debate. We evaluated a national, multihospital patient data base to examine recent trends in ruptured aneurysm therapies and to compare peri-procedural outcomes between clipping and coiling treatments.

MATERIALS AND METHODS: The Premier Perspective data base was used to identify patients hospitalized between 2006–2011 for ruptured aneurysm who underwent clipping or coiling therapy. A propensity score model, representing the probability of receiving clipping, was generated for each patient by use of relevant patient and hospital variables. After Greedy-type matching of the propensity score, the risk of in-hospital mortality and morbidity was compared between clipping and coiling cohorts.

RESULTS: A total of 5229 patients with ruptured aneurysm (1228 clipping, 4001 coiling) treated at 125 hospitals were identified. Clipping therapy frequency decreased from 27% in 2006 to 21% in 2011. After propensity score adjustment, in-hospital mortality risk was similar between groups (OR = 0.94 [95% CI, 0.73–1.21]; $P = .62$). However, unfavorable outcomes were more common after clipping compared with coiling, including discharge to long-term care (OR = 1.32 [95% CI, 1.12–1.56]; $P = .0006$), ischemic complications (OR = 1.51 [95% CI, 1.24–1.83]; $P = .0009$), neurologic complications (OR = 1.64 [95% CI, 1.18–2.27]; $P = .0018$), and other surgical complications (OR = 1.55 [95% CI, 1.05–2.33]; $P = .0240$).

CONCLUSIONS: This study of a data base of multiple hospitals in the United States demonstrates that clipping of ruptured cerebral aneurysms resulted in greater adjusted morbidity compared with coiling.

ABBREVIATIONS: ICD-9 = International Classification of Diseases 9th Revision; ISAT = International Subarachnoid Aneurysm Trial

The relative merits of treating ruptured aneurysms with clipping versus coiling continue to be a topic of debate. The International Subarachnoid Aneurysm Trial (ISAT) demonstrated a 7.4% decrease in absolute risk of death or dependency (modified Rankin score, 4–5) at 1 year, with 23.5% of patients randomly assigned to coiling dependent or dead at 1 year compared with 30.9% randomly assigned to clipping.¹ However, because ISAT only enrolled patients who were deemed suitable to receive either clipping or coiling therapy, representing only 22% of patients who were screened,² the generalizability of the results has been called into question.³ Despite this criticism, multiple reports show a trend toward increasing use of coiling over clipping for patients

with ruptured cerebral aneurysms.^{4–7} Studies of large patient data bases that compared clipping and coiling treatments yielded mixed results, with some demonstrating worse outcomes after clipping^{8,9} and others demonstrating worse outcomes after coiling.^{6,10} In addition, the nonrandomized studies may have been affected by selection bias. To address this disparity in study findings and the concern of potential selection bias, we identified patients hospitalized for ruptured cerebral aneurysm between 2006–2011 by use of a large multihospital data base and performed a propensity score analysis to compare peri-procedural outcomes between patients of similar clinical and demographic characteristics who were treated with clipping or coiling.

MATERIALS AND METHODS

Study Population

The Perspective data base (Premier, Charlotte, North Carolina) is a voluntary, fee-supported collection of data developed to assess the quality and resource utilization of health care delivery within the United States.¹¹ As of 2011, the Perspective data base consisted of approximately 15% of hospitalizations nationwide and repre-

Received February 13, 2013; accepted after revision April 15.

From the Departments of Radiology (J.S.M., R.J.M., D.F.K., G.L., H.J.C.), Health Sciences Research (J.F.), and Neurosurgery (D.F.K., G.L., H.J.C.), Mayo Clinic, Rochester Minnesota.

Please address correspondence to Jennifer S. McDonald, PhD, Department of Radiology Mayo Clinic, 200 1st Street SW, Rochester, MN 55905; e-mail: mcdonald.jennifer@mayo.edu

<http://dx.doi.org/10.3174/ajnr.A3642>

Table 1: Patient and hospital demographics of patients with ruptured aneurysm

	Clipping	Coiling	P Value ^a
No. of patients	1228	4001	
Patients			
Age, y, median (IQR)	53 (45–62)	55 (46–65)	<.0001
Female, n (%)	814 (66)	2839 (71)	.0020
Race, n (%)			
White	742 (60)	2290 (57)	.0512
Black	193 (16)	640 (16)	.86
Hispanic	66 (5)	220 (6)	.94
Other	227 (18)	851 (21)	.0360
Admission status, n (%)			
Elective	101 (8)	480 (12)	.0002
Urgent	287 (23)	1063 (27)	.0253
Emergency	840 (68)	2458 (61)	<.0001
Admission source, n (%)			
Nonmedical source	382 (31)	1475 (37)	.0002
Transfer from hospital/care facility	350 (29)	1350 (34)	.0006
Emergency department	470 (38)	1106 (28)	<.0001
Clinic	26 (2)	70 (2)	.40
Charlson score	1 (1–2)	1 (1–2)	.0054
Endovascular procedure			
Day of procedure (range)	2 (1–3)	2 (1–2)	<.0001
Hospital			
Region, n (%)			
Midwest	186 (15)	450 (11)	.0004
South	576 (47)	1689 (42)	.0038
Northeast	266 (22)	1307 (33)	<.0001
West	200 (16)	555 (14)	.0368
No. of beds, n (range)	623 (439–725)	623 (448–683)	.19
Urban location vs rural, n (%)	1215 (99)	3908 (98)	.0051
Teaching vs nonteaching, n (%)	818 (67)	2721 (68)	.36

Note.—IQR indicates interquartile range.

^a P values derived from Wilcoxon rank sum test or Fisher exact test.

sented more than 600 US hospitals. Detailed information of a patient's hospitalization, including patient demographics, hospital information, diagnoses, procedures, discharge status, and all billed items, are recorded. Time of procedures and administration of billed items, tests, and examinations are reported in relation to the day of admission.

International Classification of Diseases, 9th Revision, Clinical Modification (ICD-9) codes were used to identify all cases of ruptured aneurysm hospitalizations (ICD-9 diagnostic code 430) recorded from 2006–2011. Patients were included if they underwent aneurysmal clipping (ICD-9 procedural code 39.51, “clipping of aneurysm”) or coiling (ICD-9 procedural codes 39.52, “other repair of aneurysm”; 39.72, “endovascular repair of occlusion of head and neck vessels”; 39.75, “endovascular embolization or occlusion of vessel[s] of head or neck by use of bare coils”; 39.76, “endovascular embolization or occlusion of vessel[s] of head or neck by using bioactive coils”; or 39.79, “other endovascular repair [of aneurysm] of other vessels”) during hospitalization. Because these diagnostic codes may not be specific for clipping or coiling, billing information was used as confirmation. Patients were included in the clipping or coiling groups if their billing record included an aneurysm clip or endovascular coil(s), respectively.

Outcome Variables

The primary outcome variables of this study were death during hospitalization, discharge to long-term care (hospice, skilled nursing facility, long-term care hospital, or rehabilitation facil-

ity), and ischemic complications (aphasia, ICD-9 diagnostic code 784.3; hemiplegia or paraplegia, 342.0–342.9; or cerebral artery occlusion, 434.0–434.9). Secondary outcomes were defined as hydrocephalus (331.3–331.4), postoperative neurologic complications (997.0–997.09), other postoperative surgical complications (997.2–997.5, 998.59, 998.0), ventriculostomy (ICD-9 procedural code 02.2), ventriculo-peritoneal shunt surgery (02.34), or tracheostomy (31.3–31.29) that occurred after clipping or coiling. Primary and secondary outcomes defined by ICD-9 codes were excluded from the analysis if they were listed as “present on admission” to specifically examine complications that occurred during hospitalization.

Statistics

Data were extracted from the Perspective data base by use of SAS (version 9.3; SAS Institute, Cary, North Carolina) and analyzed by use of JMP (version 9, SAS Institute) and R (version 2.15, <http://www.r-project.org/>). Continuous results are presented as median and interquartile range to account for nonparametric data distributions. Categorical results are presented as relative frequencies (%). Patient, procedure, and hospital covariates and outcome incidences were compared between clipping and coiling groups by use of the Wilcoxon rank sum test for continuous variables and Fisher exact test for categorical variables. Propensity score adjustment by use of 1:1 matching methods was performed by use of the MatchIt package in R.¹²

Propensity Score Analysis

Propensity score analysis was performed as previously described.¹³ Propensity scores, representing the probability of receiving clipping treatment, were calculated for each patient in the clipping and coiling groups by use of a logistic regression model. Twenty-seven covariates were used to generate this propensity score, including patient variables (age, sex, race, admission status, admission source, priority of ruptured aneurysm diagnosis, Charlson comorbidity score [calculated from ICD-9 diagnostic codes as previously described¹⁴], and payor source), clipping/coiling procedure variables (priority of procedure and day of procedure), and hospital variables (region, number of beds, urban or rural location, and teaching or nonteaching status). After propensity score generation, patients treated with clipping and those treated with coiling underwent 1:1 nearest-neighbor (Greedy-type) matching of the logit of the propensity score with a caliper width of 0.25 of the standard deviation of the score. Matching was performed without replacement, and both treated and control units not meeting matching criteria were excluded. Each propensity score–derived matched pair was assigned a unique pair ID by use of an R script. Improvement in covariate balance after match-

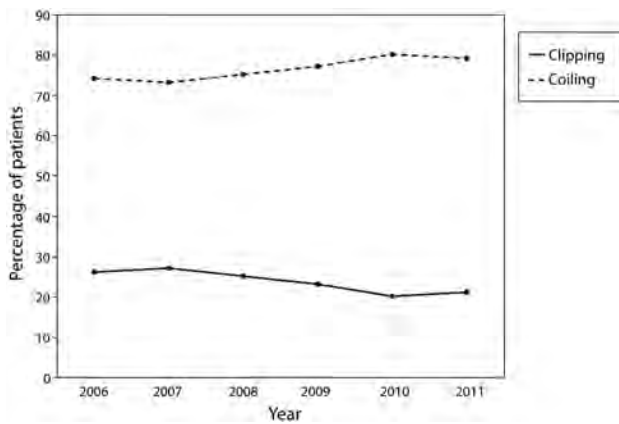


FIG 1. Trends in use of clipping and coiling of ruptured aneurysms from 2006–2011.

ing was analyzed by means of conditional logistic regression, conditioned on the pair ID. Odds ratios of primary and secondary outcomes were calculated after matching by means of the Fisher exact test.

Sensitivity Analysis

Sensitivity analysis was performed as described by Lin et al¹⁵ to assess whether observed differences in outcomes between clipping and coiling groups could be completely attributed to an unmeasured confounder. The lower 95% confidence interval of the odds ratio of the primary outcome that was the closest to 1.00 when comparing of clipping and coiling groups was used for this analysis. Discharge to long-term care was chosen for sensitivity analysis because the lower 95% confidence interval (1.12) was closest to equivalency of all primary outcomes significantly different between clipping and coiling groups.

RESULTS

Patient Demographics

Between 2006–2011, a total of 5229 patients from 125 unique medical centers were hospitalized with ruptured aneurysms. Within this cohort, 1228 (23%) patients underwent clipping and 4001 patients (77%) underwent coiling (Table 1). Significant differences between patients treated with clipping and those treated with coiling were observed for most patient and hospital variables. Specifically, patients who underwent clipping were younger (median age of 53 versus 55 years, $P < .0001$), more likely to have an emergency admission (68% versus 61%, $P < .0001$), and were more likely to be admitted from the emergency department (38% versus 28%, $P < .0001$) compared with patients who underwent coiling. Most hospitals that performed clipping or coiling were urban (99% clipping and 98% coiling) and classified as teaching hospitals (67% clipping and 68% coiling).

Temporal Trends in Clipping versus Coiling

Trends in the use of clipping and coiling were examined from 2006–2011. The proportion of patients who underwent clipping decreased from 27% in 2006 to 21% in 2011 (Fig 1).

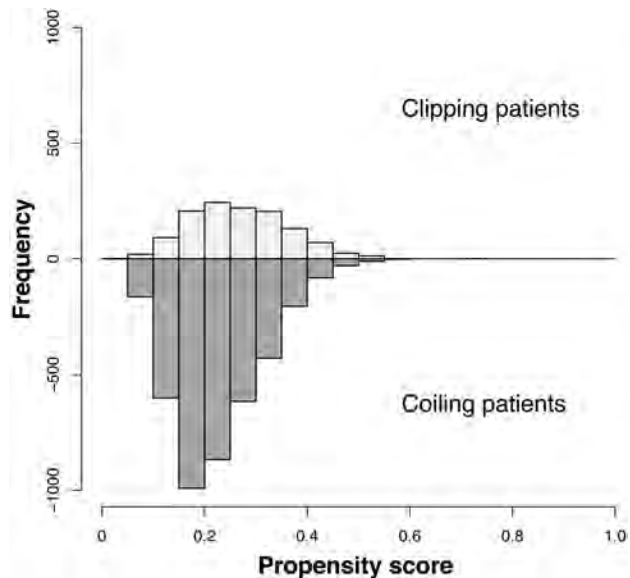


FIG 2. Distribution of propensity scores in the study population. Patients who underwent clipping are shown above the x-axis; patients who underwent coiling are shown below the x-axis.

Propensity Score–Adjusted Characteristics

The distribution of unmatched propensity scores for the clipping and coiling groups is shown in Fig 2. Propensity score distributions were very similar between clipping and coiling groups. After 1:1 matching, 1227 patients treated with clipping and 1227 treated with coiling were matched on the basis of similarities in their demographic and clinical characteristics (Table 2). After matching, all covariates were statistically indistinguishable between the clipping and coiling groups.

Propensity Score–Adjusted Outcomes

Propensity score–adjusted outcome incidence rates and odds ratios are shown in Table 3. After 1:1 matching, the likelihood of in-hospital mortality was similar between the matched clipping and coiling groups (Table 3; OR = 0.94 [95% CI, 0.73–1.21], $P = .62$). There was, however, significantly more morbidity in patients treated with clipping compared with those treated with coiling, as reflected by an increased likelihood of discharge to long-term care (OR = 1.32 [95% CI, 1.12–1.56], $P = .0006$), ischemic complications (OR = 1.51 [95% CI, 1.24–1.83], $P = .0009$), postoperative neurologic complications (OR = 1.64 [95% CI, 1.18–2.27], $P = .0018$), and other postoperative surgical complications (OR = 1.55 [95% CI, 1.05–2.33], $P = .0240$). The likelihood of ventriculostomy, ventriculoperitoneal shunt surgery, or tracheostomy was similar between clipping and coiling groups.

Sensitivity Analysis

The Perspective data base lacks information on cerebral aneurysm size and location. We therefore examined how these and other unmeasured confounders could affect our findings through the use of a sensitivity analysis. This sensitivity analysis (Fig 3) examined the relationship between confounder prevalence in the clipping and coiling groups and the odds ratio of the confounder with respect to discharge to long-term care. For example, if the prevalence of an unmeasured confounder in the clipping group was

Table 2: Patient and hospital demographics of patients matched by propensity score

	Clipping	Coiling	P Value ^a
No. of patients	1227	1227	
Patients			
Age, y, median (IQR)	53 (45–62)	53 (45–63)	.19
Female, n (%)	814 (66)	798 (65)	.49
Race, n (%)			
White	741 (60)	740 (60)	.97
Black	193 (16)	196 (16)	.86
Hispanic	66 (5)	66 (5)	.99
Other	227 (19)	225 (18)	.92
Admission status, n (%)			
Elective	101 (8)	100 (8)	.94
Urgent	287 (23)	309 (25)	.27
Emergency	839 (68)	818 (67)	.31
Admission source, n (%)			
Nonmedical source	382 (30)	368 (31)	.52
Transfer from hospital/care facility	350 (29)	370 (30)	.35
Emergency department	469 (38)	458 (37)	.59
Clinic	26 (2)	31 (3)	.50
Charlson score	1 (1–2)	1 (1–2)	.34
Endovascular procedure			
Day of procedure (range)	2 (1–3)	2 (1–2)	.99
Hospital			
Region, n (%)			
Midwest	189 (15)	185 (15)	.81
South	576 (47)	568 (46)	.74
Northeast	266 (22)	257 (21)	.59
West	200 (16)	213 (17)	.47
No. of beds (range)	623 (439–725)	620 (440–683)	.85
Urban location vs rural, n (%)	1214 (99)	1213 (99)	.83
Teaching vs nonteaching, n (%)	817 (67)	811 (66)	.79

Note:—IQR indicates interquartile range.

^a P values derived from conditional logistic regression, controlling for paired data through conditional estimation.

15% (dashed vertical line) and 5% in the coiling group (light gray curve), the odds ratio of the confounder would need to be ~2.2 (point “A”) or higher to account for the significant differences observed in discharge to long-term care. If the prevalence of the confounder increased to 10% in the coiling group, the odds ratio would need to be ≥ 4.3 (point “B”) to account for the observed significant differences in Table 3. Estimates from the Prospective Registry of Subarachnoid Aneurysms Treatment (PRESAT) trial showed that the treatment frequency of large aneurysms was similar between clipping and coiling groups, whereas coiling was preferentially used in posterior circulation aneurysms compared with clipping (22.5% versus 4.5%).¹⁶ On the basis of these differences, the confounder odds ratio required to nullify the observed differences in discharge to long-term care approaches infinity because of the asymptotic nature of this function. Given these results, the other measured outcomes would not be affected by treatment disparities in aneurysm size or location.

DISCUSSION

Our analysis of a large sample of the US population treated for ruptured aneurysm from 2006–2011 found an increasing trend in the proportion of aneurysms treated by coiling versus surgical clipping. After propensity score adjustment, patients treated with coiling and those treated with clipping had a similar likelihood of in-hospital mortality, but patients treated with clipping demonstrated an increased likelihood of morbidity, as defined by discharge

to long-term care facilities, ischemic complications, and other postoperative complications, as compared with patients treated with coiling. These results suggest that surgical clipping of ruptured aneurysms generally results in a higher peri-procedural risk of morbidity compared with coiling.

Our findings offer substantial advances over previous corroborating retrospective studies that demonstrated worse outcomes after clipping as compared with coiling.^{8,9} First, we performed propensity score adjustment by use of numerous patient and hospital covariates to minimize the impact of selection bias on the observed treatment outcomes. Second, we performed a sensitivity analysis to measure the effect of a possible unmeasured confounder on our results. Finally, the Perspective data base contains hospitalizations through 2011, enabling an examination of more current clinical practices and patient outcomes compared with these previous studies.

Compared with our study that demonstrated a 5% lower risk of death or discharge to long-term care in the coiling cohort compared with the clipping cohort, the ISAT investigators found a 10.8% decrease in absolute risk of death or dependency at 2 months in the coiling cohort compared with the clipping cohort.¹ The

more favorable results from the ISAT study probably can be explained by their exclusion of patients with more guarded initial clinical presentations that probably would put them at higher risk for peri-procedural morbidity and mortality. In contrast, a propensity score–adjusted Canadian study of clipping versus coiling of ruptured intracranial aneurysms treated between 1995–2004 concluded that coiling increased the risk of death or subsequent readmission for SAH (hazard ratio = 1.25 [95% CI, 1.00–1.55], $P = .04$).⁶ Despite somewhat dissimilar end points, the results of this study led the authors to question the generalizability of the ISAT results. However, the Ontario study was performed at an earlier stage in the development of endovascular coiling compared with ISAT, which may explain the worse outcomes with coiling.

A study of the Nationwide Inpatient Sample by Qureshi et al⁵ reported different findings in the United States, demonstrating that the in-hospital mortality rates for SAH admissions decreased from 27–24% ($P = .003$) before and after publication of the ISAT results. These observed improvements in outcome probably are a result of multiple factors including shifts in treatment to higher-volume centers,¹⁷ increased operator experience in treating aneurysms with coiling, and technical and procedural improvements that have increased the percentage of aneurysms that are amenable to endovascular coiling.¹⁸ Additionally, the frequency of coiling increased from 8% in the 3 years before publication of ISAT to

Table 3: Patient outcomes after 1:1 matching by propensity score

	Incidence in Clipping	Incidence in Coiling	OR ^a (95% CI)	P Value
In-hospital mortality	146/1227 (12%)	154/1227 (13%)	0.94 (0.73–1.21)	.62
Discharge to long-term care	520/1227 (42%)	438/1227 (36%)	1.32 (1.12–1.56)	.0006
Ischemic complications ^b	331/1227 (27%)	256/1227 (21%)	1.51 (1.24–1.83)	.0009
Hydrocephalus	445/1227 (36%)	500/1227 (41%)	0.83 (0.70–0.98)	.0210
Postop neuro complications	109/1227 (9%)	69/1227 (6%)	1.64 (1.18–2.27)	.0018
Other postop surgical complications	70/1227 (6%)	46/1227 (4%)	1.55 (1.05–2.33)	.0240
Ventriculostomy	462/1227 (38%)	457/1227 (37%)	1.02 (0.86–1.20)	.84
Ventriculoperitoneal shunt surgery	148/1227 (12%)	174/1227 (14%)	0.83 (0.65–1.06)	.11
Tracheostomy	159/1227 (13%)	157/1227 (13%)	1.01 (0.80–1.29)	.90

Note:—Postop indicates postoperative.

^a Odds ratio of clipping versus coiling.

^b Defined as aphasia, hemiplegia, or paraplegia or cerebral artery occlusion not present at admission.

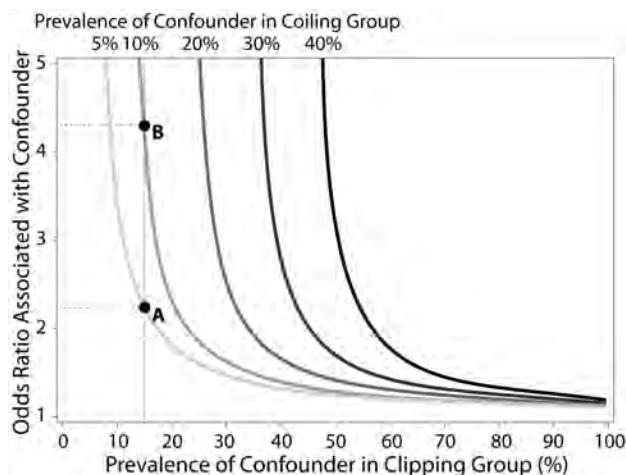


FIG 3. Sensitivity analysis of unmeasured confounders. Sensitivity analysis was performed by use of the lower 95% confidence interval of the odds ratio of discharge to long-term care (1.12). The x-axis represents the hypothetical prevalence of an unmeasured confounder in the clipping group; y-axis represents the hypothetical odds ratio associated with this unmeasured confounder. Curved lines represent the required strength of unmeasured confounder (defined by odds ratio[s]) that would be required to nullify the observed differences in discharge to long-term care between treated groups at selected confounder prevalence rates within the coiling group (5%, 10%, 20%, 30%, and 40%). For a given prevalence within the coiling group, a single unmeasured confounder could potentially nullify significant differences in study outcomes if the data point representing associated odds ratio and clipping prevalence is on or above the depicted curve. Point A depicts an example of a confounder with a prevalence of 15% in the clipping group and 5% in the coiling group; in this case, an odds ratio of approximately 2.2 is needed to nullify the significant difference in discharge to long-term care. If the prevalence of the same confounder increased to 10% in the coiling group, an odds ratio of approximately 4.3 (point B) would be needed to nullify the significant difference.

43% in the following 3 years. These results suggest that the incorporation of ISAT results into practice had a favorable impact on mortality. The randomized Barrow Ruptured Aneurysm Trial (BRAT)¹⁹ provides further evidence to support a shift toward coiling. A poor outcome with death or disability (modified Rankin score >2) at 1 year occurred in 33.7% of the patients assigned to clipping and in 23.2% of the patients assigned to coiling ($P = .02$). Although most aneurysms randomized to the coil treatment arm in BRAT were treated by coiling, a substantial number crossed over to clipping, which indicates that surgery continues to be an important therapeutic option in many patients.

The increasing proportion of patients with ruptured aneurysm treated with coiling relative to clipping probably reflects how physicians are incorporating the evolving literature into their practice. Despite public debate over the results of the ISAT trial, neurosurgeons are increasingly referring patients with SAH for endovascular coiling instead of clipping. However, because it is possible that an overly aggressive application of coil embolization could result in a higher complication rate that would offset the benefits of coiling demonstrated in ISAT and BRAT, it is essential that high-quality surgical clipping be available as a complementary treatment option for ruptured cerebral aneurysms. Ideally, ruptured intracranial aneurysms would be treated in centers offering high-quality treatment with open surgical as well as endovascular techniques. The balance between clipping and coiling will vary somewhat between centers, depending on local expertise, and may shift as we learn more about the relative strengths of clipping versus coiling for specific clinical scenarios.

Intracranial aneurysm size and location are important clinical variables used to guide treatment decisions but are not available in the Perspective data base. Because the distributions of aneurysm location and size are expected to differ in the clipping and coiling cohorts, these variables represent potentially important unmeasured confounders. The Hunt and Hess Scale and the Glasgow Coma Scale were also not present in the Perspective data base and also represent potential confounders. If the distribution of these variables were sufficiently disparate between cohorts and were associated with an unfavorable outcome, such an unmeasured confounder could potentially account for the more favorable outcomes observed in the coiling group. Data from the PRESAT trial provide reasonable estimates of the disparities in ruptured aneurysm size and location for patients treated with clipping versus coiling. Given the observed prevalence rates of aneurysm size and distribution in coiling and clipping cohorts, neither variable is a sufficiently powerful unmeasured confounder to nullify the observed differences in discharge to long-term care. However, if other confounders such as a poor Glasgow Coma Scale were present at a substantially higher prevalence in the clipping group (eg, >4-fold), they might be able to account for our findings.

Our study has several additional limitations. First, because patients were not randomly assigned to clipping or coiling in our retrospective analysis of the Perspective data base, selection bias may exist. Although propensity score adjustment minimized differences between the clipping and coiling patient groups, other unmeasured variables not contained within the data base, such as

clinical presentation, may exist and contribute to selection bias. A randomized trial would be necessary to definitively assess the efficacy of treatment of unruptured cerebral aneurysms. Second, coding inaccuracies are known to occur within administrative data bases.²⁰ Such inaccuracies, however, are expected to occur randomly with equal prevalence in both clipping and coiling groups. Third, whereas we intentionally excluded complications that were present on admission to only examine complications that occurred during hospitalization, it is possible that some complications were coded incorrectly and occurred independently of clipping or coiling treatment. Finally, long-term outcomes cannot be evaluated in the Perspective data base. However, because the ISAT study demonstrated that 2-month outcomes were reasonably predictive of 1-year outcomes,²¹ shorter-term outcomes are reasonable surrogate markers for long-term outcomes. Conversely, it might be argued that a higher recurrence rate associated with coiling relative to clipping could result in hemorrhages and/or retreatment procedures that negate some of the improved outcome during initial hospitalization. The results of ISAT,²² the CARAT (Cerebral Aneurysm Rerupture After Treatment)²³ study, and BRAT¹⁹ demonstrate that it is extremely unlikely that the initial treatment benefit of endovascular coil embolization could be overshadowed by delayed hemorrhages or complications of retreatment.

CONCLUSIONS

In patients presenting to a large group of US hospitals with ruptured cerebral aneurysms between 2006–2011, surgical clipping was associated with significantly greater morbidity risk than endovascular coiling but with similar in-hospital mortality. Our evaluation of the Perspective data is by no means a randomized study but rather a retrospective look at outcomes on the basis of prevailing practices. Observational data from large clinical data bases can complement the findings of prospective clinical trials because the data base may better reflect real-world practice.

Disclosures: Jennifer S. McDonald—UNRELATED: Grants/Grants Pending: GE Healthcare.* David F. Kallmes—UNRELATED: Consultancy: Medtronic,* ev3,* Codman,* GE.* Comments: Clinical trials planning and implementation, Core Lab services, Cost-effectiveness assessment; Grants/Grants Pending: MicroVention,* Sequent,* Micrus,* Benvenue*; Royalties: UVA Patent Foundation, Comments: Spine Fusion; Travel/Accommodations/Meeting Expenses Unrelated to Activities Listed: MicroVention.* Giuseppe Lanzino—UNRELATED: Consultancy: ev3/Covidien.* Harry J. Cloft—UNRELATED: Grants/Grants Pending: Cordis Endovascular* (*money paid to institution).

REFERENCES

- Molyneux AJ, Kerr RS, Yu LM, et al. **International subarachnoid aneurysm trial (ISAT) of neurosurgical clipping versus endovascular coiling in 2143 patients with ruptured intracranial aneurysms: a randomised comparison of effects on survival, dependency, seizures, rebleeding, subgroups, and aneurysm occlusion.** *Lancet* 2005;366:809–17
- Molyneux A, Kerr R, Stratton I, et al. **International subarachnoid aneurysm trial (ISAT) of neurosurgical clipping versus endovascular coiling in 2143 patients with ruptured intracranial aneurysms: a randomised trial.** *Lancet* 2002;360:1267–74
- Nichols DA, Brown RD Jr, Meyer FB. **Coils or clips in subarachnoid haemorrhage?** *Lancet* 2002;360:1262–63
- Klompshouwer EG, Dings JT, van Oostenbrugge RJ, et al. **Single-center experience of surgical and endovascular treatment of ruptured intracranial aneurysms.** *AJNR Am J Neuroradiol* 2011;32:570–75
- Qureshi AI, Vazquez G, Tariq N, et al. **Impact of international subarachnoid aneurysm trial results on treatment of ruptured intracranial aneurysms in the United States.** *J Neurosurg* 2011;114:834–41
- O’Kelly CJ, Kulkarni AV, Austin PC, et al. **The impact of therapeutic modality on outcomes following repair of ruptured intracranial aneurysms: an administrative data analysis.** *J Neurosurg* 2010;113:795–801
- Gnanalingham KK, Apostolopoulos V, Barazi S, et al. **The impact of the international subarachnoid aneurysm trial (ISAT) on the management of aneurysmal subarachnoid haemorrhage in a neurosurgical unit in the UK.** *Clin Neurol Neurosurg* 2006;108:117–23
- Dumont AS, Crowley RW, Monteith SJ, et al. **Endovascular treatment or neurosurgical clipping of ruptured intracranial aneurysms: effect on angiographic vasospasm, delayed ischemic neurological deficit, cerebral infarction, and clinical outcome.** *Stroke* 2010;41:2519–24
- Hoh BL, Chi YY, Lawson MF, et al. **Length of stay and total hospital charges of clipping versus coiling for ruptured and unruptured adult cerebral aneurysms in the Nationwide Inpatient Sample database 2002 to 2006.** *Stroke* 2010;41:337–42
- Cowan JA Jr, Ziewacz J, Dimick JB, et al. **Use of endovascular coil embolization and surgical clip occlusion for cerebral artery aneurysms.** *J Neurosurg* 2007;107:530–35
- Premier Research Services. **Premier Perspective Database.** Charlotte, North Carolina: 2012
- Ho DE, Imai K, King G, et al. **MatchIt: Nonparametric Preprocessing for Parametric Causal Inference.** 2011. <http://gking.harvard.edu/matchit>. Accessed June 11, 2013.
- McDonald RJ, McDonald JS, Bida JP, et al. **Intravenous contrast induced nephropathy: causal or coincident phenomenon?** *Radiology* 2013;267:106–18
- Quan H, Sundararajan V, Halfon P, et al. **Coding algorithms for defining comorbidities in ICD-9-CM and ICD-10 administrative data.** *Med Care* 2005;43:1130–39
- Lin DY, Psaty BM, Kronmal RA. **Assessing the sensitivity of regression results to unmeasured confounders in observational studies.** *Biometrics* 1998;54:948–63
- Taki W, Sakai N, Suzuki H. **Determinants of poor outcome after aneurysmal subarachnoid hemorrhage when both clipping and coiling are available: Prospective Registry of Subarachnoid Aneurysms Treatment (PRESAT) in Japan.** *World Neurosurg* 2011;76:437–45
- Leake CB, Brinjikji W, Kallmes DF, et al. **Increasing treatment of ruptured cerebral aneurysms at high-volume centers in the United States.** *J Neurosurg* 2011;115:1179–83
- Coley S, Sneade M, Clarke A, et al. **Cerecye coil trial: procedural safety and clinical outcomes in patients with ruptured and unruptured intracranial aneurysms.** *AJNR Am J Neuroradiol* 2012;33:474–80
- McDougall CG, Spetzler RF, Zabramski JM, et al. **The Barrow ruptured aneurysm trial.** *J Neurosurg* 2012;116:135–44
- Berthelsen CL. **Evaluation of coding data quality of the HCUP National Inpatient Sample.** *Top Health Inf Manage* 2000;21:10–23
- Molyneux AJ, Kerr R, Langham J, et al. **Applicability of coiling for subarachnoid haemorrhage.** *Lancet* 2005;366:1924
- Molyneux AJ, Kerr RS, Birks J, et al. **Risk of recurrent subarachnoid haemorrhage, death, or dependence and standardised mortality ratios after clipping or coiling of an intracranial aneurysm in the international subarachnoid aneurysm trial (ISAT): long-term follow-up.** *Lancet Neurol* 2009;8:427–33
- Johnston SC, Dowd CF, Higashida RT, et al. **Predictors of rehemorrhage after treatment of ruptured intracranial aneurysms: the cerebral aneurysm rerupture after treatment (CARAT) study.** *Stroke* 2008;39:120–25

Diffusion-Weighted Imaging of Orbital Masses: Multi-Institutional Data Support a 2-ADC Threshold Model to Categorize Lesions as Benign, Malignant, or Indeterminate

A.R. Sepahdari, L.S. Politi, V.K. Aakalu, H.J. Kim, and A.A.K. Abdel Razek



ABSTRACT

BACKGROUND AND PURPOSE: DWI has been increasingly used to characterize orbital masses and provides quantitative information in the form of the ADC, but studies of DWI of orbital masses have shown a range of reported sensitivities, specificities, and optimal threshold ADC values for distinguishing benign from malignant lesions. Our goal was to determine the optimal use of DWI for imaging orbital masses through aggregation of data from multiple centers.

MATERIALS AND METHODS: Source data from 3 previous studies of orbital mass DWI were aggregated, and additional published data points were gathered. Receiver operating characteristic analysis was performed to determine the sensitivity, specificity, and optimal ADC thresholds for distinguishing benign from malignant masses.

RESULTS: There was no single ADC threshold that characterized orbital masses as benign or malignant with high sensitivity and specificity. An ADC of less than $0.93 \times 10^{-3} \text{ mm}^2/\text{s}$ was more than 90% specific for malignancy, and an ADC of less than $1.35 \times 10^{-3} \text{ mm}^2/\text{s}$ was more than 90% sensitive for malignancy. With these 2 thresholds, 33% of this cohort could be characterized as “likely malignant,” 29% as “likely benign,” and 38% as “indeterminate.”

CONCLUSIONS: No single ADC threshold is highly sensitive and specific for characterizing orbital masses as benign or malignant. If we used 2 thresholds to divide these lesions into 3 categories, however, a majority of orbital masses can be characterized with >90% confidence.

ABBREVIATIONS: ROC = receiver operating characteristic analysis

Orbital space-occupying lesions represent a heterogeneous group that includes benign tumors, malignant tumors, inflammatory lesions, vascular lesions, and infections.¹ Frequent nonclassic clinical presentations, challenging pathologic evaluation, and risks associated with biopsy are strong reasons to develop better noninvasive diagnostic and imaging tools for orbital disease.

Imaging with CT and MR can be helpful in establishing a diagnosis through demonstration of characteristic patterns of ana-

tomic involvement and through features such as CT attenuation, MR imaging signal intensity, and pattern of contrast enhancement.²⁻⁹ Nevertheless, imaging is frequently nonspecific, and significant room for improvement remains in imaging diagnosis.

DWI has been increasingly used to characterize solid masses in the head and neck, aiding in the distinction of benign and malignant lesions.¹⁰ Several retrospective studies have characterized orbital masses with DWI, and some have attempted to determine optimal quantitative ADC thresholds and their sensitivity and specificity in distinguishing malignant from benign lesions.¹¹⁻¹⁸ These studies have shown somewhat conflicting results and have been limited by single-institution designs and potential selection bias inherent to their patient populations. Specifically, some studies have suggested that a single ADC threshold can be both highly sensitive and specific for predicting malignancy,¹⁶ whereas other results have contradicted this statement.^{11,14}

To resolve these outstanding conflicts, we performed an analysis of aggregated data by using all available published data points on the DWI of orbital masses, including aggregated source data from the 3 largest published case series on this topic.^{14,16,17} The

Received January 23, 2013; accepted after revision April 9.

From the Department of Radiological Sciences (A.R.S., H.J.K.), David Geffen School of Medicine, University of California, Los Angeles, Los Angeles, California; Department of Neuroradiology (L.S.P.), San Raffaele Institute of Science, Milan, Italy; Department of Ophthalmology and Visual Sciences (V.K.A.), University of Illinois at Chicago, Chicago, Illinois; and Diagnostic Radiology Department (A.A.K.A.R.), Mansoura Faculty of Medicine, Mansoura, Egypt.

No conflicting relationship exists for any author.

Please address correspondence to Ali R. Sepahdari, MD, 757 Westwood Plaza, Suite 1621D, Los Angeles, CA 90095; e-mail: asephdari@mednet.ucla.edu; ali.sephdari@gmail.com

Indicates article with supplemental on-line table.

<http://dx.doi.org/10.3174/ajnr.A3619>

purpose of this study was to better determine what ADC thresholds can be used to predict either benign or malignant histology with high confidence.

MATERIALS AND METHODS

Review of Published Literature

To conduct an initial meta-analysis, the lead author (A.R.S.) performed a MEDLINE search to identify published data on the DWI of orbital masses. The search strings included “orbit” OR “orbital” AND “DWI” OR “diffusion-weighted,” as well as “head and neck” AND “DWI” OR “diffusion-weighted.” One hundred forty-three results were obtained, as of February 2013. These were reviewed, and studies that did not describe the DWI of orbital space-occupying lesions were excluded, leaving 11 studies. Studies of exclusively intraocular tumors and of demyelinating optic neuritis were excluded in this process. Of these 11, one was excluded because its data were wholly duplicated in a more expansive follow-up study from the same authors. The remaining 10 studies, which described 260 orbital masses, were further analyzed.^{11,12,14,16,17,19-23} The lesions described in each of these studies were characterized as either lymphoma, metastasis, nonlymphomatous primary malignancy, benign mass, inflammatory disease, vascular malformation, or infection. The distribution of lesions across the studies is summarized in the On-line Table.

The review of the literature revealed only 2 studies that reported sufficient quantitative metrics (sensitivity, specificity, positive predictive value, negative predictive value) to permit meta-analysis, both from this study’s authors.^{14,16} It was not possible to reconstruct these data from the published results of the other studies, either because of a small sample size or the way the data were summarized. In place of a meta-analysis, we attempted to aggregate as many raw data points as could be obtained on the basis of source data from the study authors’ previous works and ADC values of individual tumors that could be obtained from the literature. All tumors with reported ADC values were included. In some cases, multiple lesions with the same diagnosis were reported as an average and SD of the group. These data were excluded from further analysis because it was impossible to incorporate them into the receiver operating characteristic analysis (ROC). To assess for a systematic bias in lesion distribution, we compared the distribution of lesions from the published data and from the final analysis group against historical data from the largest published series of orbital masses by Shields et al.¹ These data are summarized in Table 1.

Data Collection and Analysis

The de-identified data used in this study comprised source data from 3 previously published case series of orbital mass DWI by the authors of this study, consisting of ADC and corresponding clinical/pathologic diagnosis for 189 cases.^{14,16,17} These data were collected with the approval of the respective local institutional review boards/ethics committees, with technical methods as previously described.^{14,16,17} Thirteen additional orbital mass ADC values were obtained through review of the literature. In total, 98 benign lesions and 104 malignant masses were studied. The re-

Table 1: Distribution of lesions by category in published studies of DWI, analysis group of this study, and in the largest reported clinical series by Shields et al, 2004^a

	Pre-Exclusion		Shields et al, 2004
	Published Data of Orbital DWI	Final Analysis Group	
Lymphoma	57	46	123
Metastasis	21	20	91
Malignant primary	50	38	219
Benign primary	51	27	182
Inflammatory	48	39	193
Vasculogenic	25	24	169
Infection	8	8	13

^a Any lesions from the Shields et al¹ series that were likely to be excluded in studies of orbital DWI were removed. Capillary hemangioma was categorized as a benign primary tumor, reflecting current understanding. Nonmalignant lymphocytic or histiocytic processes were categorized as inflammatory disease.

maining 58 cases were excluded either because quantitative ADC analysis was not performed by the original authors or because the data were reported in a summarized fashion that did not allow the extraction of individual data points.

The data included DWI studies performed on MR imaging machines from different vendors, with different field strengths and different technical parameters. To determine the equivalence of the DWI techniques across institutions, we compared the most commonly occurring lesions across the authors’ source datasets with each other by using Kruskal-Wallis analysis. Lymphomas from the 3 source datasets (6, 32, and 6 tumors) and inflammatory lesions from the 3 source datasets (20, 13, and 6 lesions) were compared.

The data were then grouped into benign and malignant categories. For each of these categories, descriptive statistics, Student *t* tests, and ROC were performed. These analyses were performed for all lesions in aggregate and for the authors’ source datasets separately. Sensitivity and specificity of various ADC thresholds for distinguishing benign from malignant masses were determined.

Lymphoma and inflammatory lesions were also compared with each other separately because there is considerable clinical and radiologic overlap in these conditions. As mentioned above, descriptive statistics, Student *t* tests, and ROC were performed.

In consideration of the disproportionately large number of lymphoma lesions in our dataset, which may skew the results through characteristically low ADC, ROC was also performed, comparing benign lesions and malignant tumors, after excluding lymphomas.

RESULTS

Lesions Analyzed

The final analysis group consisted of 202 patients with 98 benign lesions and 104 malignant lesions. The most common benign lesions were inflammatory masses ($n = 39$), vascular lesions ($n = 24$), and optic nerve sheath meningiomas ($n = 11$). The most common malignant lesions were lymphoma ($n = 46$) and metastases ($n = 20$). The data are summarized in Table 2. The composition of the final analysis group of 202 subjects was similar to the composition of the 260 subjects imaged with DWI before exclusion of unavailable data points (Table 1 and Fig 1), though with a modest reduction in the proportion of benign primary lesions.

Both groups contained a larger proportion of lymphoma lesions than would be expected on the basis of available epidemiologic data.¹ When lymphomas were excluded, the composition of the pre-exclusion group, final analysis group, and the epidemiologic data was similar (Fig 1).

Validation of ADC across Techniques

There was no significant difference in the ADC of lymphoma across the authors' source datasets ($P = .98$). Likewise, there was no significant difference in ADC of inflammatory lesions across these datasets ($P = .42$). These data are summarized in Table 2.

Table 2: Summarized ADC values of commonly occurring lesions

Lesion (No.)	ADC ($10^{-3} \text{ mm}^2/\text{s}$) (mean \pm SD)	Range
Benign (98)	1.42 \pm 0.41	0.72–2.78
Inflammatory (39)	1.40 \pm 0.31	0.93–2.28
Cavernous hemangioma (ie, encapsulated venous malformation) (12)	1.23 \pm 0.20	0.73–1.44
Optic nerve sheath meningioma (11)	0.99 \pm 0.20	0.56–1.28
Other vascular (15)	1.58 \pm 0.40	0.98–2.26
Other benign (22)	1.67 \pm 0.51	1.00–2.78
Malignant (104)	0.90 \pm 0.37	0.34–2.08
Lymphoma (46)	0.66 \pm 0.09	0.44–0.91
Metastasis (20)	1.20 \pm 0.31	0.64–2.08
Rhabdomyosarcoma (12)	0.72 \pm 0.31	0.34–1.31
Carcinoma (9)	1.15 \pm 0.12	1.04–1.39
Other malignant (17)	1.19 \pm 0.47	0.34–2.12

Descriptive Characteristics

Benign lesions showed an ADC of $1.43 \pm 0.41 \times 10^{-3} \text{ mm}^2/\text{s}$ (mean). Malignant lesions showed ADC of $0.90 \pm 0.36 \times 10^{-3} \text{ mm}^2/\text{s}$ (Table 3). Figure 2 shows a scatterplot of lesion categories with corresponding ADCs. There were significant differences between benign and malignant lesions with respect to ADC ($P < .0001$), and these differences were visually apparent (Fig 3). Significant differences remained ($P < .0001$), even after exclusion of lymphomas.

ADC Performance in Distinguishing Benign from Malignant Lesions

The area under the ROC curve for aggregated data was 0.84. An ADC threshold of less than $0.93 \times 10^{-3} \text{ mm}^2/\text{s}$ resulted in a 60% sensitivity and 96% specificity for malignancy. A more lenient threshold of ADC less than $1.35 \times 10^{-3} \text{ mm}^2/\text{s}$ resulted in 90% sensitivity for malignancy, but only 49% specificity. When lymphomas were excluded, the area under the ROC curve dropped to 0.73. The $0.93 \times 10^{-3} \text{ mm}^2/\text{s}$ threshold resulted in only a 28% sensitivity for malignancy, with a 96% specificity. Figure 4 shows the ROC curve for distinguishing benign from malignant lesions. Table 4 shows the sensitivities and specificities of various ADC values for distinguishing benign from malignant lesions.

ADC Performance in Distinguishing Lymphoma from Inflammatory Disease

Lymphomas showed an ADC of $0.67 \pm 0.09 \times 10^{-3} \text{ mm}^2/\text{s}$. Inflammatory lesions showed an ADC of $1.40 \pm 0.31 \times 10^{-3} \text{ mm}^2/\text{s}$. There was no overlap between lymphoma and inflammatory lesions. Only 2 of 46 lymphomas had an ADC of greater than $0.8 \times 10^{-3} \text{ mm}^2/\text{s}$, which approached the range of the lowest ADC inflammatory lesions. An ADC threshold of less than $0.92 \times 10^{-3} \text{ mm}^2/\text{s}$ distinguished lymphoma from inflammation with 100% sensitivity (95% confidence interval, 92%–100%) and 100% specificity (95% confidence interval, 91%–100%).

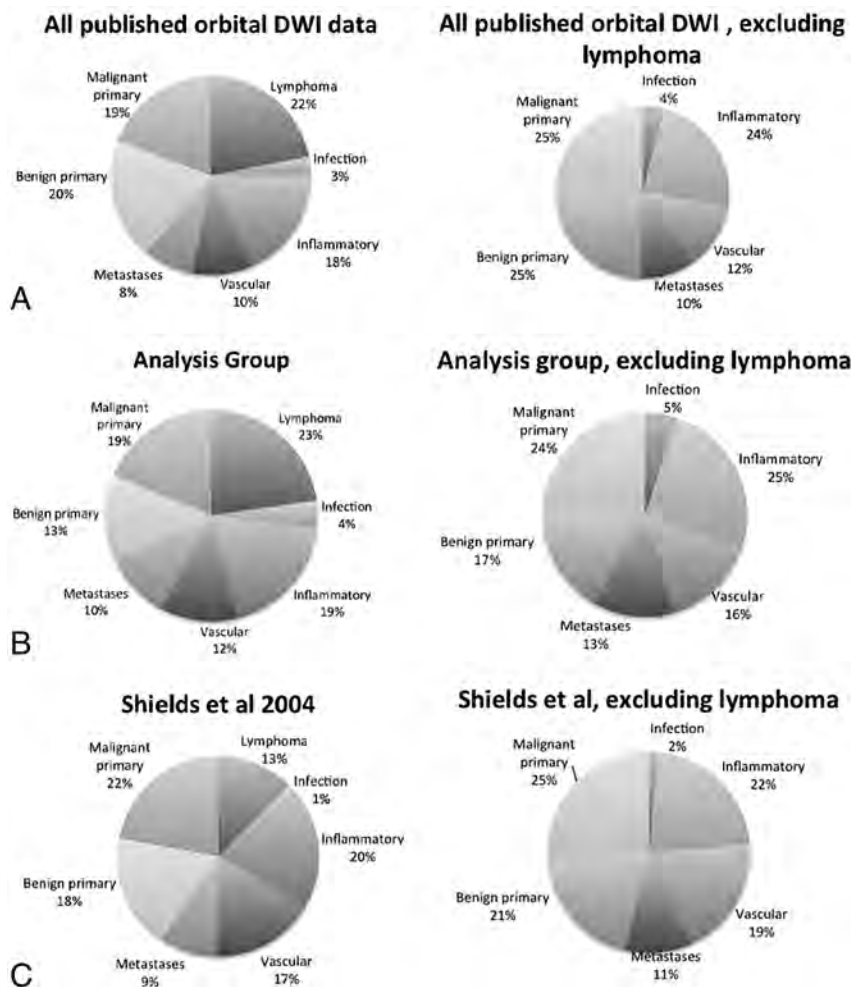


FIG 1. Lesion distribution by category. The left column shows the relative proportion of lesions encountered in all published studies of orbital DWI (A), in this analysis (B), and by Shields et al¹ during a 30-year period (C). The published literature and our analysis group contain a higher proportion of lymphoma cases than would be predicted by Shields et al. Otherwise, the relative proportion of lesions across these 3 groups is similar, as is seen after exclusion of lymphomas (right column).

Table 3: Descriptive statistics of orbital lesion ADC across the largest source datasets (ADC in units of $10^{-3} \text{ mm}^2/\text{s}$)

	All Lesions (n = 183)	Sepahdari et al ¹³ (n = 50)	Politi et al ¹⁷ (n = 90)	Razek et al ¹⁶ (n = 43)
Benign lesion ADC (mean, 95% CI)	1.42 ± 0.41 (1.34–1.51)	1.36 ± 0.41 (1.22–1.51)	1.39 ± 0.42 (1.25–1.54)	1.53 ± 0.35 (1.37–1.67)
Malignant lesion ADC (mean, 95% CI)	0.90 ± 0.37 (0.83–0.98)	1.02 ± 0.42 (0.80–1.24)	0.88 ± 0.36 (0.79–0.98)	0.80 ± 0.34 (0.65–0.95)
Lymphoma ADC (mean, 95% CI)	0.67 ± 0.09 (0.64–0.69)	0.69 ± 0.16 (0.58–0.86) ^a	0.67 ± 0.07 (0.60–0.75)	0.67 ± 0.07 (0.60–0.73) ^a
Inflammatory lesion ADC (mean, 95% CI)	1.40 ± 0.31 (1.30–1.50)	1.42 ± 0.37 (1.24–1.60)	1.45 ± 0.26 (1.29–1.60)	1.24 ± 0.13 (1.18–1.33) ^a
Area under ROC curve (95% CI)	0.84 (0.79–0.90)	0.74 (0.58–0.89)	0.86 (0.79–0.94)	0.95 (0.87–1.0)

^a The 25th–75th percentile range was reported due to a sample size too small to assume normal distribution.

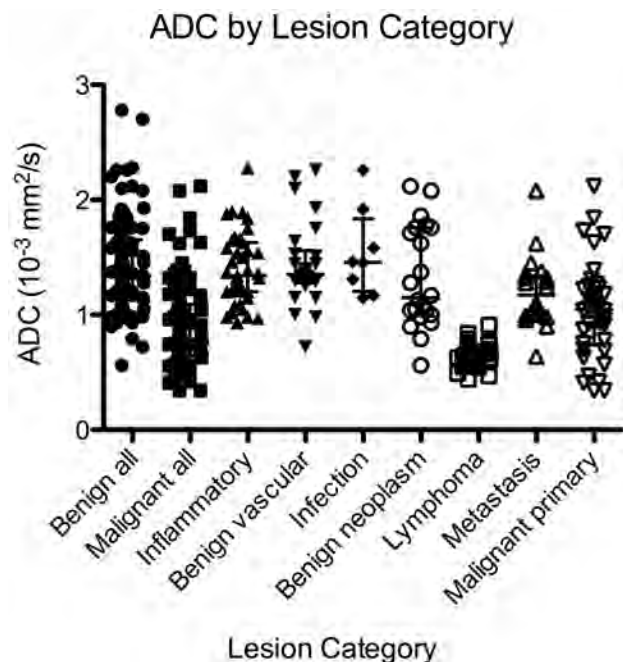


FIG 2. Scatterplot of ADC by lesion category shows consistently low ADC for lymphoma and a wide distribution of ADC for nonlymphoma malignancies.

DISCUSSION

This analysis showed that DWI produces equivalent quantitative ADC values across a variety of MR imaging scanners and techniques, a finding that is in concert with expectations based on previous investigation.²⁴ There were significant differences between benign and malignant lesions, though with notable overlap. ADC was highly accurate in distinguishing lymphoma from inflammatory disease.

Previous studies of orbital mass DWI have demonstrated its technical feasibility and potential clinical uses. These studies have conflicted somewhat in their results, however, and each has been limited by a retrospective, single-institution design. Therefore, the role of DWI in evaluating orbital masses remains unclear. Aggregating data from multiple institutions removes some of the selection bias inherent in the individual studies. Furthermore, this analysis verifies that quantitative ADC values are generalizable across a range of MR imaging scanners and techniques.

Previous studies have conflicted in their reports of the overall sensitivity and specificity of DWI for differentiating benign from malignant lesions and have conflicted slightly in their optimal ADC thresholds. Sepahdari et al¹⁴ reported an optimal threshold value of $1.0 \times 10^{-3} \text{ mm}^2/\text{s}$ for differentiating benign from malignant lesions, with an associated 63% sensitivity and 86% specificity. Razek et al¹⁶ reported an optimal threshold value of $1.15 \times 10^{-3} \text{ mm}^2/\text{s}$, with a sensitivity of 95% and specificity of 91%.

Politi et al¹⁷ did not specifically address the question of differentiating benign from malignant lesions, but they reported an ADC threshold of $0.775 \times 10^{-3} \text{ mm}^2/\text{s}$ for distinguishing lymphoma from nonlymphoma lesions with a 96% sensitivity and 93% specificity. Roshdy et al¹¹ did not attempt to calculate a threshold ADC value and associated sensitivity and specificity, but they did note overlap between benign and malignant lesions.

The results of this multi-institutional analysis indicate that there is no single ADC threshold that is both sensitive and specific for distinguishing benign from malignant lesions. On the basis of these results, we propose a 2-threshold model for characterizing orbital masses with DWI: 1) “likely malignant,” for lesions with a >90% probability of malignancy, based on an ADC less than $0.93 \times 10^{-3} \text{ mm}^2/\text{s}$ (33% of this cohort); 2) “likely benign,” for lesions with a >90% probability of benignity, based on an ADC greater than $1.35 \times 10^{-3} \text{ mm}^2/\text{s}$ (29% of this cohort); and 3) “indeterminate,” for lesions with ADCs between 0.93 and $1.35 \times 10^{-3} \text{ mm}^2/\text{s}$ (38% of this cohort).

In general, the optimal clinical use of DWI for evaluating an orbital mass will depend on the differential diagnosis dictated by other clinical and imaging data. For example, differentiation between lymphoma and atypical lymphocytic infiltrate or other orbital inflammatory diseases is a common diagnostic dilemma,⁸ for which DWI proves quite useful. On occasion, it can be difficult to distinguish an infantile hemangioma (capillary hemangioma) or a vascular malformation from a rhabdomyosarcoma in a pediatric patient,²⁵ another task for which DWI would seem well-suited.²¹ There are, however, tasks for which DWI may be limited. There was overlap in the ADC of optic nerve sheath meningioma and lymphoma, and DWI may also fail to distinguish these lesions in cases in which the imaging appearance and clinical findings overlap. The clinical and conventional imaging data should always be weighted appropriately when evaluating any single case, to ensure that the DWI information contributes to the analysis rather than detracting from it. In a practical setting, we believe that DWI is best used as a tool to further refine a short differential provided by the clinical presentation and the other imaging data.

There were 4 major limitations to this study. The first is that the data were acquired on multiple scanner types, with slight differences in acquisition technique and methods of measuring ADC. This feature is both a strength and a weakness of the study design. Although less technical standardization weakens the internal validity of the data, equivalent ADC values of similar lesions across multiple datasets suggest that quantitative ADC measurements are robust across multiple platforms. The second limitation is that some of the results may not be generalizable across all practices. The sensitivity, specificity, and accuracy of DWI in distinguishing benign from malignant lesions depend on the study population because there is heterogeneity in lesions. This study

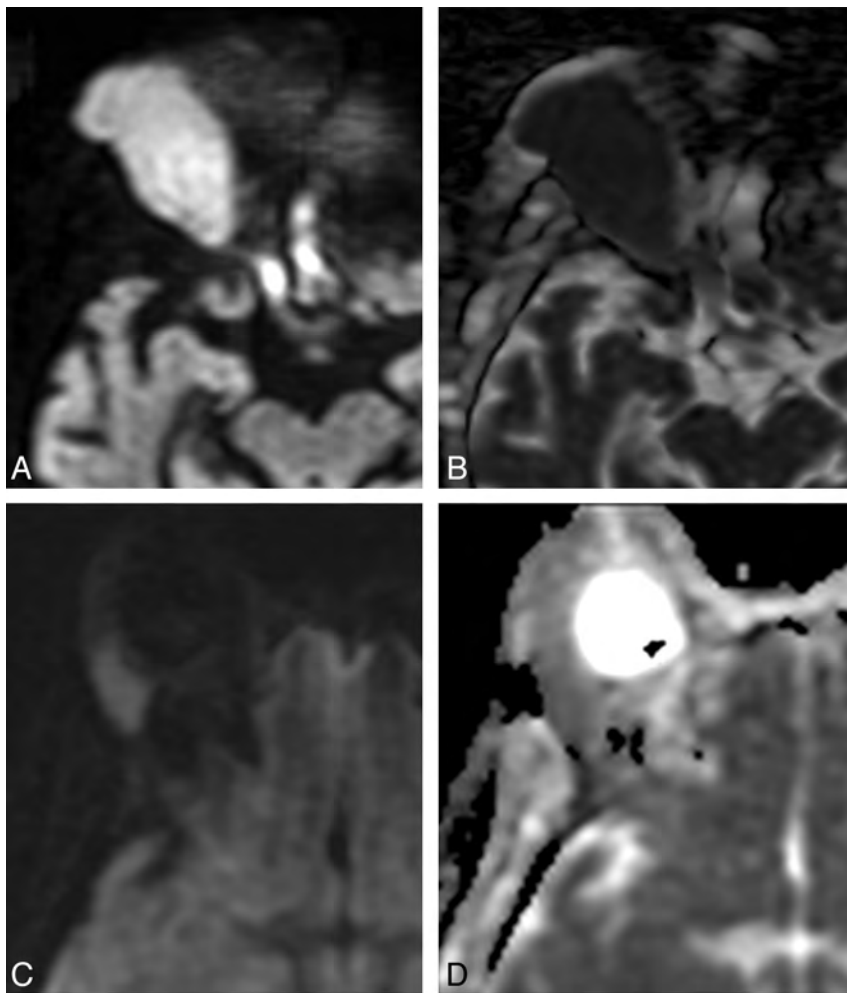


FIG 3. Comparison between orbital lymphoma (A and B) and orbital inflammatory disease (C and D). A, Axial DWI shows a right orbital mass with marked hyperintensity. B, Corresponding axial ADC map shows dark signal, indicating low ADC and hypercellularity typical of lymphoma. ADC of this lesion was $0.65 \times 10^{-3} \text{ mm}^2/\text{s}$. C, Axial DWI in a different patient shows a lacrimal gland mass with less intense signal compared with A. D, Corresponding axial ADC map shows intermediate signal, brighter than adjacent brain parenchyma, reflective of the lower cellularity seen in orbital inflammatory lesions. The ADC of this lesion was $1.09 \times 10^{-3} \text{ mm}^2/\text{s}$.

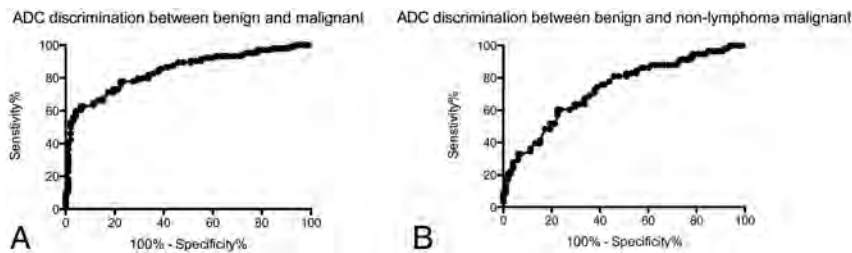


FIG 4. Receiver operating characteristic curve analysis of ADC for distinguishing benign from malignant masses (A) shows high specificities with increasing sensitivity up to 60%, at which point additional gains in sensitivity are offset by larger losses in specificity. When lymphomas are removed from the analysis (B), the performance of ADC diminishes.

includes a larger number of patients with lymphoma and a larger proportion of lymphomas compared with other malignancies than would be expected in an unselected group of patients based on available epidemiologic data.¹ This fact likely improves the observed sensitivity and specificity of DWI for distinguishing benign from malignant lesions, due to the characteristic very low

ADC of lymphoma. When lymphoma lesions were removed from the analysis, the ability of DWI to differentiate benign from malignant lesions dropped. Nevertheless, there were still significant differences between benign and malignant lesions.

The results of this ad hoc subgroup analysis should be interpreted cautiously because the removal of lymphoma lesions reduces the sample size and introduces other biases. A third limitation is the inability to quantify variability in ADC measurements. A degree of intraobserver and interobserver variability in the measurement of lesion ADC is expected, and a degree of scan-to-scan variation in ADC is also expected. Without the ability to quantify these factors, it can be difficult to interpret the results of a single ADC measurement in a single patient. Overall, the effect of measurement error between or within observers on a single scan has been shown to be small,²⁶ and the variability in ADC between different scanners is similarly small.²⁷

Finally, there are multiple areas of potential bias that could not be addressed by the study design. There may be a degree of selection bias within studies, with selective exclusion of some data points or publication bias related to exclusion of results that do not support a role for DWI. The exclusion of published studies for which ADC values could not be obtained could also affect the results. Note that 2 lymphomas and 3 rhabdomyosarcomas reported by Roshdy et al¹¹ showed higher average ADC than was observed in our group but were excluded because the ADC data were reported as an average. Specifically, Roshdy et al reported 2 lacrimal gland lymphomas whose average ADC overlapped that in the inflammatory lesions we observed. Our study may therefore overestimate the true performance of DWI in distinguishing lymphoma from inflammatory disease.

CONCLUSIONS

This analysis of multi-institutional data confirms that benign and malignant orbital tumors have significant differences in ADC. There was no single ADC threshold that was both highly sensitive and specific for predicting malignancy. On the basis of these results, we propose a “likely malignant” threshold ADC of $<0.93 \times 10^{-3} \text{ mm}^2/\text{s}$, a “likely benign” threshold ADC of $>1.35 \times 10^{-3} \text{ mm}^2/\text{s}$, and an “indeterminate range” ADC be-

Table 4: Sensitivity and specificity of various ADC threshold values for distinguishing benign from malignant lesions

ADC (10^{-3} mm ² /s)	Sensitivity (%)	Specificity (%)	Likelihood Ratio of Positive Results
0.72	40	99	39
0.82	54	97	17
0.93	60	96	14
1.03	67	85	4.3
1.13	77	77	3.4
1.23	80	66	2.3
1.33	89	54	1.8
1.42	92	41	1.6
1.52	93	34	1.4

tween 0.93 and 1.35×10^{-3} mm²/s when evaluating orbital masses with DWI. Knowledge of the expected ADC values of common lesions may also be helpful in organizing the differential diagnosis determined by other clinical and imaging data. DWI may be particularly helpful in distinguishing inflammatory disease from lymphoma.

ACKNOWLEDGEMENTS

We would like to thank Dr. Sahar M. Elkharnay, of King Khaled Eye Specialist Hospital and Mansoura University Faculty of Medicine, for providing data for this study.

REFERENCES

- Shields J, Shields C, Scartozzi R. Survey of 1264 patients with orbital tumors and simulating lesions. 1. The 2002 Montgomery Lecture, part 1. *Ophthalmology* 2004;111:997–1008
- Mafee M, Karimi A, Shah J, et al. Anatomy and pathology of the eye: role of MR imaging and CT. *Neuroimaging Clin North Am* 2005;15:23–47
- Mafee MF, Edward DP, Koeller KK, et al. Lacrimal gland tumors and simulating lesions: clinicopathologic and MR imaging features. *Radiol Clin North Am* 1999;37:219–39, xii
- Mafee MF, Goodwin J, Dorodi S. Optic nerve sheath meningiomas: role of MR imaging. *Radiol Clin North Am* 1999;37:37–58, ix
- Mafee MF, Dorodi S, Pai E. Sarcoidosis of the eye, orbit, and central nervous system: role of MR imaging. *Radiol Clin North Am* 1999;37:73–87, x.
- Valvassori GE, Sabnis SS, Mafee RF, et al. Imaging of orbital lymphoproliferative disorders. *Radiol Clin North Am* 1999;37:135–50, x–xi
- Carroll GS, Haik BG, Fleming JC, et al. Peripheral nerve tumors of the orbit. *Radiol Clin North Am* 1999;37:195–202, xi–xii
- Akansel G, Hendrix L, Erickson BA, et al. MRI patterns in orbital malignant lymphoma and atypical lymphocytic infiltrates. *Eur J Radiol* 2005;53:175–81
- Smoker WR, Gentry LR, Yee NK, et al. Vascular lesions of the orbit: more than meets the eye. *Radiographics* 2008;28:185–204, quiz 325
- Razek AA. Diffusion-weighted magnetic resonance imaging of head and neck. *J Comput Assist Tomogr* 2010;34:808–15

- Roshdy N, Shahin M, Kishk H, et al. MRI in diagnosis of orbital masses. *Curr Eye Res* 2010;35:986–91
- Kapur R, Sepahdari AR, Mafee MF, et al. MR imaging of orbital inflammatory syndrome, orbital cellulitis, and orbital lymphoid lesions: the role of diffusion-weighted imaging. *AJNR Am J Neuroradiol* 2009;30:64–70
- Sepahdari AR, Kapur R, Aakalu VK, et al. Diffusion-weighted imaging of malignant ocular masses: initial results and directions for further study. *AJNR Am J Neuroradiol* 2012;33:14–19
- Sepahdari AR, Aakalu VK, Setabutr P, et al. Indeterminate orbital masses: restricted diffusion at MR imaging with echo-planar diffusion-weighted imaging predicts malignancy. *Radiology* 2010;256:554–64
- Sepahdari AR, Aakalu VK, Kapur R, et al. MRI of orbital cellulitis and orbital abscess: the role of diffusion-weighted imaging. *AJR Am J Roentgenol* 2009;193:W244–50
- Razek AA, Elkharnay S, Mousa A. Differentiation between benign and malignant orbital tumors at 3-T diffusion MR-imaging. *Neuro-radiology* 2011;53:517–22
- Politi LS, Forghani R, Godi C, et al. Ocular adnexal lymphoma: diffusion-weighted MR imaging for differential diagnosis and therapeutic monitoring. *Radiology* 2010;256:565–74
- de Graaf P, Pouwels PJ, Rodjan F, et al. Single-shot turbo spin-echo diffusion-weighted imaging for retinoblastoma: initial experience. *AJNR Am J Neuroradiol* 2012;33:110–18
- Srinivasan A, Dvorak R, Perni K, et al. Differentiation of benign and malignant pathology in the head and neck using 3T apparent diffusion coefficient values: early experience. *AJNR Am J Neuroradiol* 2008;29:40–44
- Maeda M, Kato H, Sakuma H, et al. Usefulness of the apparent diffusion coefficient in line scan diffusion-weighted imaging for distinguishing between squamous cell carcinomas and malignant lymphomas of the head and neck. *AJNR Am J Neuroradiol* 2005;26:1186–92
- Lope LA, Hutcheson KA, Khademian ZP. Magnetic resonance imaging in the analysis of pediatric orbital tumors: utility of diffusion-weighted imaging. *J AAPOS* 2010;14:257–62
- Yang BT, Wang YZ, Dong JY, et al. MRI study of solitary fibrous tumor in the orbit. *AJR Am J Roentgenol* 2012;199:W506–11
- Kamano H, Noguchi T, Yoshiura T, et al. Intraorbital lobular capillary hemangioma (pyogenic granuloma). *Radiat Med* 2008;26:609–12
- Chenevert TL, Galbán CJ, Ivancevic MK, et al. Diffusion coefficient measurement using a temperature-controlled fluid for quality control in multicenter studies. *J Magn Reson Imaging* 2011;34:983–87
- Chung EM, Specht CS, Schroeder JW. From the archives of the AFIP: pediatric orbit tumors and tumorlike lesions: neuroepithelial lesions of the ocular globe and optic nerve. *Radiographics* 2007;27:1159–86
- Bilgili Y, Unal B. Effect of region of interest on interobserver variance in apparent diffusion coefficient measures. *AJNR Am J Neuroradiol* 2004;25:108–11
- Sasaki M, Yamada K, Watanabe Y, et al. Variability in absolute apparent diffusion coefficient values across different platforms may be substantial: a multivendor, multi-institutional comparison study. *Radiology* 2008;249:624–30

4D-CT for Preoperative Localization of Abnormal Parathyroid Glands in Patients with Hyperparathyroidism: Accuracy and Ability to Stratify Patients by Unilateral versus Bilateral Disease in Surgery-Naïve and Re-Exploration Patients

H.R. Kelly, L.M. Hamberg, and G.J. Hunter

ABSTRACT

BACKGROUND AND PURPOSE: 4D-CT is an emerging technique that uses high-resolution images, multiplanar reformats, and perfusion characteristics to identify abnormal parathyroid glands in patients with hyperparathyroidism. This study evaluates the accuracy of 4D-CT for localization and lateralization of abnormal parathyroid glands in preoperative planning for minimally invasive parathyroidectomy vs bilateral neck exploration at a tertiary referral center.

MATERIALS AND METHODS: Radiology, pathology, and operative reports were retrospectively reviewed for 208 patients with hyperparathyroidism who underwent 4D-CT and parathyroid surgery between May 2008 and January 2012. 4D-CT performance in localizing side and site was determined by use of surgical and pathologic findings as a reference.

RESULTS: Of 208 patients, 155 underwent initial surgery and 53 underwent re-exploration parathyroid surgery. No lesions were found in 8 patients (3.8%). A total of 284 lesions were found in 200 patients; 233 were correctly localized by 4D-CT (82.0%). Of the 200 patients with parathyroid lesions, 146 underwent unilateral and 54 bilateral neck exploration. 4D-CT correctly identified unilateral vs bilateral disease in 179 (89.5%) of 200. 4D-CT correctly localized parathyroid lesions in 126 of the unilateral cases (86.3%). In the re-exploration cohort, 4D-CT correctly identified unilateral vs bilateral disease in 46 (95.8%) of 48. There was no statistically significant difference in subgroups stratified by surgery type (primary or subsequent) and number of scan phases (3 or 4) ($P > .56$).

CONCLUSIONS: 4D-CT leverages modern high-resolution CT scanning and dynamic contrast enhancement to localize abnormal parathyroid glands in patients with hyperparathyroidism of any cause and can be used for planning minimally invasive parathyroidectomy vs bilateral neck exploration.

ABBREVIATIONS: EMR = electronic medical record; PPV = positive predictive value

Hyperparathyroidism is caused by overproduction of parathyroid hormone by a single adenoma, multigland hyperplasia or multiple adenomata. In primary hyperparathyroidism, a single adenoma is the cause in most cases (75%–85%), with multiple adenomas or multigland hyperplasia found in a smaller subset of patients (approximately 4% and 10%, respectively).^{1,2} In secondary and tertiary hyperparathyroidism, excess parathyroid hor-

mone is usually secreted by multiple hyperplastic glands.³ The only therapeutic option for complete cure of primary hyperparathyroidism is surgery, with reported success rates of greater than 95% for the reference standard of bilateral neck exploration performed by an experienced surgeon.⁴ Minimally invasive parathyroidectomy with a unilateral surgical approach is rapidly becoming the standard of care in an effort to lower complication rates, reduce costs, shorten hospital stays, and improve cosmetic results.⁴⁻⁶ Preoperative localization and lateralization of abnormal parathyroid glands are integral to the performance of unilateral minimally invasive parathyroidectomy.⁷ Preoperative imaging is also integral to operative planning in patients with recurrent hyperparathyroidism undergoing redo surgery.⁸ At most institutions, the current favored approach to preoperative imaging for hyperparathyroidism includes a combination of sonography and technetium Tc99m sestamibi scanning, with a reported combined sensitivity of 74%–95% for single-gland disease.⁸ However, the sensitivities reported for multigland disease and multiple adeno-

Received December 20, 2012; accepted after revision April 5, 2013.

From the Division of Diagnostic Neuroradiology (H.R.K., G.J.H.), Massachusetts General Hospital/Harvard Medical School, Boston, Massachusetts; Department of Radiology (H.R.K.), Massachusetts Eye and Ear Infirmary/Harvard Medical School, Boston, Massachusetts; and Department of Radiology (L.M.H.), Brigham and Women's Hospital/Harvard Medical School, Boston, Massachusetts.

Recipient of the Radiologist-In-Training Award for results previously presented in part at the Annual Meeting of the American Society of Head and Neck Radiology, September 2011; San Diego, California.

Please address correspondence to Hillary R. Kelly, MD, Massachusetts General Hospital, Division of Neuroradiology, 55 Fruit St, GRB-273A, Boston, MA 02114; e-mail: hkelly2@partners.org

<http://dx.doi.org/10.3174/ajnr.A3615>

mata are much lower, in the range of 15%–35% for sonography and 30%–44% for technetium Tc99m sestamibi.⁸

4D-CT has been proposed as an alternative or adjunctive method for preoperative localization of abnormal parathyroid glands in patients with primary hyperparathyroidism.^{9–13} Multiple recent studies have indicated that 4D-CT may be especially useful for preoperative localization in patients with negative or inconclusive results on sonography and technetium Tc99m sestamibi studies, reoperative parathyroid patients, patients with mild hypercalcemia, and in patients with multigland disease.^{14–18} However, previously published reports have predominantly evaluated cohorts with small numbers of patients and have focused on specific patient populations with strict exclusion criteria. One study with a large group of patients included only those with sporadic primary hyperparathyroidism who had a single adenoma identified by 4D-CT and were undergoing initial parathyroidectomy, excluding patients with multigland disease, prior surgery, concomitant thyroid disease, mediastinal ectopic parathyroid glands, and multiple endocrine neoplasia syndromes.¹²

The purpose of our study was to assess the accuracy of 4D-CT for localizing and characterizing the number of parathyroid adenomas and/or hyperplasia in a large group of unselected patients evaluated at a tertiary care center. Our hypothesis was that 4D-CT may be used to accurately predict the site and number of parathyroid lesions and thus allow planning for a minimally invasive, unilateral surgical approach vs a conventional bilateral neck exploration. Furthermore, we hypothesized that the accuracy of 4D-CT is not reduced in those patients who have undergone prior parathyroid surgery.

MATERIALS AND METHODS

Patients

This retrospective study was approved by our institutional review board, waiving consent in accordance with the Health Insurance Portability and Accountability Act. We began performing 4D-CT examinations at our institution in May 2008. Patients were included in the study if they carried a clinical and biochemical diagnosis of hyperparathyroidism, had 4D-CT for preoperative localization between May 2008 and July 2011, and subsequently underwent surgical exploration between May 2008 and January 2012. Inclusion criteria also included the availability of the operative report and final pathology report. Patient demographic data including age and sex were obtained from the electronic medical record (EMR).

CT Technique

Examinations were performed on a 16- or 64-multidetector row CT scanner (LightSpeed 16 Pro and Discovery CT750 HD; GE Healthcare, Milwaukee, Wisconsin) with use of the following standardized protocol. Patients were supine, head first in the scanner. The scanner manufacturer-supplied head holder was used for all scans. Patients' arms were extended caudally by use of manufacturer-supplied straps, specifically designed to reduce shoulder artifacts. Scanning extended from the carina to the maxillary teeth. Scanning parameters for each phase were 140 kVp, 180–300 mA by automatic exposure control (Auto-mA algorithm; GE Healthcare), 1-second rotation time, 1.375 pitch, a

0.625-mm detector configuration with a beam width of 10-mm for the 16-section scanner and 40 mm for the 64-section scanner, and 1.25-mm section thickness reconstructed at 1-mm centers. The first phase was acquired before the administration of intravenous contrast material. Iodinated contrast material (Isovue 370; Bracco Diagnostics, Princeton, New Jersey) was then administered at a dose of 100 mL at an infusion rate of 4 mL per second via an 18-gauge catheter, followed by 40 mL of saline at an infusion rate of 4 mL per second. The second phase was acquired 30 seconds after the start of intravenous contrast administration. A third delayed phase was acquired 30 seconds after the completion of the second phase (approximately 45–48 seconds after the start of the injection of contrast, depending on the length of the patient, table speed, and gantry rotation). For the examinations performed between May 2008 and June 9, 2010, a fourth "late-delayed" phase was acquired 45 seconds after the completion of the third "early delayed" phase. Only the initial 3 phases were acquired for all examinations performed between June 10, 2010, and June 2011.

Image Processing and Analysis

Standardized postprocessing was performed on all studies yielding multiplanar reformations, including a "true axial" plane parallel to the vocal cords, coronal, and sagittal planes orthogonal to the true axial plane, as well as bilateral anterior sagittal oblique planes parallel to the sternocleidomastoid muscles. All examinations and images were reviewed prospectively on a PACS workstation (Impax 5.3; Agfa HealthCare, Greenville, South Carolina) by a board-certified neuroradiologist (G.J.H.) with more than 17 years of experience and a Certificate of Added Qualification in neuroradiology. Additional 3D postprocessing, kinetic analysis, and volume-rendered images were also created and were reviewed as deemed necessary for image analysis by the interpreting neuroradiologist and/or as requested by the referring surgeon (Advantage Windows Workstation, ADW 4.2; GE Healthcare). A formal report was entered into the EMR for each study, with a detailed anatomic description of the location of the abnormal parathyroid lesion(s), if any were identified. Biochemical information, clinical history, and prior sonography and technetium Tc99m sestamibi imaging results (if available) were reviewed at the time of image interpretation.

Retrospective Review of Imaging Results

For each patient who met the criteria for inclusion into our study, the radiology report was retrieved from the EMR, and the side and anatomic location of the abnormal parathyroid lesion(s) were recorded by a neuroradiologist (H.R.K.) without knowledge of the operative findings. Localization of presumptive parathyroid lesions was with respect to the midline as defined by the trachea and was extended vertically into the mediastinum. Anatomic localization was refined by reference to the adjacent thyroid gland and the sternal notch or level of the clavicular heads. These landmarks are used by the surgeons to plan the correct access for adenoma resection. If the patient had prior surgery, any clips marking resected tissue were also used as reference points. When necessary and appropriate, additional reference points included the level of the carotid bifurcation, the hyoid bone, or mediastinal structures

such as the aortic arch and carina. No reinterpretation of the images was performed at the time of this retrospective review. The results of any prior sonography and technetium Tc99m sestamibi imaging were also retrieved from the EMR, and the side and anatomic location of the parathyroid lesion(s) were recorded as indicated in the official reports. In a typical setting, the anatomic location provided by sonography or technetium Tc99m sestamibi imaging was with respect to the thyroid gland.

Retrospective Review of Operative and Pathologic Results

The surgical findings, as recorded in the operative note in the EMR, were used as the reference standard for final anatomic location of parathyroid lesions. Surgical nomenclature for the location of abnormal tissue was with reference to the thyroid gland or, if the lesion was ectopic, with reference to mediastinal or hyoid structures as appropriate, and matched the classification used by the radiologists. The pathologic findings were used as the reference standard for a definitive diagnosis of abnormal parathyroid tissue. The operative and pathology reports were retrieved from the EMR, and the findings were recorded for each patient in a separate data base blinded to the imaging findings. The anatomic location, as labeled by the surgeon when submitted to pathology, was also recorded. If multiple lesions were identified and removed, all lesions were recorded. This data base was then merged with the imaging results. The 4D-CT, sonography, and/or technetium Tc99m sestamibi studies were recorded as concordant with the operative and pathologic results if a parathyroid lesion was removed from the same location (relative to anatomic landmarks) as predicted by that imaging study.

Statistical Analysis

Excel 2011 (Microsoft Corporation, Redmond, Washington) was used for all statistical analysis. Accuracy and positive predictive value (PPV) of localization were determined as the number of patients in whom each imaging technique correctly identified the anatomic location of the pathology-proven lesion(s), expressed as a percentage of the total number of abnormal parathyroid glands found and removed at surgery. In patients with multiple lesions, correct identification of the location of each lesion by the imaging study was required for it to be considered concordant with surgery and pathology. Patients with mediastinal lesions were included in the localization analysis. To evaluate any potential effect on the results because of the change in protocol from 4-phase to 3-phase, we repeated localization analyses with the patient cohort stratified by the 2 protocol subgroups. In these 2 subgroups, we undertook further stratification to distinguish between patients undergoing parathyroid surgery for the first time and those who had undergone prior parathyroid surgery. The Fisher exact test was used to test the null hypothesis of no difference between subgroups. A P value of $< .05$ was considered significant.

RESULTS

A total of 275 patients underwent 4D-CT scans in the study period. Of these, 67 did not proceed to surgery and were excluded from further evaluation. The remaining 208 patients all had radiologic, operative, and pathology reports available in the EMR and were analyzed. There were 30 men (mean age, 57.3 years;

median age, 57.5 years; age range, 21–82 years) and 178 women (mean age, 59.8 years; median age, 61 years; age range, 18–87 years).

There were 155 patients who underwent primary surgery. Of these, 90 had a 4-phase 4D-CT scan, and 65 patients underwent a 3-phase 4D-CT scan. In the 4-phase subgroup, 140 abnormal parathyroid glands were found at surgery in 89 patients, and 109 lesions were correctly localized with an accuracy of 77.9% (109/140). 4D-CT identified 18 potential lesions that were not adenomatous or hyperplastic, giving a PPV of 85.8% (109/127). In the 3-phase subgroup, 93 parathyroid lesions were found at surgery in 63 patients. A total of 81 lesions were correctly localized with an accuracy of 87.1% (81/93). 4D-CT identified 10 potential lesions that were not adenomas, giving a PPV of 89.0% (81/91). No significant difference was observed between these 2 populations ($P > .57$).

There were 53 patients who underwent a second surgery. Of these, 36 patients had a 4-phase 4D-CT scan and 17 patients underwent a 3-phase 4D-CT scan. In the 4-phase subgroup, 32 parathyroid lesions were found at surgery in 33 patients, and 27 lesions were correctly localized with an accuracy of 84.4% (27/32). 4D-CT identified 10 potential lesions that were not adenomas, giving a PPV of 73.0% (27/37). In the 3-phase subgroup, 19 parathyroid adenomas were found at surgery in 15 patients, and 16 lesions were correctly localized with an accuracy of 84.2% (16/19). 4D-CT identified 2 potential lesions that were not adenomas, giving a PPV of 88.9% (16/18). No significant difference was observed between these 2 populations ($P > .56$).

Stratification of the patients by surgery, but not by phase, also revealed no significant difference in the results obtained from the primary vs the repeated surgery data ($P > .65$). As no differences were identified among any of the subgroups, the data were pooled and the final results were 284 parathyroid adenomas identified at surgery in 200 patients. No lesions were identified in 8 patients (3.8%). Of the 284 lesions, 4D-CT correctly identified 233 (82.0%). In addition to the correctly identified lesions, 4D-CT indicated 40 potential lesions that were not found at surgery, were found to be normal glands, or were nonparathyroid structures such as exophytic thyroid nodules or lymph nodes (false-positive results) with a PPV of 85.3% (233/273).

Of the 200 patients in whom abnormal parathyroid tissue was found, 146 underwent unilateral neck exploration and 54 underwent bilateral neck exploration. 4D-CT correctly identified unilateral vs bilateral disease in 179 (89.5%) of these 200 patients, including the mediastinal lesions. In the 146 patients who underwent unilateral surgery, 4D-CT correctly identified the side and location of the abnormal gland(s) in 126 cases (86.3%). Considering the repeated surgery cohort separately, 4D-CT correctly discriminated between unilateral and bilateral disease in 46 (95.8%) of the 48 cases.

Preoperative technetium Tc99m sestamibi examination results were available in 167 of 200 patients with abnormal parathyroid tissue at surgery (140 who underwent primary parathyroidectomy; 27 who underwent re-exploration surgery). Technetium Tc99m sestamibi was concordant with the surgical findings in 45 (26.9%) of the 167 patients. In an additional 12 patients, technetium Tc99m sestamibi localized 1 lesion correctly but failed to

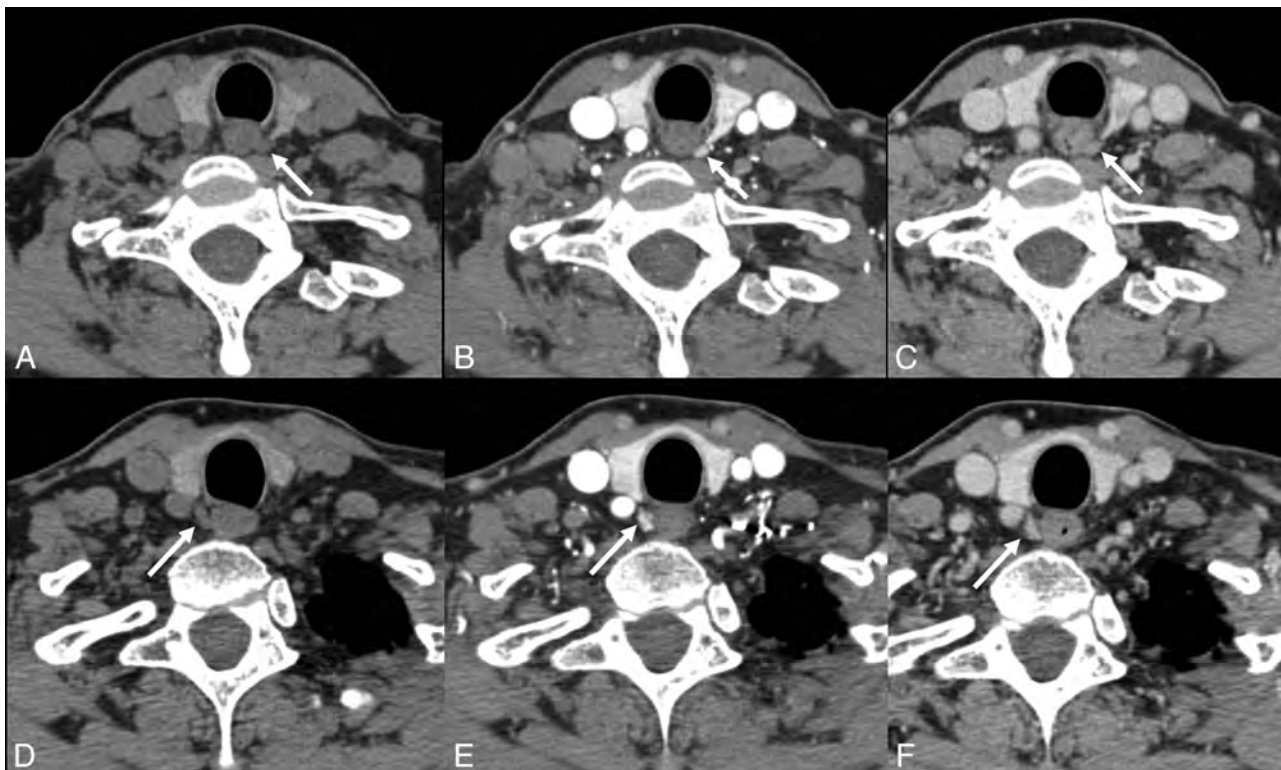


FIG 1. A 63-year-old woman with primary hyperparathyroidism. No lesions were identified on sonography or technetium Tc99m sestamibi. 4D-CT demonstrates avidly enhancing lesions in the orthotopic superior location (arrows) bilaterally with rapid washout of contrast greater than that of the adjacent thyroid gland (A and D: noncontrast phase; B and E: initial postcontrast “arterial” phase; C and F: delayed postcontrast phase). This patient underwent bilateral exploration, and bilateral superior parathyroid adenomas were found at surgery.

identify additional abnormal parathyroid lesions in the same patient. Technetium Tc99m sestamibi was discordant with the surgical and pathologic findings in 110 patients (65.9%).

Preoperative sonography examination results were available in 165 of 200 patients with abnormal parathyroid tissue at surgery (137 who underwent primary parathyroidectomy; 28 who underwent re-exploration surgery). Sonography was concordant with the surgical findings in 43 (26.1%) of 165 patients. In an additional 18 patients, sonography localized 1 lesion correctly but failed to identify additional abnormal parathyroid lesions, or suggested additional lesions that were not present at surgery. Sonography results were discordant with the surgical and pathologic findings in 104 patients (63%).

Abnormal parathyroid glands were identified correctly by both technetium Tc99m sestamibi and sonography in only 15 of the 208 patients. The 4D-CT and surgical findings were concordant with the technetium Tc99m sestamibi and sonography results in all 15 patients.

Fig 1 is an example of a case in which sonography and technetium Tc99m sestamibi results were negative, but 4D-CT correctly predicted bilateral disease and the locations of the abnormal parathyroid glands. Fig 2 is an example of a complicated case from the reoperative group in which 4D-CT correctly lateralized and localized the site of disease.

DISCUSSION

Unilateral minimally invasive parathyroidectomy has become increasingly used as the favored technique for treatment of hyper-

parathyroidism from any cause.^{6,7} Successful deployment of minimally invasive parathyroidectomy requires accurate information concerning the location of parathyroid lesions. If the preoperative localization studies indicate multigland or ectopic disease, minimally invasive parathyroidectomy may not be the correct choice, and a conventional bilateral neck exploration should be performed. In patients with no prior surgery and with only single-gland disease located in the neck, 4D-CT by use of a 4-phase protocol initially adopted at our institution has been reported to provide accuracy for localization of 93.7%.¹² In our study, a more heterogeneous group of patients has been considered, including those with multigland disease (including patients with secondary or tertiary hyperparathyroidism), those undergoing a second surgery because of persistent hyperparathyroidism, and those with parathyroid lesions in ectopic locations. Furthermore, protocols by use of 4- or 3-phase acquisition techniques have also been evaluated in these groups. Although there was variability in the localization accuracy in the subgroups, with the lowest accuracy seen in the 4-phase, primary surgery cohort (77.9%) and the highest accuracy in the 3-phase, primary surgery cohort (87.1%), statistical analysis indicated that all of the subgroups were equivalent ($P > .56$), with a pooled accuracy of 82%.

Arguably the most challenging patients are those with multigland and/or recurrent disease who are undergoing a second surgery. In this particular subgroup, localization accuracy was 84% in our study, whereas previous studies by other groups recorded accuracies of 88% and 73%^{16,14} in similar patient cohorts. Vari-

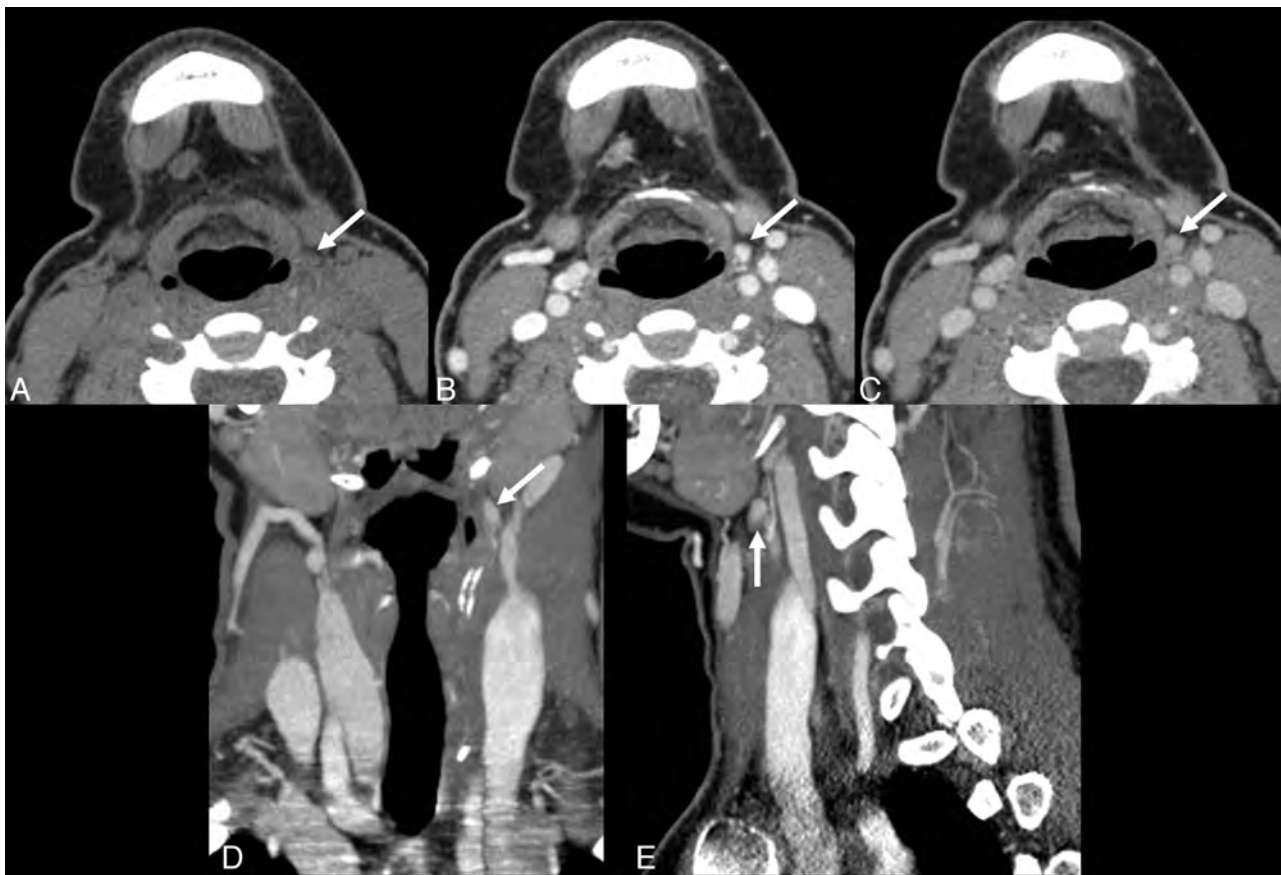


FIG 2. A 26-year-old woman with persistent primary hyperparathyroidism after undergoing a 7-hour neck exploratory procedure including the upper mediastinum and a left hemithyroidectomy, as the left inferior gland could not be found. 4D-CT demonstrates a small lesion high in the left neck at the level of the hyoid bone (arrows). Perfusion characteristics are suggestive of a parathyroid adenoma, with a lesion lower in attenuation than the thyroid gland on the initial noncontrast phase (A), and rapid uptake of contrast (B) and rapid washout of contrast (C), greater than that of the thyroid gland (*not shown*). (D: coronal reformatted image in the “arterial” phase; E: sagittal reformatted image in the “arterial” phase). At surgery, a parathyroid adenoma was found in the left carotid sheath, at the apex of ectopic thymic tissue, consistent with an undescended left inferior parathyroid gland.

ability in these results likely reflects the small numbers of patients studied: 48 in our group, 45 in the study by Mortenson et al,¹⁶ and 21 in the study by Lubitz et al.¹⁴ Although overall localization accuracy was 82%, discrimination between unilateral and bilateral disease in this cohort was successful in 46 (95.8%) of 48 patients. This improvement is important because surgery in the re-operative neck is often more difficult, and patients are at increased risk for significant morbidity.¹⁶ Improved preoperative localization and lateralization may prevent unnecessary dissection and complications.^{16,19}

In our patient population, neither sonography nor technetium Tc99m sestamibi scanning provided adequate localization. The success rate for localization by technetium Tc99m sestamibi and/or sonography was approximately 27% in our 200 unselected patients. This rate was markedly lower than that recorded in the literature.⁸ The low accuracies and rates of concordance of these primary localization methods in our cohort likely reflect the referral pattern of the endocrine surgeons in our practice. Deployment of 4D-CT is biased toward complex or difficult cases, ie, when sonography and/or technetium Tc99m sestamibi results are negative, or if the results of those 2 studies are discordant. Thus, our cohort consists of unselected, potentially complex patient cases, and this trend is reflected in lower identification rates com-

pared with the results from cohorts of relatively uncomplicated patient cases.^{12,13}

Many different protocols have been advocated in the literature for 4D-CT. These are typically 2-phase scans with imaging acquired only after contrast^{20,21} or imaging acquired both before and after contrast.¹¹ Assessment of such protocols demonstrates significantly lower rates of accuracy compared with our current 3-phase protocol (Hunter GJ, Ginat DT, Kelly HR, et al; unpublished data, 2013).

The change from a 4- to a 3-phase protocol was made to reduce the effective dose of a 4D-CT study from approximately 28 mSv to 21 mSv.¹² We believe the benefit of accurate localization represents a favorable risk-benefit ratio to patients needing surgery for hyperparathyroidism. The current 3-phase protocol balances the need for sufficient data against unnecessary phases. As our results demonstrate, the move from 4 to 3 phases has not decreased accuracy in localization but has decreased the effective dose. Further reduction to a 2- or single-phase study is likely to be counterproductive, as the decrease in effective dose (an indeterminate delayed risk) may result in a disproportionately greater decrease in accuracy of localization (an immediate benefit).

There were several limitations in this study. First, this study

was retrospective and could not prospectively address the accuracy of 4D-CT in all patients with hyperparathyroidism. As multigland disease and ectopic glands are more likely to be missed by the traditional initial imaging studies of sonography and technetium Tc99m sestamibi, our patient population was also likely skewed toward more complex or difficult cases by the referral bias mentioned above. Furthermore, the accuracies reported in this study reflected the results of 4D-CT, as interpreted by a single neuroradiologist with 7 years of experience with this technique and evaluation of more than 900 cases. Therefore, our study was not able to assess interobserver variability. Interpretation of the images is time consuming and, in our cohort, may be nontrivial; if adequate time is not devoted to interpretation, accuracy rates will be compromised. Finally, the overall accuracy of 4D-CT is likely to vary by institution, CT scanner, experience and interest of the interpreter, and CT protocol technique used to generate the images.

CONCLUSIONS

4D-CT is an accurate technique for preoperative localization of parathyroid lesions in patients with hyperparathyroidism regardless of cause or prior parathyroid surgical history, and can be used to stratify patients to unilateral minimally invasive parathyroidectomy vs bilateral neck exploration.

ACKNOWLEDGMENTS

The authors thank Dr. Elkan Halpern for assistance in providing statistical advice during manuscript revision.

REFERENCES

1. The American Association of Clinical Endocrinologists and the American Association of Endocrine Surgeons position statement on the diagnosis and management of primary hyperparathyroidism. *Endocr Pract* 2005;11:49–54
2. Fraser WD. Hyperparathyroidism. *Lancet* 2009;374:145–58
3. Tominaga Y, Tanaka Y, Sato K, et al. **Histopathology, pathophysiology, and indications for surgical treatment of renal hyperparathyroidism.** *Semin Surg Oncol* 1997;13:78–86
4. Greene AB, Butler RS, McIntyre S, et al. **National trends in parathyroid surgery from 1998 to 2008: a decade of change.** *J Am Coll Surg* 2009;209:332–43
5. Udelsman R, Lin Z, Donovan P. **The superiority of minimally invasive parathyroidectomy based on 1650 consecutive patients with primary hyperparathyroidism.** *Ann Surg* 2011;253:585–91
6. Kunstman JW, Udelsman R. **Superiority of minimally invasive parathyroidectomy.** *Adv Surg* 2012;46:171–89
7. Fraker DL, Harsono H, Lewis R. **Minimally invasive parathyroidectomy: benefits and requirements of localization, diagnosis, and intraoperative PTH monitoring. Long-term results.** *World J Surg* 2009;33:2256–65
8. Johnson NA, Carty SE, Tublin ME. **Parathyroid imaging.** *Radiol Clin North Am* 2011;49:489–509
9. Rodgers SE, Hunter GJ, Hamberg LM, et al. **Improved preoperative planning for directed parathyroidectomy with 4-dimensional computed tomography.** *Surgery* 2006;140:932–40
10. Beland MD, Mayo-Smith WW, Grand DJ, et al. **Dynamic MDCT for localization of occult parathyroid adenomas in 26 patients with primary hyperparathyroidism.** *AJR Am J Roentgenol* 2011;196:1:61–65
11. Kutler DI, Moquete R, Kazam E, et al. **Parathyroid localization with modified 4D-computed tomography and ultrasonography for patients with primary hyperparathyroidism.** *Laryngoscope* 2011;121:1219–24
12. Hunter GJ, Schellingerhout D, Vu TH, et al. **Accuracy of four-dimensional CT for the localization of abnormal parathyroid glands in patients with primary hyperparathyroidism.** *Radiology* 2012;264:789–95
13. Cheung K, Wang TS, Farrokhyar F, et al. **A meta-analysis of preoperative localization techniques for patients with primary hyperparathyroidism.** *Ann Surg Oncol* 2012;19:577–83
14. Lubitz CC, Hunter GJ, Hamberg LM, et al. **Accuracy of 4-dimensional computed tomography in poorly localized patients with primary hyperparathyroidism.** *Surgery* 2010;148:1129–37
15. Eichhorn-Wharry LI, Carlin AM, Talpos GB. **Mild hypercalcemia: an indication to select 4-dimensional computed tomography scan for preoperative localization of parathyroid adenomas.** *Am J Surg* 2011;201:334–38
16. Mortenson MM, Evans DB, Lee JE, et al. **Parathyroid exploration in the reoperative neck: improved preoperative localization with 4D-computed tomography.** *J Am Coll Surg* 2008;206:888–95
17. Chazen JL, Gupta A, Dunning A, et al. **Diagnostic accuracy of 4D-CT for parathyroid adenomas and hyperplasia.** *AJNR Am J Neuroradiol* 2012;33:429–33
18. Starker LF, Mahajan A, Bjorklund P, et al. **4D parathyroid CT as the initial localization study for patients with de novo primary hyperparathyroidism.** *Ann Surg Oncol* 2011;18:1723–28
19. Lew JI, Solorzano CC. **Surgical management of primary hyperparathyroidism: state of the art.** *Surg Clin North Am* 2009;89:1205–25
20. Gafton AR, Glastonbury CM, Eastwood JD, et al. **Parathyroid lesions: characterization with dual-phase arterial and venous enhanced CT of the neck.** *AJNR Am J Neuroradiol* 2012;33:949–52
21. Welling RD, Olson JA Jr, Kranz PG, et al. **Bilateral retropharyngeal parathyroid hyperplasia detected with 4D multidetector row CT.** *AJNR Am J Neuroradiol* 2011;32:E80–82

Imaging Findings in Auto-Atticotomy

M. Manasawala, M.E. Cunnane, H.D. Curtin, and G. Moonis

ABSTRACT

BACKGROUND AND PURPOSE: An acquired attic cholesteatoma may spontaneously drain externally into the external auditory canal, leaving a cavity in the attic with the shape of the original cholesteatoma but now filled with air, a phenomenon referred to as “nature’s atticotomy” or auto-atticotomy. We describe and quantify the CT appearance of the auto-atticotomy cavity as it pertains to the appearance of the scutum and the lateral attic wall.

MATERIALS AND METHODS: Twenty-one patients with erosion of the scutum and loss of the lower attic wall on MDCT were identified during a 5-year span. Images were assessed for measureable widening of the space between the ossicles and the lower lateral attic wall in the axial and coronal planes. Three measurements of the lateral attic were made on the axial images. Findings were compared with the same measurements in 20 control subjects.

RESULTS: The 21 patients had a characteristic blunting of the scutum with loss of the lower lateral attic wall and widening of the lateral attic, consistent with an auto-atticotomy. There was a statistically significant ($P < .001$) widening of the lateral attic dimensions in the axial plane in the patients with auto-atticotomy.

CONCLUSIONS: Spontaneously evacuated cholesteatoma may mimic a surgical atticotomy on MDCT. Scutal erosion and attic enlargement with a smoothly contoured bony remodeling of the lower lateral attic wall in a patient with no history of surgery suggest that a cholesteatoma was previously present and spontaneously drained.

An atticotomy is a surgical approach through the external auditory canal to the attic of the middle ear, whereby the scutum and the lower lateral wall of the attic are surgically removed for access. An auto-atticotomy (also called “nature’s atticotomy”) refers to an enlarged lateral attic with absence of the scutum and lower lateral wall of the attic in a patient without a history of surgery.¹⁻³ This entity results from a deep retraction pocket or a cholesteatoma that has eroded the bone and then spontaneously drained into the external auditory canal. The wall of the original cholesteatoma remains, and so the air-filled defect is lined by keratinizing squamous epithelium. The appearance of an atticotomy and an auto-atticotomy is similar on CT. The purpose of this article was to describe the findings of auto-atticotomy on multidetector CT of the temporal bone.

MATERIALS AND METHODS

The study was approved by the Human Studies Committee of our hospital, and review of on-line medical records was performed in all patients and controls. The images were prospectively collected by 2 of the authors (practicing head and neck radiologists) during a 5-year period from MDCT scans of the temporal bone viewed in daily readouts. The inclusion criteria were the following: 1) apparent absence or blunting of the scutum and/or smooth bony remodeling of the lateral attic wall on MDCT, and 2) no history of prior otologic surgical intervention. This yielded 21 patients (12 men and 9 women, 27–88 years of age) who fulfilled the inclusion criteria; additionally, all had a history of chronic otitis media. Twelve patients had confirmation of pars flaccida cholesteatoma by histology, 2 patients had evidence of pars flaccida cholesteatoma on clinical examination, and 8 patients had deep attic retraction pockets on clinical examination. These 8 patients all had history of intermittently draining ears. We also retrospectively evaluated MDCT of the temporal bone in 20 control subjects. These control subjects had been referred to the radiology department for unrelated symptoms such as tinnitus or sensorineural hearing loss and did not have any history of prior

Received January 18, 2013; accepted after revision March 22.

From the Department of Radiology (M.M.), Abington Memorial Hospital, Abington, Pennsylvania; Department of Radiology (G.M.), Beth Israel Deaconess Medical Center, Boston, Massachusetts; and Department of Radiology (M.E.C., H.D.C., G.M.), Massachusetts Eye and Ear Infirmary, Boston, Massachusetts.

Please address correspondence to Gul Moonis, MD, Department of Radiology, Massachusetts Eye and Ear Infirmary, 243 Charles St, Boston, MA 02215; e-mail: gmoonis@bidmc.harvard.edu

<http://dx.doi.org/10.3174/ajnr.A3791>

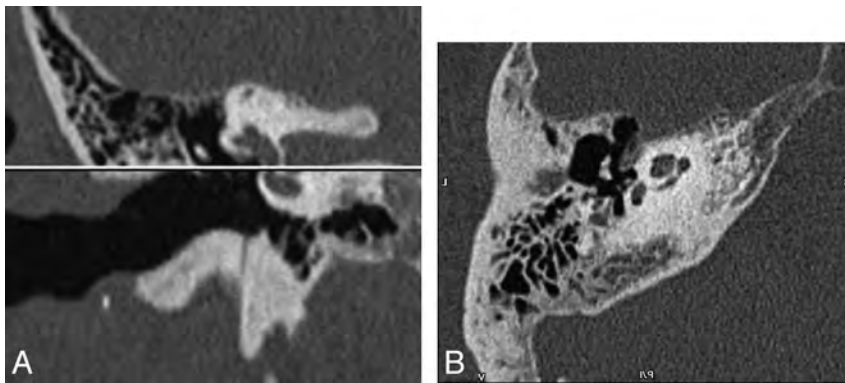


FIG 1. A, Coronal MDCT image depicts the location of the axial plane at the base of the scutum. B, Axial MDCT image at the level where the first bone image appears superior to the air-containing external auditory canal. The malleoincudal junction is well-seen.

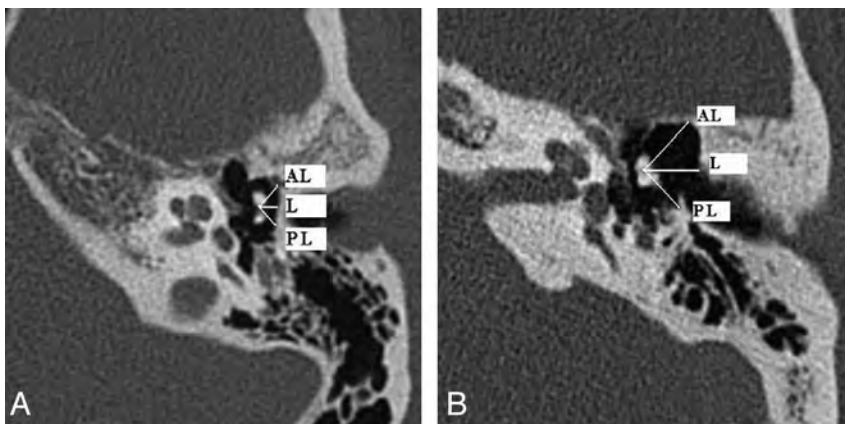


FIG 2. A, Lateral attic measurements in a healthy subject. Axial MDCT demonstrates anterolateral (AL), lateral (L), and posterolateral (PL) measurements from the center of the malleoincudal articulation at the level of the base of the scutum in a healthy subject. B, Lateral attic measurements in a 27-year-old patient with a history of cholesteatoma. There is a left auto-atticotomy with smooth remodeling and widening of the anterolateral (AL), lateral (L), and posterolateral (PL) walls of the attic.

Table 1: Lateral, anterolateral, and posterolateral attic measurements (mm) in patients

Patients	Lateral	Anterolateral	Posterolateral
A	3.6	4.6	3.8
B	3.8	4.5	3.7
C	5	4.4	3.2
D	3.6	5	3.3
E	3.2	4	2.5
F	4.3	3.8	3.7
G	4.3	4.1	4.5
H	2.3	3.3	2.3
I	4.8	4.4	6.9
J	3.7	3.6	4.3
K	3.9	4.1	4.1
L	3.7	3.6	3.9
M	7.5	4.3	4.5
N	3.7	4.2	3.5
O	4.7	5.5	3.9
P	3.9	4	3.4
Q	5.4	7.4	4.2
R	3.5	3.6	4.7
S	3.5	4.8	3.3
T	3.8	5.2	4.4
U	4.1	4.2	3.8

middle ear inflammatory disease or surgery of the temporal bone; their tympanic membranes were normal at otoscopy.

All subjects had imaging performed on a 40-section multidetector CT scanner (Somatom Sensation scanner; Siemens, Erlangen, Germany). The raw data were acquired helically with 0.6-mm collimation and 0.55 pitch at 320 mAs and 120 kV(peak), with the scan excursion plotted from the arcuate eminence through the mastoid tip. The raw data from each ear were separated and reconstructed into 0.6 (section thickness) \times 0.2 mm (reconstruction interval) axial images in bone algorithms at a display FOV of 100 mm and a matrix of 512 \times 512. The data were displayed in 3 orthogonal planes on the scanner console. The technologist scrolled through the sagittal data to find an image on which the anterior and posterior limbs of the lateral semicircular canal were displayed in cross-section. An axial dataset was made in a standardized plane parallel to the lateral semicircular canal by placing the reference line connecting the anterior and posterior limbs of the canal. Axial images were reformatted at 0.6 (image thickness) \times 0.5 (distance between images) mm. Coronal images (0.6 \times 0.5 mm) were made in a plane perpendicular to the axial images.

The images were visually inspected for scutal erosion, widening of the lateral attic, middle ear opacification, ossicular

erosion, and mastoid opacification. To quantify our subjective visual impression of the auto-atticotomy changes, we performed the following measurements: An axial image was chosen that demonstrated the malleoincudal junction at the level of the base of the scutum. For this purpose, the base of the scutum was determined to be the first bone image superior to the air-containing external auditory canal and was reproducibly seen in all cases (Fig 1A, -B). Three measurements were obtained for each case. A lateral measurement was made from the center of the malleoincudal junction to the base of the scutum, and subsequent measurements were made at a 45° angle anterior and a 45° angle posterior to this initial measurement (Fig 2A, -B and Tables 1 and 2).

We performed statistical analysis by using the Statistical Package for the Social Sciences, Version 13.0 software (IBM, Armonk, New York). We used the Mann-Whitney *U* test, a nonparametric test to assess whether there was a statistically significant difference between the 2 samples of observations in patients and controls.

RESULTS

The lateral attic dimension measured an average of 4.11 \pm 1.05 mm in patients compared with 2.37 \pm 0.37 mm in healthy sub-

Table 2: Lateral, anterolateral, and posterolateral attic measurements (mm) in controls

Controls	Lateral	Anterolateral	Posterolateral
AA	2.8	2.7	2.7
BB	3	3.4	3
CC	2.4	3	2.6
DD	1.9	3.6	2.2
EE	2	3.1	2.3
FF	1.8	2.4	2
GG	1.8	2.6	1.9
HH	2.5	4.2	2.3
II	2.3	3.8	2.6
JJ	2.3	3.2	2.5
KK	2.9	3.6	2.3
LL	2.1	3.2	2.3
MM	2.2	2.3	2.4
NN	2.3	3.1	2.3
OO	2.5	2.7	2.2
PP	2.9	3.8	2.9
QQ	2.1	2.6	2.4
RR	2.3	2.4	2.3
SS	2.6	3.6	3.3
TT	2.8	3.6	3.2

jects. These results represented a significant statistical difference between the 2 groups with a 2-tailed *P* value of < .001.

The anterolateral attic dimension measured an average of 4.41 ± 0.88 in patients compared with 3.15 ± 0.54 mm in healthy subjects. These results represented a significant statistical difference between the 2 groups with a 2-tailed *P* value of < .001.

The posterolateral attic dimension measured an average of 3.90 ± 0.93 mm in patients compared with 2.49 ± 0.37 mm in healthy subjects. These results represented a significant statistical difference between the 2 groups with a 2-tailed *P* value of < .001.

Overall, 12/21 patients (57%) demonstrated minimal or no soft-tissue opacification within the middle ear cavity. Nine patients had nonspecific middle ear opacification. Mastoid underpneumatization and/or opacification was seen in 17/21 (80%) patients. Ossicular erosion was seen in 10/21 (47%) patients.

DISCUSSION

Pars flaccida or primary acquired cholesteatoma most commonly forms in the Prussak space lateral to the ossicles and may result in medial ossicular displacement and/or erosion. Lateral expansion causes erosion of the scutum and lower lateral wall of the attic.⁴⁻⁷ Histologically, cholesteatoma is a cystic structure containing exfoliated keratin lined by stratified keratinizing squamous epithelium. The outer layer of the cyst lining or sac is composed of perimatrix or lamina propria.⁸ There are multiple theories to explain the pathogenesis of bony destruction associated with cholesteatomas, including remodeling from local pressure and recruitment of osteoclasts that are enzymatically active.⁹

At imaging (usually CT), a cholesteatoma classically is seen as a soft-tissue mass adjacent to the ossicles with erosion of the ossicles or the scutum. If the cholesteatoma drains spontaneously into the external auditory canal, the bony changes remain but the mass is no longer visualized. Instead, the “cavity” is now filled with air.

An auto-mastoidectomy has been described referring to external evacuation of the contents of a cholesteatoma that had replaced much of the mastoid, leaving behind its outer mem-

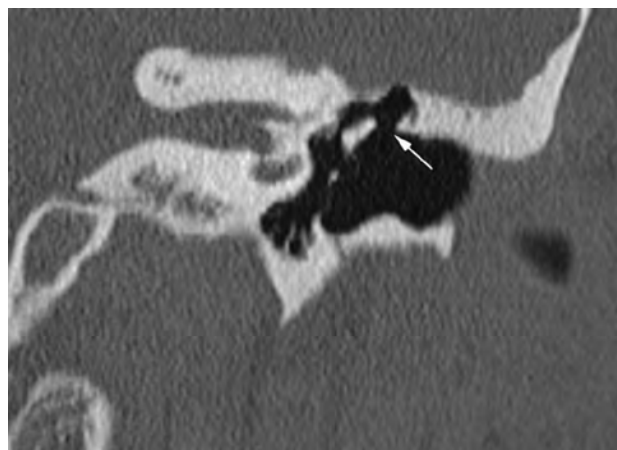


FIG 3. Auto-atticotomy in a 35-year-old patient with a remote history of draining ear. Coronal MDCT demonstrates scutal absence (arrow) mimicking the appearance of a surgical atticotomy. Note the lack of soft-tissue inflammatory changes.

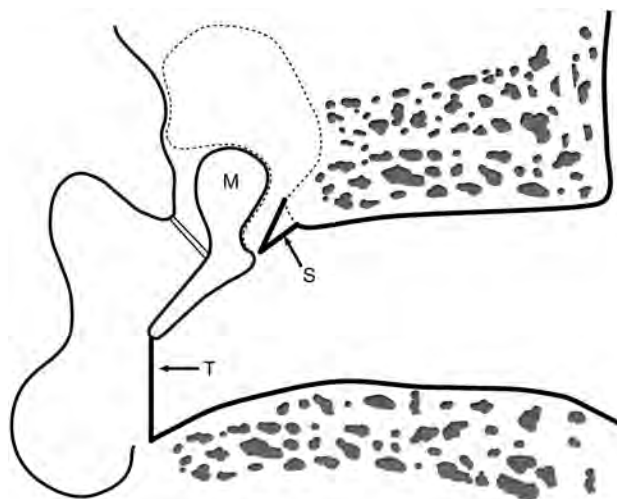


FIG 4. Schematic drawing demonstrating the surgical atticotomy margins (dotted line). S indicates scutum; T, tympanic membrane; M, malleus.

brane and a remodeled temporal bone without a soft-tissue mass. This is also referred to as “mural cholesteatoma” or “unusual cholesteatoma shell.”^{3,10,11} Auto-atticotomy can be considered to be the same external decompression process, though less extensive than an auto-mastoidectomy (Fig 3). The auto-atticotomy may mimic a surgical atticotomy performed for limited attic cholesteatomas, with removal of the scutum and lower lateral attic wall (Fig 4). The size and shape of an auto-atticotomy cavity reflects the size, shape, and location of the original cholesteatoma that produced it.¹² It is possible that we are seeing a higher incidence of auto-atticotomy compared with auto-mastoidectomy due to detection earlier in the course of the disease because imaging is more easily available.

Pars flaccida cholesteatomas most commonly erode the scutum and lower lateral wall of the attic. Scutal erosion was noted in all patients in our series because this was an inclusion criterion. On MDCT, scutal erosion is typically evaluated in the coronal plane as blunting of the normally sharply pointed bone ridge. However, this erosion can also be appreciated in the axial plane

where there is widening of the space between the ossicles and the lower lateral attic wall. Smooth lateral expansion of this bony margin can be visualized in a single axial plane image and, in our experience, therefore can occasionally be more noticeable or can support the diagnosis in questionable cases.

Regarding the lateral attic wall, the remodeling of the scutum may be centered either anteriorly, posteriorly, or laterally.¹¹ In our series, there was a predilection for anterolateral remodeling, with approximately two-thirds of patients (13/21) demonstrating the greatest widening of the anterolateral measurement (Fig 2B). Approximately one-fourth of the patients (5/21) demonstrated a posterolateral directionality, with the greatest widening of the posterolateral measurement. A smaller number of patients (2/21) demonstrated scutal erosion in a more straight-lateral fashion, with the greatest widening of the straight-lateral (lateral) measurement. The direct lateral dimension corresponds to the plane of the coronal images and therefore is well-depicted on coronals. The anterolateral and posterolateral measurements lie at a 45° angle from the coronal plane. In patients with the maximum widening along these axes, the coronal plane might underestimate the extent of attic remodeling. In our study, evaluation of the lateral attic in the coronal plane alone would have underestimated the degree of widening in most of our patients. For this reason, we recommend evaluation on the axial plane as well as the coronal plane.

Nearly half (12/21) of our patients demonstrated auto-atticotomy changes without any CT indication of a residual attic or Prussak space cholesteatoma as evidenced by a soft-tissue component (Fig 3). It is thus especially important to be aware of this imaging appearance, which can alert the clinician to the presence of a previously evacuated cholesteatoma.

For otologists, the dividing line between a deep retraction pocket and a drained cholesteatoma may be difficult to define. It is conceivable that a deep or large retraction pocket can, by itself, create an auto-atticotomy with erosion of the scutum.¹³ A retraction pocket against the long process of the incus has been noted to cause erosion.¹⁴ So too, a deep retraction pocket could theoretically cause blunting at the scutum without ever forming a collection of keratin or mass. However, a deep retraction pocket seen on clinical examination could also simply represent a previously evacuated cholesteatoma with the outer wall left behind. Once the cholesteatoma evacuates and the keratin reaches the external canal, the “sac” may never obstruct again and there would be no further drainage. The keratin would simply evacuate at the normal rate via the external auditory canal. This process would be appreciated by the otologist as a retraction pocket and may present as a conductive hearing loss without mass or drainage. This differentiation is not crucial because most otologists would treat a deep retraction pocket and an auto-atticotomy from a drained cholesteatoma similarly, depending on the symptoms, including the frequency of drainage and accumulation of debris.¹⁵

There are other potential or theoretic explanations for loss of the scutum in the absence of soft tissue. The development of the external auditory canal occurs as an invagination of the first branchial cleft, which touches the endoderm of the ascending first branchial pouch to form the tympanic membrane. Mesoderm then grows between the 2 layers, and the mature tympanic membrane is formed of all 3 layers.¹⁶ Theoretically, the pouch could invaginate further than normal

at the superior aspect of the tympanic membrane, but the presence of chronic inflammatory disease in the middle ear and mastoids in almost all of our patients makes this finding unlikely to be a congenital or developmental variant.

CONCLUSIONS

Evacuated attic cholesteatomas may be difficult to recognize on CT due to the absence of soft tissue. We propose that widening of the lateral attic and scutal erosion are findings that help to accurately diagnose these patients. We emphasize careful attention to the axial images along the base of the scutum, which can help in recognizing subtle anterior or posterior remodeling of the lateral attic wall and can support questionable findings on coronal images.

Disclosures: Mary E. Cunnane—UNRELATED: Other: WorldCare Clinical, Comments: payment for reviewing radiology studies on patients entered into drug trials for head and neck cancer. Hugh D. Curtin—UNRELATED: Payment for Lectures (including service on Speakers Bureaus): 1 lecture in Continuing Medical Education but am not sponsored by any company and do not get paid for lecturing; I am not on any Speakers Bureaus, Royalties: none other than books and lecturing; nothing from outside companies related to health care, Travel/Accommodations/Meeting Expenses Unrelated to Activities Listed: If I lecture outside Boston, someone is usually paying meeting expenses and travel (various universities). The International Institute for Continuing Medical Education pays for my travel to a meeting sponsored by Mt. Sinai Hospital.

REFERENCES

1. Nadol JB, Shuknecht HF. **Office examination of the ear.** In: Nadol JB, McKenna MJ, eds. *Surgery of the Ear and Temporal Bone*. 2nd ed. New York: Lippincott Williams & Wilkins; 2004:5
2. Sadé J. **Retraction pockets and attic cholesteatomas.** *Acta Otorhinolaryngol Belg* 1980;34:62–84
3. Swartz JD, Hagiwara M. **Inflammatory diseases of the temporal bone.** In: Som PM, Curtin HD, eds. *Head and Neck Imaging*. 5th ed. Philadelphia: Elsevier Mosby; 2011:1207
4. Kikuchi S, Yamasoba T, Iinuma T. **An analysis of bone destruction in cholesteatomas by high resolution computed tomography.** *Auris Nasus Larynx* 1993;20:11–17
5. Mafee MF, Kumar A, Yannias DA, et al. **Computed tomography of the middle ear in the evaluation of cholesteatomas and other soft-tissue masses: comparison with pluridirectional tomography.** *Radiology* 1983;148:465–72
6. Nagar GT. **Theories on the origin of attic retraction cholesteatoma.** In: *Proceedings of the Shambaugh Fifth International Workshop on Microsurgery and Fluctuant Hearing Loss*, Huntsville, Alabama. 1977;127–52
7. Swartz JD. **The middle ear and mastoid.** In: Swartz JD, Loevner LA, eds. *Imaging of the Temporal Bone*. 4th ed. New York: Thieme; 2009:115
8. Olszewska E, Wagner M, Bernal-Sprekelsen M, et al. **Etiopathogenesis of cholesteatoma.** *Eur Arch Otorhinolaryngol* 2004;261:6–24
9. Breinlich T, Giebel W. **Histochemical studies of cholesteatoma.** *Arch Otorhinolaryngol* 1984;240:95–101
10. Baráth K, Huber AM, Stampfli P, et al. **Neuroradiology of cholesteatomas.** *AJNR Am J Neuroradiol* 2011;32:221–29
11. Nardis PF, Teramo M, Giunta S, et al. **Unusual cholesteatoma shell: CT findings.** *J Comput Assist Tomogr* 1988;12:1084–85
12. Vignaud J, Dulac GL, Francois J. **Temporal Fosses Nasales, Caviles Accessoires.** In: Fischgold H, ed. *Traite de Radiodiagnostic*. Paris, France: Masson; 1974
13. Sadé J. **Pathogenesis of attic cholesteatoma.** *J Royal Soc Med* 1978;71:716–32
14. Borgstein J, Gerritsma TV, Bruce IA. **Erosion of the incus in pediatric posterior tympanic membrane retraction pockets without cholesteatoma.** *Int J Pediatr Otorhinolaryngol* 2008;72:1419–23
15. Ars B. **Tympanic membrane: retraction pocket.** *Acta Otorhinolaryngol Belg* 1995;49:163–71
16. Curtin HD, Gupta R, Bergeron RT. **Embryology, anatomy and imaging of the temporal bone.** In: Curtin HD, Som PM, eds. *Head and Neck Imaging*. 5th ed. Philadelphia: Elsevier Mosby; 2011:1058

Tympanic Plate Fractures in Temporal Bone Trauma: Prevalence and Associated Injuries

C.P. Wood, C.H. Hunt, D.C. Bergen, M.L. Carlson, F.E. Diehn, K.M. Schwartz, G.A. McKenzie, R.F. Morreale, and J.I. Lane

ABSTRACT

BACKGROUND AND PURPOSE: The prevalence of tympanic plate fractures, which are associated with an increased risk of external auditory canal stenosis following temporal bone trauma, is unknown. A review of posttraumatic high-resolution CT temporal bone examinations was performed to determine the prevalence of tympanic plate fractures and to identify any associated temporal bone injuries.

MATERIALS AND METHODS: A retrospective review was performed to evaluate patients with head trauma who underwent emergent high-resolution CT examinations of the temporal bone from July 2006 to March 2012. Fractures were identified and assessed for orientation; involvement of the tympanic plate, scutum, bony labyrinth, facial nerve canal, and temporomandibular joint; and ossicular chain disruption.

RESULTS: Thirty-nine patients (41.3 ± 17.2 years of age) had a total of 46 temporal bone fractures (7 bilateral). Tympanic plate fractures were identified in 27 (58.7%) of these 46 fractures. Ossicular disruption occurred in 17 (37.0%). Fractures involving the scutum occurred in 25 (54.4%). None of the 46 fractured temporal bones had a mandibular condyle dislocation or fracture. Of the 27 cases of tympanic plate fractures, 14 (51.8%) had ossicular disruption ($P = .016$) and 18 (66.6%) had a fracture of the scutum ($P = .044$). Temporomandibular joint gas was seen in 15 (33%) but was not statistically associated with tympanic plate fracture ($P = .21$).

CONCLUSIONS: Tympanic plate fractures are commonly seen on high-resolution CT performed for evaluation of temporal bone trauma. It is important to recognize these fractures to avoid the preventable complication of external auditory canal stenosis and the potential for conductive hearing loss due to a fracture involving the scutum or ossicular chain.

ABBREVIATIONS: HRCT = high-resolution CT; TMJ = temporomandibular joint; TPF = tympanic plate fracture

There are many reports in the literature describing CT of temporal bone trauma,¹⁻⁴ detailing fracture plane orientations,⁴⁻⁶ ossicular disruptions, otic capsule involvement,^{4,5} associations with air in the temporomandibular joint (TMJ),⁷ facial nerve injury,⁴⁻⁶ and fracture mimics, to name a few broad categories.⁸ Temporal bone fractures involving the tympanic plate (Figs 1 and 2), however, are under-recognized and have received little attention beyond isolated case reports involving mandibular trauma.⁸⁻¹⁵ The tympanic plate of the temporal bone is a U-shaped structure forming the anterior wall, floor, and part of the posterior wall of the external auditory canal. The limited lit-

erature concerning tympanic plate fracture (TPF) suggests that these types of fractures are uncommon.^{4,10,11,16} Most literature on direct and indirect CT findings of temporal bone trauma was published in the pre-/early multidetector CT era^{1,3,7,17,18} or was based solely on non-high-resolution CT (HRCT) imaging,¹⁹ however, it is possible that posttraumatic TPFs are under-recognized or overlooked by the inexperienced observer. TPFs are important to identify, given the potential for the clinically significant long-term complications of external auditory canal stenosis and trismus.²⁰ The purpose of this study was to retrospectively review acute posttraumatic HRCT temporal bone studies to determine the true incidence of TPF and to identify other associated temporal bone injuries.

MATERIALS AND METHODS

Institutional review board approval with waived consent was obtained for this Health Insurance Portability and Accountability Act-compliant research study. A retrospective review was under-

Received January 17, 2013; accepted after revision March 29.

From the Departments of Radiology (C.P.W., C.H.H., D.C.B., F.E.D., K.M.S., G.M., J.I.L.) and Otolaryngology (M.L.C.) and Media Support Services (R.M.), Mayo Clinic, Rochester, Minnesota.

Please address correspondence to Christopher P. Wood, MD, Department of Radiology, Mayo Clinic, 200 First St SW, Rochester, Minnesota 55905; e-mail: wood.christopher@mayo.edu

<http://dx.doi.org/10.3174/ajnr.A3609>

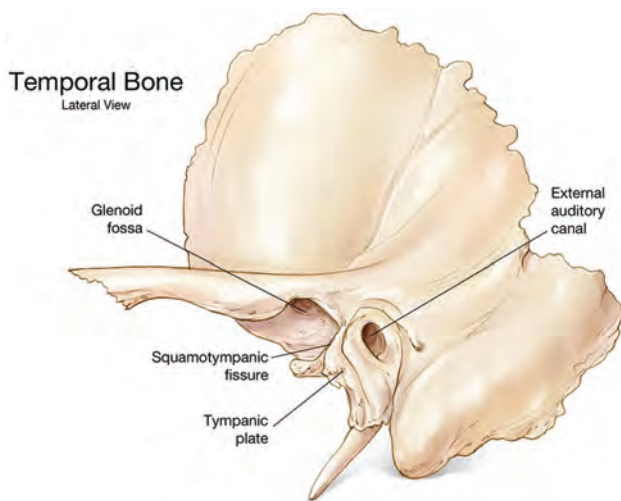


FIG 1. External sagittal view of the left temporal bone depicting the tympanic plate as it forms part of the anterior wall of the external auditory canal.

taken of patients with acute trauma who underwent a HRCT examination of the temporal bone at a level 1 trauma center from July 2006 to March 2012. Two hundred sixty-three patients were identified on the basis of a search of a radiology report database during this time for CT reports containing the keywords “temporal bone” and “fracture,” followed by a visual review of each study to confirm the presence of a definable fracture through the temporal bone on HRCT, which yielded 58 patients. Studies were excluded if they were performed as a follow-up to a prior temporal bone HRCT, were not acquired using a HRCT temporal bone protocol, were of unacceptable image quality due to excessive motion/dental scatter, or were performed for ballistic injuries (19 patients). This process yielded 39 patients, 7 of whom had bilateral fractures that were analyzed as 2 separate cases, producing a total of 46 HRCT temporal bone fractures that met the inclusion criteria.

HRCT of the temporal bone had been acquired without contrast on either a Definition, Definition AS+, or Definition Flash scanner (Siemens, Erlangen, Germany), using 12×0.3 mm or 16×0.3 mm collimation, 120 kV (peak), 0.8 pitch, and a 300-mm FOV. The source data were reconstructed into 0.5-mm sections at 0.3-mm increments in the axial, coronal, and Pöschl planes (Fig 3A) by using a bone kernel algorithm. These 46 HRCT cases were then reviewed on a PACS workstation by 3 neuroradiologists (C.P.W., C.H.H., and J.L.), each with a Certificate of Added Qualification, and a neuroradiology fellow (D.C.B.), respectively, for consensus diagnosis. At the review, readers were blinded to the original radiology report and clinical history. Consensus review was performed to ensure that the interpretation generated was representative of a typical group of neuroradiologists and to decrease any expectation bias. Each of the above 3 planar reformats was reviewed before a finding was determined, and subtle findings were confirmed by comparison with the opposite side in cases of unilateral fractures.

Cases were assessed for multiple variables. The fracture plane orientation was classified as either transverse, longitudinal, or mixed. These planes were determined relative to the axis of the

petrous ridge, with fracture orientations considered longitudinal if $<30^\circ$, transverse if $>70^\circ$, or mixed if a combination of both planes was present.⁴ TPF was confirmed if there was a visible fracture extending through the tympanic plate that was clearly distinct from the petrotympanic fissure (Fig 3B). Fracture extension through the otic capsule was assessed for involvement of the vestibule, semicircular canals, and/or cochlea. The entire course of the facial nerve through the temporal bone was followed for the presence of fracture involvement, including the tympanic and mastoid segments. Facial nerve canal fracture was designated if there was a clear intersection between the course of the fracture and the labyrinthine segment or anterior genu of the facial nerve, while perigeniculate involvement was determined if the fracture line passed within 2 mm of the anterior genu on any planar reformat.

The scutum and internal auditory canal were examined for any fracture involvement. Ossicular integrity was assessed for the presence of subluxation/dislocation of either the malleoincudal joint, incudostapedial joint, or both. Ossicular complex displacement was determined if the entire ossicular chain was notably displaced from its expected location due to either ligamentous rupture or fracture of bony attachment sites. Images were reviewed by using lung windows for the presence of pneumocephalus, pneumolabyrinth, or air in the TMJ fossa. The CT boundaries of the TMJ fossa were defined by its bony margins: anteriorly by the articular tubercle, posteriorly by the tympanic plate, and medially and laterally by the condylar head width. Images were evaluated for mandibular condyle dislocation or fracture.

An otolaryngology chief resident (M.L.C.) performed a retrospective review of each patient’s electronic medical record, assessing any potential clinical consequences of the temporal bone trauma. Statistical analysis was performed using a commercially available software package (JMP, Version 9.0; SAS Institute, Cary, North Carolina). The Pearson χ^2 test was used to determine the association between TPF and ossicular disruption; fracture plane orientation; fractures involving the otic capsule, facial nerve canal, scutum, or mandibular condyle; mandibular condylar dislocation; pneumocephalus; pneumolabyrinth; and TMJ gas. A *P* value $< .05$ was considered statistically significant.

RESULTS

Thirty-nine unique patients (41.3 ± 17.2 years of age; 33 men, 6 women) were identified who had undergone temporal bone HRCT in the acute setting. Seven of these patients had bilateral temporal bone fractures, which yielded a total of 46 distinct temporal bone fractures that were evaluated. The CT features of temporal bone fractures and TPF are listed in Table 1. The distribution of fracture orientations was transverse in 2 (4.4%), longitudinal in 18 (39.1%), and mixed in 26 (56.5%). The otic capsule was involved in only 4 cases (9%). Pneumocephalus was present in 16 cases (35%). TMJ gas was seen in 15 (33%) cases. TPFs were identified in 27 (58.7%) cases and were most conspicuous on the Pöschl view (Figs 4 and 5). Ossicular disruption was seen in 17 (37.0%) cases. Fractures involving the scutum were seen in 25 (54.4%) cases. None of the 46 temporal bone fractures, including the TPF cases, had an associated mandibular condyle dislocation or fracture. A fracture extending to involve the inter-

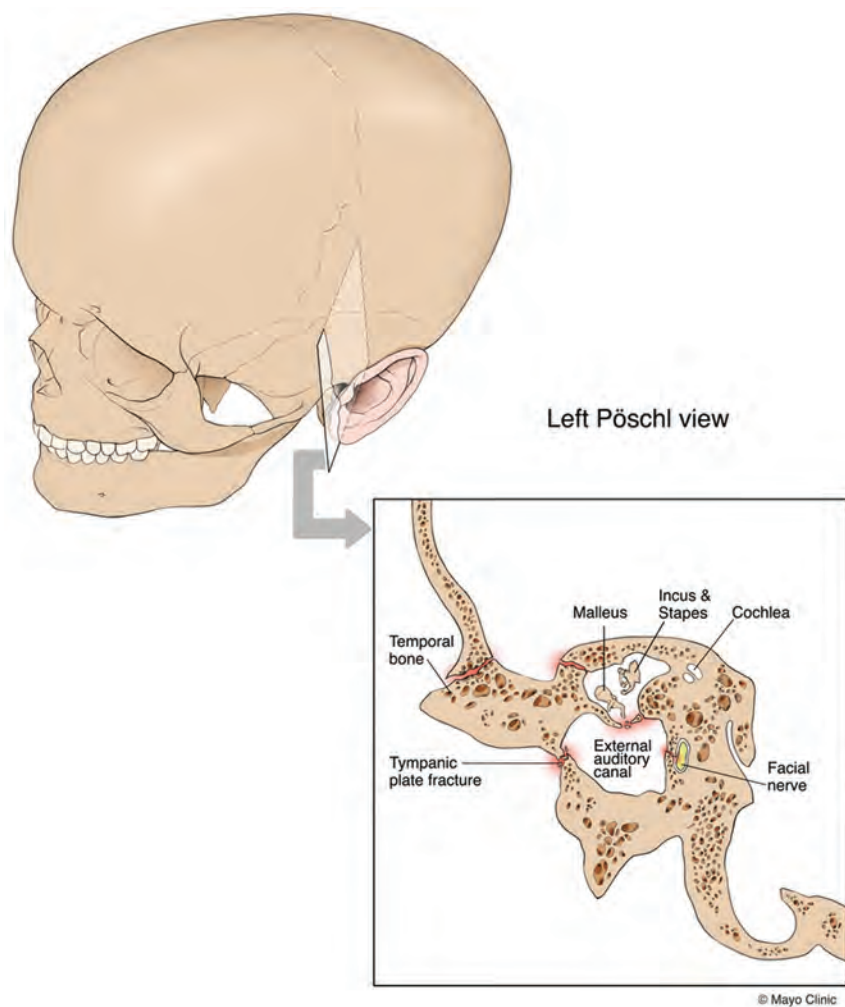


FIG 2. Oblique 3D view of the skull, including the external portion of the left temporal bone and the Pöschl plane for CT reformatting superimposed. This Pöschl plane view is depicted in the inset along with a TPF and some of the possible associated traumatic injuries.

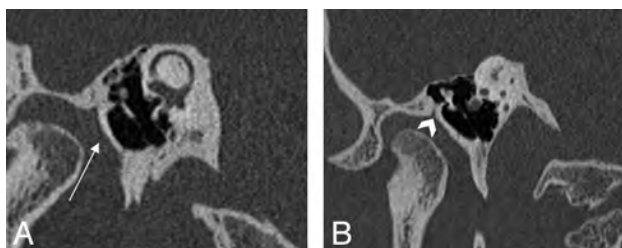


FIG 3. HRCT images with Pöschl views in the same patient demonstrating the tympanic plate (A, white arrow) and the petrotympanic fissure (B, arrowhead).

nal auditory canal occurred in only 1 (2%) case. Pneumolabyrinth was identified in only 1 (2%) case.

Statistical analysis revealed the following positive associations with TPF (Table 2): Of the 27 cases of TPF, 14 (51.8%) had associated ossicular disruption ($P = .016$) and 18 (66.6%) had an associated fracture of the scutum ($P = .044$). There was no correlation between fracture plane orientation and TPF. In addition, fracture plane orientation was not predictive of ossicular disruption or scutum fracture. There was no statistical difference between unilateral-versus-bilateral temporal bone fractures and the

frequency of TPF ($P = .52$). Twenty-two fractures were found that involved the course of the facial nerve in the temporal bone. Twenty-one of these involved the geniculate/perigeniculate region, and 1 involved the tympanic segment. There was no correlation between TPF and fractures involving the segments of the facial nerve ($P = .56$). The presence of gas within the TMJ fossa was not predictive of a TPF ($P = .21$). The review of the patient posttraumatic clinical courses was unrevealing, especially because clinical parameters were often incompletely documented.

DISCUSSION

Fractures of the temporal bone are common in cases of major head trauma, with a reported incidence of 3%–22% in patients with skull fractures.^{5,21} Temporal bone fractures frequently have associated complications such as hearing loss, cranial neuropathy or dysfunction, CSF leak, and vestibulopathy occurring in 5%–10% of cases.^{22,23} Previously Schuberger et al⁶ noted that 48% of patients with temporal bone fractures had ossicular chain disruption, facial nerve damage, or a CSF leak.⁶ Subsequently, Dahiya et al⁵ reported a higher incidence of facial paralysis, CSF leaks, profound hearing loss, and more frequent intracranial complications when temporal bone fractures involved the otic capsule compared with those that spared the

bony labyrinth. Patients with temporal bone fractures often have coexistent major intracranial injuries because a significant force is required to fracture the temporal bone.²⁴

The tympanic part of the temporal bone is a U-shaped structure forming the anterior wall (or posterior margin of the glenoid fossa), floor, and part of the posterior wall of the external auditory canal. The tympanic plate is this anterior wall segment of the tympanic portion of the temporal bone, interposed between the external auditory canal and the glenoid fossa (Fig 1). The plate is subjacent to the squamous part of the temporal bone, from which it is separated by a contiguous set of fissures running along the anterosuperior external auditory canal: the squamotympanic fissure laterally and the petrotympanic fissure medially. The petrotympanic fissure permits passage of the chorda tympani nerve (via the canal of Huguier), fibers from the anterior ligament of the malleus, and the anterior tympanic branch of the internal maxillary artery.²⁵ Identification of this contiguous fissure (best visualized in the Pöschl plane) is important to avoid mistaking it for a temporal bone fracture and in localizing the tympanic plate.

In our study, TPFs (Fig 2) were commonly seen on HRCT of the temporal bone in acute trauma. This finding is in contradis-

Table 1: Clinical and CT features of temporal bone fractures

	No. of Temporal Bone Fractures (n = 46)
Fracture orientation	
Transverse	2 (4.4%)
Longitudinal	18 (39.1%)
Mixed	26 (56.5%)
Otic capsule involvement	4 (9%)
Pneumocephalus	16 (35%)
TMJ gas	15 (33%)
TPF	27 (58.7%)
Ossicular disruption	17 (37.0%)
Fractures involving scutum	25 (54.4%)

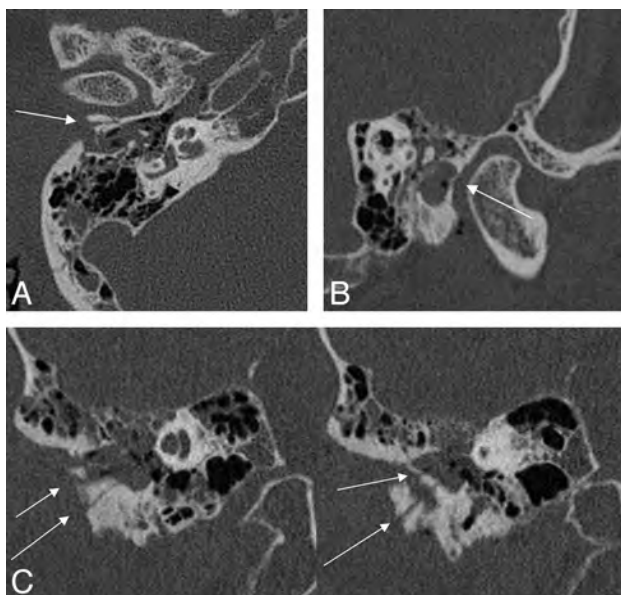


FIG 4. A 66-year-old intoxicated man, status post 2 falls within an hour, each of which led to his head striking a cement floor. Right tympanic plate fractures demonstrated on HRCT. Axial (A), Pöschl (B), and coronal (C) plane views. Tympanic plate fracture is demonstrated by white arrows.

tion to the purportedly “rare” and “uncommon” occurrence of TPF reported in the literature.^{10,11,16} One explanation for this under-reporting could be that TPFs in our study were most conspicuous on the Pöschl plane, which is generally not included on routine CT examinations. Most interesting, a study in 1988 mentioned the benefits of direct sagittal CT in temporal bone evaluation including the external auditory canal and for TMJ trauma, but it did not mention TPF.²⁶

Most, if not all, of the articles referencing a low incidence of tympanic plate injuries were written in the context of mandibular trauma, detailing a blow to the chin driving the mandibular condyles posteriorly and then impacting the tympanic plate. While this mechanism makes intuitive sense, none of our cases had evidence of a mandibular fracture or dislocation. In addition, in the present study the tympanic plate was typically never fractured in isolation, suggesting an alternative fracture mechanism. Both Valvassori²⁷ and Ghorayeb and Yeakley²⁸ briefly noted fracture extension into the glenoid fossa in most of their temporal bone fracture cases, often in association with a longitudinal or mixed fracture, respectively. Although specific mechanisms of injury

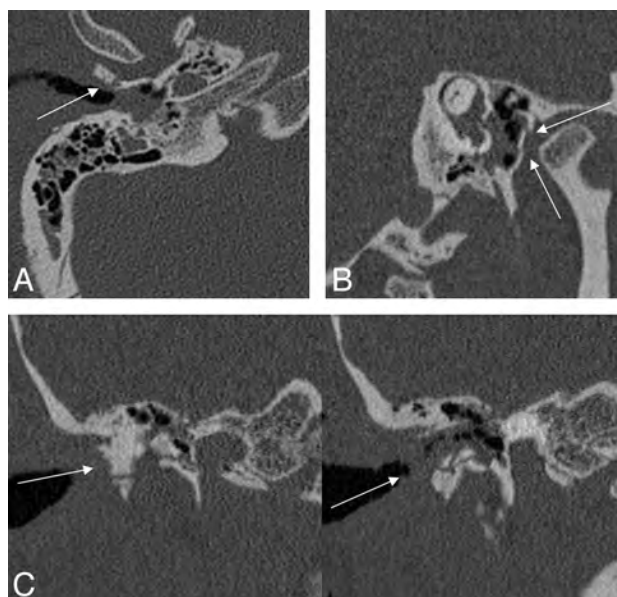


FIG 5. A 21-year-old woman, status post motor vehicle collision, with bilateral tympanic plate fractures (only the right one is shown). The complex nature of the right tympanic plate fracture is demonstrated by the white arrows on the axial (A), Pöschl (B), and coronal (C) plane images.

Table 2: Tympanic plate fractures and associations

	No. of TPFs (n = 27)	P Value
Ossicular disruption	14 (51.8%)	.016
Scutum fracture	18 (66.6%)	.044
Bilateral TPF	7 (25.9%)	.52
CT evidence of CN VII involvement	14 (51.9%)	.56
Gas within TMJ fossa	11 (40.7%)	.21

Note:—CN indicates cranial nerve.

were not provided, their studies appeared to be based on patient populations experiencing blunt nonpenetrating trauma, similar to our patient group.

In our study, there was a statistically significant association between ossicular injury and TPF. This could merely represent extension of an adjacent fracture plane, given the close anatomic relationship of the tympanic plate and the ossicles. Alternative mechanisms of ossicular injury due to TPF should also be considered, such as damage to the anterior ligament of the malleus. This ligament anchors the malleolar head to the anterior wall of the tympanic cavity and spina angularis of the sphenoid.^{25,29} However, to reach its sphenoid insertion, the fibers of the anterior ligament of the malleus must course through the petrotympanic fissure. Because the tympanic plate borders the petrotympanic fissure, a TPF could disrupt these passing fibers and lead to ossicular injury. A second explanation could be related to the lateral ligament of the malleus, which connects the malleolar neck to the osseous margins of the tympanic notch and runs inferior to the scutum.²⁵ Given the correlation between fractures of the tympanic plate and scutum in our study, the association between TPF and ossicular injury could be due to lateral ligament damage from a scutum fracture. Regardless of which ligament is disrupted, either could destabilize the ossicles and transfer additional strain on the remaining ligaments and joints, ultimately contributing to ossicular injury.

Potential long-term complications of TPF are well-documented in the literature, including external auditory canal stenosis, TMJ dysfunction, prolapse of the mandibular condyle into the external auditory canal, and facial nerve paresis.^{9,10} External auditory canal stenosis can vary from mild to complete occlusion with variable degrees of conductive hearing loss. Stenosis presumably occurs from marked comminution and displacement of the tympanic plate, resultant loss of anterior wall structural integrity, callus formation, and fibrous inflammation.²⁰ The management and treatment of external auditory canal stenosis are beyond the scope of this article, but the mainstay of preventive treatment is packing of the canal in cases at high risk for the development of stenosis. Early identification of this injury and medical management can reduce the need for surgery in cases of fixed stenosis. Surgery often involves canaloplasty to remove fixed narrowing and bony irregularities, excision of any soft-tissue stenosis, and/or skin grafting, often with restenosis rates as high as 27%.²⁰ TMJ dysfunction is another possible long-term complication, though acutely there is usually trismus and pain due to regional soft-tissue and retrodiscal inflammation.¹⁰ For these reasons, it is important for the radiologist to document the presence of a TPF.

The present study has several limitations. This is a retrospective review and is limited as such. Cases were identified from a cohort of patients in whom some type of temporal bone fracture in an acute setting had been reported by a neuroradiologist. Hence, there exists the potential for having missed cases not appreciated by the initial neuroradiologist, thereby excluding more subtle cases of temporal bone trauma. There may be a referral bias because we are a tertiary care center. In addition, because our institution is a large referral center, many patients had limited or no long-term follow-up after their initial injury and acute care. Future work could include more detailed prospective clinical follow-up and outcomes for these types of patients.

CONCLUSIONS

TPFs are commonly seen on dedicated HRCT performed for the evaluation of acute temporal bone trauma, which is in contradistinction to previous literature concerning CT imaging of temporal bone trauma. TPFs were most conspicuous on the Pöschl view. It is important to recognize these fractures to avoid the preventable complication of external auditory canal stenosis and its potential impact on conductive hearing loss with a fracture involving the scutum or ossicular chain.

REFERENCES

- Holland BA, Brant-Zawadzki M. **High-resolution CT of temporal bone trauma.** *AJR Am J Roentgenol* 1984;143:391–95
- Cannon CR, Jahrsdoerfer RA. **Temporal bone fractures: review of 90 cases.** *Arch Otolaryngol* 1983;109:285–88
- Kahn JB, Stewart MG, Diaz-Marchan PJ. **Acute temporal bone trauma: utility of high-resolution computed tomography.** *Am J Otol* 2000;21:743–52
- Zayas JO, Feliciano YZ, Hadley CR, et al. **Temporal bone trauma and the role of multidetector CT in the emergency department.** *Radiographics* 2011;31:1741–55
- Dahiya R, Keller JD, Litofsky NS, et al. **Temporal bone fractures: otic capsule sparing versus otic capsule violating clinical and radiographic considerations.** *J Trauma* 1999;47:1079–83
- Schubiger O, Valavanis A, Stuckmann G, et al. **Temporal bone fractures and their complications: examination with high resolution CT.** *Neuroradiology* 1986;28:93–99
- Betz BW, Wiener MD. **Air in the temporomandibular joint fossa: CT sign of temporal bone fracture.** *Radiology* 1991;180:463–66
- Kwong Y, Yu D, Shah J. **Fracture mimics on temporal bone CT: a guide for the radiologist.** *AJR Am J Roentgenol* 2012;199:428–34
- Psimopoulou M, Antoniadis K, Magoudi D, et al. **Tympanic plate fracture following mandibular trauma.** *Dentomaxillofac Radiol* 1997;26:344–46
- Gomes MB, Guimaraes SM, Filho RG, et al. **Traumatic fractures of the tympanic plate: a literature review and case report.** *Cranio* 2007;25:134–37
- Coulier B. **Tympanic plate fracture following mandibular trauma with emphasis on 3D imaging.** *JBR-BTR* 2011;94:85
- Conover GL, Crammond RJ. **Tympanic plate fracture from mandibular trauma.** *J Oral Maxillofac Surg* 1985;43:292–94
- Akers JO, Narang R, DeChamplain RW. **Posterior dislocation of the mandibular condyle into the external ear canal.** *J Oral Maxillofac Surg* 1982;40:369–70
- Mintz SM, Horowitz Y. **Fracture of a condyle and associated tympanic plate.** *Oral Surg Oral Med Oral Pathol* 1992;73:515–16
- Chong VF, Fan YF. **Technical report: external auditory canal fracture secondary to mandibular trauma.** *Clin Radiol* 2000;55:714–16
- Iannetti G, Martucci E. **Fracture of glenoid fossa following mandibular trauma.** *Oral Surg Oral Med Oral Pathol* 1980;49:405–08
- Liebetrau R, Draf W, Kahle G. **Temporal bone fractures: high resolution CT.** *J Otolaryngol* 1993;22:249–52
- Johnson DW, Hasso AN, Stewart CE 3rd, et al. **Temporal bone trauma: high-resolution computed tomographic evaluation.** *Radiology* 1984;151:411–15
- Exadakylos AK, Sclabas GM, Nuyens M, et al. **The clinical correlation of temporal bone fractures and spiral computed tomographic scan: a prospective and consecutive study at a level I trauma center.** *J Trauma* 2003;55:704–06
- Luong A, Roland PS. **Acquired external auditory canal stenosis: assessment and management.** *Curr Opin Otolaryngol Head Neck Surg* 2005;13:273–76
- Saraiya PV, Aygun N. **Temporal bone fractures.** *Emerg Radiol* 2009;16:255–65
- Amin Z, Sayuti R, Kahairi A, et al. **Head injury with temporal bone fracture: one year review of case incidence, causes, clinical features and outcome.** *Med J Malaysia* 2008;63:373–76
- Brodie HA, Thompson TC. **Management of complications from 820 temporal bone fractures.** *Am J Otol* 1997;18:188–97
- Travis LW, Stalnaker RL, Melvin JW. **Impact trauma of the human temporal bone.** *J Trauma* 1977;17:761–66
- Gray H. *Anatomy of the Human Body.* Philadelphia: Lea & Febiger; 1918
- Mafee MF, Kumar A, Tahmoressi CN, et al. **Direct sagittal CT in the evaluation of temporal bone disease.** *AJR Am J Roentgenol* 1988;150:1403–10
- Valvassori GE. **Approach to the study of temporal bone trauma.** *Rev Laryngol Otol Rhinol (Bord)* 1985;106:63–66
- Ghorayeb BY, Yeakley JW. **Temporal bone fractures: longitudinal or oblique? The case for oblique temporal bone fractures.** *Laryngoscope* 1992;102:129–34
- Lemmerling MM, Stambuk HE, Mancuso AA, et al. **CT of the normal suspensory ligaments of the ossicles in the middle ear.** *AJNR Am J Neuroradiol* 1997;18:471–77

Optimal Contrast Concentration for CT-Guided Epidural Steroid Injections

P.G. Kranz, M. Abbott, D. Abbott, and J.K. Hoang

EBM
1

ABSTRACT

BACKGROUND AND PURPOSE: Contrast is used in CT-guided epidural steroid injections to ensure proper needle placement. Once injected, undiluted contrast often obscures the needle, hindering subsequent repositioning. The purpose of this investigation was to establish the optimal contrast dilution for CT-guided epidural steroid injections.

MATERIALS AND METHODS: This investigation consisted of an initial phantom study, followed by a prospective, randomized, single-center trial assessing a range of contrast dilutions. In the phantom study, a phantom housing a chamber containing a 22-gauge needle and various dilutions of contrast was scanned, and images were evaluated for needle visibility. On the basis of these results, concentrations of 66, 100, 133, and 150 mg/mL iodine were selected for evaluation in a clinical study. Patients presenting for CT-guided epidural steroid injections were randomly assigned to a contrast dilution, and images from the procedure were evaluated by 2 readers blinded to the contrast assignment. Needle visibility was scored by use of a 5-point scale.

RESULTS: In the phantom study, the needle was not visible at contrast concentrations of ≥ 133 mg/mL. In the clinical study, needle visibility was strongly associated with contrast concentration ($P < .0001$). Significant improvements in visibility were found in 66 mg/mL and 100 mg/mL compared with higher iodine concentrations; no difference was found comparing 66 mg/mL with 100 mg/mL iodine. Neither injection location (cervical versus lumbar) nor technique (interlaminar versus transforaminal) influenced visibility scores.

CONCLUSIONS: For CT-guided epidural steroid injections, the optimal contrast concentration is 66–100 mg/mL iodine. Because these concentrations are not commercially available, proceduralists must dilute their contrast for such procedures.

ABBREVIATIONS: ESI = epidural steroid injections; ILESI = interlaminar epidural steroid injection; TFESI = transforaminal epidural steroid injection; CTF = CT fluoroscopy

Imaging guidance is a critical component of safe and accurate needle placement during spinal epidural steroid injections (ESI).^{1–6} The injection of contrast medium during such image-guided procedures provides information on patterns of injectate spread and helps to avoid complications caused by inadvertent intrathecal or intravascular needle placement. When the pattern of injected contrast shows that the needle position is not ideal, the proceduralist may reposition the needle.

Although conventional fluoroscopy remains the most widely used technique for guidance, CT fluoroscopy (CTF) has become

increasingly used because of its ability to provide cross-sectional needle localization and excellent visualization of the regional soft tissues.^{7–10} When CT guidance is used, however, the attenuation of many commercially available contrast agents is often sufficient to obscure the needle tip after injection. This can hinder attempts at needle repositioning, and as a result, several authors have advocated the use of dilute contrast for CT-guided procedures. The recommendations for the degree of contrast dilution vary widely, have generally been empirically selected, and, to our knowledge, have not been systematically evaluated previously.

The purpose of this investigation was to establish the optimal iodine concentration in contrast material for use in CT-guided spine procedures. Our study design included a phantom study for the purpose of acquiring preliminary data, followed by a prospective, randomized trial of various contrast dilutions in conditions mirroring routine clinical practice.

MATERIALS AND METHODS

This investigation was conducted in 2 parts. The first part was a phantom study designed to narrow the range of contrast dilutions

Received January 4, 2013; accepted after revision March 20.

From the Departments of Radiology (P.G.K., M.A., J.K.H.) and Biostatistics and Bioinformatics (D.A.), Duke University Medical Center, Durham, North Carolina.

Paper previously presented in part at: Annual Meeting of the American Society of Neuroradiology, April 26, 2012; New York, New York.

Please address correspondence to Peter G. Kranz, MD, Department of Radiology, Box 3808, Duke University Medical Center, Durham, NC 27710; e-mail: peter.kranz@duke.edu

EBM
1 Evidence-Based Medicine Level 1.

<http://dx.doi.org/10.3174/ajnr.A3626>

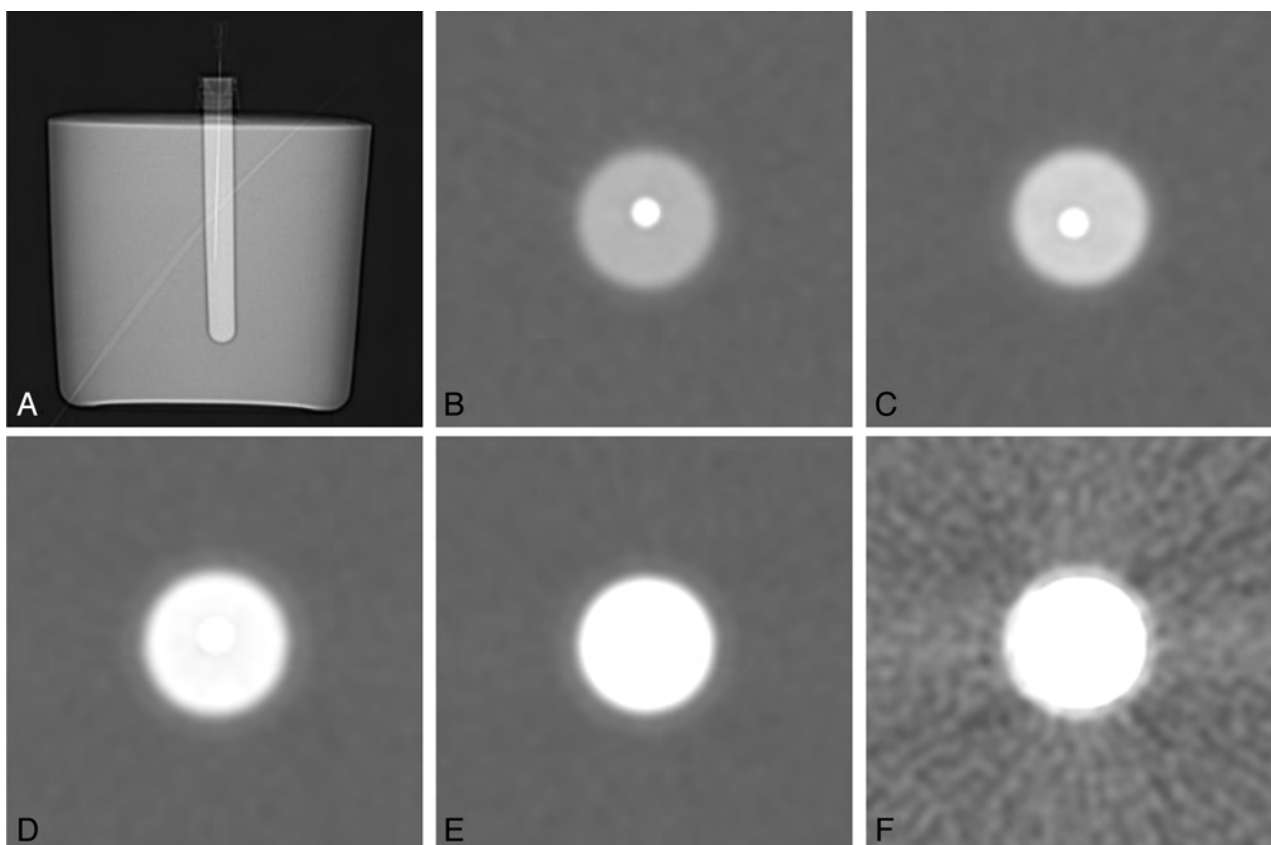


FIG 1. Phantom study assessing needle visibility. *A*, Scout image from CT demonstrating the configuration of the phantom. The central chamber houses contrast and a 22-gauge needle. Axial cross-sectional images of the chamber are shown with various contrast dilutions: 50 mg/mL (*B*), 66 mg/mL (*C*), 100 mg/mL (*D*), 133 mg/mL (*E*), and 150 mg/mL (*F*).

to be tested. The second part was a prospective, randomized, single-center trial assessing a range of contrast dilutions in actual CTF-guided epidural steroid injections. The study was approved by our local institutional review board and was compliant with the Health Insurance Portability and Accountability Act.

Part I: Phantom Study

We constructed a 15-cm-diameter cylindrical phantom composed of ballistics-grade gelatin (12% wt/vol) that housed a central cylindrical chamber capable of holding contrast. Contrast dilutions were prepared by diluting commercially available contrast medium containing 200 mg/mL iodine (iopamidol; Isovue-M 200, Bracco Diagnostics, Princeton, New Jersey) with preservative-free sterile saline to achieve 5 final iodine concentrations: 50, 66, 100, 133, and 150 mg/mL. The phantom's central chamber was filled with various dilutions of contrast, and a 22-gauge needle was secured into place, centered along the long axis of the chamber. The phantom was placed in a clinical CT scanner (LightSpeed 16; GE Healthcare, Milwaukee, Wisconsin) containing each contrast dilution and was scanned by use of the axial technique at a tube current of 10 mA and peak voltage of 120 kVp (Fig 1). The images were then reviewed by a neuroradiologist by use of the scanner's preset window/level setting for CTF procedures (window and level setting: 4000/465). Needle visibility was assessed by use of a 3-point scoring system, with a score of 0 indicating clear visibility of the needle against the background contrast, a score of 1 indicating borderline visibility, necessitating adjustment of the

window and level settings, and a score of 2 indicating inability to visualize the needle.

Part II: Clinical Study

On the basis of the results of the phantom study, we selected 4 contrast concentrations for use in the clinical study: 66, 100, 133, and 150 mg/mL iodine. Subjects were recruited from among adult patients presenting to a single neuroradiologist for CTF-guided interlaminar or transforaminal epidural steroid injections in the cervical or lumbar spine. A contraindication to iodinated contrast, such as a prior allergic reaction, was an exclusion criterion.

Once enrolled, subjects were randomly assigned to one of the contrast dilutions on the basis of a predetermined randomization schedule, and the clinically indicated procedure was performed. For patients scheduled for multiple injections in a single visit, a single-contrast dilution was used for all injections performed at that visit. All scans were performed on the same clinical scanner, which was the same scanner used to scan the phantom. For each procedure, tube current settings were at the discretion of the proceduralist and were based on body habitus and injection location.

Image Analysis

Images from the procedures were reviewed by use of a standardized window and level setting (4000/465) by 2 neuroradiologists, each with 5 years of experience performing CTF-guided steroid injections. The readers were blinded to the assigned contrast dilution. One of the readers was the same radiologist who per-

formed the injections; however, image review occurred 5 months after the end of patient enrollment, thereby mitigating the chance that any particular dilution could be recalled during analysis. Images were scored according to a 5-point scoring system (Table 1), which expanded the 3-point system used in the phantom study. Scores of -2 and -1 were added to account for the need to achieve adequate anatomic soft tissue contrast when performing clinical procedures. Representative examples of injections scored as optimal and at the extremes of the 5-point scale are shown in Fig 2. In 4 cases in which the readers disagreed by 2 points, the case was jointly reviewed by both readers and a consensus score was determined. Injection technique (interlaminar epidural steroid injection [ILESIs] versus transforaminal epidural steroid injection [TFESIs]) was also recorded.

Data Analysis

Data were analyzed with the use of SAS software (version 9.3, SAS Institute, Cary, North Carolina). Because there was more than 1 injection per subject in some cases, visibility scores were analyzed by means of the generalized estimating equations test of difference, assuming a multinomial distribution and a cumulative logit link function. A value of $P = .05$ was considered to be statistically significant for analysis of the effect of contrast concentration on needle visibility. Follow-up contrast statements in the generalized estimating equations test of difference model comparing multiple individual contrast concentrations as well as the effect of injection type (ie, ILESIs versus TFESIs) were analyzed with the use of a Bonferroni-corrected significance threshold of 0.0083.

RESULTS

In the phantom study, iodine concentrations of 50 and 66 mg/mL were associated with clear needle visualization, 100 mg/mL was found to be borderline for needle visualization, and concentra-

tions of 133 mg/mL and higher resulted in nonvisualization of the needle. Dilutions in the range of 66–150 mg/mL were selected for the clinical study because we anticipated that there would be a further reduction in iodine concentration as the contrast was injected and dispersed into the soft tissues.

In the clinical study, a total of 42 patients receiving a total of 60 injections were enrolled and randomly assigned. Mean patient age was 64 years (range, 20–89). There were 19 men and 23 women. Lumbar injections accounted for 55 of 60 procedures. Of the cervical injections, 3 were TFESIs and 2 were ILESIs. There was a similar proportion of TFESIs and ILESIs, with TFESIs accounting for 28 of 60 of all injections (47%) and ILESIs accounting for the remainder (53%). Tube current settings for the procedure ranged from 20–70 mA.

Needle visibility was found to be highly associated with contrast concentration ($P < .0001$). No association was found between visibility scores and anatomic location (cervical versus lumbar) ($P = .61$) or the combined variables of anatomic location and contrast concentration ($P = .20$).

Visibility scores for the individual contrast dilutions are presented in Table 2. Generally, concentrations of ≥ 133 mg/mL showed substantial numbers of injections in which the contrast was too concentrated to allow needle visualization (ie, score of $+2$). Of the concentrations < 133 mg/mL, a concentration of 66 mg/dL demonstrated the greatest percentage of optimal scores (44%) but was also assigned a score indicating unacceptable soft tissue contrast (ie, score of -2) in 21% of cases. Overall inadequate visibility (ie, a score of $+2$ or -2) was found in 8 of 32 cases for the 100 mg/mL concentration and 8 of 34 cases for the 66 mg/mL concentration.

With the use of a Bonferroni-corrected significance threshold of 0.0083, significant differences were found in visibility between the following dilutions: 66 mg/mL versus 133 mg/mL ($P < .0001$), 66 mg/mL versus 150 mg/mL ($P = .0004$), and 100 mg/mL versus 133 mg/mL ($P = .0005$). No difference was found in visibility between the 66 mg/mL and 100 mg/mL concentrations ($P = .069$).

Table 1: Five-point scoring system for the clinical study

	Too Concentrated		Optimal		Too Dilute
Visibility score	+2	+1	0	-1	-2
Needle tip	Not visible	Borderline	Visible	Visible	Visible
Soft tissue contrast	Adequate	Adequate	Adequate	Borderline	Not acceptable

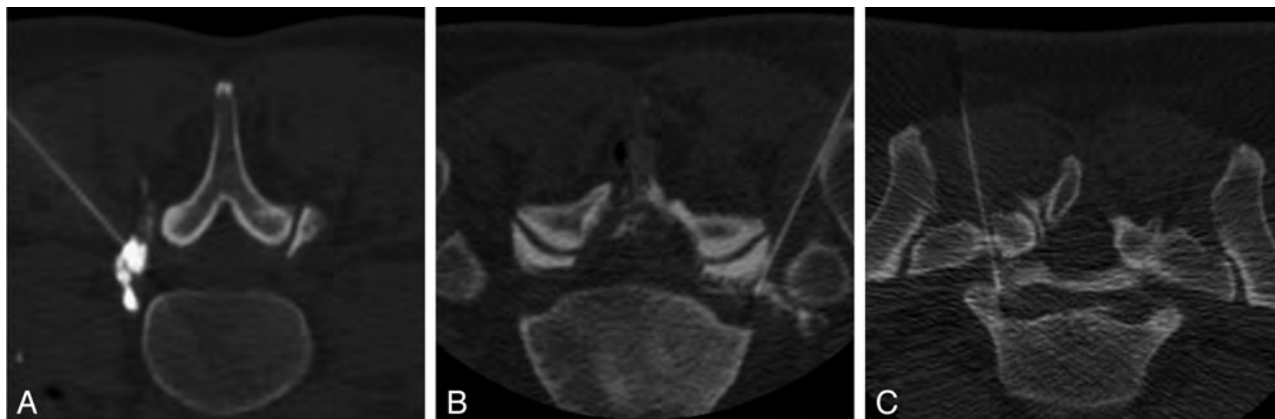


FIG 2. Axial CTF images show representative examples of visibility scores on the basis of our 5-point scoring system. A, Score of $+2$. The contrast is too dense to visualize the location of the needle tip. B, Score of 0. The needle tip can be distinguished from the injected contrast; adequate soft tissue contrast is also provided. C, Score of -2 . The injected contrast is too dilute to provide adequate soft tissue contrast.

Table 2: Visibility scores for the clinical study

	Visibility Score				
	-2	-1	0	+1	+2
Total scores (<i>n</i> = 120) (2 readers)	<i>n</i> = 9 (7.5%)	<i>n</i> = 10 (8.3%)	<i>n</i> = 34 (28.3%)	<i>n</i> = 25 (20.8%)	<i>n</i> = 42 (35.0%)
Iodine concentration					
66 mg/mL (<i>n</i> = 34)	<i>n</i> = 7 (20.6%)	<i>n</i> = 5 (14.7%)	<i>n</i> = 15 (44.1%)	<i>n</i> = 6 (17.6%)	<i>n</i> = 1 (2.9%)
100 mg/mL (<i>n</i> = 32)	<i>n</i> = 2 (6.3%)	<i>n</i> = 5 (15.6%)	<i>n</i> = 9 (28.1%)	<i>n</i> = 10 (31.3%)	<i>n</i> = 6 (18.8%)
133 mg/mL (<i>n</i> = 26)	<i>n</i> = 0 (0%)	<i>n</i> = 0 (0%)	<i>n</i> = 2 (7.7%)	<i>n</i> = 3 (11.5%)	<i>n</i> = 21 (80.8%)
150 mg/mL (<i>n</i> = 28)	<i>n</i> = 0 (0%)	<i>n</i> = 0 (0%)	<i>n</i> = 8 (28.6%)	<i>n</i> = 6 (21.4%)	<i>n</i> = 14 (50.0%)
Injection technique					
Ilesi (<i>n</i> = 64)	<i>n</i> = 0 (0%)	<i>n</i> = 3 (4.7%)	<i>n</i> = 14 (21.9%)	<i>n</i> = 17 (26.6%)	<i>n</i> = 30 (46.9%)
TFESI (<i>n</i> = 56)	<i>n</i> = 9 (16.1%)	<i>n</i> = 7 (12.5%)	<i>n</i> = 20 (35.7%)	<i>n</i> = 8 (14.3%)	<i>n</i> = 12 (21.4%)

Table 3: Comparison of visibility scores on the basis of combined iodine concentration and injection technique

Iodine Concentration + Injection Technique	P Value ^a
(66 mg/mL and TFESI) versus (100 mg/mL and TFESI)	.011
(66 mg/mL and Ilesi) versus (100 mg/mL and Ilesi)	.016
(66 mg/mL and Ilesi) versus (66 mg/mL and TFESI)	.051
(100 mg/mL and Ilesi) versus (100 mg/mL and TFESI)	.021

^a P values are based on results of generalized estimating equations test of difference contrast statements with the use of a Bonferroni-corrected significance threshold of 0.0083.

To determine whether either the 66 mg/mL or 100 mg/mL concentration was superior for a particular injection technique (Ilesi versus TFESI), we examined multiple combinations of contrast concentration and injection technique. These included comparison of visibility scores for TFESI with scores for Ilesi at both 66 mg/mL and 100 mg/mL iodine, as well as scores for TFESI injections performed at 66 mg/mL with those performed at 100 mg/mL, and Ilesi scores for the same concentrations (Table 3). Although we observed trends for several of these combinations, none of these comparisons achieved statistical significance by use of the corrected significance threshold of 0.0083.

DISCUSSION

The role of contrast in ESI is to confirm the epidural and extravascular location of the needle tip and to examine the spread of injectate toward the therapeutic target. In cases in which the contrast pattern indicates an undesirable needle position necessitating repositioning of the needle, the contrast attenuation must not obscure the visibility of the needle tip. Our investigation demonstrated that iodine concentration was highly associated with needle visibility ($P < .0001$) during CT-guided ESI and that at or above iodine concentrations of 133 mg/mL, the contrast was too attenuated to allow needle visualization. Furthermore, our results suggest that the optimal iodine concentration for such procedures is 66–100 mg/mL. Because commercially available contrast media used for spinal injections generally are available with iodine concentration of 180–200 mg/mL and higher, proceduralists seeking to optimize needle visibility during CT-guided spine procedures must dilute their contrast.

To our knowledge, ours is the first investigation to systematically evaluate the effect of contrast concentration on needle visibility in CT-guided procedures. Previous authors have recommended the use of dilute contrast for use in CT-guided procedures, but the suggested dilutions have generally been empirically determined and vary widely among authors. For cervical TFESI, contrast dilutions of 1:10, 1:2, 1:1, and 3:1 have been reported by different authors, with the use of either saline or local anesthetic as the diluent.^{7,10-13} A report of CT-guided celiac plexus neurolysis technique recommended the use of a contrast dilution of 1:4 with anesthetic.¹⁴ In many cases, the dilution ratios were reported,

but details of the contrast medium being diluted or its iodine concentration were not specified. Thus, our study aimed to systematically determine the optimal iodine concentration for use in CT-guided ESI. In our investigation, the contrast concentrations that produced the highest proportions of acceptable scores correspond to dilutions of 1:1 (100 mg/mL) or 1:2 (66 mg/mL).

Visibility is particularly important when performing CT-guided procedures requiring high degrees of precision in needle placement, such as with cervical epidural steroid injections (Fig 3). In a previous investigation, we found that needle repositioning was necessary after contrast injection in 16% of cervical TFESIs because of the undesirable spread of contrast in the epidural space, subperiosteal injection, or intravascular injection.¹⁵ In cases in which critical neural and vascular structures are in close proximity to the target needle placement, the inability to visualize the needle tip and make controlled adjustments to its position increases the risk for catastrophic consequences. The need to decrease iodine concentration to allow visibility of the needle must be balanced against the need for adequate soft tissue contrast. Overdilution of contrast could result in inability to confidently confirm epidural location of the needle, failure to adequately assess the extent and direction of spread of injectate in the epidural space, or failure to detect intrathecal or intravascular injection. The ideal concentration of contrast would permit needle visibility while maintaining good visibility of the contrast as it disperses in the soft tissues surrounding the injection site.

The 5-point scoring system that we used for the clinical study was designed to balance these competing needs. We found that needle visibility against the background contrast pool is no longer possible at concentrations ≥ 133 mg/mL under phantom conditions and is unacceptable in most clinical cases. Notably, we did not find a statistically significant difference in visibility scores between the 66 mg/mL and 100 mg/mL concentrations, nor did we identify a subgroup on the basis of injection location or technique in which one concentration or the other was superior. We did find that at a concentration of 100 mg/mL iodine, most unacceptable visibility scores resulted from a contrast concentration too high to allow needle visibility. Conversely, at 66 mg/dL, most unacceptable scores resulted from overdiluted contrast and insufficient

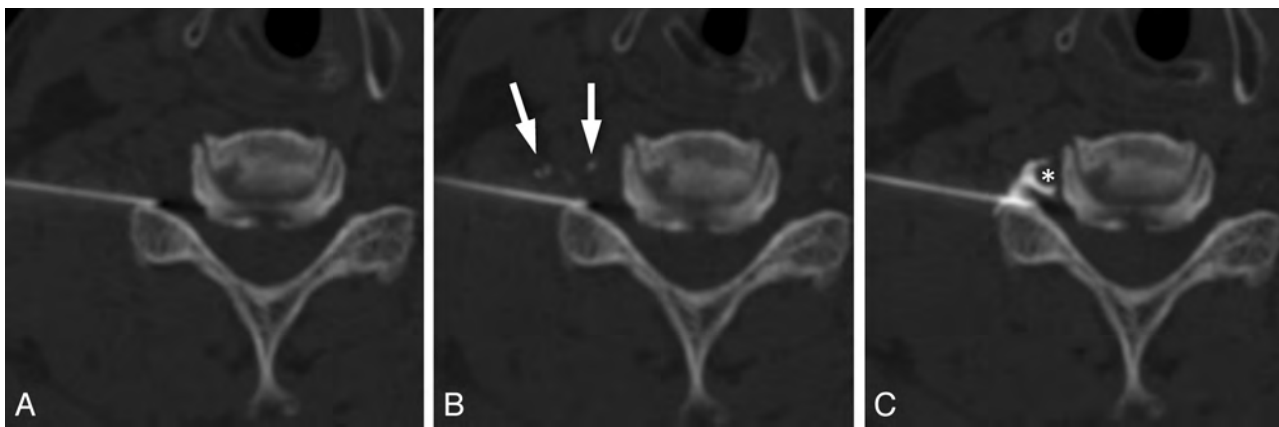


FIG 3. Importance of precise needle placement in cervical epidural steroid injections. *A*, Axial CTF image obtained before contrast injection. *B*, Image obtained immediately after contrast injection shows transient filling of small vessels (arrows). No epidural spread is seen. *C*, Image obtained after advancing the needle <2 mm demonstrates foraminal epidural contrast spread, with no vascular filling. Note the close proximity of the needle tip to the vertebral artery (*). This case highlights the importance of accurate localization of the needle tip and the need to be able to make small but precise adjustments in needle position during epidural injections.

soft tissue contrast. Yet, for both dilutions, there were cases scored as too concentrated (ie, score of +2) as well as others scored as too dilute (ie, score of -2), suggesting that some component of needle visibility may depend on idiosyncratic factors related to the anatomy or tissue composition of the injection site or individual perceptual differences by the scorers. Although our investigation focused on ESI, a variety of other CT-guided procedures use contrast injection, and we would anticipate that our results would be generalizable to other techniques in which contrast is injected into soft tissue.

There are several limitations to this investigation. First, the number of injections in this prospective investigation was selected to evaluate our primary hypothesis that there would be a difference in needle visibility on the basis of concentration. There are subgroups of injections, however, for which our total number of subjects may be insufficiently powered to detect differences. With larger numbers, it is possible that differences in optimal contrast concentration could be found between interlaminar epidural and transforaminal injections in which we observed nonsignificant trends or between cervical and lumbar injections. Second, the degree to which any single contrast attenuation is considered optimal may be in part influenced by the specific considerations of the procedure being performed, the relative hazards of overdilution versus underdilution of contrast in any particular context, and by the subjective preferences of the proceduralist. Our determination of optimal iodine concentration should be considered a general guide but can be tailored according to the needs of individual cases and operators.

CONCLUSIONS

Optimal iodine concentration in contrast used during CT-guided spine procedures is 66–100 mg/mL. This range provides the greatest balance between visualizing the needle and providing adequate tissue contrast. Because these concentrations are not currently commercially available, the use of a 2:1 or 1:1 dilution of contrast by proceduralists performing CT-guided ESI would be necessary, assuming a starting contrast concentration of 200 mg/mL iodine.

REFERENCES

1. Provenzano DA, Fanciullo G. Cervical transforaminal epidural steroid injections: should we be performing them? *Reg Anesth Pain Med* 2007;32:169–70
2. McGrath JM, Schaefer MP, Malkamaki DM. Incidence and characteristics of complications from epidural steroid injections. *Pain Med* 2011;12:726–31
3. Benny B, Azari P, Briones D. Complications of cervical transforaminal epidural steroid injections. *Am J Phys Med Rehabil* 2010;89:601–07
4. White AH, Derby R, Wynne G. Epidural injections for the diagnosis and treatment of low-back pain. *Spine* 1980;5:78–86
5. Stojanovic MP, Vu TN, Caneris O, et al. The role of fluoroscopy in cervical epidural steroid injections: an analysis of contrast dispersal patterns. *Spine* 2002;27:509–14
6. Glaser SE, Shah RV. Root cause analysis of paraplegia following transforaminal epidural steroid injections: the 'unsafe' triangle. *Pain Physician* 2010;13:237–44
7. Wald JT, Maus TP, Geske JR, et al. Safety and efficacy of CT-guided transforaminal cervical epidural steroid injections using a posterior approach. *AJNR Am J Neuroradiol* 2012;33:415–19
8. Chang A, Pochert S, Romano C, et al. Safety of 1000 CT-guided steroid injections with air used to localize the epidural space. *AJNR Am J Neuroradiol* 2011;32:E175–77
9. Silbergleit R, Mehta BA, Sanders WP, et al. Imaging-guided injection techniques with fluoroscopy and CT for spinal pain management. *Radiographics* 2001;21:927–39
10. Wagner AL. CT fluoroscopic-guided cervical nerve root blocks. *AJNR Am J Neuroradiol* 2005;26:43–44
11. Hoang JK, Apostol MA, Kranz PG, et al. CT fluoroscopy-assisted cervical transforaminal steroid injection: tips, traps, and use of contrast material. *AJR Am J Roentgenol* 2010;195:888–94
12. Miller TS, Fruauff K, Farinhas J, et al. Lateral decubitus positioning for cervical nerve root block using CT image guidance minimizes effective radiation dose and procedural time. *AJNR Am J Neuroradiol* 2013;34:23–28
13. Kranz PG, Raduazo PA. Technique for CT fluoroscopy-guided cervical interlaminar steroid injections. *AJR Am J Roentgenol* 2012;198:675–77
14. Wang PJ, Shang MY, Qian Z, et al. CT-guided percutaneous neurolytic celiac plexus block technique. *Abdom Imaging* 2006;31:710–18
15. Hoang JK, Massoglia DP, Apostol MA, et al. CT-guided cervical transforaminal steroid injections: where should the needle tip be located? *AJNR Am J Neuroradiol* 2013;34:688–92

Intramedullary Spinal Cord Metastases: Visibility on PET and Correlation with MRI Features

P.M. Mostardi, F.E. Diehn, J.B. Rykken, L.J. Eckel, K.M. Schwartz, T.J. Kaufmann, C.P. Wood, J.T. Wald, and C.H. Hunt



ABSTRACT

BACKGROUND AND PURPOSE: Studies systematically evaluating the detection of intramedullary spinal cord metastasis with PET are lacking. Our purpose was to evaluate the visibility of intramedullary spinal cord metastasis on PET in a single institutional series and to correlate PET and MR imaging features.

MATERIALS AND METHODS: Patients were included if pretreatment MR imaging identifying an intramedullary spinal cord metastasis and an [¹⁸F] FDG-PET examination near the time of MR imaging were available. PET examinations were retrospectively reviewed, with reviewers blinded and then unblinded to the PET report and MR imaging findings. PET intramedullary spinal cord metastasis features were compared with and correlated with previously analyzed MR imaging lesion characteristics. Original clinical PET reports were reviewed.

RESULTS: The final study sample was 10 PET examinations in 10 patients with 13 intramedullary spinal cord metastases. In 7 (70%) patients, retrospective blinded review demonstrated convincing evidence of 10 (77%) intramedullary spinal cord metastases. Three MR imaging features correlated with intramedullary spinal cord metastases being visible on PET compared with those nonvisible, respectively: larger lesion enhancement size: mean size: 32.1 mm versus 6.0 mm ($P = .038$); larger longitudinal extent of T2 signal abnormality: mean 5.6 versus 1.0 segments ($P = .0081$); and larger ratio of extent of T2 signal abnormality to contrast enhancement: 3.8 versus 1.0 ($P = .0069$). Intramedullary spinal cord metastasis was confidently reported clinically in 2 (20%) patients, accounting for 5 (38%) intramedullary spinal cord metastases.

CONCLUSIONS: Most intramedullary spinal cord metastases can be detected on PET when performed near the time of pretreatment MR imaging. However, intramedullary spinal cord metastases may not be clinically reported on PET. Larger lesions with more edema are more likely to be visible. The spinal cord should be specifically and carefully assessed on PET for evidence of intramedullary spinal cord metastases to provide timely diagnosis.

ABBREVIATIONS: ISCM = intramedullary spinal cord metastasis; [¹⁸F] = fluorine 18; SUVmax = maximum standardized uptake value

Intramedullary spinal cord metastases (ISCMs) are rare and devastating manifestations of metastatic neoplasm. They are present at autopsy in 0.9–2.1% of patients with cancer^{1,2} and comprise 1–4% of spinal metastases.^{1–3} Early detection is important because ISCMs indicate a poor prognosis, and treatment may slow neurologic deterioration.⁴ However, ISCMs can be asymptomatic, especially at early stages, and are historically difficult to

detect with imaging.^{3,5} MR imaging is the cornerstone of spinal cord imaging,⁶ but this technique is generally not indicated for screening of asymptomatic patients.

[¹⁸F] FDG-PET is the primary imaging technique used for whole-body screening for metastases and therefore is a technique that ideally locates most sites of metastases, including intraspinal. However, there are only scattered case reports of visualization of ISCMs on PET.^{7–12} No large series systematically evaluating the detection of ISCMs with PET have been reported. The purpose of the current study was to retrospectively evaluate the visibility of ISCMs on PET in a single institutional series of patients with ISCMs, and to correlate PET and MR imaging features.

MATERIALS AND METHODS

Institutional review board approval with waived consent was obtained for this Health Insurance Portability and Accountability Act–compliant retrospective research study.

Received March 8, 2013; accepted after revision April 13.

From the Mayo Medical School (P.M.M.), and Division of Neuroradiology (F.E.D., L.J.E., K.M.S., T.J.K., C.P.W., J.T.W., C.H.H.), Department of Radiology, Mayo Clinic, Rochester, Minnesota; and Division of Neuroradiology (J.B.R.), Department of Radiology, University of Minnesota, Minneapolis, Minnesota.

Paper previously presented at: Annual Symposium of the American Society of Spine Radiology, February 2013; Scottsdale, Arizona.

Please address correspondence to Felix E. Diehn, MD, 200 1st St SW, Rochester, MN 55905; e-mail: Diehn.felix@mayo.edu

Indicates article with supplemental on-line tables.

<http://dx.doi.org/10.3174/ajnr.A3618>

Subjects

A search of the radiologic and clinical databases at our institution from 1999–2011 had previously yielded a group of 45 patients with 64 ISCMs, in whom pretreatment MR imaging had identified the ISCM.¹³ For inclusion in the current study, this group was refined to those patients in whom a PET scan (either PET/CT or PET only) was also available for electronic review. It was assumed that the number of potential cases of ISCM seen on PET at our institution but not imaged with MR imaging (and thus not included in our 45-patient cohort) would be negligible or nonexistent, given that patients would be expected to undergo spinal MR imaging if an ISCM was first suggested at PET. When multiple PET examinations were available for a patient, only the examination closest to the MR imaging was included in the study. PET examinations performed more than 60 days before or more than 14 days after the pretreatment diagnostic MR imaging were excluded. The purpose of these criteria was to exclude PET examinations that were estimated to have a high likelihood of predating the development of an ISCM (those performed more than 60 days before MR imaging) and to exclude PET examinations in which the PET appearance probably would have been affected by the preceding treatment of an ISCM (those performed more than 14 days after MR imaging).

PET Acquisition

Although there was some variability in PET scanner technology, given the more than 10-year time period over which the imaging was performed, our standard [¹⁸F] FDG-PET protocol was followed for patient preparation and imaging. Patient preparation included 4 hours of fasting, such that the finger-stick blood glucose level was in the desired range, between 70–180 mg/dL, before injection of the [¹⁸F] FDG radiotracer. The injected activity was 15 mCi of [¹⁸F] FDG ($\pm 10\%$), with an uptake time of 60–70 minutes.

All PET images were obtained on General Electric scanners (GE Healthcare, Milwaukee, Wisconsin). Because of the evolving nature of our clinical practice over the course of the study, the scanner types changed with emerging technology. Only 1 of the patients in this study was imaged on a PET only scanner (Advance NX series). The other 9 patients were all imaged on PET/CT scanners: 3 on Discovery 690 series, 1 on Discovery ST series, 2 on Discovery RX series, and 3 on Discovery DLS series.

PET/CT acquisition parameters were helical scan, 0.5 seconds rotation time; pitch, 0.984; table speed, 39.37 mm/rotation; section thickness, 3.75 mm; kVp 120. A 3D PET acquisition toward the feet was used with bed position of 3 minutes.

Image Review

Two radiologists (F.E.D., neuroradiology faculty member with an American Board of Radiology certification and a Certificate of Added Qualification in neuroradiology; C.H.H., neuroradiology and nuclear medicine faculty member with an American Board of Radiology certification, Certificate of Added Qualification—eligible for neuroradiology and nuclear medicine) and a 4th-year medical student (P.M.M.) retrospectively reviewed the PET examinations for evidence of ISCMs in multiplanar fashion on an electronic workstation in consensus fashion. The reviewers were first blinded and, after complete initial review of the PET

examinations, subsequently unblinded to the clinical PET report and all MR imaging findings. When concurrent CT was available, images were reviewed both without and with the CT data. Multiple characteristics were analyzed on PET for ISCMs that were identified: lesion location (spinal levels), maximal superior-inferior extent (number of vertebral body segments), morphology of FDG uptake (fusiform versus round), and maximum standardized uptake value (SUV_{max}) of the ISCM. SUV_{max} of the mediastinal blood pool was measured on all PET examinations. The SUV_{max} of both the ISCMs and of the mediastinal blood pool was determined by placing a circular region of interest over the area that included the subjective maximum uptake. Several MR imaging lesion characteristics previously analyzed by 2 radiologists (F.E.D. and J.B.R., a neuroradiology fellow with an American Board of Radiology certification)^{13,14} were noted: lesion location, maximal superior-inferior enhancement length (size [mm] and extent [number of vertebral body segments]), extent of T2 signal abnormality (number of vertebral segments), ratio of extent of T2 signal abnormality to contrast enhancement, and presence/absence of “rim” and “flame” signs,¹³ 2 postgadolinium MR imaging findings specific for ISCM.

Clinical Review

The original clinical PET interpretations were reviewed to assess whether any of the following were reported: the ISCM(s), the primary neoplasm, additional metastatic disease (including specifically CNS, non-CNS, and skeletal spinal column metastases). Note that these clinical interpretations were issued by subspecialty trained nuclear medicine physicians at a large academic medical center. The time interval (days) between the PET and MR imaging examinations was calculated. For cases in which the PET report did not describe the ISCM(s) but PET occurred before the MR imaging, a review of the electronic medical record was performed to assess whether there was an impact on clinical care of the patient.

Statistical Analysis

PET and MR imaging findings were compared for each patient, in consensus by the 3 reviewers. Spinal segment localization on PET was considered concordant with that on MR imaging if at least a portion of the PET location overlapped with the MR imaging location. One-way *t* test assuming unequal variances was performed to assess correlation of the following features with visibility of ISCMs on PET: number of days between MR imaging and PET and all aforementioned MR imaging features except for location. Contingency testing was performed to assess the relationship of the primary tumor pathology (lung cancer and melanoma) with the ability to detect ISCM on PET/CT. Bivariate linear coefficient analysis was performed to assess the correlation of the length of the ISCM on MR imaging (contrast enhancement) and on PET, by use of both the size measurement (mm) on MR imaging and longitudinal extent (number of vertebral segments) on both MR imaging and PET. Descriptive statistics were obtained by use of Excel 2010 (Microsoft Corporation, Redmond, Washington). Additional analyses were conducted with the use of SAS

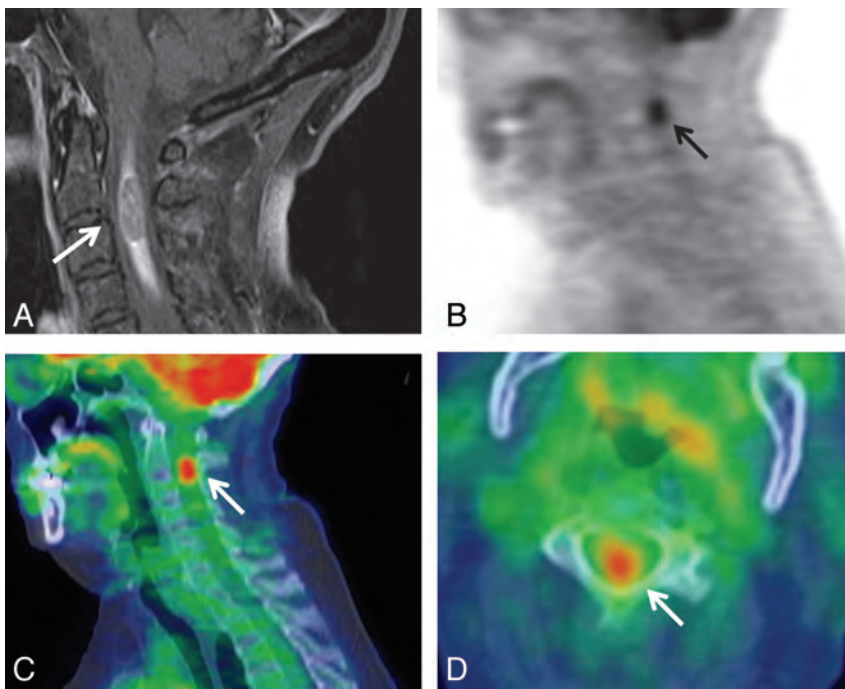


FIG 1. Solitary ISCM visible on PET. A 69-year-old woman (patient 8 in On-line Table 1) with non-small cell lung cancer underwent PET 13 days after MR imaging. A, Postcontrast fat-suppressed sagittal T1WI; B, sagittal PET only image; C, sagittal, and D, axial PET/CT fused images. The cervical cord ISCM was identified on original clinical and retrospective review. The location of the FDG avid ISCM in the upper cervical cord (C2–3) corresponds to the lesion location on MR imaging (C1–5) (arrows). SUVmax of the ISCM was 5.1 ($2.0 \times$ that of blood pool). The clinical PET report favored a primary spinal cord neoplasm.

version 9.3 (SAS Institute, Cary, North Carolina). Statistical significance was defined as a value of $P < .05$.

RESULTS

Summary of Subjects

Of the 49 patients with 70 ISCMs and available pretreatment MR imaging, 17 (35%) had a total of 32 PET examinations performed. Twenty-two PET examinations from 7 (41%) of these 17 patients were excluded; 16 PET examinations were excluded because the PET examination was performed more than 60 days before the MR imaging and 6 because the PET was more than 14 days after the pretreatment MR imaging. The final study sample was 10 PET examinations (9 PET/CT and 1 PET only) in 10 patients with 13 ISCMs. Patient individual and group characteristics are shown in On-line Tables 1 and 2, respectively. The mean age was 61 years (range, 37–75), and 6 (60%) were female. The primary malignancies were lung cancer in 5 (50%) patients (8 ISCMs) and melanoma in 5 (50%) patients (5 ISCMs). Four of the 5 lung cancer patients had non-small cell carcinoma and 1 had small-cell lung carcinoma. Nine (90%) patients had a solitary ISCM (Figs 1, 3, and 4), whereas 1 (10%) patient with lung cancer harbored multiple ISCMs (Fig 2).

The mean interval between MR imaging and PET was 11 days (range, 49 days before to 13 days after). PET occurred before or on the day of MR imaging in 8 (80%) of patients. Other metastases were present on the PET report in 9 (90%) patients; 7 (70%) patients had non-CNS, nonspine metastases, 2 (20%) patients had other CNS metastases, and 1 (10%) patient had skeletal spinal column metastases reported (On-line Table 2).

ISCM Findings on PET

ISCM characteristics, including findings on PET, are displayed in On-line Tables 1 and 2, on an individual and group basis. On retrospective, blinded review of PET, there was convincing evidence of 10 of 13 (77%) ISCMs in 7 of 10 (70%) patients (Figs 1–4). The location of FDG uptake for each of these 10 ISCMs was concordant with the location of the contrast-enhancing lesion on MR imaging (for example, Figs 1–4). For the 1 patient with multiple ISCMs, each ISCM was found and even 2 adjacent lesions at the T4 and T4–5 levels were discretely visualized on PET, as on MR imaging (Fig 2). Furthermore, the ISCM extent on PET (number of vertebral segments) correlated with the measured enhancing lesion size (mm) on MR imaging ($R^2 = 0.803$; $P = .0004$). The ISCM extent on PET did not correlate with the longitudinal extent of enhancement on MR imaging ($P = .151$). The average SUVmax was 6.7 (range, 3.3–9.9). For each ISCM, the SUVmax of the lesion was greater than that of the mediastinal blood pool. The FDG avid lesions had round morphology in 8

(80%) cases (for example, Figs 1, 2, and 4).

Three (23%) ISCMs in 3 (30%) patients could not be seen retrospectively on PET, despite unblinding of reviewers to the MR imaging results. These 3 ISCMs were also not described in the original clinical PET interpretations. The PET examinations were performed 7 days before MR imaging in 2 of these patients and 21 days before MR imaging in another. In all 3 (100%) patients, other metastases were reported on the original clinical PET interpretation (On-line Table 2). In none of the 10 patients did unblinding of reviewers to the MR imaging findings and PET report change the retrospective interpretation of the PET.

Correlation of Clinical and MR Imaging Features with ISCM Visibility on PET

There was no association between either the type of primary malignancy or the time interval between the MR imaging and PET and the visibility of ISCM on PET ($P = .25$, $P = .7$, respectively). Three MR imaging features correlated with ISCM visibility on PET (On-line Table 2): 1) larger lesion enhancement size: mean size of lesions visible versus not visible on PET, 32.1 mm versus 6.0 mm, respectively ($P = .038$); 2) larger extent of T2 signal abnormality: mean of 5.6 versus 1.0 segments ($P = .0081$); and 3) larger ratio of extent of T2 signal abnormality to contrast enhancement: 3.8 versus 1.0 ($P = .0069$). MR imaging features that did not correlate with ISCM visibility on PET were extent of lesion contrast enhancement (number of vertebral segments) ($P = .11$) and the presence of the “rim” sign ($P = .50$), “flame” sign ($P = .50$), either sign ($P = .23$), or both signs ($P = .53$).

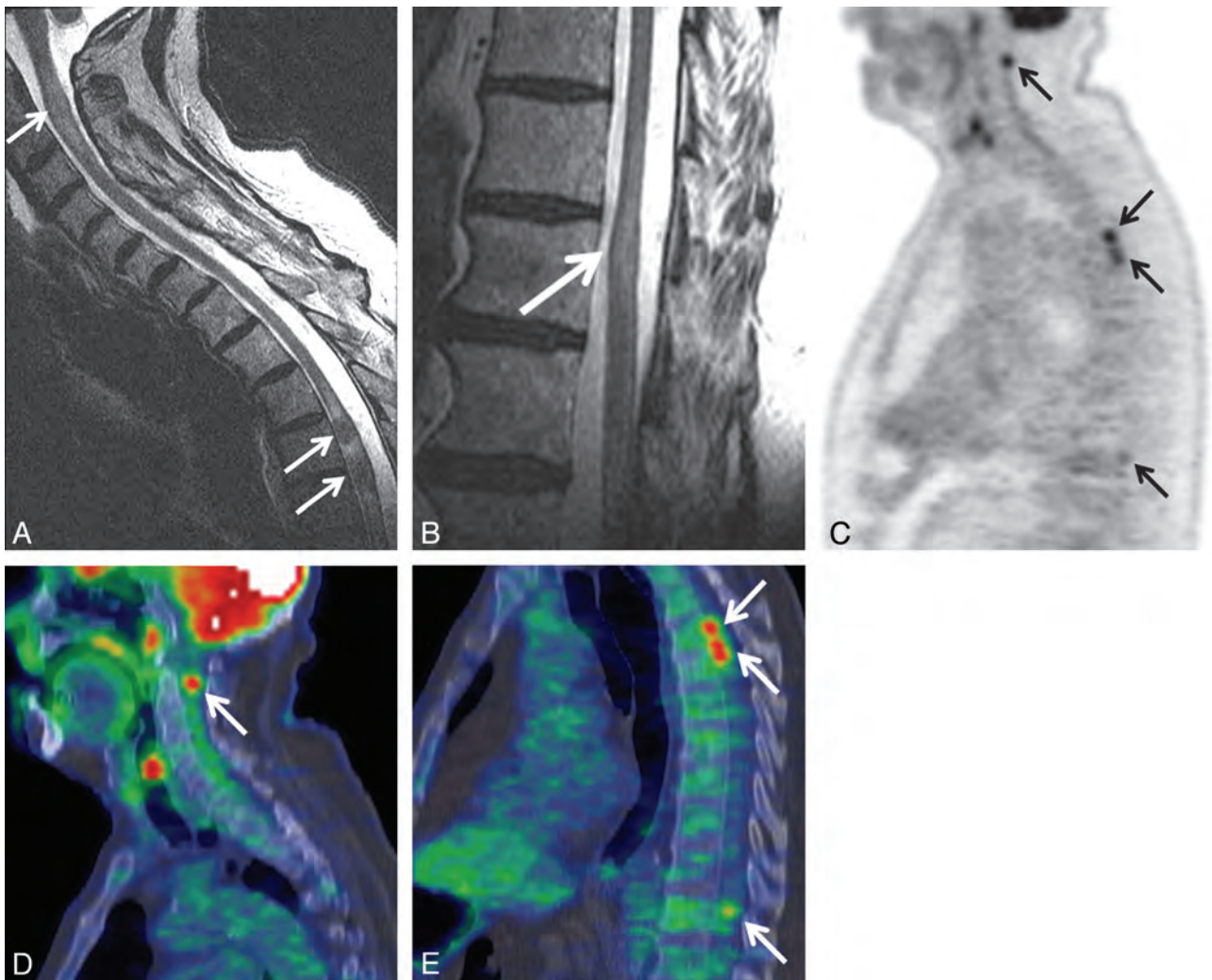


FIG 2. Patient with multiple ISCMs, all visible on PET. A 73-year-old man (patient 5 in On-line Table 1) with non-small cell lung cancer underwent PET 5 days before MR imaging. Precontrast sagittal T2WI of the cervicothoracic (A) and lower thoracic (B) regions; C, sagittal entire spine PET only image; sagittal cervicothoracic (D) and thoracic (E) region PET/CT fused images. Several cervical and thoracic cord ISCMs were identified on original clinical and retrospective review of the PET examination, including 2 immediately adjacent metastases at T4 and T4–5. The locations on MR imaging (C2; T4; T4–5; T11) correlate with those on PET (C1–2; T4; T5; T10) (arrows). SUVmax of the ISCMs ranged from 5.3–9.9 (2.9–5.5 × that of blood pool). (Note: Postcontrast sagittal T1WI from the same patient showing enhancement of the ISCMs is included in Reference 14, Fig 1, in which the figure emphasized the asymptomatic status of some patients with ISCM).

Clinical Reporting of ISCMs on PET

Of the 10 patients with 13 ISCMs, ISCMs were confidently prospectively reported in the original clinical PET report in 2 (20%), accounting for 5 of 13 (38%) ISCMs (for example, Fig 2). In 1 patient, a cord lesion was reported, but a primary cord neoplasm was favored, at least in part because of lack of other evidence of FDG metastatic disease (Fig 1). In 7 of 10 (70%) patients with 7 of 13 (54%) ISCMs, the ISCMs were not reported (Figs 3 and 4). In 4 of these 7 (57%) patients and 4 of 7 (57%) ISCMs, the ISCMs were identified on blinded, retrospective review (Figs 3 and 4). These ISCMs ranged in size from 7–114 mm on MR imaging. The PET examinations were performed 49 days and 1 day prior in 2 patients, on the day of MR imaging in 1 patient, and 7 days after MR imaging in 1 patient. Of these 4 ISCMs visible on retrospective review but not clinically reported, the lack of identification on PET probably had clinical impact in 1 patient. The patient shown in Fig 3 had PET performed while having lower extremity symptoms. It was not until the MR imaging 49 days

later that the ISCM of the conus with leptomeningeal spread in the cauda equina was formally diagnosed and subsequently treated with steroids and radiation.

DISCUSSION

The present study shows that most ISCMs can be detected on PET when this is performed near the time of diagnostic MR imaging. PET is often performed prior to spine MR imaging and may thus be the first imaging study to reveal an ISCM. However, ISCMs may not be clinically reported on PET, as the minority of ISCMs in the minority of patients had been confidently clinically reported in this study. This can have clinical impact. Larger lesions with more edema are more likely to be visible on PET, but even subcentimeter ISCMs can be detected.

These results are clinically relevant in several ways. We hope that these results will stimulate those who read PET primarily to focus on the spinal cord as part of their search pat-

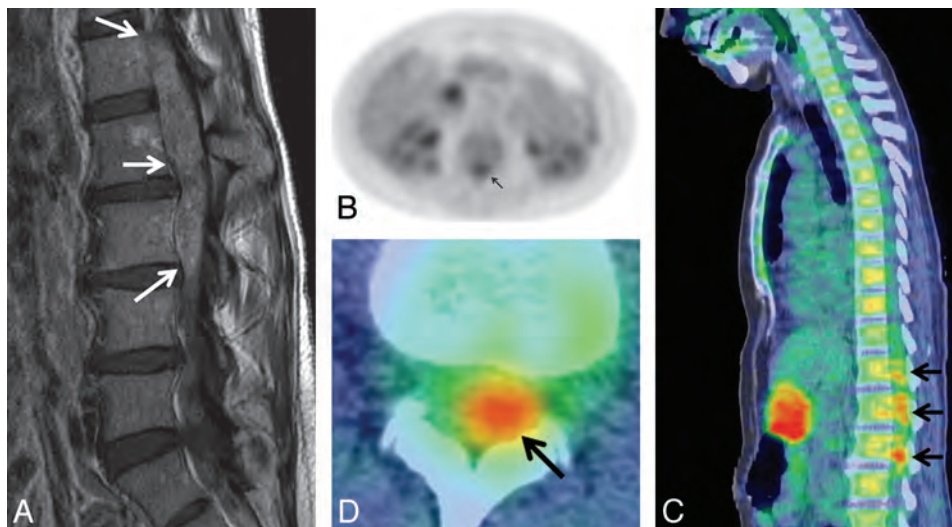


FIG 3. ISCM not originally clinically reported, probably with clinical impact. A 57-year-old woman (patient 2 from On-line Table 1) with melanoma underwent PET 49 days before MR imaging. *A*, Postcontrast sagittal T1WI; *B*, axial PET only image; *C*, sagittal and *D*, axial PET/CT fused images. The fusiform, patchy lower spinal canal uptake (conus and cauda equina region) was not described in the original clinical PET report. It was not until the MR imaging nearly 2 months later that the large exophytic ISCM arising from the conus was formally diagnosed and treated. Note that only a single sagittal PET/CT section is shown; on review of multiple adjacent images; the PET uptake appears contiguous. This is the largest ISCM in this series. The location of enhancing lesions on MR imaging (L1–4) corresponds with PET uptake (T12/L1–L3/4) (arrows). SUVmax was 5.4 ($3.0 \times$ that of blood pool).

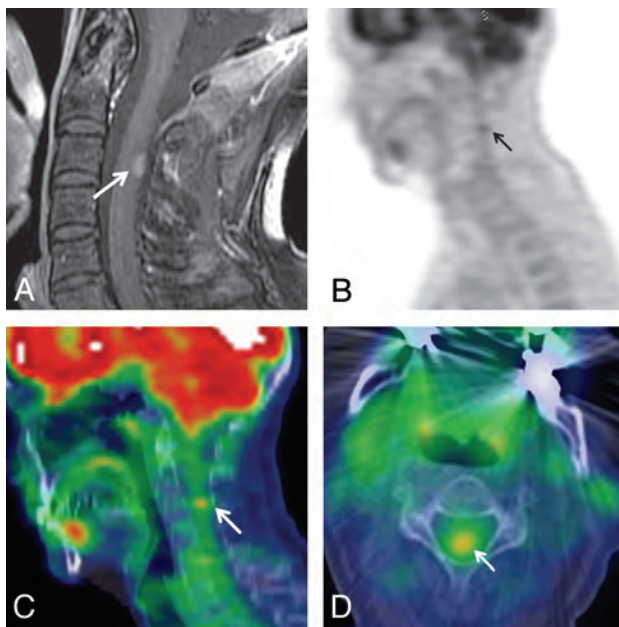


FIG 4. Smallest ISCM visible on PET, not clinically reported. A 54-year-old woman (patient 9 from On-line Table 1) with non-small cell lung cancer underwent PET 1 day before MR imaging. *A*, Post-contrast sagittal T1WI; *B*, sagittal PET only image; *C*, sagittal, and *D*, axial PET/CT fused images. A small, 7-mm cervical ISCM (arrows) was not described on the original clinical PET report. The location of the FDG avid ISCM in the upper cervical cord (C3–4) corresponds to the lesion location on MR imaging (C3) (arrows). The SUVmax was 3.3 ($1.9 \times$ that of blood pool).

tern. Missing ISCMs can delay diagnosis, and identifying and treating ISCM(s) early improves outcomes.^{15,16} The fact that ISCMs can be asymptomatic or present with minimal neurologic symptoms^{7-9,12,14,15} also underscores the importance of detecting the lesions on early imaging, even when other evidence of metastatic disease is present, as there was for most

patients in the current study. Similarly, the results of our study should encourage those who do not interpret PET primarily but correlate with it when interpreting MR imaging to actually review the PET images, not just the interpretation. Finally, PET may be considered as an alternative to MR imaging for the evaluation for ISCMs in certain settings, including in patients for whom MR imaging is contraindicated and those already undergoing PET for disease staging. Patients suspected of having ISCM with equivocal spinal cord findings on MR imaging who cannot receive intravenous gadolinium may also be good candidates for PET.

Our study adds to the existing literature describing PET findings of ISCMs, which is otherwise limited to case reports.⁷⁻¹² This is the first study starting with a large number of ISCMs identified on MR imaging to evaluate the conspicuity of ISCMs on PET and how visibility on PET correlates with MR imaging features. Note that in a recent neuroimaging study assessing PET findings of 9 intramedullary spinal cord tumors, only primary spinal cord tumors were included; primary tumors can also demonstrate increased uptake on PET.¹⁷

There are several possible reasons for nondiagnosis and the low clinical identification rate of ISCMs on the original PET reports for patients in the current study. These probably include lack of specific attention to the spinal cord, lack of familiarity with the appearance or even their existence (as these lesions are rare), confounding or distracting uptake in the immediately adjacent vertebral column, satisfaction of search (as other sites of FDG avid metastatic disease were often present), and the small size of some of the lesions. As part of the CNS, the spinal cord may also be overlooked on PET just as the intracranial contents are often not well scrutinized on this technique. Specifically, MR imaging has been shown to have superior sensitivity and specificity in detecting intracranial metastases, even in FDG avid malignancies.^{18,19} Contributory factors are that inherent phys-

ologic FDG uptake within the brain limits visualization of superimposed FDG avid lesions and that MR imaging has superior spatial sensitivity. Moreover, Lee et al²⁰ showed that approximately one-third of lung cancer brain metastases appeared hypometabolic on PET.

Limitations of this study include those inherent to a retrospective study. The time span over which data were collected leads to differences in the MR imaging and PET imaging techniques. Another limitation is that the MR imaging and PET images were interpreted by consensus review and despite blinding, readers were aware that there was at least 1 ISCM in each case. Although the exclusion criteria limiting the time interval between PET and MR imaging examinations may have eliminated some patients who harbored an ISCM that could have been visible on PET, we chose those criteria to minimize the possibility of “false-negative” PET examinations as the result of an ISCM either not yet having developed or already having been treated. Additionally, 10 patients with 13 ISCMs is a relatively small series, but this is the largest such series to be published to our knowledge. Some factors may overestimate the sensitivity of PET for ISCMs, such as the fact that the consensus reviewers knew at least 1 ISCM was present in each case; others may underestimate, such as the fact that not all malignancies are FDG avid.

Future work may include studying a larger patient population, potentially across multiple centers, to allow further identification of factors that affect ISCM conspicuity on PET. Some small ISCMs in this series could be detected on PET, whereas others could not, and we could not discover an explanation for this in this current work. Identifying such tumor or patient characteristics may help determine patients for whom PET is or is not a reliable screening tool for ISCMs.

CONCLUSIONS

We describe the PET findings from a large series of ISCMs and correlate these with MR imaging features. The results should be helpful to radiologists. Most ISCMs are visible on PET when this is performed near the time of diagnostic MR imaging, but they may not be clinically reported on PET. Larger lesions with more edema are more likely to be visible on PET. The spinal cord should be specifically and carefully assessed on PET for evidence of ISCMs to provide timely and accurate diagnosis. In some settings, such as when MR imaging is contraindicated, PET may be considered as an option to evaluate for ISCM.

REFERENCES

1. Chason JL, Walker FB, Landers JW. **Metastatic carcinoma in the central nervous system and dorsal root ganglia: a prospective autopsy study.** *Cancer* 1963;16:781–87
2. Costigan DA, Winkelman MD. **Intramedullary spinal cord metastasis: a clinicopathological study of 13 cases.** *J Neurosurg* 1985;62:227–33
3. Edelson RN, Deck MD, Posner JB. **Intramedullary spinal cord metastases: clinical and radiographic findings in nine cases.** *Neurology* 1972;22:1222–31
4. Lee SS, Kim MK, Sym SJ, et al. **Intramedullary spinal cord metastases: a single-institution experience.** *J Neurooncol* 2007;84:85–89
5. Reddy SC, Vijayamohan G, Rao GR. **Delayed CT myelography in spinal intramedullary metastasis.** *J Comput Assist Tomogr* 1984;8:1182–85
6. Sze G, Krol G, Zimmerman RD, et al. **Intramedullary disease of the spine: diagnosis using gadolinium-DTPA-enhanced MR imaging.** *AJR Am J Roentgenol* 1988;151:1193–204
7. Jayasundera MV, Thompson JF, Fulham MJ. **Intramedullary spinal cord metastasis from carcinoma of the lung: detection by positron emission tomography.** *Eur J Cancer* 1997;33:508–09
8. Komori T, Delbeke D. **Leptomeningeal carcinomatosis and intramedullary spinal cord metastases from lung cancer: detection with FDG positron emission tomography.** *Clin Nucl Med* 2001;26:905–07
9. Nguyen NC, Sayed MM, Taalab K, et al. **Spinal cord metastases from lung cancer: detection with F-18 FDG PET/CT.** *Clin Nucl Med* 2008;33:356–58
10. Jeon MJ, Kim TY, Han JM, et al. **Intramedullary spinal cord metastasis from papillary thyroid carcinoma.** *Thyroid* 2011;21:1269–71
11. Pellegrini D, Quezel MA, Bruetman JE. **Intramedullary spinal cord metastasis.** *Arch Neurol* 2009;66:1422
12. Poggi MM, Patronas N, Buttman JA, et al. **Intramedullary spinal cord metastasis from renal cell carcinoma: detection by positron emission tomography.** *Clin Nucl Med* 2001;26:837–39
13. Rykken JB, Diehn FE, Hunt CH, et al. **Rim and flame signs: post-gadolinium MRI findings specific for non-CNS intramedullary spinal cord metastases.** *AJNR Am J Neuroradiol* 2013;34:908–15
14. Rykken JB, Diehn FE, Hunt CH, et al. **Intramedullary spinal cord metastases: MRI and relevant clinical features from a 13-year institutional case series.** *AJNR Am J Neuroradiol* 2013;34:2043–49
15. Sung WS, Sung MJ, Chan JH, et al. **Intramedullary spinal cord metastases: a 20-year institutional experience with a comprehensive literature review.** *World Neurosurg* 2013;79:576–84
16. Kalayci M, Cagavi F, Gul S, et al. **Intramedullary spinal cord metastases: diagnosis and treatment: an illustrated review.** *Acta Neurochir* 2004;146:1347–54
17. Tomura N, Ito Y, Matsuoka H, et al. **PET findings of intramedullary tumors of the spinal cord using [18F] FDG and [11C] methionine.** *AJNR Am J Neuroradiol* 2013;34:1278–83
18. Krüger S, Mottaghy FM, Buck AK, et al. **Brain metastasis in lung cancer: comparison of cerebral MRI and 18F-FDG-PET/CT for diagnosis in the initial staging.** *Nuklearmedizin* 2011;50:101–06
19. Pfannenbergl C, Aschoff P, Schanz S, et al. **Prospective comparison of 18F-fluorodeoxyglucose positron emission tomography/computed tomography and whole-body magnetic resonance imaging in staging of advanced malignant melanoma.** *Eur J Cancer* 2007;43:557–64
20. Lee HY, Chung JK, Jeong JM, et al. **Comparison of FDG-PET findings of brain metastasis from non-small-cell lung cancer and small-cell lung cancer.** *Ann Nucl Med* 2008;22:281–86

Analysis of Related Factors on the Deformity Correction of Balloon Kyphoplasty

C. Xu, H.-X. Liu, and H.-Z. Xu



ABSTRACT

BACKGROUND AND PURPOSE: Balloon kyphoplasty is a minimally invasive surgical approach for treating vertebral compression fractures, including osteoporotic vertebral compression fractures. The purpose of this study was to determine the effect of balloon inflation and postural reduction on balloon kyphoplasty for the deformity correction of vertebral compression fractures and to explore the correlative factors affecting the deformity correction.

MATERIALS AND METHODS: A retrospective study of 72 patients (75 levels) who had undergone balloon kyphoplasty was conducted. Imaging data and clinical features were collected and analyzed. Independent-samples *t* test analysis was used to find the possible factors affecting deformity correction.

RESULTS: Postural correction in the overextending position significantly increased anterior middle vertebral height, kyphotic angle, and Cobb angle (each $P < .05$). There was no significant difference in anterior, middle vertebral height, kyphotic angle, and Cobb angle between postural reduction and balloon dilation (each $P > .05$). The improvement on the Visual Analog Scale was notable ($P < .05$). Among a variety of factors, the fracture type (wedge type and biconcave type) affected both the height restoration ($P = .003$) and kyphotic angle reduction ($P = .007$). The bone cement injected volume was related to height restoration ($P = .011$) and kyphotic angle reduction ($P = .018$).

CONCLUSIONS: Balloon inflation was useless for deformity correction. The deformity correction was attributed to postural reduction with cement strengthening. The most significant factors affecting deformity correction were the fracture type and bone cement injected volume.

ABBREVIATIONS: VCF = vertebral compression fracture; KA = kyphotic angle; BMI = body mass index; BMD = bone mineral density; IBT = inflatable bone tamp; HA = height of anterior vertebra; HM = height of middle vertebra; HP = height of posterior vertebra

Osteoporosis is a condition in which the bones lose calcium and become more likely to break. In other words, osteoporosis is a disease of the skeleton in which bones become brittle and prone to fracture.¹ Bone mineral attenuation reduction is the fundamental basis for the diagnosis of osteoporosis. Osteoporotic vertebral compression fracture (VCF) is the most common complication of osteoporosis. Osteoporosis causes the vertebra to become thin and fragile, increasing the chance of compressing with even minor injury, and, over time, the person with osteoporosis can become hunched over or stooped. During the past 2 decades, balloon kyphoplasty has proved to be a minimally invasive technique for treating VCFs, including osteoporotic VCFs. The inflat-

able bone tamp (IBT) expands slowly, thus providing a preformed low-pressure cavity for bone cement to be injected in. The aim of this procedure is to relieve pain and to correct deformity of the fractured vertebral body.²⁻⁵ The benefits of balloon kyphoplasty compared with percutaneous vertebroplasty are better vertebral height restoration and less cement leakage.⁶ Nevertheless, some scholars have observed the existence of dynamic and latent mobility of VCFs.^{7,8} Improvement in fractured vertebral height and restoration of sagittal alignment have been ascribed to postural reduction combined with IBT dilation. However, whether the radiographic changes would be significant after removing the interference of postural factors is unknown.

In this retrospective study, we determined whether IBT inflation offers an additional advantage of realigning the spinal column and regaining height in the index vertebral body and investigated related factors that could contribute to deformity correction.

MATERIALS AND METHODS

Patient Data

We retrospectively reviewed all consecutive patients with VCFs who were treated with balloon kyphoplasty at our institution with

Received February 26, 2013; accepted after revision April 3.

From the Department of Orthopedic Surgery, The Second Affiliated Hospital of Wenzhou Medical College, Wenzhou, Zhejiang, People's Republic of China.

Please address correspondence to Dr Hua-Zi Xu, Department of Orthopedic Surgery, The Second Affiliated Hospital of Wenzhou Medical College, 109 Xueyuanxi Rd, Wenzhou, Zhejiang, People's Republic of China; e-mail: derek1226@163.com

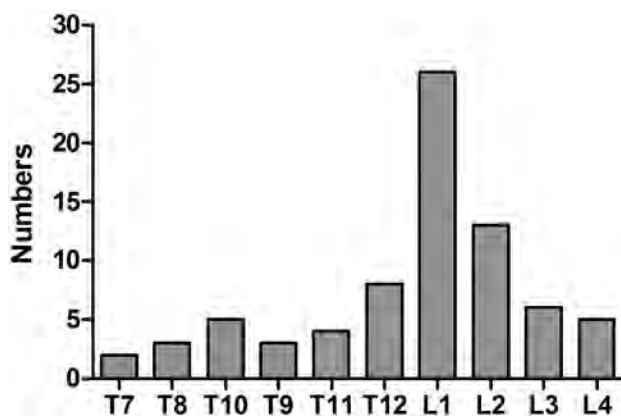
Indicates article with supplemental on-line table

<http://dx.doi.org/10.3174/ajnr.A3617>

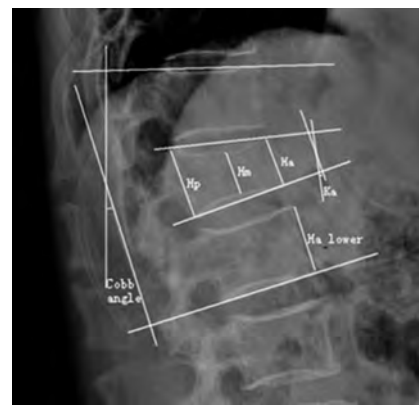
Table 1: Classifications and data of patients

Classifications	Data
Total No. of cases	72 (75 fractured vertebrae)
Average age, y	71.47 ± 1.42 (57–86 y)
<70	26 (36.1%)
≥70	46 (63.9%)
Sex	
Male	20 (27.8%)
Female	52 (72.2%)
BMD	
> -2.5	19 (26.4%)
≤ -2.5	53 (73.6%)
BMI ^a	
<24	30 (41.7%)
≥24	42 (58.3%)
Type of fracture	
Wedge	48 (66.7%)
Biconcave	24 (33.3%)
Cement injected volume	
<6 mL	28 (38.9%)
≥6 mL	44 (61.1%)

^a BMI = weight (kg)/height² (m²).

**FIG 1.** Index vertebra distribution.

verbal informed consent between March 2011 and October 2012. Institutional review board approval and written informed consent were obtained. Selection criteria were 1) elderly (>50 years), 2) thoraco-lumbar vertebrae, 3) minor injury or no history of trauma, 4) the constant ache and fatigue in thoraco-lumbar vertebrae that can significantly affect daily life, 5) being diagnosed with osteoporosis or osteopenia by dual-energy x-ray absorptiometry (Lunar Prodigy-DXA; Lunar Radiation, Madison, Wisconsin), 6) imaging (x-ray, CT scan, or MR imaging) showing thoraco-lumbar vertebral morphologic change, and 7) fresh fractures (the duration between presentation or injury and surgery was ≤3 weeks). The exclusion criteria were 1) fractures older than 3 weeks' duration, 2) pathologic fracture, 3) vertebral body height fully recovered after postural reduction, and 4) MR imaging signal findings only, without the index vertebral morphologic change. Seventy-two consecutive patients were enrolled in the study according to the above criteria. There were 52 (72.2%) women and 20 (27.8%) men, ranging in age between 57–86 years (mean age, 71.5 years). A total of 75 vertebral bodies were treated in this group (Table 1). The level of the fracture was distributed between T7 and L4, and was most prevalent in the thoraco-lumbar junction (Fig 1). Of all patients treated, 69 had a single vertebral fracture

**FIG 2.** Illustration showing the measurement of anterior (HA), middle (HM), and posterior (HP) portions of fractured vertebral height; kyphotic angle (KA); Cobb angle; and vertebral heights 1 level above (upper) and below (lower) the index vertebra.

and 3 had multiple lesions. The categoric variables, including sex, age, bone mineral density (BMD), body mass index (BMI), fracture type, and bone cement injected volume, were checked and classified (Table 1). Patients were grouped according to categoric variables and the radiographic outcomes for each and were then compared. For all patients, x-ray, CT scan, and MR imaging were performed before surgery and x-ray again after the procedure.

Operative Technique

The patient was positioned prone on a radiolucent operating bed that allowed for anteroposterior and lateral imaging, with the thoraco-lumbar junction hyperextended by cushions. Cushions were positioned under the iliac crests and both sides of the upper thorax. The operating bed was flexed as needed to increase extension at the thoraco-lumbar junction. General anesthesia was the most comfortable option for patients experiencing pain and was used in all procedures. A 1–2-cm skin incision was made lateral to the desired entry point of the pedicle to percutaneously place an IBT (Shandong Guan-long Medical Utensils Co, Shandong Province, China) into the collapsed vertebral body through a bipedicular approach. IBT inflation was performed to create a low-pressure cavity for cement injection. Inflation continued until the IBT reached 300 psi or the maximum size was reached. The IBTs were removed, and viscous bone cement (polymethylmethacrylate; Tianjin Synthetic Materials Research Institute, Tianjin, China) was injected through the working cannula. The whole therapeutic process was monitored and recorded by the C-arm digitalized x-ray system.

Imaging Parameters and Clinical Outcomes

Each fractured vertebra was sequentially measured for its height of anterior vertebra (HA), height of middle vertebra (HM), height of posterior vertebra (HP), kyphotic angle (KA), and Cobb angle⁹ in the midsagittal plane on a PACS. Kyphotic angle was the angle defined by the intersection of superior and inferior endplate of the fractured body. Determination of the Cobb angle measurement was taken from the superior endplate of the vertebra 1 level above the treated vertebra to the inferior endplate of the vertebral body 1 level below the treated vertebra. The vertebral heights 1 level above and below the index vertebra were also calculated (measurement method is

Table 2: Imaging parameters during balloon kyphoplasty ($\bar{x} \pm s$)

	Preoperative	Prone	Balloon Inflated	Postoperative
HA, mm	21.30 \pm 5.34 ^a	26.37 \pm 4.34	26.47 \pm 4.41 ^b	25.61 \pm 4.50 ^c
HM, mm	17.88 \pm 4.65 ^a	21.57 \pm 4.28	21.76 \pm 4.38 ^b	21.24 \pm 4.24 ^c
HP, mm	27.97 \pm 4.64	27.96 \pm 4.65	28.07 \pm 4.68	27.98 \pm 4.65

^a $P < .05$ for preoperative versus prone.

^b $P > .05$ for balloon inflated versus prone.

^c $P < .05$ for postoperative versus preoperative.

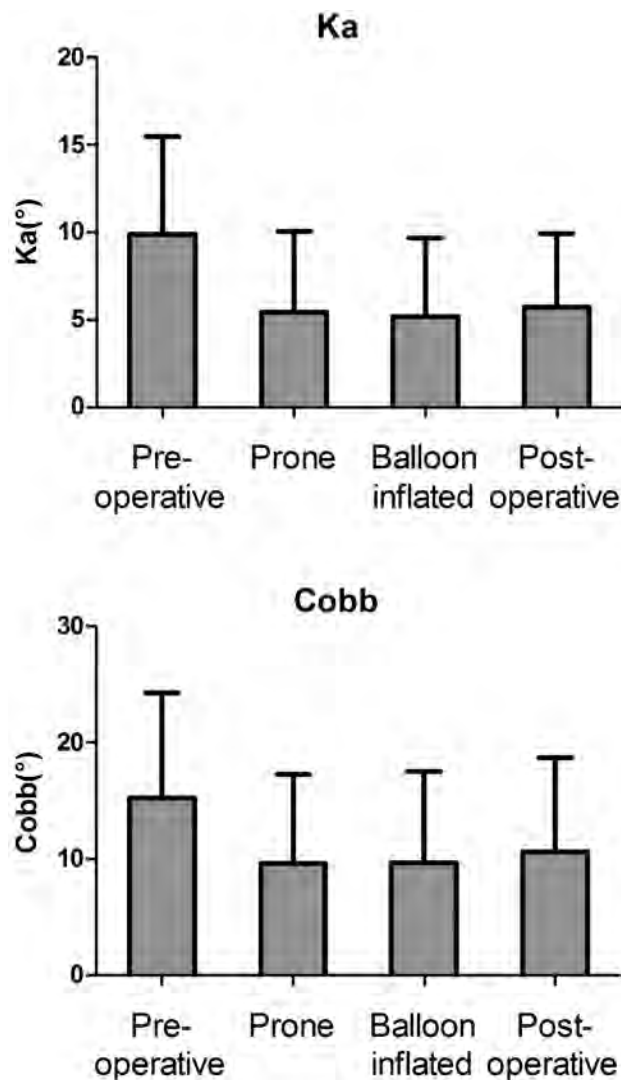


FIG 3. Change of the KA and Cobb angle during balloon kyphoplasty ($\bar{x} \pm s$). Note: Prone compared with preoperative, $P < .05$; balloon inflated compared with prone, $P > .05$; postoperative compared with preoperative, $P < .05$.

shown in Fig 2). Initial index vertebra height = $(\text{height}_{\text{upper}} + \text{height}_{\text{lower}})/2$. Height restoration ratio was calculated as follows: $(\text{height}_{\text{postop}} - \text{height}_{\text{preop}})/(\text{height}_{\text{normal}} - \text{height}_{\text{preop}}) \times 100\%$. These data were taken from lateral radiographs and analyzed at 4 different time points: 1) preoperative (standing), 2) intraoperatively (placing the patient in prone hyperextension position), 3) after inflation of the IBT, and 4) postoperative (standing). The clinical outcomes were measured with the Visual Analog Scale, which patients were asked to complete before and after surgery. All parameters were measured and recorded by one surgeon.

Statistical Analysis

All statistical analysis, including mean values and standard deviations, were performed with the use of commercially available software (SPSS 19 for Windows; IBM, Armonk, New York) with the significance level setting at level $P = .05$. The statistical significance of differ-

ent time points was assessed with the paired t test. Categorical variables (sex, age, BMD, fracture type, BMI, and bone cement injected volume) were compared and evaluated by means of the independent-sample t test. A value of $P < .05$ was considered to show a statistically significant difference.

RESULTS

We examined whether patients who were treated with kyphoplasty obtained height restoration and kyphosis rectification. Changes in measured parameters before vertebral augmentation, after postural positioning on the table, after IBT inflation, and after the procedure are presented in Table 2, the On-line Table, and Fig 3. Imaging of a typical case is shown in Fig 4.

Vertebral body height and KA were markedly affected by placing the patient in the hyperextended prone position with extended posture at the commencement of the procedure. Minor further improvement in vertebral height (Table 2, $P > .05$), KA (Fig 3, $P > .05$), and Cobb angle (Fig 3, $P > .05$) were noted after IBT dilation in comparison with the hyperextended position time point.

In a comparison of preoperative and postoperative measurements, significant improvement in compressed vertebral body deformity was noted. HA and HM improved significantly ($P < .05$), from 21.30 ± 5.34 mm to 25.61 ± 4.50 mm, and from 17.88 ± 4.65 mm to 21.24 ± 4.24 mm, respectively. HP was nearly unchanged after treatment, which improved from 27.97 ± 4.64 mm to 27.98 ± 4.65 mm with no significance ($P > .05$). The KA dramatically ($P < .05$) fell from $9.90 \pm 5.59^\circ$ to $5.69 \pm 4.25^\circ$. The Cobb angle dropped significantly, from $15.21 \pm 9.05^\circ$ to $10.61 \pm 8.08^\circ$ ($P < .05$).

Clinical symptom (low back pain), which was assessed by the Visual Analog Scale, significantly ($P = .003$) decreased from a mean of 8.2 ± 0.8 points (range, 7–10 points) before surgery to 2.1 ± 1.0 points (range, 0–4 points) 1 day after surgery. All patients were satisfied with the results. The mean bone cement injected volume was 6.2 mL (range, 2.7–8.0 mL). The leakage of cement into paravertebral soft tissue or veins was detected in 6 cases (8.33%). However, no complications related to cement leakage were noted.

All patients benefited significantly ($P < .05$) from being placed in prone position at the time of surgery (Table 2 and Fig 3). HA increased from 21.30 ± 5.34 mm to 26.37 ± 4.34 mm and HM increased from 17.88 ± 4.65 mm to 21.57 ± 4.28 mm. The KA and Cobb angle separately reduced from $9.90 \pm 5.59^\circ$ to $5.41 \pm 4.62^\circ$ and from $15.21 \pm 9.05^\circ$ to $9.61 \pm 7.67^\circ$.

The possible correlative factors, including sex, age, BMD, fracture type, BMI, and bone cement injected volume, were classified and analyzed respectively (On-line Table). When comparing the categorical variables, we found that fracture type and bone cement

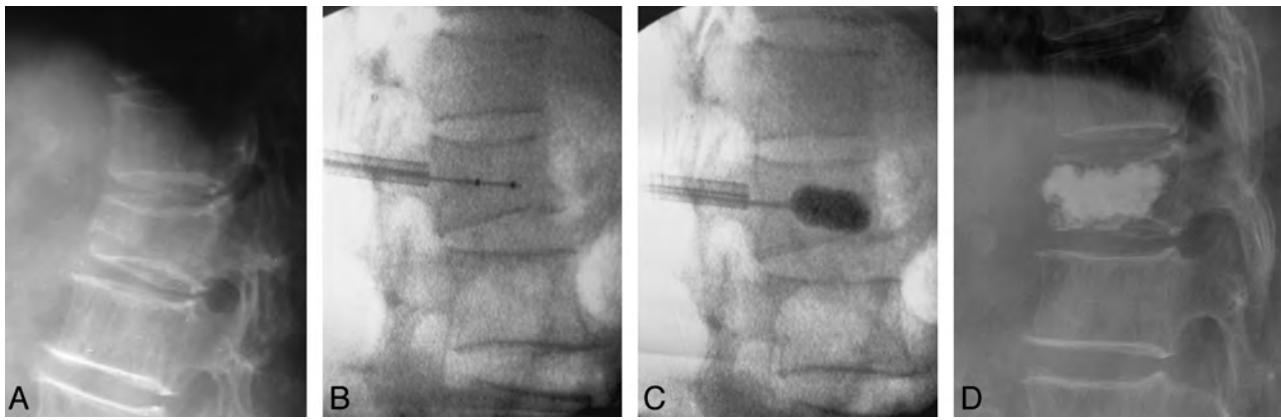


FIG 4. X-ray films of a typical patient: 69-year-old woman with a T12 vertebral compression fracture (wedge type). A, Preoperative standing lateral, HA, HM, KA, and Cobb were 20.20 mm, 24.57 mm, 17.27°, and 14.55°, respectively; B, intraoperative prone position lateral, HA, HM, KA, and Cobb were 25.33 mm, 25.23 mm, 8°, and 7°, respectively; C, intraoperative IBT inflated, HA, HM, KA, and Cobb were 25.33 mm, 25.23 mm, 8°, and 7°, respectively; D, postoperative standing lateral, HA, HM, KA, and Cobb were 24.82 mm, 24.91 mm, 8.56°, and 7.12°, respectively.

injected volume showed statistically significant correlation with height restoration ($P = .003$, $P = .011$) and KA reduction, ($P = .007$, $P = .018$) from the results of independent-samples *t* test analysis. The kyphosis correction of the wedge type group and >6 mL group were significantly larger than the biconcave type group and the <6 mL group, respectively.

DISCUSSION

The efficacy of balloon kyphoplasty for treatment of VCFs has been widely accepted by most spine surgeons.^{10,11} However, it was recently reported that both percutaneous vertebroplasty and balloon kyphoplasty appeared to be effective at producing rapid relief of pain resulting from VCFs and showed similar orders of magnitude of height restoration.¹²⁻¹⁵ This phenomenon occurred because almost all collapsed vertebral bodies exhibited “dynamic and latent fracture mobility.”^{7,8} Nevertheless, some authors^{16,17} support the viewpoint that beyond fracture mobility, a statistically significant further reduction by inflation of the balloon tamp was achieved in every patient.

The results obtained from our study demonstrate that spontaneous reduction in the hyperextended prone position with subsequent cement injection after balloon kyphoplasty resulted in both significant reduction in pain and significant improvement in vertebral deformity, including vertebral height and KA. After hyperextended prone positioning was established, IBT inflation did not appear to significantly further improve vertebral height or KA. Although IBT did not produce additional restoration, it was still an important tool that aided in controlling the distribution of cement during the procedure and compacted the bone fragments, so the bone tunnel was sealed and the incidence of leakage was reduced.

Ligamentotaxis, or manipulative reduction, has been used to prevent the development of postoperative kyphosis in unstable thoraco-lumbar burst fractures.¹⁸ In our study, we refer to postural reduction as ligamentotaxis, confining patients to the supine position overnight before surgery and placing cushions under the upper chest and the iliac crests during surgery. The anterior column of the compressed vertebra was destroyed, whereas the anterior longitudinal ligament and fibrous ring remained intact,

which were important structures in limiting dispersive stress. Through stretching of the anterior longitudinal ligament and the fibrous ring, ligamentotaxis effectively reconstructed the compressed anterior column while adding stability and restoring the sagittal profile. The postural reduction technique created a maximum effect on deformity correction. Research by Cawley et al¹⁹ supports our opinion that IBT inflation did not significantly further increase vertebral height or Cobb angle.

To examine the effect of balloon kyphoplasty on the deformity correction for the collapsed vertebral bodies, we collected and analyzed several parameters before and after the operation. According to statistics, the fracture type and cement injected volume might have an effect on the deformity correction, which would help in forecasting the prognosis of the operation.

The selected cases were divided into 2 groups on the basis of the type of fracture— anterior wedge type and biconcave type—by use of a semiquantitative technique developed by Genant et al.²⁰ The anterior wedge type fracture was mainly affected by the buckling stress, thus HA and KA appeared obviously deformed. The endplates (upper and lower) of biconcave fractured vertebrae, which are also known as vertical-compression type endplates, were compressed by their adjacent intervertebral disks. Lee et al²¹ put forward that the compressed vertebral body configuration was only associated with height restoration. However, we found that this factor showed a statistically significant correlation with height restoration and KA reduction. The kyphosis correction of the wedge type group was significantly larger than the biconcave type group. Thus, the aim of treatment for VCFs with small KA was restoring the middle portion height, increasing vertebral strength and stiffness, and quickly relieving pain.

The bone cement injection was terminated when adequate filling of the vertebral body was achieved or if leakage occurred. How do we define “adequate”? The ideal cement injection volume should be required to meet the following 2 conditions: maximum therapeutic effect and minimum side effects. We observed that a larger volume of bone cement achieved better correction effect (On-line Table). Nevertheless, increasing numbers of studies showed²²⁻²⁵ that bone cement injection volume had no corre-

lation with pain relief and had a positive correlation with bone cement leakage rate. In the clinic, many factors influenced the cement injection volume, such as the severity of osteoporosis, the degree of compression, the region of fracture, and so forth. Further study to evaluate these factors would be valuable.

We expected that BMD would have affected the deformity correction and that the change in vertebral height would be especially common in patients with severe osteoporosis because of the presence of unstable nonunion states in these patients, but the result was not as good as we had hoped. This discordance might be limited by the number and age of patients. Surgical treatment for VCFs does not address continued loss of bone attenuation or the progressive increase in fracture risk caused by underlying osteoporosis. Therefore, patients with confirmed osteoporotic VCFs should receive anti-osteoporosis treatment, such as a bisphosphonate, supplemented with adequate doses of calcium and vitamin D, and should pay more attention to the adjacent vertebral fracture after the balloon kyphoplasty.²⁶

As short-term observational research from a single center, the lack of a sufficient number of cases and long-term effects assessment are limitations of this study. Although all of the data were measured accurately by one spine surgeon, some measurement errors are still inevitable.

CONCLUSIONS

Balloon kyphoplasty is a minimally invasive surgical approach for treating VCFs, including osteoporotic VCFs. It can provide an effective and safe therapeutic effect for VCFs with low BMD. Deformity correction of the index vertebral body in early fractures appears to occur as the result of hyperextended postural reduction with subsequent cement strengthening. IBT does not appear to contribute significantly to additional deformity correction in these early fractures when maximum hyperextension postural correction is used. In view of these facts, how to make the selection depends on cost and the spine surgeon's skill. The predominant correlative factors affecting deformity correction were the fracture type and cement injected volume.

ACKNOWLEDGMENTS

We thank Mr Shi at the Second Affiliated Hospital of Wenzhou Medical College for support and technical assistance.

REFERENCES

- Lindsay R, Burge R, Strauss DM. **One year outcomes and costs following a vertebral fracture.** *Osteoporosis Int* 2005;16:78–85
- Barr JD, Barr MS, Lemley TJ, et al. **Percutaneous vertebroplasty for pain relief and spinal stabilization.** *Spine* 2000;25:923–28
- Lieberman I, Dudeny S, Reinhardt MK, et al. **Initial outcome and efficacy of 'kyphoplasty' in the treatment of painful osteoporotic vertebral compression fractures.** *Spine* 2001;26:1631–37
- Phillips FM, Ho E, Campbell-Hupp M, et al. **Early radiographic and clinical results of balloon kyphoplasty for the treatment of osteoporotic vertebral compression fractures.** *Spine* 2003;28:2260–67
- Bouza C, López T, Magro A, et al. **Efficacy and safety of balloon kyphoplasty in the treatment of vertebral compression fractures: a systematic review.** *Eur Spine J* 2006;15:1050–67
- Taylor RS, Taylor RJ, Fritzell P, et al. **Balloon kyphoplasty and vertebroplasty for vertebral compression fractures: a comparative systematic review of efficacy and safety.** *Spine* 2006;31:2747–55
- McKiernan F, Faciszewski T, Jensen R, et al. **Latent mobility of osteoporotic vertebral compression fractures.** *J Vasc Intervent Radiol* 2006;17:1479–87
- McKiernan F, Jensen R, Faciszewski T, et al. **The dynamic mobility of vertebral compression fractures.** *J Bone Miner Res* 2003;18:24–29
- Phillips FM, Ho E, Campbell-Hupp M, et al. **Early radiographic and clinical results of balloon kyphoplasty for the treatment of osteoporotic vertebral compression fractures.** *Spine* 2003;28:2260–65
- Wardlaw D, Cummings SR, Van Meirhaeghe J, et al. **Efficacy and safety of balloon kyphoplasty compared with non-surgical care for vertebral compression fracture (FREE): a randomised controlled trial.** *Lancet* 2009;373:1016–24
- Eck JC, Nachtigall D, Humphreys SC, et al. **Comparison of vertebroplasty and balloon kyphoplasty for treatment of vertebral compression fractures: a meta-analysis of the literature.** *Spine J* 2008;8:488–97
- Hiwatashi A, Moritani T, Numaguchi Y, et al. **Increase in vertebral body height after vertebroplasty.** *AJNR Am J Neuroradiol* 2003;24:185–89
- Teng MM, Wei CJ, Wei LC, et al. **Kyphosis correction and height restoration effects of percutaneous vertebroplasty.** *AJNR Am J Neuroradiol* 2003;24:1893–900
- Hiwatashi A, Westesson PL, Yoshiura T, et al. **Kyphoplasty and vertebroplasty produce the same degree of height restoration.** *AJNR Am J Neuroradiol* 2009;30:669–73
- Mathis JM. **Percutaneous vertebroplasty or kyphoplasty: which one do I choose?** *Skeletal Radiol* 2006;35:629–31
- Voggenreiter G. **Balloon kyphoplasty is effective in deformity correction of osteoporotic vertebral compression fractures.** *Spine* 2005;30:2806–12
- Shindle MK, Gardner MJ, Koob J, et al. **Vertebral height restoration in osteoporotic compression fractures: kyphoplasty balloon tamp is superior to postural correction alone.** *Osteoporos Int* 2006;17:1815–19
- Silva MB, Zaninelli EM, Benato ML, et al. **Evaluation of the reduction by ligamentotaxis in thoracolumbar burst fractures.** *Columna Columna* 2010;9:126–31
- Cawley DT, Sexton P, Murphy T, et al. **Optimal patient positioning for ligamentotaxis during balloon kyphoplasty of the thoracolumbar and lumbar spine.** *J Clin Neurosci* 2011;18:834–36
- Genant HK, Wu CY, van Kuijk C, et al. **Vertebral fracture assessment using a semiquantitative technique.** *J Bone Miner Res* 2009;8:1137–48
- Lee JH, Kwon JT, Kim YB, et al. **Segmental deformity correction after balloon kyphoplasty in the osteoporotic vertebral compression fracture.** *J Korean Neurosurg Soc* 2007;42:371–76
- Baroud G, Crookshank M, Bohner M. **High-viscosity cement significantly enhances uniformity of cement filling in vertebroplasty: an experimental model and study on cement leakage.** *Spine* 2006;31:2562–68
- Lee IJ, Choi AL, Yie MY, et al. **CT evaluation of local leakage of bone cement after percutaneous kyphoplasty and vertebroplasty.** *Acta Radiol* 2010;51:649–54
- Venmans A, Klazen CA, van Rooij WJ, et al. **Postprocedural CT for perivertebral cement leakage in percutaneous vertebroplasty is not necessary—results from VERTOS II.** *Neuroradiology* 2011;53:19–22
- Boonen S, Van Meirhaeghe J, Bastian L, et al. **Balloon kyphoplasty for the treatment of acute vertebral compression fractures: 2-year results from a randomized trial.** *J Bone Miner Res* 2011;26:1627–37
- Rho YJ, Choe WJ, Chun YI. **Risk factors predicting the new symptomatic vertebral compression fractures after percutaneous vertebroplasty or kyphoplasty.** *Eur Spine J* 2012;21:905–11

Vertebral Augmentation in Patients with Multiple Myeloma: A Pooled Analysis of Published Case Series

O.A. Khan, W. Brinjikji, and D.F. Kallmes



ABSTRACT

BACKGROUND AND PURPOSE: Studies examining the efficacy of vertebroplasty and kyphoplasty in patients with vertebral fractures from multiple myeloma are limited. We sought to perform a systematic review of published case studies examining changes in pain, disability, and analgesic drug use in patients with multiple myeloma who have undergone vertebral augmentation.

MATERIALS AND METHODS: We performed a pooled analysis of published case series of vertebral augmentation in patients with multiple myeloma. Twenty-three studies (9 kyphoplasty, 12 vertebroplasty, and 2 of both) with data on 923 patients were identified from a PubMed search. Quantitative outcome data included the Visual Analog Scale, the Brief Pain Inventory, the Short Form 36 Health Survey, and the Oswestry Disability Index. Time periods were consolidated into 3: postoperatively ≤ 1 week, 1 week to 1 year, and ≥ 1 year. Change in analgesic use was also studied. Data were compared by using nonparametric tests and matched t tests for temporally linked data.

RESULTS: Patients achieved a decrease in pain across all consolidated time periods. Pain, as measured on a 10-point scale, decreased by 4.8 points up to 1 week, 4.6 points up to 1 year, and 4.4 points after a year ($P < .001$). Decrease in pain was apparent early after treatment and was sustained with time. Kyphoplasty and vertebroplasty were equally effective in reducing pain scores because differences between procedures for each time period were insignificant ($P < .9$ for < 1 week, $P < 1.0$ for ≤ 1 year, and $P < .9$ for > 1 year).

CONCLUSIONS: Our analysis demonstrates that vertebral augmentation is effective in patients with multiple myeloma.

ABBREVIATIONS: ODI = Oswestry Disability Index

Multiple myeloma is a neoplasm resulting from the proliferation of plasma cells which invade bone and release factors leading to bone fragility.¹ Fifty-five to 70 percent of patients develop bony lesions that are localized primarily in the vertebrae.² Vertebral augmentation has become an increasingly common treatment to alleviate pain caused by vertebral compression fractures.³ Randomized and nonrandomized controlled trials of patients with osteoporosis and solid metastatic neoplasms have shown that vertebroplasty and kyphoplasty reduce pain, decrease patient use of analgesic drugs, improve functional disability, and increase vertebral height.⁴⁻⁷ Complication rates are low, attributed commonly to cement leakage.^{8,9} Vertebroplasty and kyphoplasty are increasingly used to palliate vertebral lesions in myeloma. However, data are limited to small experiential case series.

We conducted a literature-based analysis of published case series. The aim was to compile and analyze data on vertebral augmentation procedures in multiple myeloma.

MATERIALS AND METHODS

Study Identification

A review of the literature was performed by using PubMed. “Vertebroplasty” or “Kyphoplasty and Myeloma” were used as controlled vocabulary, and descriptors were identified by using MeSH. Studies of vertebroplasty and/or kyphoplasty published in the English language were considered in patients with myeloma, with a minimum of 15 patients, and those that contained ≥ 1 of the following parameters: numeric pain assessment scores for pre- and postoperative pain (Visual Analog Scale, Brief Pain Inventory, Short Form 36 Health Survey), numeric Oswestry Disability Index (ODI) assessment for pre- and postoperative disability, rate of cement leakage (as detected on CT and plain film), and change in patient analgesic drug use. A summary of our search strategy is provided in Fig 1.

Data Extraction

Data on pain, disability, and analgesic use were consolidated into 3 time periods: postoperatively ≤ 1 week, ≤ 1 year, and > 1 year. The percentage of studies showing benefit and the extent of ben-

Received February 17, 2013; accepted after revision April 8.

From the Departments of Radiology (O.A.K., W.B., D.F.K.) and Neurosurgery (D.F.K.), Mayo Clinic, Rochester, Minnesota.

Please address correspondence to Waleed Brinjikji, MD, Mayo Clinic, OL 1-115, 200 First St SW, Rochester, MN 55905; e-mail: brinjikji.waleed@mayo.edu

Indicates article with supplemental on-line tables.

<http://dx.doi.org/10.3174/ajnr.A3622>

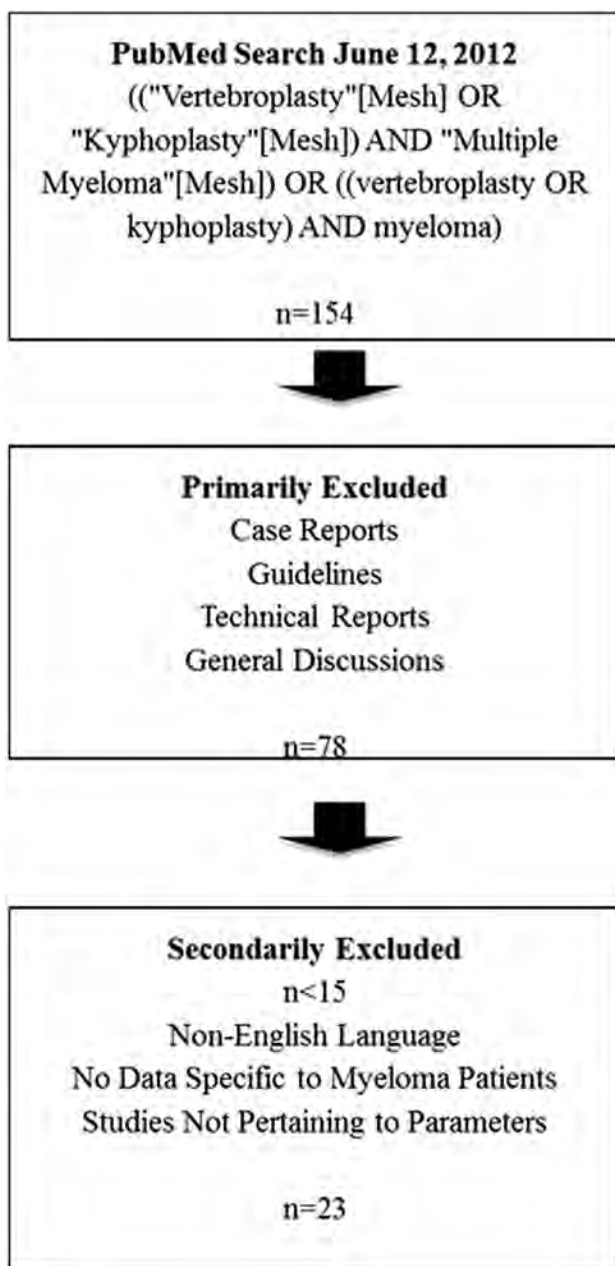


FIG 1. Search criteria used in PubMed data base.

efit were calculated. We looked for immediate or delayed benefit, and, if immediate, whether this benefit was sustained.

We collected data on the following complications: infection, pulmonary embolism, myocardial infarction, subsequent vertebral body compression fractures at untreated levels, neurologic symptoms requiring revision surgery, and transient postoperative pain. Outcome and complications rates of kyphoplasty were compared with those of vertebroplasty.

Statistical Analysis

Statistical analysis was performed by JMP software, Version 9 (SAS, Cary, North Carolina). For the purpose of descriptive and analytical analysis, mean scores were used (when unavailable, median scores were treated as means), and pain assessment from the Visual Analog Scale, the Short Form Health Survey 36, and the

Brief Pain Inventory was combined. Data were compared by using nonparametric tests (χ^2 and Wilcoxon rank tests). Matched *t* tests for temporally linked data were used. Statistical significance was taken as a 2-tailed *P* value < .05.

RESULTS

There were 23 studies (9 kyphoplasty, 12 vertebroplasty, and 2 of both) with data on 923 patients. Twenty patients had multiple treatment sessions; thus, data on 943 procedures were extracted from the literature search. Of 22 studies that reported separate data on the 2 procedures, there were 367 kyphoplasty treatments and 576 vertebroplasty patients. Sex data were available for 760 patients (82.3%). There were 215 men and 215 women for vertebroplasty studies, 153 men and 98 women for kyphoplasty studies, and 47 men and 32 women for a study that did not differentiate between the procedures.¹⁰ The mean age of the total patient population was 64.6 years (range, 28–92 years), while the mean age of patients who underwent kyphoplasty was 63.6 years (range, 28–90 years), and that of those who underwent vertebroplasty was 65.9 years (range, 35–92 years). These data are summarized in On-line Table 1. Spinal augmentation was performed on 1872 levels. Detailed anatomic localization of the fractures was not available. Data recorded in the studies ranged anywhere from 24 hours to 4 years postprocedure.

Nineteen studies reported on pre- and postprocedure pain (On-line Table 2). There was no significant difference in mean pain reduction between vertebroplasty and kyphoplasty at ≤ 1 week (2.8 points \pm 0.4 versus 2.8 points \pm 0.4, *P* = .9). Similarly, no difference in pain reduction was found at 1 week to 1 year postprocedure as vertebroplasty patients had a mean pain reduction compared with baseline of 2.5 points \pm 0.4 versus 2.5 points \pm 0.5 for kyphoplasty patients (*P* = 1.00). At >1 year postprocedure, vertebroplasty patients had a mean pain reduction of 2.9 points \pm 0.6 compared with 2.7 points \pm 0.4 for kyphoplasty patients (*P* = .9). When we combined pain outcomes of vertebroplasty and kyphoplasty patients, mean pain reduction at ≤ 1 week postprocedure was 4.8 points \pm 0.56 (*P* < .001). This improvement in pain was sustained to >1 year postprocedure (mean pain reduction, 4.4 points \pm 0.48; *P* < .001). There was no significant reduction in pain when comparing postprocedural pain scores at different time points (Table 1).

Three studies reported ODI scores at ≤ 1 week postprocedure, 6 studies reported ODI scores at 1 week to 1 year post procedure, and 4 studies reported ODI scores at >1 year postprocedure (On-line Table 3). There was no significant decrease in ODI at ≤ 1 week postprocedure (mean decrease of 39.2, *P* = .37), at 1 week to 1 year postprocedure (mean decrease of 40.7, *P* = .14), or at >1 year postprocedure (mean decrease of 46.5, *P* = .88). Seven studies reported a percentage decrease in analgesic use at ≤ 1 week postprocedure, 7 studies reported a percentage decrease in analgesic use at 1 week to 1 year postprocedure, and 3 studies reported a percentage decrease in analgesic use at >1 year postprocedure (On-line Table 4). There was a significant decrease in analgesic use at ≤ 1 week postprocedure (81.9%, *P* = .002) and at 1 week to 1 year postprocedure (85.0%, *P* = .003). These data are summarized in Table 2.

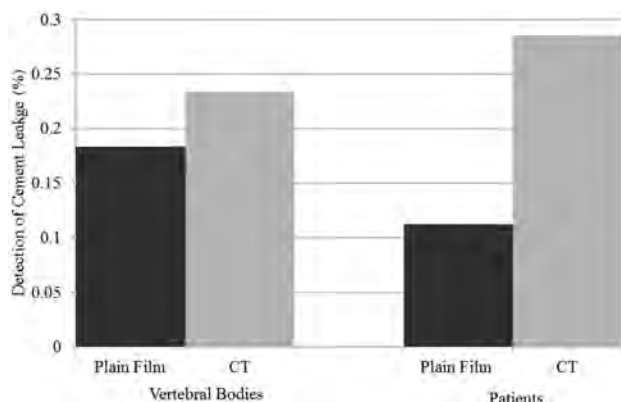
Cement leakage was detected with either plain film or CT. Twelve studies reported leakages in terms of the number of vertebral bodies, while 5 studies reported leakage in terms of the number of patients. Plain film identified 18% (49/267, median = 0.15,

Table 1: Pain scores in relation to time period

Pain Comparison	No. of Studies	Mean Difference ± SE	P Value
Preprocedure compared with ≤1 week postprocedure	11	4.8 ± 0.56	<.001
Preprocedure compared with 1 week–1 year postprocedure	14	4.6 ± 0.49	<.001
Preprocedure compared with >1 year postprocedure	14	4.4 ± 0.48	<.001
≤1 Week postprocedure compared with 1 week–1 year postprocedure	9	0.077 ± 0.11	<.481
≤1 Week postprocedure compared with >1 year postprocedure	7	0.49 ± 0.49	<.132
1 week–1 year postprocedure compared with >1 year postprocedure	10	0.33 ± 0.25	<.276

Table 2: Change in ODI and analgesic use

	Mean Decrease in ODI from Baseline (range)		% Patients with Decrease in Analgesic Drug Use from Baseline (range)	
		P		P
≤1 Week	39.2 (16.3–75.0)	.37	81.9 (53.7–100)	.002
1 Week–1 year	40.7 (16.3–75.0)	.14	85.0 (46.1–100)	.003
>1 Year	46.5 (14.5–75.0)	.88	89.1 (57.7–100)	.08

**FIG 2.** Detection of leakage with plain film versus CT.

range = 0.04–0.38) of vertebrae as having cement leakage, while CT identified 23% (255/1090, median = 0.23, range = 0.05–0.49). When we considered studies that presented leakage in terms of the number of patients, plain film identified 11% (9/80, median = 0.12, range = 0.07–0.17) of patients as having leakage, while CT identified almost 29% (22/77, median = 0.28, range = 0.03–0.53). CT in both cases was associated with more cases of leakage; however, the correlation was not significant (vertebrae *P* value = .75, patient *P* value = 1.0). These data are summarized in Fig 2. Postprocedural pain score was not associated with cement leakage (coefficient $-0.096 \pm SE 1.34$, *P* = .9450).

The most common complication was new vertebral fractures at untreated vertebral bodies. This occurred in 7.3% of vertebroplasty patients (42/576) and 6.8% of kyphoplasty patients (25/367). There was no difference in the rate of this complication between groups (*P* = .78). Infection, pulmonary embolism, myocardial infarction, and neurologic symptoms requiring revision surgery occurred in <1% of vertebroplasty and kyphoplasty patients. These data are summarized in Table 3.

DISCUSSION

Although vertebroplasty and kyphoplasty have been shown to be beneficial in patients with metastatic cancer and osteoporosis, studies depicting outcomes in patients with multiple myeloma are limited. Our analysis of published studies demonstrates that spinal augmentation in patients with myeloma is effective, with decreased postoperative pain and decreased analgesic drug use. The benefit was seen

immediately on augmentation and was sustained for the duration of the reported follow-up periods (maximum of 4 years). We further demonstrated that complication rates associated with treatment of these patients are low; this finding suggests that treatment of these patients is safe. Vertebroplasty and kyphoplasty had similar safety and efficacy rates in this study.

Randomized controlled trials have been performed for patients with osteoporosis or solid metastatic cancers who underwent spinal augmentation procedures. The treatment has consistently demonstrated decreased postoperative pain, disability, and analgesic use following vertebral augmentation procedures.^{4–7} Previous studies have shown that vertebroplasty and kyphoplasty differ in their postprocedure effectiveness.⁷ However, we did not find any statistically significant difference between the 2 procedures among patients with myeloma. Similar to patients with myeloma, those with osteoporosis also appeared to achieve early and sustained pain relief.¹¹ Because the pain relief is generally achieved almost immediately postprocedure, it appears that the mechanism of benefit is anatomic (one hypothesis is that cement stabilization of vertebrae relieves pressure that fractures place on spinal nerves).³ There appears to be a similar percentage of decrease in pain scores for patients with osteoporotic compression fracture compared with those with multiple myeloma undergoing spine augmentation.⁴

When we studied cement leakage, simple cement leakage without other adverse events is generally not considered a complication but rather a stopping point for cement injection. While our study did show that CT is a superior means of detecting cement leakage, we do not advocate the routine use of CT for cement leakage detection because this is generally clinically irrelevant. Furthermore, most studies that include plain film follow-up only obtain frontal and lateral views. Oblique views are generally not obtained; this practice may limit the sensitivity of plain film in the detection of cement leakage.

Limitations

Intrinsic limitations of this review relate mainly to the design (including publication bias and use of studies that differed in adjunctive therapy, disease stage, and other factors) and the combined use of prospective and retrospective case series. Combining data that were reported differentially across studies required non-conventional compilation, which calls for uniformity in reporting future outcomes. The small sample size of relevant studies served as an additional limitation. Vertebral height was initially another parameter that was of interest to our study. However, a vast majority of studies did not report these data. An effort was made to contact authors but this proved to be unsuccessful.

Table 3: Complication rates

Reported Symptomatic Complications	Overall Rate	Vertebroplasty Rate	Kyphoplasty Rate	P
Infection	1/943	1/576	0/367	.64
Pulmonary embolism	1/943	0/576	1/367	.21
Myocardial infarction	1/943	0/576	1/367	.21
Vertebral body compression fractures at untreated levels	67/943	42/576	25/367	.78
Neurologic symptoms requiring revision surgery	2/943	0/576	2/367	.08
Transient perioperative pain	6/943	4/576	2/367	.78

CONCLUSIONS

This review served as a unique analysis of pooled data that demonstrated that vertebral augmentation is safe and effective in patients with multiple myeloma. Further prospective studies are needed to evaluate complication rates and confirm the immediate and sustained benefit of vertebral body augmentation in these patients.

Disclosures: David Kallmes—UNRELATED: Consultancy: ev3,* Medtronic,* Grants/Grants Pending: MicroVention,* ev3,* Sequent Medical,* Royalties: University of Virginia Patent Foundation, Travel/Accommodations/Meeting Expenses Unrelated to Activities Listed: MicroVention.* *Money paid to the institution.

REFERENCES

- Edwards CM, Zhuang J, Mundy GR. The pathogenesis of the bone disease of multiple myeloma. *Bone* 2008;42:1007–13
- Masala S, Fiori R, Massari F, et al. Percutaneous kyphoplasty: indications and technique in the treatment of vertebral fractures from myeloma. *Tumori* 2004;90:22–26
- Mathis JM, Barr JD, Belkoff SM, et al. Percutaneous vertebroplasty: a developing standard of care for vertebral compression fractures. *AJNR Am J Neuroradiol* 2001;22:373–81
- Papanastassiou ID, Phillips FM, Van Meirhaeghe J, et al. Comparing effects of kyphoplasty, vertebroplasty, and non-surgical management in a systematic review of randomized and non-randomized controlled studies. *Eur Spine J* 2012;21:1826–43
- Rhyne A 3rd, Banit D, Laxer E, et al. Kyphoplasty: report of eighty-two thoracolumbar osteoporotic vertebral fractures. *J Orthop Trauma* 2004;18:294–99
- McGirt MJ, Parker SL, Wolinsky JP, et al. Vertebroplasty and kyphoplasty for the treatment of vertebral compression fractures: an evidenced-based review of the literature. *Spine J* 2009;9:501–08
- Han S, Wan S, Ning L, et al. Percutaneous vertebroplasty versus balloon kyphoplasty for treatment of osteoporotic vertebral compression fracture: a meta-analysis of randomised and non-randomised controlled trials. *Int Orthop* 2011;35:1349–58
- Levine SA, Perin LA, Hayes D, et al. An evidence-based evaluation of percutaneous vertebroplasty. *Manag Care* 2000;9:56–60, 63
- Bouza C, Lopez-Cuadrado T, Cediell P, et al. Balloon kyphoplasty in malignant spinal fractures: a systematic review and meta-analysis. *BMC Palliat Care* 2009;8:12
- Mendoza TR, Koyalagunta D, Burton AW, et al. Changes in pain and other symptoms in patients with painful multiple myeloma-related vertebral fracture treated with kyphoplasty or vertebroplasty. *J Pain* 2012;13:564–70
- Gill JB, Kuper M, Chin PC, et al. Comparing pain reduction following kyphoplasty and vertebroplasty for osteoporotic vertebral compression fractures. *Pain Physician* 2007;10:583–90
- Chen LH, Hsieh MK, Niu CC, et al. Percutaneous vertebroplasty for pathological vertebral compression fractures secondary to multiple myeloma. *Arch Orthop Trauma Surg* 2012;132:759–64
- Yang Z, Tan J, Xu Y, et al. Treatment of MM-associated spinal fracture with percutaneous vertebroplasty (PVP) and chemotherapy. *Eur Spine J* 2012;21:912–19
- Trumm C, Jakobs T, Pahl A, et al. CT fluoroscopy-guided percutaneous vertebroplasty in patients with multiple myeloma: analysis of technical results from 44 sessions with 67 vertebrae treated. *Diagn Interv Radiol* 2012;18:111–20
- Kasperk C, Haas A, Hillengass J, et al. Kyphoplasty in patients with multiple myeloma a retrospective comparative pilot study. *J Surg Oncol* 2012;105:679–86
- Basile A, Cavalli M, Fiumara P, et al. Vertebroplasty in multiple myeloma with osteolysis or fracture of the posterior vertebral wall: usefulness of a delayed cement injection. *Skeletal Radiol* 2011;40:913–19
- Anselmetti GC, Manca A, Montemurro F, et al. Percutaneous vertebroplasty in multiple myeloma: prospective long-term follow-up in 106 consecutive patients. *Cardiovasc Intervent Radiol* 2012;35:139–45
- Masala S, Volpi T, Fucci FP, et al. Percutaneous osteoplasty in the treatment of extraspinal painful multiple myeloma lesions. *Support Care Cancer* 2011;19:957–62
- Astolfi S, Scaramuzza L, Logroscino CA. A minimally invasive surgical treatment possibility of osteolytic vertebral collapse in multiple myeloma. *Eur Spine J* 2009;18(suppl 1):115–21
- Masala S, Anselmetti GC, Marcia S, et al. Percutaneous vertebroplasty in multiple myeloma vertebral involvement. *J Spinal Disord Tech* 2008;21:344–48
- McDonald RJ, Trout AT, Gray LA, et al. Vertebroplasty in multiple myeloma: outcomes in a large patient series. *AJNR Am J Neuroradiol* 2008;29:642–48
- Tran Thang NN, Abdo G, Martin JB, et al. Percutaneous cementoplasty in multiple myeloma: a valuable adjunct for pain control and ambulation maintenance. *Support Care Cancer* 2008;16:891–96
- Köse KC, Cebesoy O, Akan B, et al. Functional results of vertebral augmentation techniques in pathological vertebral fractures of myelomatous patients. *J Natl Med Assoc* 2006;98:1654–58
- Khanna AJ, Reinhardt MK, Togawa D, et al. Functional outcomes of kyphoplasty for the treatment of osteoporotic and osteolytic vertebral compression fractures. *Osteoporos Int* 2006;17:817–26
- Pflugmacher R, Kandziora F, Schroeder RJ, et al. Percutaneous balloon kyphoplasty in the treatment of pathological vertebral body fracture and deformity in multiple myeloma: a one-year follow-up. *Acta Radiol* 2006;47:369–76
- Bosnjaković P, Ristic S, Mrvic M, et al. Management of painful spinal lesions caused by multiple myeloma using percutaneous acrylic cement injection. *Acta Chir Jugosl* 2009;56:153–58
- Huber FX, McArthur N, Tanner M, et al. Kyphoplasty for patients with multiple myeloma is a safe surgical procedure: results from a large patient cohort. *Clin Lymphoma Myeloma* 2009;9:375–80
- Zou J, Mei X, Gan M, et al. Kyphoplasty for spinal fractures from multiple myeloma. *J Surg Oncol* 2010;102:43–47
- Julka A, Tolhurst SR, Srinivasan RC, et al. Functional outcomes and height restoration for patients with multiple myeloma-related osteolytic vertebral compression fractures treated with kyphoplasty. *J Spinal Disord Tech* 2012 Jun 1. [Epub ahead of print]
- Lane JM, Hong R, Koob J, et al. Kyphoplasty enhances function and structural alignment in multiple myeloma. *Clin Orthop Relat Res* 2004;49–53
- Garland P, Gishen P, Rahemtulla A. Percutaneous vertebroplasty to treat painful myelomatous vertebral deposits—long-term efficacy outcomes. *Ann Hematol* 2011;90:95–100
- Lim BS, Chang UK, Youn SM. Clinical outcomes after percutaneous vertebroplasty for pathologic compression fractures in osteolytic metastatic spinal disease. *J Korean Neurosurg Soc* 2009;45:369–74
- Dudeny S, Lieberman IH, Reinhardt MK, et al. Kyphoplasty in the treatment of osteolytic vertebral compression fractures as a result of multiple myeloma. *J Clin Oncol* 2002;20:2382–87

3T MRI Quantification of Hippocampal Volume and Signal in Mesial Temporal Lobe Epilepsy Improves Detection of Hippocampal Sclerosis

A.C. Coan, B. Kubota, F.P.G. Bergo, B.M. Campos, and F. Cendes



ABSTRACT

BACKGROUND AND PURPOSE: In mesial temporal lobe epilepsy, MR imaging quantification of hippocampal volume and T2 signal can improve the sensitivity for detecting hippocampal sclerosis. However, the current contributions of these analyses for the diagnosis of hippocampal sclerosis in 3T MRI are not clear. Our aim was to compare visual analysis, volumetry, and signal quantification of the hippocampus for detecting hippocampal sclerosis in 3T MRI.

MATERIALS AND METHODS: Two hundred three patients with mesial temporal lobe epilepsy defined by clinical and electroencephalogram criteria had 3T MRI visually analyzed by imaging epilepsy experts. As a second step, we performed automatic quantification of hippocampal volumes with FreeSurfer and T2 relaxometry with an in-house software. MRI of 79 healthy controls was used for comparison.

RESULTS: Visual analysis classified 125 patients (62%) as having signs of hippocampal sclerosis and 78 (38%) as having normal MRI findings. Automatic volumetry detected atrophy in 119 (95%) patients with visually detected hippocampal sclerosis and in 10 (13%) with visually normal MR imaging findings. Relaxometry analysis detected hyperintense T2 signal in 103 (82%) patients with visually detected hippocampal sclerosis and in 15 (19%) with visually normal MR imaging findings. Considered together, volumetry plus relaxometry detected signs of hippocampal sclerosis in all except 1 (99%) patient with visually detected hippocampal sclerosis and in 22 (28%) with visually normal MR imaging findings.

CONCLUSIONS: In 3T MRI visually inspected by experts, quantification of hippocampal volume and signal can increase the detection of hippocampal sclerosis in 28% of patients with mesial temporal lobe epilepsy.

ABBREVIATIONS: EEG = electroencephalography; HS = hippocampal sclerosis; MTLE = mesial temporal lobe epilepsy

Mesial temporal lobe epilepsy (MTLE) is the most common form of epilepsy in adults.¹ Although hippocampal sclerosis (HS) is the main pathologic substrate in patients with MTLE, there are several other causes and some patients may have normal MR imaging findings and no specific histopathologic changes de-

tected postoperatively.^{1,2} HS can be reliably detected on MRI,² and quantitative analysis of hippocampal formation improves the sensitivity for detecting this pathology.^{3,4} With advances in the MR imaging field in the past decades, the current contributions of these postprocessing MR imaging tools for the detection of hippocampal pathology, especially in tertiary epilepsy centers, are not clear.

The histopathology of HS is characterized by loss of specific neurons and synaptic reorganization of surviving cells,⁵ and in MR images, this is observed as volume reduction and signal hyperintensity in T2 images.^{6,7} Quantification of hippocampal volume has advantages over visual analysis for the detection of subtle and bilateral hippocampal abnormalities.^{2,8} Equally, the quantification of hippocampal T2 signal, especially with relaxometry, can improve the MR imaging diagnosis of HS.^{9,10} Both volume and hippocampal signal quantification measurements have good correlation with histopathologic findings of HS.⁴

Currently, these techniques are considered reliable and reproducible for the detection of hippocampal pathology.¹¹ However,

Received January 28, 2013; accepted after revision April 10.

From the Neuroimaging Laboratory, Department of Neurology, State University of Campinas, Campinas, São Paulo, Brazil.

Ana C. Coan was responsible for the study concept and design, patient selection and recruitment, MRI visual analysis, interpretation of the data, and manuscript writing. Bruno Kubota contributed the relaxometry analysis; Felipe Bergo, volumetry analysis; Brunno M. Campos, patient recruitment and volumetry analysis; Fernando Cendes, study concept and design, review of patient selection, MRI visual analysis, interpretation of the data, manuscript writing, and reviewing.

This study was funded by São Paulo Research Foundation, grants 2005/56578-4 and 2009/54552-9. Dr Cendes received support from Conselho Nacional de Desenvolvimento Científico e Tecnológico, Brazil.

Please address correspondence to Fernando Cendes, MD, Departamento de Neurologia, Faculdade de Ciências Médicas—UNICAMP, Cidade Universitária Zeferino Vaz, Campinas São Paulo, Brazil, CEP 13083-970; e-mail: fcendes@unicamp.br

Indicates open access to non-subscribers at www.ajnr.org

<http://dx.doi.org/10.3174/ajnr.A3640>

hippocampal volumetry by manual segmentation is time-consuming and depends on the expertise of the examiner. These 2 features have limited its use in clinical practice. Recently automatic analyses have been shown to be promising; however, there are few studies comparing their efficacy with the visual analyses of high-quality MR imaging by experts in the field.^{12,13}

Although it is clear that in studies with 1.5T MR imaging, volumetry and relaxometry have significantly higher sensitivity than the qualitative analysis of MR imaging,^{8,9} today most epilepsy centers work with 3T MRI and specific epilepsy protocols, which make the determination of MR imaging signs of HS by visual analysis easier and more accurate.¹⁴ It has been reported that there is no difference in the hippocampal volume measures of 1.5 and 3T^{15,16} and that quantitative measures in 3T MRI can demonstrate ultrastructural details of HS pathology not detectable with lower field scanners.¹⁷ Once the sensitivity to visually detect signs of HS at 3T is higher,¹⁴ the question that remains is whether the use of hippocampal measurements in these higher field MRIs still adds information to the clinical practice.

In this study, we aimed to evaluate whether the quantification of hippocampal volume and T2 signal in MRI acquired at 3T has a higher sensitivity in detecting MR imaging signs of HS than the visual analysis of these images by epilepsy imaging experts. Our hypothesis was that though the scanners with higher field and specific epilepsy protocols have improved the visual detection of MR imaging signs of HS, the use of techniques to measure the abnormal hippocampal volume and T2 signal can still further improve the detection of HS in patients with otherwise normal MRI findings.

MATERIALS AND METHODS

Patients

This was a prospective study of patients followed at the Epilepsy Clinic of University of Campinas with a clinical and electroencephalographic diagnosis of MTLE according to International League Against Epilepsy criteria,¹⁸ who consecutively underwent 3T MRI between August 2009 and April 2012. An informed consent form approved by the Ethics Committee of Universidade Estadual de Campinas was signed by all patients before acquisition of MR imaging. Patients with symptomatic MTLE due to lesions other than HS (tumor, vascular malformations, gliosis, focal cortical dysplasia) were excluded.

MR Imaging Epilepsy Protocol and Visual Analysis

All patients underwent an MR imaging epilepsy protocol with a 3T Inera Achieva scanner (Philips Healthcare, Best, the Netherlands), which included the following:

Coronal images perpendicular to the long axis of the hippocampus, defined at the sagittal image: 1) T2WI multiecho (3-mm-thick, no gap, voxel size = $0.89 \times 1 \times 3$ mm, TR = 3300 ms, TE = 30/60/90/120/150 ms, matrix = 200×180 , FOV = 180×180 , TSE factor = 5; EPI factor = 5, flip angle = 90°); 2) T1WI inversion recovery (3-mm-thick, no gap, voxel size = $0.75 \times 0.75 \times 3$ mm, TR = 3550 ms, TE = 15 ms, TI = 400 ms, matrix = 240×229 , FOV = 180×180 , TSE factor = 7), 3) FLAIR (fat-suppressed = spectral-attenuated inversion recovery, fat-suppressed power = 1, four-mm-thick, section gap = 1 mm, voxel

size = $0.89 \times 1.1 \times 2.4$ mm, TR = 12,000 ms, TE = 140 ms, TI = 2850 ms, matrix = 180×440 , FOV = 200×200).

Axial images parallel to the long axis of the hippocampus: FLAIR (fat-suppressed = spectral-attenuated inversion recovery, fat-suppressed power = 1, four-mm-thick, section gap = 1 mm, voxel size = $0.89 \times 1.1 \times 2.4$ mm, TR = 12,000 ms, TE = 140 ms, TI = 2850 ms, matrix = 224×160 , FOV = 200×200).

T1WI volume: isotropic voxels of 1 mm, acquired in the sagittal plane (1-mm-thick, no gap, flip angle = 8° , TR = 7.0 ms, TE = 3.2 ms, matrix = 240×240 , FOV = 240×240).

T2WI volume: isotropic voxels of 1.5 mm, acquired in the sagittal plane (no gap, TR = 1800 ms, TE = 340 ms, matrix = 140×140 , FOV = 230×230 , TSE factor = 120; flip angle = 90° ; geometry-corrected).

MR imaging sequences were corrected for gradient nonlinearity during the reconstruction step in the scanner.

As a first step, MRI was visually analyzed by 2 epilepsy imaging experts (A.C.C. and F.C.) and the images were classified as having normal findings or signs of HS. Classic signs of HS were as follows: reduction of volume and abnormal shape observed on T1 images and increased signal observed in T2 and FLAIR images. Images were carefully examined by the investigators in light of the clinical and electroencephalography (EEG) data of each patient because this routine of MR imaging evaluation for the investigation of focal epilepsies is used in most epilepsy centers. Special attention was given to rule out subtle signs of focal cortical dysplasia, such as sulcal morphology abnormalities, focal increase of cortical thickness, FLAIR focal signal hyperintensities, or small transmantle signs.

Hippocampal Volumetry

As the second step, quantification of hippocampal volume and signal was performed. A group of 79 healthy controls (with similar age and sex distribution) was used for comparison (60% female; median age, 42 years; range, 21–70 years). Automatic volumetric analysis was performed with FreeSurfer software (Version 5.1.0; <http://surfer.nmr.mgh.harvard.edu>) by using T1WI volume. Hippocampal volumes were corrected for individual brain (supratentorial) volumes, and corrected hippocampal volumes smaller than 2 SDs (absolute value and/or asymmetry index, defined by the ratio of the smaller over the larger hippocampus of each individual) from the mean of controls were considered as having atrophy.

Hippocampal Signal Quantification

For signal quantification, we used relaxometry analysis of T2 multiecho images (3-mm sections, TR = 3300, TE = 30/60/90/120/150 ms, matrix = 200×176 , FOV = 1802×180) with After-voxel, a medical image visualization tool written by Felipe Bergo (<http://www.liv.ic.unicamp.br/~bergo/aftervoxel>). For this analysis, a region of interest was manually defined in 3 different MR imaging sections, including the hippocampus of each individual (1 in the head, 1 in the body, and 1 in the tail of the hippocampus) by an investigator blinded to the results of the MR imaging visual evaluation (B.K.). To make the ROI placement more consistent among patients, we defined the section of the hippocampus head as the first in which it was possible to see the temporal horn of the lateral ventricle and therefore to appropriately separate the hippocampal for-

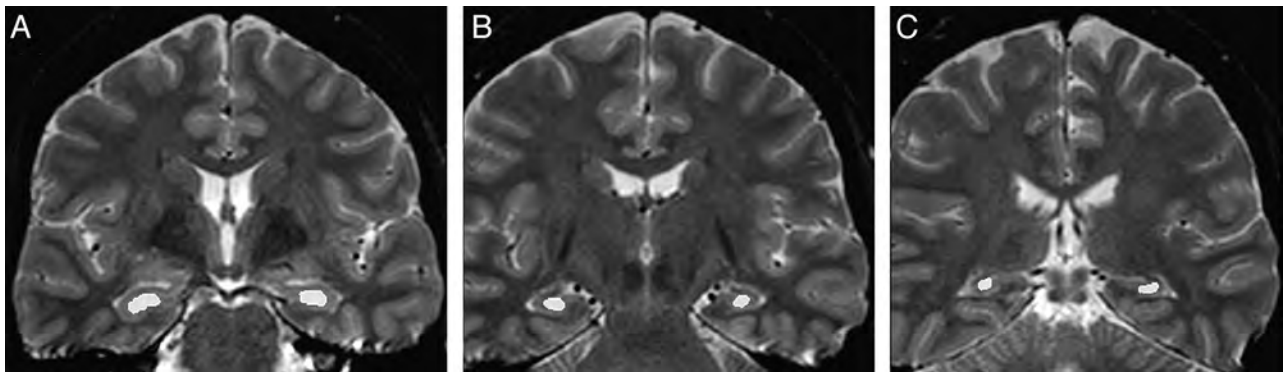


FIG 1. T2 relaxometry in Aftervoxel software. Example of regions of interest manually defined in the head (A), body (B), and tail (C) of the hippocampus of a patient with MTLE.

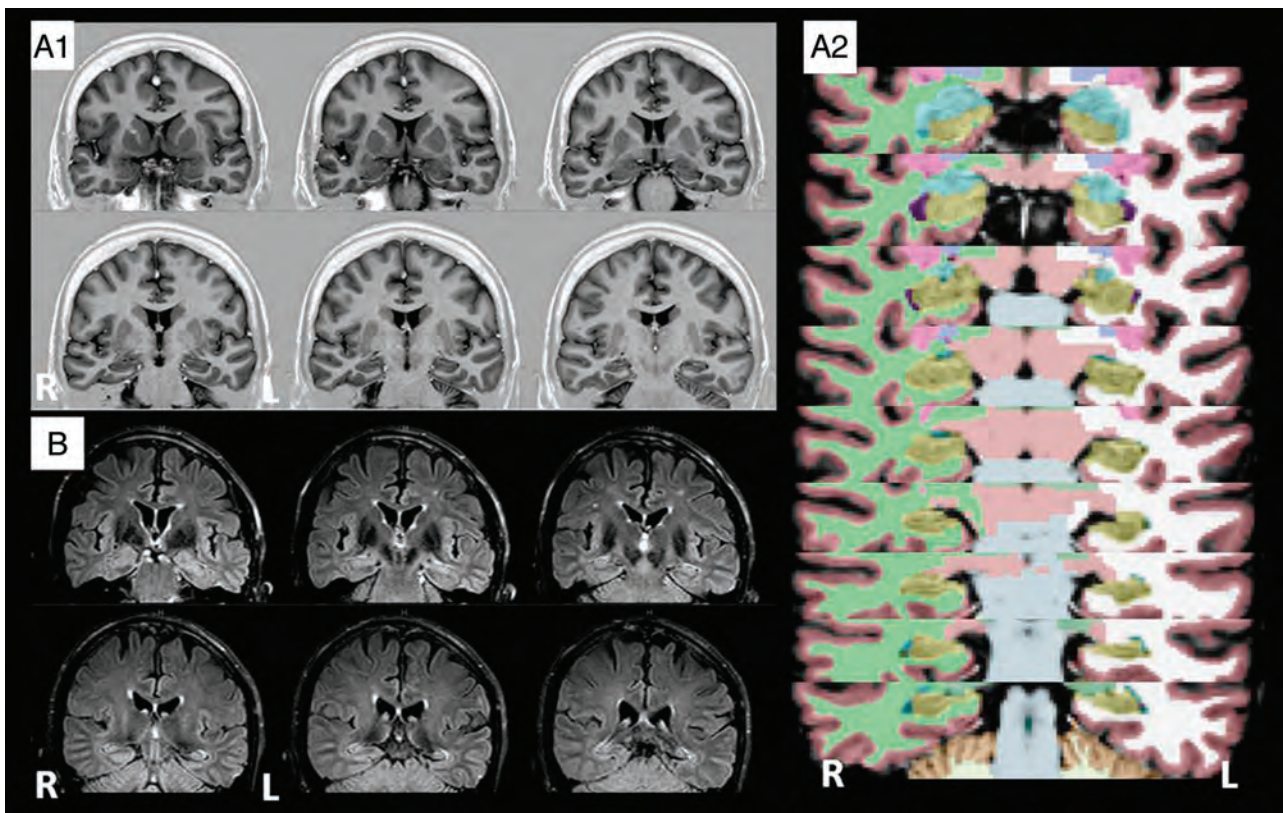


FIG 2. MR imaging signs of HS detected by quantification analysis. Examples of 2 patients with normal MR imaging findings by visual analysis and HS signs detected by quantification techniques. A, A 67-year-old male patient, with MTLE and left EEG seizure focus. His seizures started at 5 years of age and were characterized by an aura described as *jamaïs vu* followed by a hipometer complex partial seizure. MR imaging volumetry detected significant left reduced hippocampal volume. A1, T1WI in which both hippocampi were considered normal by visual analysis. A2, FreeSurfer volumetry images in which the hippocampi are shown in yellow. Corrected volume of the left hippocampus: 3.50 cm³ (z score = -2.20 SDs). B, A 28-year-old male patient with MTLE and left seizure focus. His seizures started at 11 years of age and were characterized by an aura described as fear and an epigastric sensation followed by loss of consciousness and manual automatisms. MR imaging T2 relaxometry detected significant left increased hippocampal signal. Left hippocampus T2 signal: 111.40 (z score = 3.52 SDs).

mation from the amygdala. The body of the hippocampus was defined in the fourth coronal section after the region of interest of the hippocampus head, and the tail was defined in the third coronal section after the hippocampus body, in which it was also possible to visualize the quadrigeminal plate. The ROIs were manually drawn to include the larger area of the hippocampus in that section but also to carefully avoid contamination of the hippocampal signal with CSF signal (Fig 1). The mean T2 signal from the 3 sections of each hippocampus was used as the final measurement. Hippocampal signal

values higher than 2 SDs from the mean of the control group composed of the same individuals in the volumetry analysis (absolute value and/or asymmetry index, defined by the ratio of higher and lower hippocampal signals of each individual) were considered hyperintense signal.

RESULTS

Two hundred seventeen patients fulfilled the inclusion criteria. However, after detailed MR imaging visual analysis, 14 patients

3T MRI signs of HS detected by visual or quantification analysis^a

MRI Visual Analysis	Volumetry	Relaxometry	Volumetry + Relaxometry
MTLE-HS (125/203; 62%)	119/125 (95%)	103/125 (82%)	124/125 (99%)
MTLE-NL (78/203; 38%)	10/78 (13%)	15/78 (19%)	22/78 (28%)
Concordance with EEG laterality	95% had concordant EEG* and 5% discordant	94% had concordant EEG** and 6% discordant	

Note:—NL, indicates normal MRI.

^a First column shows the frequency of HS signs detected by visual analysis. The other columns show the percentages of HS signs detected by quantification of hippocampal volume ("Volumetry") and T2 MRI signal ("Relaxometry") alone (second and third columns, respectively) or when considered together (fourth column). In the last line, for each technique the concordance with the laterality of the seizure focus is described as defined by ictal and interictal scalp EEG.

* Excluding the 9 patients and ** the 12 patients with bilateral non-lateralizing EEG.

were thought to have subtle signs of focal cortical dysplasia and were excluded. The final group was then composed of 203 patients (129 female, 74 male; median age, 46 years; range, 17–74 years). There was no difference in sex or age distribution between patients and controls (Sex, χ^2 , $P = .527$; age, t test, $P = .072$). According to ictal and interictal scalp EEG, 184 patients had unilateral temporal epileptic focus (117 left MTLE and 67 right MTLE) and 19 had bitemporal epileptic focus.

In this group, 176 (87%) patients had drug-resistant seizures, while 27 (13%) had been free of seizures for at least 2 years.

MR Imaging Visual Analysis

MR imaging visual analysis detected 125 (62%) patients with signs of HS (62 left, 54 right, 6 bilateral with left-sided predominance, 3 bilateral with right-sided predominance). For the remaining 78 (38%) patients, MRI had normal findings by visual analyses. Although the qualitative analysis detected signs of hippocampal sclerosis in 62% of patients, one cannot say in how many it failed to detect HS because the remaining 38% of patients may or may not have had HS in their histology, even though they all had MTLE.

Concordance of MR Imaging Visual Analysis and the EEG Epileptic Focus

From the 125 patients with MTLE with HS signs detected by visual analysis, 117 had unilateral epileptic focus (defined by ictal and interictal EEG); in 88% (103/117), the side of signs with HS was concordant with the epileptic focus, and it was contralateral in 7.5% (9/117). In the remaining 4% (5/117), the MR imaging signs of HS were bilateral and symmetric.

MR Imaging Quantification Analysis

Automatic volumetry analysis detected hippocampal atrophy in 119 (95%) patients with visual signs of HS and in 10 (13%) patients with visually normal MR imaging findings. Relaxometry detected hyperintense T2 signal in 103 (82%) patients with visual signs of HS and in 15 (19%) patients with visually normal MR imaging findings (Fig 2). Considered together, volumetry plus relaxometry detected signs of HS in all except 1 (124; 99%) patient with visual signs of HS and in 22 (28%) patients with visually normal MR imaging findings (Table). Therefore, the use of combined hippocampal volumetry and T2 relaxometry increased the sensitivity to detect MR imaging signs of HS in 28% compared with visual analysis.

Volumetry detected bilateral hippocampal atrophy in 9 patients (8 with visual signs of HS and 1 with visually normal MR imaging findings). Relaxometry detected bilateral hippocampal hyperintense signal in 22 patients (20 with visual signs of HS and 2 with visually normal MR imaging findings). In patients who had

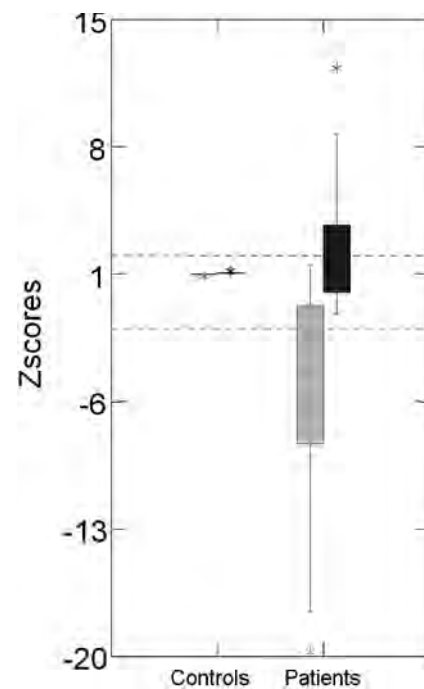


FIG 3. Z score distribution of the hippocampal asymmetry index for volumetry and T2 relaxometry analyses. On the left side is the boxplot graphic of z scores of the volumetry asymmetry index (gray) and T2 relaxometry asymmetry index (black) of controls. On the right side is the boxplot graphic of z scores of the volumetry asymmetry index (gray) and T2 relaxometry asymmetry index (black) of patients with MTLE.

bilateral hippocampal abnormalities detected by the quantification methods, there was marked asymmetry.

The laterality of the hippocampal abnormality detected by both absolute values and the asymmetry index in volumetry and T2 relaxometry analysis was concordant in all cases. The asymmetry index had a higher sensitivity to detect the hippocampal volume reduction (76% [98 patients] had significant hippocampal volume reduction detected by the absolute volume and 98% [126 patients] were detected by asymmetry index) and a lower sensitivity to detect T2 hyperintense signal (92% [109 patients] with significant hippocampal T2 hyperintense signal detected by the absolute volume and 70% [82 patients] detected by asymmetry index). The distribution of the hippocampal asymmetry index for volumetry and T2 relaxometry in patients and controls is shown in Fig 3.

Figure 4 demonstrates the z score distribution of hippocampal volumes and T2 signal in controls (right and left hippocampus) and patients (hippocampi ipsi- and contralateral to the epileptic focus).

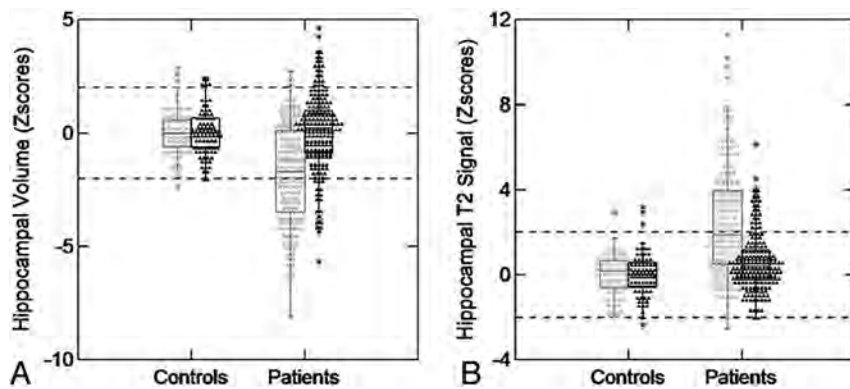


FIG 4. Z score distribution of hippocampal volumes and T2 signal in patients with MTLE and controls. **A,** Boxplot graphic shows z scores of hippocampal volumetry for controls and patients with MTLE. On the left side of the graphic are shown the hippocampal volumes of controls (white circles = right hippocampi; mean volume, $4.28 \pm 0.35 \text{ cm}^3$; black triangles = left hippocampi; mean volume, $4.21 \pm 0.32 \text{ cm}^3$). On the right side of the graphic are shown the hippocampal volumes of patients (white circles = hippocampi ipsilateral to the epileptic focus; mean volume, $3.78 \pm 0.51 \text{ cm}^3$; black triangles = hippocampi contralateral to the epileptic focus; mean volume, $4.28 \pm 0.56 \text{ cm}^3$). **B,** Boxplot graphic shows z scores of hippocampal T2 relaxometry for controls and patients with MTLE. On the left side of the graphic is the hippocampal T2 signal of controls (white circles = right hippocampi; mean signal, 96.77 ± 4.05 ; black triangles = left hippocampi; mean signal, 96.98 ± 4.10). On the right side of the graphic is the hippocampal T2 signal of patients (white circles = hippocampi ipsilateral to the epileptic focus; mean signal, 105.49 ± 7.88 ; black triangles = hippocampi contralateral to the epileptic focus; mean signal, 99.10 ± 5.01).

Concordance of MR Imaging Visual and Quantification Analysis

The side of the HS detected by MR imaging visual and volumetry analysis was concordant in all except 1 case (118/119, 99%). The patient with discordant volumetry and MR imaging visual analysis had a subtle hippocampal atrophy and clear hyperintense T2 signal on the left hippocampus by visual analysis, which was concordant with the T2 relaxometry.

The side of the abnormal hippocampal signal detected by relaxometry was concordant with the visual analysis in 96% (99/103). In the remaining 4 patients, 2 had bilateral asymmetric hippocampal abnormalities on visual analyses and the relaxometry lateralized to the side with less hippocampal atrophy by both visual and automatic volumetry, and the other 2 patients had unilateral hippocampal atrophy (concordant by visual and automatic volumetry) and the relaxometry lateralized to the side contralateral to the atrophy and hyperintense T2 signal defined by visual analysis.

Concordance of MR Imaging Quantification Analysis and the EEG Epileptic Focus

From the 129 patients with MTLE with hippocampal atrophy detected by volumetry, 120 had unilateral epileptic focus (defined by ictal and interictal EEG) and in 95% (114/120) the side of epileptic focus was correctly lateralized by volumetry. From the 118 patients with MTLE with hippocampal T2 signal hyperintensity detected by relaxometry, 106 had unilateral epileptic focus and in 94% (100/106) the side of epileptic focus was correctly lateralized by volumetry.

There was no significant difference in the frequency of concordance of signs of HS or hippocampal atrophy detected by visual analysis with the side of the epileptic focus (88% of concordance by visual analyses and 95% of concordance by volumetry analysis, $\chi^2, P = .054$) and no difference in the frequency of concordance

of visual signs of HS or hippocampal hyperintense signal detected by relaxometry with the side of the epileptic focus (88% of concordance by visual analyses and 94% of concordance by relaxometry analysis, $\chi^2, P = .099$). The small additional gain of the quantification analyses was secondary to better discrimination of the bilateral hippocampal abnormalities.

Concordance of Histopathology and MR Imaging Visual and Quantification Analyses

Nineteen patients (10%) underwent surgical treatment (anterior temporal lobectomy or selective amygdalohippocampectomy) due to refractory seizures. Of those, all except 1 individual had confirmed histopathology of HS. In patients with a histopathology of HS, visual analysis and volumetry detected abnormal hippocampi in all cases and relaxometry detected hyperintense signal

in 15/18 (83%) patients. The patient with a normal hippocampus on histology had no signs of HS detected by either visual or quantitative methods.

DISCUSSION

The detection of MR imaging signs of HS can help to define seizure etiology and to indicate surgical treatment for patients with drug-resistant MTLE. We demonstrated here that even in 3T MRI analyzed in tertiary centers by epilepsy experts, hippocampal volume and signal quantification can significantly improve the detection of signs of HS in patients with otherwise normal MRI findings by using an epilepsy protocol.

MR imaging has significantly improved the detection of pathologies related to epilepsy.¹⁹ It is safe, noninvasive, and widely available in epilepsy centers. However, a variable but significant number of patients with focal epilepsies have normal MRI findings and unknown seizure etiology.²⁰⁻²⁴

From the beginning of MR imaging use in epilepsy, special attention has been given to HS because it is the main pathologic feature associated with the most common epilepsy in adults.¹ Hippocampal volume and signal have been used for research purposes but also in epilepsy clinics to help in the evaluation of drug-resistant focal epilepsies. Quantification of hippocampal volume and signal in MRI cannot only detect signs of HS but can consistently help to lateralize the seizure focus in patients with MTLE who are surgical candidates.⁸ For these individuals, the prognosis of surgical resection of the temporal lobe ipsilateral to HS detected by MRI is excellent.²¹ Today, most of the tertiary epilepsy centers have 3T MRI available and visual signs of HS have been more easily detected.¹⁴ In this context, the contribution of MR imaging quantification methods to detect HS in 3T MRI has not been previously evaluated. Here we demonstrated that with 3T MRI, adequate epilepsy protocols, and expert visual evaluation, quan-

tification analysis can still improve the detection of subtle signs of HS in 28% of patients.

The detection of more subtle MR imaging abnormalities in patients with focal epilepsies depends on both the quality of MR imaging acquisition protocol and the experience of the examiner in reading MRIs of patients with epilepsy. A previous study²⁰ showed that “nonexperts” reported 61% of standard MR imaging as having normal findings or as showing no focal abnormality, while epilepsy “expert” examiner reassessments of the same standard MRIs classified 28% of these scans as technically inadequate and considered only 22% of these standard MR imaging scans as having normal findings. More important, by using a dedicated epilepsy MR imaging protocol, the same group of “experts” described focal MR imaging abnormalities in 91% of the same group of patients (they did not include hippocampal volumetry or T2 relaxometry).²⁰ Also, in this context, MRIs are always evaluated in the light of clinical, neuropsychological, and EEG data. In this article, we reproduced this optimal visual evaluation of MRI in patients with MTLE: Two epileptologists with expertise in MR imaging evaluation of patients with focal epilepsies reviewed the images of all patients (acquired with an extensive epilepsy protocol) in the context of clinical and EEG data. Even in this most favorable circumstance, quantification of hippocampal volume and signal significantly increased the detection of signs of HS.

In our series, only 1 patient with visual signs of HS had normal volumetry and signal quantification. In this patient, by visual analysis, we observed normal hippocampal volume and a localized hyperintense signal in the body of the hippocampus, contralateral to the epileptic focus determined by EEG. This pattern of subtle and localized hippocampal abnormality (restricted to the hippocampal body) is not commonly seen. We believe that this discordance could be overcome if more sections of the coronal MR imaging sequence were added to the relaxometry analysis. However, this addition would add time to the procedure and would probably result in limited improvement in the detection rate (<1%).

The increase of patients with detectable MR imaging abnormalities compatible with the site of the seizure-onset origin is significantly important for drug-resistant focal epilepsies. With quantitative analysis of 1.5T MRI, a group of patients with MTLE remains with no detectable structural abnormalities even when HS is confirmed after surgical removal of the mesial temporal structures.²² For patients with drug-resistant MTLE and normal MR imaging findings, invasive procedures, which have high cost and morbidity, are often necessary to evaluate the potential target for surgical intervention,²³ and yet for these individuals, the rate of seizure freedom is lower than that for those with MRI signs of HS.^{24,25} Histopathology of HS is only found in a limited number of patients with MTLE with normal MR imaging findings undergoing surgery, but those with positive hippocampal pathology are the ones with better surgical outcomes.^{24,26} It is necessary to improve noninvasive techniques that could more efficiently select the individuals with MTLE with subtle HS to better select surgical patients and improve outcomes. In this context, we believe that the use of hippocampal quantification measures in 3T MRI, as we showed in this article, can help in the recognition of these individuals with hippocampal sclerosis not detected by visual analysis

who could benefit from surgical procedures for control of drug-resistant seizures. The complete benefit of the use of hippocampal quantification measurements in 3T MRI in the presurgical evaluation of patients with drug-resistant MTLE could be assessed with follow-up and surgical outcome data of these patients.

In this study, we were not able to satisfactorily determine the specificity of the quantification procedures in the detection of HS. To achieve this goal, a correlation of these findings with the criterion standard, histopathology, would be necessary. We were only able to evaluate the histopathologic findings in 10% (19 patients) of our group. In the sample of our patients undergoing surgery, the specificity of hippocampal volumetry and T2 signal quantification was 100% (all patients with abnormal hippocampal volume or T2 signal had confirmed histopathology of HS, and the only patient with a normal hippocampus by these quantification techniques had normal histopathology). However, this specificity is biased because all patients who underwent surgery in our group had similar findings in both visual and quantification analysis, and the visual analysis was used in the selection of the patients for the surgical procedure. However, a good correlation of volume and signal abnormalities detected by quantification analysis and histopathology of HS has been previously demonstrated.²⁷ Also, in our group of patients, the laterality of abnormal hippocampal volume and signal was highly concordant with the laterality of the epileptic focus defined by EEG recordings.

Currently, most studies of hippocampal volumetry apply manual hippocampal delimitation, and whether manual²⁸ or automatic analysis has higher sensitivity and specificity is still debatable.^{12,13} Despite this controversy, in the clinical context, the quantification of hippocampal abnormalities must be as fast and practical as possible. In this article, we used automated volumetry and a simple manual signal quantification in which it is necessary only to define a small region of interest in 3 sections of the T2 scan of each patient, without the need to define precisely the borders of the hippocampus. We think that this optimized hippocampal quantification protocol can be easily applied to all patients with drug-resistant focal epilepsies as a parallel and additional analysis for the routine evaluation of MRI in specialized epilepsy centers. Although FreeSurfer software is not approved for clinical use by the US Food and Drug Administration, as far as we know, there is at least 1 software approved for automated volumetric analyses of brain MRI.²⁷ However, this has only been evaluated for the detection of hippocampal abnormalities on 1.5T scanners.¹³

In 1.5T MRI, a good correlation of volume and signal abnormalities detected by quantification analysis and histopathology of HS has been demonstrated.²⁹ More recently, histologic studies have proposed that different patterns of neuronal loss in the hippocampus might be associated with different seizure outcome after surgical removal of the temporal lobe.³⁰ Also, it has been shown that quantitative measures in 3T MRI can demonstrate ultrastructural details of HS pathology not detectable with lower field scanners.^{17,31} These *in vivo* quantitative measurements of this detailed HS pathology on 3T MR imaging scanners might contribute, in the future, to the better selection of patients with drug-resistant MTLE who will benefit from surgical procedures.

CONCLUSIONS

In MRI performed with a 3T scanner and visually inspected by imaging experts, quantification of hippocampal volume and T2 signal can increase the detection of signs of HS in approximately 28% of patients with MTLE. Today, these MR imaging quantification methods are easily available and not very time-consuming, and they could be used as routine diagnostic tools for patients with drug-resistant focal epilepsies and visually normal MRI findings after further validation for clinical use.

Disclosures: Ana C. Coan—RELATED: Grant: Fundação de Amparo à Pesquisa do Estado de São Paulo (FAPESP) (São Paulo Research Foundation), Comments: PhD scholarship, UNRELATED: Payment for Lectures (including service on Speakers Bureau): Novartis. Bruno Kubota—RELATED: Grant: FAPESP, Comments: scientific scholarship. Felipe P.G. Bergo—RELATED: Grant: FAPESP, Comments: Postdoctoral scholarship funding from a government agency. Postdoctoral project includes the subject of this study but is not limited to it, UNRELATED: Grants/Grants Pending: FAPESP. Fernando Cendes—RELATED: Grants: FAPESP and Conselho Nacional de Desenvolvimento Científico e Tecnológico, Brazil.* Comments: FAPESP grants 2005/56578-four and 2009/54552-9. *Money paid to the institution.

REFERENCES

- Engel J. Introduction to temporal lobe epilepsy. *Epilepsy Res* 1996;26:141–50
- Van Paesschen W, Connolly A, King MD, et al. The spectrum of hippocampal sclerosis: a quantitative magnetic resonance imaging study. *Ann Neurol* 1997;41:41–51
- Cendes F, Leproux F, Melanson D, et al. MRI of amygdala and hippocampus in temporal lobe epilepsy. *J Comput Assist Tomogr* 1993;17:206–10
- Van Paesschen W, Sisodiya S, Connolly A, et al. Quantitative hippocampal MRI and intractable temporal lobe epilepsy. *Neurology* 1995;45:2233–40
- Sloviter RS. The neurobiology of temporal lobe epilepsy: too much information, not enough knowledge. *C R Biol* 2005;328:143–53
- Jackson GD, Berkovic SF, Tress BM, et al. Hippocampal sclerosis can be reliably detected by magnetic resonance imaging. *Neurology* 1990;40:1869–75
- Berkovic SF, Andermann F, Olivier A, et al. Hippocampal sclerosis in temporal lobe epilepsy demonstrated by magnetic resonance imaging. *Ann Neurol* 1991;29:175–82
- Cendes F, Andermann F, Gloor P, et al. MRI volumetric measurements of amygdala and hippocampus in temporal lobe epilepsy. *Neurology* 1993;43:719–25
- Jackson GD, Connolly A, Duncan JS, et al. Detection of hippocampal pathology in intractable partial epilepsy. Increased sensitivity with quantitative magnetic resonance T2 relaxometry. *Neurology* 1993;43:1793–1793-99
- Bernasconi A, Bernasconi N, Caramanos Z, et al. T2 relaxometry can lateralize mesial temporal lobe epilepsy in patients with normal MRI. *Neuroimage* 2000;12:739–46
- Duncan JS. Neuroimaging methods to evaluate the etiology and consequences of epilepsy. *Epilepsy Res* 2002;50:131–40
- Hammers A, Heckemann R, Koeppe MJ, et al. Automatic detection and quantification of hippocampal atrophy on MRI in temporal lobe epilepsy: a proof-of-principle study. *Neuroimage* 2007;36:38–47
- Farid N, Girard HM, Kemmotsu N, et al. Temporal lobe epilepsy: quantitative MR volumetry in detection of hippocampal atrophy. *Radiology* 2012;264:542–50
- Knake S, Triantafyllou C, Wald LL, et al. 3T phased array MRI improves the presurgical evaluation in focal epilepsies: a prospective study. *Neurology* 2005;65:1026–31
- Briellmann, RS, Syngieniotis, A, Jackson, GD. Comparison of hippocampal volumetry at 1.5 T and at 3 T. *Epilepsia* 2001;42:1021–24
- Scorzin JE, Kaaden S, Quesada CM, et al. Volume determination of amygdala and hippocampus at 1.5 and 3.0 T MRI in temporal lobe epilepsy. *Epilepsy Res* 2008;82:29–37
- Howe KL, Dimitri D, Heyn C, et al. Histologically confirmed hippocampal structural features revealed by 3T MR imaging: potential to increase diagnostic specificity of mesial temporal sclerosis. *AJNR Am J Neuroradiol* 2010;31:1682–89
- Proposal for revised classification of epilepsies and epileptic syndromes: Commission on Classification and Terminology of the International League Against Epilepsy. *Epilepsia* 1989;30:389–99
- McLachlan RS, Nicholson RL, Black S, et al. Nuclear magnetic resonance imaging, a new approach to the investigation of refractory temporal lobe epilepsy. *Epilepsia* 1985;26:555–62
- Von Oertzen J, Urbach H, Jungbluth S, et al. Standard magnetic resonance imaging is inadequate for patients with refractory focal epilepsy. *J Neurol Neurosurg Psychiatry* 2002;73:643–47
- Berkovic SF, McIntosh AM, Kalnins RM, et al. Preoperative MRI predicts outcome of temporal lobectomy: an actuarial analysis. *Neurology* 1995;45:1358–63
- Jackson GD, Kuzniecky RL, Cascino GD. Hippocampal sclerosis without detectable hippocampal atrophy. *Neurology* 1994;44:42–46
- Cohen-Gadol AA, Bradley CC, Williamson A, et al. Normal magnetic resonance imaging and medial temporal lobe epilepsy: the clinical syndrome of paradoxical temporal lobe epilepsy. *J Neurosurg* 2005;102:902–09
- Bell ML, Rao S, So EL, et al. Epilepsy surgery outcomes in temporal lobe epilepsy with a normal MRI. *Epilepsia* 2009;50:2053–60
- Schwartz TH, Jeha L, Tanner A, et al. Late seizures in patients initially seizure free after epilepsy surgery. *Epilepsia* 2006;47:567–73
- Sylaja PN, Radhakrishnan K, Kesavadas C, et al. Seizure outcome after anterior temporal lobectomy and its predictors in patients with apparent temporal lobe epilepsy and normal MRI. *Epilepsia* 2004;45:803–08
- Brewer JB. Fully-automated volumetric MRI with normative ranges: translation to clinical practice. *Behav Neurol* 2009;21:21–28
- Pardoe HR, Pell GS, Abbott DF, et al. Hippocampal volume assessment in temporal lobe epilepsy: how good is automated segmentation? *Epilepsia* 2009;50:2586–92
- Cascino GD, Jack CR, Parisi JE, et al. Magnetic resonance imaging-based volume studies in temporal lobe epilepsy: pathological correlations. *Ann Neurol* 1991;30:31–36
- Blümcke I, Pauli E, Clusmann H, et al. A new clinico-pathological classification system for mesial temporal sclerosis. *Acta Neuropathol* 2007;113:235–44
- Hanamiya M, Korogi Y, Kakeda S, et al. Partial loss of hippocampal striation in medial temporal lobe epilepsy: pilot evaluation with high-spatial-resolution T2-weighted MR imaging at 3.0 T1. *Radiology* 2009;251:873–81

MRI Findings in Autoimmune Voltage-Gated Potassium Channel Complex Encephalitis with Seizures: One Potential Etiology for Mesial Temporal Sclerosis

A.L. Kotsenas, R.E. Watson, S.J. Pittock, J.W. Britton, S.L. Hoyer, A.M.L. Quek, C. Shin, and C.J. Klein



ABSTRACT

BACKGROUND AND PURPOSE: Autoimmune voltage-gated potassium channel complex encephalitis is a common form of autoimmune encephalitis. Patients with seizures due to this form of encephalitis commonly have medically intractable epilepsy and may require immunotherapy to control seizures. It is important that radiologists recognize imaging characteristics of this type of autoimmune encephalitis and suggest it in the differential diagnosis because this seizure etiology is likely under-recognized. Our purpose was to characterize MR imaging findings in this patient population.

MATERIALS AND METHODS: MR imaging in 42 retrospectively identified patients (22 males; median age, 56 years; age range, 8–79 years) with seizures and voltage-gated potassium channel complex autoantibody seropositivity was evaluated for mesial and extratemporal swelling and/or atrophy, T2 hyperintensity, restricted diffusion, and enhancement. Statistical analysis was performed.

RESULTS: Thirty-three of 42 patients (78.6%) demonstrated enlargement and T2 hyperintensity of mesial temporal lobe structures at some time point. Mesial temporal sclerosis was commonly identified (16/33, 48.5%) at follow-up imaging. Six of 9 patients (66.7%, $P = .11$) initially demonstrating hippocampal enhancement and 8/13 (61.5%, $P = .013$) showing hippocampal restricted diffusion progressed to mesial temporal sclerosis. Conversely, in 6 of 33 patients, abnormal imaging findings resolved.

CONCLUSIONS: Autoimmune voltage-gated potassium channel complex encephalitis is frequently manifested as enlargement, T2 hyperintensity, enhancement, and restricted diffusion of the mesial temporal lobe structures in the acute phase. Recognition of these typical imaging findings may help prompt serologic diagnosis, preventing unnecessary invasive procedures and facilitating early institution of immunotherapy. Serial MR imaging may demonstrate resolution or progression of radiologic changes, including development of changes involving the contralateral side and frequent development of mesial temporal sclerosis.

ABBREVIATIONS: Ab = autoantibody; CASPR2 = contactin-associated protein-like 2; LGII = leucine-rich glioma-inactivated protein I; MTS = mesial temporal sclerosis; VGKC = voltage-gated potassium channel complex

Limbic encephalitis, typically characterized clinically by the subacute onset of partial and secondary generalized seizures, memory loss, and neuropsychiatric changes can be of either infectious or autoimmune etiology. Herpes simplex encephalitis is the most common infectious agent that targets the limbic region. Autoimmune limbic encephalitis may occur as a paraneoplastic phenomenon associated with certain tumors or may occur in the absence of a neoplasm.^{1–3} Autoimmune voltage-gated potassium

channel complex (VGKC) encephalitis is one of the most common forms of autoimmune encephalitis. It is frequently found in the absence of associated tumor.^{4,5} VGKC autoantibodies (Abs) have been reported in 6% of patients with long-standing seizures⁶ and in up to 11% when both acute and chronic presentations are considered.⁷ Furthermore, autoimmune VGKC encephalitis may be more common than paraneoplastic autoimmune encephalitis.⁸ Because the hippocampus and associated limbic structures contain attenuated concentrations of potassium channels and due to the inherent epileptogenic potential of these structures, it is not surprising that alteration of the neuronal electrochemical function by this class of Ab would predispose to seizure activity. Comprehensive information is lacking as to whether VGKC autoimmunity leads to longitudinal loss of neurons in the mesial temporal regions or whether this ion channel Ab disorder is without significant long-term radiologic or histopathologic sequelae. Autoimmune VGKC encephalitis can be diagnosed by serologic test-

Received February 5, 2013; accepted after revision March 19.

From the Departments of Radiology (A.L.K., R.E.W., S.L.H.), Neurology (S.J.P., J.W.B., A.M.L.Q., C.S., C.J.K.), and Laboratory Medicine and Pathology (S.J.P., C.J.K.), Mayo Clinic, Rochester Minnesota; and Department of Medicine (A.M.L.Q.), National University Health System, Singapore.

Paper previously presented in part at: 49th Annual Meeting of the American Society of Neuroradiology, June 4–9, 2011; Seattle, Washington.

Please address correspondence to Amy L. Kotsenas, MD, Mayo Clinic, 200 1st St SW, Rochester, MN 55905; e-mail: kotsenas.amy@mayo.edu

<http://dx.doi.org/10.3174/ajnr.A3633>

ing and is potentially treatable with immunotherapy.^{5,6,8-11} However, it is suspected that this condition is greatly underdiagnosed and undertreated.^{9,12} Because the long-term consequences of limbic encephalitis and seizures are frequently significant and the immune aspect of this disease is potentially treatable, it is important that neuroradiologists recognize the existence of this newly identified entity and its imaging characteristics to raise the possibility in the differential diagnosis when appropriate. In this study, we characterize MR imaging findings in autoimmune VGKC encephalitis.

MATERIALS AND METHODS

Institutional review board approval was obtained, and informed consent was waived for this retrospective review. Patients were identified by the following 2 mechanisms: 1) A search of the Mayo Clinic Life Sciences System (a clinical data repository containing patient demographics, diagnoses, hospital and clinical notes, laboratory results, and pathology data obtained from multiple clinical and hospital source systems) by using the keywords “voltage-gated potassium channel” or “VGKC” and “seizures,” “epilepsy,” “encephalitis” or “encephalopathy” identified 11 patients presenting between January 1, 2001, and June 1, 2008, seropositive for VGKC Ab with associated seizures; 2) From June 1, 2008, to June 30, 2010, comprehensive serologic evaluation of patients with unexplained neurologic symptoms was performed at our institution, identifying 1992 patients who were seropositive for VGKC Ab.¹³ A search of this data base identified 33 additional patients with associated seizures.

Chart reviews were performed on these 44 patients. All available imaging was reviewed by 2 neuroradiologists with 13 and 12 years of experience, consensus was reached at the time of interpretation, and results were tabulated. Initial MR imaging was evaluated for the presence of T2 signal hyperintensity in the mesial temporal lobes and extratemporal regions, hippocampal and amygdala swelling, restricted diffusion, and abnormal enhancement. All available follow-up imaging, including short-term (≤ 1 year) and later studies, was assessed for progression or regression of these findings and for the presence of T2 hyperintensity or atrophy indicative of mesial temporal sclerosis (MTS). When MTS was present, the time to its development from the time of first imaging abnormality was recorded.

Statistical Analysis

Statistical analysis was performed by using the JMP software package (Version 9.0; SAS Institute, Cary, North Carolina). χ^2 analysis was used to determine the association between the development of MTS and patient age. The Fisher exact test was used to determine the association between the development of MTS and each of the following: sex, enhancement, restricted diffusion, and leucine-rich glioma-inactivated protein 1 (LGI1) or contactin-associated protein-like 2 (CASPR2) subunit status. Only 2-tailed tests were used. A *P* value of $< .05$ was considered significant.

RESULTS

Clinical Findings

Clinical results are summarized in the Table. Forty-four VGKC Ab-positive patients with seizures were identified. Two were excluded because their imaging was no longer available for review. MR imaging and clinical findings of the remaining 42 patients (22 males;

Clinical findings in autoimmune VGKC encephalitis with seizures

Characteristic	Data (No.)
Patients seropositive for VGKC with seizure with MR imaging	
No.	42
Age (yr) (mean)	8–79 (53.5)
Sex	22 Males (52.4%)
Associated tumor (9) (21.4%)	
Prostate adenocarcinoma	3
Multiple myeloma	2
Colon carcinoma	2
NHL	1
Thymoma	1
Seizure type	
Partial/partial complex	27 (62.3%)
With secondary generalization	3
Tonic-clonic	8 (19%)
With status epilepticus	1
Focal motor	5 (11.9%)
Subclinical/EEG evidence only	2 (5.8%)
Additional neurologic symptoms	
Cognitive decline/confusion	16
Memory deficits	13
Dizziness	5
Sensory changes/paresthesias	4
Personality changes	3
Visual aura/hallucinations	3
Nausea/vomiting	3
Headache	2
Treatment	
Immunotherapy	32 (76.2%)
IVMP alone	18 (56.3%)
IVIG	5 (15.6%)
IVMP/plasmapheresis	3 (9.4%)
IVMP/IVIG	2 (6.3%)
Oral prednisone	2 (6.3%)
IVIG/plasmapheresis	1 (3.1%)
IV dexamethasone (Decadron)	1 (3.1%)
None	10 (23.8%)

Note:—EEG indicates electroencephalography; NHL, Non-Hodgkin lymphoma; IVIG, IV immunoglobulin; IVMP, IV methylprednisolone.

median age, 56 years; age range, 8–79 years) were reviewed. The clinical aspects of 18 patients in this cohort have previously been published, but that prior report did not include detailed analysis of MR imaging findings.⁵ Nine patients (21.4%) had malignancies. One (patient 10, with a thymoma) also had concurrent CRMP5 and GAD65 Abs. Thirty-three patients lacked a tumor diagnosis after a median clinical follow-up of 18 months (range, 1 month to 8.5 years). Two patients, both female, presented in the pediatric age range (8 and 16 years of age), and neither had malignancy.

All 42 patients had seizures. Thirty-five had seizures at presentation. The other 7 developed seizures 1–6 months after initial neurologic symptom onset. Partial seizures were most common, occurring in 27. Only 1 patient, a 46-year-old woman with alcoholism, developed status epilepticus. In 11 patients, seizure was the only neurologic symptom. Additional neurologic symptoms in the other 31 patients are listed in the Table.

Quantitative VGKC Ab levels were available for 33 patients, and autoantibody subtyping was available in 32. Twenty-two (68.8%) were positive for the LGI1 subtype, 3 (9.4%) were positive for the CASPR2 subtype, and 7 (21.9%) were negative for both subtypes. No patients were positive for both LGI1 and CASPR2 subtypes.



FIG 1. A 66-year-old man with autoimmune VGKC epilepsy. Coronal FLAIR at presentation (A), 7-month follow-up (B), and 46-month follow-up (C) demonstrate progression from unilateral increased signal intensity and enlargement of the left hippocampus (A) to left MTS (arrow, B) and finally progression to bilateral MTS (arrows, C).

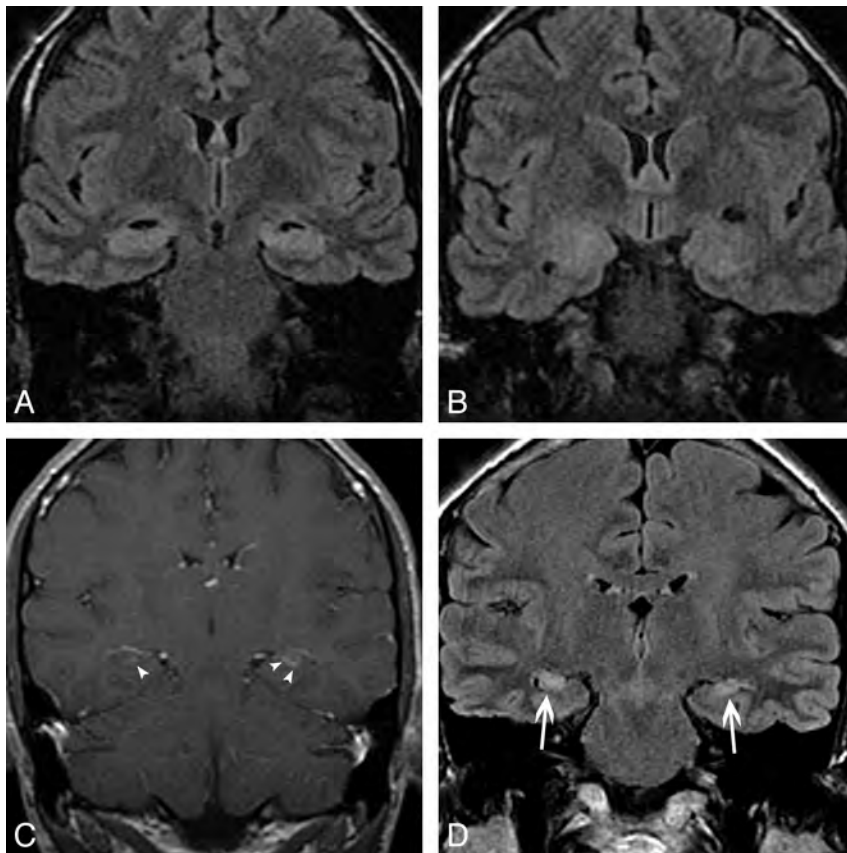


FIG 2. A 25-year-old man with autoimmune VGKC epilepsy. Imaging at presentation demonstrates enlargement and increased signal intensity in the bilateral hippocampi (A) and bilateral amygdalae (B) on coronal FLAIR, with faint ill-defined enhancement (arrowheads) of the hippocampi (C) on coronal contrast-enhanced T1. Follow-up coronal FLAIR imaging (D) at 4 years demonstrates progression to bilateral MTS (arrows).

Thirty-two patients (76.2%) were treated with immunotherapy as outlined in the Table. Initiation of treatment ranged from 1 week to 3 years after symptom onset, which varied depending on seizure frequency, clinical response, and clinical course.

Initial MR Imaging Findings

There was variability in the imaging protocol performed during the 10-year span of this study, and in some cases, initial

imaging was performed at outside institutions. This resulted in variability in the specific sequences obtained, particularly in the availability of diffusion-weighted and contrast-enhanced images. All patients had T2 and/or FLAIR sequences available for review. Thirteen patients had normal MR imaging findings at presentation. In the 29 (69%) cases with abnormal MR imaging findings at presentation, imaging findings revealed enlargement of the amygdala and/or hippocampus with associated signal hyperintensity on T2-weighted images. Of these, findings were unilateral in 15 patients (35.7%; 9 left-sided; Fig 1A). Findings were bilateral in 14 (33.3%; Fig 2A, -B). In 10 patients post-contrast-enhanced T1-weighted imaging was not performed. In those that had post-contrast-enhanced T1-weighted imaging, 9/32 cases (28.1%) demonstrated mild, ill-defined enhancement in areas of T2 hyperintensity (Fig 2C). In 12 patients, DWI was not performed. In the 30 patients in whom DWI was performed, 13/30 cases (43%) showed associated restricted diffusion in areas of T2 hyperintensity (Fig 3A, -B). Twenty-four patients had both DWI and post-contrast-enhanced T1-weighted

imaging; 5 (20.8%) of these patients had both restricted diffusion and abnormal enhancement. No case showed findings of hemorrhage.

Only 2 patients demonstrated nonmesial temporal findings; in 1, there was T2 hyperintensity and restricted diffusion in the left perisylvian cortex and right caudate nucleus in addition to involvement of the left hippocampus. This patient was previously reported in a case series of VGKC Ab encephala-

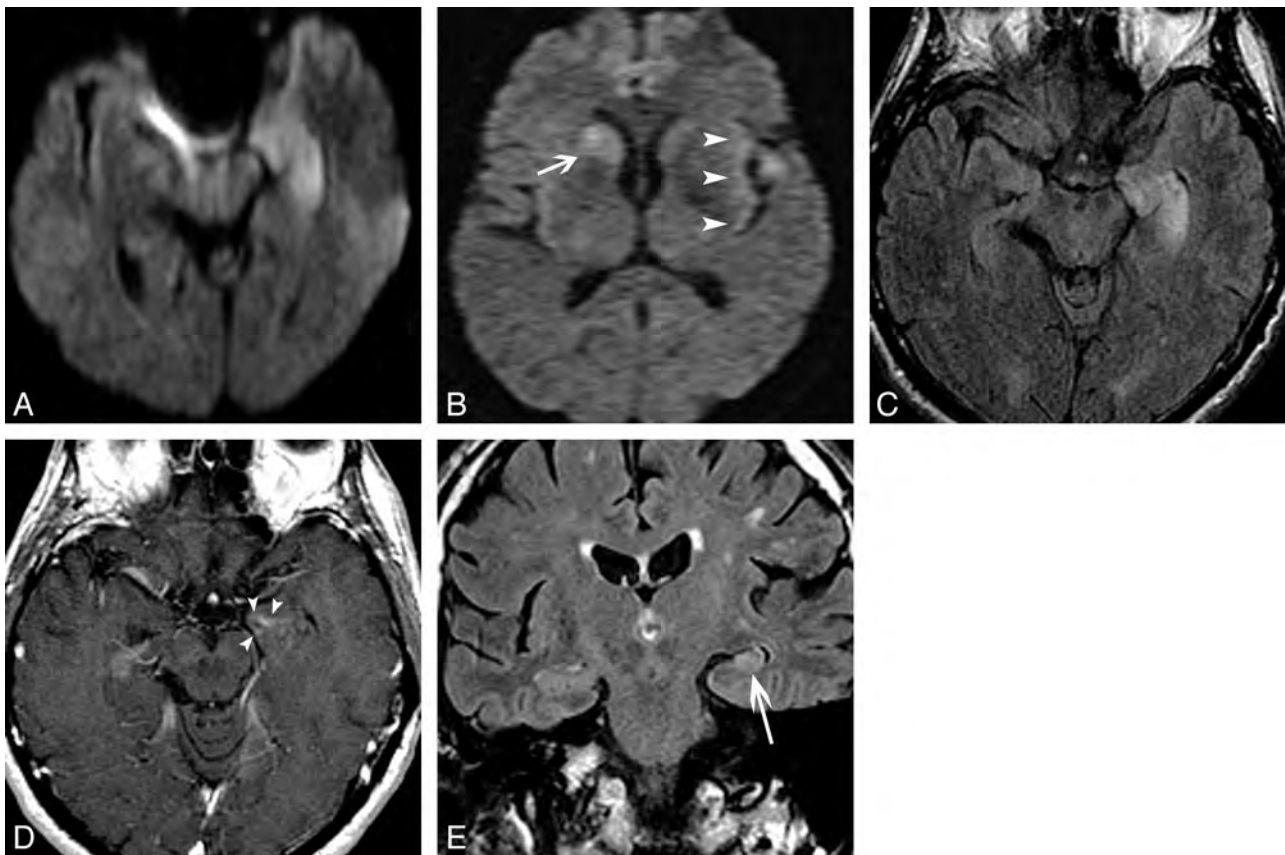


FIG 3. A 60-year-old man with autoimmune VGKC epilepsy. Initial imaging findings (not shown) were normal. At 1-month follow-up, axial diffusion-weighted imaging demonstrates restricted diffusion in the left hippocampus (A), left perisylvian cortex (arrowheads), and right caudate nucleus (arrow, B). Axial FLAIR (C) shows enlargement and increased signal intensity of the left hippocampus, and axial contrast-enhanced T1-weighted image (D) shows faint ill-defined enhancement (arrowheads) in the left hippocampus. Coronal FLAIR (E) 3 years after presentation shows progression to left MTS (arrow).

litis mimicking Creutzfeldt-Jakob disease.¹⁴ The second case demonstrated T2 hyperintensity and restricted diffusion in the left insula in addition to the left hippocampus. There were no changes in the inferior frontal lobes or cingulate gyrus in any case.

In 1 patient referred to our institution, imaging findings of right hippocampal and amygdala enlargement and T2 hyperintensity had been interpreted as a glioma, leading to temporal lobectomy at the outside institution. Pathology demonstrated moderate-to-marked gliosis with scant chronic perivascular inflammatory T-lymphocyte infiltrates and no evidence of neoplasm.

Follow-Up MR Imaging Findings

Subsequent short-term follow-up studies (<1 year) showed progression to bilateral abnormalities in 28.6% with initially negative ($n = 3$) or unilateral ($n = 5$) presentations (Fig 1C). In total, 33 patients (78.6%) demonstrated medial temporal abnormalities at some point during the disease course.

Hippocampal atrophy and T2 hyperintensity consistent with MTS were identified in 16 of 33 patients (48.5%) at follow-up imaging, ranging from 2 to 39 months (median 7 months; 75% quartile 13 months; 25% quartile 3 months) (Fig 4); bilateral in 6 (Fig 1B, -C and Fig 3C) and unilateral in 10. The patients who developed MTS were older (60.25 ± 17.9 years versus 48.9 ± 12.4 years, $P = .02$) and more likely to be male ($n = 12/16$, 75%; $P = .03$). Nine (40.9%, $P =$

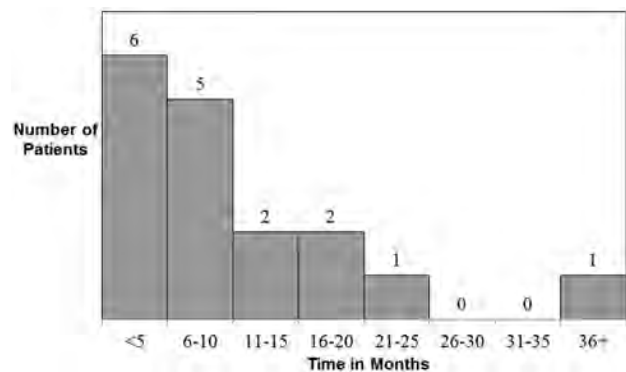


FIG 4. Time to development of MTS from initial MR imaging abnormality.

.43) patients positive for LGI1 and none positive for CASPR2 developed MTS.

In patients with initial associated enhancement, 6/9 (66.7%, $P = .11$) developed MTS, and in patients with initial restricted diffusion, 8/13 (61.5%, $P = .03$) developed MTS. In all 5 patients who showed both restricted diffusion and abnormal enhancement, there was progression to MTS.

Conversely, in 5 of 33 patients (15.2%), abnormal findings resolved on follow-up imaging with immunotherapy treatment (1–49 months; mean, 19 months; Fig 5). In 1 additional patient,

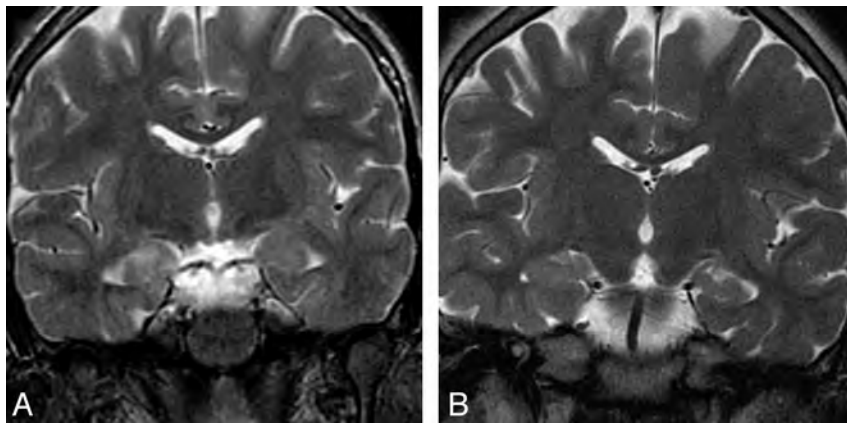


FIG 5. A 74-year-old man with autoimmune VGKC epilepsy. Coronal FSE T2 image (A) shows mild enlargement and increased signal in the right hippocampus. Follow-up coronal FSE T2 (B) at 1 year shows resolution of hyperintense signal and enlargement of the right hippocampus.

findings resolved without specific treatment. None of the immunotherapy-responsive patients demonstrated enhancement or restricted diffusion at any time point. Nine patients did not have long-term imaging follow-up at our institution, including 4 with initially negative imaging findings.

DISCUSSION

Our study demonstrates that initial MR imaging findings associated with autoimmune VGKC encephalitis included uni- or bilateral amygdala and/or hippocampal enlargement and T2 hyperintensity in 78.6% of patients at some time point during the disease course. Nearly half of our patients also demonstrated restricted diffusion; a quarter showed associated mild ill-defined contrast enhancement, and a minority demonstrated extratemporal findings. These findings are nonspecific and are similar to those associated with infectious limbic encephalitis¹⁵ and diverse paraneoplastic limbic encephalitides^{2,16} and to those demonstrated in several smaller series of autoimmune VGKC encephalitis.^{1,8-10,17,18} Our study emphasizes the need to include autoimmune VGKC encephalitis in the differential diagnosis of patients presenting with these MR imaging findings.

Many VGKC Ab–positive patients can present with seizures and epilepsy as the primary clinical feature in the absence of memory loss and neuropsychiatric symptoms that are frequently present in the full clinical spectrum of limbic encephalitis.⁵ Furthermore, while some authors have indicated that autoimmune VGKC encephalitis may present as a monophasic illness, others have reported progression, with patients shown to develop bilateral temporal lobe involvement with time.^{18,19} Our imaging study would support the finding that radiologic progression is common because greater than a quarter (28.6%) of our patients with initially negative study findings or only unilateral findings progressed to bilateral involvement. Whether these changes represent pathology due to persistent CNS inflammation, reflect damage done secondarily by recurrent seizures, or both remains unclear, and prospective longitudinal follow-up will be required to answer this question.

Patients with autoimmune VGKC encephalitis tend to have an unusually high seizure burden⁵; this may account, in part, for the

development of MTS seen in nearly half of our cohort at long-term follow-up. This also implicates VGKC autoimmunity as one potential etiology for “cryptogenic” MTS. Radiologic features of MTS are without a specific pathologic cause, and investigation for VGKC autoimmunity has not been reported in idiopathic MTS.²⁰ Our findings would argue for the need to consider VGKC autoimmunity as a pathologic mechanism of MTS among such patients. In our cohort, patients who developed MTS were significantly more likely to be male and older than those who were responsive to immunotherapy. Most who developed MTS did so within a year of initial imaging abnormality.

While diffusion-weighted imaging was not included on all initial MR imaging examinations, a statistically significant number of patients with initial imaging findings of T2 hyperintensity and swelling of the mesial temporal lobe structures and associated restricted diffusion progressed to MTS. Restricted diffusion can be seen with recent seizure activity or status epilepticus.^{21,22} Only 1 of our patients with restricted diffusion had status epilepticus. Unfortunately, this patient did not have long-term follow-up imaging at our institution. Restricted diffusion is more commonly seen in ischemia/infarction and is reflective of cytotoxic edema, typically indicative of irreversible cell damage. Perhaps patients with autoimmune VGKC encephalitis who present with restricted diffusion should be targeted for more prompt or aggressive immunotherapy in an effort to prevent progression to MTS.

Similarly, there was a trend to develop MTS in two-thirds of patients whose scans demonstrated mild ill-defined enhancement in the hippocampus. This suggests that enhancement and its presumed association with breakdown of the blood-brain barrier may be a marker for more severe or irreversible damage to the hippocampus. This was not statistically significant, likely secondary to the small number of patients with enhancement and follow-up imaging available for review at our institution. Potential association of contrast enhancement and ultimate development of MTS should be confirmed with prospective studies involving larger numbers of patients. All 5 patients who had both contrast-enhancement and restricted diffusion went on to develop MTS. Therefore, we suggest that patients imaged for suspected autoimmune limbic encephalitis should have diffusion-weighted imaging and receive contrast as part of the imaging work-up when issues such as impaired renal function or pregnancy do not preclude its use.

T2 hyperintensity and enlargement were confined to the hippocampus and/or amygdala in all except 2 cases in this series, findings that would be atypical for other etiologies of limbic encephalitis. Nevertheless, the imaging findings of our VGKC Ab–positive patients were not entirely specific for limbic encephalitis in all cases. Consideration for glioma, herpes simplex encephalitis, infarction, and Creutzfeldt-Jakob disease delayed diagnosis in some. One of our patients had temporal lobectomy performed at

an outside institution for suspicion of glioma, further supporting the value of assessing for VGKC Ab. Only 1 patient demonstrated extratemporal findings of restricted diffusion in a distribution similar to that of Creutzfeldt-Jakob disease.¹⁴ There was no evidence of hemorrhage in any case in our series as may be seen in herpes encephalitis.

Interpretation of longitudinal imaging findings in this study was complicated by several factors. First is the long time span during which imaging was obtained, from January 2001 to June 2010. During this decade-long period, the imaging equipment and quality of imaging changed, potentially casting doubts on the consistency of the imaging evaluations. This difference may have underestimated the detection of findings on poorer quality examinations performed at earlier time points. Furthermore, imaging findings are presumed to be reflecting a dynamic pathologic process, likely reflecting not only the primary pathologic autoimmune inflammatory process but also findings associated with engendered seizure activity and those of a superimposed response to immunotherapy and antiepileptic drug treatments. Due to the retrospective nature of our study, we did not specifically assess differences in seizure burden in patients who developed MTS versus those who did not. We propose that future prospective studies may be helpful in addressing this question. Finally, due to the retrospective nature of our study, in some cases, it was difficult to temporally relate treatment regimens with specific imaging findings. However, imaging findings resolved in 14.7% of our patients with some form of immunotherapy treatment. Future prospective studies are anticipated to permit more discrete analysis of the various contributors to the evolution of imaging findings.

CONCLUSIONS

The most common initial findings in autoimmune VGKC encephalitis with seizures are T2 hyperintensity and swelling of the limbic structures, though extratemporal involvement does not preclude a diagnosis of this condition. Recognition of these imaging findings and inclusion of autoimmune VGKC encephalitis in the differential diagnosis with other forms of limbic encephalitis may prompt appropriate serologic evaluation to confirm the diagnosis, which may in turn facilitate early institution of immunotherapy and prevent unnecessary invasive procedures. This study also demonstrates that serial MRI should be considered in patients with suspected autoimmune VGKC epilepsy, to demonstrate the following: delayed development of radiologic changes in patients who previously had normal MR imaging findings; evolution of changes involving the contralateral side, suggesting ongoing inflammatory activity radiologically; and progression to MTS. Future prospective work should be performed to answer the important question of how commonly otherwise “cryptogenic” MTS relates to a remote effect of VGKC autoimmunity.

Disclosures: Sean J. Pittock—UNRELATED: Consultancy: Alexian Pharmaceuticals,* MedImmune,* Grants/Grants Pending: ROI NS065829,* Guthy-Jackson Charitable Foundation,* Payment for Lectures (including service on Speakers Bureaus): American Academy of Neurology,* American Neurological Association,* Patents (planned, pending or issued): patents relating to AQP4 antibodies for the diagnosis of neuromyelitis optica and AQP4 autoantibody as a cancer marker. *Money paid to the institution.

REFERENCES

1. Ances BM, Vitaliani R, Taylor RA, et al. **Treatment-responsive limbic encephalitis identified by neuropil antibodies: MRI and PET correlates.** *Brain* 2005;128:1764–77
2. Gultekin SH, Rosenfeld MR, Voltz R, et al. **Paraneoplastic limbic encephalitis: neurological symptoms, immunological findings and tumour association in 50 patients.** *Brain* 2000;123:1481–94
3. Lucchinetti CF, Kimmel DW, Lennon VA. **Paraneoplastic and oncologic profiles of patients seropositive for type 1 antineuronal nuclear autoantibodies.** *Neurology* 1998;50:652–57
4. Graus F, Saiz A, Lai M, et al. **Neuronal surface antigen antibodies in limbic encephalitis: clinical-immunologic associations.** *Neurology* 2008;71:930–36
5. Quek AM, Britton JW, McKeon A, et al. **Autoimmune epilepsy: clinical characteristics and response to immunotherapy.** *Arch Neurol* 2012;69:582–93
6. Majoie HJ, de Baets M, Renier W, et al. **Antibodies to voltage-gated potassium and calcium channels in epilepsy.** *Epilepsy Res* 2006;71:135–41
7. McKnight K, Jiang Y, Hart Y, et al. **Serum antibodies in epilepsy and seizure-associated disorders.** *Neurology* 2005;65:1730–36
8. Vincent A, Buckley C, Schott JM, et al. **Potassium channel antibody-associated encephalopathy: a potentially immunotherapy-responsive form of limbic encephalitis.** *Brain* 2004;127(pt 3):701–12
9. Barajas RF, Collins DE, Cha S, et al. **Adult-onset drug-refractory seizure disorder associated with anti-voltage-gated potassium-channel antibody.** *Epilepsia* 2010;51:473–77
10. Buckley C, Oger J, Clover L, et al. **Potassium channel antibodies in two patients with reversible limbic encephalitis.** *Ann Neurol* 2001;50:73–78
11. Thieben MJ, Lennon VA, Boeve BF, et al. **Potentially reversible autoimmune limbic encephalitis with neuronal potassium channel antibody.** *Neurology* 2004;62:1177–82
12. Vincent A, Irani SR, Lang B. **The growing recognition of immunotherapy-responsive seizure disorders with autoantibodies to specific neuronal proteins.** *Curr Opin Neurol* 2010;23:144–50
13. Klein CJ, Lennon VA, Aston PA, et al. **Insights from LGI1 and CASPR2 potassium channel complex autoantibody subtyping.** *JAMA Neurol* 2013;70:229–34
14. Geschwind MD, Tan KM, Lennon VA, et al. **Voltage-gated potassium channel autoimmunity mimicking Creutzfeldt-Jakob disease.** *Arch Neurol* 2008;65:1341–46
15. Tüzün E, Dalmau J. **Limbic encephalitis and variants: classification, diagnosis and treatment.** *Neurologist* 2007;13:261–71
16. Lawn ND, Westmoreland BF, Kiely MJ, et al. **Clinical, magnetic resonance imaging, and electroencephalographic findings in paraneoplastic limbic encephalitis.** *Mayo Clin Proc* 2003;78:1363–68
17. Bien CG, Elger CE. **Limbic encephalitis: a cause of temporal lobe epilepsy with onset in adult life.** *Epilepsy Behav* 2007;10:529–38
18. Urbach H, Soeder BM, Jeub M, et al. **Serial MRI of limbic encephalitis.** *Neuroradiology* 2006;48:380–86
19. Chatzikonstantinou A, Szabo K, Ottomeyer C, et al. **Successive affection of bilateral temporomesial structures in a case of non-paraneoplastic limbic encephalitis demonstrated by serial MRI and FDG-PET.** *J Neurol* 2009;256:1753–55
20. **National Institutes of Health Consensus Conference: Surgery for Epilepsy.** *JAMA* 1990;264:729–33
21. Diehl B, Najm I, Ruggieri P, et al. **Periictal diffusion-weighted imaging in a case of lesional epilepsy.** *Epilepsia* 1999;40:1667–71
22. Kim JA, Chung JI, Yoon PH, et al. **Transient MR signal changes in patients with generalized tonicoclonic seizure or status epilepticus: periictal diffusion-weighted imaging.** *AJNR Am J Neuroradiol* 2001;22:1149–60

Intracranial Arteries in Individuals with the Elastin Gene Hemideletion of Williams Syndrome

D.P. Wint, J.A. Butman, J.C. Masdeu, A. Meyer-Lindenberg, C.B. Mervis, D. Sarpal, C.A. Morris, and K.F. Berman



ABSTRACT

BACKGROUND AND PURPOSE: Williams syndrome, a rare genetic disorder with a striking neurobehavioral profile characterized by extreme sociability and impaired visuospatial construction abilities, is caused by a hemideletion that includes the elastin gene, resulting in frequent supravalvular aortic stenosis and other stenotic arterial lesions. Strokes have been reported in Williams syndrome. Although the extracranial carotid artery has been studied in a sample of patients with Williams syndrome, proximal intracranial arteries have not.

MATERIALS AND METHODS: Using MRA, we studied the intracranial vessels in 27 participants: 14 patients with Williams syndrome (age range, 18–44 years; mean age, 27.3 ± 9.1; 43% women) and 13 healthy control participants with similar age and sex distribution (age range, 22–52 years; mean age, 33.4 ± 7.6; 46% women). All participants with Williams syndrome had hemideletions of the elastin gene. Blinded to group allocation or to any other clinical data, a neuroradiologist determined the presence of intracranial vascular changes in the 2 groups.

RESULTS: The Williams syndrome group and the healthy control group had similar patency of the proximal intracranial arteries, including the internal carotid and vertebral arteries; basilar artery; and stem and proximal branches of the anterior cerebral artery, MCA, and posterior cerebral arteries. The postcommunicating segment of the anterior cerebral artery was longer in the Williams syndrome group.

CONCLUSIONS: Despite the elastin haploinsufficiency, the proximal intracranial arteries in Williams syndrome preserve normal patency.

ABBREVIATIONS: ACA = anterior cerebral artery; SVAS = supravalvular aortic stenosis; SVPS = supravalvular pulmonic stenosis

Williams syndrome (On-line Mendelian Inheritance in Man number, 194050) is a multisystem disorder characterized neurologically by remarkable hypersociability along with a distinct deficit in visuospatial construction abilities.^{1–3} Intellectual ability ranges from average for the general population to severe disability, with most people performing in the borderline to mod-

erate range.² With an estimated prevalence of 1 in 7500 live births,⁴ Williams syndrome results from a hemizygous contiguous microdeletion on chromosome 7. The missing band, an approximately 1.6-megabase span at 7q11.23, codes for more than 20 proteins, including elastin.⁵

As a major component of distensible tissues such as the skin, lungs, and vascular walls, elastin plays an important role in normal physiologic functioning.⁶ Elastin deficiency results in fibroblast proliferation in arterial walls,^{7,8} leading to altered mural elasticity and macrostructural deformities, best described for the great arteries and heart.^{9,10} The reported prevalence of cardiovascular structural abnormalities in Williams syndrome hovers at approximately 75% (70%–82%).^{11–13} Supravalvular aortic stenosis (SVAS) and peripheral pulmonary artery stenosis are the most common cardiovascular deformities.^{11,14} Arterial narrowing may be isolated or may occur simultaneously in numerous locations, including the aortic arch; the descending aorta; and the pulmonary, coronary, renal, and mesenteric arteries.³ Aneurysmal dilation may occur after stent placement or other procedures to correct the stenotic lesions,¹⁵ or may rarely manifest spontaneously, particularly in adults.¹⁶

A widespread misunderstanding, derived from the distribution of arterial involvement in giant-cell arteritis,¹⁷ holds that the

Received February 8, 2013; accepted after revision April 8.

From the Section on Integrative Neuroimaging, Clinical Brain Disorders Branch (D.P.W., J.C.M., A.M.-L., D.S., K.F.B.), National Institute of Mental Health, and Radiology and Imaging Sciences, Warren G. Magnuson Clinical Center (J.A.B.), Intramural Research Program, National Institutes of Health, Bethesda, Maryland; Neurodevelopmental Sciences Laboratory (C.B.M.), Department of Psychological and Brain Sciences, University of Louisville, Louisville, Kentucky; and Department of Pediatrics (C.A.M.), University of Nevada School of Medicine, Las Vegas, Nevada.

D.P.W. is currently at the Cleveland Clinic Lou Ruvo Center for Brain Health, Las Vegas, Nevada. A.M.-L. is currently at the Central Institute of Mental Health, Mannheim, Germany. D.S. is currently at the North Shore-LIJ Health System, Glen Oaks, New York.

This work was funded by the NIMH Intramural Research Program, Bethesda, Maryland, and by a grant from the National Institute of Neurological Disorders and Stroke (R01 NS35102) to C.B.M.

Please address correspondence to Karen F. Berman, MD, 10 Center Dr 3C111, Bethesda, MD 20892; e-mail: bermank@mail.nih.gov

Indicates open access to non-subscribers at www.ajnr.org

Indicates article with supplemental on-line table.

<http://dx.doi.org/10.3174/ajnr.A3641>

intracranial arteries do not have elastic layers in their walls. In reality, although the external elastic lamina, between the media and adventitia, is lost a few millimeters after the large arteries perforate the dura to enter the cranial cavity, the internal elastic lamina, in the media, is present. Therefore, the elastin gene hemideletion in Williams syndrome could be associated with arterial stenosis or dilation and compromised hemodynamic function.^{17,18} However, only a few case reports have documented cerebrovascular disease in Williams syndrome. They include spontaneous dissection of the internal carotid artery, leading to an MCA infarction, in an adult¹⁹; 3 patients with striatocapsular infarctions: an adult²⁰ and a child²¹ with clean cerebral vessels on angiography, and a child with stenosis of the supraclinoid carotid and M1 segment of the MCA²²; and narrowing of proximal intracranial arteries in 3 children and a young adult with multiple cerebral infarcts.²³⁻²⁵ In addition, an adult had a cardiogenic stroke after a myocardial infarction.²⁶ Finally, intracerebral hemorrhages, possibly resulting from aneurysmal arteriolar thinning, have been documented in 2 cases.^{27,28} The extracranial carotid arteries have been studied in Williams syndrome with sonography and have been found to lack stenotic or aneurysmal lesions but have been found to have increased media thickness.²⁹ However, although the potential for intracranial cerebral arterial abnormalities in Williams syndrome would constitute a substantial clinical risk factor, the proximal intracranial arterial tree has not been studied systematically in this disorder by use of a prospective design in a population without acute symptoms. To address this gap in knowledge, we used MRA to determine the prevalence of anomalies of the proximal intracranial arterial tree in adults with Williams syndrome.

MATERIALS AND METHODS

Participant Selection and Genetic Testing

Study procedures were approved by the CNS Institutional Review Board of the National Institutes of Health. Participants gave written consent after being informed of the nature and purposes of the study. Fourteen normal-IQ white adults with Williams syndrome gave written consent to participate after being informed of the nature and purposes of the research and were enrolled in the study. All of the participants in this group exhibited the physical features and cognitive profile typical of Williams syndrome, were in good physical health, and did not take any psychotropic medication. Genetic testing had been performed by use of fluorescent in situ hybridization according to standard procedures.³⁰ Thirteen of these participants had the classic 1.6-megabase hemideletion in 7q11.23,¹ and 1 participant had a shorter hemideletion that included the gene coding for elastin. The MR imaging data from 13 healthy control participants, who were not receiving medications, were used for comparison. The control participants were recruited by advertisement and were matched for sex, age, and IQ to the group with Williams syndrome. All study participants were right-handed.

History and Examination

The participants and their parents provided histories of medical and psychiatric diagnoses and treatments, which were supplemented with medical record review. Each participant also under-

went physical and neurologic examination on entry into the study.

Image Acquisition

MR imaging was performed on a Signa 1.5T scanner (GE Healthcare, Milwaukee, Wisconsin) at the National Institutes of Health Nuclear Magnetic Resonance Research Center, by use of a standard head coil. Six T1WIs (TR, 12 ms; TE, 5.2 ms; FOV, 24 mm; resolution, 0.94 × 0.94 × 1.2 mm) were registered and averaged to create a high-resolution structural image for each participant. The major intracranial arteries were imaged by 3D time-of-flight MRA, with the following parameters: field of view, 22 cm; TR, 35 ms; TE, 3.4 ms; flip angle, 20°; section thickness, 1.4 mm; and acquisition time, 6 minutes.

Image Analysis

Images were processed from DICOM format on an Advantage Workstation (AW 4.1; GE Healthcare). Brain MR images were reformatted into double-oblique views to permit analysis of the cerebral midline. Vessels in the circle of Willis were partitioned from the rest of the MRA to increase signal-to-noise ratio. The arteries evaluated included the intracranial portion of the internal carotid and vertebral arteries; basilar artery; and stem and proximal branches of the anterior cerebral, middle cerebral, and posterior cerebral arteries. A neuroradiologist (J.A.B.) with expertise in the interpretation of high-resolution MR imaging and MRA performed qualitative analyses of the images, by using maximum-intensity projection reconstructions. He was blinded to the name, sex, genetic/diagnostic status, physical appearance, and cognitive performance of the participants. Any vascular abnormalities, including stenosis and vasospasm, as well as vascular variants were recorded.

Statistical Analyses

We did not make any assumptions as to the direction of the findings and therefore used 2-tailed statistics. Nominal data were analyzed with the Fisher exact test; age was analyzed with the Student *t* test. Correlations were explored with the non-parametric Spearman correlation.

RESULTS

Demographics

Age and sex of the participants were similar in the Williams syndrome and control groups. The average age of the 14 participants with Williams syndrome was 27.3 ± 9.1 years, compared with 33.4 ± 7.6 years for the 13 participants in the control group (*P* = .11). Each group included 6 women (*P* = .58).

Medical Histories

Medical findings in participants with Williams syndrome are detailed in Table 1. A total of 12 (86%) had a history of at least 1 cardiovascular illness. SVAS was present in 9 (64%) and supravalvular pulmonic stenosis (SVPS) in 3 (21%). Mitral valve abnormalities were recorded in 3 (21%). Four participants (29%) had histories of hypertension. Gastrointestinal tract difficulties, present in 11 (79%) participants with Williams syndrome, included hernias, constipation, diverticular disease, and rectal

Table 1: Medical findings in participants with Williams syndrome

Participant	Age (y)	Pulse (bpm)	Blood Pressure (mm Hg)		Medical History	Cardiovascular History
			Systolic	Diastolic		
1	18	84	130	90	Inguinal hernia	Hypertension
2	18		Not available		Hypercalcemia, joint limitation	SVAS
3	18	72	90	70	Chronic otitis media, hip subluxation, kyphosis, constipation	Ventricular septal defect, SVPS, prolonged Q-T interval
4	19	64	110	80	Constipation	Negative
5	22	64	130	80	Chronic otitis media, scoliosis, rectal prolapse, constipation	Mitral valve prolapse, hypertension
6	22		Not available		Left conductive hearing loss, chronic otitis media, joint limitation	SVAS, mitral valve prolapse
7	23	64	120	60	Inguinal hernia, umbilical hernia, joint impairment	SVAS, SVPS, mitral valve prolapse
8	24	80	130	80	Chronic otitis media, inguinal hernia, joint impairment	SVAS, peripheral pulmonary stenosis, hypertension
9	29	72	120	92	Hypercalcemia	SVAS
10	30	76	120	70	Inguinal hernia	SVAS, SVPS
11	33	68	165	100	Constipation, inguinal hernia	SVAS, hypertension, renal artery stenosis
12	37	100	110	70	Diverticulitis, constipation	SVAS, carotid bruit
13	44	62	120	91	Hypercalcemia, kyphosis, chronic abdominal pain, constipation	SVAS
14	45	96	130	85	Diverticulitis	No history of hypertension

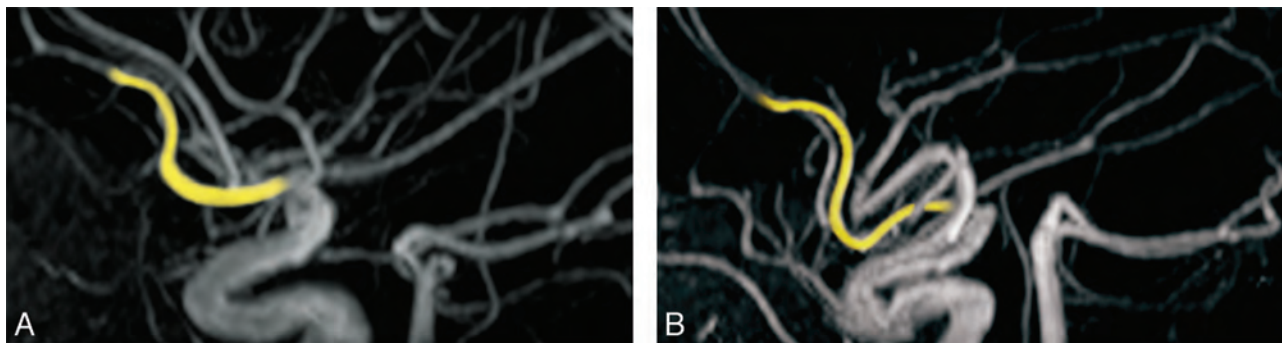


FIGURE. Anterior cerebral artery configuration in Williams syndrome. MRA from a normally developing person (A) and a participant with Williams syndrome (B) showing elongation of the postcommunicating segment of the anterior cerebral artery in the participant with Williams syndrome.

prolapse. Other than the cognitive changes reported elsewhere,^{1,31} the most common neurologic abnormalities were clumsy or uncoordinated gait (79%) and poor cerebellar function (71%).

Imaging Findings

MR imaging and MRA findings are listed in the On-line Table.

Structural MR Images

There was a tendency toward a higher prevalence of atypical gross structural findings in the brains of the Williams syndrome group. Eight participants with Williams syndrome vs 4 control participants had at least 1 morphologic anomaly ($P = .252$). The most frequently noted neuroanatomic finding was a small or unusually shaped corpus callosum, which was present in 6 members of the Williams syndrome group and in 2 of the control participants ($P = .209$). In 5 of the participants with Williams syndrome who had callosal anomalies, the irregularity was in the anterior portion (rostrum or genu) of the corpus callosum. Other findings in the Williams syndrome group were descended cerebellar tonsils and a thickened calvarium. Two

control participants were thought to have small-appearing cerebellar hemispheres.

MRA

Most importantly, there were no stenoses or other hemodynamically significant lesions in either group. Enlarged collaterals were not noted. However, incidental anomalies on MRA were significantly more frequent in the Williams syndrome group. The Figure depicts a specific variation in the course of the anterior cerebral artery (ACA) that was noted only in members of the Williams syndrome group. Typically, the A2 postcommunicating segment of the ACA courses horizontally and then ascends along the genu of the corpus callosum before dividing into the callosomarginal and pericallosal arteries. In 6 of the participants with Williams syndrome, but in none of the matched control participants ($P = .016$), A2 deviated inferiorly before turning toward the callosal genu. No correlation was observed between this ACA variant and the presence of either hypertension or SVAS-SVPS. The other MRA findings in participants with Williams syndrome and in the control group are listed in the On-line Table.

Table 2: Prevalence of medical conditions in patients with Williams syndrome

Medical Condition	Study			
	Wint et al ^a (n = 14)	AAP ^b (n = 315)	Cherniske et al ^c (n = 20)	
	n	%	%	%
Cardiovascular	12	86	80	70
SVAS	9	64	75	65
SVPS	3	21	25	15
Peripheral pulmonary stenosis	1	7	50	—
Mitral valve prolapse	3	21	—	15
Other	1	7	—	35
Hypertension	4	29	50	60
Gastrointestinal	11	79	—	75
Inguinal hernia	5	36	40	—
Constipation	7	50	40	25
Diverticular disease	3	21	30	40
Rectal prolapse	1	7	15	—
Neurologic				
Hyperreflexia	7	50	75	65
Gait disturbance	11	79	60	70
Ataxia	10	71	—	—
Skeletal	6	43	50	—
Spinal	3	21	60	60
Peripheral	5	36	50	55
Chronic otitis	4	29	50	—

Note:—This is a comparison of the prevalence of medical problems in this study's participants with those reported in 2 large studies of Williams syndrome. The number of participants with each condition is listed in the leftmost column.

^a Present study.

^b American Academy of Pediatrics, 2001.³²

^c Cherniske et al, 2004.³³

DISCUSSION

In this first systematic study of cerebral vasculature in patients with Williams syndrome, we have documented that, except for a minor difference in the anatomic configuration of the ACA, the major intracranial arteries in Williams syndrome were similar to those of matched healthy control participants. Because the resolution of MRA does not allow analysis of submillimeter arterial vessels, such as those that penetrate the cerebral cortex, a possibility still remains that elastin deficiency could affect the patency of those arteries. A strength of our study was that it included adults with Williams syndrome, rather than children, allowing us to explore the end result of possible developmental changes during childhood and adolescence. However, it is important to stress that our study was cross-sectional; it did not allow us to predict arterial changes in later adulthood. It could be argued that our sample was skewed, because it included only adults with a normal IQ. However, the cardiovascular findings in our sample (Table 1) are essentially indistinguishable from those of the general Williams syndrome population (Table 2).¹¹⁻¹³ The relatively small incidence of peripheral pulmonary stenosis in our sample of adult patients with Williams syndrome reflects that peripheral pulmonary artery stenosis is often present in infancy and usually improves with time.³² Therefore, peripheral pulmonary artery stenosis is less frequent in our sample of adults than in the much younger sample from the American Academy of Pediatrics (Table 2). Furthermore, the prevalence of various medical illnesses in our participants is comparable to the corresponding prevalence reported in previous studies of children and adults with Williams syndrome that included the full range of intellectual ability associated with this syndrome (Table 2),^{32,33} suggesting that the cerebrovascular findings in our study may be generalized to the wider

Williams syndrome population with no presenting neurologic complaints.

Careful qualitative analysis of MRA for each participant revealed no lesions of hemodynamic significance in the large intracranial arteries, an important negative finding in a population that, by virtue of cardiovascular anomalies and hypertension, could be at elevated risk for stroke. Although only approximately 12 cases of stroke in patients with Williams syndrome have been reported in the literature, the true incidence of stroke in this population is unknown.³⁴ Our findings suggest that most large-artery strokes in Williams syndrome may be related to mechanisms other than significant intracranial arterial involvement. A subset of recorded strokes may be attributable to cardiac or aortic risk factors, which are present in a high proportion of people with Williams syndrome and were documented in some instances of stroke in this syndrome.²⁶ The association with extracranial disorder is likely to occur in cases where no cerebrovascular abnormalities were detected by angiography.^{20,21}

Even in the few stroke cases in which stenotic lesions were documented in the major intracranial vessels,²²⁻²⁴ the possibility of embolism with recanalization cannot be completely ruled out. In some patients, stroke onset was clearly timed to surgical procedures for the correction of aortic disease.²⁵ Furthermore, the presence of small distal microinfarcts in the brain of a person with Williams syndrome studied at autopsy suggests that cardioarterial disease in this population may predispose to embolic infarction.³⁵

Although by using MRA we did not detect hemodynamically significant lesions in our participants with Williams syndrome, we encountered an atypical ACA morphologic feature that was common and specific to Williams syndrome. The usual course of the subgenual ACA was altered in 6 members of the Williams syndrome group by an inferiorly directed “loop” of A2 just proximal to the upward turn of the ACA (Figure). The unusual morphologic pattern of A2 may be a result of the same mechanism that is thought to cause SVAS and SVPS, namely, focal overproliferation of the arterial laminar cells. In the case of the ACA, excessive growth would necessarily impel a downward extension. It is also possible that the ACA develops normally, but A2 is displaced inferiorly because the ACA is “too long” for the unusually short and flat cerebrum and callosum that have been observed in this and other studies of Williams syndrome.³⁶

CONCLUSIONS

In summary, by using MRA we did not detect stenoses or other hemodynamically significant lesions of the proximal intracranial arteries in Williams syndrome, attended by elastin deficiency and stenotic lesions in other arteries. However, most of the partici-

pants with Williams syndrome and, therefore, elastin haploinsufficiency had unusual cerebrovascular morphologic features. Most of the characteristics involved an elongation of the postcommisural segment of the ACA.

Disclosures: Dylan Wint—RELATED: Support for Travel to Meetings for the Study or Other Purposes: National Institutes of Health.* Joseph Masdeu—RELATED: Grant: National Institutes of Health Intramural Research Program*; UNRELATED: Royalties: Lippincott Williams and Wilkins, Elsevier, Comments: Books and book chapters; Travel/Accommodations/Meeting Expenses Unrelated to Activities Listed: American Academy of Neurology; Other: American Society of Neuroimaging, Comments: Editorship of the *Journal of Neuroimaging*. Andreas Meyer-Lindenberg—UNRELATED: Board Membership: Advisory Boards: AstraZeneca, Hoffmann-La Roche, Outcome Europe Sarl; Consultancy: Alexza Pharmaceuticals; Payment for Lectures (including service on speaker bureaus): Bristol-Myers Squibb, H. Lundbeck A/S, Janssen Cilag, Lilly Deutschland GmbH, Pfizer Pharma GmbH, Servier. Carolyn Mervis—RELATED: Grant: NIH*; Support for Travel to Meetings for the Study or Other Purposes: NIH.* Colleen Morris—RELATED: Grant: University of Louisville.* Comments: This was a subcontract on a grant to Dr. Carolyn Mervis from NINDS. *Money paid to institution.

REFERENCES

- Meyer-Lindenberg A, Kohn P, Mervis CB, et al. **Neural basis of genetically determined visuospatial construction deficit in Williams syndrome.** *Neuron* 2004;43:623–31
- Mervis CB, John AE. **Cognitive and behavioral characteristics of children with Williams syndrome: implications for intervention approaches.** *Am J Med Genet C Semin Med Genet* 2010;154C:229–48
- Pober BR. **Williams-Beuren syndrome.** *N Engl J Med* 2010;362:239–52
- Strømme P, Bjørnstad PG, Ramstad K. **Prevalence estimation of Williams syndrome.** *J Child Neurol* 2002;17:269–71
- Morris CA, Thomas IT, Greenberg F. **Williams syndrome: autosomal dominant inheritance.** *Am J Med Genet* 1993;47:478–81
- Kiely CM, Sherratt MJ, Shuttleworth CA. **Elastic fibres.** *J Cell Sci* 2002;115:2817–28
- O'Connor WN, Davis JB Jr, Geissler R, et al. **Supravalvular aortic stenosis. Clinical and pathologic observations in six patients.** *Arch Pathol Lab Med* 1985;109:179–85
- Li DY, Brooke B, Davis EC, et al. **Elastin is an essential determinant of arterial morphogenesis.** *Nature* 1998;393:276–80
- Lacolley P, Boutouyrie P, Glukhova M, et al. **Disruption of the elastin gene in adult Williams syndrome is accompanied by a paradoxical reduction in arterial stiffness.** *Clin Sci (Lond)* 2002;103:21–29
- Urbán Z, Riazi S, Seidl TL, et al. **Connection between elastin haploinsufficiency and increased cell proliferation in patients with supravalvular aortic stenosis and Williams-Beuren syndrome.** *Am J Hum Genet* 2002;71:30–44
- Collins RT 2nd, Kaplan P, Somes GW, et al. **Long-term outcomes of patients with cardiovascular abnormalities and Williams syndrome.** *Am J Cardiol* 2010;105:874–78
- Yau EK, Lo IF, Lam ST. **Williams-Beuren syndrome in the Hong Kong Chinese population: retrospective study.** *Hong Kong Med J* 2004;10:22–27
- Del Pasqua A, Rinelli G, Toscano A, et al. **New findings concerning cardiovascular manifestations emerging from long-term follow-up of 150 patients with the Williams-Beuren-Beuren syndrome.** *Cardiol Young* 2009;19:563–67
- Ahmad Z, Vettukattil J. **Pulmonary artery diverticulum: an angiographic marker for Williams syndrome.** *Pediatr Cardiol* 2010;31:611–14
- Geggel RL, Gauvreau K, Lock JE. **Balloon dilation angioplasty of peripheral pulmonary stenosis associated with Williams syndrome.** *Circulation* 2001;103:2165–70
- McKenna AJ, Craig B, Graham AN. **Williams syndrome in an adult.** *J Card Surg* 2010;25:339–42
- Wilkinson IM, Russell RW. **Arteries of the head and neck in giant cell arteritis. A pathological study to show the pattern of arterial involvement.** *Arch Neurol* 1972;27:378–91
- Ortiz PP, Sarrat R, Daret D, et al. **Elastin variations implicating in vascular smooth muscle cells phenotype in human tortuous arteries.** *Histol Histopathol* 2000;15:95–100
- Vanacker P, Thijs V. **Spontaneous cervical artery dissection in adult Williams syndrome.** *Cerebrovasc Dis* 2009;27:309–10
- Wollack JB, Kaifer M, LaMonte MP, et al. **Stroke in Williams syndrome.** *Stroke* 1996;27:143–46
- Lee WD, Hsu JJ, Huang FC, et al. **Ischemic stroke in Williams-Beuren syndrome: a case report.** *Kaohsiung J Med Sci* 2009;25:212–16
- Soper R, Chaloupka JC, Fayad PB, et al. **Ischemic stroke and intracranial multifocal cerebral arteriopathy in Williams syndrome.** *J Pediatr* 1995;126:945–48
- Kaplan P, Levinson M, Kaplan BS. **Cerebral artery stenoses in Williams syndrome cause strokes in childhood.** *J Pediatr* 1995;126:943–45
- Ardinger RH, Jr, Goertz KK, Mattioli LF. **Cerebrovascular stenoses with cerebral infarction in a child with Williams syndrome.** *Am J Med Genet* 1994;51:200–02
- Sim YW, Lee MS, Kim YG, et al. **Unpredictable postoperative global cerebral infarction in the patient of Williams syndrome accompanying Moyamoya disease.** *J Korean Neurosurg Soc* 2011;50:256–59
- Blanc F, Wolff V, Talmant V, et al. **Late onset stroke and myocardial infarction in Williams syndrome.** *Eur J Neurol* 2006;13:e3–4
- Kawai M, Nishikawa T, Tanaka M, et al. **An autopsied case of Williams syndrome complicated by Moyamoya disease.** *Acta Paediatr Jpn* 1993;35:63–67
- Kalbhenn T, Neumann LM, Lanksch WR, et al. **Spontaneous intracerebral hemorrhage and multiple infarction in Williams-Beuren syndrome.** *Pediatr Neurosurg* 2003;39:335–38
- Sadler LS, Gingell R, Martin DJ. **Carotid ultrasound examination in Williams syndrome.** *J Pediatr* 1998;132:354–56
- Lowery MC, Morris CA, Ewart A, et al. **Strong correlation of elastin deletions, detected by FISH, with Williams syndrome: evaluation of 235 patients.** *Am J Hum Genet* 1995;57:49–53
- Meyer-Lindenberg A, Hariri AR, Munoz KE, et al. **Neural correlates of genetically abnormal social cognition in Williams syndrome.** *Nat Neurosci* 2005;8:991–93
- Committee on Genetics. **American Academy of Pediatrics: Health care supervision for children with Williams syndrome.** *Pediatrics* 2001;107:1192–204
- Cherniske EM, Carpenter TO, Klaiman C, et al. **Multisystem study of 20 older adults with Williams syndrome.** *Am J Med Genet* 2004;131A:255–64
- Beslow LA, Jordan LC. **Pediatric stroke: the importance of cerebral arteriopathy and vascular malformations.** *Childs Nerv Syst* 2010;26:1263–73
- Galaburda AM, Bellugi UV. **Multi-level analysis of cortical neuroanatomy in Williams syndrome.** *J Cogn Neurosci* 2000;12 Suppl 1:74–88
- Schmitt JE, Eliez S, Warsofsky IS, et al. **Corpus callosum morphology of Williams syndrome: relation to genetics and behavior.** *Dev Med Child Neurol* 2001;43:155–59

Evaluation of Diffusivity in the Anterior Lobe of the Pituitary Gland: 3D Turbo Field Echo with Diffusion-Sensitized Driven-Equilibrium Preparation

A. Hiwatashi, T. Yoshiura, O. Togao, K. Yamashita, K. Kikuchi, K. Kobayashi, M. Ohga, S. Sonoda, H. Honda, and M. Obara



ABSTRACT

BACKGROUND AND PURPOSE: 3D turbo field echo with diffusion-sensitized driven-equilibrium preparation is a non-echo-planar technique for DWI, which enables high-resolution DWI without field inhomogeneity-related image distortion. The purpose of this study was to evaluate the feasibility of diffusion-sensitized driven-equilibrium turbo field echo in evaluating diffusivity in the normal pituitary gland.

MATERIALS AND METHODS: First, validation of diffusion-sensitized driven-equilibrium turbo field echo was attempted by comparing it with echo-planar DWI. Five healthy volunteers were imaged by using diffusion-sensitized driven-equilibrium turbo field echo and echo-planar DWI. The imaging voxel size was $1.5 \times 1.5 \times 1.5 \text{ mm}^3$ for diffusion-sensitized driven-equilibrium turbo field echo and $1.5 \times 1.9 \times 3.0 \text{ mm}^3$ for echo-planar DWI. ADCs measured by the 2 methods in 15 regions of interests (6 in gray matter and 9 in white matter) were compared by using the Pearson correlation coefficient. The ADC in the pituitary anterior lobe was then measured in 10 volunteers by using diffusion-sensitized driven-equilibrium turbo field echo, and the results were compared with those in the pons and vermis by using a paired *t* test.

RESULTS: The ADCs from the 2 methods showed a strong correlation ($r = 0.79$; $P < .0001$), confirming the accuracy of the ADC measurement with the diffusion-sensitized driven-equilibrium sequence. The ADCs in the normal pituitary gland were $1.37 \pm 0.13 \times 10^{-3} \text{ mm}^2/\text{s}$, which were significantly higher than those in the pons ($1.01 \pm 0.24 \times 10^{-3} \text{ mm}^2/\text{s}$) and the vermis ($0.89 \pm 0.25 \times 10^{-3} \text{ mm}^2/\text{s}$, $P < .01$).

CONCLUSIONS: We demonstrated that diffusion-sensitized driven-equilibrium turbo field echo is feasible in assessing ADC in the pituitary gland.

ABBREVIATIONS: DSDE = diffusion-sensitized driven-equilibrium; EP = echo-planar; TFE = turbo field echo

DWI is widely used to diagnose cerebrovascular diseases, intracranial tumors, and inflammation.¹⁻¹⁰ However, it is difficult to evaluate skull base structures by the most common imaging technique used with echo-planar (EP)-DWI. Previous studies have revealed the efficacy of DWI for skull base tumors such as pituitary adenoma; however, they are mostly limited to macroadenomas large enough to calculate the ADC by using EP sequences.³⁻⁷ Compared with EP-DWI, 3D diffusion-sensitized

driven-equilibrium turbo field echo (DSDE-TFE) obtained DWI has higher spatial resolution and fewer susceptibility artifacts.¹¹ To our knowledge, to date, the diffusivity of the normal pituitary gland has not been fully evaluated, especially in those glands surrounded by aerated sphenoid sinuses. Therefore, the purpose of this study was to evaluate the feasibility of DSDE-TFE in evaluating diffusivity in the normal pituitary gland.

MATERIALS AND METHODS

The study was conducted with approval of the involved institutional review boards. Written informed consent was obtained from each participant. First, we validated DSDE-TFE and compared it with EP-DWI. Then, ADC measurement in the anterior lobe of the pituitary gland was performed.

Imaging Technique

All participants underwent MR imaging with a 3T system (Achieva Quasar Dual; Philips, Best, the Netherlands) with an 8-channel head coil. Figure 1 shows a diagram of our DSDE preparation sequence.

Received February 8, 2012; accepted after revision March 26.

From the Departments of Clinical Radiology (A.H., T.Y., O.T., K.Y., K. Kikuchi, H.H.) and Molecular Imaging and Diagnosis (O.T.), Graduate School of Medical Sciences, Kyushu University, Fukuoka, Japan; Division of Radiological Technology (K. Kobayashi, M.O., S.S.), Department of Medical Technology, Kyushu University Hospital, Fukuoka, Japan; and MR Clinical Science (M.O.), Philips Electronics Japan, Tokyo, Japan.

Please address correspondence to Akio Hiwatashi, MD, PhD, Department of Clinical Radiology, Graduate School of Medical Sciences, Kyushu University, 3-1-1 Maidashi, Higashi-ku, Fukuoka 812-8582, Japan; e-mail hiwatashi@radiol.med.kyushu-u.ac.jp

Indicates open access to non-subscribers at www.ajnr.org

<http://dx.doi.org/10.3174/ajnr.A3620>

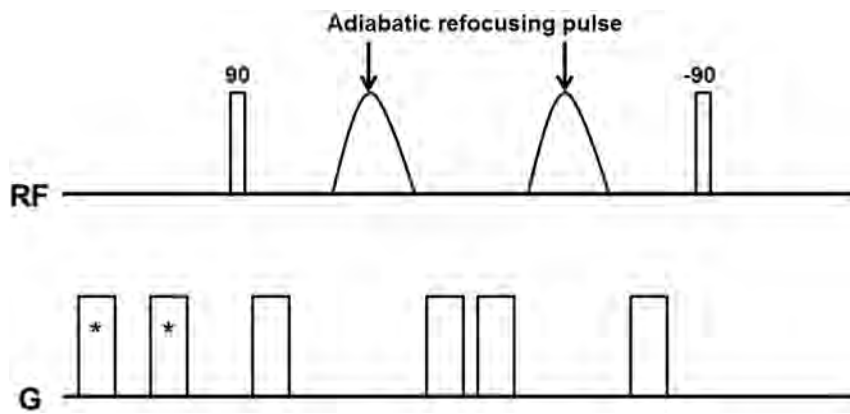


FIG 1. Diagram of DSDE sequences used in this study. Asterisk indicates prepulse gradients for eddy current compensation.

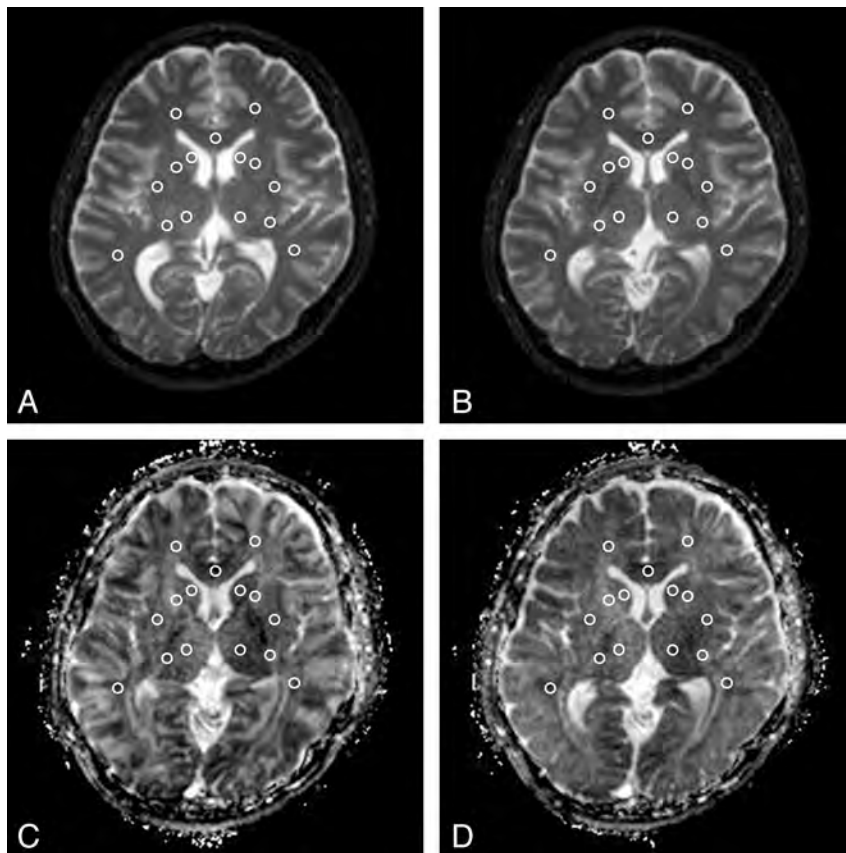


FIG 2. ROI placement. Fifteen ROIs were placed at the bilateral caudate head, putamen, thalamus, anterior limb of the internal capsule, posterior limb of the internal capsule, frontal white matter, temporal white matter, and the genu of the corpus callosum on a b_0 map (DSDE-TFE, A; EP-DWI, B) and then were copied to the ADC map derived from DSDE-TFE (C) and EP-DWI (D).

The DSDE-TFE has 2 distinct components: first, the DSDE preparation and, second, the segmented 3D TFE data acquisition.¹¹ The DSDE preparation is an extension of the motion-sensitized driven-equilibrium preparation, which has been used for black-blood imaging of large vessels.^{12,13} Motion-sensitized driven-equilibrium preparation has also been applied to brain imaging for the detection of metastatic tumors.¹⁴ Compared with motion-sensitized driven-equilibrium preparation, the DSDE-prepared sequence has stronger motion-sensitizing gradients, which enable diffusion-weighting in

the anteroposterior direction. DSDE preparation was originally developed to reduce distortion in the imaging of peripheral nerves,¹¹ and it was then optimized for skull base imaging in the present study. Adiabatic refocusing pulses and additional gradients inserted in front of the sequence were used to reduce B0 and B1 inhomogeneity and eddy current effects.^{11,15} Data acquisition by using TFE was performed immediately after the DSDE preparation. To eliminate T1 effects in the acquired signal by TFE, we used a phase-cycling scheme.^{16,17}

The imaging parameters for the DSDE-TFE were as follows: TR/TE = 6.2/3 ms, flip angle = 10°, echo-train length = 75, b factors = 0, 500 s/mm², sensitivity-encoding factor = 2, FOV = 240 mm, voxel size = 1.5 × 1.5 × 1.5 mm³, number of signal averages = 2, and acquisition time = 5 minutes 22 seconds. The imaging parameters for the EP-DWI were as follows: TR/TE = 3000/62 ms, b factors = 0, 500 s/mm² (anteroposterior direction), sensitivity encoding factor = 2.5, FOV = 240 mm, matrix = 160 × 128, section thickness/gap = 3/0 mm, voxel size = 1.5 × 1.9 × 3 mm³, number of signal averages = 2, and acquisition time = 48 seconds. Because coverage of DSDE-TFE was limited by 36-mm thickness, acquisition of EP-DWI coincided with that of DSDE-TFE. Sagittal T1-weighted images were also obtained to separate the anterior and the posterior lobes of the pituitary gland. The imaging parameters for T1-weighted images were as follows: TR/TE = 450/13 ms, FOV = 150 mm, matrix = 224 × 180, section thickness/gap = 3/0 mm, voxel size = 0.7 × 0.8 × 3 mm³, number of signal averages = 2, and acquisition time = 2 minutes 44 seconds.

Analysis

Validation Study. The DSDE-TFE dataset was originally imaged in the axial plane. The data were reformatted to the axial plane (3-mm-thick). Both the DSDE-TFE and EP-DWI datasets were saved in the DICOM format. ADC maps were calculated on a personal computer by using ImageJ, Version 1.44p, for Windows software (National Institutes of Health, Bethesda, Maryland). Fifteen ROIs were placed on b_0 images and then were copied to ADC maps. They were located at the bilateral caudate head, putamen, thalamus, anterior limb of the internal capsule, posterior limb of the internal capsule, frontal white matter, temporal white matter, and the genu of the corpus callosum by a neuroradiologist

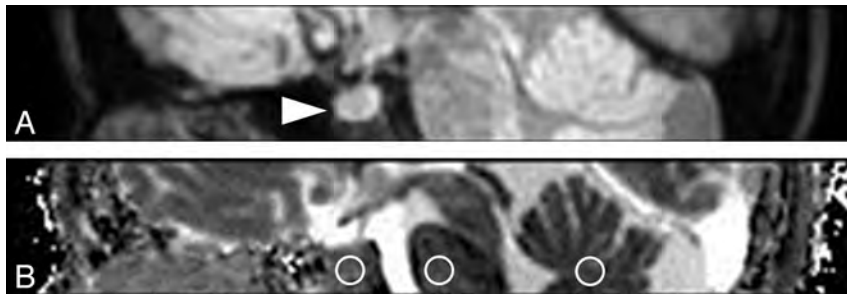


FIG 3. Sagittal reformatted DWI (A) and ADC map derived from DSDE-TFE (B). The normal anterior lobe of the pituitary gland is clearly visualized without image degradation (arrowhead, A). Three ROIs are placed at the anterior lobe of the pituitary gland, pons, and vermis (circles, B).

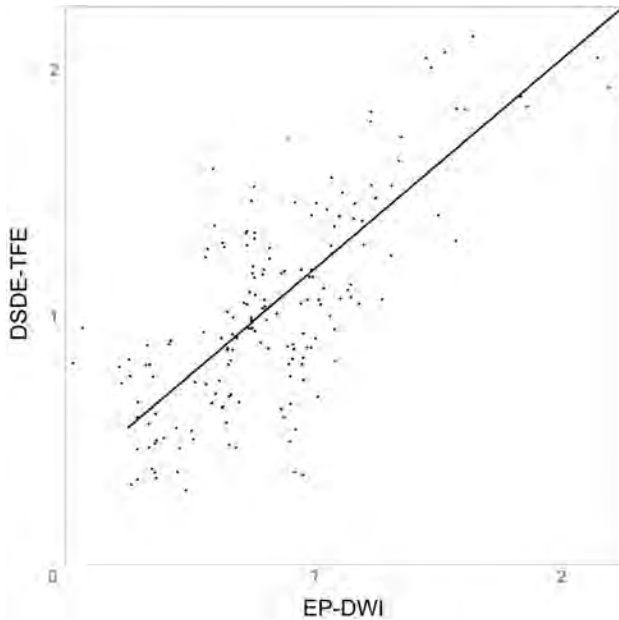


FIG 4. Graph shows the relationship of ADC between DSDE-TFE and EP-DWI ($\times 10^{-3} \text{ mm}^2/\text{s}$). There is a significant correlation in ADC measurements between DSDE-TFE and EP-DWI ($r = 0.79, P < .0001$). $\text{ADC}_{\text{DSDE-TFE}} = \text{ADC}_{\text{EP-DWI}} \times 0.849 + 0.340$.

(A.H., with 15 years' experience in neuroradiology, Fig 2). Statistical analysis was performed by the same author by using the statistical software JMP, Version 9.0.2 (SAS Institute, Cary, North Carolina). The Pearson correlation coefficient was used for analysis. P values $< .05$ were considered significant.

ADC Measurement in the Pituitary Gland. The DSDE-TFE data were reformatted to the sagittal plane (3-mm-thick). Both the DSDE-TFE and EP-DWI datasets were saved in the DICOM format. ADC maps were calculated in the same manner. Three ROIs were placed at the anterior lobe of the pituitary gland, pons, and vermis on the midsagittal plane by the same rater (Fig 3). The posterior lobe of the pituitary gland was excluded by sagittal T1-weighted images for comparison. The statistical analysis was performed with a paired t test in the same manner as that used for the validation study above. P values $< .05$ were considered significant.

RESULTS

Validation Study

The validation study included 5 healthy volunteers (5 men; age range, 30–46 years; median age, 36 years).

On DSDE-TFE, the ADCs of the 15 ROIs ranged from $0.32 \times 10^{-3} \text{ mm}^2/\text{s}$ to $2.13 \times 10^{-3} \text{ mm}^2/\text{s}$ (mean, $1.07 \pm 0.41 \times 10^{-3} \text{ mm}^2/\text{s}$). On EP-DWI, the ADCs ranged from $0.26 \times 10^{-3} \text{ mm}^2/\text{s}$ to $2.19 \times 10^{-3} \text{ mm}^2/\text{s}$ (mean, $0.86 \pm 0.38 \times 10^{-3} \text{ mm}^2/\text{s}$). There was a significant correlation in the ADC measurement between DSDE-TFE and EP-DWI ($r = 0.79, P < .0001$; Fig 4).

ADC Measurement in the Pituitary Gland

ADC measurement in the pituitary gland included 10 healthy volunteers (6 men and 4 women; age range, 25–46 years; median age, 33 years).

DSDE-TFE provided images of the pituitary gland without distortion in all 10 subjects. The ADCs in the anterior lobe of the pituitary gland ranged from $1.16 \times 10^{-3} \text{ mm}^2/\text{s}$ to $1.54 \times 10^{-3} \text{ mm}^2/\text{s}$. In the pons, the ADCs ranged from $0.68 \times 10^{-3} \text{ mm}^2/\text{s}$ to $1.38 \times 10^{-3} \text{ mm}^2/\text{s}$, and in the vermis, the ADCs ranged from $0.63 \times 10^{-3} \text{ mm}^2/\text{s}$ to $1.35 \times 10^{-3} \text{ mm}^2/\text{s}$. The ADCs in the anterior lobe of the pituitary gland (mean, $1.37 \pm 0.13 \times 10^{-3} \text{ mm}^2/\text{s}$) were significantly higher than those in the pons ($1.01 \pm 0.24 \times 10^{-3} \text{ mm}^2/\text{s}$) and vermis ($0.89 \pm 0.25 \times 10^{-3} \text{ mm}^2/\text{s}$, $P < .01$, Fig 5).

DISCUSSION

To our knowledge, this is the first report to evaluate the diffusivity of the normal pituitary gland. We revealed a strong correlation in ADC measurements between DSDE-TFE and EP-DWI ($r = 0.79, P < .0001$) in several brain structures in healthy subjects. The DSDE-TFE technique was originally reported as one of the nerve sheath imaging techniques.¹¹ Obara et al¹¹ reported a qualitative evaluation of DSDE-TFE, but there has been no quantitative evaluation. The present study is thus also the first to validate ADC calculations by using this technique.

We observed that the ADCs of brain structures obtained by using DSDE-TFE ($1.07 \pm 0.41 \times 10^{-3} \text{ mm}^2/\text{s}$) were higher than those obtained by using EP-DWI ($0.86 \pm 0.38 \times 10^{-3} \text{ mm}^2/\text{s}$). For DSDE-TFE, adiabatic refocusing pulses and additional gradients inserted in front of the sequence were used to reduce B0 and B1 inhomogeneity and eddy current effects.^{11,15} However, further development is required to achieve less variation in measurement.

In this study, DSDE-TFE provided visualization of the pituitary gland without distortion of the images in all 7 subjects. Due to the severe susceptibility artifacts, it is impossible to evaluate the normal pituitary gland with EP-DWI. Therefore, previous studies by using EP-DWI were mainly limited to pituitary macroadenoma, apoplexy, abscess, or other parasellar lesions.^{3–7} Other researchers applied non-EP-DWI such as single-shot fast spin-echo,⁸ line scan,⁹ and periodically rotated overlapping parallel lines with enhanced reconstruction¹⁰ DWI for sellar and parasellar lesions to overcome image degradation. In the present study, we used DSDE-TFE, which enabled us to obtain a 3D dataset and high spatial resolution ($1.5 \times 1.5 \times 1.5 \text{ mm}^3$). We may apply this technique to other skull base and head and neck structures in the future.

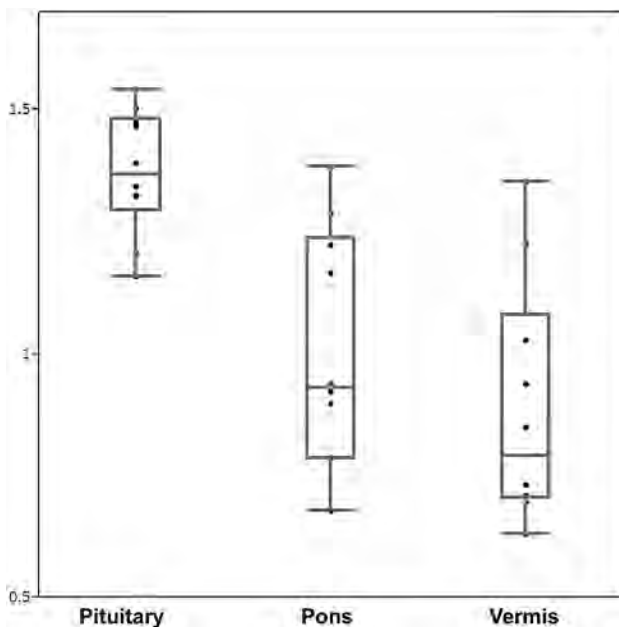


FIG 5. Graph of ADCs in the anterior lobe of the pituitary gland, pons, and vermis ($\times 10^{-3}$ mm²/s). The ADCs in the anterior lobe of the pituitary gland ($1.37 \pm 0.13 \times 10^{-3}$ mm²/s) are significantly higher than those in the pons ($1.01 \pm 0.24 \times 10^{-3}$ mm²/s) and vermis ($0.89 \pm 0.25 \times 10^{-3}$ mm²/s, $P < .01$).

We observed that the ADCs in the anterior lobe of the pituitary gland ($1.37 \pm 0.13 \times 10^{-3}$ mm²/s) were significantly higher than those in the pons ($1.01 \pm 0.24 \times 10^{-3}$ mm²/s) and vermis ($0.89 \pm 0.25 \times 10^{-3}$ mm²/s). Even in the previous reports that used non-EP-DWI, there was no mention of the diffusivity of the normal pituitary gland. We suspect that the lack of myelination and hypervascularity in the normal pituitary gland may contribute to the increased diffusivity compared with the pons and vermis.^{18,19} Further studies are needed to investigate this possibility.

Limitations of this study included the low b-values and 1 direction of the diffusion-weighting. We were able to obtain DWI with DSDE-TFE at b-values higher than 500 s/mm², but it was sometimes difficult to obtain ADC maps, probably due to insufficient eddy current compensations. We are trying to apply DWI in >3 directions, but further technical developments are required. We also tried to evaluate the diffusivity of the posterior lobe, but it was difficult, despite the high spatial resolution of our images ($1.5 \times 1.5 \times 1.5$ mm³). Limited coverage (36 mm) and the longer acquisition time (5 minutes 22 seconds) of DSDE-TFE (36 mm) compared with EP-DWI are other disadvantages. We could not compare the pituitary gland, vermis, and pons on the sagittal plane consistently. The absence of a criterion standard for pituitary ADC is also a limitation. We did not have a normal pituitary gland on postmortem examination or in surgical specimens in this study. Histopathologic correlation is required in the future.

CONCLUSIONS

By using DSDE-TFE, it was possible to obtain ADC maps with high resolution and fewer susceptibility artifacts compared with EP-DWI. The 3D DSDE-TFE technique enabled us to evaluate the diffusivity in the normal pituitary gland, which was higher than that in the pons and vermis.

Disclosures: Koji Yamashita—RELATED: Grant: Grants-in-Aid for Scientific Research, Comments: Grant-in-Aid for Young Scientists (JSPS KAKENHI grant number 23791432).

REFERENCES

1. Le Bihan D, Breton E, Lallemand D, et al. MR imaging of intravoxel incoherent motions: application to diffusion and perfusion in neurologic disorders. *Radiology* 1986;161:401–07
2. Provenzale JM, Sorensen AG. Diffusion-weighted MR imaging in acute stroke: theoretic considerations and clinical applications. *AJR Am J Roentgenol* 1999;173:1459–67
3. Rogg JM, Tung GA, Anderson G, et al. Pituitary apoplexy: early detection with diffusion-weighted MR imaging. *AJNR Am J Neuroradiol* 2002;23:1240–45
4. Yamasaki F, Kurisu K, Satoh K, et al. Apparent diffusion coefficient of human brain tumors at MR imaging. *Radiology* 2005;235:985–91
5. Pierallini A, Caramia F, Falcone C, et al. Pituitary macroadenomas: preoperative evaluation of consistency with diffusion-weighted MR imaging—initial experience. *Radiology* 2006;239:223–31
6. Takao H, Doi I, Watanabe T. Diffusion-weighted magnetic resonance imaging in pituitary abscess. *J Comput Assist Tomogr* 2006;30:514–16
7. Boxerman JL, Rogg JM, Donahue JE, et al. Preoperative MRI evaluation of pituitary macroadenoma: imaging features predictive of successful transphenoidal surgery. *AJR Am J Roentgenol* 2010;195:720–28
8. Kunii N, Abe T, Kawamo M, et al. Rathke's cleft cysts: differentiation from other cystic lesions in the pituitary fossa by use of single-shot fast spin-echo diffusion-weighted MR imaging. *Acta Neurochir (Wien)* 2007;149:759–69
9. Suzuki C, Maeda M, Hori K, et al. Apparent diffusion coefficient of pituitary macroadenoma evaluated with line-scan diffusion-weighted imaging. *J Neuroimaging* 2007;34:228–35
10. Mahmoud OM, Tominaga A, Amatya VJ, et al. Role of PROPELLER diffusion-weighted imaging and apparent diffusion coefficient in the evaluation of pituitary adenomas. *Eur J Radiol* 2011;80:412–17
11. Obara M, Takahara T, Honda M, et al. Diffusion weighted MR nerve sheath imaging (DW-NSI) using diffusion-sensitized driven-equilibrium (DSDE). In: *Proceedings of the 19th Annual Meeting and Exhibition of the International Society for Magnetic Resonance in Medicine*, Montreal, Quebec, Canada. May 7–13, 2011;19:4023
12. Koktzoglou I, Li D. Diffusion-prepared segmented steady-state free precession: application to 3D black-blood cardiovascular magnetic resonance of the thoracic aorta and carotid artery walls. *J Cardiovasc Magn Reson* 2007;9:33–42
13. Wang J, Yarnykh VL, Hatsukami T, et al. Improved suppression of plaque-mimicking artifacts in black-blood carotid atherosclerosis imaging using a multislice motion-sensitized driven-equilibrium (MSDE) turbo spin-echo (TSE) sequence. *Magn Reson Med* 2007;58:973–81
14. Nagao E, Yoshiura T, Hiwatashi A, et al. 3D turbo spin-echo sequence with motion-sensitized driven-equilibrium preparation for detection of brain metastases on 3T MR imaging. *AJNR Am J Neuroradiol* 2011;32:664–70
15. Nezafat R, Stuber M, Ouwerkerk R, et al. B1-insensitive T2 preparation for improved coronary magnetic resonance angiography at 3 T. *Magn Reson Med* 2006;55:858–64
16. Coremans J, Spanoghe M, Budinsky L, et al. A comparison between different imaging strategies for diffusion measurements with the centric phase-encoded turboFLASH sequence. *J Magn Reson* 1997;124:323–42
17. Thomas DL, Pell GS, Lythgoe MF, et al. A quantitative method for fast diffusion imaging using magnetization-prepared turbo-FLASH. *Magn Reson Med* 1998;39:950–60
18. Miki Y, Matsuo M, Nishizawa S, et al. Pituitary adenomas and normal pituitary tissue: enhancement patterns on gadopentetate-enhanced MR imaging. *Radiology* 1990;177:35–38
19. Sakamoto Y, Takahashi M, Korogi Y, et al. Normal and abnormal pituitary glands: gadopentetate dimeglumine-enhanced MR imaging. *Radiology* 1991;178:441–45

Diffusion-Weighted Imaging of the Pituitary Gland

In this issue of the *American Journal of Neuroradiology*, you will find the article “Evaluation of Diffusivity in the Anterior Lobe of the Pituitary Gland: 3D Turbo Field Echo with Diffusion-Sensitized Driven-Equilibrium Preparation” by Hiwatashi et al.¹ I enjoyed reading this article and found it to be a nice “proof of principle” regarding the use of “diffusion-sensitized driven-equilibrium turbo field echo” to image the anterior pituitary gland.¹ In my clinical practice, I have found diffusion-weighted imaging to have particular utility in neuroimaging...well beyond the classic assessment for acute brain ischemia or infarction or pyogenic abscess formation. I like the idea of “squeezing out” as much information as possible from each of our MR images to help identify and characterize neuropathology. It is also helpful, I think, to approach each neuroimaging examination and sequence in terms of its physiologic basis and known or presumed “added value.” For example, in terms of DWI, I like to think about its physiologic basis as the diffusion of water. As we consider new technical variants and/or adding sequences to our brain MR imaging, I propose that we need to critically appraise “the literature” and developments communicated at meetings of “organized radiology.” In this context, I would like to comment on this article.

There have been quite a few recent publications regarding pituitary gland/sellar/parasellar imaging and a few of these are listed here: “Imaging of the Pituitary: Recent Advances” by Chaudhary and Bano,² “Rathke’s Cleft Cysts: Differentiation from Other Cystic Lesions in the Pituitary Fossa by Use of Single-Shot Fast Spin-Echo Diffusion-Weighted Imaging” by Kunii et al,³ “A Pituitary Abscess Showing High Signal Intensity on Diffusion-Weighted Imaging” by Takayasu et al,⁴ “Role of PROPELLER Diffusion Weighted Imaging and Apparent Diffusion Coefficient in the Evaluation of Pituitary Adenomas” by Mahmoud et al,⁵ and “Role of PROPELLER Diffusion Weighted Imaging and Apparent Diffusion Coefficient in the Diagnosis of Sellar and Parasellar Lesions” by Mahmoud et al.⁶ I thought that the authors of the “Evaluation of Diffusivity in the Anterior Lobe of the Pituitary Gland: 3D Turbo Field Echo with Diffusion-Sensitized Driven-Equilibrium Preparation” did a good job at not only sharing their results but also conveying the relative advantages and disadvantages of this technique for this use, at least currently.¹ According to these authors, they were able to image the an-

terior lobe of the pituitary gland with diffusivity and without distortion, make measurements, and compare these values with internal controls.¹ The “scientist in me” appreciates the approach of assessing what “normal range” is before we proceed to measuring pathologic values. This is also in keeping, I think, with the “modern” notions of quantitative imaging and personalized medicine. To the best of my reading, it would appear that the authors were able to acquire volumetric data and with high spatial resolution (please see the article for details)¹; this was especially enticing to me and it is pleasant to think of a future sella/pituitary protocol MR readout with capabilities like these! Some challenges shared by the authors include that the sequence has “limited coverage,” “longer acquisition time,” a single direction, “difficulty” assessing the posterior lobe of the pituitary gland and “absence of a ‘criterion standard’ for pituitary ADC.”¹ I think that the specific values for ADC presented in this article are of limited utility, but as a “proof of concept,” I found it quite appealing. I hope that you will, too.

REFERENCES

1. Hiwatashi A, Yoshiura T, Togao O, et al. **Evaluation of diffusivity in the anterior lobe of the pituitary gland: 3D turbo field echo with diffusion-sensitized driven-equilibrium preparation.** *AJNR Am J Neuroradiol* 2014;35:95–98.
2. Chaudhary V, Bano S. **Imaging of the pituitary: recent advances.** *Indian J Endocrinol Metab* 2011;15(Suppl 3):S216–23
3. Kunii N, Abe T, Kawamo M, et al. **Rathke’s cleft cysts: differentiation from other cystic lesions in the pituitary fossa by use of single-shot fast spin-echo diffusion-weighted imaging.** *Acta Neurochir (Wien)* 2007;149:759–69
4. Takayasu T, Yamasaki F, Tominaga A, et al. **A pituitary abscess showing high signal intensity on diffusion-weighted imaging.** *Neurosurg Rev* 2006;29:246–48
5. Mahmoud OM, Tominaga A, Amatya VJ, et al. **Role of PROPELLER diffusion weighted imaging and apparent diffusion coefficient in the evaluation of pituitary adenomas.** *Eur J Radiol* 2011;80:412–17
6. Mahmoud OM, Tominaga A, Amatya VJ, et al. **Role of PROPELLER diffusion weighted imaging and apparent diffusion coefficient in the diagnosis of sellar and parasellar lesions.** *Eur J Radiol* 2011;80:420–27

M.E. Mullins

Department of Radiology and Imaging Sciences
Emory University
Atlanta, Georgia

<http://dx.doi.org/10.3174/ajnr.A3648>

Brain MR Findings in Patients with Systemic Lupus Erythematosus with and without Antiphospholipid Antibody Syndrome

Y. Kaichi, S. Kakeda, J. Moriya, N. Ohnari, K. Saito, Y. Tanaka, F. Tatsugami, S. Date, K. Awai, and Y. Korogi



ABSTRACT

BACKGROUND AND PURPOSE: Antiphospholipid syndrome may affect the incidence and pathogenesis of cerebrovascular diseases in patients with systemic lupus erythematosus. We compared the spectrum of MR findings in patients with systemic lupus erythematosus with and without antiphospholipid syndrome.

MATERIALS AND METHODS: We identified 256 patients with systemic lupus erythematosus (45 with, 211 without antiphospholipid syndrome) who underwent MR studies; in 145 (57%), we detected abnormalities. These were categorized as large territorial, lacunar, localized cortical, and borderzone infarctions and as microembolisms, basal ganglia lesions, callosal lesions, hemorrhages, and white matter hyperintensity on T2-weighted and/or FLAIR images, and as stenotic arterial lesions on MR angiograms. Logistic regression analysis was performed to compare the MR findings in patients with systemic lupus erythematosus with and without antiphospholipid syndrome, with patient age and antiphospholipid syndrome as the covariates.

RESULTS: Abnormal MR findings were more common in patients with systemic lupus erythematosus with antiphospholipid syndrome (73% versus 53%). Large territorial ($P = .01$), lacunar ($P = .01$), localized cortical ($P < .01$), borderzone infarcts ($P < .01$), basal ganglia lesions ($P = .03$), stenotic arterial lesions ($P = .04$), and the rate of positive findings on MR imaging ($P = .01$) were significantly associated with antiphospholipid syndrome. Irrespective of age, significantly more patients with antiphospholipid syndrome manifested lacunar infarcts in the deep white matter ($P < .01$), localized cortical infarcts in the territory of the MCA ($P < .01$), bilateral borderzone infarcts ($P < .01$), and anterior basal ganglia lesions ($P = .01$).

CONCLUSIONS: Abnormal MR findings were more common in patients with systemic lupus erythematosus with than in those without antiphospholipid syndrome. Large territorial infarctions, lacunar infarctions in the deep white matter, localized cortical infarctions in the MCA territory, bilateral borderzone infarctions, anterior basal ganglia lesions, and stenotic arterial lesions are common MR findings in patients with systemic lupus erythematosus with antiphospholipid syndrome.

ABBREVIATIONS: aPL = antiphospholipid antibodies; APS = antiphospholipid syndrome; GRE = gradient echo; SLE = systemic lupus erythematosus; WMH = white matter hyperintensity

Systemic lupus erythematosus (SLE) is an autoimmune disease that frequently manifests with involvement of the central nervous system.^{1,2} A previous autopsy study of neuropsychiatric SLE revealed various types of brain lesions including global ischemic changes, parenchymal edema, microhemorrhages, glial

hyperplasia, diffuse neuronal/axonal loss, resolved infarction, microthromboemboli, blood vessel remodeling, acute infarction, acute macrohemorrhages, and resolved intracranial hemorrhages.³ A wide spectrum of MR findings in patients with SLE has also been reported.³ SLE is a heterogeneous disease characterized by multisystem autoimmunity, leading to an array of clinical presentations. In addition, there is also a small subset of patients with SLE who show persistently negative antinuclear antibody tests despite having the typical clinical features of SLE. These variabilities can add to the difficulty of timely diagnosis and intervention.⁴ Understanding the wide spectrum of brain pathologic conditions in patients with SLE may help to render an appropriate diagnosis.

Antiphospholipid syndrome (APS) is characterized by antiphospholipid antibodies (aPL) and specific thromboembolic phenomena, including deep venous thrombosis and spontaneous

Received September 12, 2012; accepted after revision April 5, 2013.

From the Department of Radiology (Y. Kaichi, S.K., J.M., N.O., Y. Korogi) and First Department of Internal Medicine (K.S., Y.T.), University of Occupational and Environmental Health, School of Medicine, Kitakyushu, Japan; and Department of Diagnostic Radiology (Y. Kaichi, F.T., S.D., K.A.), Graduate School of Biomedical Sciences, Hiroshima University, Hiroshima, Japan.

Please address correspondence to Shingo Kakeda, MD, PhD, Department of Radiology, University of Occupational and Environmental Health, 1-one Iseigaoka, Yahatanishi-ku, Kitakyushu 807-8555, Japan; e-mail: kaichi@hiroshima-u.ac.jp

Indicates article with supplemental on-line tables.

<http://dx.doi.org/10.3174/ajnr.A3645>

abortions.⁵ However, both events are relatively common in the general population and in subjects with autoimmune diseases. Moreover, in patients with thrombosis or spontaneous abortion in whom APS is strongly suspected, conventional aPL are repeatedly negative.⁶ This condition has been called “seronegative APS.”⁷ Therefore, the correct identification of patients with APS can be a complex task. The diagnosis of APS affects treatment options; an antiplatelet and/or anticoagulation therapy is recommended for neuropsychiatric SLE related to aPL, especially for thrombotic cerebrovascular disease.⁸ Therefore, it is important to investigate MR findings in patients with SLE with APS and those without APS. The association of aPL/APS with neurologic involvement has been established,^{9,10} but there has been limited reporting of differences in MR findings in patients with SLE with APS and those without APS.¹¹ That study concluded that infarc-

tions and infarcts with white matter hyperintensity (WMH) were more common in patients with SLE with APS, but the study population was relatively small and the specific nature of the MR findings was not described in detail. We characterize the spectrum of MR findings in a large series of patients with SLE and compare our findings in patients with SLE with APS and those without APS.

MATERIALS AND METHODS

Patients

This retrospective study was approved by our institutional review board; informed consent was waived. We reviewed the data base of patient charts entered between May 2004 and June 2011 and selected 261 patients diagnosed with SLE on the basis of American Rheumatism Association criteria for the classification of SLE.¹² At our institution, a screening brain MR imaging has been routinely performed for the assessment of patients with SLE.

Exclusion criteria included unsatisfactory images because of artifacts and a history of other neurologic disease. Thus, on the basis of these exclusion criteria, we eliminated 2 patients whose image quality was inadequate and 3 because they had a brain tumor, osmotic myelinolysis, or multiple sclerosis. Consequently, 256 patients with SLE who underwent brain MR study were included. Of these, 211 (82.4%) did not and 45 (17.6%) did have APS diagnosed according to Sapporo criteria.^{10,13}

We reviewed patient demographic data for vascular risk factors (diabetes mellitus, defined as a random glucose level >11.1 mmol/L, a fasting blood glucose level >7.0 mmol/L, HbA1c >6.5%, or current use of antidiabetic drugs), hypertension (blood pressure >140/90 mm Hg, or current treatment with anti-

hypertensive drugs), past and current smoking, dyslipidemia (LDL cholesterol >3.64 mmol/L, HDL cholesterol <0.91 mmol/L, triglyceride >1.7 mmol/L, or receiving treatment), obesity (body mass index >26 kg/m²), duration of SLE (interval between diagnosis and brain MR study), and previous treatments (corticosteroids and immunomodulatory drugs).

MR Imaging

All studies were performed on a 1.5T or 3T MR system (Signa Excite, GE Healthcare, Milwaukee, Wisconsin) by use of a dedicated 8-channel phased-array coil (USA Instruments, Aurora, Ohio). The imaging parameters were 4000/85/1/13.4/1 minute, 50 seconds (repetition time msec/echo time msec/NEX/echo spacing/imaging time), with an echo-train length of 14 at 1.5T, and 4500/85/1/10.9/2 minutes, 10 seconds, with an echo-train length of 16 at 3T for T2-weighted FSE imaging. They were 8000/115/2000/2/8.0/2 minutes, 40 seconds (repetition time msec/echo time msec/

MRI findings in patients with SLE

MRI findings	Patients With SLE, No. (%)		Occlusions or Stenotic Lesions of Arteries, No. (%)	
	No.	(%)	No.	(%)
Infarction/infarction-like lesions	69	(27)	8	(12)
Large territorial infarctions	23	(9)	6	(26)
Lacunar infarctions	23	(9)	2	(9)
Localized cortical infarctions	19	(7)	2	(11)
Borderzone infarctions	11	(4)	2	(18)
Basal ganglia lesions	11	(4)	0	0
Callosal lesions	3	(1)	1	(33)
Acute microemboli	4	(2)	0	0
Other lesions	118	(46)		
Hemorrhages	6	(2)		
WMH	108	(42)		
Stenotic arterial lesions	9	(4)		
Abnormal findings	145	(57)		

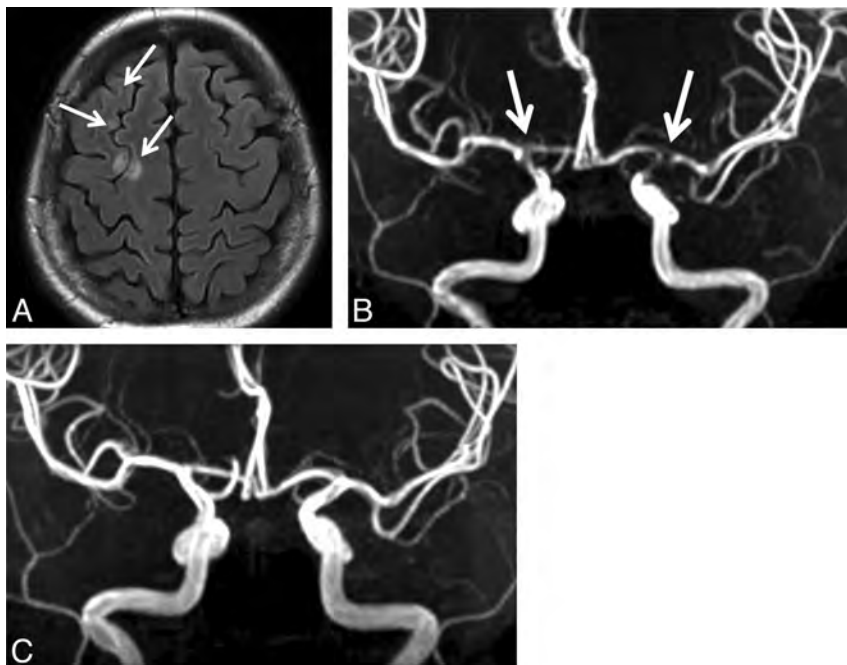


FIG 1. A 34-year-old woman with SLE with APS. A, Axial FLAIR image shows right borderzone infarction (arrows). B, MR imaging study performed 3 days after symptom onset shows evidence of marked narrowing of the bilateral internal carotid artery and the M1 segment of the bilateral MCA (arrows). C, Follow-up MRA study performed 60 days after symptom onset shows recovery of the arterial stenosis.

inversion time/NEX/echo spacing/imaging time), with an echo-train length of 30 at 1.5T, and 12,000/140/2600/2/9.1/3 minutes, 20 seconds, with an echo-train length of 30 at 3T for FLAIR imaging. At both field strengths, T2-weighted and FLAIR images were acquired at a section thickness of 5 mm, an intersection gap of 2.5 mm, an FOV of 22 cm, and a matrix of 256 × 192. In addition, all patients underwent our standard brain MR imaging protocol including T1WI, DWI, and 3D TOF intracranial MRA. The following imaging parameters at 3T were used: 2500/10/90/320 × 224/22 × 22/1 minute, 30 seconds (TR msec/TE msec/flip angle/section thickness/matrix/FOV/imaging time), for T1WI and 6000/minimum/not available/5/128 × 256/22 × 22/30 seconds for DWI. The imaging parameters for 3D TOF MRA were 30 msec/6.3 msec/20°/1 mm/18 cm/256 × 256/4 minutes, 32 seconds (repetition time msec/echo time msec/flip angle/section thickness/FOV/matrix/imaging time), at 1.5T; they were 30 msec/3.3 msec/20°/1 mm/18 cm/384 × 224/4 minutes, 37 seconds, at 3T. In 29 of 256 patients with SLE (11%), gradient echo (GRE) T2WI scans were obtained on 1.5T or 3T systems.

MR Imaging Analysis

Two neuroradiologists (S.K. and Y. Kaichi) reviewed the MR images and categorized their findings as normal (grade 1), as infarction or infarction-like lesions (large territorial, lacunar, localized cortical, or bilateral or unilateral borderzone infarctions; acute multiple or single micro-embolisms; basal ganglia; or callosal lesions; grade 2), and as other lesions (WMH, macro- or microhemorrhages, stenotic arterial lesions on MRA; grade 3). We found various kinds of destructive brain lesions in this study, for some of which we could not identify the specific MR findings suggesting cerebral infarctions according to the previous observations. Therefore, we defined them as infarction-like lesions.

Large territorial infarction¹⁴ was defined as an infarct that involved all or a large part of the territory of the anterior cerebral artery, MCA, or posterior cerebral artery; the cerebellum; or the brain stem in a characteristic pattern of a large vessel occlusion. The readers defined acute multiple or single microemboli as small hyperintense foci <3 mm in the cortex and/or subcortical white matter on DWI. Localized cortical infarction¹⁵ was recorded when there were single or multifocal ischemic lesions in the cortex. Therefore, this category included chronic small cortical infarcts suggestive of microembolism and acute cortical lesions >3 mm.¹⁶

Borderzone infarction was defined according to the templates of Bogousslavsky and Regli¹⁷ and the atlas of Damasio.¹⁸ Lacunar infarction, defined as a CSF-filled cavity with increased peripheral signal on FLAIR <15 mm in diameter,¹⁹ was subclassified into basal ganglia, deep white matter, or brain stem infarction. Lesions larger than lacunar infarcts were recorded as basal ganglia lesions; their location was divided into anterior, middle, and posterior. Callosal lesions were defined as abnormally hyperintense areas in any part of the corpus callosum on DWI, T2WI, or FLAIR scans. WMH was identified as ill-defined hyperintensity ≥5 mm on both T2-weighted FSE and FLAIR images, and WHM was rated according to the scale of Fazekas et al,²⁰ in which grade 1 = punctate foci, grade 2 = incipient confluence of foci, and grade 3 = large confluent areas. In the present study, we made a distinction

between WMH and perivascular space on the basis of the MR findings in a previous report²¹; the perivascular space was visualized as hyperintense regions on T2WI and as hypointense regions on T1WI and formed punctuate or tubular structures of usually <3 mm in diameter, and usually located in conformity with the path of perforating brain vessels, which run perpendicular to the brain surface. Micro- and macrohemorrhages were defined as hemorrhages ≤5 mm and >5 mm in diameter on the basis of T2WI findings, because only 29 of the 256 patients (11%) underwent GRE T2WI.²² Stenotic arterial lesions were recorded when there was either complete occlusion or stenosis of >50% on MRA images. Because of the limited FOV and spatial resolution of MRA images, the assessed intracranial vessels included segments of the internal carotid artery, the middle cerebral artery (M1 [the sphenoidal segment], M2 [the insular segment], M3 [the opercular segment]), and the anterior cerebral artery (A1 [the segment from the origin of the anterior cerebral artery to the anterior communicating artery] and A2 [the infracallosal segment]).

Statistical Analysis

We compared the differences in the baseline characteristics of patients with SLE with and without APS by use of logistic regression analysis. To compare MR findings in patients with SLE with and without APS, logistic regression was also applied to correct for confounding age and APS, resulting in an adjusted odds ratio. Differences of $P < .05$ were considered statistically significant.

RESULTS

Whereas the demographic and clinical characteristics were not significantly different between patients with and without APS, the median disease duration was longer in those with APS ($P = .05$) (On-line Table 1).

Our MR findings on all patients with SLE are summarized in the Table. The most common finding was WMH. Infarcts and infarct-like lesions were seen in 69 of the 256 patients (27%); only 8 of the 69 (12%) harbored stenotic lesions on major intracranial arteries. On MRA images, the relevant artery manifested stenotic lesions in 6 (26%) of 23 patients with large territorial, 2 (9%) of 23 with lacunar, and 2 (18%) of 11 with borderzone infarcts. In 1 patient with borderzone infarction, the initial MRA scan showed marked narrowing of the bilateral internal carotid artery and the M1 segment of the bilateral MCA; follow-up MRA revealed resolution of the arterial stenoses. In this patient, we considered vasculitis or arterial vasospasm a likely diagnosis (Fig 1). No stenotic lesion on the relevant artery was seen in patients with basal ganglia lesions and acute micro-embolism in the cortex and/or subcortical white matter.

On-line Table 2 is a comparison of the MR imaging findings in patients with SLE with and without APS. More patients with than without APS demonstrated abnormal findings (73% versus 53%). The incidence of large territorial, lacunar, localized cortical, and borderzone infarcts; acute microemboli; basal ganglia lesions; callosal lesions; and stenotic arterial lesions was higher in patients with APS than in those without APS.

We performed logistic regression analysis to compare MR findings in patients with SLE with and without APS, with patient age and APS as the covariates. Large territorial, localized cortical

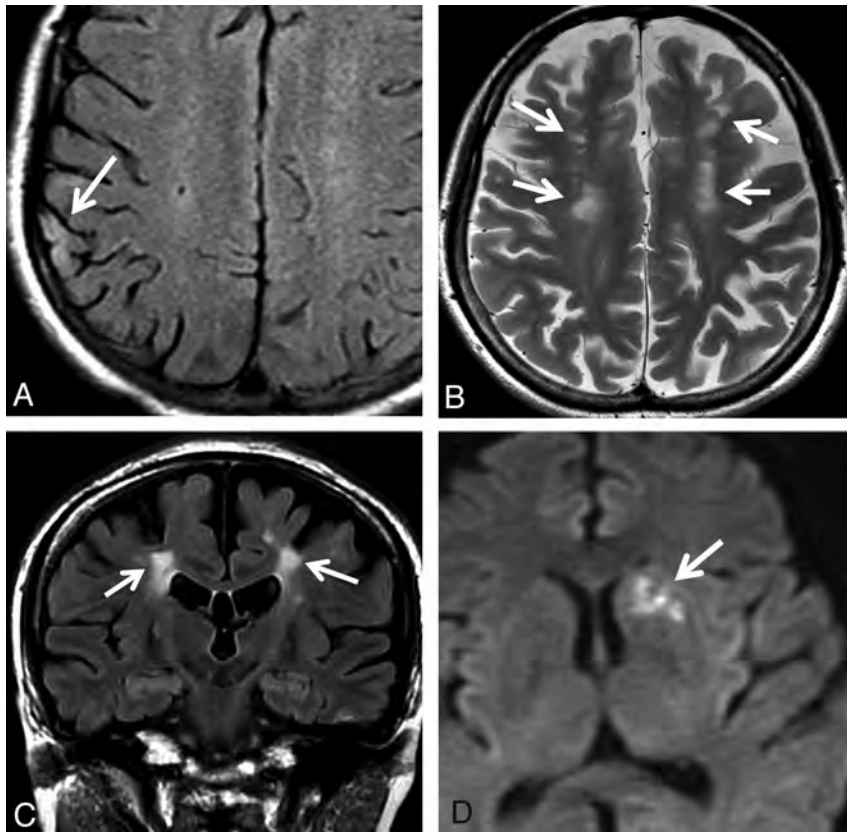


FIG 2. A, Sixteen-year-old boy with SLE with APS. Axial FLAIR image shows localized cortical infarction (arrow). B and C, Thirty-nine-year-old woman with SLE with APS. Axial T2WI (B) and coronal FLAIR image (C) show bilateral borderzone infarction (arrows). MRA revealed no abnormality (image not shown). D, Forty-five-year-old woman with SLE with APS. Axial DWI image shows a lesion in the left anterior basal ganglia (arrow).

(Fig 2A), and borderzone infarctions (Fig 2B, -C); basal ganglia lesions (Fig 2D); lacunar infarcts; stenotic arterial lesions; and the total number of patients with abnormal findings were significantly associated with APS (On-line Table 3). The incidence of large territorial infarctions in the cerebellum was significantly higher in patients with APS than in those without APS ($P = .02$). Localized cortical infarctions in the MCA area were significantly associated with APS ($P < .01$). Bilateral but not unilateral borderzone infarcts were associated with APS ($P < .01$). All basal ganglia lesions were in the anterior zone (7/7). Stenotic arterial lesions were seen in the ICA and MCA. WHM, lacunar infarcts, and the total number of patients with abnormal findings were significantly associated with age. Although acute microembolism in the cortex and/or subcortical white matter was associated with age ($P = .03$), the association was not significant because the number of patients was small. We found that abnormal findings and lacunar infarcts were associated with patient age and APS status.

DISCUSSION

We compared brain MR findings in a large number of patients with SLE on the basis of their APS status. Our logistic regression analysis demonstrated that the incidence of large territorial infarcts, lacunar infarcts in the deep white matter, localized cortical infarcts in the MCA area, bilateral borderzone infarcts, anterior basal ganglia lesions, and stenotic arterial lesions was significantly

higher in patients with SLE with APS than in those without APS, regardless of their age.

Large Territorial Infarcts

Arterial thrombosis rather than arterial sclerosis has been proposed as a major cause of territorial infarction in patients with APS.^{4,23} Our patients with and without APS manifested infarcts/infarct-like lesions in the absence of stenotic lesions in the cerebral arteries. This suggests thromboembolism as the main mechanism leading to lesions associated with cerebrovascular disease in patients with SLE with and without APS, though the presence of APS may further promote their development.

Localized Cortical Infarcts

The small arterial anastomoses between gyri of the cerebral cortex may help to prevent the development of cortical infarction.²⁴ In patients with SLE, thromboembolism or small-vessel thrombosis promoted by the association of APS may result in the occlusion of small cortical arteries and the eventual development of localized infarcts.

Bilateral Borderzone Infarcts

Borderzone infarcts occur at characteristic locations at the junction between the external (cortical) and internal (subcortical) territory. Internal borderzone infarcts are thought to be attributable to hemodynamic compromise,²⁵ whereas external borderzone infarcts have been attributed to embolism not necessarily associated with hypoperfusion.^{26,27} We observed both internal and external borderzone infarcts in patients with SLE without stenotic lesions on the relevant artery. Therefore, besides thromboembolism, different etiologies such as small-vessel injury may play a role in the development of borderzone infarcts. According to Atsumi et al,²⁸ the induction of endothelin-1 by aPL may contribute to an increase in the arterial tone and ultimately lead to vasospasm and the occlusion of small vessels. In 1 of our patients with borderzone infarction who presented with marked narrowing of the bilateral internal carotid arteries and the M1 segment of the bilateral MCA, vasculitis or arterial vasospasm was suspected. This suggests that hemodynamic compromise secondary to vasculitis or arterial vasospasm may represent a possible mechanism resulting in borderzone infarctions.

Anterior Basal Ganglia Lesions

Significantly more patients with SLE with APS than those without APS presented with anterior basal ganglia lesions. None of the patients with such lesions manifested stenotic lesions on the relevant MCA, suggesting that APS induces substantial neuronal injury caused by small-vessel injury. A clot of the M1 segment of the MCA often leads to caudate and/or putaminal

infarction. Therefore, another explanation for basal ganglia lesions might be the infarction caused by the clot of the M1 segment after recanalization. Other factors, for example, demyelination,²⁹ metabolic abnormalities,³⁰ and vasculitis or vasospasm,²⁸ must be considered as etiologic factors in the development of basal ganglia lesions. However, the mechanism(s) responsible for the high incidence of lesions in the anterior part remains to be identified.

Stenotic Arterial Lesions

We found that significantly more patients with SLE with APS than those without APS presented with stenotic arterial lesions, and these lesions were not associated with age. Moreover, in 1 of our patients, follow-up MRA study revealed resolution of the arterial stenosis. This suggests that the main cause of arterial stenosis is not associated with arteriosclerosis but with aPL/APS-related vasculitis or arterial vasospasm.

White Matter Hyperintensity

Compared with healthy individuals, WMH was a more common finding in patients with SLE and those with primary APS.³¹ Although the specific mechanism, SLE per se or APS, resulting in the manifestation of WMH remains unknown, various pathologic conditions, not only small-vessel occlusion but also demyelination, may play a contributory role. The incidence of WMH was higher in our patients with SLE than in asymptomatic volunteers studied by others,²⁹ but there was no significant difference among our patients with SLE with APS and those without APS. Moreover, WMH was significantly associated with age. The WMHs seen in patients with SLE are therefore not necessarily related to thromboembolism or small-vessel injury promoted by the presence of aPL.

Miscellaneous Lesions

The reported incidence of lacunar infarction in patients with aPL is 9%.³² Our observation that this rate was higher in patients with SLE with APS than in those without APS (20% versus 7%) suggests that thromboembolism or small-vessel injury promoted by the presence of aPL may produce lacunar infarcts in patients with SLE with APS. Because lacunar infarcts were significantly associated with patient age and APS, however, they are not a characteristic finding in patients with SLE with APS. Whereas up to 42% of patients with SLE with uremia, thrombocytopenia, and hypertension have cerebral hemorrhages,^{33,34} their incidence in our patients with SLE with APS and those without APS was not different.

The presence of multiple microemboli implies that they arose at the same time, suggesting that their source is a proximal rather than a more distal independent microvascular occlusive event. Because the number of patients with cerebral hemorrhage and acute microemboli in the cortex and/or subcortical white matter was small in our study, we cannot comment on the difference in their incidence rate in patients with SLE with APS and those without APS.

Our retrospective study has some limitations. First, we evaluated patients with different phases of the disease as a single group, and we did not differentiate between acute and chronic infarctions. Moreover, we could not take neurologic symptoms into consideration because in most patients it was not possible to evaluate the association between their symptoms and MR findings.

Second, because many patients received therapy with antiplatelet, antihypertensive, and antilipemic drugs before undergoing MR imaging, we cannot rule out the possibility that these treatments affected our findings. Nonetheless, we posit that drug treatments did not play a major role because the clinical characteristics were not significantly different between patients with SLE with APS and those without APS. Third, because our study included neither healthy age-matched control subjects nor patients with primary APS, we did not assess the difference in the incidence of cerebral lesions in patients with SLE and control subjects. Fourth, we could not evaluate hemorrhagic lesions exactly because few of our patients underwent GRE T2WI. Last, we did not determine the incidence of large territorial infarcts, lacunar infarcts in the deep white matter, localized cortical infarcts in the territory of the MCA, bilateral borderzone infarcts, anterior basal ganglia lesions, and stenotic arterial lesions in patients with primary APS.

CONCLUSIONS

Our study of a large series of patients with SLE shows that APS is a significant risk factor for cerebral lesions. Our characterization of the spectrum of MR findings suggests that large territorial infarcts, lacunar infarcts in the deep white matter, localized cortical infarcts in the territory of the MCA, bilateral borderzone infarcts, anterior basal ganglia lesions, and stenotic arterial lesions are particularly common MR findings in patients with SLE with APS.

Disclosures: Kazuo Awai—UNRELATED: Consultancy: Daiichi-Sankyo Ltd; Employment: Toshiba Medical Systems,* Bayer Pharmaceutical,* Daiichi-Sankyo Ltd,* Eizai Ltd* (*money paid to institution).

REFERENCES

1. Johnson RT, Richardson EP. **The neurological manifestations of systemic lupus erythematosus.** *Medicine* 1968;47:337–69
2. O'Connor JF, Musher DM. **Central nervous system involvement in systemic lupus erythematosus: a study of 150 cases.** *Arch Neurol* 1966;14:157–64
3. Sibbitt WL Jr, Brooks WM, Kornfeld M, et al. **Magnetic resonance imaging and brain histopathology in neuropsychiatric systemic lupus erythematosus.** *Semin Arthritis Rheum* 2010;40:32–52
4. Kim JH, Choi CG, Choi SJ, et al. **Primary antiphospholipid antibody syndrome: neuroradiologic findings in 11 patients.** *Korean J Radiol* 2000;1:5–10
5. Golstein M, Meyer O, Bourgeois P, et al. **Neurological manifestations of systemic lupus erythematosus: role of antiphospholipid antibodies.** *Clin Exp Rheumatol* 1993;11:373–79
6. Bertolaccini ML, Gomez S, Pareja JF, et al. **Antiphospholipid antibody tests: spreading the net.** *Ann Rheum Dis* 2005;64:1639–43
7. Rodríguez García JL, Khamashta MA. **Clinical advances of interest in the diagnosis and treatment of patients with antiphospholipid syndrome.** *Rev Clin Esp* 2013;213:108–13
8. Bertias GK, Ioannidis JP, Aringer M, et al. **Eular recommendations for the management of systemic lupus erythematosus with neuropsychiatric manifestations: report of a task force of the Eular Standing Committee for Clinical Affairs.** *Ann Rheum Dis* 2010;69:2074–82
9. Harris EN, Gharavi AE, Asherson RA, et al. **Cerebral infarction in systemic lupus: association with anticardiolipin antibodies.** *Clin Exp Rheumatol* 1984;2:47–51
10. Harris EN, Gharavi AE, Mackworth, et al. **Lupoid sclerosis: a possible pathogenetic role for antiphospholipid antibodies.** *Ann Rheum Dis* 1985;44:281–83
11. Valdes-Ferrer SI, Vega F, Cantu-Brito C, et al. **Cerebral changes in**

- SLE with or without antiphospholipid syndrome: a case-control MRI study.** *J Neuroimaging* 2008;18:62–65
12. Hochberg MC. **Updating the American College of Rheumatology revised criteria for the classification of systemic lupus erythematosus.** *Arthritis Rheum* 1997;40:1725
 13. Wilson WA, Gharavi AE, Koike T, et al. **International consensus statement on preliminary classification criteria for definite antiphospholipid syndrome: report of an international workshop.** *Arthritis Rheum* 1999;42:1309–11
 14. Lodder J, Hupperts R, Boreas A, et al. **The size of territorial brain infarction on CT relates to the degree of internal carotid artery obstruction.** *J Neurol* 1996;243:345–49
 15. Bang OY, Ovbiagele B, Liebeskind DS, et al. **Clinical determinants of infarct pattern subtypes in large vessel atherosclerotic stroke.** *J Neurol* 2009;256:591–99
 16. Kimura K, Minematsu K, Koga M, et al. **Microembolic signals and diffusion-weighted MR imaging abnormalities in acute ischemic stroke.** *AJNR Am J Neuroradiol* 2001;22:1037–42
 17. Bogousslavsky J, Regli F. **Unilateral watershed cerebral infarcts.** *Neurology* 1986;36:373–77
 18. Damasio H. **A computed tomographic guide to the identification of cerebral vascular territories.** *Arch Neurol* 1983;40:138–42
 19. Fisher CM. **Lacunar strokes and infarcts: a review.** *Neurology* 1982;32:871–76
 20. Fazekas F, Kleinert R, Offenbacher H, et al. **The morphologic correlate of incidental punctate white matter hyperintensities on MR images.** *AJNR Am J Neuroradiol* 1991;12:915–21
 21. Wuerfel J, Haertle M, Waiczies H, et al. **Perivascular spaces: MRI marker of inflammatory activity in the brain?** *Brain* 2008;131:2332–40
 22. Chao CP, Kotsenas AL, Broderick DF. **Cerebral amyloid angiopathy: CT and MR imaging findings.** *Radiographics* 2006;26:1517–31
 23. Aron AL, Gharavi AE, Shoenfeld Y. **Mechanisms of action of antiphospholipid antibodies in the antiphospholipid syndrome.** *Int Arch Allergy Immunol* 1995;106:8–12
 24. Duvernoy HM, Delon S, Vannson JL. **Cortical blood vessels of the human brain.** *Brain Res Bull* 1981;7:519–79
 25. Derdeyn CP, Khosla A, Videen TO, et al. **Severe hemodynamic impairment and border zone–region infarction.** *Radiology* 2001;220:195–201
 26. Torvik A. **The pathogenesis of watershed infarcts in the brain.** *Stroke* 1984;15:221–23
 27. Chaves CJ, Silver B, Schlaug G, et al. **Diffusion- and perfusion-weighted MRI patterns in borderzone infarcts.** *Stroke* 2000;31:1090–96
 28. Atsumi T, Khamashta MA, Haworth RS, et al. **Arterial disease and thrombosis in the antiphospholipid syndrome: a pathogenic role for endothelin 1.** *Arthritis Rheum* 1998;41:800–07
 29. Karussis D, Leker RR, Ashkenazi A, et al. **A subgroup of multiple sclerosis patients with anticardiolipin antibodies and unusual clinical manifestations: do they represent a new nosological entity?** *Ann Neurol* 1998;44:629–34
 30. Sabet A, Sibbitt WL Jr, Stidley CA, et al. **Neurometabolite markers of cerebral injury in the antiphospholipid antibody syndrome of systemic lupus erythematosus.** *Stroke* 1998;29:2254–60
 31. Hachulla E, Michon-Pasturel U, Leys D, et al. **Cerebral magnetic resonance imaging in patients with or without antiphospholipid antibodies.** *Lupus* 1998;7:124–31
 32. Provenzale JM, Barboriak DP, Allen NB, et al. **Patients with antiphospholipid antibodies: CT and MR findings of the brain.** *AJR* 1996;167:1573–78
 33. Asherson RA, Mercey D, Phillips G, et al. **Recurrent stroke and multi-infarct dementia in systemic lupus erythematosus: association with antiphospholipid antibodies.** *Ann Rheum Dis* 1987;46:605–11
 34. Provenzale JM, Heinz ER, Ortel TL, et al. **Antiphospholipid antibodies in patients without systemic lupus erythematosus: neuroradiologic findings.** *Radiology* 1994;192:531–37

Prevalence of Radiologically Isolated Syndrome and White Matter Signal Abnormalities in Healthy Relatives of Patients with Multiple Sclerosis

T. Gabelic, D.P. Ramasamy, B. Weinstock-Guttman, J. Hagemeyer, C. Kennedy, R. Melia, D. Hojnacki, M. Ramanathan, and R. Zivadinov



ABSTRACT

BACKGROUND AND PURPOSE: The exact prevalence of WM signal abnormalities in healthy relatives of MS patients and their impact on disease development has not been fully elucidated. The purpose of this study was to compare WM signal abnormality characteristics and the prevalence of radiologically isolated syndrome in healthy control subjects selected randomly from the population with the healthy relatives of patients with MS.

MATERIALS AND METHODS: Healthy control subjects ($n = 150$) underwent physical and 3T MR imaging examinations. Healthy control subjects were classified as non-familial healthy control subjects ($n = 82$) if they had no family history of MS or as healthy relatives of patients with MS ($n = 68$) if they had ≥ 1 relative affected with MS. The presence of radiologically isolated syndrome was evaluated according to the Okuda criteria; dissemination in space on MR imaging and fulfillment of radiologically isolated syndrome criteria were also evaluated according to Swanton criteria.

RESULTS: There was a significantly higher total volume of WM signal abnormality in the healthy relatives of patients with MS compared with the non-familial healthy control subjects ($P = .024$ for signal abnormality ≥ 3 mm in size and $P = .025$ for all sizes). Periventricular localization and the number of lesions in all groups ($P = .034$ and $P = .043$) were significantly higher in the healthy relatives of patients with MS; 8.8% of the healthy relatives of patients with MS and 4.9% of non-familial healthy control subjects showed ≥ 9 WM signal abnormalities; 2.9% of subjects in the healthy relatives of patients with MS group and 2.4% of non-familial healthy control subjects fulfilled radiologically isolated syndrome according to the Okuda criteria, whereas 10.3% and 3.7% of subjects fulfilled radiologically isolated syndrome according to the Swanton criteria. In the healthy relatives of patients with MS, smoking was associated with the presence of WM signal abnormalities, whereas obesity was related to the presence of ≥ 9 WM signal abnormalities and to fulfillment of radiologically isolated syndrome according to the Swanton criteria.

CONCLUSIONS: The frequency of WM signal abnormalities and radiologically isolated syndrome is higher in the healthy relatives of patients with multiple sclerosis patients compared with non-familial healthy control subjects.

ABBREVIATIONS: DAWM = dirty-appearing white matter; DIS = dissemination in space; HC = healthy control subject; non-FHC = non-familial healthy control subject; PD = proton attenuation; RIS = radiologically isolated syndrome; SAV = signal abnormality volume

Multiple sclerosis is an inflammatory autoimmune demyelinating disorder of the CNS.¹ Although MS is predominantly a sporadic disease, a genetic predisposition to developing

familial MS is well accepted.² Although the exact definition of familial MS is not yet established, familial patients with MS are considered to be those with ≥ 1 first-degree relative affected with MS,² although some authors use a definition that is based on the presence of 2 first-degree relatives.³ In a recent meta-analysis, the risk of development of MS was 18.2% for monozygotic twins of patients with MS, 4.6% for dizygotic twins, and 2.7% for siblings.⁴ The risk of development of MS in a first-degree relative of the affected patient is 30- to 50-fold higher than in the general population,⁵ whereas second- and third-degree relatives also showed an increased risk for development of MS.⁶

Whether familial or non-familial MS are different forms of the disease is not fully elucidated yet.⁷ Differences in disease progression in familial MS were observed in several studies demonstrating earlier age of onset and increased probability of a progressive

Received March 5, 2013; accepted after revision April 19.

From the Buffalo Neuroimaging Analysis Center (T.G., D.P.R., J.H., C.K., R.M., R.Z.), The Jacobs Neurological Institute (B.W.-G., D.H., R.Z.), Department of Neurology, and Department of Pharmaceutical Sciences (M.R.), State University of New York, Buffalo, New York; and Department of Neurology (T.G.), Referral Centre for Demyelinating Disease of the Central Nervous System, University Hospital Centre Zagreb, Zagreb, Croatia.

Please address correspondence to Robert Zivadinov, MD, PhD, FAAN, Department of Neurology, School of Medicine and Biomedical Sciences, The Jacobs Neurological Institute, 100 High St, Buffalo, NY 14203; e-mail: rzivadinov@bnac.net

Indicates open access to non-subscribers at www.ajnr.org

<http://dx.doi.org/10.3174/ajnr.A3653>

clinical course.⁸ However, other studies did not show clinical differences among familial and non-familial healthy control subject (non-fMS) forms.^{2,9} Nevertheless, MR imaging studies by use of nonconventional techniques showed MR imaging differences between familial and non-familial MS.¹⁰⁻¹²

In 2009, Okuda et al¹³ introduced the term “radiologically isolated syndrome” (RIS) to describe subjects who show incidental brain MR imaging WM lesions suggestive of MS and who fulfill Barkhof criteria for dissemination in space (DIS)¹⁴ but have no signs or symptoms of the disease. Overall, the prevalence of RIS is, according to postmortem studies, in a range of 0.06–0.7%, with an age range of 16–70.^{13,15} However, the McDonald 2010 criteria for DIS¹⁶ substituted Barkhof criteria¹⁴ with the Swanton criteria for DIS.¹⁷ Swanton DIS criteria require the presence of ≥ 1 WM lesion in ≥ 2 of the brain regions (juxtacortical, periventricular, or infratentorial) or in the spinal cord.¹⁷ The value of the Swanton criteria for DIS¹⁷ was not evaluated with respect to the diagnosis of RIS.

Previous MR imaging studies showed that asymptomatic relatives of patients with MS display significant magnetization transfer ratio changes in CNS WM signal abnormality, indicative of MS pathology,^{3,18} though some other studies showed no differences in the magnetization transfer ratio of WM in the siblings of patients with MS.¹⁹ Studies with the use of conventional brain MR imaging showed WM signal abnormalities consistent with MS in the healthy relatives of patients with MS,²⁰⁻²² with 4% of non-familial healthy control subjects (non-fHC) and 10% of healthy control subjects with familial MS (HC) fulfilling Barkhof criteria¹⁴ for DIS.²⁰ However, these studies had several limitations including the number of enrolled subjects, strength of the MR imaging field, and use of more conservative criteria for RIS.¹³ As a result, the exact prevalence of RIS and the WM signal abnormalities in asymptomatic MS relatives is not yet fully defined.

The aim of this pilot study was to compare WM signal abnormality characteristics in a large cohort of non-fHCs and healthy relatives of patients with MS by use of 3T MR imaging. We also determined the prevalence of RIS in HC groups, according to both the Barkhof¹⁴ and Swanton¹⁷ MR imaging criteria for DIS and investigated association between the presence of vascular risk factors and RIS.

MATERIALS AND METHODS

Subjects

This was a pilot study in which HCs without known CNS pathology or neurologic complaints were recruited from the following volunteer sources: hospital personnel, respondents to a local newspaper advertisement, and relatives of the patients with MS who are followed in our center. The inclusion criteria were: fulfilling the health screen questionnaire requirements containing information regarding medical history (illnesses, surgeries, vascular and environmental risk factors, medications, family history of MS, etc), fulfilling the health screen requirements on physical examination, having ≥ 1 relative with MS followed in our center (for the healthy relatives of patients with MS), and being able to undergo MR imaging scanning. Exclusion criteria included preexisting medical conditions known to be associated with CNS pathology (eg, neurodegenerative disorder, cerebrovascular disease, cognitive impairment, history of psychiatric disorders, seizures, and trauma, etc). All subjects underwent physical, neurologic, and MR imaging examinations and were assessed with a structured ques-

tionnaire administered in person by a trained interviewer unaware of the subjects' healthy control status.²³ Race/ethnicity was determined according to the US Census Bureau.

Subjects with unknown relatives affected by MS were classified as non-fHC and familial HCs were classified according to the number of family members affected by clinically definitive MS¹⁶ by use of previously proposed definitions.^{2,3} In particular, sporadic HCs had to have at least 1 affected relative (first-, second-, or third-degree), whereas familial HCs had to have ≥ 1 affected first-degree relative plus ≥ 1 affected first-, second-, or third-degree relative. Family members were classified into first-, second-, and third-degree relatives as described previously.¹⁰ There were 47 subjects in sporadic and 21 subjects in familial HC subgroups. Both subgroups were merged into 1 group composed of healthy relatives of patients with MS.

Subjects were evaluated for diagnostic criteria of RIS, proposed by Okuda et al (Table 1 and Fig 1).¹³ If the subjects fulfilled DIS on MR imaging according to Barkhof criteria¹⁴ and satisfied Okuda diagnostic criteria for RIS,¹³ they were classified as having RIS-Okuda. We also applied modified Okuda criteria¹³ in which the DIS on MR imaging (section A2 of the Okuda criteria) was evaluated according to DIS Swanton criteria (Table 1 and Fig 1).¹⁷ If the subjects fulfilled these modified RIS criteria, they were classified as having RIS-Swanton. As required in the Okuda criteria, only lesions ≥ 3 mm were considered in RIS analysis.¹³

The study was approved by our local Health Sciences Institutional Review Board, and written informed consent was obtained from all subjects.

MR Imaging Acquisition

All subjects were examined on a 3T Signa Excite HD 12.0 Twin Speed 8-channel scanner (GE Healthcare, Milwaukee, Wisconsin). MR imaging sequences included multi-planar dual fast spin-echo proton attenuation (PD) and T2WI as well as FLAIR. Pulse sequence characteristics for 3T MR imaging were as follows: all scans were acquired with a 256×256 matrix and a 25.6-cm FOV for an in-plane resolution of 1×1 mm² with a phase FOV of 75% and 1 average. Sequence-specific parameters were as follows: for the PD/T2: 3-mm-thick sections with no gap, TE1/TE2/TR = 12/95/3000 ms, echo-train length = 14, and for the FLAIR scans, 3-mm-thick sections with no gap, TE/TI/TR = 120/2100/8500 ms.

MR Imaging Analysis

The MR imaging analyses were blinded to the subject demographic and clinical characteristics.

To facilitate combined analysis, each subject's relevant T2/PD images were co-registered to the FLAIR by use of a rigid body (6 *df*) registration.²⁴ The FLAIR image was used to outline WM signal abnormalities, whereas the co-registered T2/PD images were used to confirm the presence of WM signal abnormalities. Additionally, the T2/PD images were used to check for infratentorial WM signal abnormalities because FLAIR imaging is known to be insensitive in this area. The WM signal abnormality number and volume (WM-SAV) were outlined by means of a semi-automated edge detection contouring/thresholding technique as described previously.²⁵ All WM signal abnormalities were divided into in-

Table 1: Proposed diagnostic criteria for radiologically isolated syndrome

Okuda RIS criteria ¹³
1) MRI criteria
a) Ovoid, well-circumscribed, and homogeneous foci with or without involvement of corpus callosum.
b) T2 hyperintensities measuring >3 mm in size fulfilling at least 3 of 4 Barkhof criteria ¹⁴ for DIS, which are: 1) ≥ 9 lesions or ≥ 1 gadolinium-enhancing lesion, 2) ≥ 3 periventricular lesions, 3) ≥ 1 juxtacortical lesion, and 4) ≥ 1 infratentorial lesion.
c) CNS white matter anomalies are not consistent with a vascular pattern.
2) No historical accounts of remitting clinical symptoms consistent with neurologic dysfunction.
3) The MRI anomalies do not account for clinically apparent impairments in social, occupational, or generalized areas of functioning.
4) The MRI anomalies are not due to the direct physiologic effects of substances (eg, drug abuse, toxic exposure) or a medical condition.
5) Exclusion of individuals with MRI phenotypes suggestive of leukoaraiosis or extensive white matter pathology lacking involvement of the corpus callosum.
6) The MRI anomalies are not better accounted for by another disease process.
Swanton RIS criteria ¹⁷
1) MRI criteria
a) DIS defined as presence of ≥ 1 T2 lesion in ≥ 2 of the following brain regions (periventricular, juxtacortical, and infratentorial) or in the spinal cord.
2) No historical accounts of remitting clinical symptoms consistent with neurologic dysfunction.
3) The MRI anomalies do not account for clinically apparent impairments in social, occupational, or generalized areas of functioning.
4) The MRI anomalies are not due to the direct physiologic effects of substances (eg, drug abuse, toxic exposure) or a medical condition.
5) Exclusion of individuals with MRI phenotypes suggestive of leukoaraiosis or extensive white matter pathology lacking involvement of the corpus callosum.
6) The MRI anomalies are not better accounted for by another disease process.

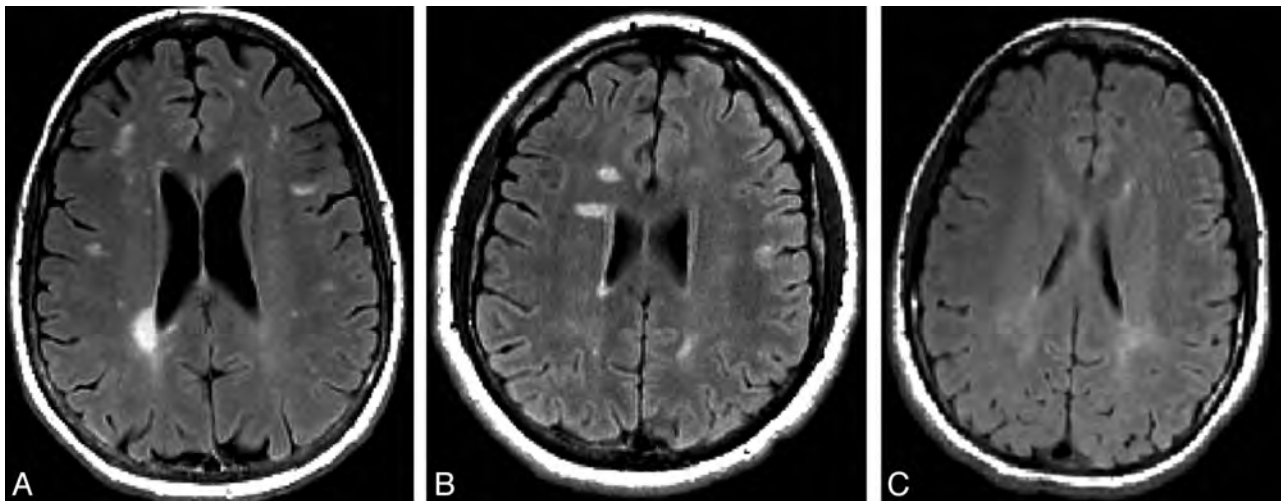


FIG 1. Representative images of the healthy relatives of patients with MS fulfilling Okuda criteria¹³ for radiologically isolated syndrome (RIS) (A) fulfilling modified Okuda criteria¹³ for RIS in which the dissemination in space on MR imaging was evaluated by use of Swanton criteria (RIS-Swanton),¹⁷ (B) or presenting with dirty-appearing white matter (C).

dividual ROIs ≥ 3 mm in size (equivalent to ≥ 14.1 mm³) and ROIs of all sizes (including those <3 mm in size). The regional localization of WM signal abnormalities was determined on the basis of their presence in the juxtacortical, periventricular, infratentorial, and deep WM regions.

In addition, we outlined areas of dirty-appearing white matter (DAWM). The DAWM was defined as a uniform, nonfocal area of signal increase on the FLAIR/T2/PD-weighted sequence at 3T, with a subtly increased signal intensity compared with the contralateral signal intensity of normal-appearing WM but less than that of WM signal abnormalities, as previously proposed.²⁶ The DAWM measurement was not based on a size, as shown in Fig 1. The DAWM showed a border of areas that were not sharply defined compared with focal WM lesions and was tapered off toward the normal-appearing WM.

Statistical Analysis

Statistical analyses were performed with the Statistical Package for the Social Sciences, version 16.0 (IBM, Armonk, New York). Demographic, clinical, and MR imaging differences were tested between non-fHCs and the healthy relatives of patients with MS as well as between sporadic and familial HC subgroups. There were no significant differences between sporadic and familial HC subgroups in any of the exploited variables. Therefore, to decrease the number of multiple comparisons, all analyses were performed between non-fHCs and the healthy relatives of patients with MS. For statistics between the groups, the *t* test, χ^2 test, and Mann-Whitney rank sum *U* test were used as appropriate.

To explore whether there was a relationship between the presence of WM signal abnormalities, ≥ 9 WM signal abnormalities,

Table 2: Demographic and clinical characteristics of non-familial healthy control subjects and the healthy relatives of patients with multiple sclerosis

	Non-Familial HCs (n = 82)	Healthy Relatives of Patients with MS (n = 68)	P Value
Age, y, mean (SD) median	39.8 (14.3) 43	39.5 (16.6) 43	.917
Sex, female n (%)	57 (69.5)	45 (66.2)	.663
Race/ethnicity, n (%)			.180
White	64 (78.1)	62 (91.2)	
Black	12 (14.6)	4 (5.9)	
Other	6 (7.3)	2 (2.9)	
Vascular risk factors, n (%)			
Heart disease	8 (9.8)	13 (19.1)	.085
Smoking	22 (27.5)	19 (27.9)	.979
Hypertension	17 (20.7)	15 (22.1)	.442
Obesity n (%) ^a			.582
BMI <18.5	2 (2.4)	2 (2.9)	
BMI 18.5–24.9	34 (41.5)	25 (36.8)	
BMI 25–29.9	26 (31.7)	17 (25.0)	
BMI >30	13 (15.8)	18 (26.5)	
Autoimmune diseases, n (%)			
Systemic lupus erythematosus	0	0	NA
Rheumatoid disorder	1 (1.2)	2 (2.9)	.474
Psoriasis	0	1 (1.5)	.279
Diabetes mellitus type 1	1 (1.2)	0	.352
Migraine, n (%)	10 (12.2)	13 (19.1)	.282

Note:—BMI indicates body mass index.

BMI <18.5 represents underweight, BMI 18.5–24.9 represents normal weight, BMI 25–29.9 represents overweight, and BMI >30 represents obesity. The differences between the groups were compared by means of the Student *t* test or the χ^2 test.

^aData missing for 13 subjects.

Table 3: MRI white matter signal abnormality (≥ 3 mm in size) characteristics of non-familial healthy control subjects and the healthy relatives of patients with multiple sclerosis

	Non-Familial HCs (n = 82)	Healthy Relatives of Patients With MS (n = 68)	P Value
Subjects with WM SAs, n (%)	21 (25.6)	20 (29.4)	.603
Subjects with WM JC SAs, n (%)	4 (4.9)	7 (10.3)	.205
Subjects with WM PVL SAs, n (%)	7 (8.5)	13 (19.1)	.058
Subjects with WM IT SAs, n (%)	0 (0)	1 (1.5)	.271
Subjects with DWM SAs, n (%)	20 (24.4)	17 (25.0)	.931
Subjects with ≥ 9 WM SAs, n (%)	4 (4.9)	6 (8.8)	.335
WM-SAN, mean (SD), median	1.5 (4.7) 0	2.1 (5.1) 0	.527
WM JC SAN, mean (SD), median	0.06 (0.3) 0	0.19 (0.7) 0	.198
WM PVL SAN, mean (SD), median	0.32 (1.8) 0	0.40 (1.2) 0	.061
WM IT SAN mean (SD) median	0.0 (0) 0	0.0 (0.1) 0	.272
WM DWM SAN, mean (SD), median	1.1 (3.0) 0	1.5 (3.9) 0	.838
WM-SAV, mean (SD), median	166.1 (892.0)	230.4 (736.8)	.480
DAWM-SAV, ^a mean (SD), median	675.3 (554.7)	866.2 (669.3)	.054
WM-SAV + DAWM-SAV, mean (SD), median	842.3 (1079.7)	1096.5 (1026.6)	.024

Note:—SAs indicates signal abnormalities; SAN, signal abnormality number; JC, juxtacortical, PVL, periventricular; IT, infratentorial; DWM, deep white matter; SAV, signal abnormality volume.

Differences between the groups were compared by means of the χ^2 test or Mann-Whitney *U* test.

The SAV is expressed in millimeters cubed (mm³).

^aDAWM calculation was not related to the size of the hyperintensities.

the fulfillment of RIS-Okuda and RIS-Swanton criteria, and the presence of vascular risk factors (hypertension, heart disease, smoking, obesity, and diabetes mellitus type 1) as well as migraine, we used a multivariate logistic regression model in which age and sex were used as covariates and the vascular risk factors were used as independent variables. The dependent variables were the presence of WM signal abnormalities, ≥ 9 WM signal abnormalities, and the fulfillment of RIS-Okuda as well as RIS-Swanton criteria. The analyses were separately performed for non-fHCs

and the healthy relatives of patients with MS. All *P* values were calculated by means of a 2-tailed test. Given the pilot nature of the study, a *P* value of <.05 was considered statistically significant, and a *P* value of <.1 was considered a trend.

RESULTS

Subject Characteristics

A total of 150 subjects divided into the 2 groups according to their familial characteristics (non-fHCs = 82, healthy relatives of patients with MS = 68) were enrolled in this study.

The demographic and clinical characteristics of the subjects are listed in Table 2. There were no age, sex, or race differences between the study groups. There were also no significant differences between the groups in respect to the presence of vascular risk factors, autoimmune diseases, or migraine.

WM Signal Abnormality

Characteristics of the Groups

MR imaging characteristics of WM signal abnormalities and their regional localization are presented in Tables 3 and 4. WM signal abnormalities were divided into 2 groups: those with size ≥ 3 mm (Table 3) and those with all sizes (Table 4). There was significantly higher WM-SAV + DAWM-SAV in the healthy relatives of patients with MS as compared with non-fHCs (1.10 mL versus 0.84 mL, *P* = .024 for those ≥ 3 mm in size, and 1.13 mL versus 0.87 mL, *P* = .025 for all sizes). A trend was observed in the healthy relatives of patients with MS group compared with non-fHCs for DAWM-SAV (866.2 mm³ versus 675.3 mm³, *P* = .054 for signal abnormality >3 mm and all lesion size groups).

In all lesion size groups, more healthy relatives of patients with MS presented with WM signal abnormalities located in the periventricular WM (20.6% versus 8.5%, *P* = .034) and their number was higher (0.57 versus 0.41,

P = 0.43) compared with non-fHCs. In the ≥ 3 mm lesion group, a trend was observed in the healthy relatives of patients with MS for the periventricular signal abnormality localization and number compared with non-fHC (19.1% versus 8.5%, *P* = .058 and 0.40 versus 0.32, *P* = .061, respectively).

In total, 29.4% of the healthy relatives of patients with MS showed WM signal abnormalities versus 25.6% in non-fHCs for signal abnormality ≥ 3 mm in size (Table 3). The corresponding percentages

of WM signal abnormalities of all sizes were 41.2% in the healthy relatives of patients with MS group and 35.4% in the non-fHC group.

Classification of Subjects According to Criteria for DIS and RIS

Six (8.8%) subjects in the healthy relatives of patients with MS group and 4 (4.9%) in non-fHCs showed ≥ 9 WM signal abnormalities (≥ 3 mm size, Table 3). Of these, all subjects had lesions in 2 location categories in the healthy relatives of patients with MS group, whereas there were 3 of 4 in non-fHCs. The percentages of ≥ 9 WM signal abnormality of all sizes were 11.8% and 6.1% in the healthy relatives of patients with MS group and the non-fHC group, respectively. These differences were not significant.

Two (2.9%) subjects in the healthy relatives of patients with MS group and 2 (2.4%) non-fHCs fulfilled RIS-Okuda criteria (Table 5). Ten subjects fulfilled the RIS-Swanton: 7 (10.3%) in the

healthy relatives of patients with MS and 3 (3.7%) non-fHCs. These differences were not significant. Localization characteristics of WM signal abnormalities are listed in Table 5.

Relationship Between Vascular Risk Factors and RIS and WM Signal Abnormality Findings

In multivariate regression analysis in which the presence of WM signal abnormalities was used as a dependent variable, smoking ($B = 0.44, P = .024$) was the only variable associated with the healthy relatives of patients with MS.

In multivariate regression analysis in which ≥ 9 WM signal abnormalities was used as a dependent variable, obesity (body mass index > 30) was the only variable associated with the healthy relatives of patients with MS ($B = 0.56, P = .003$).

In multivariate regression analysis in which RIS-Swanton was used as a dependent variable, obesity ($B = 0.29, P = .019$) was the

only variable associated with the healthy relatives of patients with MS. No association was found in non-fHCs for all 3 dependent variables.

No association between vascular risk factor variables and RIS-Okuda criteria was found in any HC group.

DISCUSSION

Subjects with WM signal abnormalities suggestive for MS but without history of MS symptoms or neurologic deficit may be at an increased risk for development of the disease. This pilot study included a large cohort of 150 HCs with or without familial history of MS that were collected prospectively by use of 3T MR imaging. We assessed the prevalence of WM signal abnormalities and of RIS in the study groups, also applying the Swanton MR

Table 4: MRI white matter signal abnormality (all sizes) characteristics of non-familial healthy control subjects and the healthy relatives of patients with multiple sclerosis

	Non-Familial HCs (n = 82)	Healthy Relatives of Patients with MS (n = 68)	P Value
Subjects with WM SAs, n (%)	29 (35.4)	28 (41.2)	.465
Subjects with WM JC SAs, n (%)	4 (4.9)	7 (10.3)	.205
Subjects with WM PVL SAs, n (%)	7 (8.5)	14 (20.6)	.034
Subjects with WM IT SAs, n (%)	1 (1.2)	1 (1.5)	.894
Subjects with DWM SAs, n (%)	28 (34.1)	26 (38.2)	.603
Subjects with ≥ 9 WM SAs, n (%)	5 (6.1)	8 (11.8)	.219
WM-SAN, mean (SD) median	2.5 (7.5) 0	3.8 (10) 0	.386
WM JC SAN, mean (SD) median	0.07 (0.3) 0	0.19 (0.7) 0	.207
WM PVL SAN, mean (SD) median	0.41 (2.1) 0	0.57 (1.9) 0	.043
WM IT SAN, mean (SD) median	0.01 (0.1) 0	0.01 (0.1) 0	.894
WM DWM SAN, mean (SD) median	1.9 (5.3) 0	3.1 (8.5) 0	.468
WM-SAV, mean (SD) median	198.2 (1085.2)	259.7 (784.4)	.338
DAWM-SAV, ^a mean (SD) median	675.3 (554.7)	866.2 (669.3)	.054
WM-SAV + DAWM-SAV, mean (SD) median	873.5 (1233.5)	1125.9 (1076.8)	.025

Note:—SAs indicates signal abnormalities; SAN, signal abnormality number; JC, juxtacortical; PVL, periventricular; IT, infratentorial; DWM, deep white matter; SAV, signal abnormality volume.

Differences between the groups were compared by means of the χ^2 test or Mann-Whitney *U* test.

The SAV is expressed in millimeters cubed (mm³).

^a DAWM calculation was not related to the size of the hyperintensities.

Table 5: Non-familial healthy control subjects and the healthy relatives of patients with multiple sclerosis fulfilling Okuda criteria for RIS or fulfilling modified Okuda criteria for RIS in which the dissemination in space on MRI was evaluated by use of Swanton criteria (RIS-Swanton)

	Non-Familial HCs (n = 82)	Healthy Relatives of Patients with MS (n = 68)	P Value
RIS-Okuda criteria ¹³			
Non-RIS	80	66	.849
RIS	2	2	
Subject 1	>9 WM SA: 5 JC, 3 PVL, 13 DWM	>9 WM SA: 5 JC, 3 PVL, 13 DWM	
Subject 2	>9 WM SA: 1 JC, 8 PVL, 11 DWM	>9 WM SA: 1 JC, 8 PVL, 11 DWM	
Total	82	68	
Modified Okuda criteria (RIS-Swanton ^{13,17})			
Non-RIS	79	61	.105
RIS	3	7	
Subject 1	>9 WM SA: 2 JC, 5 PVL, 9 DWM	>9 WM SA: 5 JC, 3 PVL, 13 DWM	
Subject 2	>9 WM SA: 1 JC, 15 PVL, 18 DWM	>9 WM SA: 1 JC, 8 PVL, 11 DWM	
Subject 3	>9 WM SA: 2 JC, 1 PVL, 7 DWM	>9 WM SA: 2 JC, 1 PVL, 7 DWM	
Subject 4	>9 WM SA: 1 JC, 1 PVL, 11 DWM	>9 WM SA: 1 JC, 1 PVL, 24 DWM	
Subject 5		>9 WM SA: 1 JC, 1 PVL, 7 DWM	
Subject 6		>9 WM SA: 1 JC, 1 PVL, 8 DWM	
Subject 7		2 JC, 2 PVL 3 DWM	
Total	82	68	

Note:—SA indicates signal abnormality; JC, juxtacortical; PVL, periventricular; DWM, deep white matter.

Differences between the groups were compared by means of the χ^2 test. The regional localization data for subjects fulfilling RIS criteria are presented on individual subject level.

imaging criteria for DIS.¹⁷ There was a significantly higher total volume of WM signal abnormalities (including WM-SAV + DAWM-SAV) in subjects with familial MS history. In these subjects, significantly more WM signal abnormalities (only for all WM signal abnormality sizes) were located in periventricular WM compared with non-fHCs. No significant differences were observed between the groups for presence, number, or localization of juxtacortical, infratentorial, and deep WM signal abnormalities. Although more subjects in the group with familial history of MS presented with RIS according to Okuda et al¹³ or modified Okuda criteria (in which DIS was evaluated according to the Swanton MR imaging criteria), the differences were not significant. Interestingly, in the healthy relatives of MS patients in multivariate regression models, smoking was associated with the presence of WM signal abnormalities, while obesity was related to the presence of ≥ 9 WM signal abnormalities and fulfillment of RIS-Swanton criteria. This is in line with recently reported data in pediatric patients with MS.²⁷

Increasing diagnostic application of MR imaging, especially at higher strength field, results in an increased number of abnormal incidental findings with potential clinical significance.^{28,29} Several postmortem and MR imaging studies aimed to establish the prevalence of demyelinating lesions, possibly indicative of RIS.²⁸⁻³¹ Disadvantages of postmortem studies are related to the fact that they are usually performed at late stages of the disease (autopsies) or in selected atypical early cases (biopsies), which analyze the brain only in 1 anatomic part. In comparison with MR imaging, pathologic assessment does not allow observation of the evolution of pathologic changes over time. A recent MR imaging meta-analysis included 15,559 healthy adults and found only 9 cases of definite demyelination (0.06%).²⁸ This meta-analysis included studies performed on MR imaging magnets with field strengths 1T or 1.5T. The most common reason for performing MR imaging among patients later identified as having RIS is headache,¹⁵ which is also described as a presenting MS symptom in some cases.³² Compared with these previous studies, the present one evaluated asymptomatic HCs with no signs or symptoms of MS. Despite this, the prevalence of RIS on the basis of RIS-Okuda or RIS-Swanton criteria was higher in subjects with (2.9% and 10.3%, respectively) compared with those without (2.4% and 3.7%, respectively) family MS history.

Although the incidence of MS among relatives is increased in affected families,¹ there are only a few MR imaging studies that evaluated the WM signal abnormalities of asymptomatic healthy relatives of patients with MS.²⁰⁻²² All were performed on 1T or 1.5T MR imaging. In the current study, we used 3T MR imaging, which can substantially increase the detection of WM and DAWM abnormalities.^{33,34} A previous 3T versus 1.5T comparison study in patients with MS and HCs showed regional predilection of WM signal abnormality detection in periventricular, pericallosal, cortical/juxtacortical, and infratentorial regions on 3T MR imaging.³³ The correlation of MR imaging findings with clinical status is also stronger at 3T compared with 1.5T MR imaging.³⁵ The use of 3T may be one of the reasons why we found a significantly higher total volume of WM signal abnormalities (including WM-SAV + DAWM-SAV) in patients with familial MS history as compared with those without history. Regional predilection and number of WM signal abnormalities was detected only for the

periventricular area in the healthy relatives of patients with MS. No regional predilection of WM signal abnormalities has been detected between the study groups for both the presence and number of other anatomic sites. Previous studies in asymptomatic healthy relatives of patients with MS did not report WM signal abnormality number or size.²⁰⁻²² Our study showed no significant differences between the HC groups in the presence or number of WM signal abnormalities ≥ 3 mm in size or when all WM signal abnormalities, independent of the size, were added to the total count.

WM signal abnormalities on MR imaging are more frequent in older individuals and in subjects presenting with vascular risk factors^{36,37}; therefore their presence in asymptomatic individuals should be interpreted with caution. No differences between the HC with or without familial MS history were found for demographic characteristics, vascular risk factors, migraine, or the presence of autoimmune diseases considered in this study. However, in regression analysis, we found that only the relatives of subjects with MS who showed WM signal abnormalities or had ≥ 9 WM signal abnormalities and fulfilled RIS-Swanton criteria had elevated smoking and obesity vascular risk factors. It could be hypothesized that these risk factors may play a different role in formation of WM signal abnormalities in individuals genetically susceptible for MS, as are relatives of patients with MS. A recent study suggested that primary lipid abnormality in DAWM may be involved in demyelination and axonal degeneration of patients with MS,³⁸ and obesity was recently suggested as linked with increased morbidity for MS.²⁷

Persons with RIS are at an increased risk of development of MS.^{39,40} During a follow-up period of 2–5 years, approximately one-third of patients had clinical symptoms characteristic of MS.^{39,40} Increased risk for clinical conversion was observed in younger subjects, with a higher number of lesions, presence of infratentorial lesions, pathologic evoked potentials, positive oligoclonal bands, and spinal cord lesions.⁴⁰ The limitation of our study was that it was a cross-sectional pilot study that did not include spinal cord MR imaging, and no information is currently available about longitudinal follow-up of the enrolled subjects.

This is the first study in which the Swanton MR imaging criteria for DIS¹⁷ were integrated in the Okuda criteria for RIS.¹³ The prevalence of RIS-Swanton in the healthy relatives of patients with MS was increased compared with those without, whereas no differences were found when RIS-Okuda criteria¹³ were applied. Future longitudinal studies should determine whether asymptomatic HCs fulfilling RIS-Swanton criteria have an increased risk of development of MS as compared with RIS-Okuda criteria.¹³ De Stefano et al²⁰ reported that 7.1% of the relatives of patients with MS fulfilled Barkhof criteria¹⁴ on MR imaging for DIS. Although 8.8% of the healthy relatives of patients with MS showed ≥ 9 WM signal abnormalities, only 2.9% presented with RIS-Okuda. However, 2.4% of HCs without MS family history also fulfilled RIS-Okuda criteria in the present study, compared with none fulfilling Barkhof criteria for DIS¹⁴ in the De Stefano et al²⁰ study. The reasons for these differences are not clear and should be further explored.

To establish the long-term value of RIS Okuda and Swanton criteria on clinical and imaging follow-up of our study cohort, a 5-year follow-up is planned. Because the treatment of RIS is controversial, possible differences in the conversion rate of clinical and

imaging characteristics between the RIS Okuda/Swanton criteria may influence future treatment decisions at the stage of RIS.

CONCLUSIONS

The healthy relatives of patients with MS show more frequent WM signal abnormalities as compared with those without and are more likely to present with RIS when Swanton criteria for DIS are applied.

ICMJE Disclosures: Robert Zivadinov—UNRELATED: Consultancy: Biogen Idec, EMD Serono, Teva Pharmaceuticals, Genzyme-Sanofi, Novartis; Grants/Grants Pending: Biogen Idec,* EMD Serono,* Teva Pharmaceuticals,* Novartis,* Genzyme-Sanofi*; Payment for Lectures (including service on speaker's bureaus): Biogen Idec, EMD Serono, Teva Pharmaceuticals, Genzyme-Sanofi, Novartis. Bianca Weinstock-Guttman—UNRELATED: Consultancy: Biogen Idec, Teva Neurosciences, EMD Serono, Novartis, Genzyme, Acorda; Grants/Grants Pending: Payment for Lectures (including service on speakers bureaus): Teva Neuroscience, Biogen Idec, EMD Serono, Novartis, Pfizer, Genzyme, and Acorda. David Hojnacki—UNRELATED: Consultancy: Teva, Biogen, EMD, Pfizer; Payment for Lectures (including service on speaker's bureaus): Teva, Biogen, EMD, Pfizer. Murali Ramanathan—UNRELATED: Grants/Grants Pending: National Multiple Sclerosis Society,* Department of Defense*; Other: Self-published textbook on Pharmacy Calculations (*money paid to institution).

REFERENCES

1. Compston A, Coles A. **Multiple sclerosis.** *Lancet* 2002;359:1221–31
2. Weinschenker BG, Bulman D, Carriere W, et al. **A comparison of sporadic and familial multiple sclerosis.** *Neurology* 1990;40:1354–58
3. Siger-Zajdel M, Filippi M, Selmaj K. **MTR discloses subtle changes in the normal-appearing tissue from relatives of patients with MS.** *Neurology* 2002;58:317–20
4. O'Gorman C, Lin R, Stankovich J, et al. **Modelling genetic susceptibility to multiple sclerosis with family data.** *Neuroepidemiology* 2013;40:1–12
5. Sadovnick AD, Yee IM, Ebers GC, et al. **Effect of age at onset and parental disease status on sibling risks for MS.** *Neurology* 1998;50:719–23
6. Prokopenko I, Montomoli C, Ferrai R, et al. **Risk for relatives of patients with multiple sclerosis in central Sardinia, Italy.** *Neuroepidemiology* 2003;22:290–96
7. Ramagopalan SV, Dobson R, Meier UC, et al. **Multiple sclerosis: risk factors, prodromes, and potential causal pathways.** *Lancet Neurol* 2010;9:727–39
8. Hensiek AE, Seaman SR, Barcellos LF, et al. **Familial effects on the clinical course of multiple sclerosis.** *Neurology* 2007;68:376–83
9. Ebers GC, Koopman WJ, Hader W, et al. **The natural history of multiple sclerosis: a geographically based study: 8: familial multiple sclerosis.** *Brain* 2000;123(Part 3):641–49
10. Tipirneni A, Weinstock-Guttman B, Ramanathan M, et al. **MRI characteristics of familial and sporadic multiple sclerosis patients.** *Mult Scler* Dec 11, 2012 [Epub ahead of print]
11. Siger-Zajdel M, Selmaj K. **Magnetisation transfer ratio analysis of normal appearing white matter in patients with familial and sporadic multiple sclerosis.** *J Neurol Neurosurg Psychiatry* 2001;71:752–56
12. Siger-Zajdel M, Selmaj KW. **Proton magnetic resonance spectroscopy of normal appearing white matter in familial and sporadic multiple sclerosis.** *J Neurol* 2005;252:830–32
13. Okuda DT, Mowry EM, Beheshtian A, et al. **Incidental MRI anomalies suggestive of multiple sclerosis: the radiologically isolated syndrome.** *Neurology* 2009;72:800–05
14. Barkhof F, Filippi M, Miller DH, et al. **Comparison of MRI criteria at first presentation to predict conversion to clinically definite multiple sclerosis.** *Brain* 1997;120(Part 11):2059–69
15. Granberg T, Martola J, Kristoffersen-Wiberg M, et al. **Radiologically isolated syndrome: incidental magnetic resonance imaging findings suggestive of multiple sclerosis, a systematic review.** *Mult Scler* 2013;19:271–80
16. Polman CH, Reingold SC, Banwell B, et al. **Diagnostic criteria for multiple sclerosis: 2010 revisions to the McDonald criteria.** *Ann Neurol* 2011;69:292–302
17. Swanton JK, Fernando K, Dalton CM, et al. **Modification of MRI criteria for multiple sclerosis in patients with clinically isolated syndromes.** *J Neurol Neurosurg Psychiatry* 2006;77:830–33
18. De Stefano N, Stromillo ML, Rossi F, et al. **Improving the characterization of radiologically isolated syndrome suggestive of multiple sclerosis.** *PLoS One* 2011;6:e19452
19. Filippi M, Campi A, Martino G, et al. **A magnetization transfer study of white matter in siblings of multiple sclerosis patients.** *J Neurol Sci* 1997;147:151–53
20. De Stefano N, Cocco E, Lai M, et al. **Imaging brain damage in first-degree relatives of sporadic and familial multiple sclerosis.** *Ann Neurol* 2006;59:634–39
21. Tienari PJ, Salonen O, Wikstrom J, et al. **Familial multiple sclerosis: MRI findings in clinically affected and unaffected siblings.** *J Neurol Neurosurg Psychiatry* 1992;55:883–86
22. Lynch SG, Rose JW, Smoker W, et al. **MRI in familial multiple sclerosis.** *Neurology* 1990;40:900–03
23. Dolic K, Weinstock-Guttman B, Marr K, et al. **Risk factors for chronic cerebrospinal venous insufficiency (CCSVI) in a large cohort of volunteers.** *PLoS One* 2011;6:e28062
24. Jenkinson M, Bannister P, Brady M, et al. **Improved optimization for the robust and accurate linear registration and motion correction of brain images.** *Neuroimage* 2002;17:825–41
25. Zivadinov R, Rudick RA, De Masi R, et al. **Effects of IV methylprednisolone on brain atrophy in relapsing-remitting MS.** *Neurology* 2001;57:1239–47
26. Seewann A, Vrenken H, van der Valk P, et al. **Diffusely abnormal white matter in chronic multiple sclerosis: imaging and histopathologic analysis.** *Arch Neurol* 2009;66:601–09
27. Langer-Gould A, Brara S, Beaver B, et al. **Childhood obesity and risk of pediatric multiple sclerosis and clinically isolated syndrome.** *Neurology* 2013;80:548–52
28. Morris Z, Whiteley WN, Longstreth WT Jr, et al. **Incidental findings on brain magnetic resonance imaging: systematic review and meta-analysis.** *BMJ* 2009;339:b3016
29. Weber F, Knopf H. **Incidental findings in magnetic resonance imaging of the brains of healthy young men.** *J Neurol Sci* 2006;240:81–84
30. Engell T. **A clinical patho-anatomical study of clinically silent multiple sclerosis.** *Acta Neurol Scand* 1989;79:428–30
31. Wasay M, Rizvi F, Azeemuddin M, et al. **Incidental MRI lesions suggestive of multiple sclerosis in asymptomatic patients in Karachi, Pakistan.** *J Neurol Neurosurg Psychiatry* 2011;82:83–85
32. D'Amico D, La Mantia L, Rigamonti A, et al. **Prevalence of primary headaches in people with multiple sclerosis.** *Cephalalgia* 2004;24:980–84
33. Di Perri C, Dwyer MG, Wack DS, et al. **Signal abnormalities on 1.5 and 3 Tesla brain MRI in multiple sclerosis patients and healthy controls: a morphological and spatial quantitative comparison study.** *Neuroimage* 2009;47:1352–62
34. Sicotte NL, Voskuhl RR, Bouvier S, et al. **Comparison of multiple sclerosis lesions at 1.5 and 3.0 Tesla.** *Invest Radiol* 2003;38:423–27
35. Stankiewicz JM, Glanz BI, Healy BC, et al. **Brain MRI lesion load at 1.5T and 3T versus clinical status in multiple sclerosis.** *J Neuroimaging* 2011;21:e50–56
36. Enzinger C, Smith S, Fazekas F, et al. **Lesion probability maps of white matter hyperintensities in elderly individuals: results of the Austrian stroke prevention study.** *J Neurol* 2006;253:1064–70
37. Gouw AA, Seewann A, van der Flier WM, et al. **Heterogeneity of small vessel disease: a systematic review of MRI and histopathology correlations.** *J Neurol Neurosurg Psychiatry* 2011;82:126–35
38. Laule C, Pavlova V, Leung E, et al. **Diffusely abnormal white matter in multiple sclerosis: further histologic studies provide evidence for a primary lipid abnormality with neurodegeneration.** *J Neuropathol Exp Neurol* 2013;72:42–52
39. Lebrun C, Bensa C, Debouverie M, et al. **Unexpected multiple sclerosis: follow-up of 30 patients with magnetic resonance imaging and clinical conversion profile.** *J Neurol Neurosurg Psychiatry* 2008;79:195–98
40. Okuda DT, Mowry EM, Cree BA, et al. **Asymptomatic spinal cord lesions predict disease progression in radiologically isolated syndrome.** *Neurology* 2011;76:686–92

Right Insular Atrophy in Neurocardiogenic Syncope: A Volumetric MRI Study

J.B. Kim, S.-i. Suh, W.-K. Seo, S.-B. Koh, and J.H. Kim



ABSTRACT

BACKGROUND AND PURPOSE: Alterations in the central autonomic network are hypothesized to play a role in the pathophysiologic mechanism underlying neurocardiogenic syncope; however, few data are available regarding the structural changes of the brain in this condition. We used voxel-based morphometry and regional volumetry to identify possible neuroanatomic correlates.

MATERIALS AND METHODS: We prospectively studied 32 patients with neurocardiogenic syncope with a positive response to the head-up tilt test and 32 controls who had no history of syncope. We used voxel-based morphometry to compare GM volumes between patients and controls. In addition, regional volumes of structures known to be included in the central autonomic network were measured and compared between the groups. Correlation analyses were also performed between clinical variables and anatomic data.

RESULTS: Voxel-based morphometry showed a significant GM volume reduction in the right insular cortex in patients with neurocardiogenic syncope compared with controls (corrected $P = .033$). Regional volumetry showed a significant reduction of right insular volumes in patients compared with controls ($P = .002$, MANCOVA). Smaller right insular volumes in patients with neurocardiogenic syncope were related to larger drops in systolic ($P = .020$) and diastolic ($P = .003$) blood pressures during the head-up tilt test.

CONCLUSIONS: We observed a novel finding of right insular atrophy in patients with neurocardiogenic syncope with a positive response to the head-up tilt test, implicating the role of right insular dysfunction in the pathophysiologic mechanism underlying neurocardiogenic syncope. Our findings further support the hypothesis that right insular dysfunction may cause a decrease in sympathetic activity and a reciprocal increase in parasympathetic activity, leading to syncope.

ABBREVIATIONS: BP = blood pressure; HR = heart rate; HUT = head-up tilt test; NCS = neurocardiogenic syncope; VBM = voxel-based morphometry

Neurocardiogenic syncope (NCS) (simple fainting or vasovagal syncope) is the most frequent cause of syncope.^{1,2} It refers to a condition in which autonomic cardiovascular reflexes become inappropriate in response to triggers, leading to transient cerebral hypoperfusion and loss of consciousness with spontaneous recovery.³⁻⁵ Although the pathophysiologic mechanism of NCS remains incompletely understood, paradoxical compensatory reflex has been suggested as the most probable mechanism.^{3,6}

Reduction of cardiac ventricular volume activates baroreceptor-mediated sympathetic outflow, which causes vigorous contraction of an empty cardiac ventricle. In turn, activation of mechanoreceptors in the ventricular wall might trigger an inhibitory response through increasing vagal tone, resulting in paradoxical bradycardia and hypotension.^{3,6} This widely accepted “ventricular theory” basically includes increased parasympathetic activity caused by alteration of autonomic controls in the CNS.⁷ Therefore, the understanding of CNS structures involved in the autonomic control system might be crucial for elucidating fundamental mechanisms of NCS.

To our knowledge, there is 1 voxel-based morphometry (VBM) study that investigated changes in brain structures in patients with NCS.⁸ VBM is an objective and fully validated method, which can detect regionally specific differences in GM structures on a voxelwise comparison between groups.⁹ In the present study, we applied VBM and regional volumetry to identify the structural GM changes associated with NCS. In addition, we investigated possible relationships between the structural changes and clinical variables such as disease duration, frequency of syncope attacks, and blood pressure (BP) and heart rate (HR) changes during head-up tilt test (HUT).

Received March 3, 2013; accepted after revision March 29.

From the Departments of Neurology (J.B.K., W.-K.S., S.-B.K., J.H.K.) and Radiology (S.-i.S.) Korea University Guro Hospital, Korea University College of Medicine, Seoul, Korea.

This work was supported in part by the National Research Foundation of Korea Grant funded by the Korean Government (Grant No. 20100004827, 20110005418) and a Korea University Grant (to J.H. Kim). We certify that there is no conflict of interest.

Please address correspondence to Ji Hyun Kim, MD, PhD, Department of Neurology, Korea University Guro Hospital, Korea University College of Medicine, 152-703, Guro-dong Ro 148, Guro-gu, Seoul, Republic of Korea; email: jhkim.merrf@gmail.com

Indicates open access to non-subscribers at www.ajnr.org

<http://dx.doi.org/10.3174/ajnr.A3611>

MATERIALS AND METHODS

Subjects

Consecutive patients with NCS were prospectively recruited from the outpatient clinic at the Neurology Department, Korea University Guro Hospital, from January 2010 to April 2012. Inclusion criteria were as follows: 1) unequivocal symptoms of syncope (defined as transient loss of consciousness and postural tone with spontaneous recovery) and presyncope (defined as a state of lightheadedness, muscular weakness, and feeling faint without complete loss of consciousness); 2) orthostatic stress as the only trigger of syncope and a positive response to HUT (as described below); 3) no history of syncope relevant to situational syncope or carotid sinus hypersensitivity; 4) absence of any abnormal findings on electroencephalography; 5) no history of epileptic seizure; 6) no evidence of developmental and neurologic abnormalities; 7) neither abnormal nor unusual findings on conventional MR imaging; 8) no evidence of cardiogenic syncope based on electrocardiography and echocardiography; 9) no history of diabetes, parkinsonism, and peripheral neuropathy; and 10) no history of significant head injury, alcohol or psychotropic drug abuse, or neurologic and psychiatric disorders. Demographic and clinical data such as age of onset, disease duration, and the number of syncope and presyncope attacks were obtained through interviews with the patients and their family members and reviews of medical records.

For group comparison, 32 right-handed healthy volunteers matched for age and sex were recruited to serve as control subjects. All control subjects underwent neurologic examination and a detailed interview to ensure that they did not have the following: 1) a history of syncope and presyncope; 2) a history of headache disorders, significant head injury, neurologic, psychiatric, or systemic disorders; and 3) a history of alcohol or psychotropic drug abuse. The local ethics committee approved the study protocol, and all participants gave written informed consent before study inclusion.

Head-Up Tilt Test

None of the patients were on any medications at the time of the HUT examination. Orthostatic BP recording was performed with a sphygmomanometer cuff over the brachial artery and a monitor console displaying systolic and diastolic BP. Simultaneous HR recording was performed as well. After a 20-minute rest in the supine position and measurement of baseline BP and HR, each subject was positioned at an angle of 70° from the supine position for as long as 45 minutes or until syncope occurred on a standard electrically driven tilt table with a footboard. Serial measurement of BP and HR was performed every 2 minutes during HUT. Pharmacologic provocation was not performed.¹⁰ The response to HUT was defined as positive when the development of symptoms recognized by the patients was similar to those of spontaneous syncope in association with hypotension, bradycardia, or both.^{4,11,12} As soon as syncope occurred, the patient was rapidly returned to the supine position. Changes in BP and HR were measured from the baseline to the onset of the syncope attack.

MR Imaging Acquisition

MR images were acquired on a Trio 3T scanner (Siemens, Erlangen, Germany) with a 12-channel phased array head coil. For volumetric analysis, a high-resolution 3D MPRAGE sequence was acquired with

the following parameters: TR = 1780 ms, TE = 2.34 ms, matrix = 256 × 256, FOV = 256 × 256 mm, voxel dimension = 1 mm³. For identification of structural abnormalities, the following conventional MR images were acquired: axial T2-weighted and FLAIR images (4-mm thickness), oblique coronal T2-weighted and FLAIR images perpendicular to the long axis of the hippocampus (3-mm thickness), and gadolinium-enhanced axial T1-weighted images (5-mm thickness). The MR images of all participants were reviewed by a board-certified neuroradiologist (S.-i.S.) for any structural abnormalities, and findings were reported as normal.

Voxel-Based Morphometry

Data were processed and analyzed by using SPM8 (Wellcome Department of Imaging Neuroscience, London, UK), where we applied VBM implemented in the VBM8 toolbox (<http://dbm.neuro.uni-jena.de/vbm.html>) with default parameters. Images were bias-corrected, tissue-classified, and registered by using linear (12-parameter affine) and nonlinear transformations, within a unified segmentation model.¹³ Subsequently, analyses were performed on the volumes of the GM segments, which were multiplied by nonlinear components derived from the normalization matrix to compensate for possible volume changes during the nonlinear spatial normalization procedure. These modulated GM images were then smoothed with an 8-mm full width at half maximum isotropic Gaussian kernel. The analyses of modulated GM images can detect regional differences in GM volume.

Regionally specific differences in GM volume between patients with NCS and control subjects were assessed by using ANCOVA with total intracranial volume, age, and sex as nuisance variables. An absolute GM threshold of 0.2 (of a maximum value of 1) was used to avoid possible edge effects around the border between GM and WM. Two contrasts were defined to examine both increases and reductions in GM volume between the groups. Statistical significance was set at a height threshold of $P < .001$ and an extent threshold of cluster-level $P < .05$, corrected for multiple comparisons by using family-wise error.

Regional Volumetry

Cortical reconstruction and volumetric segmentation were performed by using FreeSurfer software (Version 5.1.0, <http://surfer.nmr.mgh.harvard.edu>). The technical details of the procedures are described elsewhere.¹⁴⁻¹⁷ Briefly, image preprocessing procedures included removal of nonbrain tissue,¹⁷ automated Talairach transformation, segmentation of the subcortical WM and deep GM volumetric structures,¹⁵ intensity normalization, tessellation of the GM/WM boundary, automated topology correction,¹⁸ and surface deformation to detect GM/WM and GM/CSF boundaries. Subsequent to cortical reconstruction, the cortex was subdivided into units on the basis of gyral and sulcal structures.¹⁹ This parcellation method was shown to be valid and reliable, with high intraclass correlation coefficients between the manual and automated procedures for volume measurement of 34 cortical regions of interest.¹⁹ A volume at each vertex was computed as the average area of the triangles around the vertex multiplied by the thickness at the vertex. The volume of a parcellated cortex was then computed as the sum of the volumes of the vertices in each parcellation.

Demographic data, clinical characteristics, and regional volumetry of patients with NCS and controls^a

	Patients with NCS (n = 32)	Controls (n = 32)	P Value
Clinical features			
Age (yr)	24.1 ± 6.9	24.8 ± 5.2	.655
Male sex (No.) (%)	11 (34.4)	12 (37.5)	.794
Age of onset (yr)	20.8 ± 7.1		
Disease duration (yr)	4.3 ± 4.7		
No. of total syncope and presyncope attacks	38.4 ± 74.4		
Head-up tilt test findings			
Baseline systolic BP (mm Hg)	109.5 ± 12.2		
Baseline diastolic BP (mm Hg)	62.0 ± 9.6		
Baseline mean HR (beats/min)	67.7 ± 10.0		
Change in systolic BP (mm Hg)	-40.5 ± 15.3		
Change in diastolic BP (mm Hg)	-18.3 ± 10.1		
Change in HR (beats/min)	-33.5 ± 15.8		
Volume of structure (mm³)			
R rostral anterior cingulate	2288 ± 416.3	2461 ± 425.2	.137
R caudal anterior cingulate	2386 ± 555.6	2488 ± 639.3	.498
R insula	7323 ± 689.1	8011 ± 932.5	.002
R amygdala	1755 ± 232.2	1829 ± 184.9	.339
L rostral anterior cingulate	2791 ± 484.6	3141 ± 589.7	.014
L caudal anterior cingulate	1819 ± 494.8	2142 ± 711.5	.063
L insula	7234 ± 649.5	7657 ± 701.0	.018
L amygdala	1770 ± 216.2	1816 ± 229.1	.963

Note:—R indicates right; L, left.

^aThe values are presented as means. An independent t test and χ^2 test were used to compare between-group differences in age and sex, respectively. MANCOVA adjusting for age, sex, and estimated total intracranial volume was performed to compare regional volumes of each structure between the groups.

The automated procedures for volumetric measurements of the subcortical GM structures were described in detail previously.¹⁵ Briefly, this procedure automatically provided segments and labels for up to 40 unique structures and assigned a neuro-anatomic label to each voxel in an MR imaging volume on the basis of probabilistic information estimated automatically from a manually labeled training set. A Bayesian segmentation procedure was then performed, and the maximum a posteriori estimate of the labeling was computed. The segmentation uses 3 pieces of information to disambiguate labels: 1) the prior probability of a given tissue class occurring at a specific atlas location, 2) the likelihood of the image intensity given that tissue class, and 3) the probability of the local spatial configuration of labels given the tissue class. This technique has previously been shown to be comparable in accuracy with manual labeling.¹⁵ All segmentations were visually inspected for accuracy before inclusion in the analysis.

Among the automatically segmented regions, we focused on 3 cortical regions (rostral anterior cingulate, caudal anterior cingulate, and insula) and 1 subcortical region (amygdala) in each hemisphere, which are known to be parts of the central autonomic network.^{20–22} Volumes of the 8 regions were automatically measured and compared between patients and controls by using MANCOVA, adjusting for age, sex, and estimated total intracranial volume. Post hoc univariate tests with a Bonferroni correction were performed to follow the significant main effects yielded by the MANCOVA. Statistical significance was set at $P < .00625$ (.05/8). Correlation analyses were performed between the normalized volumes of 8 structures (each regional GM volume corrected for estimated total intracranial volume) and clinical parameters such as disease duration, total frequency of syncope and

presyncope, and BP and HR changes during HUT (Spearman correlation analysis, $P < .05$). Statistical analyses were performed by using the Statistical Package for Social Sciences (Version 19.0; IBM, Armonk, New York).

RESULTS

Clinical Characteristics

Thirty-two right-handed patients and 32 controls were enrolled in this study. Clinical characteristics and the results of HUT are summarized in the Table. There were no differences in age and sex between patients and controls. The mean age of onset was 20.8 ± 7.1 years (range, 11–39 years), the mean duration of NCS was 4.3 ± 4.7 years (range, 1–22 years), and the mean number of total syncope and presyncope attacks (mean number of attacks per year \times disease duration in years) was 38.4 ± 74.4 (range, 2–300).

All patients showed positive responses to HUT. Mean baseline systolic BP was 109.5 ± 12.2 mm Hg (range, 87–148 mm Hg), mean baseline diastolic BP was

62.0 ± 9.6 mm Hg (range, 47–81 mm Hg), and mean baseline HR was 67.7 ± 10.0 beats/min (range, 52–86 beats/min). During HUT, mean change of systolic BP was -40.5 ± 15.3 mm Hg (range, -16 to -81 mm Hg), mean change of diastolic BP was -18.3 ± 10.1 mm Hg (range, 0 to -36 mm Hg), and mean change of HR was -33.5 ± 15.8 beats/min (range, -5 to -65 beats/min). According to the Vasovagal Syncope International Study (VASIS) classification,²³ 31 of 32 patients had a type 1 mixed response and 1 patient had a type 3 vasodepressor response.

Voxel-Based Morphometry and Regional Volumetry

VBM showed a significant GM volume reduction in the right insular cortex in patients with NCS compared with control subjects (family-wise-error-corrected $P = .033$; cluster size = 1178 voxels [3976 mm³]; peak z score = 4.06; Montreal Neurological Institute coordinates of local maxima = 42, 3, -6; resolution element count = 1.5) (Fig 1). No region of a significant GM volume increase was found in patients compared with controls at the same threshold (family-wise-error-corrected $P < .05$).

Regional volumes of 8 GM structures are presented in the Table. Volumes of the right insular cortex were significantly reduced in patients with NCS compared with controls (7323 ± 689.1 versus 8011 ± 932.5 mm³, $P = .002$) (Fig 2). Volumes of the left rostral anterior cingulate cortex ($P = .014$) and left insular cortex ($P = .018$) were also reduced in patients compared with controls; however, the statistical significance of these 2 structures did not survive multiple comparisons by using a Bonferroni correction ($P < .00625$).

Smaller right insular volumes in patients with NCS were related to larger drops in systolic ($r = -.410$, $P = .020$) and diastolic ($r = -.507$, $P = .003$) BP during HUT (Fig 3). There were no

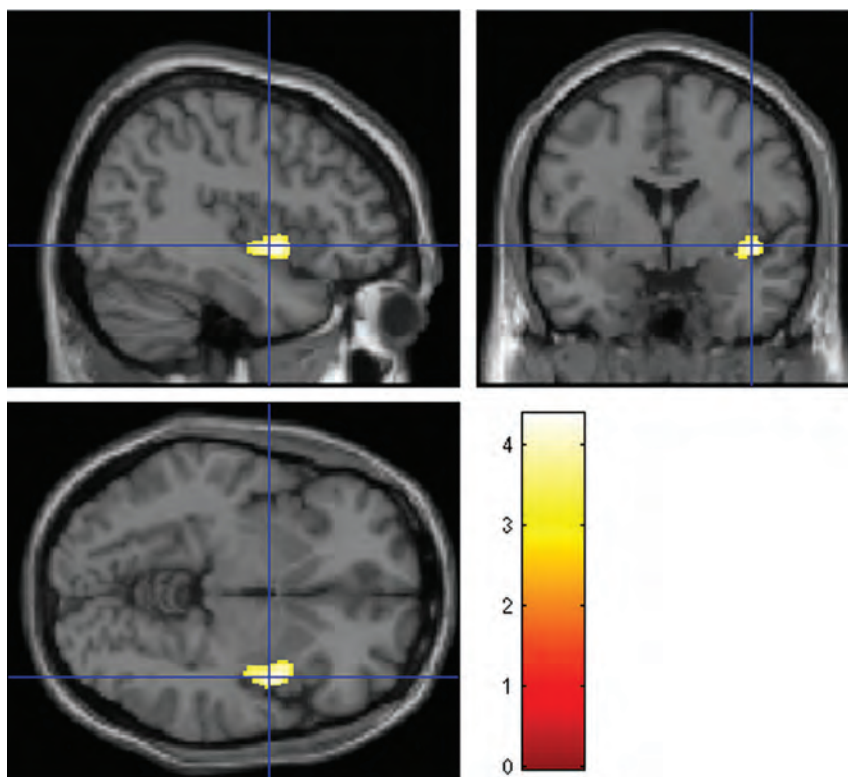


FIG 1. Statistical parametric maps showing regional differences in GM volume between 32 patients with NCS and 32 controls. Orthogonal images show a reduction of GM volume in the right insula in patients with NCS compared with controls, superimposed on a standard template ($P < .05$, cluster-level-corrected for multiple comparisons by using family-wise error). The color bar represents the T values. The left side of each image is the left side of brain.

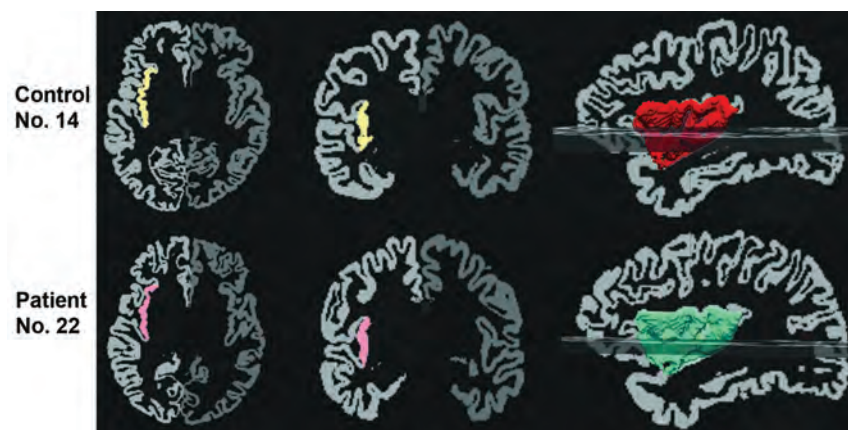


FIG 2. An illustration of segmentation and volume measurement of the right insula in a control subject (upper row, volume = 8119 mm³) and a patient (lower row, volume = 7247 mm³). The automatically segmented insular cortex is superimposed on axial (first column) and coronal (second column) GM images, and the third column illustrates a 3D reconstructed image of the right insula. The left side of each image is the right side of brain.

correlations between right insular volumes and other clinical variables including HR changes, disease duration, and number of total syncope and presyncope attacks (all $P > .05$). Volumes of the left rostral anterior cingulate and left insular cortices were not correlated with any clinical variables (all $P > .05$).

DISCUSSION

This study attempted to explore cerebral structural changes associated with pathophysiologic mechanisms underlying NCS. Using

VBM, we found that patients with NCS had regional atrophy in the right insular cortex. We also observed a significant reduction of whole right insular volume in patients with NCS compared with controls, consistent with the VBM finding. Moreover, smaller right insular volumes in patients with NCS were related to larger drops in both systolic and diastolic BP during HUT, suggesting an important involvement of the right insular cortex in NCS.

Among the regions belonging to the central autonomic network, the insular cortex has been recognized as playing a crucial role in cardiovascular modulation.^{20,21,24-26} An increase in nocturnal BP and occurrence of QT prolongation and cardiac arrhythmias were more frequently observed in patients with stroke with involvement of the insular cortex compared with those without insular involvement.^{27,28} Damage to the right insular cortex was associated with impairment in sympathovagal balance, supporting an important implication of the right insular cortex in autonomic control of cardiovascular activity.^{29,30} Several lines of evidence indicate that there is a hemispheric lateralization of cardiovascular autonomic control of the insular cortex. A study investigating heart rate variability changes during intracarotid amobarbital injection in patients with temporal lobe epilepsy showed sympathetic activation with left hemisphere injection and parasympathetic activation with right hemisphere injection.³¹ An intraoperative study before temporal lobectomy in patients with epilepsy demonstrated that BP and HR decreased with left insular stimulation, whereas BP and HR increased with right insular stimulation.²⁴ These findings strongly support a critical role of the left insula in parasympathetic cardiovascular control and of the right insula in sympathetic control.

There is a reciprocal interaction between sympathetic and parasympathetic control of cardiac autonomic functions.^{32,33} Damage confined to the left insular cortex by acute stroke could shift cardiovascular balance toward an increase in basal sympathetic tone and a decrease in parasympathetic tone.³⁴ Likewise, our finding could be interpreted as right insular atrophy in NCS being associated with a decrease in sympathetic activity and a reciprocal increase in parasympathetic activity, resulting in a drop in BP and syncope. Our speculation

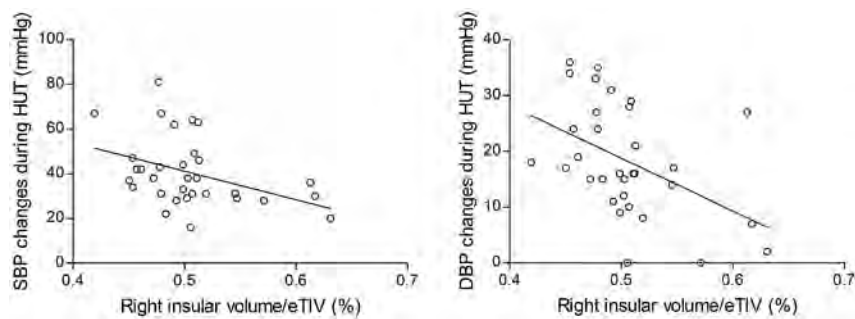


FIG 3. The relationship between the volume of the whole right insular cortex and BP changes in patients with NCS. Normalized right insular volume (raw volume/estimated total intracranial volume [eTIV] \times 100) was negatively correlated with the extent of drops in systolic BP (SBP) (left panel, $r = -.410$, $P = .020$) and diastolic BP (DBP) (right panel, $r = -.507$, $P = .003$) during the head-up tilt test (Spearman correlation, $P < .05$).

might be further supported by the findings of greater right insular volume reductions in relation to larger drops in both systolic and diastolic BP during HUT.

There are only a few studies evaluating hemodynamic and structural changes of the brain in patients with NCS. Studies by using SPECT showed decreases in regional cerebral blood flow in multiple cortical regions, yielding inconsistent results across the studies.³⁵⁻³⁷ The results of these SPECT studies might be interpreted as a consequence of cerebral hypoperfusion rather than a specific cause of NCS. To our knowledge, there is only 1 exploratory VBM study that showed a reduction of GM volume in the medulla in patients with NCS. The study suggested that NCS may be associated with structural changes of the medulla, which predisposes the patient to abnormal cardiovascular homeostasis and recurrent syncope.⁸ However, we did not observe any GM volume changes in the brain stem, even by using a lenient threshold of uncorrected $P < .01$. This difference could not be properly explained but might, in part, be ascribed to different sample sizes, MR scanners, and patient characteristics. Because a substantial number of conditions can mimic NCS,⁵ only patients with orthostatic stress and a positive response to HUT were included in our study. In their study, only 2 of 18 patients had orthostatic stress as a main trigger of syncope, and the remaining patients had variable triggers such as emotional distress, blood phobia, instrumentation, or pain.⁸ Because NCS comprises a heterogeneous group of conditions based on pathophysiologic classification of the principal triggers of syncope,⁴ the differences in the patient populations included might account for the inconsistency between the studies.

There are several limitations to our study. First, the current study is cross-sectional, and thus interpretation of our results with respect to a causal relationship is limited. Given that GM atrophy found in VBM could be a reflection of neuropathologic changes in many brain disorders such as temporal lobe epilepsy, Alzheimer disease, and schizophrenia,³⁸ we hypothesized that right insular atrophy may represent a primary underlying pathology and therefore act as the specific cause that promotes NCS. Conversely, taken together with our finding of a trend toward significance for regional volume reductions of the left insula and anterior cingulate cortex in patients with NCS, it seems possible that right insular atrophy might be a consequence of repeated attacks of cerebral hypoperfusion. Further prospective study incorporating a longitudinal design would provide a hint of the causal relationship between

insular atrophy and disease progression. Second, we did not measure heart rate variability, a representative indicator of autonomic cardiovascular functions that can quantify both sympathetic and parasympathetic activities. Therefore, examination of HUT without heart rate variability measurement may be insufficient to support our speculation that patients with NCS have decreased sympathetic activity and reciprocally increased parasympathetic activity.

CONCLUSIONS

We have observed a novel finding of right insular atrophy in patients with

NCS with a positive response to HUT, implicating a role of right insular dysfunction in the pathophysiologic mechanism underlying NCS. Together with previous investigations, our findings suggest that right insular atrophy may be associated with a decrease in sympathetic activity and a reciprocal increase in parasympathetic activity, resulting in cerebral hypoperfusion and syncope. Confirmation of our findings in larger, more homogeneous datasets of patients with NCS is warranted.

Disclosures: Ji Hyun Kim—RELATED: Grant: This work was supported in part by the National Research Foundation of Korea Grant funded by the Korean Government (Grant No. 20100004827, 20110005418) and a Korea University Grant.

REFERENCES

- Chen-Scarabelli C, Scarabelli TM. Neurocardiogenic syncope. *BMJ* 2004;329:336–41
- Mathias CJ, Deguchi K, Schatz I. Observations on recurrent syncope and presyncope in 641 patients. *Lancet* 2001;357:348–53
- Kaufmann H. Neurally mediated syncope: pathogenesis, diagnosis, and treatment. *Neurology* 1995;45(4 suppl 5):S12–18
- Moya A, Sutton R, Ammirati F, et al. Guidelines for the diagnosis and management of syncope (version 2009). *Eur Heart J* 2009;30:2631–71
- McKeon A, Vaughan C, Delanty N. Seizure versus syncope. *Lancet Neurol* 2006;5:171–80
- Abboud FM. Neurocardiogenic syncope. *N Engl J Med* 1993;328:1117–20
- Mosqueda-Garcia R, Furlan R, Tank J, et al. The elusive pathophysiology of neurally mediated syncope. *Circulation* 2000;102:2898–906
- Beacher FD, Gray MA, Mathias CJ, et al. Vulnerability to simple faints is predicted by regional differences in brain anatomy. *Neuroimage* 2009;47:937–45
- Ashburner J, Friston KJ. Voxel-based morphometry: the methods. *Neuroimage* 2000;11:805–21
- Kapoor WN, Smith MA, Miller NL. Upright tilt testing in evaluating syncope: a comprehensive literature review. *Am J Med* 1994;97:78–88
- Grubb BP. Neurocardiogenic syncope and related disorders of orthostatic intolerance. *Circulation* 2005;111:2997–3006
- Brignole M, Menozzi C, Gianfranchi L, et al. Carotid sinus massage, eyeball compression, and head-up tilt test in patients with syncope of uncertain origin and in healthy control subjects. *Am Heart J* 1991;122:1644–51
- Ashburner J, Friston KJ. Unified segmentation. *Neuroimage* 2005;26:839–51
- Dale AM, Fischl B, Sereno MI. Cortical surface-based analysis. I.

- Segmentation and surface reconstruction. *Neuroimage* 1999;9:179–94
15. Fischl B, Salat DH, Busa E, et al. **Whole brain segmentation: automated labeling of neuroanatomical structures in the human brain.** *Neuron* 2002;33:341–55
 16. Fischl B, van der Kouwe A, Destrieux C, et al. **Automatically parcellating the human cerebral cortex.** *Cereb Cortex* 2004;14:11–22
 17. Ségonne F, Dale AM, Busa E, et al. **A hybrid approach to the skull stripping problem in MRI.** *Neuroimage* 2004;22:1060–75
 18. Ségonne F, Pacheco J, Fischl B. **Geometrically accurate topology-correction of cortical surfaces using nonseparating loops.** *IEEE Trans Med Imaging* 2007;26:518–29
 19. Desikan RS, Segonne F, Fischl B, et al. **An automated labeling system for subdividing the human cerebral cortex on MRI scans into gyral based regions of interest.** *Neuroimage* 2006;31:968–80
 20. Nagai M, Hoshida S, Kario K. **The insular cortex and cardiovascular system: a new insight into the brain-heart axis.** *J Am Soc Hypertens* 2010;4:174–82
 21. Benarroch EE. **The central autonomic network: functional organization, dysfunction, and perspective.** *Mayo Clin Proc* 1993;68:988–1001
 22. Kimmerly DS, O’Leary DD, Menon RS, et al. **Cortical regions associated with autonomic cardiovascular regulation during lower body negative pressure in humans.** *J Physiol* 2005;569:331–45
 23. Kurbaan AS, Franzén AC, Bowker TJ, et al. **Usefulness of tilt test-induced patterns of heart rate and blood pressure using a two-stage protocol with glyceryl trinitrate provocation in patients with syncope of unknown origin.** *Am J Cardiol* 1999;84:665–70
 24. Oppenheimer SM, Gelb A, Girvin JP, et al. **Cardiovascular effects of human insular cortex stimulation.** *Neurology* 1992;42:1727–32
 25. Oppenheimer S. **Cerebrogenic cardiac arrhythmias: cortical lateralization and clinical significance.** *Clin Auton Res* 2006;16:6–11
 26. Williamson JW, Fadel PJ, Mitchell JH. **New insights into central cardiovascular control during exercise in humans: a central command update.** *Exp Physiol* 2006;91:51–58
 27. Sander D, Klingelhofer J. **Changes of circadian blood pressure patterns after hemodynamic and thromboembolic brain infarction.** *Stroke* 1994;25:1730–37
 28. Eckardt M, Gerlach L, Welter FL. **Prolongation of the frequency-corrected QT dispersion following cerebral strokes with involvement of the insula of Reil.** *Eur Neurol* 1999;42:190–93
 29. Colivicchi F, Bassi A, Santini M, et al. **Cardiac autonomic derangement and arrhythmias in right-sided stroke with insular involvement.** *Stroke* 2004;35:2094–98
 30. Tokgözoğlu SL, Batur MK, Top uoğlu MA, et al. **Effects of stroke localization on cardiac autonomic balance and sudden death.** *Stroke* 1999;30:1307–11
 31. Yoon BW, Morillo CA, Cechetto DF, et al. **Cerebral hemispheric lateralization in cardiac autonomic control.** *Arch Neurol* 1997;54:741–44
 32. Kollai M, Koizumi K. **Reciprocal and non-reciprocal action of the vagal and sympathetic nerves innervating the heart.** *J Auton Nerv Syst* 1979;1:33–52
 33. Malliani A, Pagani M, Lombardi F, et al. **Cardiovascular neural regulation explored in the frequency domain.** *Circulation* 1991;84:482–92
 34. Oppenheimer SM, Kedem G, Martin WM. **Left-insular cortex lesions perturb cardiac autonomic tone in humans.** *Clin Auton Res* 1996;6:131–40
 35. İlgin N, Olguntürk R, Kula S, et al. **Brain perfusion assessed by 99mTc-ECD SPECT imaging in pediatric patients with neurally mediated reflex syncope.** *Pacing Clin Electrophysiol* 2005;28:534–39
 36. Töyry JP, Kuikka JT, Lansimies EA. **Regional cerebral perfusion in cardiovascular reflex syncope.** *Eur J Nucl Med* 1997;24:215–18
 37. Joo EY, Hong SB, Lee M, et al. **Cerebral blood flow abnormalities in patients with neurally mediated syncope.** *J Neurol* 2011;258:366–72
 38. Kakeda S, Korogi Y. **The efficacy of a voxel-based morphometry on the analysis of imaging in schizophrenia, temporal lobe epilepsy, and Alzheimer’s disease/mild cognitive impairment: a review.** *Neuroradiology* 2010;52:711–21

Cerebral Abnormalities in Adults with Ataxia-Telangiectasia

D.D.M. Lin, P.B. Barker, H.M. Lederman, and T.O. Crawford



ABSTRACT

SUMMARY: Ataxia-telangiectasia, an autosomal recessive disorder caused by defect of the ataxia-telangiectasia mutated gene, is characterized by progressive neurologic impairment with cerebellar atrophy, ocular and cutaneous telangiectasia, immunodeficiency, heightened sensitivity to ionizing radiation and susceptibility to developing lymphoreticular malignancy. Supratentorial brain abnormalities have been reported only rarely. In this study, brain MRI was performed in 10 adults with ataxia-telangiectasia having stable neurologic impairment. Intracerebral telangiectasia with multiple punctate hemosiderin deposits were identified in 60% of subjects. These lesions were apparently asymptomatic. They are similar in appearance to radiation-induced telangiectasia and to cryptogenic vascular malformations. Also noted, in the 2 oldest subjects, was extensive white matter T2 hyperintensity, and in 1 of these a space-occupying fluid collection consistent with transudative capillary leak and edema as evidenced by reduced levels of metabolites on MR spectroscopic imaging. Asymptomatic supratentorial vascular abnormalities appear to be common in adults with ataxia-telangiectasia.

ABBREVIATIONS: A-T = ataxia-telangiectasia; AFP = alpha-fetoprotein; ATM = ataxia telangiectasia mutated; MRSI = MR spectroscopic imaging

Ataxia-telangiectasia (A-T) is an autosomal recessive neurodegenerative disorder associated with a single defective gene localized to chromosome 11 (11q22–23)¹ that is estimated to affect 1 in 40,000–300,000 people.^{2,3} The causative gene, termed *ataxia telangiectasia mutated* (ATM), is constitutively expressed in all eukaryotic cells and encodes a serine-threonine kinase key to a number of important cellular responses, including the DNA damage response and associated cell-cycle checkpoint regulation.⁴ The range of clinical features manifested by people with A-T is similarly broad and dramatic, including telangiectatic vessels on the bulbar conjunctivae and skin, humeral and cell-mediated immunodeficiency, and an array of cerebellar and other neurologic

impairments.⁵ Affected persons also manifest both heightened sensitivity to ionizing radiation and enhanced susceptibility to malignant disease, chiefly lymphoreticular in nature.^{6–8}

MR imaging is the favored technique of neuroimaging for patients suspected to have A-T because of its superior tissue contrast, as well as the absence of ionizing radiation. Cerebellar atrophy is the most consistent finding, though it is usually not present in the preschool years when most patients first seek neurologic consultation.⁹ The supratentorial brain is typically normal on MR imaging.^{10,11} A few cases have been reported of patients with A-T, mostly adults surviving into their second and third decades of life, in whom cerebral white matter abnormalities of 2 types have been described. One pattern consists of multiple T1 and T2 hypointense foci suggestive of hemosiderin, thought to be related to thrombosis and vascular leaks from multiple capillary telangiectasias.¹² The other pattern, described in a single child and in a few adult patients,^{11,13–15} is T2/FLAIR hyperintensity on long TR sequences that simulates leukodystrophy. The purpose of this study was to analyze the MR imaging features of the supratentorial brain in a small series of young adults with A-T, all otherwise healthy and neurologically stable for years, though they were manifesting substantial persistent neurologic deficits.

Case Series

This study was approved by the local institutional review board (NA_00014314 and NA_00012201). Ten adult participants with A-T (4 men, 6 women; mean age, 23.4 ± 4.5 years; age range,

Received May 31, 2011; accepted after revision March 13, 2013.

From the Departments of Radiology and Radiological Science (D.D.M.L., P.B.B.), Pediatrics (H.M.L., T.O.C.), and Neurology (T.O.C.), Johns Hopkins University School of Medicine, Baltimore, Maryland.

This publication was made possible by the Johns Hopkins Institute for Clinical and Translational Research (ICTR), which is funded in part by grant number ULI TR 000424-06 from the National Center for Advancing Translational Sciences (NCATS), a component of the National Institutes of Health (NIH), and the NIH Roadmap for Medical Research. Its contents are solely the responsibility of the authors and do not necessarily represent the official view of the Johns Hopkins ICTR, NCATS, or NIH. Additional support was provided by NIH grant P41EB015909 and the Ataxia Telangiectasia Children's Project, Boca Raton, Florida.

Please address correspondence to Doris D.M. Lin, MD, PhD, Russell H. Morgan Department of Radiology and Radiological Science, Johns Hopkins University School of Medicine, 600 North Wolfe St, Phipps B-100, Baltimore, MD 21287; e-mail: ddmlin@jhmi.edu

Indicates open access to non-subscribers at www.ajnr.org

<http://dx.doi.org/10.3174/ajnr.A3646>

Characteristics of adults with ataxia-telangiectasia

Participant	Age/Sex	Age of Onset ^a	AFP ^b (ng/mL)	Chromatid Breaks/Cell ^c	SWI Lesions	WM T2 Hyperintensity	Additional MRI Findings
1	21/F	1	498	2.02	Multiple	None	—
2	21/F	1	123	NA	1	None	—
3	25/F	2	1	2.20	None	None	—
4	20/M	1	400	NA	Multiple	None	—
5	22/M	3	240	NA	Multiple	None	—
6	23/F	1.5	224	1.48	Several	None	—
7	19/F	2	14	1.34	None	None	—
8	21/F	1.5	384	2.58	None	None	—
9	34/M	3	484	2.14	Innumerable	Present	—
10	28/M	2	715	1.92	Innumerable	Present	Cystic mass

Note:—NA indicates not available.

^a Age (years) at first inquiry to physician for neurologic concern.

^b Normal < 10 ng/mL.

^c Measured after in vitro exposure to x-irradiation (1.0 Gy); normal range, 0.06-0.34 (Thomas GH and Lederman HM, personal communication).

19–34 years; Table) constitute the case series here reviewed. Eight of these patients were enrolled in a research study¹⁶ to collect CSF, and they underwent MR imaging scans as a safety measure before lumbar puncture. The ninth participant was neurologically stable but underwent clinical MR imaging to evaluate chronic headaches. The final participant underwent MR imaging for clinical concerns but had experienced no new symptoms or signs in several years. The research brain MR imaging studies were performed at 3T and consisted of T1, T2, and SWI. For the 2 clinical studies, in addition to conventional sequences, proton MR spectroscopic imaging (MRSI; TR, 1500 ms; TE, 280 ms) was acquired at 1.5T.

All participants were followed in the Ataxia-Telangiectasia Clinical Center at our institution and underwent MR imaging between 2005 and 2008. At the time of MR imaging evaluation, all participants had stable neurologic impairments of variable severity, including ataxia, dystonia, various forms of tremor, dysarthria, oculomotor abnormalities, distal diminished sensibility to light touch and position, and decreased or absent distal tendon reflexes. All used a wheelchair for mobility. The diagnosis of A-T was by fulfillment of established clinical criteria,^{5,9} including these and other characteristic clinical features, and laboratory studies of elevated alpha-fetoprotein (AFP); increased lymphocyte chromosomal breaks after in vitro radiation exposure; and, in some cases, demonstration of absent ATM protein on Western blot analysis or demonstration of predicted protein-null homozygous mutations of ATM (Table).

On MR imaging, all participants had manifest cerebellar atrophy, whereas the supratentorial brain showed no sign of volume loss. In 6 participants, SWI showed few to innumerable punctate signal voids, suggesting hemosiderin deposits, scattered throughout the cerebral white matter. Four of these 6 were in the research-acquired group, and in these 4 participants, the punctate lesions were inconspicuous on other pulse sequences, including T2-weighted FSE images. In the 2 participants (participants 9 and 10) scanned for clinical concerns (but, like the research-acquired group, absent of any recent change in neurologic function) additional findings of white matter T2 hyperintensity were present, surrounding and highlighting some of these lesions. No signal abnormalities were evident in the cerebellum or brain stem.

In participant 9 (Fig 1), a 34-year-old man who was evalu-

ated for chronic headache, innumerable punctate lesions were best seen on SWI. Several clusters of these lesions were surrounded by T2/FLAIR hyperintensity in the white matter and were associated with mild mass effect (Fig 1A). In these regions of white matter hyperintense T2 signal abnormality—in contrast to the surrounding normal-appearing white matter—¹H-MRSI showed a diminution of all examined metabolites, suggesting reduced cellularity with edema, or perhaps gliosis (Fig 1B). No increase of choline was evident, arguing against an active demyelinating process. No abnormal elevation of lactate was found in any of the brain regions or in the CSF.

In participant 10 (Fig 2), a 28-year-old man who underwent MR imaging simply because of concern for his advancing age, there was an ovoid T2 hyperintense and T1 hypointense space-occupying lesion lined by hemosiderin deposits and surrounded by vasogenic edema (Fig 2A). Some of the T2 dark lesions showed contrast enhancement, suggesting telangiectatic vessels. Within the surrounding white matter T2 hyperintensity, MRSI (Fig 2B) again showed the decrease of all metabolites in a pattern similar to that apparent in participant 9. The right frontal lesion was virtually devoid of any metabolites, consistent with a fluid collection.

DISCUSSION

This case series identifies a spectrum of supratentorial white matter findings in adults with A-T. Combined with the experience of a few reported individual cases,^{12,17} it is apparent that patients with A-T frequently manifest scattered small white matter hypointensities that most likely represent tiny hemosiderin deposits related to telangiectatic vessels. These lesions were most conspicuous on SWI. The presence of these asymptomatic lesions in 6 of 10 neurologically stable patients > 19 years old contrasts with their absence in a younger reported cohort¹⁸ of 8 patients with A-T (mean age, 13 years; age range, 9–19 years), as well as our general experience at the Johns Hopkins Ataxia Telangiectasia Clinical Center reviewing several hundred initial diagnostic MR imaging scans. Although age-related differences in sensitivity or other technical differences are possible confounders, the most plausible explanation is that these are acquired lesions, passing over a threshold of MR imaging detectability in early adult years.

Disabling mutation of the ATM gene responsible for A-T

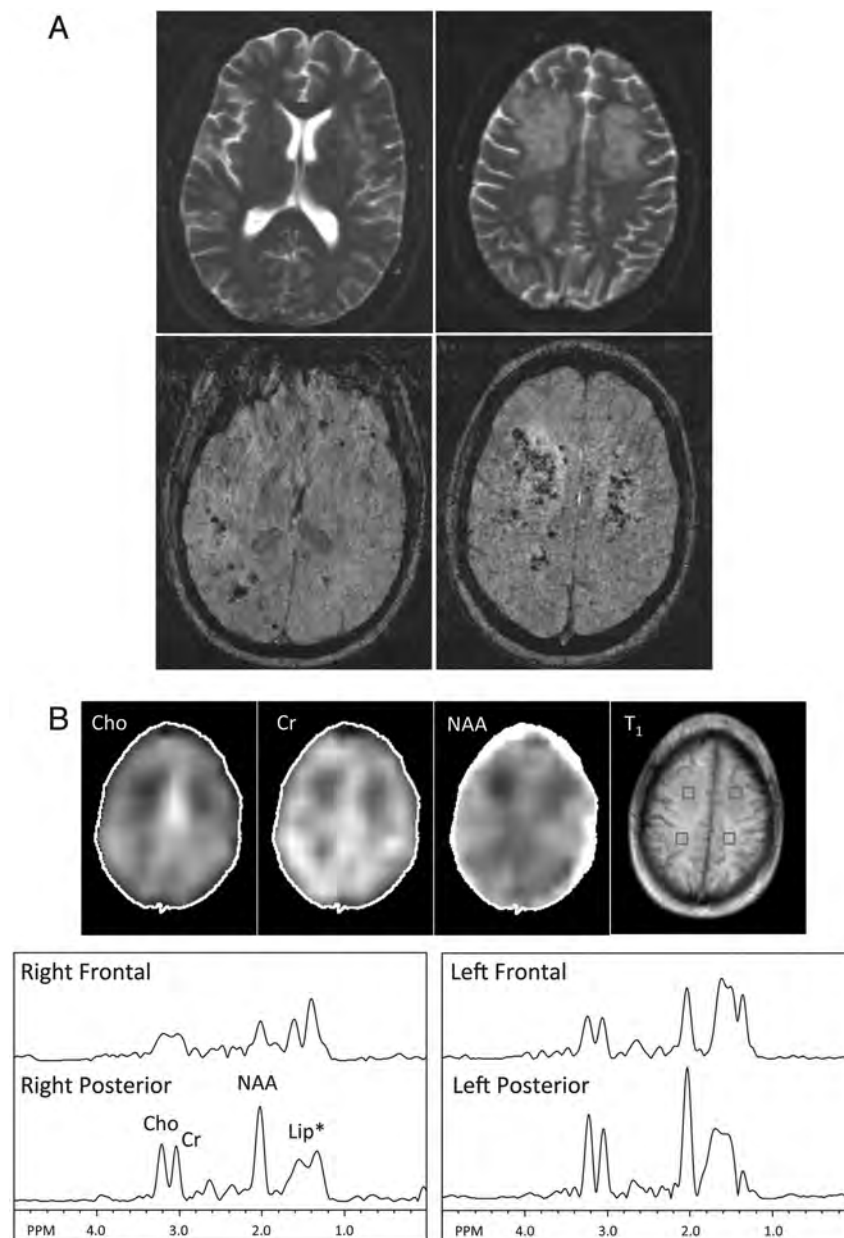


FIG 1. MR imaging and MRSI in participant 9, a 34-year-old man with A-T who had experienced chronic headaches. *A*, Top: T2-weighted images show multifocal confluent hyperintensity in the frontal and parietal white matter bilaterally. A few punctate hypointense foci suggestive of hemosiderin deposits can be identified in the left frontal white matter. Bottom: SWI shows innumerable foci of susceptibility consistent with hemosiderin deposits scattered throughout the bilateral cerebral white matter, some clustered within the confluent T2 hyperintensity. *B*, MRSI metabolite maps (Cho = choline, Cr = creatine, NAA = N-acetylaspartate) and corresponding T1-weighted MR imaging showing voxel locations for selected spectra in the left and right frontal and posterior white matter. Lower levels of Cho, Cr, and NAA are seen, particularly in the right frontal region corresponding to T2 hyperintense white matter, compared with the spectra obtained from the posterior centrum semiovale where more normal-appearing white matter was found. Note the broad peak (approximately 1.5 ppm) upfield from NAA in all brain regions is related to scalp lipid contamination that results from head motion during the scan.

has pleiotropic cellular effects.^{4,19,20} Among the most prominent of these is disruption of the cell-cycle arrest and other cellular responses to DNA damage. Identification of the specific impaired ATM-kinase pathway responsible for formation of deep white matter telangiectasia is unknowable, though this is an appropriate target for research. The ocular and cutaneous telangiectasias that are part of the defining feature of A-T appear in light-exposed superficial regions. A similar vascular pathologic pattern in ATM-deficient mice²¹ that arises in the retina with diminished retinal vasculature attenuation is asso-

ciated with increased vascular endothelial growth factor expression (implicated in angiogenesis), decreased tight junction protein occludin expression, and perturbed astrocytic interaction with endothelial cells, as well as increased vascular permeability with deposits of hemosiderin; however, this model differs from the deep brain lesions demonstrated in this case series by its relationship to light exposure.²² Another plausible explanation is offered by growing evidence that ATM mediates vascular endothelial cell senescence.^{23,24}

The imaging findings reported here in A-T are reminiscent

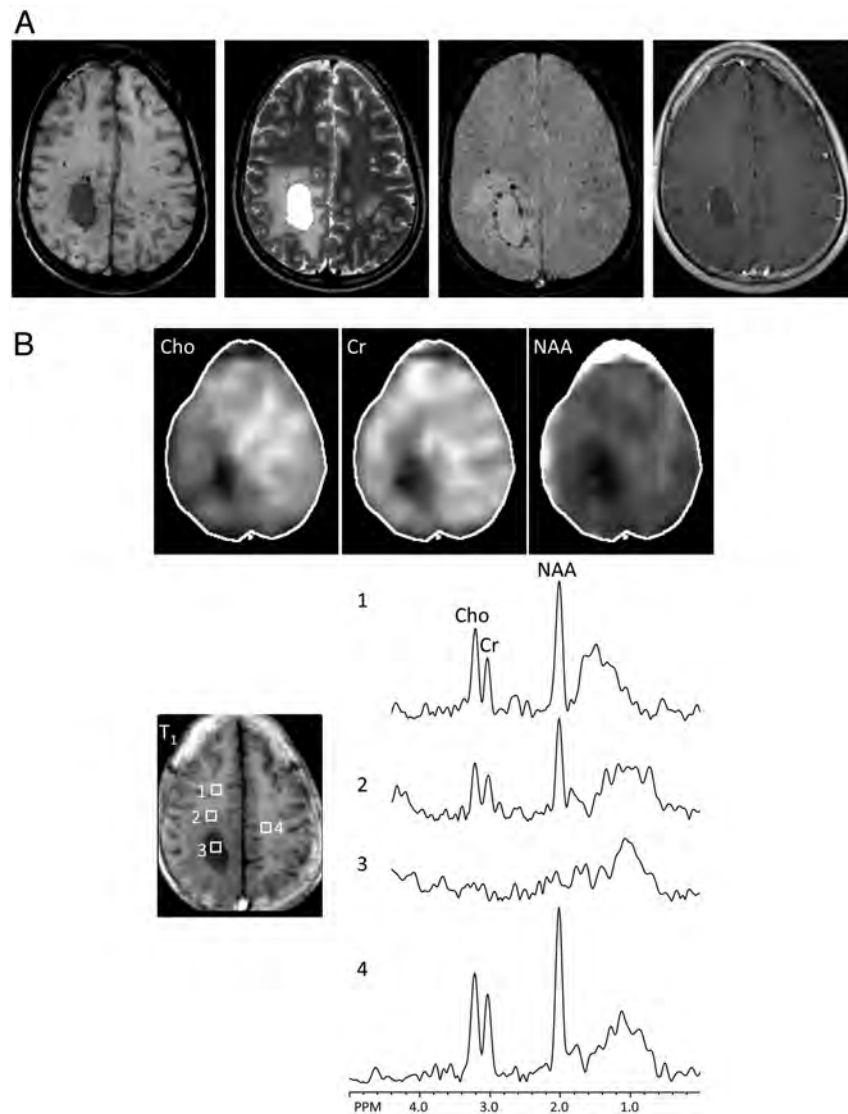


FIG 2. A 28-year-old man with no recent changes in neurologic function underwent scanning because of concern for advancing age. *A*, A T1 hypointense, T2 hyperintense, mild rim-enhancing lesion in the right parietal white matter, with surrounding T2 hyperintensity suggestive of vasogenic edema. The contrast enhancement corresponds to punctate T2 hypointense hemosiderin deposits that outline the ovoid lesion, in addition to a few isolated foci, suggestive of telangiectasia. *B*, MRSI shows complete signal void in the right parietal ovoid lesion (ROI 3), compatible with a fluid collection. Within the surrounding white matter T2 hyperintensity, all metabolites are decreased (ROI 2), compared with normal-appearing white matter regions (ROIs 1 and 4). Residual lipid signals upfield from NAA are the result of head motion.

of those seen in radiation-induced vascular malformations and white matter injuries. Vascular telangiectasias are reported more frequently in patients after CNS irradiation.²⁵⁻²⁷ Parenchymal radiation-associated MR imaging changes typically manifest as progressive, mild to moderate T2 prolongation in the periventricular white matter,²⁵ which may be the result of vascular abnormalities leading to parenchymal ischemia and white matter degeneration. It is not clear, however, whether similar mechanisms cause the white matter changes seen in older patients with A-T.

An unusual finding, identified in our 2 oldest participants (ages 34 and 28 years), was that of white matter T2/FLAIR hyperintensities. Similar hyperintensities have been the topic of individual case reports,^{11,14,15} although we believe that these differ from the single case report of a child with diffuse white matter signal simulating leukodystrophy,¹³ a pattern we have

not otherwise seen. Although MR spectroscopy and MRSI have been previously reported in A-T,^{17,18} abnormalities (eg, reduced NAA) were found only in the atrophic cerebellum, and MR spectroscopy abnormality has not previously been reported in the supratentorial compartment. In one of the reported cases,¹⁴ these white matter signal changes were thought to represent demyelination, but the associated low level of all metabolites found in our MRSI investigation of similar T2 appearance lesions suggests that these white matter signal abnormalities represent reduced cellularity rather than active demyelination or ischemia. The peculiar appearance of a discrete fluid-filled cavity surrounded by the hemosiderin lesions in participant 10 of our series can be best explained by a transudative or exudative process related to leaky capillary telangiectasia.

A spectrum of supratentorial MR imaging abnormalities

seem to be common in adults with A-T. These are asymptomatic, or possibly their associated signs and symptoms are lost amid the many otherwise stable neurologic impairments that such patients endure. Six of 10 participants in our current study manifested deep cerebral telangiectatic vessels best visualized on the SWI sequence, whereas the 2 oldest participants also manifested parenchymal lesions and white matter signal abnormalities. The vascular lesions have many similarities to those seen in patients after therapeutic radiation. The pathogenesis of these lesions is unknown, but candidates include impaired DNA damage response, oxidative damage, enhanced senescence, or any combination of these 3 changes. The prognosis of these MR imaging changes is unclear and will require longitudinal studies.

Disclosures: Howard Lederman—RELATED: Grant: A-T Children's Project*; Support for Travel to Meetings for the Study or Other Purposes: A-T Children's Project.*
*Money paid to institution.

REFERENCES

- Savitsky K, Bar-Shira A, Gilad S, et al. **A single ataxia telangiectasia gene with a product similar to PI-3 kinase.** *Science* 1995;268:1749–53
- Crawford TO. **Ataxia telangiectasia.** *Semin Pediatr Neurol* 1998;5:287–94
- Sedgwick R, Border E. Ataxia-telangiectasia. In: de Jong J, ed. *Handbook of Clinical Neurology*. Amsterdam: Elsevier 1991;347–423
- Ciccio A, Elledge SJ. **The DNA damage response: making it safe to play with knives.** *Mol Cell* 2010;40:179–204
- Crawford TO, Mandir AS, Lefton-Greif MA, et al. **Quantitative neurologic assessment of ataxia-telangiectasia.** *Neurology* 2000;54:1505–09
- Canman CE, Lim DS. **The role of ATM in DNA damage responses and cancer.** *Oncogene* 1998;17:3301–08
- Canman CE, Lim DS, Cimprich KA, et al. **Activation of the ATM kinase by ionizing radiation and phosphorylation of p53.** *Science* 1998;281:1677–79
- Taylor AM, Harnden DG, Arlett CF, et al. **Ataxia telangiectasia: a human mutation with abnormal radiation sensitivity.** *Nature* 1975;258:427–29
- Cabana MD, Crawford TO, Winkelstein JA, et al. **Consequences of the delayed diagnosis of ataxia-telangiectasia.** *Pediatrics* 1998;102:98–100
- Farina L, Uggetti C, Ottolini A, et al. **Ataxia-telangiectasia: MR and CT findings.** *J Comput Assist Tomogr* 1994;18:724–27
- Sardanelli F, Parodi RC, Ottonello C, et al. **Cranial MRI in ataxia-telangiectasia.** *Neuroradiology* 1995;37:77–82
- Ciemins JJ, Horowitz AL. **Abnormal white matter signal in ataxia telangiectasia.** *AJNR Am J Neuroradiol* 2000;21:1483–85
- Chung EO, Bodensteiner JB, Noorani PA, et al. **Cerebral white-matter changes suggesting leukodystrophy in ataxia telangiectasia.** *J Child Neurol* 1994;9:31–35
- Habek M, Brinar VV, Rados M, et al. **Brain MRI abnormalities in ataxia-telangiectasia.** *Neurologist* 2008;14:192–95
- Opeskin K, Waterston J, Nirenberg A, et al. **Ataxia telangiectasia with long survival.** *J Clin Neurosci* 1998;5:471–73
- Dziedziatowska M, Qi G, You J, et al. **Proteomic characterization of cerebrospinal fluid from ataxia-telangiectasia (A-T) patients using a LC/MS-based label-free protein quantification technology.** *Int J Proteomics* 2011;2011:578903
- Wallis LI, Griffiths PD, Ritchie SJ, et al. **Proton spectroscopy and imaging at 3T in ataxia-telangiectasia.** *AJNR Am J Neuroradiol* 2007;28:79–83
- Lin DD, Crawford TO, Lederman HM, et al. **Proton MR spectroscopic imaging in ataxia-telangiectasia.** *Neuropediatrics* 2006;37:241–46
- Guo Z, Kozlov S, Lavin MF, et al. **ATM activation by oxidative stress.** *Science* 2010;330:517–21
- McKinnon PJ. **ATM and ataxia telangiectasia.** *EMBO Rep* 2004;5:772–76
- Raz-Prag D, Galron R, Segev-Amzaleg N, et al. **A role for vascular deficiency in retinal pathology in a mouse model of ataxia-telangiectasia.** *Am J Pathol* 2011;179:1533–41
- Leemput J, Masson C, Bigot K, et al. **ATM localization and gene expression in the adult mouse eye.** *Mole Vis* 2009;15:393–416
- Chen J, Goligorsky MS. **Premature senescence of endothelial cells: Methusaleh's dilemma.** *Am J Physiol Heart Circ Physiol* 2006;290:H1729–39
- Zhan H, Suzuki T, Aizawa K, et al. **Ataxia telangiectasia mutated (ATM)-mediated DNA damage response in oxidative stress-induced vascular endothelial cell senescence.** *J Biol Chem* 2010;285:29662–70
- Gaensler EH, Dillon WP, Edwards MS, et al. **Radiation-induced telangiectasia in the brain simulates cryptic vascular malformations at MR imaging.** *Radiology* 1994;193:629–36
- Koike S, Aida N, Hata M, et al. **Asymptomatic radiation-induced telangiectasia in children after cranial irradiation: frequency, latency, and dose relation.** *Radiology* 2004;230:93–99
- Lew SM, Morgan JN, Psaty E, et al. **Cumulative incidence of radiation-induced cavernomas in long-term survivors of medulloblastoma.** *J Neurosurg* 2006;104:103–07

Differences in the Angiographic Evaluation of Coiled Cerebral Aneurysms between a Core Laboratory Reader and Operators: Results of the Cerecyte Coil Trial

I. Rezek, R.K. Lingineni, M. Sneade, A.J. Molyneux, A.J. Fox, and D.F. Kallmes

ABSTRACT

BACKGROUND AND PURPOSE: Independent evaluation of angiographic images is becoming widely applied in the assessment of treatment outcomes of cerebral aneurysms. In the current study, we assessed the agreement between an independent core laboratory and the operators regarding angiographic appearance in a recent randomized, controlled trial.

MATERIALS AND METHODS: Data were derived from the Cerecyte Coil Trial. Angiographic images of each coiled aneurysm, taken immediately after embolization and at 5- to 7-month follow-up, were evaluated by the operator at the treating center and by an independent neuroradiologist at the core laboratory. For the purpose of this study, images were interpreted on a 3-point scale to provide uniformity for analysis; grade 1: complete occlusion, grade 2: neck remnant; and grade 3: sac filling. “Unfavorable angiographic appearance” was defined as grade 3 at follow-up or interval worsening of grade between the 2 time points.

RESULTS: The study included 434 aneurysms. Immediately after embolization, grade 3 was reported by operators in 39 (9%) compared with 52 (12%) by the core laboratory ($P = .159$). On follow-up, grade 3 was reported by operators in 44 (10%) compared with 81 (19%) by the core laboratory ($P < .0001$). Overall, operators noted unfavorable angiographic appearance in 78 (18%) compared with 134 (31%) by the core laboratory ($P < .0001$). At every time point, agreement between the core laboratory and the operators was slight.

CONCLUSIONS: Unfavorable angiographic appearance was noted almost twice as frequently by an independent core laboratory as compared with the operators. Planning of trials and interpretation of published studies should be done with careful attention to the mode of angiographic appearance interpretation.

Angiographic imaging represents the principal metric for evaluating endovascular treatment of cerebral aneurysms and comparing the efficacy of different coil types. The relationship between complete or stable aneurysm occlusion and incomplete occlusion and the risk of delayed aneurysm re-bleeding remains uncertain. Angiographic results are also used to decide on whether further treatment is considered. Treatment success and indications for further management, including the possibility of an additional intervention, are highly dependent on angiographic appearance in the belief that patients with incomplete occlusion are at risk of hemorrhage, though the size of this risk is unknown.

Most previous literature included assessments of angiographic appearance on the basis of readings performed in the treating center(s).¹⁻³ However, other investigators,⁴⁻¹¹ especially in the setting of randomized, controlled trials,⁹⁻¹¹ have used an independent core laboratory for angiographic assessment. Independent core laboratories represent a centralized approach and can provide a standard operating procedure for imaging review. In this respect, they are used to provide a more objective assessment within a trial setting than may be possible at treating centers. This suggested objectivity may also result from the core laboratory being blinded to treatment settings, using the same prespecified systematic reviewing protocols, and usually consisting of more experienced reviewers. On the other hand, operators, being aware of the details of the patient status and the procedure, may have a hands-on sense of “success” when considering the risk-benefit ratio of adding more coils to the treated aneurysm. Also, there is currently no study addressing the degree of objectivity of operators judging their own procedural results at the end of prolonged risk procedures.

Reported angiographic appearance after endovascular treatment has varied widely in previous studies.¹²⁻¹⁵ Many factors are

Received February 21, 2013; accepted after revision March 28.

From the Departments of Radiology (I.R., D.F.K.), and Health Sciences Research (R.K.L.), and Neurosurgery (D.F.K.), Mayo Clinic, Rochester, Minnesota; Oxford Neurovascular and Neuroradiology Research Unit (M.S., A.J.M.), Nuffield Department of Surgical Sciences, University of Oxford, Oxford, United Kingdom; and Department of Neuroradiology (A.J.F.), Sunnybrook Health Sciences Centre, Toronto, Ontario, Canada.

Please address correspondence to Issa Rezek, MD, Department of Radiology, Mayo Clinic, 200 1st St SW, Rochester, MN 55905; e-mail: rezek.issa@mayo.edu

<http://dx.doi.org/10.3174/ajnr.A3623>

Table 1: Definitions of the scales of assessment used

Angiographic Assessment Scale in the Current Study	Operator Angiographic Assessment Scale ^a	Core Laboratory Angiographic Assessment Scale Immediately after Embolization	Core Laboratory Angiographic Assessment Scale at Follow-Up
Grade 1	Complete occlusion	Apparently complete occlusion or overlapping coils/neck	Complete occlusion
Grade 2	Subtotal occlusion or neck remnant	Neck remnant	Stable neck appearance/neck remnant
Grade 3	Incomplete occlusion/aneurysm filling	Inflow/incomplete occlusion (body filling)	Residual filling

^a Cases assessed as “failed embolization” by the operators were excluded from the analysis of this study.

known to influence angiographic appearance, including aneurysm size, neck diameter, initial rupture status, and follow-up duration.^{10,16-18} However, the influence of core laboratory interpretation on outcomes for research purposes, compared with operator evaluations at the treating centers, remains poorly studied.^{19,20} In the current study, we assessed the agreement between an independent core laboratory and the operators at the treating centers regarding angiographic outcomes in a recent randomized, controlled trial.

MATERIALS AND METHODS

All data were derived from the Cerecyte Coil Trial.^{9,21} The trial compared patients with either a ruptured or unruptured aneurysm treated with bioactive Cerecyte coils (Micrus Endovascular, San Jose, California) or bare platinum coils. Details about patient enrollment and inclusion/exclusion criteria are described elsewhere.^{9,21} Briefly, patients with 1 aneurysm deemed suitable for endovascular treatment were enrolled into the trial and randomly assigned to either receiving Cerecyte or bare platinum coils. There were 23 participating centers worldwide. Aneurysms were imaged by DSA immediately after embolization and by either DSA or MR angiography at 5–7 months of follow-up. Each imaging session was evaluated by the operator and by an independent core laboratory. The core laboratory consisted of a single, experienced neuroradiologist who did not have access to the center evaluations and was blinded to the type of coil used. In a similar fashion, the operators at the treating centers were blinded to the core laboratory assessment. Images of the studied aneurysms were sent to the core laboratory reader on compact discs for assessment without further details about the procedure other than vessel location of the target aneurysm. More details about the process of sending images are described elsewhere.⁹

Angiographic appearance was evaluated at the core laboratory and each of the treating centers by use of predefined scales that are summarized in Table 1. Operators evaluated angiographic images immediately after embolization and at follow-up by use of a 4-point scale, including 1) complete occlusion; 2) subtotal occlusion or neck remnant; 3) incomplete occlusion/aneurysm filling; and 4) failed embolization. The core laboratory used a slightly modified 4-point scale immediately after embolization and another one at follow-up. The core laboratory scale immediately after embolization included 1) apparently complete occlusion; 2) overlapping coils/neck; 3) neck remnant; and 4) inflow/incomplete occlusion (body filling). The core laboratory scale at follow-up included 0, no change compared with immediate postembolization DSA; 1, complete occlusion; 2, stable neck appearance/neck remnant; and 3, residual filling. For the purposes of this study, and after confirming with the core laboratory

reader about the definitions of the scale points, we considered “complete occlusion” from operator readings to be equivalent to “apparently complete,” “overlapping coils/neck,” or “complete occlusion” from core laboratory readings (grade 1 for the purposes of the current study); “subtotal occlusion or neck remnant” to be equivalent to “neck remnant” or “stable neck appearance/neck remnant” (grade 2 for the purposes of the current study); and “incomplete occlusion/aneurysm filling” to be equivalent to “inflow/incomplete (body filling)” or “residual filling” (grade 3 for the purposes of the current study). When the core laboratory reported that there was “no change” in the angiographic appearance on follow-up, the aneurysm was given the same grade of the core laboratory readings in the immediate postembolization assessment. “Failed embolization” cases were excluded from all analysis as well as cases with incomplete imaging data. Last, we defined “unfavorable angiographic appearance” as either grade 3 at follow-up or interval worsening of grade between the immediate postembolization angiogram and the follow-up imaging.

Statistical Analysis

A simple κ coefficient and a 95% CI were used to assess agreement between the core laboratory reader and the operators in evaluating angiographic appearance. Kappa scores were interpreted as follows²²: <0 as “less than chance agreement,” 0.01–0.20 as “slight agreement,” 0.21–0.40 as “fair agreement,” 0.41–0.60 as “moderate agreement,” 0.61–0.80 as “substantial agreement,” and 0.81–0.99 as “almost perfect agreement.”

The McNemar test of symmetry was used to assess the marginal homogeneity of the proportion of grade 3 immediately after embolization and at follow-up as well as the proportion of aneurysms identified as having had an “unfavorable appearance” for both the operators and core laboratory readings. All statistical analysis was performed with the use of SAS software (v9.3, SAS Institute, Cary, North Carolina).

RESULTS

Patients ($n = 497$) with 1 confirmed aneurysm suitable for coil embolization were enrolled in the trial. Of these 497 target aneurysms, 49 (9.9%) were excluded from the angiographic analysis because of incomplete imaging data and 14 (2.8%) were also excluded as the operators deemed them as “failed embolizations.” Thus, the current analysis included 434 aneurysms (87.3%) of 497 treated aneurysms that were reviewed immediately after embolization and at 5–7 months of follow-up by both the operators and core laboratory reader.

Angiographic appearance of the treated aneurysms immediately after embolization is presented in Table 2. Of the 395 (91%)

Table 2: Immediate postembolization angiographic appearance on the 3-point scale

Core Laboratory Readings	Operator Readings			Total
	Grade 1, n (%) ^a	Grade 2, n (%)	Grade 3, n (%)	
Grade 1	108 (48)	41 (24)	18 (46)	167
Grade 2	97 (43)	100 (59)	18 (46)	215
Grade 3	21 (9)	28 (17)	3 (8)	52
Total	226	169	39	434

^a Percentages follow columnar order.

Table 3: Follow-up angiographic appearance on the 3-point scale

Core Laboratory Readings	Operator Readings			Total
	Grade 1, n (%) ^a	Grade 2, n (%)	Grade 3, n (%)	
Grade 1	105 (43)	24 (16)	1 (2)	130
Grade 2	124 (51)	80 (55)	19 (43)	223
Grade 3	14 (6)	43 (29)	24 (55)	81
Total	243	147	44	434

^a Percentages follow columnar order.

Table 4: Agreement between operators and the core laboratory reader on different time point assessments

	Simple κ Coefficient (95% CI)	Interpretation
Immediately after embolization on 3-point scale	0.138 (0.067–0.209)	Slight agreement
Follow-up on 3-point scale	0.189 (0.121–0.258)	Slight agreement
Favorable versus unfavorable outcomes	0.121 (0.042–0.199)	Slight agreement

of 434 aneurysms graded either 1 or 2 by the operators, 49 were graded as 3 by the core laboratory reader. The overall number of aneurysms graded as 3 by the operators was 39 (9%) of 434 aneurysms compared with 52 (12%) graded as 3 by the core laboratory reader ($P = .159$).

Angiographic appearance of the treated aneurysms at follow-up is presented in Table 3. Of the 390 (90%) of 434 aneurysms that were graded as either 1 or 2 by the operators, 57 (16%) were graded as 3 by the core laboratory reader. The overall number of aneurysms graded as 3 by the operators was 44 (10%) of 434 aneurysms compared with 81 (19%) graded by the core laboratory reader ($P < .0001$).

Of the 356 aneurysms that had “favorable angiographic appearance” according to the operators, 86 (24%) had “unfavorable angiographic appearance” according to the core laboratory reader. The overall “unfavorable angiographic appearance” according to the operators was 78 (18%) of 434 aneurysms compared with 134 (31%) according to the core laboratory reader ($P < .0001$).

Agreement between the core laboratory reader and the operators by use of the simple κ coefficient is presented in Table 4. At every time point, agreement between the core laboratory and the operators was slight.

DISCUSSION

In the current study, we have shown that interpretation angiographic appearance for the same treated aneurysms can significantly change when reviewed by an independent core laboratory versus the treating operators. At follow-up, the rates of both unfavorable angiographic appearance, as well as those deemed as grade 3, were nearly twice as high for the core laboratory compared with the operator assessments.

Agreement between the core laboratory and operators was only “slight” after embolization and at follow-up. This appears to be far worse than the “good” agreement among readers in a single-center study.²³ These findings suggest not only that single-center studies with angiographic appearance assessed by operators are fundamentally different from those assessed by independent core laboratories but also that outcomes assessed at the treating centers are likely to be systematically more favorable than those from core laboratories, even for the same angiograms. The core laboratory recognized that some post-coiling angiograms appear complete but have coils overlapping aneurysm necks due to the view needed to separate parent vessel from coils not being available. An example is some anterior communicating aneurysms best viewed with a basal submental vertex view, but not done at the time of coiling.

The impact of core laboratory evaluation of outcomes has previously been studied in cardiology and its superiority over operator readings suggested.^{24–28} A recent systematic review and meta-analysis of the endovascular literature for cerebral aneurysms¹⁹ found that studies that used an independent core laboratory reported higher numbers of unfavorable angiographic outcomes as compared with treating center evaluations, but the quality of evidence was low for the heterogeneity of the literature studies. The current study, which allowed direct comparison of individual cases from a randomized cohort instead of relying on literature reviews, adds additional evidence for the impact of core lab readings on reported outcomes. Another group of investigators²⁰ has shown that core laboratory evaluation of immediate angiographic images resulted in doubling the number of incompletely occluded aneurysms when compared with treating center evaluation, similar to our own findings.

The current study had some limitations. First, to achieve uniformity of the reviews as much as possible between core laboratory reader and operators at the treating centers, we had to exclude 13% of the aneurysms for the various reasons that were listed earlier. We could not standardize the level of experience and former training of the core laboratory reader with the individual operators and also account for the variations between readers from different centers. Also, the Cerecyte Coil Trial was not set up to answer the specific question of comparing the core laboratory and operator readings. One of the resulting challenges of the differently oriented design was the ambiguity of the boundaries between the grades of each scale that was used. The possible misperception of the scale definitions among readers can, in part, explain some of the resulting differences. The core laboratory reader of the Cerecyte Coil Trial included, for every case, a derivation of “millimeter” measurements and measured neck remnant depth establishing 2 mm as an attempted measured boundary between grade 2 and grade 3 instead of distinguishing them in the eye of the beholder. This strategy was not applied by the operators in the treating centers. The core laboratory reader received a limited amount of information about the individual cases on compact discs, which may affect the overall understanding of the procedure’s details and possibly affect the subsequent judgment. Finally, this study assesses 1 core laboratory with a single reader, which reduces the generalizability of the conclusions. A future

study would ideally recruit different core laboratory readers to assess for interreader variability.

CONCLUSIONS

Unfavorable angiographic appearance was noted almost twice as frequently by an independent core laboratory as compared with the operators at the treating centers for aneurysms treated with coil embolization. The planning of trials and interpretation of published studies should be done with careful attention to the mode of angiographic appearance interpretation. More specific attention to the consistent use of the categories of less-than-complete aneurysm obliteration may reduce the discrepancies.

Disclosures: The chief Investigator for the Cerecyte Coil Trial was Dr Andrew J. Molyneux. The trial was sponsored and funded (unrestricted research grant) by Micrus Endovascular but was independently co-ordinated by the Oxford Neurovascular & Neuroradiology Research Unit (ONNRU), Nuffield Department of Surgical Sciences, University of Oxford, Oxford, UK. The Core Laboratory was led by Dr Allan J. Fox at Sunnybrook Health Sciences Centre, Toronto, Ontario, Canada. ONNRU hold all the trial data and the data for this report was provided by ONNRU on request. ISRCTN82461286. Mary Sneade—*RELATED: Support for Travel to Meetings for the Study or Other Purposes:* Micrus Endovascular,* Comments: Travel and accommodation support for site visits as part of the Cerecyte Coil Trial protocol and meetings for the study set-up and data presentation. Andrew J. Molyneux—*RELATED: Grant:* Micrus Endovascular,* Comments: Unrestricted research grant; *Support for Travel to Meetings for the Study or Other Purposes:* Micrus Endovascular,* Comments: Attendance at ASNR Annual Meeting. Allan Fox—*RELATED: Grant:* Micrus Endovascular. Comments: Angiographic Core Laboratory for the Cerecyte Coil Trial; *Support for Travel to Meetings for the Study or Other Purposes:* Cerecyte Coil Trial. Comments: Travel expenses provided for participation in trial workshops; *OTHER RELATIONSHIPS:* Was chair of the Clinical Events Committee for the MAPS trial (randomized, parallel, control trial) organized and run by Boston Scientific. Time for work and meetings was paid on an hourly basis. David Kallmes—*RELATED:* research support Micrus for enrolling patients in the Cerecyte Clinical Trial. No funding was provided for any work related to the current paper focused on Core Laboratory outcomes. *UNRELATED: Board Membership:* Deputy Editor for *Radiology**; *OTHER RELATIONSHIPS:* Research support: Microvention (eV3) Inc, Covidien, AG, NFocus Consulting Inc, Sequent Medical Inc, Penumbra Inc, Benvenue Medical, UVA patent (*money paid to institution).

REFERENCES

1. Zang P, Liang C, Shi Q, et al. **Intraprocedural cerebral aneurysm rupture during endovascular coiling.** *Neurol India* 2011;59:369–72
2. Gallas S, Januel AC, Pasco A, et al. **Long-term follow-up of 1036 cerebral aneurysms treated by bare coils: a multicentric cohort treated between 1998 and 2003.** *AJNR Am J Neuroradiol* 2009;30:1986–92
3. Murayama Y, Nien YL, Duckwiler G, et al. **Guglielmi detachable coil embolization of cerebral aneurysms: 11 years' experience.** *J Neurosurg* 2003;98:959–66
4. Kang HS, Han MH, Lee TH, et al. **Embolization of intracranial aneurysms with Hydrogel-coated coils: result of a Korean multicenter trial.** *Neurosurgery* 2007;61:51–59
5. Cloft HJ; HEAL Investigators. **HydroCoil for Endovascular Aneurysm Occlusion (HEAL) study: 3–6 month angiographic follow-up results.** *AJNR Am J Neuroradiol* 2007;28:152–54
6. Park JH, Kang HS, Han MH, et al; Korean HydroSoft Registry Investigators. **Embolization of intracranial aneurysms with HydroSoft coils: results of the Korean multicenter study.** *AJNR Am J Neuroradiol* 2011;32:1756–61
7. Pierot L, Cognard C, Ricolfi F, et al. **Mid-term anatomic results after endovascular treatment of ruptured intracranial aneurysms with GDC and Matrix coils: analysis of the CLARITY series.** *AJNR Am J Neuroradiol* 2012;33:469–73
8. Pierot L, Leclerc X, Bonafé A, et al. **Endovascular treatment of intracranial aneurysms with Matrix detachable coils: midterm anatomic follow-up from a prospective multicenter registry.** *AJNR Am J Neuroradiol* 2008;29:57–61
9. Molyneux AJ, Clarke A, Sneade M, et al. **Cerecyte Coil Trial: angiographic outcomes of a prospective randomized trial comparing endovascular coiling of cerebral aneurysms with either Cerecyte or bare platinum coils.** *Stroke* 2012;43:2544–50

10. White PM, Lewis SC, Gholkar A, et al. **Hydrogel-coated coils versus bare platinum coils for the endovascular treatment of intracranial aneurysms (HELPS): a randomized controlled trial.** *Lancet* 2011;377:1655–62
11. Claiborne Johnson S, McDougal C, Gholkar A. **The MAPS (Matrix and Platinum Science) Trial: primary results.** In: *Proceedings of the Eighth Annual Meeting of the Society of Neurointerventional Surgery*, Colorado Springs, Colorado. July 25–28, 2011
12. Raymond J, Guilbert F, Weill A, et al. **Long-term angiographic recurrences after selective endovascular treatment of aneurysms with detachable coils.** *Stroke* 2003;34:1398–403
13. Plowman RS, Clarke A, Clarke M, et al. **Sixteen-year single-surgeon experience with coil embolization for ruptured intracranial aneurysms: recurrence rates and incidence of later rebleeding: clinical article.** *J Neurosurg* 2011;114:863–74
14. Thornton J, Debrun GM, Aletich VA, et al. **Follow-up angiography of intracranial aneurysms treated with endovascular placement of Guglielmi detachable coils.** *Neurosurgery* 2002;50:239–49
15. Guo XB, Fan YM, Zhang JN. **HydroSoft coil versus HydroCoil for endovascular aneurysm occlusion study: a single center experience.** *Eur J Radiol* 2011;79:e42–46
16. Kole MK, Pelz DM, Kalapos P, et al. **Endovascular coil embolization of intracranial aneurysms: important factors related to rates and outcomes of incomplete occlusion.** *J Neurosurg* 2005;102:607–15
17. Sluzewski M, van Rooij WJ, Slob MJ, et al. **Relation between aneurysm volume, packing, and compaction in 145 cerebral aneurysms treated with coils.** *Radiology* 2004;231:653–58
18. Fernandez Zubillaga A, Guglielmi G, Viñuela F, et al. **Endovascular occlusion of intracranial aneurysms with electrically detachable coils: correlation of aneurysm neck size and treatment results.** *AJNR Am J Neuroradiol* 1994;15:815–20
19. Rezek I, Mousan G, Wang Z, et al. **Effect of core laboratory and multiple-reader interpretation of angiographic images on follow-up outcomes of coiled cerebral aneurysms: a systematic review and meta-analysis.** *AJNR Am J Neuroradiol* 2013;34:1380–84
20. Pierot L, Cognard C, Ricolfi F, et al. **Immediate anatomic results after the endovascular treatment of ruptured intracranial aneurysms: analysis in the CLARITY series.** *AJNR Am J Neuroradiol* 2010;31:907–11
21. Coley S, Sneade M, Clarke A, et al. **Cerecyte Coil Trial: procedural safety and clinical outcomes in patients with ruptured and unruptured intracranial aneurysms.** *AJNR Am J Neuroradiol* 2012;33:474–80
22. Viera AJ, Garrett JM. **Understanding interobserver agreement: the kappa statistic.** *Fam Med* 2005;37:360–63
23. Cloft HJ, Kaufmann T, Kallmes DF. **Observer agreement in the assessment of endovascular aneurysm therapy and aneurysm recurrence.** *AJNR Am J Neuroradiol* 2007;28:497–500
24. Douglas PS, DeCara JM, Devereux RB, et al. **Echocardiographic imaging in clinical trials: American Society of Echocardiography Standards for echocardiography core laboratories: endorsed by the American College of Cardiology Foundation.** *J Am Soc Echocardiogr* 2009;22:755–65
25. Dahiya A, Bolen M, Grimm RA, et al. **Development of a consensus document to improve multireader concordance and accuracy of aortic regurgitation severity grading by echocardiography versus cardiac magnetic resonance imaging.** *Am J Cardiol* 2012;110:709–14
26. Hole T, Otterstad JE, St John Sutton M, et al. **Differences between echocardiographic measurements of left ventricular dimensions and function by local investigators and a core laboratory in a 2-year follow-up study of patients with an acute myocardial infarction.** *Eur J Echocardiogr* 2002;3:263–70
27. Baur LH, Schipperheyn JJ, van der Velde EA, et al. **Reproducibility of left ventricular size, shape and mass with echocardiography, magnetic resonance imaging and radionuclide angiography in patients with anterior wall infarction: a plea for core laboratories.** *Int J Card Imaging* 1996;12:233–40
28. Oh JK. **Is core laboratory essential for using echocardiography in clinical trials? Controlled vs random error.** *Eur J Echocardiogr* 2002;3:245–47

Last-Recorded P2Y12 Reaction Units Value Is Strongly Associated with Thromboembolic and Hemorrhagic Complications Occurring Up to 6 Months after Treatment in Patients with Cerebral Aneurysms Treated with the Pipeline Embolization Device

J.E. Delgado Almandoz, B.M. Crandall, J.M. Scholz, J.L. Fease, R.E. Anderson, Y. Kadkhodayan, and D.E. Tubman



ABSTRACT

BACKGROUND AND PURPOSE: A recent study identified a preprocedural P2Y12 reaction units value of <60 or >240 as a strong independent predictor of perioperative thromboembolic and hemorrhagic complications after treatment of cerebral aneurysms with the Pipeline Embolization Device. This study aimed to determine whether a last-recorded P2Y12 reaction units value of <60 or >240 predicts thromboembolic and hemorrhagic complications up to 6 months after treatment of cerebral aneurysms with the Pipeline Embolization Device in the same patient cohort.

MATERIALS AND METHODS: We recorded patient and aneurysm characteristics, P2Y12 receptor antagonist administered, P2Y12 reaction units value with VerifyNow, procedural variables, and thromboembolic and hemorrhagic complications up to 6 months after Pipeline Embolization Device procedures at our institution during an 8-month period. Complications causing a permanent disabling neurologic deficit or death were considered major. Multivariate regression analysis was performed to identify independent predictors of thromboembolic and hemorrhagic complications.

RESULTS: Forty-four patients underwent 48 Pipeline Embolization Device procedures at our institution during the study period. There were 11 thromboembolic and hemorrhagic complications up to 6 months after treatment in our cohort (22.9%), 5 of which were major (10.4%). A last-recorded P2Y12 reaction units value of <60 or >240 was the only independent predictor of all ($P = .002$) and major ($P = .03$) thromboembolic and hemorrhagic complications in our cohort. Most patients (71%) required, on average, 2 adjustments to the dose or type of P2Y12 receptor antagonist to remain within the 60–240 target P2Y12 reaction units range.

CONCLUSIONS: In our cohort, a last-recorded P2Y12 reaction units value of <60 or >240 was the only independent predictor of all and major thromboembolic and hemorrhagic complications up to 6 months after Pipeline Embolization Device procedures.

ABBREVIATIONS: DAT = dual antiplatelet therapy; ICH = parenchymal intracerebral hemorrhage; PED = Pipeline Embolization Device; PRU = P2Y12 reaction units

Endovascular treatment of cerebral aneurysms with the Pipeline Embolization Device (PED; Covidien/ev3, Irvine, California) requires its deployment within the lumen of the parent artery to allow the vessel to endothelialize along the PED and exclude the aneurysm from the circulation. This process carries the risk of thromboembolic complications because platelets could become activated, adhere to the PED, form thrombus, and cause either in

situ PED thrombosis or distal thromboembolization. Hence, PED procedures are usually performed under dual antiplatelet therapy (DAT) with aspirin and a P2Y12 receptor antagonist such as clopidogrel, prasugrel, or ticagrelor. However, DAT carries the risk of hemorrhagic complications, with parenchymal intracerebral hemorrhage (ICH) being the most potentially devastating.

Case series of 12–191 patients with cerebral aneurysms treated with the PED have reported a wide range of thromboembolic and hemorrhagic complications, with the risk of cerebral infarction ranging from 0% to 14% and the risk of ICH ranging from 0% to 11%.^{1–16} Among other factors, the variability in thromboembolic and hemorrhagic complications after PED procedures could be due to differences in patient responses to the P2Y12 receptor antagonists administered while the PED endothelializes.

The P2Y12 receptor plays a central role in platelet activation and aggregation. Clopidogrel and prasugrel cause irreversible inhibition of the P2Y12 receptor, while ticagrelor causes reversible

Received February 11, 2013; accepted after revision April 15.

From the Division of Interventional Neuroradiology, Neuroscience Institute, Abbott Northwestern Hospital, Minneapolis, Minnesota.

Paper previously presented in part at: Ninth Annual Meeting of the Society of NeuroInterventional Surgery, July 23–26, 2012, San Diego, California; and International Stroke Conference 2013, February 6–8, 2013, Honolulu, Hawaii.

Please address correspondence to Jossler E. Delgado Almandoz, MD, Division of Interventional Neuroradiology, Neuroscience Institute, Abbott Northwestern Hospital, 800 E 28th St, Minneapolis, MN 55407; e-mail: jossler.delgado@crlmed.com

Indicates open access to non-subscribers at www.ajnr.org

Indicates article with supplemental on-line table

<http://dx.doi.org/10.3174/ajnr.A3621>

inhibition of this receptor. VerifyNow (Accumetrics, San Diego, California) is a point-of-care platelet function test that measures the degree of P2Y12 receptor inhibition after stimulation with adenosine diphosphate, a P2Y12 receptor agonist. This assay has been found to correlate strongly with light transmittance aggregometry, the criterion standard for quantification of platelet reactivity, in patients treated with clopidogrel, prasugrel, or ticagrelor.¹⁷⁻²⁰ VerifyNow results are reported in P2Y12 reaction units (PRUs), with a lower PRU value corresponding to a higher degree of P2Y12 receptor inhibition and, hence, a decreased likelihood of platelet activation and aggregation; and a higher PRU value corresponding to a lower degree of P2Y12 receptor inhibition and, hence, an increased likelihood of platelet activation and aggregation. A recent study of 44 patients who underwent 48 PED procedures for treatment of cerebral aneurysms at our institution found that a preprocedural PRU value of <60 or >240 measured with VerifyNow was the strongest independent predictor of perioperative thromboembolic and hemorrhagic complications occurring up to postoperative day 30.¹⁶

The aim of this study was to determine whether a last-recorded PRU value of <60 or >240 (up to the occurrence of a complication, if any) predicts thromboembolic and hemorrhagic complications occurring up to 6 months after treatment in the same cohort of patients with cerebral aneurysms treated with the PED at our institution.

MATERIALS AND METHODS

Our study was approved by the institutional review board of our hospital and conducted in compliance with the Health Insurance Portability and Accountability Act. We conducted a retrospective analysis to examine the predictors of thromboembolic and hemorrhagic complications occurring up to 6 months after treatment in patients who underwent treatment of cerebral aneurysms with the PED at our institution from November 17, 2011 to July 23, 2012.

Medical Record Review

We recorded baseline patient characteristics, dose and type of P2Y12 receptor antagonist administered, P2Y12 receptor inhibition with the VerifyNow test (in PRUs) up to the occurrence of a thromboembolic or hemorrhagic complication (if any), aspirin dose, aneurysm characteristics, number of PEDs deployed, technical difficulties, procedure time, postprocedural corticosteroid regimen, and the incidence and severity of thromboembolic and hemorrhagic complications occurring up to 6 months after the PED procedure. Procedures were considered technically difficult if there was PED herniation into the aneurysm, incomplete PED opening requiring balloon angioplasty for adequate wall apposition, PED migration during deployment requiring a second PED to cover the aneurysm neck, or concurrent treatment of another cerebral aneurysm. Thromboembolic and hemorrhagic complications were reviewed by a panel of 3 neurointerventionalists and were designated "major" if they caused a permanent disabling neurologic deficit or death.

DAT Protocol

P2Y12 receptor inhibition was assessed with the VerifyNow test in all patients before the procedure and 10 and 30 days after any

changes to the dose or type of P2Y12 receptor antagonist administered, after changes to medications that may affect clopidogrel or prasugrel metabolism, or at any time if the patient was symptomatic with abnormal bruising/bleeding or focal neurologic deficits.

The target P2Y12 receptor inhibition initially was 80–200 PRUs and was subsequently expanded to 60–240 PRUs after July 27, 2012. For most elective PED procedures (83%), DAT was started 10 days before the procedure with 325 mg aspirin daily and 75 mg clopidogrel daily. The clopidogrel response was assessed the day before the procedure. Clopidogrel hyporesponders received a 60-mg prasugrel loading dose the day before the procedure followed by 10 mg prasugrel daily, and the initial prasugrel response was assessed on the day of the procedure. Clopidogrel hyper-responders were placed on every other day, every third day, every Monday and Friday, every fourth day, or every fifth day dosing regimens as needed to reach the target PRU range. Prasugrel hyporesponders received a 180-mg loading dose of ticagrelor followed by 90 mg twice a day with the initial ticagrelor response assessed before the procedure. Prasugrel hyper-responders in follow-up testing initially had the daily prasugrel dose reduced to 5 mg and, if needed, were subsequently placed on every other day or every third day dosing regimens to reach the target PRU range. Although the aforementioned adjustments to the dose or type of the P2Y12 receptor antagonist administered were made according to the preprocedural PRU value, elective PED procedures were not rescheduled to a later date to reach the target PRU range before PED deployment.

For urgent/emergent PED procedures, a 60-mg loading dose of prasugrel was administered followed by 10 mg prasugrel daily, with the initial prasugrel response assessed before the procedure and follow-up testing performed as described above.

PED Procedure

The PED procedure was performed with the patient under general anesthesia by a team of 2 neurointerventionalists by using transfemoral access in a dedicated biplanar neuroangiographic unit (Axiom Artis; Siemens, Erlangen, Germany). Heparinization was used throughout the procedure to achieve an activated clotting time 2–2.5 times baseline. A triaxial system was used with a 6F long sheath (Shuttle; Cook, Bloomington, Indiana), a distal access catheter (ReFlex; Covidien/ev3 or Neuron; Penumbra, Alameda, California), and a Marksman microcatheter (Covidien/ev3). A 0.016-inch (Headliner; Terumo, Tokyo, Japan) or 0.014-inch (Traxcess; MicroVention, Aliso Viejo, California or Avigo; Covidien/ev3) microwire was used to advance the Marksman microcatheter across the aneurysm neck. The PED device was deployed across the aneurysm neck under fluoroscopic guidance. A post-deployment DynaCT (Siemens) angiography performed to ensure adequate PED vessel wall apposition and aneurysm neck coverage. Final biplanar angiography was performed to document patency of the intracranial vasculature. Hemostasis was achieved with an Angio-Seal device (St. Jude Medical, Minnetonka, Minnesota). Heparinization was not continued postprocedure.

Statistical Analysis

Statistical analysis was performed using MedCalc 11.1 software package (MedCalc Software, Mariakerke, Belgium). First, we per-

Table 1: Thromboembolic and hemorrhagic complications occurring up to 6 months after treatment of cerebral aneurysms with the PED according to last-recorded PRU value

	All Complications			Thromboembolic Complications			Hemorrhagic Complications		
	All (%)	Major ^a (%)	P Value ^b	All (%)	Major ^a (%)	P Value ^b	All (%)	Major ^a (%)	P Value ^b
All procedures (n = 48)	11 (22.9)	5 (10.4)		6 (12.5)	1 (2.1)		5 (10.4)	4 (8.3)	
PRU <60 (n = 9)	5 (55.6)	3 (33.3)		1 (11.1)	0		4 (44.4)	3 (33.3)	
PRU 60–240 (n = 37)	4 (10.8)	1 (2.7)		3 (8.1)	0		1 (2.7)	1 (2.7)	
PRU >240 (n = 2)	2 (100)	1 (50)	<.001/.011	2 (100)	1 (50)	.014/.042	0		.004/.036

^a Resulting in death or permanent disabling neurologic deficits.

^b For difference in all/major complications.

formed univariate analysis with the χ^2 or Fisher exact test for each variable to identify the predictors of all and major thromboembolic and hemorrhagic complications occurring up to 6 months after treatment in our cohort. Then, we performed multivariate regression analysis to identify the independent predictors of all and major thromboembolic and hemorrhagic complications occurring up to 6 months after treatment in our cohort. A *P* value \leq .05 was considered statistically significant.

RESULTS

From November 17, 2011, to July 23, 2012, forty-four patients underwent 48 PED procedures to treat 54 cerebral aneurysms at our institution. Thirty-six patients were women (81.8%), and 8, men (18.2%). Mean age was 59.2 years (median, 63 years; range, 31–81 years). Seven patients had a remote history of subarachnoid hemorrhage (15.9%), and 10, a family history of cerebral aneurysms (22.7%). Ten aneurysms were symptomatic (18.5%), 11 had recurred after coiling (20.4%), and 27 were incidental (50%). Mean maximum aneurysm size was 8.4 mm (median, 5.8 mm; range, 1.9–27.6 mm). Mean aneurysm neck size was 4.8 mm (median, 4 mm; range, 1.1–17 mm). Mean procedure time was 67.7 minutes (median, 50.5 minutes; range, 28–220 minutes). Seventeen procedures were technically difficult (35.4%), with a mean procedure time of 108.7 minutes (median, 91 minutes; range, 56–220 minutes). Mean number of PEDs deployed was 1.3 (range, 1–5).

Mean last-recorded PRU value up to the occurrence of a thromboembolic or hemorrhagic complication (if any) was 130.2 (median, 132.5; range, 0–292). Mean time interval from initiation of DAT to the last P2Y12 receptor inhibition test up to the occurrence of a thromboembolic or hemorrhagic complication (if any) was 103.3 days (median, 83 days; range, 7–233 days).

Thromboembolic and Hemorrhagic Complications Occurring Up to 6 Months after Treatment of Cerebral Aneurysms with the PED and Associated Last-Recorded PRU Values

Table 1 summarizes the incidence of thromboembolic and hemorrhagic complications occurring up to 6 months after treatment in our cohort according to the last-recorded PRU value, using a PRU value of >240 as a proposed cutoff for P2Y12 receptor underinhibition²¹ and a PRU value of <60 as a proposed cutoff for P2Y12 receptor overinhibition.

There were 6 thromboembolic (12.5%) and 5 hemorrhagic (10.4%) complications occurring up to 6 months after treatment in our cohort. Of these, 5 were major (10.4%): Three resulted in a permanent disabling neurologic deficit (6.2%, one thromboembolic, 2 hemorrhagic), and 2 ICHs resulted in death (4.2%).

The 4 perioperative thromboembolic complications in our cohort (one of which was major) have been described previously.¹⁶ There were 2 additional thromboembolic complications occurring after the perioperative period in our cohort: 1 patient with an asymptomatic delayed PED thrombosis after treatment of a blister ICA aneurysm identified at the time of the 6-month follow-up angiogram (PRU 193), and 1 patient with a delayed perforator infarction causing nondisabling deficits in short-term memory and executive planning after treatment of an anterior cerebral artery aneurysm (PRU 205, Fig 1). The patient with the major perioperative thromboembolic complication had a markedly elevated PRU value (PRU 292) at the time of the complication.

The 4 perioperative hemorrhagic complications in our cohort (3 of which were major) were all ICHs ipsilateral to the PED and have been described previously.¹⁶ An additional ICH contralateral to the PED occurred on postoperative day 50 in a patient with postmortem examination–proven amyloid angiopathy at the site of the ICH (PRU 58, Fig 2). Of note, 80% of hemorrhagic complications, including 3 of the 4 major complications (75%), occurred in patients who had decreased PRU values shortly before (PRU 0) or at the time of the ICH (PRU 2, 10, and 58).

Overall, 4 of the 5 (80%) major thromboembolic and hemorrhagic complications occurring up to 6 months after treatment in our cohort occurred in patients who had markedly elevated (292, thromboembolic complication) or decreased (0, 10, 58, hemorrhagic complications) PRU values shortly before or at the time of the complication.

Predictors of Thromboembolic and Hemorrhagic Complications Occurring Up to 6 Months after Treatment of Cerebral Aneurysms with the PED

The On-line Table summarizes the predictors of thromboembolic and hemorrhagic complications occurring up to 6 months after treatment in our cohort. In univariate analysis, a last-recorded PRU value of <60 or >240 ($P < .001$) and a technically difficult procedure ($P = .036$) were predictors of all thromboembolic and hemorrhagic complications occurring up to 6 months after treatment in our cohort, while a last-recorded PRU value of <60 or >240 ($P = .01$) was the only predictor of major thromboembolic and hemorrhagic complications occurring up to 6 months after treatment in our cohort.

In multivariate regression analysis, a last-recorded PRU value of <60 or >240 was the only independent predictor of all ($P = .002$) and major ($P = .03$) thromboembolic and hemorrhagic complications occurring up to 6 months after treatment in our cohort.

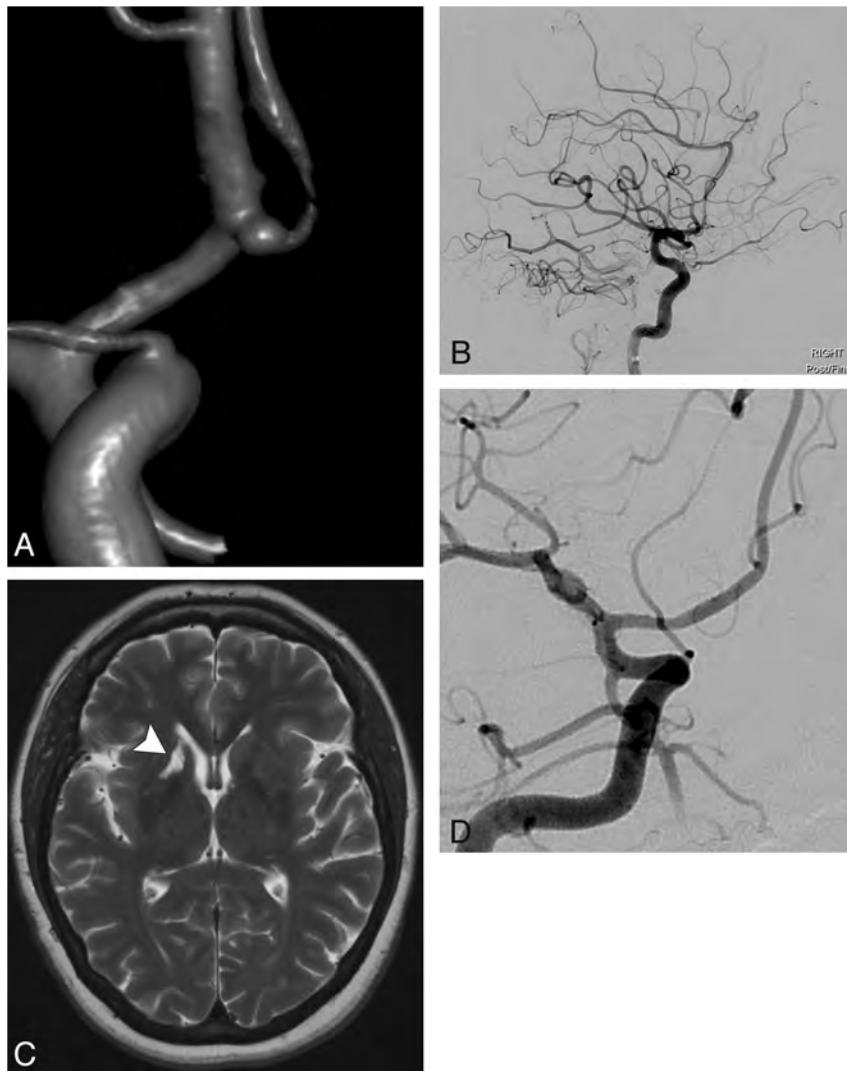


FIG 1. A 47-year-old patient with a family history of ruptured cerebral aneurysms presented with a small right anterior cerebral artery aneurysm identified at screening. The patient elected to undergo endovascular treatment with the PED. *A*, 3D image demonstrates a 2-mm right A1/A2 segment anterior cerebral artery aneurysm with the anterior communicating artery arising from the aneurysm sac. *B*, Final lateral right ICA angiogram after uncomplicated deployment of a single 2.5×10 mm PED across the aneurysm neck demonstrates patent cerebral vasculature. The patient demonstrated conversion to a clopidogrel hyper-response (PRU 52) 30 days after initiation of DAT and underwent 2 clopidogrel dose adjustments to remain within the target P2Y12 receptor inhibition range of 60–240 PRU. A final dosing regimen of 75 mg clopidogrel every third day was instituted 94 days after initiation of DAT. At the time of the 6-month follow-up angiogram, the patient's spouse stated that for the past 3–4 months the patient had experienced memory deficits, cognitive changes, and weight gain. MR imaging examination of the brain was performed immediately, and P2Y12 receptor inhibition testing showed a PRU of 205. *C*, T2WI demonstrates an old infarction in the right caudate head, anterior limb of the right internal capsule, and right putamen (arrowhead), consistent with a perforator infarction (likely in the territory of the right recurrent artery of Heubner), which was not present in pretreatment imaging. *D*, Six-month follow-up catheter angiogram demonstrates complete exclusion of the right anterior cerebral artery aneurysm from the circulation with a widely patent PED but no flow across the anterior communicating artery. The patient underwent neurologic and neuropsychological consultation and had nondisabling deficits in short-term memory, attention, problem solving, and self-regulation with near-complete resolution after outpatient rehabilitation.

Variability in Clopidogrel Response and Clinical Management of DAT

Table 2 summarizes the final P2Y12 receptor antagonist dosing regimen administered and associated major thromboembolic and hemorrhagic complications occurring up to 6 months after treatment in our cohort.

Forty-two patients underwent elective PED procedures (95.5%), and 2 patients were started on aspirin/prasugrel DAT for urgent/emergent PED procedures (4.5%) in our cohort. With the initial target P2Y12 receptor inhibition range of 80–200 PRUs as the reference, in preprocedural testing 11 patients were considered clopidogrel hyporesponders (26.2%; mean PRU, 272.8; median, 262; range, 207–399), 9 patients were considered clopidogrel hyperresponders (21.4%; mean PRU, 48.1; median, 54; range, 9–73), and 22 patients were within the target PRU range (52.4%; mean PRU, 141.9; median, 155.5; range, 83–197).

Among the 22 patients who were initially within the target PRU range, 17 became clopidogrel hyperresponders in follow-up testing (77.3%; mean PRU, 23.4; median, 10; range, 1–78). Among these, 7 were symptomatic (41.2%; five with abnormal bruising/bleeding and 2 with ICH). Mean time from initiation of DAT to conversion to a clopidogrel hyper-response was 41.6 days (median, 30 days; range, 16–200 days). No patients became clopidogrel hyporesponders in follow-up P2Y12 receptor inhibition testing.

During the study period, 31 patients required at least 1 adjustment to the dose or type of P2Y12 receptor antagonist administered to remain within the expanded target P2Y12 receptor inhibition range of 60–240 PRUs (70.5%), with a mean of 2.1 adjustments per patient (median, 2; range, 1–5) and a mean time from initiation of DAT to last adjustment of 49.9 days (median, 43 days; range, 8–149 days). Four patients temporarily exhibited a PRU of >240 after a dose adjustment (12.9%; 3 prasugrel, 1 clopidogrel) without experiencing thromboembolic complications.

DISCUSSION

The overall incidence of thromboembolic (12.5%) and hemorrhagic (10.4%) complications up to 6 months after PED procedures in our cohort is within the range of previously published studies (0%–14% and 0%–11%, respectively).^{1–15} The overall risk of major complications causing a permanent disabling neurologic deficit or death in our cohort was 10.4%, which is higher than the risk of serious complications associated with endosaccular aneurysm treatment with coils (approximately 3%–4%). However, the target patient population for PED procedures is usually those with

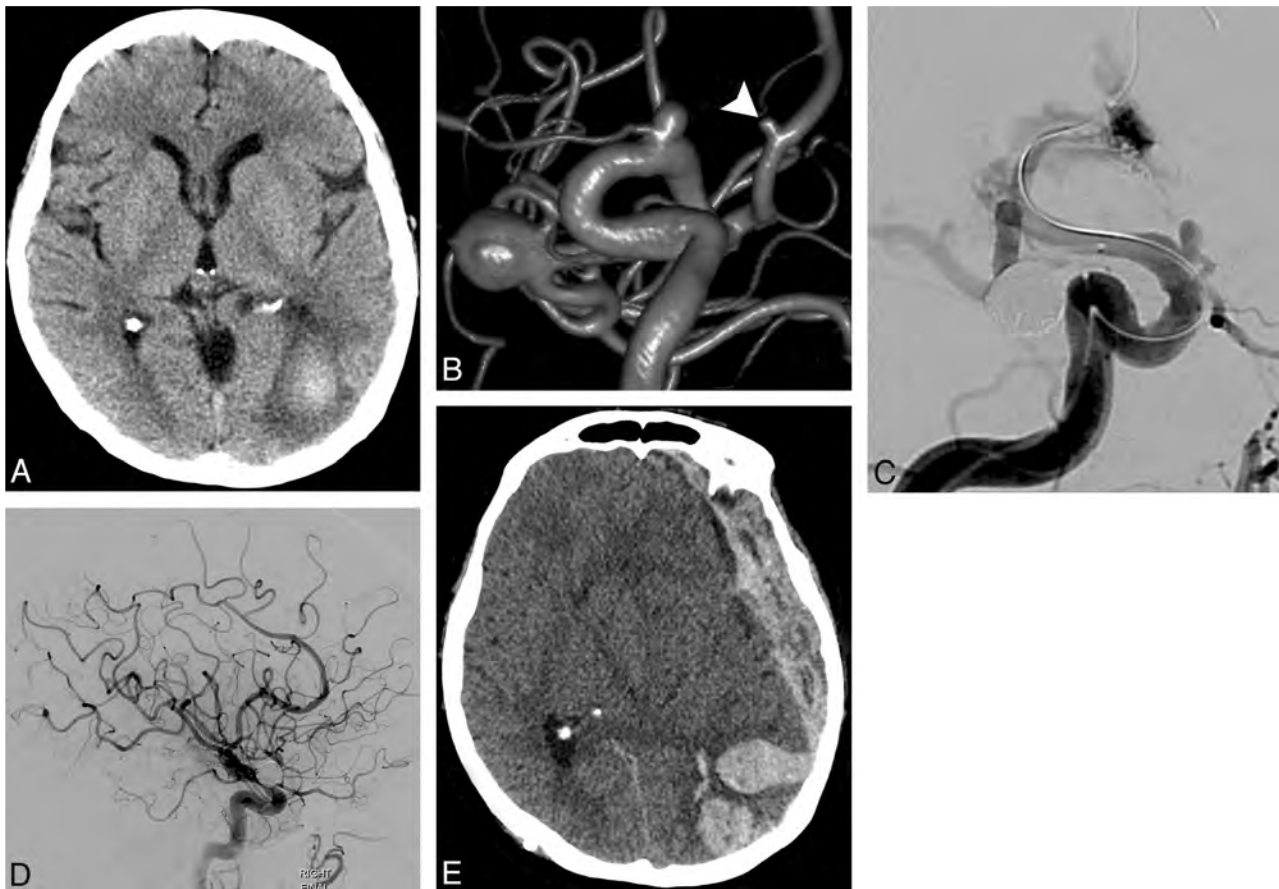


FIG 2. A 63-year-old patient with a long-standing history of cigarette smoking presented with a 3-week history of visual disturbance. *A*, NCCT demonstrates a subacute ICH in the left occipital lobe. The patient underwent further evaluation with contrast-enhanced brain MR imaging, CTA, and conventional angiography, none of which demonstrated an etiology for the ICH. *B*, 3D image of a right ICA angiogram demonstrates 3 incidental cerebral aneurysms, with a 2-mm right A2 segment anterior cerebral artery aneurysm (arrowhead). There were 2 additional incidental left-sided cerebral aneurysms, not in the vicinity of the ICH (not shown). Three months after presentation, a repeat contrast-enhanced brain MR image showed expected evolution of the left occipital ICH without new foci of hemorrhage or abnormal enhancement. The patient expressed a strong desire to undergo endovascular treatment of all the incidental cerebral aneurysms, despite the fact that amyloid angiopathy was the leading differential diagnosis for the ICH. After careful discussion with the patient and family regarding the risk of potentially-devastating rehemorrhage, DAT with aspirin and clopidogrel was instituted, and the right MCA bifurcation aneurysm was treated uneventfully with stent-assisted coil embolization. *C*, Sixteen days later, balloon-assisted coil embolization of the 2-mm right anterior cerebral artery aneurysm was complicated by aneurysm rupture. Hemostasis was achieved with immediate balloon inflation, and the aneurysm was ultimately treated with several coils and a 2.5 × 12 mm PED across its neck. *D*, Final lateral right ICA angiogram demonstrates patent cerebral vasculature. The patient recovered from the subarachnoid hemorrhage and was discharged to a rehabilitation facility on postoperative day 25. The patient demonstrated conversion to a clopidogrel hyper-response (PRU 34) 26 days after initiation of DAT and underwent 3 clopidogrel dose adjustments in an attempt to reach the target P2Y12 receptor inhibition range of 60–240 PRU. A dosing regimen of 75-mg clopidogrel every fourth day was instituted 65 days after initiation of DAT, but follow-up P2Y12 receptor inhibition testing had not been completed. *E*, On postoperative day 50, the patient was found unresponsive at home. NCCT demonstrates a recurrent left occipital ICH with extensive subdural extension causing a severe rightward midline shift. PRU at the time of the ICH was 58. The patient died that evening. Postmortem examination revealed amyloid angiopathy affecting the left occipital lobe.

large and wide-neck aneurysms, which are either not treatable by coil embolization or are at an increased risk of recurrence, requiring multiple treatments. Nevertheless, the higher risk of major thromboembolic and hemorrhagic complications associated with flow diversion must be strongly considered when offering this treatment technique to patients with potentially coilable or clipable cerebral aneurysms.

The issue of P2Y12 receptor underinhibition in patients undergoing coronary interventions has been well-studied in the cardiology literature, and a PRU cutoff of >240 has been proposed to indicate significant residual platelet reactivity.²¹ In our cohort, 26% of patients were considered clopidogrel hyporesponders in preprocedural testing using a PRU cutoff of >200 (using a PRU cutoff of >240, 21% of patients would have been considered

clopidogrel hyporesponders). The proportion of clopidogrel hyporesponders in our cohort was lower than that reported by Akbari et al²² (32.9%) and Lee et al²³ (42.9%) in patients undergoing various types of neurointerventional procedures also tested with VerifyNow using a <40% “P2Y12% inhibition” cutoff. Although 4 patients in our cohort experienced nondisabling thromboembolic complications with last-recorded PRU values of <240 (including a delayed asymptomatic PED thrombosis and a delayed perforator infarction), the patient with the major disabling thromboembolic complication had a last-recorded PRU value of >240 (PRU 292).

The important issue of P2Y12 receptor overinhibition in patients undergoing PED procedures has not been well examined in the literature. In our cohort, 21% of patients were considered

clopidogrel hyper-responders in preprocedural testing using a PRU cutoff of <80 (using a PRU cutoff of <60, 14% of patients would have been considered clopidogrel hyper-responders). Our findings are similar to those reported by Goh et al²⁴ in a cohort of 47 patients undergoing various types of neurointerventional procedures also tested with VerifyNow (15% using a >72% “P2Y12% inhibition” cutoff). Most important, using a PRU cutoff of <80, we evidenced a conversion to a clopidogrel hyper-response in follow-up testing in 77% of patients who had initially been within the target PRU range in preprocedural testing (using a PRU cutoff of <60, sixty percent of patients would have exhibited a conversion). Overall, P2Y12 receptor overinhibition was evidenced in 62% (PRU cutoff of <80) to 50% (PRU cutoff of <60) of patients who received clopidogrel in our cohort.

While the etiology of perioperative ICHs ipsilateral to the PED is likely multifactorial, P2Y12 receptor overinhibition in the perioperative period may play an important role. In our cohort, 3 of the 4 patients (75%) with perioperative ICHs were found to have P2Y12 receptor overinhibition with markedly decreased PRU values (0, 2, 10) at the time of or just before the ICH. Similarly, Goh et al²⁴ also found that P2Y12 receptor overinhibition in the perioperative period placed patients undergoing various types of neurointerventional procedures at significantly increased risk of experiencing major perioperative hemorrhagic complications (43%). A study of 133 coil embolization procedures to treat unruptured cerebral aneurysms reported a 30% rate of periprocedural thromboembolic diffusion-weighted imaging-positive lesions within 72 hours of the intervention.²⁵ Furthermore, a

pathologic study of 3 patients who had fatal ICHs after PED procedures demonstrated basophilic material occluding the blood vessels around the ICH,²⁶ which may represent the hydrophilic coating of the catheters or wires used in these procedures. Therefore, it is plausible that some of the perioperative ICHs ipsilateral to the PED could be explained by hemorrhagic transformation of subclinical infarctions caused by embolization of different types of embolic materials (air bubbles, atherosclerotic plaque, thrombus, or hydrophilic coating from the catheters or wires) in the setting of P2Y12 receptor overinhibition. Moreover, the occurrence of a fatal amyloid ICH contralateral to the PED outside the perioperative period in 1 patient with a decreased PRU value (PRU 58) in our cohort underscores the importance of avoiding P2Y12 receptor overinhibition for the entire duration of

Table 2: Final P2Y12 receptor antagonist dosing regimen and associated major thromboembolic and hemorrhagic complications occurring up to 6 months after treatment in patients with cerebral aneurysms treated with the PED

	No. of Patients (%)	Major Complications (%)	Outside Target P2Y12 Receptor-Inhibition Range (PRU 60–240) ^a (%)
All patients	44 (100)	5 (11.4)	4 (80)
Clopidogrel	31 (71)	3 (9.7)	3 (100)
150 mg daily	3 (9.7)	1 Infarction, 1 ICH (66.7)	2 (100)
75 mg daily	15 (48.3)	0	
75 mg QOD	2 (6.5)	0	
75 mg Q3D	3 (9.7)	0	
75 mg QMF	5 (16.1)	0	
75 mg Q4D	2 (6.5)	1 ICH (50) ^b	1 (100)
75 mg Q5D	1 (3.2)	0	
Prasugrel	12 (27)	2 (16.7)	1 (50)
10 mg daily	6 (50)	1 ICH (16.7)	1 (100)
5 mg daily	5 (41.7)	1 ICH (20)	0
5 mg QOD	1 (8.3)	0	
Ticagrelor	1 (2)	0	
90 mg BID	1 (100)		

Note:—QOD indicates every other day; Q3D, every third day; QMF, every Monday and Friday; Q4D, every fourth day; Q5D, every fifth day; BID, twice a day.

^a Shortly before or at the time of a major complication.

^b Recurrent ICH with subdural extension contralateral to the PED on postoperative day 50 in a patient with postmortem examination-proven amyloid angiopathy at the site of ICH (PRU 58 at the time of ICH, Fig 2).

Table 3: Current DAT protocol for PED procedures

Initiation of DAT	17 Days before procedure
Target P2Y12 receptor inhibition	PRU 60–240
Target aspirin inhibition	≥50%
Initial aspirin dose	81 mg daily
Initial clopidogrel dose	75 mg daily
Preprocedural aspirin inhibition testing ^a	After ten 81-mg aspirin doses or the day before procedure
Preprocedural P2Y12 receptor-inhibition testing	After ten 75-mg clopidogrel doses and the day before procedure
Hyporesponse to aspirin (< 50% inhibition)	Aspirin, 325 mg daily
Clopidogrel dosing schedules	0) 150 mg daily ^b ; 1) 75 mg daily; 2) 75 mg QOD; 3) 75 mg Q3D; 4) 75 mg QMF; 5) 75 mg Q5D; 6) 75 mg Q7D; 7) 75 mg PRN to reach PRU ≥60
Hyporesponse to clopidogrel (PRU > 240)	Go back 1 step in clopidogrel dosing schedule
Hyper-response to clopidogrel (PRU < 60)	PRU 40–59: advance 1 step in clopidogrel dosing schedule PRU 10–39: advance 2 steps in clopidogrel dosing schedule PRU < 10: advance 3 steps in clopidogrel dosing schedule
Reschedule procedure	PRU < 60 or >240 on the day before procedure
Postprocedural P2Y12 receptor-inhibition testing	7–10 and 30–40 Days after any clopidogrel dose adjustment, after changes to medications that may affect clopidogrel metabolism, or at any time if symptomatic with abnormal bruising/bleeding or focal neurologic deficits

Note:—QOD indicates every other day; Q3D, every third day; QMF, every Monday and Friday; Q5D, every fifth day; Q7D, once a week; PRN, dosing schedule as needed.

^a Aspirin inhibition testing performed with a standard collagen platelet aggregation assay.

^b Hyporesponders to 150-mg daily clopidogrel dose (PRU > 240) are started on ticagrelor (180 mg × 1, then 90 mg twice a day) the day before the procedure without further P2Y12 receptor-inhibition testing.

P2Y12 receptor antagonist administration to prevent major hemorrhagic complications that may not be directly related to the PED procedure.

In our cohort, a last-recorded PRU value of <60 or >240 was the only independent predictor of all and major thromboembolic and hemorrhagic complications up to 6 months after treatment of cerebral aneurysms with the PED. Although maintaining patients within the target PRU range of 60–240 has proved to be challenging in our experience—with 71% of patients requiring, on average, 2 adjustments to the dose or type of P2Y12 receptor antagonist administered—the possibility of averting major thromboembolic and hemorrhagic complications justifies the requisite time and effort. Future prospective studies are needed to determine whether active P2Y12 receptor antagonist management to maintain patients within a target P2Y12 receptor inhibition range (proposed PRU 60–240) in preprocedural and follow-up testing, including rescheduling patients who are outside this range in preprocedural testing to make the P2Y12 receptor antagonist adjustments needed to reach the target PRU range before PED deployment, could lower the risk of thromboembolic and hemorrhagic complications after PED procedures.

Following the findings of our study, we have changed our DAT protocol for PED procedures (Table 3). Due to the risk of potentially-devastating rehemorrhage, we do not institute DAT - and hence do not perform PED procedures - in patients with a history of unexplained intracranial hemorrhage or suspected amyloid angiopathy. For elective PED procedures, we currently initiate DAT 17 days before the procedure and perform 2 preprocedural P2Y12 receptor inhibition tests: the first after ten 75-mg clopidogrel doses to adjust the dosing schedule according to the PRU value (if needed), and the second the day before the procedure to ensure that the patient is within the 60–240 target PRU range before PED deployment. Elective PED deployment is not undertaken until the patient is within the 60–240 target PRU range in preprocedural testing performed no earlier than the day before the procedure. Due to the increased risk of major hemorrhagic complications with prasugrel encountered by our group and reported by Akbari et al,²² and the occurrence of a major ipsilateral ICH on postoperative day 20 in a patient receiving a 5-mg daily prasugrel dose in our cohort (PRU 185), we no longer administer prasugrel to patients considered clopidogrel hyporesponders or who must undergo urgent/emergent PED procedures. Patients who must undergo urgent/emergent PED procedures are started on ticagrelor before the procedure (180 mg × 1, then 90 mg twice a day) without P2Y12 receptor inhibition testing and are transitioned to clopidogrel on postoperative day 30 following the protocol described in Table 3. We do not perform P2Y12 receptor inhibition testing in patients who receive ticagrelor because the reversible nature of the P2Y12 receptor inhibition caused by this medication may preclude dose adjustments and the only patient whom we have tested with VerifyNow while on ticagrelor therapy consistently exhibited markedly decreased PRU values (30, 6, 8).

The limitations of our study are the modest sample size and retrospective nature.

CONCLUSIONS

In our cohort, a last-recorded PRU value of <60 or >240 was the only independent predictor of all and major thromboembolic and hemorrhagic complications occurring up to 6 months after treatment of cerebral aneurysms with the PED, and most patients required 2 adjustments to the dose or type of P2Y12 receptor antagonist administered to remain within the 60–240 target PRU range.

ACKNOWLEDGMENTS

We acknowledge Sandee K. Verootis, Radiology Department, Abbott Northwestern Hospital, for her contribution in the data collection for this study.

Disclosures: Josser E. Delgado Almandoz—RELATED: Other: Covidien/ev3, Comments: travel expenses for a Pipeline training course, UNRELATED: Consultancy: Covidien/ev3. Yasha Kadkhodayan—UNRELATED: Other: Penumbra,* Comments: site principal investigator for industry-sponsored trial. David E. Tubman—RELATED: Consulting Fee or Honorarium: MicroVention, Covidien, Lake Region Medical, UNRELATED: Consultancy: MicroVention, Covidien, Lake Region Medical, Payment for Lectures (including service on Speakers Bureaus): Covidien, Royalties: Cook, Payment for Development of Educational Presentations: Covidien. *Money paid to the institution.

REFERENCES

1. Lylyk P, Miranda C, Ceratto R, et al. **Curative endovascular reconstruction of cerebral aneurysms with the Pipeline embolization device: the Buenos Aires experience.** *Neurosurgery* 2009;64:632–42
2. Szikora I, Berentei Z, Kulcsar Z, et al. **Treatment of intracranial aneurysms by functional reconstruction of the parent artery: the Budapest experience with the Pipeline embolization device.** *AJNR Am J Neuroradiol* 2010;31:1139–47
3. Nelson PK, Lylyk P, Szikora I, et al. **The Pipeline embolization device for the intracranial treatment of aneurysms trial.** *AJNR Am J Neuroradiol* 2011;32:34–40
4. Lubicz B, Collignon L, Raphaeli G, et al. **Pipeline flow-diverter stent for endovascular treatment of intracranial aneurysms: preliminary experience in 20 patients with 27 aneurysms.** *World Neurosurg* 2011;76:114–19
5. Fischer S, Vajda Z, Aguilar Perez M, et al. **Pipeline embolization device (PED) for neurovascular reconstruction: initial experience in the treatment of 101 intracranial aneurysms and dissections.** *Neuroradiology* 2012;54:369–82
6. McAuliffe W, Wycoco V, Rice H, et al. **Immediate and midterm results following treatment of unruptured intracranial aneurysms with the Pipeline embolization device.** *AJNR Am J Neuroradiol* 2012;33:164–70
7. Deuschmann HA, Wehrsuetz M, Augustin M, et al. **Long-term follow-up after treatment of intracranial aneurysms with the Pipeline embolization device: results from a single center.** *AJNR Am J Neuroradiol* 2012;33:481–86
8. Cruz JP, Chow M, O’Kelly C, et al. **Delayed ipsilateral parenchymal hemorrhage following flow diversion for the treatment of anterior circulation aneurysms.** *AJNR Am J Neuroradiol* 2012;33:603–08
9. Colby GP, Lin LM, Gomez JF, et al. **Immediate procedural outcomes in 35 consecutive Pipeline embolization cases: a single-center, single-user experience.** *J Neurointerv Surg* 2013;5:237–46
10. Chitale R, Gonzalez LF, Randazzo C, et al. **Single center experience with Pipeline stent: feasibility, technique and complications.** *Neurosurgery* 2012;71:679–91
11. Phillips TJ, Wenderoth JD, Phatouros CC, et al. **Safety of the Pipeline embolization device in treatment of posterior circulation aneurysms.** *AJNR Am J Neuroradiol* 2012;33:1225–31
12. Saatci I, Yavuz K, Ozer C, et al. **Treatment of intracranial aneurysms using the Pipeline flow-diverter embolization device: a single-center**

- ter experience with long-term follow-up results. *AJNR Am J Neuroradiol* 2012;33:1436–46
13. O'Kelly CJ, Spears J, Chow M, et al. **Canadian experience with the Pipeline embolization device for repair of unruptured intracranial aneurysms.** *AJNR Am J Neuroradiol* 2013;34:381–87
 14. Kan P, Siddiqui AH, Veznedaroglu E, et al. **Early postmarket results after treatment of intracranial aneurysms with the Pipeline embolization device: a U.S. multicenter experience.** *Neurosurgery* 2012;71:1080–87
 15. Yu SC, Kwok CK, Cheng PW, et al. **Intracranial aneurysms: midterm outcome of Pipeline embolization device: a prospective study in 143 patients with 178 aneurysms.** *Radiology* 2012;265:893–901
 16. Delgado Almandoz JE, Crandall BM, Scholz JM, et al. **Pre-procedure P2Y12 reaction units value predicts perioperative thromboembolic and hemorrhagic complications in patients with cerebral aneurysms treated with the Pipeline Embolization Device.** *J Neurointerv Surg* 2013; 5 Suppl 3:iii3–10
 17. von Beckerath N, Pogatsa-Murray G, Wiczorek A, et al. **Correlation of a new point-of-care test with conventional optical aggregometry for the assessment of clopidogrel responsiveness.** *Thromb Haemost* 2006;95:910–11
 18. Jakubowski JA, Payne CD, Li YG, et al. **The use of the VerifyNow P2Y12 point-of-care device to monitor platelet function across a range of P2Y12 inhibition levels following prasugrel and clopidogrel administration.** *Thromb Haemost* 2008;99:409–15
 19. Varenhorst C, James S, Erlinge D, et al. **Assessment of P2Y(12) inhibition with the point-of-care device VerifyNow P2Y12 in patients treated with prasugrel or clopidogrel coadministered with aspirin.** *Am Heart J* 2009;157:562.e1–9
 20. Jeong YH, Bliden KP, Antonino MJ, et al. **Usefulness of the VerifyNow P2Y12 assay to evaluate the antiplatelet effects of ticagrelor and clopidogrel therapies.** *Am Heart J* 2012;164:35–42
 21. Bonello L, Tantry US, Marcucci R, et al. **Working group on high on-treatment platelet reactivity: consensus and future directions on the definition of high on-treatment platelet reactivity to adenosine diphosphate.** *J Am Coll Cardiol* 2010;56:919–33
 22. Akbari SH, Reynolds MR, Kadkhodayan Y, et al. **Hemorrhagic complications after prasugrel (Effient) therapy for vascular neurointerventional procedures.** *J Neurointerv Surg* 2013;5:337–43
 23. Lee DH, Arat A, Morsi H, et al. **Dual antiplatelet therapy monitoring for neurointerventional procedures using a point-of-care platelet function test: a single-center experience.** *AJNR Am J Neuroradiol* 2008;29:1389–94
 24. Goh C, Churilov L, Mitchell P, et al. **Clopidogrel hyper-response and bleeding risk in neurointerventional procedures.** *AJNR Am J Neuroradiol* 2013;34:721–26
 25. Altay T, Kang HI, Woo HH, et al. **Thromboembolic events associated with endovascular treatment of cerebral aneurysms.** *J Neurointerv Surg* 2011;3:147–50
 26. Deshmukh V, Hu YC, McDougall CG, et al. **Histopathological assessment of delayed ipsilateral parenchymal hemorrhages after the treatment of paraclinoid aneurysms with the Pipeline embolization device [abstract].** *Neurosurgery* 2012;71:E551–52

Computational Hemodynamics Analysis of Intracranial Aneurysms Treated with Flow Diverters: Correlation with Clinical Outcomes

W. Chong, Y. Zhang, Y. Qian, L. Lai, G. Parker, and K. Mitchell



ABSTRACT

BACKGROUND AND PURPOSE: Recent studies have shown promising results regarding intracranial aneurysms treated with flow diverters. However, these have had adverse effects, including delayed aneurysm occlusion, posttreatment symptoms, and rupture. The hemodynamic profiles of aneurysms treated with flow diverters were analyzed to determine the ones associated with successful and failed treatments.

MATERIALS AND METHODS: Patient-specific computational fluid dynamics were used to simulate hemodynamic profiles, including the presence of jet flow, energy loss, volume flow, and wall shear stress in 4 successful occlusions of aneurysms and 4 failed cases after flow-diverter deployment. In these 4 failed cases, hemodynamic profiles were examined again after a hypothetical second intervention. This involved replacing the failed flow diverter with a hypothetical optimally deployed flow diverter or simulated placement of a second flow diverter within the first (double hypothetical optimally deployed).

RESULTS: Where successful occlusions were achieved, a marked obliteration of jet flow was observed. Flow entering the aneurysm sac was diverted via the center of the flow diverter and joined smoothly with the continuation of flow leaving the aneurysm sac into the parent arteries. These observations were supplemented by a reduction in the other hemodynamic profiles. Aneurysm neck geometry might influence the efficacy of the flow diverter.

CONCLUSIONS: Hemodynamic indices, as calculated by using computational fluid dynamics techniques, have close correlation with flow-diverter treatment outcome. Computational fluid dynamics could be potentially useful as a planning tool for neurointerventionists by simulating an optimized flow-diverter deployment strategy before the procedure and evaluating posttreatment outcome.

ABBREVIATIONS: CFD = computational fluid dynamics; EL = energy loss; FD = flow diverter; HOFD = hypothetical optimally deployed FD; VF = volume flow; WSS = wall shear stress

Despite the availability of biologically coated aneurysm coils, the Onyx Liquid Embolic System (ev3, Irvine, California), and balloon- and stent-assisted coiling techniques, wide-neck large and giant aneurysms are very difficult and sometimes impossible to treat by endovascular means, due to significant residual and recurrence rates and unsatisfactory patient outcomes.¹⁻³

Surgical management is likewise unsatisfactory. The International Study of Unruptured Intracranial Aneurysms reported a poor 1-year patient outcome rate of up to 34% for large and giant aneurysms.⁴ Flow diverters (FDs) have provided a promising new method for the endovascular reconstruction of these types of aneurysms.^{5,6} These are fine mesh stents that divert flow away from the aneurysm sac, thereby promoting progressive thrombosis and occlusion of the aneurysm without further addition of coils or other embolic material. Currently there are 2 devices on the market, the Pipeline Embolization Device (Covidien, Irvine, California) and Silk (Balt, Montmorency, France). Long-term results are not yet available, but current experience is promising. The timeframe for complete occlusion of an aneurysm is unknown, but recent series have documented 6-month occlusion rates of 89.0%–93.3%.⁷ Of more concern are reports of delayed parenchymal or subarachnoid hemorrhage following FD treatment. These have been estimated to be up to 1.75% for the Pipeline Embolization Device and 0.8% for Silk.⁷ Hemodynamic factors and aggres-

Received December 28, 2012; accepted after revision April 5, 2013.

From the Monash Medical Centre (W.C.), Melbourne, Victoria, Australia; Australian School of Advanced Medicine (Y.Z., Y.Q., L.L.), Macquarie University, New South Wales, Australia; Royal Prince Alfred Hospital (G.P.), Sydney, New South Wales, Australia; and Royal Brisbane Hospital (K.M.), Brisbane, Queensland, Australia.

This work was partially supported by the Australian Research Council Discovery Grant DP110102985.

Please address correspondence to Yi Qian, MD, Australian School of Advanced Medicine, Macquarie University, 2 Technology Place, North Ryde 2109, NSW, Australia; e-mail: yi.qian@mq.edu.au

Indicates open access to non-subscribers at www.ajnr.org

Indicates article with supplemental on-line table

<http://dx.doi.org/10.3174/ajnr.A3790>

sive thrombus-associated autolysis of the aneurysm wall have been implicated.^{8,9}

Computational fluid dynamics (CFD) analysis has been applied in the study of the hemodynamics of aneurysm growth and rupture, as well as various types of stents, including FDs.¹⁰⁻¹⁵ The objective of this study was to analyze the hemodynamic profiles involved in successful and failed treatment by comparing 4 aneurysm cases with successful treatment outcome against 4 failed cases, through the use of CFD simulation.

MATERIALS AND METHODS

Patients and Imaging Data

After institutional ethics approval was given, 4 successful cases (patients 1–4) and 4 failed cases (patients 5–8) were studied (Online Table). A successful case was defined as a complete angiographic exclusion of the aneurysm from the circulation within 6 months. Failed cases were defined as exhibiting persistent residual aneurysms after 6 months, posttreatment rupture, and the development of increased symptoms and associated perianeurysmal MR imaging brain changes. The average aneurysm size was 4.2 mm. All 8 patients were initially treated with a Silk FD. Each Silk FD, regardless of size, is composed of forty 30- μ nitinol and eight 50- μ m platinum microfilaments; with pore sizes of 110–250 μ .^{7,11} For the successful cases, patients 1–4, the aneurysms were completely occluded by 6 months. For the failed cases 5 and 6, persistent residual aneurysms were observed at 6 months. Patient 7 developed increasing headaches and “blistering” of the aneurysm wall and brain edema on MR imaging at 3 months. Patients 6 and 7 were retreated with insertion of another FD (Silk) within the first one (double FD) at 6 months and 3 months, respectively. For patient 8, the aneurysm ruptured at 3 and a half months following FD implantation. All patients had aspirin and clopidogrel for 3 months and continued on aspirin afterward.

Vascular and Flow-Diverter Models

Commercially available packages, Mimics (Materialise, Leuven, Belgium) and CFX 13.0 (ANSYS, Canonsburg, Pennsylvania), were used to perform patient-specific CFD simulation by using fine DICOM axial sections derived from DSA or CTA. In successful cases, the optimally deployed FD was simulated as a porous media layer, 0.1 mm thick, with a flow resistance equivalent to the actual FD, as previously described.¹¹ Validation tests were performed to determine the flow-resistance parameters, and our preliminary study has been published.¹⁶ We calculated the following hemodynamic parameters: energy loss (EL), wall shear stress (WSS), and volume flow (VF) into the aneurysm sac.

EL is expressed as

$$1) \quad EL = E_{in} - E_{out} = \sum_{i=1}^{nin} \dot{m}_{i,in} \left(P_{i,in} / \rho + \frac{1}{2} u_{i,in}^2 \right) - \sum_{i=1}^{nout} \dot{m}_{i,out} \left(P_{i,out} / \rho + \frac{1}{2} u_{i,out}^2 \right),$$

where \dot{m} denotes mass flow rate; P , static pressure; and u , in- or output velocity as denoted by the subscripts $i = 1, 2, 3, u_1, u_2, u_3$.

VF rate is calculated as the summation of blood volume flowing from the artery into the aneurysm sac via the aneurysm neck.

WSS is expressed as

$$2) \quad WSS = \mu \dot{u},$$

where μ is the dynamic viscosity of blood and \dot{u} is the velocity gradient at the aneurysm wall.

The jet flow patterns were graphically represented and interpretations were made from these.

To demonstrate that EL and VF are not substantially affected by variations in inflow conditions, we tested the inflow condition at the ICA under 7 flow rates, 80, 100, 125, 150, 175, 200, and 250 mL/minute, for EL and VF for all patients. There were 8 patients, each tested with 7 flow rates, giving a total sample size of 56, resulting in 28 samples for each of the successful and unsuccessful cohorts. t tests were performed between these 2 groups.

Hypothetic Optimally Deployed Flow Diverters and Double HOFD Simulation

The porosity resistance was zeroed at the proximal portion of the FD to represent the uncovered “gap” at the aneurysm inflow of the malpositioned FD (patient 6), and it was reduced by half to simulate the stretched FD (patient 8). The porosity of the optimally deployed FDs in the failed cases 5 and 7 was not altered. The porosity characteristics, implanted positions of the FD, and FD conditions that pertain to parent arteries were optimally modified under a “what-if” condition for the failed cases. In this study, hypothetic optimally deployed (HOFD) flow diverters were simulated to substitute for the malpositioned and stretched FD for both patients 6 and 8. For all unsuccessful procedures, hypothetic placement of a second FD inside the first one (double HOFD) was simulated by increasing the porosity resistance by 10-fold.¹⁶ The HOFD and double HOFD simulations were performed under the average inflow condition at 150 mL/min.

In this study, the resulting values of EL and VF at the initial FD, HOFD, and double HOFD were all expressed as a percentage of the values obtained under conditions without FDs.

RESULTS

Jet Flow Observation

A common flow pattern for all 8 cases before deployment of the FD is a broad jet flow passing through and into the aneurysm sac. Figure 1 depicts the flow patterns of pre- and post-FD treatment. In the successful case (patient 1), before FD deployment, the jet flow impacted the aneurysm surface (Fig 1A). Following FD deployment, however, the jet flow speed significantly decreased in the aneurysm sac. In addition, the flow direction was diverted to the center of the FD with marked stasis at the periphery of the aneurysm sac (Fig 1B). This favorable flow pattern (reduction of jet flow speed, central diversion, and peripheral stasis) was observed in all successful cases. However, in the failed case (patient 6), the original jet flow pattern persisted despite the deployment of the FD stent. The jet flow speed after FD deployment (Fig 1D) did not significantly decrease compared with before (Fig 1C). These are the characteristics of an unsuccessful flow pattern.

In the posttreatment rupture case (patient 8), the jet flow through and into the aneurysm persisted after FD deployment; and though some stasis was observed near the top of the aneurysm

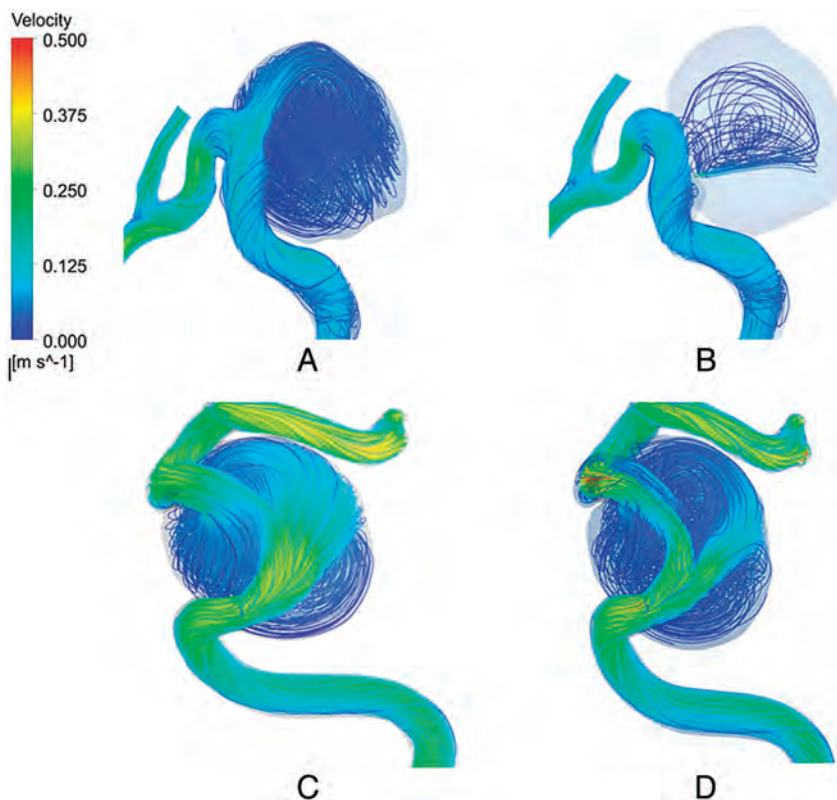


FIG 1. Flow pattern in patient 1, before FD deployment (A) and after FD deployment (B), and in patient 6, before FD (C) and after FD (D) deployment.

wall, the jet continued to impact the aneurysm surface (Fig 2B, -C) in comparison with pre-FD treatment (Fig 2A). This may be a contributory factor to the final rupture of the aneurysm. Following HOFD simulation, there was a marked decrease in inflow jet speed and redirection of jet flow toward the center of the FD (Fig 2D) and farther away from the peripheral aneurysm wall, a result similar to that exhibited by the successful case (Fig 1B).

For patient 6, the jet flow continued to resemble an unsuccessful flow pattern despite application of a HOFD (Fig 3A). Even after simulation of a double HOFD (Fig 3B), the jet flow continued to resemble an unsuccessful flow pattern, though its speed was diminished (Fig 3B). The position of the largest lobule was located directly in line with a narrow jet entering the aneurysm sac, the result of a malpositioned FD (Fig 3C). Again, even after simulation of a double HOFD at the 6-month follow-up, there is still a persistent unsuccessful jet flow pattern, though diminished (Fig 3D). A 3D reconstruction of the follow-up CTA at 6 months after deployment of the first FD revealed the presence of 2 lobules (Fig 3E). A curved CTA reconstruction (Fig 3F) demonstrated that the proximal end of the malpositioned FD was partially in the aneurysm sac and only partially in the parent artery, thereby not completely covering the inflow. At 6 months, corresponding DSA of the initial FD (Fig 3G) paralleled the CFD findings, demonstrating the largest lobule; despite deployment of a second FD within the first one (Fig 3H), the lobule persisted.

For the failed case (patient 7), the jet flow persisted with the initial FD. At the 3-month follow-up, despite the aneurysm being 90% occluded, the jet flow resembled an unsuccessful pattern.

However, with the application of a double HOFD at this stage, the jet flow changed to resemble a successful pattern.

The residual aneurysm in patient 5 was treated with a covered stent (non-flow diverter) deployed within the Silk FD after 6 months. Owing to this procedure, no further correlation with clinical or imaging studies could be conducted, though simulation of a double HOFD did not reduce jet flow.

Energy Loss and Volume Flow

Figure 4A, -B demonstrates the reduction of EL and VF for both successful cases and failed cases following initial FD treatment. Depending on the inflow condition, the SD values for EL were $\pm 1.2\%$ and $\pm 10.3\%$, while those for VF were $\pm 1.2\%$ and $\pm 3.5\%$, respectively, for successful and failed cases. However, the differences of average EL and VF between failed and successful cases were 16.44 times ($P < .001$) and 5.69 times ($P < .001$), respectively (Fig 4A, -B). The SD being significantly smaller than the difference in reduction between the 2 cohorts suggests that the inflow condition would have minimal influence on the EL and VF values in this study. Hence, the average values in the reduction of EL and VF of 2.6% and 8.5% for the successful cases, respectively, were considered favorable indices.

After simulation of a double HOFD (Fig 4C, -D), the average EL and VF of all failed cases were reduced to 6% (this reduces to 2.6% if patient 6 is omitted) and 10%, respectively.

For patient 6, the EL showed 100% after the initial FD, indicating that there was no reduction. The results also confirmed the flow pattern observations (Fig 3D) that double HOFD may not be sufficient to resist the jetting of blood flow into the aneurysm, thereby resulting in a higher EL (19%). At the 6-month follow-up, patient 6 had retreatment with double FDs, but the residue remained patent 1 month afterward.

For Patient 7, EL and VF were demonstrated to be 15.3% and 51%, respectively, following initial FD implantation. At 3 months, the aneurysm was reduced in size by over 90%, and simulation with a double HOFD demonstrated that the EL and VF were reduced to 0.68% and 12%, respectively.

For patients 6 and 8, following HOFD modifications to fully cover the aneurysm necks, EL was reduced to 49.5% and 6%, respectively. VF was reduced to 37% and 28%, respectively.

Wall Shear Stress

WSS was graphically mapped to the aneurysm model. The range between the highest and lowest values was very small, from 0 to 5 Pa. For successful patient treatments, the relatively high WSS regions that correlated with the jet flow before FD insertion disappeared after the deployment of FDs (patient 1, Fig 5A, -B). However, all 4 failed cases displayed high WSS before FD deployment,

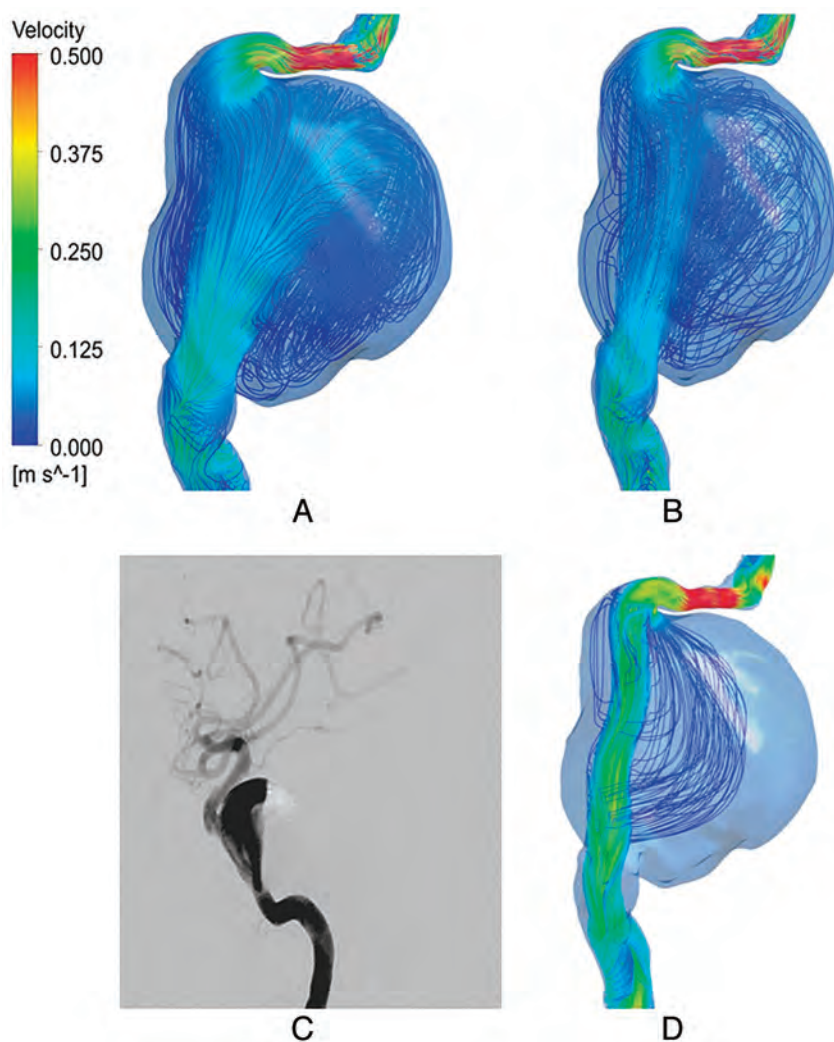


FIG 2. Flow pattern of patient 8 before (A) and after FD (B) deployment. Angiogram after FD placement (C) and after placement of an HOFD (D).

which persisted after treatment with the initial FD (eg, patient 6) (Fig 5C, -D).

DISCUSSION

The porous medium simulations are based on the works of Augsburger et al,¹¹ who concluded that this approach compared well with the real stent geometry model and allowed prediction of intra-aneurysmal flow. The effective pore size of a deployed FD would depend on the diameter and geometry of the artery, neck size of the aneurysm, and the FD size. Hence there will be variations among different aneurysms. However, in this study, we were testing the relative hemodynamic changes in the same artery/aneurysm before and after FD deployment and, in some cases, the addition of a second FD. In addition, the optimally deployed FDs should expand with a pore size to allow maximum redirection of flow from the aneurysm. Hence, we have not adjusted the porosity parameters of these FDs for the artery geometry.

Consistent with previous work in the Virtual Intracranial Stent Placement Challenge 2007,¹⁴ we showed similar therapeutic effects of the FD. Alteration of flow patterns appeared to be a remarkable differentiating feature between successful and failed

treatments. The favorable flow pattern was supplemented by a marked reduction in EL, VF, and WSS within the aneurysm sac in contrast to studies showing increased aneurysm rupture risk with high WSS and EL.^{13,15} This result suggests that jet flow speeds have a direct proportional effect on these parameters, consistent with our previous study.¹⁶

For patient 1, a successful case, there was blood flow stasis at the near-wall region in the inferior aspect (Fig 1B) with no jet flow entering this region after the initial FD deployment, indicating the occurrence of thrombosis. This case was in contrast to all the other failed cases, in which substantial jet flow into the aneurysm sac remained after the deployment of the initial FDs, via the inflow (patients 5 and 7), through the damaged portion of the FD stent (patient 8), or from the proximal gap of the malpositioned FD (patient 6). In addition, there was a variable degree of stasis at the near-wall region. In fact, in patient 6, we found that the location of the residual aneurysm corresponded with the direction at which the jet flow impacted (Fig 3C).

Our analysis also shed light on FD deployment strategies. For patient 8, as the first FD was stretched and angioplastied, the pore size of the FD could have been widened and distorted, in turn reducing the ability of the FD to divert blood to the desired direction of the parent artery and allowing more flow into the aneurysm.

Both our CFD results and a completion angiogram after the procedure indicated that a jet flow impinged on the anterior wall of the aneurysm at a point where later rupture occurred (Fig 2C). At the time of rupture, the angiogram showed the persisting jet flow, despite a considerable degree of thrombosis in the aneurysm. Kulcsár et al⁹ hypothesized that aggressive thrombosis is one factor in posttreatment rupture. Our study suggests that the interaction of unfavorable hemodynamics and thrombosis is a key part of this. The rupture was treated by vessel sacrifice. For patient 6, the first FD was malpositioned, leaving a gap between the proximal end of the FD and the aneurysm inflow. Our CFD results showed a jet flow entering the aneurysm sac through the gap, which resulted in the residual aneurysm. Even after HOFD and double HOFD, the jet flow persisted, though diminished (Fig 3); though the EL and VF were reduced, the reduction levels did not quite reach the favorable levels seen in successful treatments (Fig 4). Furthermore, the high WSS region persisted.

After the 6-month follow-up, the patient was retreated with the insertion of another FD into the first one (double FD). Despite this, the residual aneurysm lobule and jet flow persisted 1 month

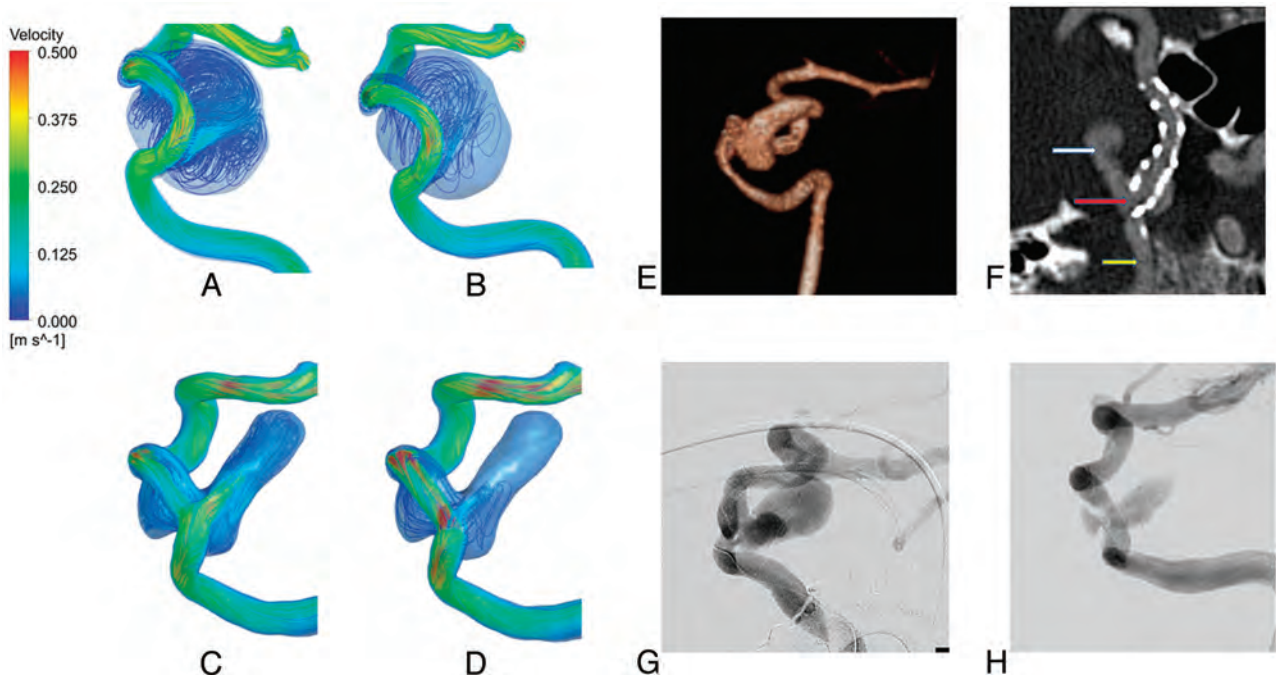


FIG 3. Flow pattern of patient 6 after placement of an HOFD (A) and double HOFD (B); a residual lobule (C); and deployment of a double HOFD at follow-up (D). 3D CTA at 6 months (E) shows the persisting lobules and malpositioned FD (F). The *white arrow* indicates the persisting lobule; *red arrow*, the proximal end of an FD partially in the neck of the aneurysm and in the parent artery; *yellow arrow*, the parent artery. DSA at 6 months with the initial FD (G) and after double FD deployment (H).

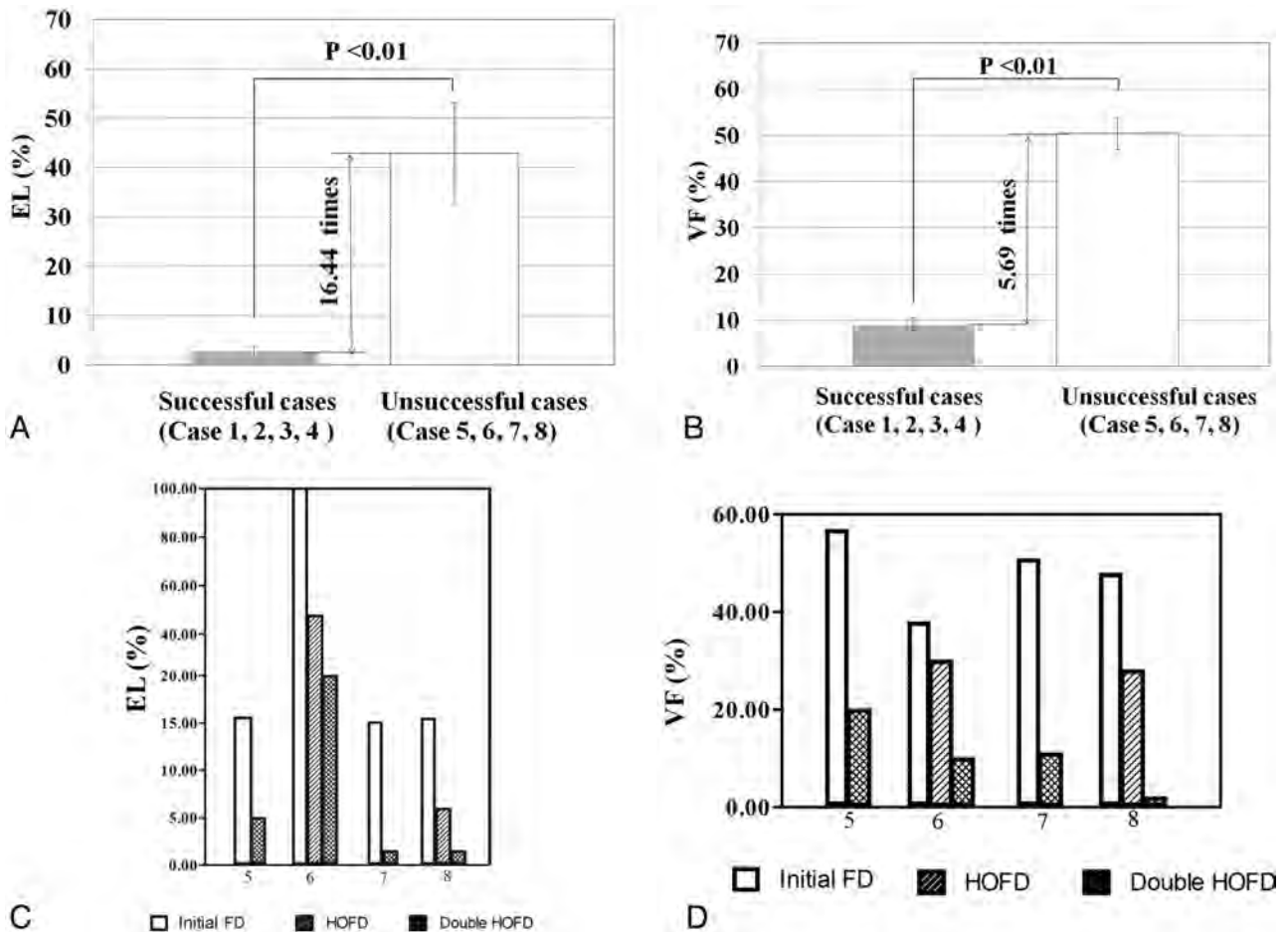


FIG 4. EL and VF results (A and B). HOFD and double EL and VF results (C and D).

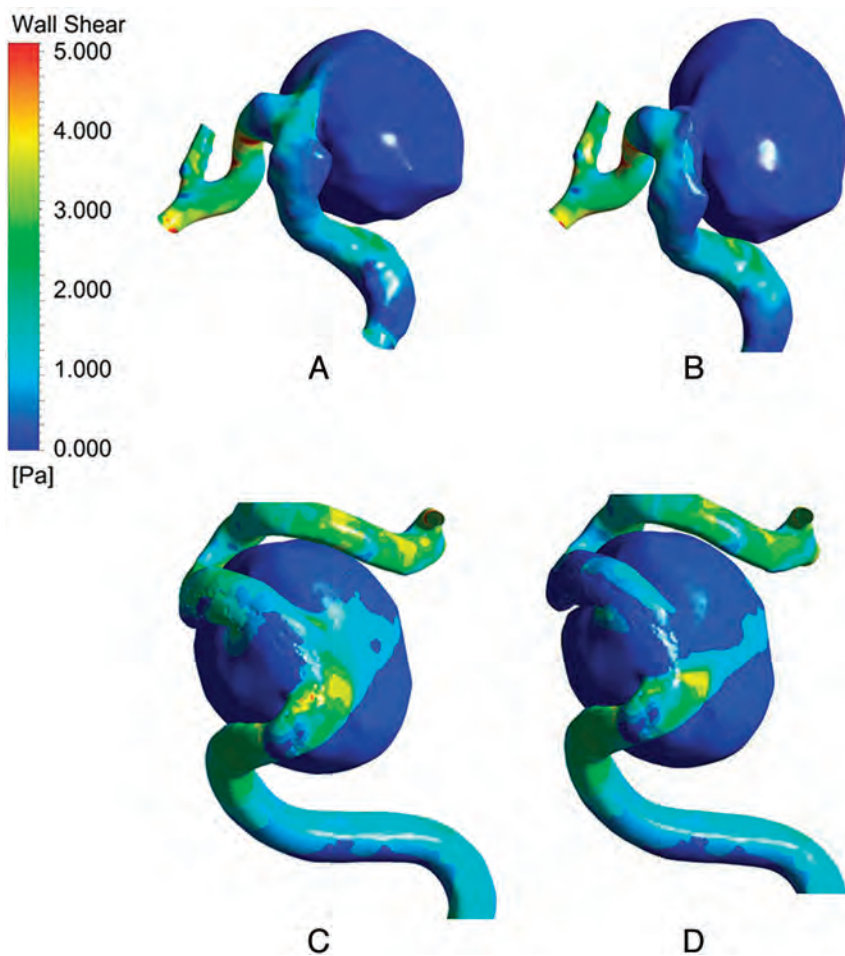


FIG 5. WSS. Patient 1 before FD deployment (A) and after initial FD deployment (B). Patient 6 before (C) and after (D) FD deployment.

later. Just as aneurysms on straight and curved vessels may be subjected to different hemodynamics,¹² the performance of an FD may vary with varying vessel curvature.¹⁶ This study suggests that the complex geometric relationship between the aneurysm neck and parent artery and the subsequent effects of this geometry on the hemodynamics after FD deployment cannot be analyzed by simple angle measurement. However, CFD can determine the resultant jet flow. It would appear in some geometry, even a double FD is not able to reverse the adverse hemodynamics (patient 6). This complex geometry may also help in understanding why the treatment was still unsuccessful in patient 5, despite the deployment of an initial intact FD in a position thought to be optimal.

For patient 7, at 3-month follow-up, areas of persistently high WSS occurred in the residual aneurysm, despite a 90% reduction in both size and inflow into the aneurysm. Simulation with a double HOFD during this time demonstrated that the inflow jet, WSS, and EL were reduced to successful levels with a VF of 12% (just above the average successful value of 8.5%). Patient 7 was treated with a double FD. This resulted in occlusion of the residual aneurysm, resolution of symptoms, and MR imaging changes. These findings suggested that hemodynamic factors continue to play a significant role in symptomatic aneurysms that are largely thrombosed, as asserted by Cebal et al.⁸

The results suggest that all parameters need to be favorable for

occlusion to occur because the jet flow is a major determinant of the other parameters.

Treatment Planning

Simulation of hypothetical situations could potentially be used for treatment planning before the procedure. If the unfavorable hemodynamic results following the initial FD in patient 8 were known, we may have re-treated with a double FD technique and potentially prevented rupture because double HOFD simulation resulted in favorable indices. As for case 6, unfavorable hemodynamic results, even with double FD, could indicate close imaging follow-up.

Limitations

The retrospective nature of this study and the small number of patients are limitations. We made assumptions in the initial estimations of porosities to simulate the maldeployed and damaged FDs and double HOFD. However, CFD flow patterns were very similar to the angiogram flow pattern (eg, patients 6 and 8), and we have validated the double HOFD porosity,¹⁶ suggesting that our assumptions are realistic. Future work, including in vitro experiments (eg, particle image velocimetry), should be performed to better simulate optimal, damaged, malpositioned and double FDs.

Other limitations include assuming that the blood vessel has a rigid arterial wall structure, models blood as a Newtonian fluid, and performs simulation under steady flow conditions. Confirming flow changes of the CFD by pre- and posttreatment angiograms may be desirable, provided the frame rate, tube angulations, and timing of injections are optimal to demonstrate the flow. If not, then it can be misleading. This work is a first approximation, and it indicates that there is good potential to better approximate the model to simulate the various parameters such as different FD geometries, sizes, and arterial geometries.

CONCLUSIONS

Patient-specific CFD, when used in conjunction with medical imaging, could help in understanding outcomes following FD deployment. Favorable hemodynamic outcomes for successful treatment of aneurysms with FDs are indicated by obliteration of the inflow jet and reduction of EL and VF and high WSS regions. Evidence collected posttreatment that points to the contrary could prompt a second intervention. We showed that a favorable treatment outcome may not have been achieved by merely placing the FD at the neck of the aneurysm sac. Instead, with FD deployment, one should consider the complex interaction among the hemodynamics, the shape of the aneurysm sac, and the geometry of the parent artery. If an optimal hemodynamic state cannot be achieved by an initial FD, a second FD within the first one (double

FD) may be beneficial. Further evaluation by refinement of CFD modeling correlated with clinical studies and in vitro experiments, including particle image velocimetry, is suggested to confirm these results.

Disclosures: Yi Qian—RELATED: Grant: The Discovery Project is supported by the Australian Research Council.* *Money paid to the institution.

REFERENCES

1. Akpek S, Arat A, Morsi H, et al. **Self-expandable stent-assisted coiling of wide-necked intracranial aneurysms: a single-center experience.** *AJNR Am J Neuroradiol* 2005;26:1223–31
2. Molyneux AJ, Cekirge S, Saatci I, et al. **Cerebral Aneurysm Multi-center European Onyx (CAMEO) trial: results of a prospective observational study in 20 European centers.** *AJNR Am J Neuroradiol* 2004;25:39–51
3. White PM, Lewis SC, Gholkar A, et al. **Hydrogel-coated coils versus bare platinum coils for the endovascular treatment of intracranial aneurysms (HELPS): a randomised controlled trial.** *Lancet* 2011;377:1655–62
4. Wiebers DO, Whisnant JP, Huston J, et al. **Unruptured intracranial aneurysms: natural history, clinical outcome, and risks of surgical and endovascular treatment.** *Lancet* 2003;362:103–10
5. Byrne JV, Beltechi R, Yarnold JA, et al. **Early experience in the treatment of intra-cranial aneurysms by endovascular flow diversion: a multicentre prospective study.** *PLoS One* 2010;5:pii
6. Lylyk P, Miranda C, Ceratto R, et al. **Curative endovascular reconstruction of cerebral aneurysms with the Pipeline embolization device: the Buenos Aires experience.** *Neurosurgery* 2009;64:632–42, discussion 642–43, quiz N636
7. Wong GK, Kwan MC, Ng RY, et al. **Flow diverters for treatment of intracranial aneurysms: current status and ongoing clinical trials.** *J Clin Neurosci* 2011;18:737–40
8. Cebal JR, Mut F, Raschi M, et al. **Aneurysm rupture following treatment with flow-diverting stents: computational hemodynamics analysis of treatment.** *AJNR Am J Neuroradiol* 2011;32:27–33
9. Kulcsár Z, Houdart E, Bonafe A, et al. **Intra-aneurysmal thrombosis as a possible cause of delayed aneurysm rupture after flow-diversion treatment.** *AJNR Am J Neuroradiol* 2011;32:20–25
10. Appanaboyina S, Mut F, Löhner R, et al. **Computational fluid dynamics of stented intracranial aneurysms using adaptive embedded unstructured grids.** *International Journal for Numerical Methods in Fluids* 2008;57:475–93
11. Augsburger L, Reymond P, Rufenacht DA, et al. **Intracranial stents being modeled as a porous medium: flow simulation in stented cerebral aneurysms.** *Ann Biomed Eng* 2011;39:850–63
12. Meng H, Wang Z, Kim M, et al. **Saccular aneurysms on straight and curved vessels are subject to different hemodynamics: implications of intravascular stenting.** *AJNR Am J Neuroradiol* 2006;27:1861–65
13. Qian Y, Takao H, Fukui K, et al. **Computational risk parameter analysis and geometric estimation for cerebral aneurysm growth and rupture.** *STROKE conference 2008, Stroke: A Journal of the American Heart Association* 2008;39:527–29
14. Radaelli AG, Augsburger L, Cebal JR, et al. **Reproducibility of haemodynamical simulations in a subject-specific stented aneurysm model: a report on the Virtual Intracranial Stenting Challenge 2007.** *J Biomech* 2008;41:2069–81
15. Shojima M, Oshima M, Takagi K, et al. **Magnitude and role of wall shear stress on cerebral aneurysm: computational fluid dynamic study of 20 middle cerebral artery aneurysms.** *Stroke* 2004;35:2500–05
16. Zhang Y, Chong W, Qian Y. **Investigation of intracranial aneurysm hemodynamics following flow diverter stent treatment.** *Med Eng Phys* 2013;35:608–15

Call for *AJNR* Editorial Fellowship Candidates

ASNR and *AJNR* are pleased once again in 2014 to join efforts with other imaging-related journals that have training programs on editorial aspects of publishing for trainees or junior staff (3–5 years after training) such as *Radiology* (Olmsted fellowship), *AJR* (Figley and Rogers fellowships [USA and international respectively]), and *Radiologia* (from Spain).

Goals:

1. Increase interest in “editorial” and publication-related activities in younger individuals.
2. Increase understanding and participation in the *AJNR* review process.
3. Incorporate into *AJNR*’s Editorial Board younger individuals who have previous experience in the review and publication process.
4. Fill a specific need in neuroradiology not offered by other similar fellowships.
5. Increase the relationship between “newer” generations of neuroradiologists and more established individuals.
6. Increase visibility of *AJNR* among younger neuroradiologists.

Activities of the Fellowship:

1. Serve as “Editorial Fellow” for one year. This individual will be listed on the masthead as such and will receive a certificate stating his/her activities at the end of the service period.
2. Review at least one manuscript per month for 12 months. Evaluate all review articles submitted to *AJNR*. Access to our electronic manuscript review system will be granted so that the candidate can learn how these systems work.
3. Be involved in the final decision of selected manuscripts together with the EIC.
4. Participate in all monthly telephone Senior Editor conference calls.
5. Participate in all meetings of the Editors and Publications Committee during the annual meetings of ASNR and RSNA as per candidate’s availability. *AJNR*/ASNR will not provide funding for this activity but may offer a discounted fee for its annual meeting.
6. Evaluate progress and adjust program to specific needs in biannual meeting or telephone conference with the EIC.
7. Write at least one editorial for *AJNR*.
8. Embark on an editorial scientific or bibliometric project that will lead to the submission of an article to *AJNR* or another appropriate journal as determined by *AJNR*’s EIC. This project can be done in conjunction with the EIC or one of the Senior Editors.
9. Serve as liaison between *AJNR* and ASNR’s Young Professionals Network and the 3 YPs appointed to *AJNR* as special consultants. Participate in meetings and telephone calls with this group. Design one electronic survey/year polling the group regarding readership attitudes and wishes.
10. Recruit trainees as reviewers as determined by the EIC.
11. Participate in Web improvement projects.
12. Potentially become a member of *AJNR*’s Editorial Board at the end of the fellowship.
13. Invite Guest Editors for *AJNR*’s News Digest to cover a variety of timely topics.

Qualifications:

1. Be a fellow in neuroradiology from North America, including Canada (this may be extended to include other countries).
2. Be a junior faculty neuroradiology member (<3 years) in either an academic and private environment.
3. Provide an “end” of fellowship report to *AJNR*’s EIC and ASNR’s Publications Committee.
4. Be an “in-training” or member of ASNR in any other category.

Application:

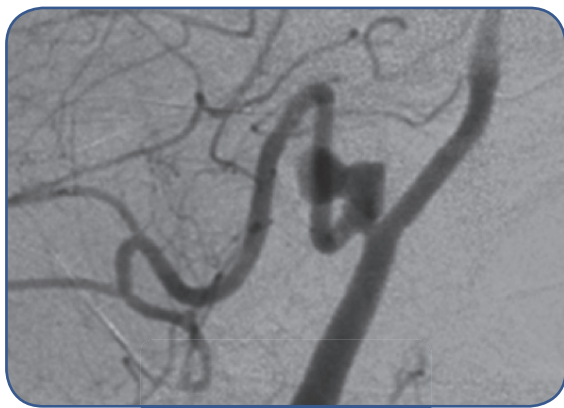
1. Include a short letter of intent with statement of goals and desired research project. CV must be included.
2. Include a letter of recommendation from the Division Chief or fellowship program director. A statement of protected time to perform the functions outlined is desirable.
3. Applications will be evaluated by *AJNR*’s Senior Editors and the Chair of the Publications Committee prior to the ASNR meeting. The name of the selected individual will be announced at the meeting.
4. Applications should be received by March 3, 2014 and sent to Ms. Karen Halm, *AJNR* Managing Editor, electronically at khalm@asnr.org.



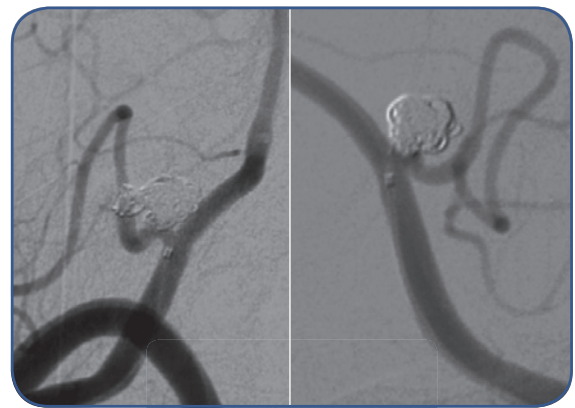
BARRICADE™ COIL SYSTEM

PERFORMANCE DELIVERED

VITOR MENDES PEREIRA, M.D. | HOSPITAL UNIVERSITY OF GENEVA (HUG) | GENEVA, SWITZERLAND

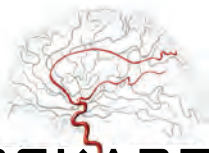


PRE-TREATMENT



POST-TREATMENT

- ◆ Female patient in her early 80's presented with an unruptured Left PICA aneurysm measuring 7mm with a 4mm neck
- ◆ The complex aneurysm had grown in size and developed a daughter sac since previous imaging
- ◆ Dense packing successfully achieved with 9 Barricade Coils
- ◆ MRA follow-up performed at 6 months showed stable treatment with no recanalization



BLOCKADE
M E D I C A L

18 TECHNOLOGY DRIVE #169, IRVINE CA 92618
P 949.788.1443 | 888.712.3502 | F 949.788.1444
WWW.BLOCKADEMEDICAL.COM



CE
0297
MKTG-030 REV. A

